1994-03

10th Annual Review of Progress in Applied Computational Electromagnetics at the Doubletree Hotel & Convention Center, Monterey,California, March 21-26, 1994,

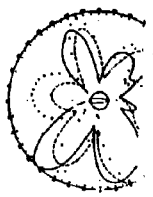

10th Annual Review of Progress in

Applied Computational Electromagnetics

at the
Doubletree Hotel & Convention Center
Monterey, California

March 21 - 26, 1994

CONFERENCE PROCEEDINGS

The 10th Anniversary ACES Conference

CONFERENCE PROCEEDINGS

VOLUME I

10th Annual Review of Progress in

APPLIED

COMPUTATIONAL

ELECTROMAGNETICS

at the

Doubletree Hotel and Convention Center

Monterey, California

March 21-26, 1994

CONFERENCE PROGRAM COMMITTEE CHAIRMAN

Andy Terzuoli

Library of Congress Catalog Card Number: 94-70636

Sponsored by

The Applied Computational Electromagnetics Society
and DOD and DOE in cooperation with IEEE, URSI, ASEE, SIAM and AMTA

VOLUME II

THE APPLIED COMPUTATIONAL ELECTROMAGNETICS SOCIETY

1995 CALL FOR PAPERS 1995

The 11th Annual Review of Progress in Applied Computational Electromagnetics

March 21-26 1995

Naval Postgraduate School, Monterey, CA

Share your knowledge and expertise with your colleagues

The Annual ACES Symposium is an ideal opportunity to participate in a large gathering of EM analysis enthusiasts. The purpose of the Symposium is to bring analysts together to share information and experience about the practical application of EM analysis using computational methods. The Symposium features four areas of interest: technical publication, demonstrations, vendor booths and short courses. All aspects of electromagnetic computational analysis are represented. The Symposium will also include invited speakers and interactive forums. Contact Ray Luebbers (814) 865-2362 for details.

1995 ACES Symposium Chairman
Ray Luebbers
Penn State University
320 EE East
University Park, PA 16802
Phone (814) 865-2352
Fax: (814) 865-7065
Email: LU4@psuvm.psu.edu

1995 ACES Symposium Administrator
Richard W. Adler
ECE Dept/Code ECAB
Naval Postgrad School
833 Dyer Rd, Room 437
Monterey, CA 93943-5121
Phone (408-646-1111)
Fax (408) 649-0300
Email: 5541304@mcimail.com

1995 ACES Symposium Co-Chairman
Richard K. Gordon
EE Dept. Univ of Mississippi
Anderson Hall, Box 41
University, MS 38677
Phone (601) 232-5388
Fax: (601) 232-7231
Email: ergordon@vm.cc.olemiss.edu

1995 ACES Symposium
Sponsored by: ACES, USAIESA, NCCOSC, NPS, DOE/LLNL, DOD/USA CECOM
In cooperation with: The IEEE Antennas and Propagation Society, the IEEE ElectromagneticCompatibility Society and USNC/URSI

1994 Conference Program Committee
for the
10th Annual Review of Progress in Applied Computational Electromagnetics
at the
Doubletree Hotel and Convention Center
Monterey, California

Conference Chairman:
Andy Terzuoli
Air Force Institute of Technology
School of Engineering
P.O. Box 3402
Dayton, OH 45401
Tel (513) 255-3636 X4717/Fax: 476-4055

Co-Chairman:
Jeff Fath and Dennis Andersh
Wright Laboratory/AARA
2010 Fifth St., Bldg 23
Wright Patterson AFB, OH 45433
Tel (916) 643-6935/Fax: 1053

Conference Advisor:
Dick Adler
ECE Dept. Code ECAB
Naval Postgraduate School
833 Dyer Rd., Room 437
Monterey, CA 93943
Tel (408) 646-1111/Fax: 649-0300

Conference/Vendor Facilitator: Jodi Nix
Veda Incorporated
5200 Springfield Pike,
Suite 200
Dayton, OH 45431
Tel (513) 476-3550/Fax: 3577

Short Course Chair:
Robert Lee
The Ohio State University
ElectroScience Laboratory
1320 Kinnear Rd.
Columbus, OH 43210-1272

Short Course Co-Chair: Jin-Fa Lee
Worcester Polytechnic Inst.
100 Institute Rd., EE Dept.
Worcester, MA 01609

1995 Conference Chairman:
Ray Luebbers
Penn-State University
320 Electrical Engineering East
University Park, PA 16802
Tel (814) 865-2362

Conference Secretary: Pat Adler

Advisory Committee:
Dick Adler, Naval Postgraduate School
Dennis Andersh, Major USAF, Wright Laboratory
Jeff Fath, Captain USAF, SM-ALC/QL
Pat Foster, Microwave and Antenna Systems
Richard K. Gordon, Univ. of Mississippi
Jim Logan, NRAD
Ray Luebbers, Penn State Univ.
Andy Peterson, Georgia Institute of Technology
John Rockway, NRAD
Andy Terzuoli, AF Institute of Technology
Frank Walker, Boeing Defense and Space Group
Perry Wheless, Univ. of Alabama

A•C•E•S 1994

10th Anniversary

Monterey, California
March 21-26, 1994

Conference Chairman:
Andy Terzuoli
Air Force Institute of Technology
School of Engineering
P.O. Box 3402 • Dayton, Ohio 45401
Tel: 513/255-3636ext4717 • Fax: 513/476-4055

Conference Co-Chairmen:
Jeff Fath and Dennis Andersh
Wright Laboratory/AARA
2010 Fifth St., Bldg 23
Wright-Patterson AFB, Ohio 45433-7001
Tel 513/255-1115 • Fax: 513/476-4414

Short Course Co-Chairman:
Rob Lee
The Ohio State University
ElectroScience Laboratory
1320 Kinnear Rd. • Columbus, Ohio 43212
Tel: 614/292-7981 • Fax: 614/292-7297

Conference Advisor:
Dick Adler
Naval Postgraduate School
ECE Dept. Code ECAB
833 Dyer Rd., Room 437
Monterey, California 93943-5121
Tel: 408/656-2382 • Fax: 408/656-2955
E-Mail: 5641304@mcimail.com

Conference Facilitator:
Jodi Nix
Veda Incorporated
5200 Springfield Pike, Suite 200
Dayton, Ohio 45431
Tel: 513/476-3850 • Fax: 513/476-3577
E-Mail: jodi@image.mtmdb.wpafb.af.mil

1995 Conference Chairman:
Ray Luebbers
The Pennsylvania State University
Electrical Engineering Dept.
University Park, Pennsylvania 16802
Tel: 814/865-2362 • Fax: 814/865-7065
E-Mail: lue@psuvm.psu.edu

APPLIED COMPUTATIONAL ELECTROMAGNETICS SOCIETY

The Tenth Annual Review of Progress in Applied Computational Electromagnetics

From The Conference Chairman To All Attendees:

On behalf of the conference committee, welcome and thank you for coming to ACES '94. Also welcome (back) to Monterey, to California, and to the Naval Postgraduate School from which we have our roots. If you are from abroad, of course, welcome (back) to the USA. If this is your first time here, an extra welcome, and an invitation to ask any of us to give you our version of where to go and what to do, or how you can become involved--we do need you!

As I write this letter, the January '94 earthquake in the Los Angeles area, and its after shocks, are still very much in the news; as we plan this enjoyable week for us all, I cannot help but think of those affected, possibly some of you. I find it remarkable that despite the numerous calamities affecting ACES' beautiful host state of California, an atmosphere of energetic hope always prevails.

For this 10th Anniversary meeting, we have tried to make it special and memorable, and to give a distinct *thank you* to Dick and Pat Adler for their years of selfless service. We tried to centralize everything around the Doubletree/Convention Center so as to give Dick and Pat *somewhat* of a break this year. We have coordinated noteworthy social events, vendor exhibits, and short courses. We deliberately tried to expand the short courses and sessions so that those of you at home with ACES can reach out to other related areas like Wavelets, Time Frequency Analysis, and Measurement Validation. We also felt that with research money being tight, if ACES was the *one* conference you went to this year, you would be able to partially diversify while here.

By way of acknowledgments and thanks, once again Dick and Pat Adler, and Pat's team of dedicated ladies who work so hard behind the scenes, not only here during the conference, but all year. Jodi Nix, who I'm sure you all talked to at least once this past year, has been the hands and feet of ACES '94 for over a year. She attended ACES '93, visited the Doubletree, gave ACES publicity at numerous other conferences this past year, and contacted countless perspective participants in various capacities. She and her team at Veda designed our letterhead, poster, flyers, etc., coordinated all the mailings, and even kept me on schedule; please thank her *every* time you see her!

Thanks to Jeff Fath, Dennis Andersh, and the Air Force Wright Laboratories for support, advice, publicity, and help with every facet of this conference; to Rob Lee and Jin Fa Lee who, as you can see, did a super job in pulling together all the short course ideas into a working reality. Ray Luebbers, the ACES '95 (despite what it says in the January announcement) Conference Chairman, did a great job in helping us out this year providing overall help and paper review.

Last but not least to my friend God I simply say *thank you, sir, and please don't let the earth shake while we are here.*

Best Wishes,
Andy Terzuoli, Chairman,
1994 ACES Conference.

Dayton, Ohio
February, 1994

ACES PRESIDENT'S STATEMENT

It's nice to be here in California in March, especially considering the frigid weather we experienced in the Midwest this past winter.

It's especially nice, however, to be here for the tenth annual conference of ACES. It's hard to believe that nine years have gone by since Ed Miller and his colleagues at LLNL convened a meeting to determine if there was a need to form a society to cater to the needs of the computational electromagnetics community. The answer was a resounding 'yes' then, and so it remains today.

ACES is unique in its attitude to the profession. It has senior-level researchers, certainly, who publish significant papers, and yet much of the email I get comes from amateur radio operators who want to use NEC in their non-professional pursuits, and naturally look to ACES to give them support in their endeavors. Perhaps that's more of a credit to NEC, but ACES started as a virtual NEC user's group, so it's nice to see that we haven't lost our roots.

Andy Terzuoli and Jodi Nix have done a great job in organizing the conference. We owe them a great debt. And how about Dick and Pat Adler? You thought they were just a couple of names who wanted your money. Now that you've had a chance to meet them, and their support staff, you can do the right thing and thank them, too.

Let me tell you how to get the most out of this conference: meet colleagues, see the acquarium, go to the banquet, have a good time. The papers will be so much better if you're in a good mood. That's what we want for you.

Harold A. Sabbagh
ACES President

ACES 1994 SHORT COURSES

MONDAY MARCH 21 — FULL DAY COURSE

"WAVELET ELECTRODYNAMICS"
by Gerald Kaiser, Dept. of Mathematical Sciences, UMass-Lowell

MONDAY MARCH 21 — FULL DAY COURSE

"TIME-FREQUENCY ANALYSIS"
by Leon Cohen, Hunter College and Graduate Center of CUNY

MONDAY MARCH 21 — FULL DAY COURSE

"GEMACS FROM A-Z"
by Buddy Coffey, Advanced EM

MONDAY MARCH 21 — HALF DAY COURSE

"FDTD FOR ANTENNAS AND SCATTERING"
by Ray Luebbers, Penn State University

MONDAY MARCH 21 — HALF DAY COURSE

"MEASUREMENT VALIDATION FOR COMPUTATIONAL ELECTROMAGNETICS"
by Al Dominek, Ohio State University

MONDAY MARCH 21 — HALF DAY COURSE

"USING MODEL-BASED PARAMETER ESTIMATION TO INCREASE EFFICIENCY AND EFFECTIVENESS OF COMPUTATIONAL ELECTROMAGNETICS"
by Ed Miller, Los Alamos National Lab

SATURDAY MARCH 26 — FULL DAY COURSE

"FINITE ELEMENT METHODS FOR ELECTROMAGNETICS"
by Jin-Fa Lee, Worcester Polytechnic Institute; Robert Lee, Ohio State University; Tom Cwik, Jet Propulsion Laboratory; and John Brauer, MacNeal-Schwendler Corporation

SATURDAY MARCH 26 — FULL DAY COURSE

"WIRE ANTENNA MODELING USING NEC"
by Richard Adler, Naval Postgraduate School; James Breakall, Penn State University; and Gerald Burke, Lawrence Livermore National Lab

SATURDAY MARCH 26 — HALF DAY COURSE

"VOLUME-INTEGRAL EQUATIONS IN EDDY-CURRENT NONDESTRUCTIVE EVALUATION"
by Hal Sabbagh, Sabbagh Associates

SATURDAY MARCH 26 — HALF DAY COURSE

"ELECTROMAGNETIC CHARACTERIZATION OF ELECTRONIC PACKAGES"
by Andreas Cangellaris, University of Arizona

SESSION 1:

RECENT IMPACTS OF MATHEMATICS ON COMPUTATIONAL ELECTROMAGNETICS

Chair: Arje Nachman

Review of FD-TD Based Algorithms for Electromagnetic Wave Propagation in Dispersive Dielectric Material

J.G. Blaschak
USAF Armstrong Laboratory
Brooks AFB, TX 78235

Abstract

The radio frequency dosimetry community is actively engaged in the assessment of the biological effects of short pulse, wide bandwidth electromagnetic sources. A key component of this effort is the development of robust and accurate numerical simulations for use in microwave pulse dosimetry prediction. Simulation algorithms based on the finite-difference time-domain (FD-TD) approximation to Maxwell's equations have the potential for significant contribution in this area and are therefore of interest to bioelectromagnetics researchers at the Armstrong Laboratory.

This study will present analysis and computational experiments designed to resolve practical, performance questions regarding the use of FD-TD based methods to model propagation in dispersive dielectrics. Some questions to be considered are:

- What effect does the accumulation of phase error, inherent to the algorithm, have on the quality of the solution?
- For a sensible level of discretization, through what distance can the algorithm be expected to accurately propagate waves?
- Using published guidelines for appropriate selection of time and space increments, what computer resources are required to produce an expected level of accuracy?

Computed results using the FD-TD algorithm will be presented using implementations of two popular formulations for dispersive dielectrics. These approaches couple the constitutive relations for the D and E fields in the material to the standard FD-TD difference scheme as either a discrete approximation to a convolution integral, or as a discrete approximation to an ordinary differential equation. The FD-TD solutions will be compared to reference solutions obtained using an exact, Fourier spectral approach designed to compute the penetrating fields in a simple, dispersive slab geometry.

Modeling Propagation and Scattering in Dispersive Dielectrics with FD-TD*

Peter G. Petropoulos,
Armstrong Laboratory, AL/OES,
Brooks AFB, Texas 78235-5102.

1. Introduction

The application of ultra-short pulsed fields in the areas of radar, hyperthermia, and biological/environmental imaging is imminent. For that reason there is a need for a thorough understanding of the short-pulse response of media whose dielectric properties are described by frequency dependent models fitted to permittivity data available for biological tissue, soils, humid atmospheres, and radar absorbing materials. In addition, the planned extension of the IEEE C95.1-1991 RF exposure standard to pulsed fields will also require qualitative and quantitative understanding of this sort to be developed. The alternative to actual measurement of the response is numerical simulation. The fact that the above mentioned problems are dispersive requires of the candidate numerical method to accurately propagate each frequency component present in the computation. This implies that the method must be non-dissipative so that it correctly models any energy loss due to physical mechanisms, and it must introduce as little artificial dispersion as possible so that the real dispersion is simulated correctly. Such nice properties are desirable for numerically capturing the Brillouin (a low-frequency aspect of the response) and Sommerfeld (a high-frequency aspect of the response) precursor phenomena in dispersive media. Lacking such a method one would like to characterise the spurious numerical attributes of existing approaches in order to control them or even alleviate them, and to develop some ability to prescribe an acceptable error level and be certain that indeed the simulation will accumulate that error and no more. In the standard FD-TD method [1] the truncation error can be neglected since it is $O(\Delta t^2 + \Delta^2)$, where Δ is the typical spatial cell size and Δt is the timestep. Assuming proper treatment of the electromagnetic boundary conditions and of the absorbing boundary condition used to truncate the computational domain one is left with the major source of error, i.e., the phase error introduced by the finite difference scheme. This error *grows* linearly with time. As a result, a given discretisation will not be suitable for an arbitrary amount of computation time, and the so called "rules of thumb" concerning the points per wavelength, N_{ppw}, have no meaning. The issue of how to choose N_{ppw} is central in FD-TD calculations in the absence of canonical solutions. In my talk I present some guidelines on how to choose the points per wavelength for FD-TD in relaxing (Debye) and lossless dielectrics.

There exist a variety of useful extensions of the popular FD-TD scheme to the modeling of pulse propagation in temporally dispersive media with complex geometry. Here I will only be concerned with a method [2] for Debye dispersive materials since most materials in the microwave are of such type. Other extensions [3] use a convolution representation of the constitutive relation and work is under way to characterize them too. I will also determine the N_{ppw} required to control the phase error of the standard FD-TD in lossless dielectrics when a small Courant number, ν, is used. The case $\nu \ll 1$ is relevant to the discussion of FD-TD for dispersive media because then the timestep is very small (as we will see the scheme in [2] requires that for accuracy the smallest

*This work was supported by contract F41624-92-D-4001 with USAF Armstrong Laboratory.

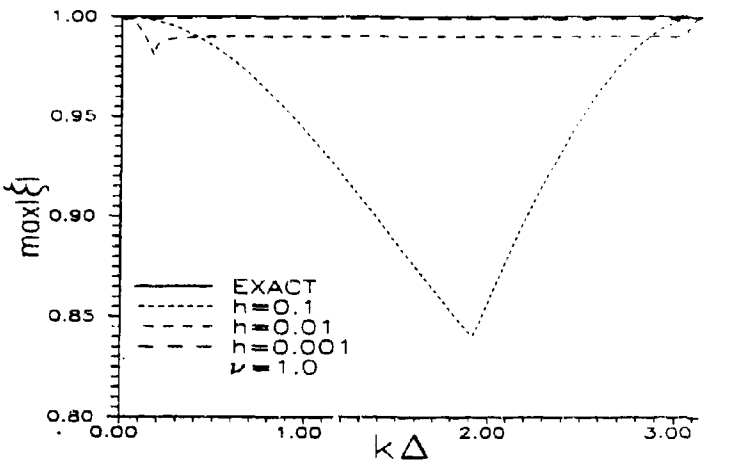

Figure 1: The maximum stability eigenvalue of the Debye medium difference schemes versus $k\Delta(= 2\pi/N_{ppw})$ for $\nu = c_\infty \Delta t/\Delta = 1$.

timescale in the problem is finely resolved) consequently, the ordinary differential equations (ODE) which are appended to the Maxwell's equations to model the dispersion are solved exactly thus leaving only the space-time discretization of the partial differential equation (PDE) part of the problem (the curl equations) to introduce the phase error. Only one dimensional problems will be considered but because temporal dispersion is not coupled to space the ideas presented here can be heuristically extended to two and three dimensions.

2. The Stability Analysis of a Debye Scheme

Details of the analysis of schemes for Debye and Lorents dispersive media can be found in [4]. Some of the text herein also appears there but the explanations are new. For demonstration I will give the essence of the approach used to determine the stability properties of the discretized coupled PDE-ODE system since from this analysis one determines how the discretization affects the *amplitude* of each frequency component in the problem on a per timestep basis.

From [2] the difference equations for the update of the magnetic, displacement, and electric field are:

$$H_{j+\frac{1}{2}}^{n+\frac{1}{2}} = H_{j+\frac{1}{2}}^{n-\frac{1}{2}} + \frac{\Delta t}{\mu_o \Delta}(E_{j+1}^n - E_j^n)$$
$$D_j^{n+1} = D_j^n + \frac{\Delta t}{\Delta}(H_{j+\frac{1}{2}}^{n+\frac{1}{2}} - H_{j-\frac{1}{2}}^{n+\frac{1}{2}}) \qquad (2.1)$$

$$E_j^{n+1} = \frac{\Delta t + 2\tau}{\alpha} D_j^{n+1} + \frac{\Delta t - 2\tau}{\alpha} D_j^n + \frac{2\tau\epsilon_\infty - \epsilon_s \Delta t}{\alpha} E_j^n,$$

where n is the discrete time index, j is the discrete spatial index, $\alpha = 2\tau\epsilon_\infty + \epsilon_s\Delta t$, τ is the medium relaxation time, ϵ_∞ is the infinite frequency relative permittivity, ϵ_s is the d.c. relative permittivity, and μ_o is the permeability of vacuum. An eigensolution solution of (2.1) is

$$\begin{Bmatrix} H_j^n \\ D_j^n \\ E_j^n \end{Bmatrix} = \begin{Bmatrix} \tilde{h} \\ \tilde{d} \\ \tilde{e} \end{Bmatrix} \xi^n e^{ikj\Delta}. \tag{2.2}$$

In (2.2) the complex valued vector $\tilde{x} = (\tilde{h}, \tilde{d}, \tilde{e})^T$ is the spatial eigenvector of the difference system which is related to initial conditions, and k is the wavenumber of the harmonic wave component whose stability and decay is determined by $|\xi|$ which is the complex time-eigenvalue we wish to find and whose magnitude will determine the stability and dissipation properties of the k-th frequency in the difference equations. Substituting (2.2) in (2.1) and after plenty of algebra we arrive to a polynomial equation for ξ. The polynomial, whose solutions give ξ as a function of the medium parameters, the timestep, and the quantity $k\Delta$ $(= 2\pi/N_{ppw})$, is as follows

$$\xi^3 + \frac{p^2(h+2) - 6\epsilon_\infty - h\epsilon_s}{2\epsilon_\infty + h\epsilon_s}\xi^2 + \frac{p^2(h-2) + 6\epsilon_\infty - h\epsilon_s}{2\epsilon_\infty + h\epsilon_s}\xi - \frac{2\epsilon_\infty - h\epsilon_s}{2\epsilon_\infty + h\epsilon_s} = 0, \tag{2.3}$$

where $p = 2\nu \sin\frac{k\Delta}{2}$, $h = \Delta t/\tau$, $\nu = \frac{c_\infty \Delta t}{\Delta}$ is the Courant number, and all permittivities are relative to ϵ_o. The speed c_∞ is the maximum wavespeed in the problem and is given by $c_\infty = c/\sqrt{\epsilon_\infty}$. The speed of light in free-space is c. The product $k\Delta$ may be thought of as wavenumber if Δ is fixed, or as inverse of points per wavelength if k is viewed as fixed. It must be emphasized that h and ν determine the amplitude (and phase error) introduced by the discretization. Taking $\tau = 8.1 \times 10^{-12}$sec, $\epsilon_s = 78.2$, and $\epsilon_\infty = 1$, we calculate numerically with IMSL routines the 3 roots of (2.3) for a variety of h and ν and examine the root of largest magnitude as a function of $k\Delta$ in the range $0 \le k\Delta \le \pi$. Figure 1 shows the result for $\nu = 1$ and three levels of time resolution, i.e., 10, 100, and 1000 timesteps per relaxation time. Numerical studies of the roots show the difference equations to be stable since it was always that $max|\xi| \le 1$ for any $k\Delta$ in the range considered as long as $\nu \le 1$ and h arbitrary. In such a graph the amount of artificial dissipation introduced by the differenced ODEs is evident since it is known that the FD-TD differenced PDEs should always have $max|\xi| = 1$ for all $k\Delta$ when $\nu \le 1$. To determine the amplitude of the k-th mode after N timesteps one merely computes the number $A \times (max|\xi(k\Delta)|)^N$ where A is the initial mode amplitude. It turned out that $max|\xi| > 1$ (instability) whenever $\nu > 1$ regardless of the medium parameters. Thus, the well-known stability restriction of the standard FD-TD scheme is preserved by this extension to Debye media. Looking at other medium parameters and media which exhibit multiple relaxation times I deduced that the amplitude error is negligible whenever $\Delta t \le O(10^{-3})\tau^{min}$ and ν is at the maximum value for stability (=1). When the timestep is thus chosen the amplitude error resembles that in the case of non-dispersive FD-TD which is labeled as EXACT on Figure 1. τ^{min} is the smallest relaxation time if the medium exhibits more than one relaxation mechanism. If ν is reduced from its maximum possible value (in 2/3 dimensions this is always the case) the timestep restriction is more severe. Note that the incident pulse duration does not enter in the analysis. Thus the minimum relaxation time must still be finely resolved by the timestep in this and other similar approaches even if the pulse duration is comparable to the longer relaxations. Thus, when the problem is stiff (it is typically) the computational resources needed to tackle realistic problems may be enormous. It would be helpful to be able to increase Δ in a controlled fashion in order to reduce the computer storage which grows geometrically when the spatial cell size is reduced. Of course one will then have to execute more timesteps to compute

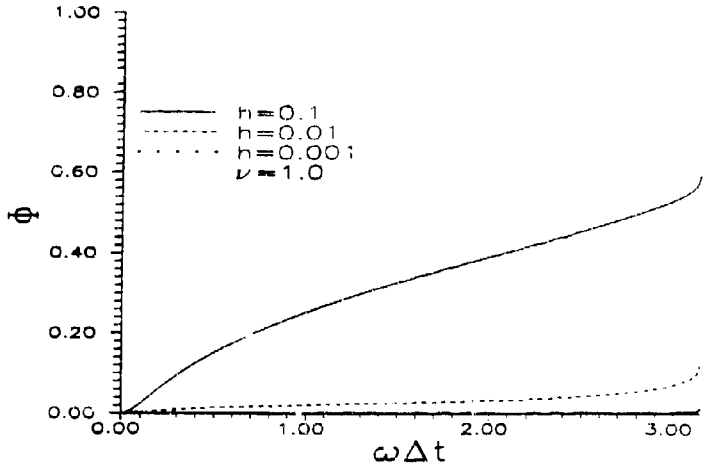

Figure 2: Phase error as a function of $h = \Delta t/\tau$ for existing Debye medium difference schemes versus $\omega\Delta t$ for Courant number $\nu = 1.0$.

in a given physical time interval but the computation time increases only linearly as Δt is reduced. Section 3 will show how to control the artificial dispersion (hence the phase error) for FD-TD in dispersive media, and Section 4 will show how to choose the spatial cell size in cases where the required timestep is very small, i.e. when one effectively reduces the Courant number, so that a prescribed amount of phase error is accumulated by the end of a prescribed computation time interval.

3. The Phase Error Analysis of a Debye Scheme

Now we will determine how the discretisation affects the *phase* of each frequency component on a per timestep basis for the scheme in the previous section. Details and some of the following text can be found in [4] but, again, the interpretations are new. The following definition of phase error is employed:

$$\Phi(\omega\Delta t) = \frac{|k_{cs}(\omega) - k_{num}(\omega\Delta t)|}{|k_{cs}(\omega)|}, \tag{3.1}$$

where $k_{num}(\omega\Delta t)$ is the numerical dispersion relation and $k_{cs}(\omega)$ is the dispersion relation of the Debye medium given by

$$k_{cs}(\omega) = \frac{\omega}{c}\sqrt{\frac{\frac{\epsilon_s}{\tau} - i\omega}{\frac{1}{\tau} - i\omega}}. \tag{3.2}$$

I have set $\epsilon_\infty = \epsilon_0$ so the expressions simplify. The ω range considered is such that $0 \leq \omega\Delta t \leq \pi$

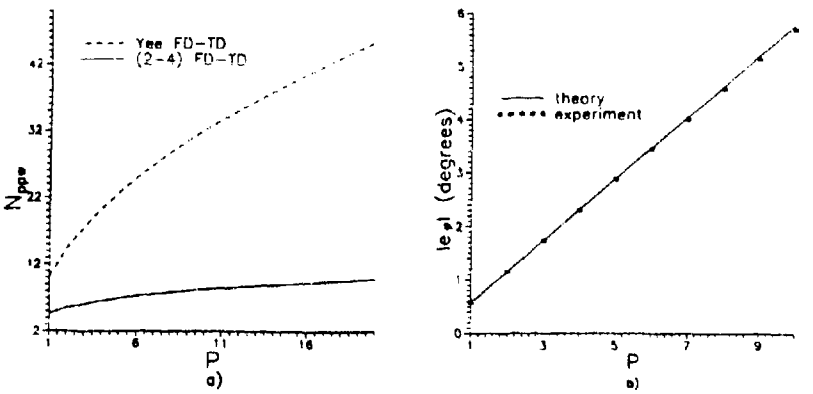

Figure 3: a) The dependence of N_{ppw} on P for an allowed phase error of 0.1 radians. For comparison the N_{ppw} required by a fourth-order FD-TD at the same error level is also graphed. b) Computed phase error (stars) growth versus the number of computation time for the Yee scheme.

given Δt. To determine the numerical dispersion relation

$$\begin{Bmatrix} H_j^n \\ D_j^n \\ E_j^n \end{Bmatrix} = \begin{Bmatrix} \tilde{h} \\ \tilde{d} \\ \tilde{e} \end{Bmatrix} e^{i(kj\Delta - \omega n\Delta t)} \tag{3.3}$$

is substituted in the difference equations (2.1). Extensive algebra gives the dependence of k_{num} on the frequency ω and on the various medium and discretisation parameters as follows

$$k_{num} = \frac{2}{\Delta} \sin^{-1}\left[\frac{\omega}{c}\frac{\Delta}{2}\frac{\sin \omega\Delta t/2}{\omega\Delta t/2}\sqrt{\frac{\frac{1}{\tau}\cos\frac{\omega\Delta t}{2} - i\omega\frac{\sin\omega\Delta t/2}{\omega\Delta t/2}}{\frac{1}{\tau}\cos\frac{\omega\Delta t}{2} - i\omega\frac{\sin\omega\Delta t/2}{\omega\Delta t/2}}}\right]. \tag{3.4}$$

By inspecting (3.4) and comparing it to (3.2) a feature emerges that is solely due to the discretization of the ODE involved. The relaxation time τ of the medium is now $\tau_{num} = \tau/\cos(\omega\Delta t/2)$, i.e., the medium actually modeled by the numerics is one with *higher* relaxation time constant. This is the source of the artificial dissipation exhibited by the maximum root of (2.3). Such artificial dissipation can be controlled by choosing Δt so that $\cos\omega\Delta t/2 \sim 1$ across the range of frequencies present in the short-pulse that propagates in the medium. In Figure 2 we show the dependence of the phase error (3.1) on the number $h = \Delta t/\tau$ as a function of $\omega\Delta t$ when $\nu = 1$, the maximum ν for stability in 1D. Again we see that the timestep guideline given in the previous

section is optimal also for the phase error since if $\Delta t \leq O(10^{-3})\Delta^{min}$ and $\nu = 1$ the phase error is that of the non-dispersive FD-TD in a 1D dielectric used with $\nu = 1$, i.e., the phase error is zero. Experimentation with various medium parameters, with media exhibiting more relaxation times and with $\nu < 1$ points to the optimality of this guideline. If ν is reduced (typical in 2/3 dimensions) the timestep estimate is more severe and the error properties of the scheme can only be determined by looking at graphs like Figures 1 and 2. In the next section a useful estimate is shown for N_{ppw}. It holds whatever the medium in cases where one needs an extremely small timestep. Finally, it is to be emphasized that if the given medium exhibits a range of relaxation times then Δt has to resolve the smallest one in the way derived here even if the incident pulse duration is comparable to the longer relaxation times. This situation occurs in simulations with realistic pulses and medium models.

4. Control of Phase Error in FD-TD for Small Timestep

For the Yee scheme in a one dimensional lossless dielectric I have determined that if one prescribes the phase error, e_ϕ, then the points per wavelength ($N_{ppw} = \lambda^{min}/\Delta$) required to discretise the spatial domain is related to P, the "electrical time," by

$$N_{ppw} \sim (\frac{1}{3})^{\frac{1}{3}} \pi^{\frac{2}{3}} (\frac{P}{e_\phi})^{\frac{2}{3}}, \tag{4.1}$$

where $P = t_c\omega^*/2\pi$, t_c is the physical computation time, ω^* is the highest frequency in the computation for which we will accept the prescribed phase error, and e_ϕ is in radians. (4.1) was derived for the Courant number $\nu \ll 1$ and this was done because my problems *required* a very small timestep and consequently a very small spatial step if I had to take $\nu = c\Delta t/\Delta = 1$. The estimate is also valid for any ν as long as $\pi/N_{ppw} \ll 1$. It would be helpful to be able to determine how to choose Δ in the case $\nu \ll 1$ since this effectively means that, for fixed ν, Δ has been *increased*. In [5] I derive the corresponding relation like (4.1) for the two dimensional FD-TD where I also verify it with simulations of propagation in a waveguide. Figure 3a) shows how N_{ppw} is related to P for a phase error of 0.1 radians, roughly 5.7°. From (4.1) the cell size is $O(\sqrt{e_\phi/t_c\omega^*})$. If we are calculating pulse propagation ω^* would be the highest frequency present thus, for fixed e_ϕ, the spatial cell size goes like $1/\sqrt{t_c}$. If we are using FD-TD to march to a steady-state in order to obtain frequency-domain information then t_c does not have any meaning apart from it being the time interval needed to reach steady-state since essentially we are solving an elliptic problem so, for fixed e_ϕ, we see that Δ goes like $1/\sqrt{\omega^*}$, where ω^* is the frequency of the time-harmonic wave forcing the problem. In this case the time t_c has been lumped in the O symbol. On Figure 3a) I have also graphed the corresponding N_{ppw} required from a fourth-order FD-TD method to achieve the same phase error as the Yee scheme in the same amount of computation time. Note that for long computation times the N_{ppw} savings (=less memory) are substantial. For the Yee scheme Figure 3b) shows a comparison between the theoretical and observed phase error for a one dimensional computation whose discretisation was designed with the guideline (4.1).

In [5] these concepts are demonstrated for two dimensional FD-TD methods where the case in favor of the fourth-order FD-TD is even stronger. We have seen in Sections 2 and 3 that the FD-TD for dispersive media require an extremely small timestep. Thus one has to look at the discretisation requirements for small Courant numbers given a fixed spatial step determined by the amount of computer memory one has. (4.1) and [4]-[5] should help in such attempts. Figure 3a) and [5] indicate that for long computation times (needed in calculations of the interaction of pulses with dispersive media) the fourth-order FD-TD should be better. Here is another reason: The fourth-order FD-TD *works best* with a small timestep since its truncation error is $O(\Delta t^2 + \Delta^4)$, it is second-order accurate in time, so if we choose $\Delta t \sim \Delta^2$ true fourth-order accuracy is obtained

at a fourth of the *total* computational cost of the standard FD-TD for the same phase error level. That is, in light of the application in dispersive media, the so called (2-4) FD-TD is a natural choice while the standard scheme needs a large amount of computational resources since in order to be accurate and the timestep restriction to be optimal it requires ν to be chosen close to its maximum value possible for stability.

References

[1] K.S. Yee, "Numerical Solution of Initial Boundary Value Problems Involving Maxwell s Equations in Isotropic Media," *IEEE Trans. Antennas Propagat.*, vol. 14, pp. 302-306, 1966.

[2] R.M. Joseph, S.C. Hagness and A. Taflove, "Direct Time Integration of Maxwell's Equations in Linear Dispersive Media with Absorption for Scattering and Propagation of Femtosecond Electromagnetic Pulses," *Optics Lett.*, vol. 16, no. 18, pp. 1412-1414, 1991.

[3] R. Luebbers, F.P. Hunsberger, K.S. Kunz, R.B. Standler and M. Schneider, "A Frequency-Dependent Finite-Difference Time-Domain Formulation for Dispersive Materials," *IEEE Trans. Electrom. Compat.*, vol. 32, no. 3, pp. 222-227, 1990.

[4] P.G. Petropoulos, "Stability and Phase Error Analysis of FD-TD Methods in Dispersive Media," *IEEE Trans. on Antennas Propagat.*, accepted, to appear January 1994.

[5] P.G. Petropoulos, "Phase Error Control for FD-TD Methods of Second and Fourth Order Accuracy," *IEEE Trans. on Antennas Propagat.*, accepted, to appear 1994.

Analysis of Finite Element Time Domain Methods in Electromagnetic Scattering

Peter Monk[1]
Dept. of Math. Sciences
University of Delaware
Newark, DE 19711, USA

A. K. Parrott and P. J. Wesson
Oxford University Computing Lab.
Parks Road
Oxford, OX1 3XD, U.K.

Abstract. In computing the RCS of complex objects, or computing the interaction of microwaves with biological tissue, one is often faced with the problem of discretizing Maxwell's equations in the presence of exotic geometries and material inhomogeneities. In these cases, the use of automatically generated unstructured tetrahedral grids is particularly attractive. These grids, in which some elements may have poor quality factors, influence the choice of discretization method. An obvious possibility is to use either standard node based continuous piecewise linear elements, or the sub-linear edge based family of Whitney elements. This paper is devoted to an analytical and numerical comparison of these two methods. We shall also discuss some implementational aspects focusing on parallel computing.

1. Introduction. In this paper we shall compare, using analytical and numerical techniques, two methods for discretizing the Maxwell system in $\mathbb{R}^3$. In order to simplify the presentation and in order to focus on essential aspects of each method we shall only consider simple wave propagation. Other aspects, such as radiation boundary conditions, will not be considered here. We wish to approximate the electric field $\boldsymbol{E}(\boldsymbol{x},t)$ and magnetic field $\boldsymbol{H}(\boldsymbol{x},t)$ that satisfy the Maxwell system.

$$\boldsymbol{E}_t - \nabla \times \boldsymbol{H} = 0 \text{ and } \boldsymbol{H}_t + \nabla \times \boldsymbol{E} = 0 \qquad \text{in } \Omega \tag{1}$$

where Ω will be either the cavity $[0,2]^3$ or the entire space $\mathbb{R}^3$. For the cavity $\Omega = [0,2]^3$ the fields are assumed to satisfy the following boundary condition:

$$\boldsymbol{n} \times \boldsymbol{E} = \boldsymbol{\gamma} \qquad \text{on } \Gamma = \text{ boundary of } \Omega, \tag{2}$$

where $\boldsymbol{n}$ is the unit outward normal to Ω and $\boldsymbol{\gamma}$ is a given tangential field. In addition, the initial fields $\boldsymbol{H}(\boldsymbol{x},0)$ and $\boldsymbol{E}(\boldsymbol{x},0)$ must be given (in our case $\boldsymbol{H}(\boldsymbol{x},0) = \boldsymbol{E}(\boldsymbol{x},0) = 0$).

We assume that Ω has been covered by an unstructured tetrahedral mesh τ_h consisting of tetrahedra of maximum diameter h. The mesh is assumed to be regular and quasi-uniform (although the latter constraint is often ignored in practice). We shall use the notation $(\boldsymbol{u},\boldsymbol{v}) = \int_\Omega \boldsymbol{u} \cdot \boldsymbol{v}\, dV$. With this notation, we can define the two methods under consideration.

1.1 Nédélec's Method. This method was proposed by Nédélec [13] and uses the lowest order edge elements of Nédélec (or Whitney elements). Precisely, the approximate electric field $\boldsymbol{E}_h(t)$ is taken to satisfy the following conditions:

[1]Research supported in part by AFOSR.

- $\boldsymbol{E}_h(t) \in H(curl;\Omega)$ where $H(curl;\Omega)$ is the set of functions in $(L^2(\Omega))^3$ with $(L^2(\Omega))^3$ curl.
- On each tetrahedron $K \in \tau_h$, $\boldsymbol{E}_h(t)|_K = \boldsymbol{a}_K + \boldsymbol{x} \times \boldsymbol{b}_K$

where $\boldsymbol{a}_K$ and $\boldsymbol{b}_K$ are piecewise constant vectors in space that depend on time. We denote the space of solution functions of the above type by U_h^N and we denote by $U_h^{N,0}$ the space of functions with homogeneous boundary data so that $U_h^{N,0} = \left\{ u_h \in U_h^N | n \times u_h = 0 \text{ on } \Gamma \right\}$. An advantage of these spaces is that $U_h^{N,0}$ is easy to construct.

Following Nédélec, the magnetic field is discretized using face based elements, so

- $\boldsymbol{H}_h(t) \in H(div;\Omega)$ where $H(div;\Omega)$ is the space of functions in $(L^2(\Omega))^3$ with $L^2(\Omega)$ divergence.
- On each tetrahedron $K \in \tau_h$, $\boldsymbol{H}_h(t)|_K = \boldsymbol{c}_K + d_K \boldsymbol{x}$ where $\boldsymbol{c}_K$ is a constant vector and d_K a scalar on each element.

We denote the space of functions of this type by V_h^N.

The discrete electric and magnetic fields $(\boldsymbol{E}_h, \boldsymbol{H}_h) \in U_h^N \times V_h^N$ satisfy the variational problem

$$(\boldsymbol{E}_{ht}, \boldsymbol{\psi}_h) - (\boldsymbol{H}_h, \nabla \times \boldsymbol{\psi}_h) = 0 \quad \forall \boldsymbol{\psi}_h \in U_h^{N,0}, \tag{3a}$$

$$(\boldsymbol{H}_{ht}, \boldsymbol{\phi}_h) + (\nabla \times \boldsymbol{E}_h, \boldsymbol{\phi}_h) = 0 \quad \forall \boldsymbol{\phi}_h \in V_h^N. \tag{3b}$$

In addition, (3) is satisfied approximately by interpolating the boundary condition at the midpoint of the edges on Γ. This method was analyzed in [11, 9]. Advantages of this method are discussed in [2]. Details of implementation, together with numerical RCS, absorbing boundary conditions and time stepping are given in [8, 7, 5]. Advantages of this method are discussed in [2]. We remark that the main advantages of this method are that the computed magnetic field is exactly divergence free and the electric field is discrete divergence free. In the case of inhomogeneous media (variable permeability, permitivity and conductivity) this method is applicable without modification.

Obvious disadvantages are that for a given mesh, many more unknowns are required to discretize the problem compared to nodal methods (but see [4] for comments on the sparsity structure of matrices for this problem). In addition the method has a low order of convergence (as we shall see in the next section).

1.2. A Node Based Method. The second method we want to examine is based on continuous piecewise linear finite elements. The discrete electric field $\boldsymbol{E}_h(t)$ satisfies:

- $\boldsymbol{E}_h(t) \in (H^1(\Omega))^3$.
- On each element $K \in \tau_h$, $\boldsymbol{E}_h(t)|_K \in (P_1)^3$ where P_1 is the set of linear polynomials.

We denote the space of such fields by U_h^S (standard elements). The magnetic field is discretized in the same way.

Due to ambiguity in the choice of a normal vector for a polyhedral domain, we prefer to use weakly enforced boundary conditions so we seek $(\boldsymbol{E}_h(t), \boldsymbol{H}_h(t)) \in (U_h^S)^2$ such that

$$(\boldsymbol{E}_t, \boldsymbol{\psi}_h) - (\nabla \times \boldsymbol{H}_h, \boldsymbol{\psi}_h) = 0 \quad \forall \boldsymbol{\psi}_h \in U_h^S, \tag{4a}$$

$$(\boldsymbol{H}_{ht}, \boldsymbol{\phi}_h + (\boldsymbol{E}_h, \nabla \times \boldsymbol{\phi}_h) = < \gamma, \boldsymbol{\phi}_h > \quad \forall \boldsymbol{\phi}_h \in U_h^S. \tag{4b}$$

Here $< u, v >= \int_\Gamma u \cdot v \, dA$. We have also programmed the use of strongly enforced boundary conditions (see [12]). This method is similar in spirit to a method investigated in [6] in two

dimensions. However we do not mass lump since mass lumping destroys the superior phase accuracy of the method.

One advantage of this method is that the fields are continuous and hence available at any point in space (for example for RCS calculations or graphics). In addition, as we shall see, the method has excellent dispersion properties. An important disadvantage is that the method does not generalize easily to allow for discontinuous permiability or permitivity.

1.3. Time Stepping. Both methods described above give rise to a system of differential equations of the form

$$M_E \frac{d\vec{E}}{dt} - C^T \vec{H} = \vec{F}, \quad \text{and} \quad M_H \frac{d\vec{H}}{dt} + C\vec{E} = \vec{G}.$$

where $\vec{E}$ and $\vec{H}$ are vectors of electric and magnetic degrees of freedom, M_E, M_H and C are matrices and $\vec{F}$ and $\vec{G}$ are data vectors. This system can be discretized conveniently by the leap-frog method [15]. Thus if Δt is the time step and $\vec{E}^n \approx \vec{E}(n\Delta t)$ with similar definitions for $\vec{H}^{n+1/2}$ and $\vec{F}^{n+1/2}$ and $\vec{G}^{n+1}$

$$M_E \frac{\vec{E}^{n+1} - \vec{E}^n}{\Delta t} - C^T \vec{H}^{n+1/2} = \vec{F}^{n+1/2}, \tag{5a}$$

$$M_H \frac{\vec{H}^{n+3/2} - \vec{H}^{n+1/2}}{\Delta t} + C\vec{E}^{n+1} = \vec{G}^{n+1}. \tag{5b}$$

Note that at each time step we shall have to solve matrix problems with matrices M_E and M_H which are sparse and positive definite.

2. Analysis of the methods.

2.1. Error Analysis. The Nédélec scheme (3) was analyzed in [11, 9] where it was shown that if $\|\cdot\|$ denotes the $(L^2(\Omega))^3$ norm then $\|(\boldsymbol{E} - \boldsymbol{E}_h)(t)\| + \|(\boldsymbol{H} - \boldsymbol{H}_h)(t)\| = O(h)$ provided $\boldsymbol{E}$ and $\boldsymbol{H}$ are smooth enough. This is an optimal estimate for the edge scheme. Using the methods of [10], it is also possible to show the same error estimate for (4), but this estimate may not be optimal. This first order convergence is very poor, but in $\mathbb{R}^2$ (using a triangle based edge method) we find that the nodal convergence rate is $O(h^2)$ which is a significant improvement over the global estimate. In this paper we shall investigate whether such "super convergence" is found in $\mathbb{R}^3$ (see the section on numerical results).

2.2. Dispersion Analysis. The error analysis above shows general global convergence. To obtain a better understanding of the wave propagation properties of (3) and (4) we perform a dispersion analysis. To do this we must use a translation invariant grid of $\mathbb{R}^3$. We start by discretizing in cube $\hat{\Omega}_h = [0, h]^3$ using six tetrahedra as shown in Figure 1 (a). Then the mesh, τ_h of $\mathbb{R}^3$ is formed by translating $\hat{\Omega}_h$ in x, y and z. We seek discrete plane wave solutions of (3) or (4). By this we mean that $\boldsymbol{E}_h(\boldsymbol{x}, t) = \hat{\boldsymbol{E}}_h(\boldsymbol{x})\exp(-i\omega t)$ and $\boldsymbol{H}_h(\boldsymbol{x}, t) = \hat{\boldsymbol{H}}_h(\boldsymbol{x})\exp(-i\omega t)$ where $\hat{\boldsymbol{E}}_h$ and $\hat{\boldsymbol{H}}_h$ have the translation property $\hat{\boldsymbol{E}}_h(\boldsymbol{x} + (jh, kh, lh)) = \hat{\boldsymbol{E}}_h(\boldsymbol{x})\exp(i\boldsymbol{k}\cdot(jh, kh, lh))$ for integer i, j, k. A similar relation holds for $\hat{\boldsymbol{H}}_h$. In order for these functions to satisfy the finite element equations, the vector $\boldsymbol{k}$ and frequency ω must satisfy a dispersion relation $\omega = \omega(\boldsymbol{k}, h)$. The finite element functions and dispersion relation may be computed by solving an eigenvalue problem on $\hat{\Omega}_h$.

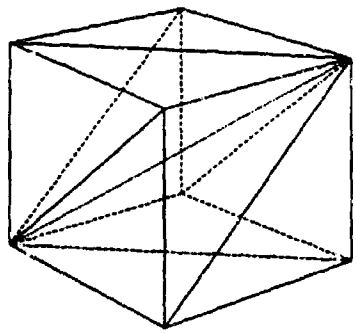

(a) Subdivision of the cube into 6 tetrahedra

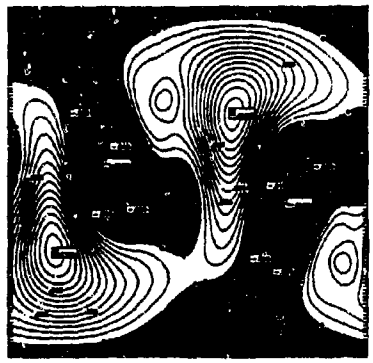

(b) Edge Element Method

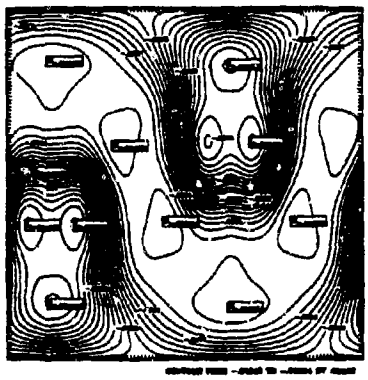

(c) Node Based Scheme

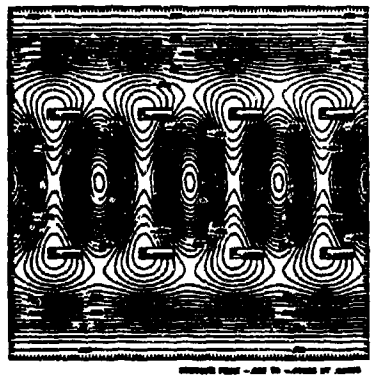

(d) Yee Scheme

Figure 1: We show contour maps of the error in the phase velocity as a function of propagation angles θ and ϕ. Panel a) shows the mesh used. Panel b) shows the phase velocity error for the edge scheme with 10 grid points per wavelength. Shading emphasizes that the error can be positive or negative depending on propagation direction. Panel c) shows the phase velocity error for the node based scheme using 14.7 gird cells per wavelength (same density of unknowns as for the edge scheme). The error is always negative and much better than for the edge scheme. Panel d) shows the corresponding plot for the Yee finite difference scheme using 14.7 grid cells per wavelength and the optimal Courant number (the other pictures do not include time stepping).

For the continuous problem (1), a plane wave solution exists if either $\omega = 0$ or $\omega = \pm|k|$. For a finite element problem the dispersion relation will no longer be exact, but we want an accurate numerical dispersion relation to ensure good phase accuracy in the numerical solution. To distinguish the finite element dispersion relation, we shall denote it by ω_h.

Using MAPLE, we can show that for the node based scheme (4), either $\omega_h = 0$ or $\omega_h = \pm|k| + O(h^4)$. This is a very highly accurate relation and justifies our interest in this method (for comparison the well known Yee finite difference scheme [15] has a dispersion relation accurate to $O(h^2)$).

For the edge method (3), we cannot compute an analytic dispersion relation. Instead we compare dispersion relations graphically. In Figure 1 (b) and (c) we show the error in the dispersion relation defined by

$$f(\theta, \phi) = \left| \frac{\omega_h(k(\theta, \phi), h)}{|k|} - 1 \right|$$

where θ and ϕ are the standard polar angles for the propagation direction and where h is chosen to correspond to 10 grid cells per wavelength for the edge method and 14.7 grid cells per wavelength for the nodal method. The choice of 10 cells per wavelength is at the lower end of the range used in practice, and has the same density of unknowns as for the node based methods with 14.7 cells per wavelength. For comparison, we also show the dispersion relation for the Yee finite difference method using 14.7 grid cells per wavelength. From Figure 1 it is quite clear that we expect the edge method (3) to have a poorer dispersion behavior than the Yee scheme, but the nodal method (4) is far superior to either.

We should also note that the edge scheme possesses parasitic modes. Finally, the grid based on subdividing a cube is optimal for neither the edge based or nodal methods. Using a uniform Sommerville grid [3], the dispersion relations for (3) and (4) improve dramatically.

3. Implementation.

In implementing the edge based method (3) it is convenient to use the Whitney forms to represent the fields on each element [1, 8]. One is left with the problem of solving the discrete problem (5) obtained form the semi-discrete problem by leap-frog discretization.

3.1. Edge Method. In this case the matrix M_E is symmetric, positive definite and sparse (see [4] for an analysis of the sparsity pattern). We use the preconditioned conjugate gradient algorithm to solve the associated matrix problem using the diagonal of the matrix as the preconditioner (see also [8]). To analyze the effectiveness of this approach we proceed as follows using the analysis of Wathen [14] Let M_E^K be the mass matrix for element $K \in \tau_h$, and let D_E^K be the diagonal matrix formed from the main diagonal of M_E^K. Then the eigenvalues of the preconditioned matrix M_E are real and lie in $[\lambda_l, \lambda_u]$ where $\lambda_l = \min_{K \in \tau_h} \lambda_K^{\min}$, $\lambda_u = \max_{K \in \tau_h} \lambda_K^{\max}$ and

$$\lambda_K^{\min} = \min_{x \neq 0} \frac{x^T M_E^K x}{x^T D_E^K x} \qquad \text{and} \qquad \lambda_K^{\max} = \max_{x \neq 0} \frac{x^T M_E^K x}{x^T D_E^K x}.$$

For the grid in Figure 1 (a) we find $\lambda_u/\lambda_l = 6.433$ which implies that at each step of the preconditioned conjugate gradient algorithm the error is decreased by a factor of approximately 0.19.

Unfortunately, the conditioning of the matrix M_E depends on the geometry of the grid. Thus λ_l and λ_u must be computed for each grid used. Nevertheless, computing λ_u and λ_l does give an a priori estimate on the number of conjugate gradient steps needed per time step. It may be worthwhile to check grids before computing and modify poor tetrahedra to improve the condition number of M_E. We note that a uniform Sommerville grid gives a condition number estimate of 5 and hence a convergence factor of 0.145 per conjugate gradient step.

For the edge method the matrix M_H in (5) can be diagonalized so (5b) can be solved rapidly.

Numerical computations of ω_h show that $\max_E \omega_h \approx 8.5$ and hence the leap frog time stepping scheme has a stability constraint of $\Delta t/h \leq 0.23$ where Δt is the time step and h is the length of the sides of the cube which underlies the tetrahedralization. The actual stability bound in the presence of boundary conditions may differ from this value.

3.2. The Node Based Method. Here both M_E and M_H are symmetric, positive definite and sparse. Thus both (5a) and (5b) give rise to linear systems that must be solved by preconditioned conjugate gradients. In this case the Wathen bound on the condition number is 5 independent of the mesh. Thus the convergence factor per conjugate gradient step is 0.145. This indicates that conjugate gradient method converges faster for the node based scheme than the edge based scheme, but one must do twice as many conjugate gradient problems.

Numerical computations of ω_h show that $\max_E \omega_h \approx 2.77$ and hence the leap frog time stepping scheme has a stability constraint of $\Delta t/h \leq 0.72$.

4. Numerical Results. In order to investigate the propagation behavior of the two methods (3) and (4) on non-uniform grids we have performed a simple computational test of the methods. We take $\Omega = [0,2]^3$ and mesh Ω by subdividing into $N \times N \times N$ cubes, then subdivide each cube into six tetrahedra (see Figure 1 (a)). Finally the mesh is randomized by moving the coordinates of each mesh point a random distance at most 0.1 (2/N) in the (x,y) plane. The time step $\Delta t \approx h/8$. The exact solution is $\boldsymbol{E} = \boldsymbol{E}_0 g(\boldsymbol{k} \cdot \boldsymbol{x} - t)$ and $\boldsymbol{H} = \boldsymbol{H}_0 g(\boldsymbol{k} \cdot \boldsymbol{x} - t)$ where $\boldsymbol{k} = (\sin(\theta)\cos(\phi), \sin(\theta)\sin(\phi), \cos(\theta))$ and $\theta = \phi = \pi/4$. Also $\boldsymbol{E}_0 = (\sin(\phi), -\cos(\phi), 0)$ and $\boldsymbol{H}_0 = (\cos(\theta)\cos(\phi), \cos(\theta)\sin(\phi), -\sin(\theta))$. Finally the function $g(t)$ is given by

$$g(t) = \begin{cases} \frac{\exp(-10(t-1)^2) - \exp(-10)}{1 - \exp(-10)} & 0 \leq t \leq 2 \\ 0 & \text{otherwise} . \end{cases}$$

The boundary data γ is computed from the exact solution.

Figure 2 shows a plot of the maximum error at the interpolation points against numbers of degrees of freedom. The slope of the line is consistent with $0(h^\delta)$ convergence with $\delta = 1$. This suggests that the error analysis mentioned earlier in the paper correctly reflects the behavior of both methods. A graph of the x component of the electrical field at $x = y = z = 1/2$ is shown in Figure 3 for the case $N = 16$. It is clear that the phase accuracy of the nodal scheme is much better than the edge scheme as is to be expected from the dispersion analysis. But the overall accuracy is worse (for the electric field).

5. Parallel Aspects. The use of a low order tetrahedral based solver increases the computational burden compared to traditional finite difference schemes. For this reason it is important to investigate parallelization of the finite element time domain code. We have done this for the edge based method (3). It turns out that the space V_h^N is no longer convenient, so we

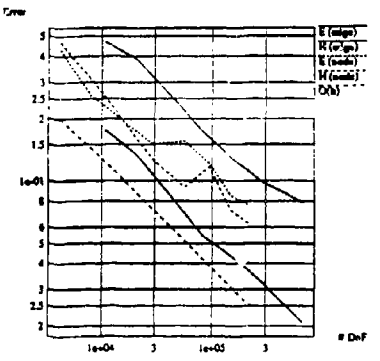

Figure 2: This figure shows a plot of the error in the nodal values of the electric and magnetic fields against the total number of degrees of freedom for the method. We show results for the edge and node based schemes and a reference line corresponding to $O(h)$ convergence. The error is computed at $t = 3$ for the numerical test discussed in the text. The slope of the lines are consistent with an error proportional to $O(h)$ for both methods which shows that our error analysis does capture the details of convergence. Note that, even allowing for differences in the number of degrees of freedom, the edge method is more accurate for the electric field although the magnetic field is worse.

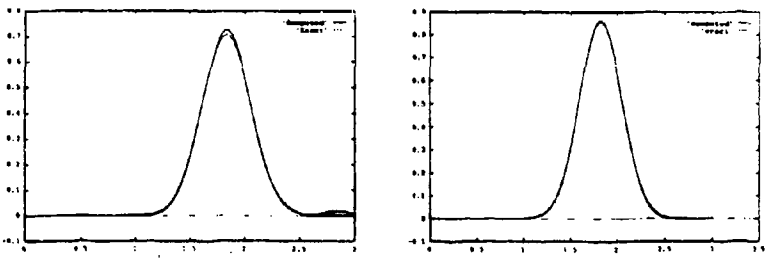

(a) Node Based Scheme

(b) Edge Element Scheme

Figure 3: We show the x component of the exact and computed electric field $\boldsymbol{E}$ at approximately $\boldsymbol{x} = (0.5, 0.5, 0.5)$ when $N = 16$ as a function of time t. The nodal result is for the node closest to the desired point, while the edge result is actually the component of $\boldsymbol{E}$ in the direction $(0.967, -0.256, 0.)$ at the point $(0.523, 0.500, 0.500)$. This is the closest edge interpolation value to the desired result. Note the poor amplitude accuracy of the node based scheme. The integration has not been carried out for a long enough time to show the superior phase accuracy of the nodal scheme.

use the space $\tilde{V}_h^N$ of piecewise constant vector fields to discretize the magnetic field. This method gives exactly the same solution as the edge/face method mentioned before, but at the cost of more degrees of freedom for the magnetic field. Parallelization aspects are discussed in more detail in [12] where we provide efficiency data using a variety of mechanisms for parallelization on message passing computers.

6. Conclusion We have given a description and comparative analysis of two finite element methods for discretizing Maxwell's equations. Despite the superior phase accuracy of the node based scheme, our calculations show that the edge based finite element method is competative. For this reason we have implemented a parallel edge based finite element solver.

It would be desirable to investigate further the source of error in the node based solver since if this source could be controlled the method could offer high phase accuracy on unstructured grids. We are now making analytical and computational investigations on this point.

References

[1] A. Bossavit, *Mixed finite elements and the complex of Whitney forms*, in The Mathematics of Finite Elements and Applications VI, J. Whiteman, ed., Academic Press, 1988, pp. 137–144.

[2] ——, *A rationale for "edge elements" in 3-D fields computations*, IEEE Trans. Mag., 24 (1988), pp. 74–79.

[3] M. Goldberg, *Three infinite families of tetrahedral space-fillers*, J. of Combinatorial Theory (A), 16 (1974), pp. 348–354.

[4] P. Kotiuga, *Essential arithmetic for evaluating three dimensional vector finite element interpolation schemes*, IEEE Trans. on Magnetics, 27 (1991), pp. 5203–5210.

[5] J-F. Lee, *Solving Maxwell's equations by finite element time domain methods*. Preprint, 1993.

[6] N. Madsen and R. Ziolkowski, *Numerical solution of Maxwell's equations in the time domain using irregular nonorthogonal grids*, Wave Motion, 10 (1988), pp. 583–596.

[7] K. Mahadevan and R. Mittra, *Radar cross section computations of inhomogeneous scatterers using edge-based finite element method in frequency and time domains*. Preprint, 1993.

[8] K. Mahadevan, R. Mittra, and P. M. Vaidya, *Use of Whitney's edge and face elements for efficient finite element time domain solution of Maxwell's equations*. Preprint, 1993.

[9] C. Makridakis and P. Monk, *Time-discrete finite element schemes for Maxwell's equations*. Submitted for publication.

[10] P. Monk, *A mixed method for approximating Maxwell's equations*, SIAM J. on Numerical Analysis, 28 (1991), pp. 1610–1634.

[11] ——, *An analysis of Nédélec's method for the spatial discretization of Maxwell's equations*, J. Comp. Appl. Math., 47 (1993), pp. 101–121.

[12] P. Monk, A. Parrott, and P. Wesson, *A parallel electromagnetic scattering code*. In preparation, 1994.

[13] J. Nédélec, *Mixed finite elements in* $\mathbb{R}^3$, Numer. Math., 35 (1980), pp. 315–341.

[14] A. Wathen, *Realistic eigenvalue bounds for the Galerkin mass matrix*, IMA J. on Numerical Analysis, 7 (1987), pp. 449–457.

[15] K. Yee, *Numerical solution of initial boundary value problems involving Maxwell's equations in isotropic media*, IEEE Trans. on Antennas and Propagation, AP-16 (1966), pp. 302–307.

Faster Single-Stage Multipole Method for the Wave Equation *

Ronald Coifman
Vladimir Rokhlin
Fast Mathematical Algorithms and Hardware Corp.

Stephen Wandzura
Hughes Research Labs

Abstract

The fast multipole method (FMM) provides a sparse decomposition of the impedance matrix arising from a discretization of an integral equation equivalent to the wave equation with radiation boundary condition. Mathematically, the sparse factorization is made possible by a diagonal representation of translation operators for multipole expansions. Physically, this diagonal representation corresponds to the complete determination of fields in the source-free region by the far fields alone.

Because the diagonal form of the translation operator is not a well behaved function, it must be filtered in numerical practice. (This does not constitute a practical limitation to the accuracy of the results obtained with the method because of the superalgebraic convergence of the multipole expansions.) In the originally published version of the FMM, the filtering was accomplished by a simple truncation of the

*This research was supported by the Advanced Research Projects Agency of the Department of Defense and was monitored by the Air Force Office of Scientific Research under Contracts No. F49620-91-C-0064 and F49620-91-C-0084. The United States Government is authorized to reproduce and distribute reprints for governmental purposes notwithstanding any copyright notation hereon.

multipole expansion of the translation operator. This sharp cutoff results in an oscillatory transfer function that is non-negligible over the entire unit sphere (i.e., in all far-field directions). Physically, the transfer function represents the effect a bounded source has on a well-separated observation region, expressed in terms of the far field of the source. This suggests that a suitable transfer function might be non-negligible only in the direction of the separation vector. It turns out that such a transfer function may be obtained by applying a smooth cutoff to the multipole expansion. Although such a transfer function requires the tabulation of far fields in a denser set of directions, the overall computational and storage requirements for a single-stage FMM are reduced to $O(N^{4/3})$ from $O(N^{3/2})$.

1 Review of FMM

The fast multipole method (FMM) for the wave equation[1, 2] gives a prescription for a sparse decomposition of the (impedance) matrix obtained by discretization of the integral kernel

$$G(\mathbf{x}-\mathbf{x}') = \frac{e^{ik|\mathbf{x}-\mathbf{x}'|}}{4\pi\,|\mathbf{x}-\mathbf{x}'|}\,. \tag{1}$$

Mathematically, this decomposition ensues from the diagonal form of the translation operator in the far-field representation[3]. For brevity, this summary relies heavily on the exposition and notation of [2].

Briefly, the FMM works by decomposing the interactions into near-field and far-field parts. This is done by dividing the scatterer into groups and classifing each pair of groups as near or far. The matrix representing the near-field part is sparse by virtue of locality. The far-field part may be factored by using

$$\frac{e^{ik|\mathbf{X}+\mathbf{d}|}}{|\mathbf{X}+\mathbf{d}|} \approx \frac{ik}{4\pi}\int d^2\hat{k}\, e^{ik\hat{\mathbf{k}}\cdot\mathbf{d}}\mathcal{T}_L(k\mathbf{X},\hat{k}\cdot\hat{\mathbf{X}})\,, \tag{2}$$

where the $\mathcal{T}$ is the diagonal representation of the translation operator:

$$\mathcal{T}_L(\kappa,\cos\theta) \equiv \sum_{l=0}^{L} i^l(2l+1)h_l^{(1)}(\kappa)P_l(\cos\theta)\,, \tag{3}$$

and X is the distance between the two members of a group pair. In the previously published version of the FMM, the sharp cutoff at $l = L$ caused the transfer function $\mathcal{T}$ to be non-negligible over a wide range of angle. As we show below, examination of $\mathcal{T}$ reveals that it may be modified so that it has support only in a narrow range of $\cos\theta$ near 1. The only cost of this modification is a denser sampling of far-field radiation patterns from the groups.

2 The Translation Operator

The transfer function $\mathcal{T}_L(\kappa, \cos\theta)$ represents the interaction between bounded source distributions separated by distance κ/k (where k is the free-space wavenumber) and θ is the angle between the displacement vector of the centers of the groups and a direction at which the far-field of the source distribution is computed. Since we expect the fields radiated from a bounded region to a well separated observation region to be given only in terms of the far-field in directions that point toward the observation region, we might expect that $\mathcal{T}_L(\kappa, \cos\theta)$ would be strongly peaked for $\cos\theta \approx 1$. Furthermore, since convergence of the multipole expansions requires $L \approx kD$, where D is the diameter of the regions, we might also expect that the peak have a width $\delta\theta \propto L/\kappa$. Numerical examination of $\mathcal{T}$ reveals that this is indeed the case; however, there are rather large oscillatory tails outside the peak. In Figure 1, $\mathcal{T}_{10}(30, \cos\theta)$ is plotted. This is the transfer function that one would use for rather small (compared to a wavelength) groups separated by 4.8 wavelengths. The oscillatory tails are reminiscent of *leakage* in power spectrum estimation using the FFT[4]. This suggests that by using a smooth "window function" to compute $\mathcal{T}$ rather than a sharp cutoff, that leakage to large angles may be reduced. In fact, this is the case; even a simple-minded cosine window function, giving

$$\tilde{\mathcal{T}}_L(\kappa, \cos\theta) = \mathcal{T}_L(\kappa, \cos\theta) + \sum_{l=L+1}^{2L} i^l (2l+1) \left[1 - \sin^2 \frac{(l-L)\pi}{2L}\right] h_l^{(1)}(\kappa) P_l(\cos\theta)\,, \quad (4)$$

produces the localized transfer function plotted in Figure 2. Naturally, because we are taking more terms in the multipole expansion of $\mathcal{T}$, we must

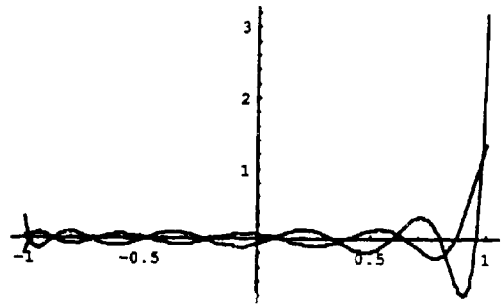

Figure 1: Real and imaginary parts of transfer function $\mathcal{T}$ of $\cos\theta$ for $L = 10$, $\kappa = 30$.

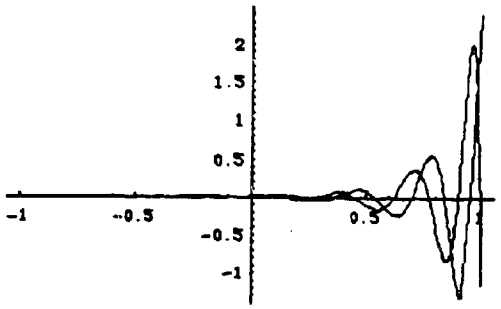

Figure 2: Real and imaginary parts of the localized transfer function $\tilde{\mathcal{T}}$ of $\cos\theta$ for $L = 10$, $\kappa = 30$.

sample the far fields in a denser set of directions appropriate to a quadrature rule for spherical integrations exact for a larger set of spherical harmonics. The trigonometric window function in Eq. (4) is only for purposes of illustration; more efficient windows should be used in practice.

3 Complexity Reduction

A detailed analysis, to be published elsewhere, reveals that the window function of I can be chosen to minimize the support in solid angle of T. This analysis confirms the intuition, implied above, that the solid angle of support of the resulting transfer function is about $\pi(kD)^2/(4\kappa^2)$, where D is the diameter of the groups. In the $\mathcal{O}\left(N^{3/2}\right)$ FMM, the operation count of the translation operator application is $\propto KM^2$, where M is the number of groups and K is the number of far-field directions tabulated. It might now seem that this count should be multiplied by a factor $\propto (kD)^2/(4\kappa^2) \propto 1/M$, giving a total count $\propto (K/M)M^2 \propto N$, which is independent of M. This is incorrect, however, because it implies that by decreasing the size of the groups that the number of directions at which the far-field is used can be reduced without limit. Actually, since we must know the far-field of each group in at least one direction for each other group, the number of directions must go to a constant for very small groups. The total operation count for application of the translation operators is thus $(bN/M^2 + c)\,M^2$, where b and c are implementation dependent constants. (Actually, a more careful analysis gives a factor of $\ln M$ in the b term, but it has no effect on the behavior for large N.) Minimizing the sum of this with the operation count for the other steps in the FMM (aN^2/M, where a is another constant), one sees that, for large problems, b is irrelevant, and the total operation count is minimized by choosing

$$M = \left(\frac{aN^2}{2c}\right)^{1/3}, \tag{5}$$

so that the total operation count is $\mathcal{O}\left(N^{4/3}\right)$. For smaller problems, where the c term does not dominate, the operation count varies roughly as $N \ln N$.

References

[1] V. Rokhlin, "Rapid solution of integral equations of scattering theory in two dimensions," *Journal of Computational Physics*, 86(2):414–439, 1990.

[2] R. Coifman, V. Rokhlin, and S. Wandzura, "The fast multipole method: A pedestrian prescription," *IEEE Antennas and Propagation Society Magazine*, 35(3):7–12, June 1993.

[3] V. Rokhlin, "Diagonal form of translation operators for the Helmholtz equation in three dimensions," *Applied and Computational Harmonic Analysis*, 1(1):82–93, December 1993.

[4] W. H. Press, B. P. Flannery, S. Teukolsky, and W. T. Vetterling, *Numerical Recipes — The Art of Scientific Computing*, Cambridge University Press, Cambridge, 1986.

An Optimal Incident Pulse for Scattering Problems

GREGORY A. KRIEGSMANN AND JONATHAN H. C. LUKE

Department of Mathematics
Center for Applied Mathematics and Statistics
New Jersey Institute of Technology
University Heights
Newark, NJ 07102

Abstract. Numerical computation of the field scattered from a body in two dimensions due to an incident plane pressure pulse is considered. In particular, we examine the process of inferring the scattered field due to one incident pulse given the scattered field due to another incident pulse. The objective is to develop an indirect method that avoids the potentially expensive direct solution of the problem. Our approach is based on a formula expressing the scattered field as a convolution of a kernel with the incident pulse profile. The most straight forward generalization of this formula to the discrete version of the scatter problem used in numerical computations does not allow the kernel to be inferred from a single numerical experiment—a difficulty we call the "multi-source problem". Preprocessing the incident pulses using simple interpolation formulas overcomes the multi-source problem giving an exact algorithm for computing the kernel. Selection of a sharp incident pulse (the Kronecker pulse) for the primary numerical experiment assures stability of this algorithm and permits extremely accurate prediction of the scattered fields for secondary incident pulses.

I. Introduction

In a recent paper [1] we presented a numerical algorithm which efficiently computes the scattering of plane incident pulses from a compact, impenetrable target. Assuming only that the numerical scheme used to solve the wave equation was linear, causal, and time invariant, we deduced an expression for the scattered field at a point as a finite convolution of the time dependent boundary data and the scattering kernel. The later is unknown in general and represents the scattering response of the target to an incident plane delta function. Our algorithm is essentially a constructive way of approximating this kernel: We simply run one numerical experiment and record the response. The incident wave for this simulation is the Kronecker pulse, which is only nonzero at one grid point, and the response is our approximation to the kernel. We then convolve the approximation to the kernel with an incident pulse to determine the scattered field.

We referred [1] to the Kronecker pulse as optimal because it affords us the simplest way of approximating the scattering kernel. Here we consider the algorithm from a slightly different point of view; we study the response of the continuous system, K_δ, to this incident pulse and estimate its deviation from the scattering kernel. Specifically, we study the difference between the field produced by convolving an incident pulse with K_δ and the exact scattered field.

This work was supported by the Air Force Office of Scientific Research under Grant No. AFOSR 91-0252 and by the Office of Naval Research under Grant N00014-92-J-1261.

II. The Scattering Kernel $K(\mathbf{x}, t)$

For the sake of simplicity, we consider only two dimensional scattering problems for the wave equation and assume that the target is convex and sound hard (or TM), although our analysis can be be generalized in the obvious manner. We therefore consider the following scattering problem:

$$\frac{\partial^2 v}{\partial t^2} = \frac{\partial^2 v}{\partial x^2} + \frac{\partial^2 v}{\partial y^2}, \qquad \mathbf{x} \in D, \quad t > 0 \tag{1a}$$

$$v = -u_{inc}(t - \mathbf{k}_{inc} \cdot \mathbf{x}), \qquad \mathbf{x} \in S, \quad t > 0 \tag{1b}$$

$$v(\mathbf{x}, 0) = v_t(\mathbf{x}, 0) = 0 \tag{1c}$$

where u_{inc} is the incident pulse, v is the scattered pulse, D is the scatterer and S is its boundary, and $\mathbf{k}_{inc}$ is the unit vector in the direction of the incident pulse. The scattered field v is also outgoing at ∞. The quantities in (1) are dimensionless; the spatial variables have been scaled with respect to a characteristic length, L, of the target, the time with respect to L/c where c is the speed of sound (light) in D, and v and u_{inc} with respect to the maximum of the incident pulse.

Taking the fourier transform of (1), denoting transformed quantities with hats, $\hat{}$, and taking ω to be the transform variable we obtain

$$\frac{\partial^2 \hat{v}}{\partial x^2} + \frac{\partial^2 \hat{v}}{\partial y^2} - \omega^2 \hat{v} = 0, \qquad \mathbf{x} \in D \tag{2a}$$

$$\hat{v} = -\hat{u}_{inc}(\omega) e^{i\omega \mathbf{k}_{inc} \cdot \mathbf{x}}, \qquad \mathbf{x} \in S \tag{2b}$$

$$\hat{v}_r + i\omega \hat{v} + \frac{\hat{v}}{2r} \sim 0, \qquad r \to \infty. \tag{2c}$$

The solution of (2) in principle is given by

$$\hat{v} = -\hat{u}_{inc}(\omega) \hat{K}(\mathbf{x}, \mathbf{k}_{inc}, \omega) \tag{3a}$$

$$\hat{K} = \int_S G(\mathbf{x}, \mathbf{x}', \omega) e^{i\omega \mathbf{k}_{inc} \cdot \mathbf{x}'} \, ds' \tag{3b}$$

where G is the greens function and ds' is the differential arc length along S.

If we take the special incident field $u_{inc} = \delta(t - \mathbf{k}_{inc} \cdot \mathbf{x})$, then $\hat{u}_{inc} \equiv 1$ and $\hat{v} = \hat{K}$ is the fourier transform of the scattered field produced an incident plane delta function. Its inverse transform $K(\mathbf{x}, t, \mathbf{k}_{inc})$ is the scattering kernel of the target. Applying the convolution theorem to (3) we obtain

$$v = \int_{-\infty}^{t} K(\mathbf{x}, t, \mathbf{k}_{inc}) u_{inc}(t - \tau) \, d\tau \tag{4}$$

which shows that the scattered field for any incident pulse can be determined from the target's response to an incident delta function. Equation (4) is the continuous version of our discrete convolution described in Reference 1.

III. The Approximate Scattering Kernel $K(\mathbf{x},t)_\delta$

We begin by defining the triangular function u_δ given by

$$u_\delta(t) = 0, \qquad t < -h \tag{5a}$$

$$u_\delta(t) = (h+t)/h^2, \qquad -h < t < 0 \tag{5b}$$

$$u_\delta(t) = (h-t)/h^2, \qquad 0 < t < h \tag{5c}$$

$$u_\delta(t) = 0, \qquad t > -h \tag{5d}$$

where h is a small positive number. The function defined in (5) is proportional to the linear interpolation of the Kronecker function that we used in our algorithm [1]. In that context h was the mesh size and our interpolation was h times bigger than u_δ.

If we take our incident pulse to be $u_{inc} = u_\delta(t - \mathbf{k}_{inc}\cdot\mathbf{x})$ and denote by K_δ the corresponding scattered field, then it follows from (4) that

$$K_\delta(\mathbf{x},t) = \int_{-\infty}^{t} K(\mathbf{x},\tau,\mathbf{k}_{inc})u_\delta(t-\tau)\,d\tau. \tag{6}$$

Since u_δ is a simple approximation to a delta function, it seems plausible that $K \sim K_\delta$ as $h \to 0$. This would then suggest in light of (4) that given any incident pulse, the produced scattered field is approximately given by

$$v \sim \int_{-\infty}^{t} K_\delta(\mathbf{x},t,\mathbf{k}_{inc})u_{inc}(t-\tau)\,d\tau. \tag{7}$$

This is the continuous version of the discrete result presented in Reference 1.

Denoting by E the difference between the approximate and exact scattered fields given by (7) and (4), respectively, we find that

$$E = \int_{-\infty}^{t} u_{inc}(t-\tau)J(\tau)\,d\tau \tag{8a}$$

$$J = K(\tau) - K_\delta(\tau) \tag{8b}$$

where the dependence of the functions on $\mathbf{x}$ and $\mathbf{k}_{inc}$ has been omitted for notational convenience. Thus, the error depends on the difference function J which according to (6) becomes

$$J(\tau) = K(\tau) - \int_{-\infty}^{t} K(p)u_\delta(\tau-p)\,dp. \tag{9}$$

Since u_δ approximates the delta function, it is clear that $J \to 0$ as $h \to 0$. The question we must therefore address is: how small is J for a fixed h?

One possible way of addressing this question goes along the following lines. Using the definition of $\hat{K}$, the evenness of $\hat{K}$, the convolution theorem, and the explicit fourier transform of u_δ we rewrite (9) as

$$J(\tau) = \frac{1}{\pi}\int_0^\infty [1 - \frac{\sin^2(\omega h/2)}{(\omega h/2)^2}]\hat{K}(\omega)\cos\omega s\, d\omega. \tag{10}$$

The ability of the function u_δ to approximate the delta function is mirrored in this frequency domain result by the bracketed term which is the difference between their fourier transforms. And if h is small enough, this term is quite small for a large range of ω. For example, if $\omega h/2 < \pi/10$, then the bracketed term is < 0.008.

In our numerical algorithm [1] we chose h small enough to resolve the highest frequency present in a class of incident functions. That is, $h \sim \pi/10\omega_M$, where ω_M is this maximum frequency. Using this ordering and the observation just made about the size of the bracketed term, we deduce the estimate

$$J(\tau) \sim \frac{1}{\pi}\int_{\omega_M}^\infty [1 - \frac{\sin^2(\omega h/2)}{(\omega h/2)^2}]\hat{K}(\omega)\cos\omega s\, d\omega. \tag{11}$$

Assuming that $\omega_M >> 1$, or equivalently $h << 1$, and that $\hat{K} \sim \omega^{-N}\hat{K}_0$, we integrate (11) by parts to obtain

$$J \sim \frac{\hat{K}_0}{\pi}\frac{\sin\omega_M\tau}{\omega_M^N\tau} \tag{12}$$

where $\hat{K}_0$ is independent of ω and N is a positive integer. The existence of $\hat{K}_0$ and N follow from greens function arguments on the helmholtz equation and boundary conditions satisfied by $\hat{K}$. Finally inserting (12) into (8a) we obtain

$$E \sim \frac{\hat{K}_0}{\pi\omega_M^N} u_{inc}(t) \tag{13}$$

which shows that the error $\to 0$ as $h \to 0$.

IV. Numerical Examples: Time Harmonic Responses

The response of a scatterer to a time harmonic incident pulse has played a major role in scattering theory for practical and theoretical reasons. Many numerical methods have been devised to tackle this problem, each with their strengths and limitations. A technique called the Finite Difference Time Domain Method (FDTD) is a relatively straightforward and robust way of computing the time harmonic scattering response of a target [2-5]. The time dependent

equations with a time periodic incident wave are solved using an explicit finite difference scheme. According to the limiting amplitude principle [6], the solution of the time dependent problem will approach a time harmonic state as long as no trapped modes are present (and this is certainly the case for compact targets). And if the explicit finite difference scheme and non-reflecting boundary condition are carefully chosen then the numerical results will give a good approximation to the time harmonic response. The rate at which the solution evolves into the time harmonic response depends upon the target shape and the polarization of the incident wave. For example, it was observed [4] that rate for sound hard (TE) targets is smaller than the rate for a soft (TM) target. Moreover, if the target shape encourages local energy confinement (e.g., a Helmholtz Resonator), then the rate can also be quite small [5]. Thus, the FDTD method may become prohibitively time consuming if the target is complex and if many frequency responses are required.

The method, presented in [1] and embodied in the discrete version of (7), may give a more economical approach than the FDTD for complex targets where the frequency response is required over a broad spectrum, Ω. Our algorithm proceeds as follows. We first use a finite difference scheme to solve (1) for the incident pulse u_δ. The temporal time step h is chosen to resolve the highest frequency present in Ω and the spatial step size is chosen to satisfy the CFL condition [7]. If the differential cross sections for different frequencies in Ω are required, then we save the response K_δ on a large circle of radius R enclosing the compact target S. Next, we choose our incident field to be the complex stepped sine wave

$$u_{inc} = \exp(-i\omega_C t)H(t) \tag{14}$$

where $H(t)$ is the Heaviside function and $\omega_C \in \Omega$. Then we convolve this function with K_δ according to the discrete version of (7); the imaginary part of v will be the approximate response of the target to a stepped sine wave incident pulse. Finally, we compute the convolution in (7) until $v(\mathbf{x}, t)$ becomes time harmonic. The amplitude of v is the differential cross section of the scatterer, $A(\theta_C, \omega_C)$. This process is then continued for those frequencies of interest in the spectrum Ω.

To illustrate the process outlined above, we determine the amplitude of the surface currents on a target in the harmonic steady state from the response to an incident Kronecker pulse. For simplicity our target is a circle of normalized radius one. We consider several wave numbers $k = 5, 8, 10$ to illustrate that the harmonic response for many frequencies can be obtained from a single computation of the response to a Kronecker pulse. The amplitude of the surface currents is shown for the three wave numbers in Figure 1. The response to the Kronecker pulse is computed using the standard explicit centered difference method in polar coordinates with $\Delta r = 0.025$, $\Delta t = 0.0025$, $\Delta\theta = 2\pi/128 \approx 0.0491$, 2000 time steps and an absorbing boundary at $r = 20$.

Because the surface currents are obtained by evaluating the convolution in our method at a single large time and because computing the convolution involves only data on the surface of the target (rather than the fields throughout the computational domain) the computational effort required to obtain the surface currents from the Kronecker scattering results is many

orders of magnitude less than the time needed to find the harmonic response directly with FDTD. Obtaining the scattering results for the Kronecker pulse is relatively expensive, but the computational cost is essentially equal to that of obtaining the harmonic response directly with FDTD for a *single* frequency. Thus, our approach gives the harmonic response for a range of frequencies for essentially the same cost as determining the harmonic response for one frequency using FDTD directly. The surface currents shown in Figure 1 contain small but noticeable errors. But these errors are no larger than then the errors suffered if FDTD is used directly. In fact, to machine accuracy the errors are the same. That is, our method predicts the surfaces currents given by the FDTD method exactly including any error inherent in the method.

References

[1] G. A. Kriegsmann and J. H. C. Luke, Journ. Comp. Physics, in press.

[2] K. S. Yee, IEEE Trans. Ant and Prop. 14, 402-412 (1968).

[3] A. Taflove and M. Brodwin, IEEE Trans. Microwave Theory 23, 888-896 (1976).

[4] G. A. Kriegsmann and C. S. Morawetz, SIAM Journ. Scientific and Statistical Computing 1, 371-385 (1980).

[5] A. Taflove and K. Umashankar, IEEE Trans. Electromagnetic Compatability 25, 433-440 (1983).

[6] C. S. Morawetz, Comm. Pure and Applied Math. 15, 349-361 (1962).

[7] R. D. Richtmeyer and K. W. Morton, "Difference Methods for Initial Value Problems", Wiley Interscience, New York, 1967.

Surface Current Amplitudes

Figure 1

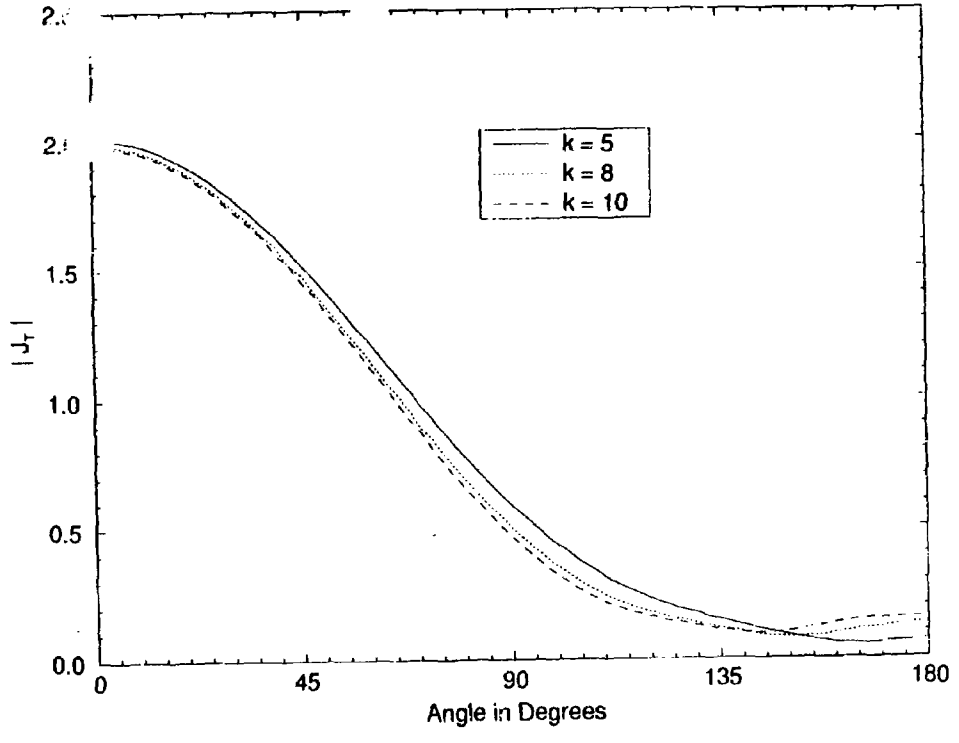

Numerical Solution of the High Frequency Asymptotic Expansion for Hyperbolic Equations

Bjorn Engquist
Emad Fatemi
Stanley Osher

Department of Mathematics
University of California, Los Angeles
Los Angeles, CA 90024

1 Introduction

The computation of high frequency electromagnetic waves is of paramount importance for calculation of reflection of radar waves from objects and radar radiation patterns. The direct calculation of the high frequency waves is not practical since the wavelength of the radiation is usually quite small compared to the size of the physical objects of interest. Therefore approximate methods have been extensively used for this type of calculations. One of the more successful approximate methods is the generalized theory of diffraction. This method relies on a high frequency asymptotic expansion of the wave equation and considers special diffracted waves from the singularities present in the media and the shape of the reflecting objects. We shall refer to these singularities that are surfaces, lines, or points as branch manifolds. Recently we have developed numerical methods for solving the partial differential equations obtained by considering the high frequency asymptotic expansion of the scalar wave equation. We expect these to replace ray-tracing methods for many high frequency calculations and they are applicable directly for the calculation of electromagnetic waves.

Maxwell's equations for the electric and magnetic fields in an isotropic homogeneous material can be written as:

$$(\epsilon E)_t = c\nabla \times H - 4\pi J \tag{1}$$

$$(\mu H)_t = \nabla \times E \tag{2}$$

$$\nabla \cdot (\epsilon E) = 4\pi\rho \tag{3}$$

$$\nabla \cdot (\mu H) = 0 \tag{4}$$

where E is the electric field, H is the magnetic field, J is the current, ρ is the charge density, c is the speed of light in the medium, and μ and ϵ are respectively electric permittivity and magnetic permeability. For electromagnetic waves the equations can be written as:

$$E_{tt} = \frac{c^2}{\epsilon\mu}\nabla^2 E \tag{5}$$

$$H_{tt} = \frac{c^2}{\epsilon\mu}\nabla^2 H \tag{6}$$

These are, of course, wave equations for the E and H vectors.

Special time harmonic high frequency solutions of the Maxwell's equations can be obtained by assuming solutions of the form,

$$E = e(\mathbf{x})e^{ik\phi(\mathbf{x})}, H = h(\mathbf{x})e^{ik\phi(\mathbf{x})}$$

where ϕ function is the phase of the wave, and k is the frequency of the wave. These solutions correspond to a high frequency plane wave and are of important practical significance. One can show that the phase satisfies an eikonal equation [8],

$$(\nabla\phi)^2 = \frac{\epsilon\mu}{c^2(\mathbf{x})} \tag{7}$$

The eikonal equation is a first order nonlinear PDE, a Hamilton-Jacobi type equation. The eikonal equation can be considered as the Hamilton-Jacobi equation for the variational problem based on Fermat's principle [8]. The usual practice has been to solve the eikonal equation by ray-tracing methods. Ray-tracing in this context is nothing but solving the eikonal equation using the method of characteristics for PDE's. Our approach relies on a direct discretization of the eikonal equation using the recently developed numerical methods for Hamilton-Jacobi equations [1].

2 Asymptotic expansion for the scalar wave equation

To develop the numerical methods we have started from the scalar wave equation in two dimensional space. The numerical methods developed for this problem are applicable to the Maxwell's equations.

$$u_{tt} = c^2\Delta u = c^2(x,y)(u_{xx} + u_{yy}) \tag{8}$$

x and y are the spatial variables, t is time. u is the amplitude of the wave, and $c(x,y)$ is the speed of the wave in the medium. High frequency solutions of the scalar wave equation can be approximated by an asymptotic expansion as introduced by Luneburg, Kline, and Keller [9], [10], [11]. The asymptotic expansion to the wave equation is obtained by expanding the solution in powers of ω^{-1} in an infinite series. The expansion is substituted in the wave equation and the sequence of the coefficients of ω^{-n} are collected and set to zero. This procedure produces an infinite system of nonlinear partial differential equations, that, together with the boundary conditions, determine the expansion. The first term and the most important term of the expansion is the

eikonal equation of geometrical optics for the phase of the wave. The remaining equations are linear hyperbolic transport equations for amplitude functions.

Here we briefly repeat the standard derivation of the asymptotic expansion. The solution to the wave equation is expanded in inverse powers of ω in the following form,

$$u(x,y,t) = e^{i\omega\phi(x,y,t)} \sum_{n=0}^{\infty} v_n(x,y,t)(i\omega)^{-n}, \tag{9}$$

where u is a complex solution of the wave equation, $\phi(x,y,t)$ is the phase of the wave, and v_n are real functions of time and space. By substituting the above expansion in the scalar wave equation and equating the coefficients of different powers of ω, the partial differential equations for the evolution of ϕ, v_0, v_1, etc are derived. Terms of order $(i\omega)^2$ are collected and the result is the eikonal equation.

$$\phi_t^2 v_0 = c^2(\phi_x^2 + \phi_y^2)v_0$$

In general v_0 is not zero and we take the square root of the equation. Here we choose the positive root.

$$\phi_t = +c(x,y)|\nabla\phi|$$

Terms of order $(i\omega)$ result in the equation for evolution of v_0.

$$2\phi_t v_{0,t} + \phi_{tt} v_0 = c^2(2\nabla\phi.\nabla v_0 + \Delta\phi v_0)$$

By collecting terms of order $(i\omega)^{-n}$ we get:

$$2\phi_t v_{n+1,t} + \phi_{tt} v_{n+1} + v_{n,tt} = c^2(2\nabla\phi \cdot \nabla v_{n+1} + \Delta\phi v_{n+1} + \Delta v_n)$$

One can solve for ϕ_t and $v_{n,t}$ and get an infinite system for evolution of the expansion coefficients.

$$\phi_t = c|\nabla\phi| \tag{10}$$

$$v_{0,t} = c^2 \frac{\nabla\phi}{|\nabla\phi|}.\nabla v_0 + \frac{(-\phi_{tt} + c^2\Delta\phi)v_0}{2|\nabla\phi|} \tag{11}$$

$$v_{n+1,t} = c^2 \frac{\nabla\phi}{|\nabla\phi|}.\nabla v_{n+1} + \frac{(-\phi_{tt} + c^2\Delta\phi)v_{n+1}}{2|\nabla\phi|} + \frac{-v_{n,tt} + c^2\Delta v_n}{2|\nabla\phi|} \tag{12}$$

The above system with the appropriate boundary conditions define the expansion.

It is possible to write the equations for evolution of v_n in conservative form by changing the variables. We define the new variables as $w_n = \frac{\phi_t v_n^2}{c^2}$, and we write the transport equations in their conservative form.

$$\phi_t = c|\nabla\phi| \tag{13}$$

$$w_{0,t} = \nabla \cdot (cw_0 \frac{\nabla\phi}{|\nabla\phi|}) \tag{14}$$

$$w_{n+1,t} = \nabla \cdot (cw_{n+1} \frac{\nabla\phi}{|\nabla\phi|}) + (\Delta v_n - \frac{v_{n,tt}}{c^2})v_{n+1} \tag{15}$$

$$v_n = c\sqrt{\frac{w_n}{\phi_t}} \tag{16}$$

The above formulation of the equations seems to be natural, based on our experience with conservation laws.

The eikonal equation for the phase is a Hamilton-Jacobi type equation. The equations for the variables w_n form a hyperbolic system. The system is essentially decoupled, since it can be truncated at any level. The first equation, the eikonal equation, can be solved independent of the others. After we compute it, we use it to solve for w_0. Similarly w_n is solved using the ϕ and w_{n-1}. The equation for w_n has a forcing term ($\Delta v_n - \frac{v_{n,tt}}{c^2}$) which has to be calculated from the previous term, w_{n-1}. If the previous term w_{n-1} is not twice differentiable in space and time, the forcing term is ambiguous. From a numerical point of view, even for smooth solutions, it is important to calculate the forcing term correctly, otherwise error would spread out to higher order terms. The ambiguity in the forcing terms could be resolved by specifying jump conditions along discontinuities of v_n. The proper conditions depend on physical considerations as well as mathematical arguments and we plan to determine them for important physical applications. Continuity of the phase across branch surfaces supplies us with the necessary boundary conditions for multivalued solutions of the phase. The situation is more complicated for the computation of v_n. For example the amount of reflected energy from a reflecting surface depends on the physical characteristics of the surface. The situation is more complex for other kinds of branch manifolds such as corners and jumps in higher order derivatives. This question of the proper boundary conditions needs to be solved for a variety of important cases, including discontinuities in the index of refraction and singularities in the shape of objects.

3 Numerical algorithm

The traditional way of solving the eikonal equation is by the method of characteristics, which, in this context is called ray tracing [13]. We apply the modern high resolution algorithms to directly compute the eikonal equation and the other equations defining the terms in the expansion. These modern techniques allow for accurate representation of singularities, which is essential in this application. The standard viscosity solution of the eikonal equation, [12], is not enough and an hierarchy of numerical solutions has to be generated. These new functions represent the multivalued character of the solution and are based on singularity detection.

Our numerical algorithm was developed based on the recently devised numerical methods for Hamilton-Jacobi type equations and high order accurate, nonoscillatory methods for hyperbolic equations. We have developed numerical algorithms to solve the equations both in conservative and nonconservative variables. We have abandoned non-conservative variables in favor of conservative variables. From a numerical and also theoretical point of view it is the natural way of writing the equations. We have only considered the first three equations of the infinite system for ϕ, w_0, and w_1, but the methods are easily applicable to an arbitrary number of terms. After the third equation the equations are exactly the same, so even the same subroutine could be used to solve them. The equations to be discretized are,

$$\phi_t = c|\nabla\phi| \tag{17}$$

$$w_{0,t} = \nabla \cdot (cw_0 \frac{\nabla\phi}{|\nabla\phi|}) \tag{18}$$

$$w_{1,t} = \nabla \cdot (cw_1 \frac{\nabla \phi}{|\nabla \phi|}) + (\Delta v_0 - \frac{v_{0,tt}}{c^2}) v_1 \tag{19}$$

$$v_0 = c\sqrt{w_0/\phi_t} \qquad v_1 = c\sqrt{w_1/\phi_t}$$

We use third order ENO interpolation and a Godunov type numerical Hamiltonian to solve the eikonal equation [1]. For solving the transport equations a first order upwind scheme is used. In principle, various sophisticated schemes developed for nonlinear conservation laws could be used to solve the transport equations. At this stage a first order scheme was sufficient.

4 Numerical examples

The reflection of high frequency waves from solid objects is an important problem.In the first example we consider the reflection of a source off a sphere. We only have calculated the phase here, but the full solution of this problem will be an essential part of our future work. An important problem for calculation of phase is computing multi-valued solutions to the eikonal equation. Usually the multi-valued nature of the solution is known *a priori*, such as in case of reflection and branch manifolds due to singularities in the index of refraction. Nevertheless there are branch manifolds that are not known *a priori*. such as the second example that we have considered here. Only after the solution to the eikonal equation is computed branch manifolds are found. We have designed a numerical procedure to do that automatically. The last example corresponds to propagation of a planar wave through a non-uniform media, in particular, a lens.

We consider the reflection of an incident wave off a sphere. This problem has all the features of reflection of high frequency waves off a convex object in a uniform medium. We consider a sphere of radius one at the origin. The source of the wave is at point $(0, 0, 2)$. We use spherical coordinates and exploit the symmetry of the problem under rotation around the z axis. The eikonal equation in (r, θ) space is written as

$$\phi_r = \sqrt{\phi_r^2 + \frac{\phi_\theta^2}{r^2}}. \tag{20}$$

We solve an eikonal equation for the incident problem and an eikonal equation for the reflected problem. The two equations are coupled only at the surface of reflection through the boundary conditions. The physical problem is posed in all of R^3 but our computational domain is $[1, 3] \times [-\pi, \pi]$. The computed solution is shown in figure 1. The viscosity solution of the eikonal equation calculates the incident and the reflected waves accurately, also it produces the phase in the shadow region of the sphere.

In a nonuniform media, the solution of the eikonal equation in general develops singularities. These singularities are generated when two wave fronts approach each other. The solution of the eikonal equation in that case becomes multivalued. But the viscosity solution of the eikonal equation only chooses one branch of the solution (conjectured to be the first wave that reaches that point). A numerical procedure was devised to recover the multi-valued solutions. When a solution becomes multivalued a discontinuity in the gradient of the phase appears. We detect this discontinuity and use the phase at that point as boundary conditions for creating the next sheet

of the solution. Using the terminology from complex analysis, the discontinuities in the gradient of the phase are branch cuts. The other branch cuts are the singularities in the index of refraction and the shape of the boundary. In figure two we show a generic situation where two sources are present and the solution is double-valued after the two waves reach other. We have superimposed the two solutions on top of each other.

In the next example we show the computed phase and amplitude for a convex lens (figure 3). The lens is implemented by taking a smooth change of index of refraction in the midule of the computational domain. The bending of the incident planar wave creates a shock starting from the focal point. The amplitude of the wave is calculated. The amplitude has a singularity on the shock, since it has to be connected to the second sheet of the solution(not done here). The proper boundary conditions for the amplitude coefficients is an important question that needs to be investigated for these applications.

5 Additional Proposed Effort

We first plan to compute problems for which the index of refraction has a known spatial discontinuity. This is fairly routine and amounts to solving an initial-boundary problem for a Hamilton-Jacobi equation.

Next, we plan to investigate appropriate boundary conditions at corners for the eikonal equation. This is well studied. We anticipate no difficulties with the numerical implementation.

An additional speculative idea involves "capturing" multivalued solutions to Hamilton-Jacobi equations directly. This has been done in one space dimension (for conservation laws, but there is an equivalence here) by Professor Yann Brenier [16]. He uses moments of the classical Vlasov equation in an original and ingenious fashion to arrive at a system of conservation laws which give the different branches of the multivalued solution. An extension to multidimensions seems difficult, but will be investigated. This would automate the code and remove the shock detection step, if successful.

Another, simpler idea is to use polar coordinates in some problems and just to allow the θ dependency to be nonperiodic. This is very promising and will be explored.

After the direct algorithm matures we expect to use it as a tool for solving the inverse problem, i.e. finding the index of refraction given a certain number of measurements. Opimization techniques e.g. those described in [14], [15] can be modified and adapted using our fast direct solvers.

Finally, we expect to extend these results to a full Maxwell's equation situation. Numerical techniques borrowed from the conservation law community such as space marching, the use of body fitted coordinates and artificial compression shall be incorporated in the resulting package.

References

[1] S. Osher and C-W Shu, High order essentially non-oscillatory schemes for Hamilton-Jacobi equations, *SIAM J. Numer. Analysis*, Vol. 28, (1991), pp. 907-927.

[2] R. N. Buchal and J. B. Keller, Boundary layer problems in diffraction theory, *Communications on Pure and Applied Mathematics, XIII* (1960), 85-114.

[3] H. Hochstadt, Asymptotic formulas for diffraction by parabolic surfaces, *Communications on Pure and Applied Mathematics, X* (1957), 311-329.

[4] D. Ludwig, Uniform asymptotic expansions at a caustic, *Communications on Pure and Applied Mathematics, XIX* (1966), 215-250.

[5] P. D. Lax, Asymptotic solutions of oscillatory initial value problems, *Duke Math J.*, Vol 24, (1957), pp. 627-646.

[6] C. Morawetz and D. Ludwig, An inequality for the reduced wave operator and the justification of geometrical optics, *Communications on Pure and Applied Mathematics, XXI*, (1968), 187-203.

[7] G. Avila and J. B. Keller, The high frequency asymptotic field of a point source in an inhomogeneous medium, *Communications on Pure and Applied Mathematics, XVI*, (1963), 363-381.

[8] M. Born and E. Wolf, Principles of Optics, Pergamon Press, sixth edition, 1989.

[9] R. Luneburg, Mathematical theory of optics, University of California press, 1964.

[10] J. B. Keller, R. Lewis, and B. Seckler, Asymptotic solution of some diffraction problems, *Communications on Pure and Applied Mathematics, IX*, (1965), 207-265.

[11] J. B. Keller, A. Geometrical Theory of Diffraction, *Calculus of variations and its Applications*, McGraw-Hill, New York, 1958, p. 27.

[12] M. Crandall and P. Lions, Viscosity solutions of Hamilton-Jacobi equations, *Trans. Amer. Math. Soc.*, 277, (1983), pp 1-42.

[13] C. H. Chapman, Ray theory and its extensions:WKBJ and Maslov seismograms, *Journal of Geophysics*, Vol. 58, (1985), pp. 27-43.

[14] F. Santosa and W. W. Symes, Linear inversion of band limited reflection seismograms, *SIAM J. Sci. Stat. Comput.*, Vol. 7, (1986), pp. 1307-1330.

[15] F. Santosa and W. W. Symes, Reconstruction of blocky impedance profiles from normal incidence reflection seismograms which are band-limited and miscalibrated, *Wave motion*, Vol. 10, (1988), pp. 209-230.

[16] Y. Brenier, Multivalued solutions can be captured, UCLA internal report, (1993).

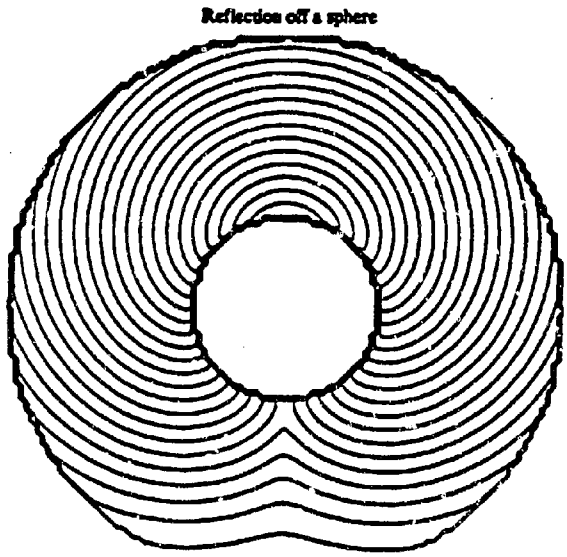

Figure 1b

Interacting Waves

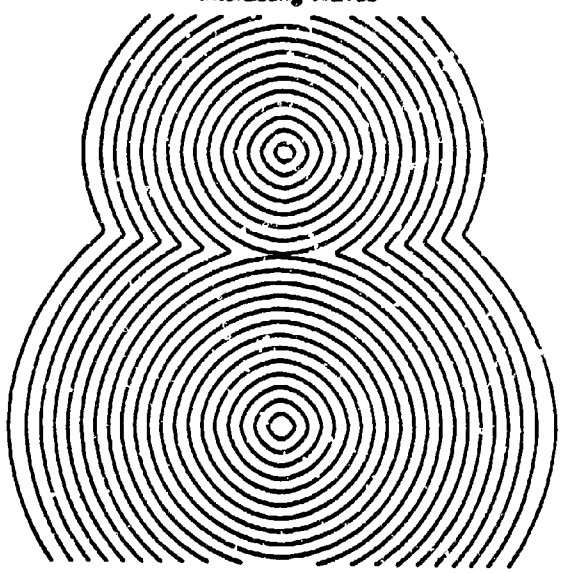

Figure 2a

Hidden Waves

Figure 2b

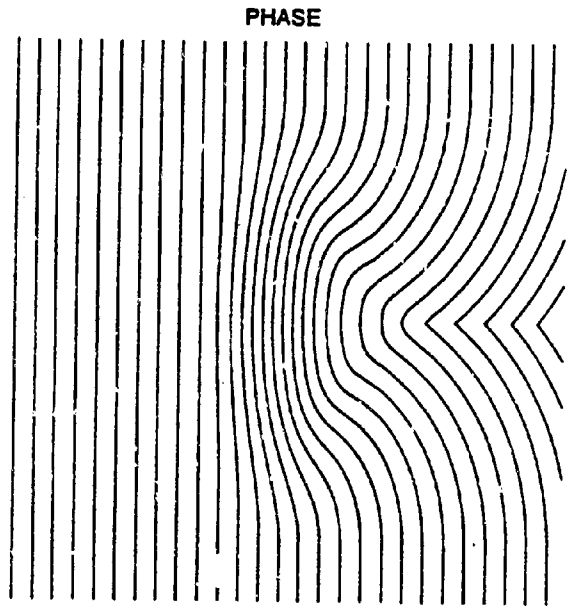

Figure 3a

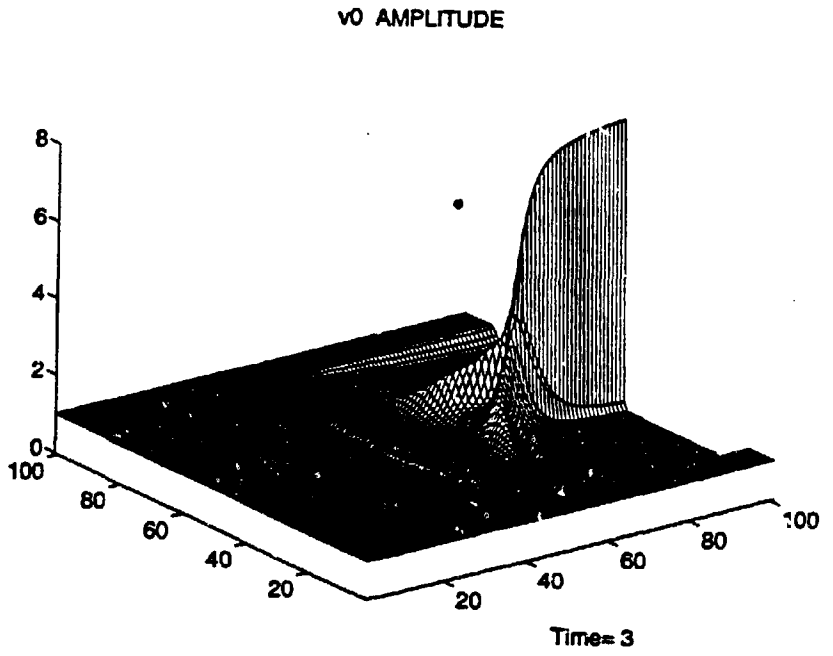

Figure 3b

A new technique for synthesis of offset dual reflector systems*

Vladimir Oliker†

Department of Mathematics and Computer Science
Emory University, Atlanta, Georgia 30322

and

Laird D. Prussner

Matis, Inc., 120 Parkwood Lane, Decatur, Georgia 30030

1 Introduction

In electromagnetics the geometric optics (GO) aproximation is used to describe offset single and dual reflector antennas when it is required to control the energy pattern and/or phase on the output aperture and at the same time minimize energy losses due to spillovers, blockage, etc. [1]. Similarly, in optics, GO is used to describe systems with one, two, or more specular reflectors that are required to transform an input Gaussian laser beam into a uniform output irradiance front and at the same time optimize certain design parameters [2].

The differential form of the energy conservation law for such systems leads to an equation for the Jacobian determinant of the map derived by ray tracing the energy wavefront. If a quasi-potential can be associated with this map then one usually arrives at an equation of Monge-Ampère type that this quasi-potential must satisfy (cf. [3], [4], [5]). The same type of equation arises in a number of other applications; for example, in inverse diffraction, nondestructive evalution, allocation of resources [6]. During the last 15 years there has been a surge in mathematical studies regarding theoretical solvability of equatuions of Monge-Ampère type and their generalizations. Still, the theory is far from being complete.

The purpose of this note is to report several results on synthesis of dual reflector systems. We discuss here only specular reflector systems with two reflectors and energy source which is a collimator. For such systems we present here a second order partial differentiil equation of Monge-Ampère type expressing the ray tracing map and the energy conservation law. Rigorous results concerning existence and uniqueness of solutions to the resulting problem are established. A detailed exposition of these results is beyond the scope of this paper and will appear elsewhere.

The numerical solution of the resulting equation and the generation of the surface points of the two reflectors is done with a specially developed software package REFSYS. The algorithms are based on our

*This research was supported by AFOSR under contract F49620-92-C-0009. The United States Government is authorized to reproduce and distribute reprints for governmental purposes notwithstanding any copyright notation herein.

†Also with Matis, Inc., 120 Parkwood Lane, Decatur, Georgia 30030.

earlier paper [7], though substantial modifications were required. Using REFSYS we can synthesize a system with two reflectors which redirects and reshapes a plane wave front and, at the same time, the system transforms the energy pattern of the input beam into a uniform (or any other, desired) energy distribution pattern across the front of the output beam. For example, our technique allows to design a two-reflector system which will transform an arbitrary elliptic input beam into an output beam with prespecified elliptical (rectangular, or general polygonal) shape. Blockage is completely avoided. The resulting reflectors are aspherical but convex, which is a substantial improvement over an earlier design of Malyak [2]. In general, the reflector surfaces are not radially symmetric. We illustrate the technique by presenting designs of two dual reflector systems converting a circular Gaussian beam into uniform circular and elliptic beams.

As it was already mentioned, Monge-Ampère equations arise in a variety of other physical problems, and we expect that our technique will apply to such problems. Inquiries regarding concrete applications are welcome.

2 The synthesis equations

2.1. The configuration of the system is shown schematically on Fig.1. We denote by α the plane $z = 0$ and by $\hat{\Omega}$ the cross section of the incoming beam I by that plane. In order to emphasize that the shape of the incoming beam is not required to be circular, on the figure, we draw $\hat{\Omega}$ as an ellipse. In general, it is allowed to be any bounded convex domain. It is assumed that the rays of the incoming beam I form a plane wavefront propagating in the positive direction $\vec{k}$ of the z axis. The input radiation pattern is given as a nonnegative function $I(x,y), (x,y) \in \hat{\Omega}$. The desired characteristics of the system are as

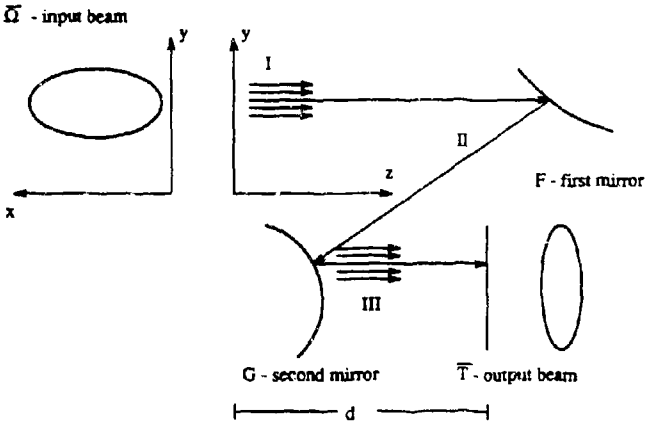

Figure 1:

follows.

- The output wavefront III is required to form a plane wave propagating in the same direction $\vec{k}$ as the incoming beam.

- The geometric shape and position of the output beam are specified by prescribing in advance the cross section of the output beam by a given plane $z = d$. We denote this cross section by $\tilde{T}$. Again, on the figure, $\tilde{T}$ is drawn as an ellipse, but it can be any bounded convex domain.

- The output radiation pattern is a prespecified in advance function $L(p,q)$, where $(p,q,d) \in \tilde{T}$.

- *Our aim is to determine the surfaces F and G which will transform the plane wave* I *with intensity $I(x,y)$ into a plane wave* III *irradiating at $\tilde{T}$ with intensity $L(p,q)$.*

Two basic physical principles are used here in deriving the analytic formulation of the problem. The first one is the Snell law of reflection, leading to the ray tracing equations, and the second one is the energy conservation law for the energy flux along differential tubes of rays. The resulting equation is a differential equation of Monge-Ampère type for a scalar function (quasi-potential) z representing the reflector F. The second surface G is determined in terms of this function, its first derivatives, and other data in the problem.

Below, we review some of the steps involved in deriving the required equation. More details can be found in [8]. We begin by tracing a typical ray through the system. Such a ray is "marked" by a point $(x,y) \in \tilde{\Omega}$. It propagates in the direction of the unit vector $\hat{k} = (0,0,1)$, strikes the first reflector F, reflects off F in the direction of the unit vector $\hat{\eta}(x,y)$, strikes the second reflector G, and reflects off it, again, in the direction $\hat{k}$. The reflector F we describe by a function $z(x,y), (x,y) \in \tilde{\Omega}$. In vector form F is given by the vector function $\mathbf{r}(x,y) = (x,y,z(x,y)), (x,y) \in \tilde{\Omega}$. Denote by $\hat{n}$ the unit normal vector on F. Put $z_x = \frac{\partial z}{\partial x}, z_y = \frac{\partial z}{\partial y}$. Then

$$\hat{n} = \frac{(-Dz,1)}{\sqrt{1+|Dz|^2}}, \quad Dz = (z_x, z_y). \tag{1}$$

The unit vector $\hat{\eta}(x,y)$ in the direction of the ray reflected off F can be found by applying Snell's law.

$$\hat{\eta} = \hat{k} - 2(\hat{k} \cdot \hat{n})\hat{n}. \tag{2}$$

Denote by $t(x,y)$ the distance from reflector F to reflector G along the ray reflected in the direction $\hat{\eta}(x,y)$ and let $s(x,y)$ be the distance from G to $\tilde{T}$ along the corresponding ray reflected off G. The total optical path length (OPL) corresponding to the ray associated with the point (x,y) is denoted by $l(x,y)$ and it is given by

$$l(x,y) = z(x,y) + t(x,y) + s(x,y). \tag{3}$$

Because $l(x,y)$ is the distance between input and output fronts, we have (see [9]):

$$l(x,y) = l = const. \tag{4}$$

It is convenient to introduce vector notation for the surface G and the output front $\tilde{T}$. Respectively, we put

$$G: \quad \mathbf{R}(x,y) = \mathbf{r}(x,y) + t(x,y)\hat{\eta}(x,y), \quad (x,y) \in \tilde{\Omega}, \tag{5}$$

$$\tilde{T}: \quad \mathbf{V}(x,y) = \mathbf{R}(x,y) + s(x,y)\hat{k}, \quad (x,y) \in \tilde{\Omega}. \tag{6}$$

Thus, a point $(p,q,d) \in \tilde{T}$ is the image of some $(x,y) \in \tilde{\Omega}$ under the ray tracing map $\mathbf{V}$, that is,

$$(p,q,d) = \mathbf{V}(x,y), \quad (x,y) \in \tilde{\Omega}. \tag{7}$$

Next, we relate the radiation pattern $I(x,y)$ of the input beam to the output radiation pattern $L(\mathbf{V}(x,y))$ on T. This relation is based on the energy conservation law for the energy flow along differential tubes of rays. Denote by $dxdy$ the area element in Ω and by $dpdq$ the area element in T. Since T is supposed to be the image of Ω under the ray tracing map $\mathbf{V}$, we have the relation

$$dpdq = |J(\mathbf{V})|dxdy,$$

where J is the Jacobian determinant of the map $\mathbf{V}$. We assign a $\pm$ sign to the Jacobian according to whether $\mathbf{V}$ preserves the orientation of Ω or reverses it.

According to the differential form of the energy conservation law [9], p. 115,

$$L(\mathbf{V}(x,y))J(\mathbf{V}(x,y)) = \pm I(x,y). \tag{8}$$

It follows from (8) that the total energy conservation equation is given by

$$\int_{\Omega} L(\mathbf{V}(x,y))|J(\mathbf{V}(x,y))|dxdy = \int_{\Omega} I(x,y)dxdy. \tag{9}$$

Using representations (5) and (6) it is possible to find an explicit expression for (8). For that we need an explicit expression for the $J(\mathbf{V})$ in terms of the function $z(x,y)$. Such an expression is found in [8] in a more general setting. To present it here we need a few more notation. Because the output front is a plane wave in the direction $\hat{k}$, the vector function $\mathbf{V}$ can be written as

$$\mathbf{V}(x,y) = \mathbf{V}_{\alpha}(x,y) + d\hat{k}, \tag{10}$$

where $\mathbf{V}_{\alpha}$ denotes the projection of the vector $\mathbf{V}$ on the plane α. Clearly, $J(\mathbf{V}) = J(\mathbf{V}_{\alpha})$ and in order to find $J(\mathbf{V})$ it suffices to compute $J(\mathbf{V}_{\alpha})$.

The position vector of the surface F is given by $\mathbf{r}(x,y) = (x,y,0) + z(x,y)\hat{k}$. Hence, it follows from (6) that

$$\mathbf{V}(x,y) = (x,y,0) + (z(x,y) + s(x,y))\hat{k} + t(x,y)\hat{\eta}(x,y). \tag{11}$$

Then (10) and (11) imply that

$$\mathbf{V}_{\alpha}(x,y) = (x,y) + t(x,y)\eta_{\alpha}(x,y), \tag{12}$$

where $\eta_{\alpha}(x,y)$ denotes the projection of the vector $\hat{\eta}(x,y)$ on the plane α.

It is shown in [8] that

$$t = \frac{1}{2}\mu(1 + |Dz|^2), \tag{13}$$

where we put $\mu = l - d$. Using formulas (1) and (2), we get

$$\eta_{\alpha} = 2(\hat{k}\cdot\hat{n})\frac{Dz}{\sqrt{1+|Dz|^2}} = \frac{2Dz}{1+|Dz|^2}.$$

Substituting this expression and (13) into (12) and recalling (7), we obtain

$$(p,q) = \mathbf{V}_{\alpha}(x,y) = (x,y) - \mu Dz(x,y), \quad (x,y) \in \tilde{\Omega}. \tag{14}$$

It follows now from (14) that

$$J(\mathbf{V}_{\alpha}) = \det\begin{pmatrix} 1+\mu z_{xx} & \mu z_{xy} \\ \mu z_{xy} & 1+\mu z_{yy} \end{pmatrix}, \tag{15}$$

where $z_{xx} = \frac{\partial^2 z}{\partial x^2}$, and similarly z_{xy} and z_{yy}.

Taking into account (10), (14), and suppressing the indication of dependence on the constant d in the function L, we have

$$L(\mathbf{V}) = L(x + \mu z_x, y + \mu z_y).$$

Thus, the main equation (8) assumes the following form:

$$L(x + \mu z_x, y + \mu z_y)[(1 + \mu z_{xx})(1 + \mu z_{yy}) - \mu^2 z_{xy}^2] = \pm I \text{ in } \Omega. \tag{16}$$

Denote by $\hat{T}_\alpha$ the projection of the region $\bar{T}$ on the plane α. Formula (14) shows that $\mathbf{V}_\alpha$ is a map from $\bar{\Omega}$ onto $\hat{T}_\alpha$ and the Jacobian determinant of this map is the same as that of map $\mathbf{V}$.

2.2. We perform now a transformation simplifying the equation (16). Introduce a new unknown function $u(x, y)$ by setting

$$\mu z(x, y) = u(x, y) - \frac{1}{2}(x^2 + y^2) + ax + bx + c, \tag{17}$$

where a, b, c are constants to be described in a moment. Then, in terms of function $u(x, y)$, the map (14) assumes the form

$$\mathbf{V}_\alpha(x, y) = (u_x(x, y) + a, u_y(x, y) + b) : \bar{\Omega} \to \hat{T}_\alpha, \tag{18}$$

where $u_x = \frac{\partial u}{\partial x}$ and $u_y = \frac{\partial u}{\partial y}$. Substituting (17) into (16), we obtain

$$L(u_x + a, u_y + b)(u_{xx}u_{yy} - u_{xy}^2) = \pm I \text{ in } \Omega, \tag{19}$$

where $u_{xx} = \frac{\partial^2 u}{\partial x^2}$, and similarly for u_{xy} and u_{yy}.

Formula (18) shows that we can choose the constants a and b so that the map $Du \equiv (u_x, u_y)$ maps $\bar{\Omega}$ into some translate $\hat{T}_\alpha^0$ of $\hat{T}_\alpha$. It is convenient to choose these constants in such a way that the origin O of the coordinate system on α is an interior point of $\hat{T}_\alpha^0$.

Obviously, the choice of the constant c in (17) affects neither the map (18) nor the equation (19). That means that any function u satisfying (18) and (19) is defined only up to a constant.

2.3. The analytic formulation of the problem stated in 2.1 is now complete. We summarize it here.

- For the given convex domain $\bar{T}$ determine the constants a, b so that $\hat{T}_\alpha^0$ is a translate of $\hat{T}$ with center at the origin O of the coordinate system on the plane α (or any other translate convenient for computations).
- Solve the equation (19) for the function $u(x, y)$.
- Assuming that μ is given, and $\mu > 0$ determine the function $z(x, y)$ from (17); the constant c can be set equal to 0. The function z completely describes the first reflector F.
- Using formulas (1) and (13) determine $\hat{n}(x, y)$ and $t(x, y)$. Then, a substitution in (5) (and a lengthy calculation that we omit) gives

$$\mathbf{R}(x, y) = (u_x + a, u_y + b, u - xu_x - yu_y + (1/2)\{[Du + \mathbf{A}]^2 - \mu^2\}), \quad (x, y) \in \bar{\Omega}, \tag{20}$$

where $\mathbf{A} = (a, b)$. Thus, we have the parametric equations of the second reflector G.

2.4. The critical step in the above procedure is to solve the equation (19). The physically interesting situation is the one when the + sign in the equations (19) is taken. We were able to investigate this problem completely but a full discussion is beyond the scope of this paper and will be presented elsewhere. We note only that this equation admits infinitely many solutions leading respectively to infinitely many

possible designs of a two-reflector system. This feature is extremely useful because it allows to select a solution satisfying additional requirements. This can be done in a way leading to an optimal design. In the test cases presented below, we construct solutions that allow to synthesize systems that convert a Gaussian circular beam into a uniform elliptic beam, have no blockage, and, in addition, map the central ray in the input beam into the central ray of the output beam. When the - sign in (19) is taken, the problem can be also investigated, but by different techniques.

3 Examples

In the examples below the input beam is circular with a Gaussian power pattern

$$I(x,y) = C exp\left(-\frac{x^2+y^2}{2\sigma^2}\right),$$

where C is a balancing constant required to enforce the energy conservation equation (9), and σ is specified below. The crossection $\hat{\Omega}$ of the input beam is given by:

$$\Omega = \{(x,y) \in \alpha \ \ |x^2+y^2 \leq 9\sigma^2\}.$$

In the first example the data as the same as in [2], Table 1, data set 1. The input beam crossection $\hat{\Omega}$ is a circle of radius 3σ, centered at the origin (0,0), the output beam is required to have a uniform energy distribution, with circular crossection $\hat{T}$ of radius 2σ, $\sigma = .125m$, and center at the point $(0, 1.396m)$: $\mu = 99.98050804m$. The parameter μ is determined from the data in [2]. The surface profile of the $y = 0$ cut of the first reflector F is shown on Fig. 2. Fig. 3 shows the spacial view of the first reflector. The surface profile of the $y = 0$ cut of the second reflector G is on Fig. 4. Fig. 5 is the spacial view of the second reflector. It is important to note, that for the same data the design presented in [2] requires nonconvex surface profiles with two "humps". Our design leads to convex profiles which should be easier to manufacture.

In our second example the input beam is the same as in the first example. The output beam is required to have an elliptic crossection, $\hat{T}$, with center at $(0, 1.396m)$, minor semiaxis 2σ in the x-direction and major semiaxis 3σ in the y-direction. The output energy distribution is required to be uniform across T. The parameter $\mu = 99.98050804m$. The surface profiles and their spacial views are shown on Figures 6 - 9. On all figures the measurement units are meters.

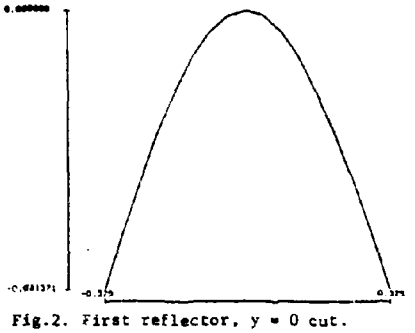

Fig.2. First reflector, y = 0 cut.

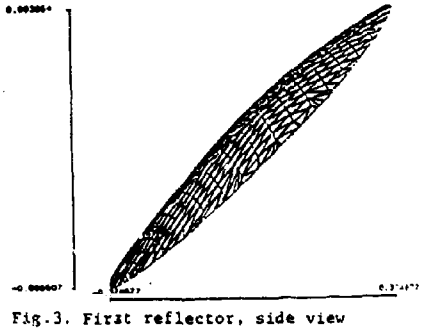

Fig.3. First reflector, side view

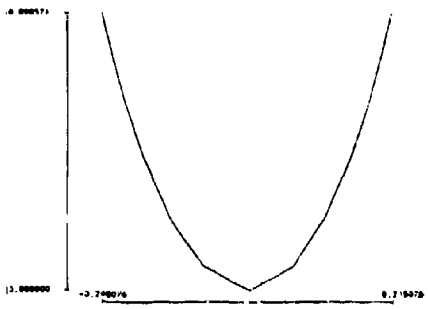

Fig.4. Second reflector, y = 0 cut.

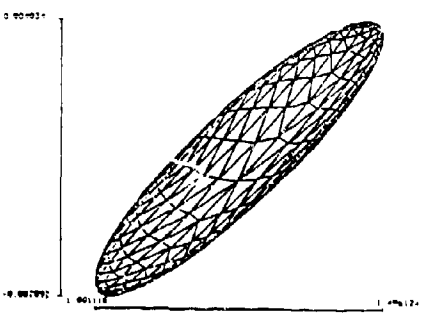

Fig.5. Second reflector, side view.

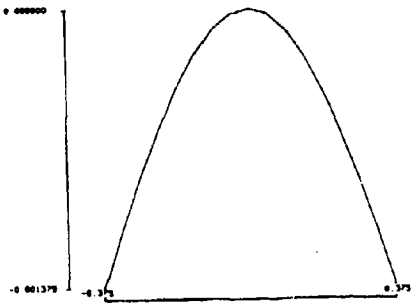

Fig.6. First reflector, y = 0 cut.

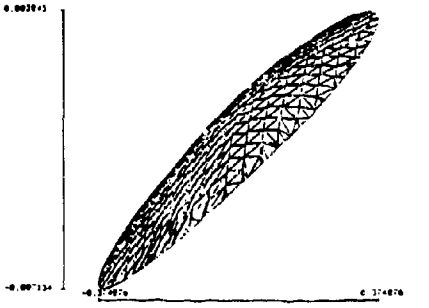

Fig.7. First reflector, side view.

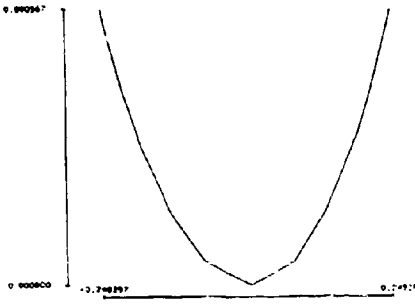

Fig.8. Second reflector, y = 0 cut.

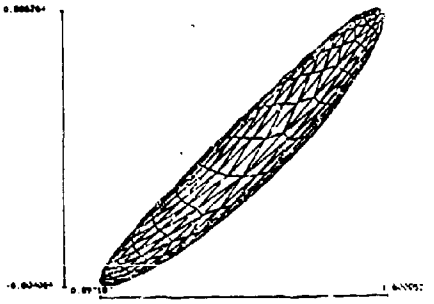

Fig.9. Second reflector, side view.

4 Summary

The design equations for a two-reflector system for reshaping, redirecting, and energy redistribution is presented. The resulting main equation is a nonlinear partial differential equation of Monge-Ampère type. Once this equation is solved, the surface data points of the reflectors are found by using formulas presented here. The results of theoretical and numerical investigation of this equation will be presented elsewhere. Using a software code REFSYS, developed by the authors, two examples of reflector systems, synthesized numerically, are presented. In contrast with some existing design techniques, our technique allows to produce noncircularly shaped output beams and uses only convex reflectors. The availability of convex reflectors is particularly important for fabrication.

References

[1] W. V. T. Rusch. Quasioptical antenna design (section 3.4). In A. W. Rudge, K. Milne, A. D. Olver, and P. Knight, editors, *The handbook of antenna design, Volumes 1 and 2*. Peter Peregrims Ltd., London, UK, 1986.

[2] P. H. Malyak. Two-mirror unobscured optical system for reshaping irradiance distribution of a laser beam. *Applied Optics*, 31(22):4377–4383, August 1992.

[3] V. I. Oliker, E. J. Newman, and L. Prussner. A formula for computing illumination intensity in a mirror optical system. *Journal of the Optical Society of America A, to appear*.

[4] V. I. Oliker and E. J. Newman. The energy conservation equation in the reflector mapping problem. *Applied Mathematics Letters*, 6(1):91–95, 1993.

[5] V. I. Oliker. On the problem of synthesis of offset dual shaped reflector antennas. In *Proceedings of the 1992 Antenna Applications Symposium*, University of Illinois, Urbana-Champaign, 1992.

[6] Y. Brenier. Décomposition polaire et réarrangement monotone des champs de vecteurs. *C.R. Acad. Sci. Paris*, 305(I):805–808, 1987.

[7] V. I. Oliker and L.D. Prussner. On the numerical solution of the equation $\frac{\partial^2 z}{\partial x^2}\frac{\partial^2 z}{\partial y^2} - (\frac{\partial^2 z}{\partial x \partial y})^2 = f$ and its discretizations, I. *Numerische Math.*, 54:271–293, 1988.

[8] V. I. Oliker. The ray tracing and energy conservation equations for mirror systems with two reflecting surfaces. *Computers and Mathematics with Applications*, 26(7):9–18, 1993.

[9] M. Born and E. Wolf. *Principles of Optics*. Pergamon Press, 4 edition, 1970.

Fast and Accurate Algorithm for Computing the Matrix Elements by the Unified Full-Wave Analysis for (M)MIC Applications

Shih-Chang Wu
Department of Electrical and Computer Engineering
New Jersey Institute of Technology
Newark, NJ 07102

Abstract — The unified full-wave analysis, which yields a fast and accurate computing algorithm for (M)MIC applications, is introduced. This new analysis method combines the advantages from the classical space-domain and spectral-domain analyses in computing the matrix elements during the moment method procedure. A frequency-independent numerical-error control algorithm is implemented to guard the numerical accuracy. A CPW short-end discontinuity was analyzed and illustrated as an example of potential applications.

I. INTRODUCTION

Recently, because of the dramatic increase in computing power and the need from the hybrid and monolithic microwave/millimeter-wave integrated circuit (MIC and MMIC) industrial, full-wave analyses have gradually been adopted in the microwave computer-aided-design software. Because that their formulations are directly derived from Maxwell's equations, full-wave analyses can accurately take into account the radiation and surface wave coupling. The space-domain method [1,2] and the spectral-domain method [3-7] are the most popular full-wave methods. Both of them utilize the same EFIEs and Green's functions to formulate electromagnetic problems; but they adopt different mathematical integration sequence in computing the sixfold integral for the mutual coupling calculation among the expansion and the test functions. As a result, the space-domain method is suitable for the modeling of arbitrarily shaped geometries and the circuits/antennas with large size compared to the wavelength. The spectral-domain method can accurately evaluates the mutual coupling between adjacent current elements; thus, it is more suitable to analyze the circuits/antennas with the size less than a wavelength. In this paper, the algorithm of the unified full-wave method, which combines the advantage from the space-domain and the spectral-domain methods, is introduced. This unified full-wave method promises an accurate mutual coupling computation for the overlap elements; while it yields high numerical efficiency and accuracy when the elements are far apart.

The unified full-wave analysis presented in this paper is formulated to characterize the multilayered coplanar waveguide (CPW) configuration. Similar approach can be extended to the microstrip or other printed circuit/antenna configurations. In the next section, the Green's function and its asymptotic expression for a multilayered CPW will be presented. The unified full-wave method will be derived. The computed reflection coefficient from a CPW short-end discontinuity will be illustrated as an application example of the presented unified full-wave method.

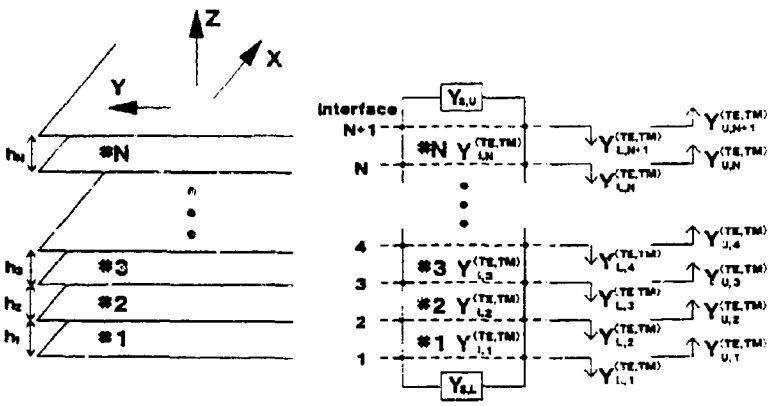

Figure 1: Multilayered substrate and its equivalent transmission line model

II. THEORY

A. Multilayered Green's Function and its Asymptotic Expression

Accurate Green's function is the essential element to solve the integral-equation formulated electromagnetic problems. The electric-field Green's function in a multilayered structure derived from an equivalent transmission line model was introduced by T. Itoh in 1980 [8]. Similar approach has been used in the derivation of the vector potentials [9]. In this paper, the derivation of the Green's function for the multilayered substrate follows that in [8]. In Fig.1, a layered substrate and its equivalent transmission line model are shown. The spectral-domain Green's function is derived by the transmission line theory and results in a recursion formula, which can be implemented numerically. In Fig.1, for a given (k_x, k_y) pair, $Y_{i,n}^{(TE,TM)}$ is the TE/TM wave admittance in the n^{th} layer. $Y_{U,n}^{(TE,TM)}$ and $Y_{L,n}^{(TE,TM)}$ are the equivalent input admittances at the n^{th} interface by looking up and down into the equivalent transmission line, respectively.

For a CPW configuration, the excitation source is horizontal electric fields on the slots. As a result, the multilayered spectral-domain Green's function at the n^{th} interface excited by the horizontal electric field source at the same interface is summarized as follows,

$$\begin{bmatrix} \tilde{J}_x \\ \tilde{J}_y \end{bmatrix}_n = -\begin{bmatrix} Y_{n,n}^{TE}\frac{k_y^2}{K^2} + Y_{n,n}^{TM}\frac{k_x^2}{K^2} & \left(-Y_{n,n}^{TE} + Y_{n,n}^{TM}\right)\frac{k_x k_y}{K^2} \\ \left(-Y_{n,n}^{TE} + Y_{n,n}^{TM}\right)\frac{k_x k_y}{K^2} & Y_{n,n}^{TE}\frac{k_x^2}{K^2} + Y_{n,n}^{TM}\frac{k_y^2}{K^2} \end{bmatrix} \begin{bmatrix} \tilde{E}_x \\ \tilde{E}_y \end{bmatrix}_n \tag{1}$$

where,

$$Y_{n,n}^{(TE,TM)} = Y_{U,n}^{(TE,TM)} + Y_{L,n}^{(TE,TM)} \tag{2}$$

$$K^2 = k_x^2 + k_y^2 \tag{3}$$

The asymptotic form of the spectral-domain Green's function is derived when the following conditions are met.

$$e^{-2\gamma_n h_n} \ll 1 \tag{4}$$

$$e^{-2\gamma_{n-1} h_{n-1}} \ll 1 \tag{5}$$

$$\frac{k_o^2 \epsilon_n \mu_n}{K^2} \ll 1 \tag{6}$$

$$\frac{k_o^2 \epsilon_{n-1} \mu_{n-1}}{K^2} \ll 1 \tag{7}$$

where $\gamma_n^2 = K^2 - k_o^2 \epsilon_n \mu_n$. Under these conditions, $Y_{U,n}^{(TE,TM)}$ and $Y_{L,n}^{(TE,TM)}$ are expressed as

$$Y_{U,n}^{(TE,TM)} = Y_{i,n}^{(TE,TM)} \left[1 + O\left(e^{-2\gamma_n h_n}\right)\right] \tag{8}$$

$$Y_{L,n}^{(TE,TM)} = Y_{i,n-1}^{(TE,TM)} \left[1 + O\left(e^{-2\gamma_{n-1} h_{n-1}}\right)\right] \tag{9}$$

And, the asymptotic expressions for $Y_{n,n}^{(TE,TM)}$ are determined to be

$$Y_{n,n}^{TE,asy} = \frac{-j\omega\epsilon_o}{k_o^2} \left(\frac{1}{\mu_{n-1}} + \frac{1}{\mu_n}\right) K \left[1 + O\left(\frac{1}{K^2}\right)\right] \tag{10}$$

$$Y_{n,n}^{TM,asy} = j\omega\epsilon_o \frac{\epsilon_{n-1} + \epsilon_n}{K^2} \left[1 + O\left(\frac{1}{K^2}\right)\right] \tag{11}$$

B. Unified Full-Wave Analysis

Full-Wave analyses, which employ the moment method to solve the electric field integral equations, were widely applied to characterize planar circuit discontinuities and printed circuit antennas. During the moment method procedure, heavily numerical effort is devoted to computing the matrix elements, which represent mutual coupling among the testing and expansion functions. The calculation of the matrix elements involves a sixfold integral as

$$Y_{m,n} = \int_{x_m} \int_{y_m} \int_{x_n'} \int_{y_n'} \int_{-\infty}^{\infty} \int_{-\infty}^{\infty} G(x, y; x_s, y_s; k_x, k_y) dk_x dk_y dy_s dx_s dy dx \tag{12}$$

The integrand $G(x, y; x_s, y_s; k_x, k_y)$ contains surface-wave poles and source-point singularity, where special care must be taken in the numerical integration. Traditionally, the calculation of the matrix element was performed either by the space-domain method or by the spectral-domain method.

The space-domain method [1,2] evaluated the (k_x, k_y) integrals in the cylindrical coordinates. Special contour integration on the complex K plane was used to account for the surface-wave contribution accurately. During the process, the precise locations of the surface-wave poles need to be pre-evaluated. In the outer space integrals, (x_s, y_s, x, y), the source-point

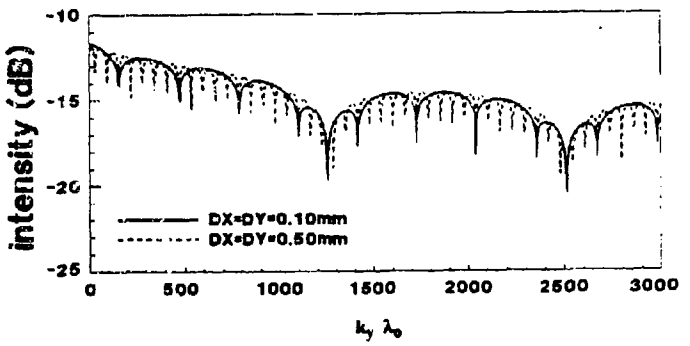

Figure 2: Comparison of the integrand behavior for two apertures of the same size but different spacing

singularity causes numerical inaccuracy when the expansion function and the testing function overlap.

The spectral-domain method utilized the properties of the Fourier-transform pairs of the expansion function and the testing function to evaluate the space integrals, (x_s, y_s, x, y), in a close form. In the (k_x, k_y) integrals, the triangular contour [10] was used to avoid the surface-wave poles. It yielded very accurate mutual-coupling computation. However, when the testing function and the expansion function are electrically far apart, the highly oscillatory integrand needs to be computed. To illustrate, the spectral-domain integrands of two rectangular apertures of the same size but different spacing are plotted in Fig.2. These two apertures are with the size of 0.05 mm × 0.05 mm and are on the dielectric substrate of (h = 0.2 mm, ϵ_r = 13.2). At 30.0 GHz, the integrands are examined at the fixed k_x, where $k_x = 50/\lambda_0$. The solid line describes the integrand behavior respected to k_y when two apertures are apart by $DX = DY$ = 0.1 mm. The dotted line represents the integrand of that when $DX = DY$ = 0.5 mm. To accurately compute this highly oscillatory integrand in the spectral domain when apertures are electrically far apart, a large integration area and dense sampling in the spectral domain are needed. Consequently, longer computing time is required.

A solution to simultaneously improve the numerical accuracy and efficiency is to combine the space-domain and spectral-domain schemes; and this leads to the unified full-wave method. With the apertures depicted in Fig.3 , the sixfold integral is decomposed into the summation of the low-frequency terms and the high-frequency asymptotic terms as

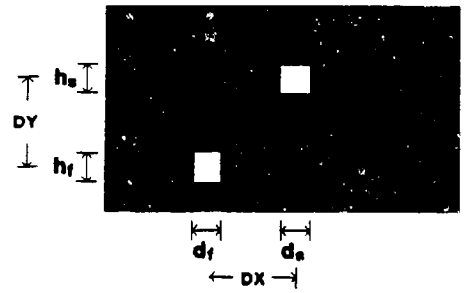

Figure 3: Aperture dimensions and relative locations

$$
\begin{aligned}
Y_{n,n}^{yy} &= \int_0^\infty \int_0^\infty -\frac{1}{\pi^2}\left[Y_{n,n}^{TE}\frac{k_y^2}{k^2} + Y_{n,n}^{TM}\frac{k_x^2}{k^2}\right] S(k_y;h_f)S(k_y;h_s)T(k_x;d_f)T(k_x;d_s)\cdot \\
&\qquad \cos(k_x DX)\cos(k_y DY)dk_x dk_y \\
&= Y_1^{yy} + Y_2^{yy} + Y_3^{yy} - Y_4^{yy} + Y_5^{yy} \qquad (13)
\end{aligned}
$$

where

$$
\begin{aligned}
Y_1^{yy} &= \int_0^{K^s} S(k_y;h_f)S(k_y;h_s)\cos(k_y DY)\left\{\int_0^{K^{asy}} -\frac{1}{\pi^2}\left[Y_{n,n}^{TE}\frac{k_y^2}{k^2} + Y_{n,n}^{TM}\frac{k_x^2}{k^2}\right]\cdot\right. \\
&\qquad \left. T(k_x;d_f)T(k_x;d_s)\cos(k_x DX)dk_x\right\}dk_y \qquad (14)
\end{aligned}
$$

$$
\begin{aligned}
Y_2^{yy} &= \int_{K^s}^{K^{asy}} S(k_y;h_f)S(k_y;h_s)\cos(k_y DY)\left\{\int_0^{K^{asy}} -\frac{1}{\pi^2}\left[\left(Y_{n,n}^{TE} - Y_{n,n}^{TE,asy}\right)\frac{k_y^2}{k^2} + \right.\right. \\
&\qquad \left.\left.\left(Y_{n,n}^{TM} - Y_{n,n}^{TM,asy}\right)\frac{k_x^2}{k^2}\right]T(k_x;d_f)T(k_x;d_s)\cos(k_x DX)dk_x\right\}dk_y \qquad (15)
\end{aligned}
$$

$$
\begin{aligned}
Y_3^{yy} &= \int_0^{K^s} S(k_y;h_f)S(k_y;h_s)\cos(k_y DY)\left\{\int_{K^{asy}}^\infty -\frac{1}{\pi^2}\left[Y_{n,n}^{TE,asy}\frac{k_y^2}{k^2} + Y_{n,n}^{TM,asy}\frac{k_x^2}{k^2}\right]\cdot\right. \\
&\qquad \left. T(k_x;d_f)T(k_x;d_s)\cos(k_x DX)dk_x\right\}dk_y \qquad (16)
\end{aligned}
$$

$$
\begin{aligned}
Y_4^{yy} &= \int_0^{K^s} S(k_y;h_f)S(k_y;h_s)\cos(k_y DY)\left\{\int_0^\infty -\frac{1}{\pi^2}\left[Y_{n,n}^{TE,asy}\frac{k_y^2}{k^2} + Y_{n,n}^{TM,asy}\frac{k_x^2}{k^2}\right]\cdot\right. \\
&\qquad \left. T(k_x;d_f)T(k_x;d_s)\cos(k_x DX)dk_x\right\}dk_y \qquad (17)
\end{aligned}
$$

$$
\begin{aligned}
Y_5^{yy} &= \int_0^\infty S(k_y;h_f)S(k_y;h_s)\cos(k_y DY)\left\{\int_0^\infty -\frac{1}{\pi^2}\left[Y_{n,n}^{TE,asy}\frac{k_y^2}{k^2} + Y_{n,n}^{TM,asy}\frac{k_x^2}{k^2}\right]\cdot\right. \\
&\qquad \left. T(k_x;d_f)T(k_x;d_s)\cos(k_x DX)dk_x\right\}dk_y \qquad (18)
\end{aligned}
$$

where the functions S and T are the Fourier transform of the PWS and the pulse functions, respectively. The constant K^{asy} is selected to satisfy the asymptotic conditions listed in (4)-(7).

K^a is selected to be less than the lowest surface wavenumber but large enough to avoid the singularity of the asymptotic expression at $K = 0$.

Y_1^{yy} and Y_2^{yy} are with double finite integrals which contain surface-wave poles. They are computed in the spectral domain by the triangular contour integration. The inner integral of Y_3^{yy} can be evaluated in a close form, and the outer finite integral is directly computed in the spectral domain. During the computation of r_4^{yy}, the space-domain scheme is used for the k_x integral to evaluate the integratible singularity analytically; and the k_y integral is performed in the spectral domain numerically. Y_5^{yy} is contributed by the asymptotic term of the integrand. A close form expression for (k_x, k_y) integral can be obtained by converting Y_5^{yy} into the space domain.

$$Y_5^{yy} = \frac{j\omega\epsilon_c}{\pi}\int_{-\frac{c_f}{2}}^{\frac{d_f}{2}}\int_{DX-\frac{d_s}{2}}^{DX+\frac{d_s}{2}}\int_{-h_f}^{h_f}\int_{DY-h_s}^{DY+h_s}\frac{\sin k_e(h_f-|y|)}{\sin k_e h_f}\frac{\sin k_e(h_s-|y-DY|)}{\sin k_e h_s}\cdot F(|x_s-x|,|y_s-y|)dy_s dy dx_s dx \tag{19}$$

where

$$F(u,v) = \frac{1}{2k_o^2}\left(\frac{1}{\mu_{n-1}}+\frac{1}{\mu_n}\right)\left[(u^2+v^2)^{-1.5}-3v^2(u^2+v^2)^{-2.5}\right]-\frac{\epsilon_{n-1}+\epsilon_n}{2}(u^2+v^2)^{-0.5} \tag{20}$$

C. Numerical Example

A comparison of the computing time between the spectral-domain method and the unified full-wave method was conducted. The test was performed on the single-layered CPW with the dielectric constant of 13.1 and the thickness of 0.2 mm. The dimensions of the two apertures, as shown in Fig.3, are equal and with $h_s = h_f = d_s = d_f = 0.05$ mm. The numerical inaccuracy for both methods was controlled to be less than 0.001%. The numerical program was executed on a 486/33 MHz PC. At 30 GHz, the computing time from each method is plotted as a function of spacing $D = DX = DY$. In Fig.4, it illustrates that the computing time of the spectral-domain method increases linearly as the spacing increases; while that of the unified full-wave method maintains near a constant.

An application example of this unified full-wave method is to characterize the CPW short-end discontinuity. The aperture electric fields of the CPW short-end was expanded into PWS and semi-infinite expansion functions as that in [7]. Fig.5 shows the calculated effective length extension of the CPW even and odd mode incidence versus frequency. Good agreement has been observed by comparing to the published data [11].

IV. CONCLUSIONS

The unified full-wave analysis, which merges the advanced schemes from the space-domain and the spectral-domain methods, was introduced. Its dynamic and accurate computational

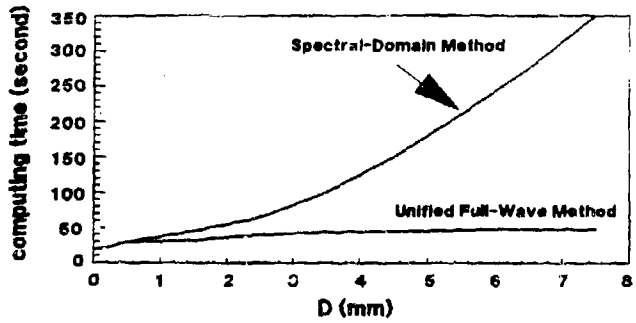

Figure 4: Computing time of two apertures with various spacing

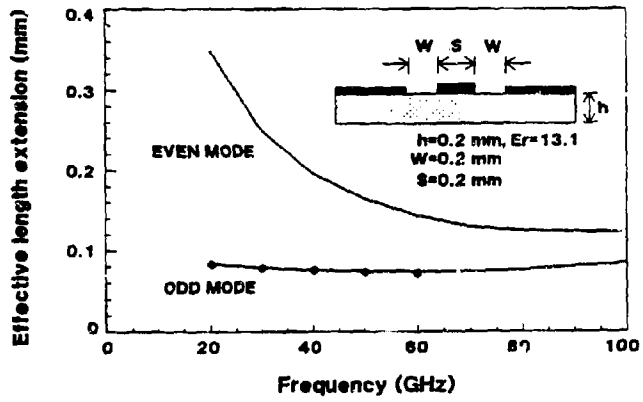

Figure 5: Effective length extension of a CPW short-end.
—— unified full-wave method, • Dib & Katehi [11]

SESSION 2:

TRANSMISSION LINE METHOD (TLM)

Chair: Wolfgang Hoefer

New Rectangular Series Node in 2D-TLM Network

Qi Zhang and Wolfgang J.R. Hoefer

NSERC/MPR Teltech Research Chair in RF Engineering
Department of Electrical and Computer Engineering
University of Victoria, Victoria, B.C., Canada V8W 3P6

Abstract

This paper presents a new modification of the transmission line matrix method of numerical analysis in two dimensions. The traditional square series mesh 2D-TLM algorithm is generalized for rectangular meshes of arbitrary aspect ratio. Reactive stubs are not needed in this scheme. The basic theory of the two-dimensional rectangular mesh is described in detail. A full dispersion analysis of the rectangular mesh is then performed for the general case, and the results are compared to the properties of the traditional square mesh.

Introduction

The transmission line matrix (TLM) method was proposed by P.B. Johns for the analysis of microwave strucnures [1]. The foundation of this method is the well-known concept of modelling field space by lumped networks[2], where these networks have been built to solve the wave equation. Using a distributed parameter transmission-line network model, the propagation space is represented by a mesh of TEM transmission lines. Electric and magnetic fields are equivalent to voltages and currents on the network. Two-dimensional propagation space can be modelled by either a shunt or a series matrix[3]. Traditional TLM schemes are restricted to square mesh elements. This affects the efficiency of the method whenever the resolution requirements differ considerably in different coordinate directions. To overcome this problem, Al-Mukhtar and Sitch proposed modifications to 'conventional TLM' which allow the mesh to be graded by means of stubs[4], but the dispersion error is increased in the mesh, and more computer memory is required. Recently, Hoefer and Sautier have proposed a more general 2D-TLM algorithm which removes the restriction that the cell must be square [5]. The basic theory of the two-dimensional rectangular TLM shunt meshes of arbitrary aspect ratio was described, and the 2D stub-free rectangular shunt node was introduced.

In this paper these concepts will be reviewed and extended to the 2D rectangular series node. The space and frequency dispersion characteristics of the rectangular series node will be derived and compared to those of the equivalent square mesh. The three-dimensional expanded node is presently being developed which incorporates the same idea, leading to a more efficient space discretization.

The Properties of the 2D Rectangular Series-Connected Network

The 2D rectangular series mesh is sketched in Fig.1. Fig.2 shows the rectangular series node and its equivalent circuit. This node represents three field components of TM modes, namely E_x, E_z and H_y.

In the rectangular series mesh the desired features are as follows[5]:

1. Impulse Synchronism: The velocities of impulses on the dispersionless link lines must be such that the transit time Δt is the same for all lines. According to this property the line velocity is proportional to the line length:

$$\frac{v_x}{v_z} = \frac{k_z}{k_x} = \frac{\Delta x}{\Delta z} = \alpha \tag{1}$$

where $\alpha = \Delta x/\Delta z$ is the aspect ratio of the rectangular element.

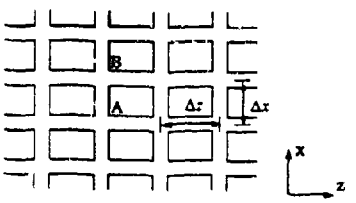

Figure 1. Two dimensional rectangular series mesh

2. Isotropic Wave Properties: In the infinitesimal limit, the plane wave network velocity v_n is the same in both coordinate directions (and in all other directions as well).

$$v_{nx} = v_{nz} \quad \text{and} \quad k_{nx} = k_{nz} \tag{2}$$

We will now determine the electrical parameters of the mesh lines such that the mesh has these two properties. To determine the slow-wave properties of the series mesh along one of the coordinate directions, it is sufficient to consider a single series cell which has its arms in the other direction short-circuited. In z-direction the mesh is characterized by a transmission line of inductance L_z and capacitance C_z per unit length. The total shunt capacitance of a cell is thus:

$$C_{tot} = C_z \Delta x \tag{3}$$

and the total series inductance of this cell is

$$L_{tot} = L_x \Delta x + L_z \Delta z \tag{4}$$

To get the capacitance and inductance per unit length in z direction, Eqs. 3 and 4 must be divided by Δz

$$C_{nz} = C_z \tag{5}$$

$$L_{nz} = \alpha L_x + L_z \tag{6}$$

The network velocity in z-direction is

$$v_{nz} = \frac{1}{\sqrt{L_{nz}C_{nz}}} = \frac{1}{\sqrt{C_z(L_z + \alpha L_x)}} \tag{7}$$

The inductance and capacitance of the link line in x-direction are L_x and C_x. The total capacitance of the cell in x-direction is

$$C_{tnx} = C_x \Delta x \tag{8}$$

and the total inductance in x-direction is

$$L_{tnx} = L_x \Delta x + L_z \Delta x \tag{9}$$

We obtain the corresponding values per unit length when dividing by Δx.

$$C_{nx} = C_x \quad \text{and} \quad L_{nx} = L_x + \frac{L_z}{\alpha} \tag{EQ 10}$$

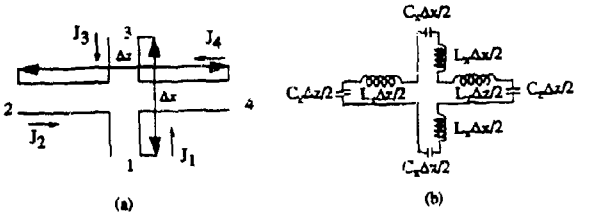

Figure 2. The unit cell of the 2D TLM series network. (a) rectangular series node. (b) equivalent lumped element model.

The network velocity in x direction is

$$v_{nx} = \frac{1}{\sqrt{C_{nx}L_{nx}}} = \frac{1}{\sqrt{C_x(L_x + \frac{L_z}{\alpha})}} \tag{EQ 11}$$

For isotropic wave property the network velocities in x- and z-direction must be equal.

$$C_x(L_x + \frac{L_z}{\alpha}) = C_z(L_z + \alpha L_x) \tag{EQ 12}$$

The phase velocities of the link lines are

$$v_x = \frac{1}{\sqrt{L_x C_x}} \quad \text{and} \quad v_t = \frac{1}{\sqrt{L_t C_t}} \tag{EQ 13}$$

From property 1 we know the ratio of phase velocities.

$$\frac{v_x}{v_t} = \frac{\Delta x}{\Delta z} = \frac{\sqrt{L_t C_t}}{\sqrt{L_x C_x}} = \alpha \tag{EQ 14}$$

Combining Eqs. 12 and 14 yields

$$1 + \frac{L_t}{\alpha L_x} = \frac{\alpha^3 L_x}{L_t} + \alpha^2 \tag{EQ 15}$$

By solving Eq. 15, the ratio of inductances can be obtained.

$$\frac{L_t}{L_x} = \frac{1}{\alpha^3} \tag{EQ 16}$$

Then we can determine the ratio of intrinsic impedances.

$$\frac{Z_{wx}}{Z_{wt}} = \frac{\sqrt{L_x C_x}}{\sqrt{L_t C_t}} = \frac{1}{\alpha^2} \tag{EQ 17}$$

The scattering matrix of this node is thus

$$[S] = \frac{1}{1+\alpha^2}\begin{bmatrix} \alpha^2 & \alpha & 1 & -\alpha \\ \alpha & 1 & -\alpha & \alpha^2 \\ 1 & -\alpha & \alpha^2 & \alpha \\ -\alpha & \alpha^2 & \alpha & 1 \end{bmatrix} \tag{EQ 18}$$

If the transmission lines are approximated by lumped inductors and capacitances as illustrated in Fig.2(b) then a pair of coupled transmission line equations can be formulated:

$$\frac{\partial I_y}{\partial x} = C_x \frac{\partial}{\partial t}(-\alpha V_t) \quad , \quad \frac{\partial I_y}{\partial z} = -C_t \alpha \frac{\partial}{\partial t}\left(\frac{V_x}{\alpha}\right) \quad \text{and} \quad \frac{\partial}{\partial z}\left(\frac{V_x}{\alpha}\right) - \frac{\partial}{\partial x}(-\alpha V_t) = -\left(\frac{L_t}{\alpha} + L_x \alpha^2\right)\left(\frac{1+\alpha^2}{2\alpha^2}\right)\frac{\partial I_y}{\partial t} \tag{EQ 19}$$

with the equivalences

$$H_y = I_y \quad , \quad E_t = -\alpha V_t \quad \text{and} \quad E_x = \frac{V_x}{\alpha} \tag{EQ 20}$$

$$\varepsilon = C_x = \alpha C_t \quad \text{and} \quad \mu = \left(\frac{L_t}{\alpha} + \alpha^2 L_x\right)\left(\frac{1+\alpha^2}{2\alpha^2}\right) \tag{EQ 21}$$

Eqs. 19 reduce to Maxwell's equations for the TM case with

$$H_x = H_z = E_y = 0 \quad \text{and} \quad \frac{\partial}{\partial y} = 0 \tag{EQ 22}$$

Thus, the series node matrix provides a solution for the H_y, E_x and E_t in the xz-plane.

The relationship between network velocity v_n and mesh line velocities v_x and v_z is the same in shunt-connected and series-connected networks. For $\alpha = 1$, the special case of a square mesh is obtained. The square mesh with a network velocity v_n is called the equivalent square mesh.

$$v_n = \frac{1}{\sqrt{C_z L_z (1+\alpha^2)}} = \frac{1}{\sqrt{C_z L_z (1+\frac{1}{\alpha^2})}} \quad \text{(EQ 23)}$$

$$v_x = v_n\sqrt{1+\alpha^2} \quad \text{and} \quad v_z = v_n\sqrt{1+\frac{1}{\alpha^2}} \quad \text{(EQ 24)}$$

$$\Delta l = \Delta x\sqrt{\frac{2}{1+\alpha^2}} = \Delta z\sqrt{\frac{2}{1+\frac{1}{\alpha^2}}} \quad \text{(EQ 25)}$$

where Δl is the mesh parameter of the equivalent square mesh.

For a given length of transmission line between nodes, it is necessary to estimate the range of frequencies for which the above approximate analysis is valid. The propagation properties of a periodic structure can be analyzed by dividing the network into individual cells and assume that a current wave travels through the network as a Floquet mode[6].

The total voltage V_c at the series node is

$$V_c = \frac{1}{1+\alpha^2}(-V_1 + \alpha^2 V_2 + V_3 - \alpha^2 V_4) \quad \text{(EQ 26)}$$

The currents into the node at the node center are denoted as J_p, where "p" is the line number. At the center of the adjacent nodes, the currents are J_p^*. J_c is the value of the current flowing around the center of the series node. For the pth branch we have

$$V_p^* = T V_p^{**} \quad \text{and} \quad V_p^{**} = T^{-1} V_p^* \quad \text{(EQ 27)}$$

where $T = e^{-jk_n\Delta l}$.

$$J^* = Y_n(V^* - V^{**}) \quad \text{(EQ 28)}$$

where Y_n is the intrinsic admittance.

For the four branches the currents can be written as

$$J_1^* = Y_n((T^{-1} - T)V_1^* - TV_c) \quad \text{and} \quad J_2^* = Y_n((T^{-1} - T)V_2^* + TV_c) \quad \text{(EQ 29)}$$

$$J_3^* = Y_n((T^{-1} - T)V_3^* + TV_c) \quad \text{and} \quad J_4^* = Y_n((T^{-1} - T)V_4^* - TV_c) \quad \text{(EQ 30)}$$

J_1^*, J_2^* and J_3^* are multiplied by -1, α^2 and $-\alpha^2$ respectively, and J_4^* is added to yield

$$-J_1^* + \alpha^2 J_2^* + J_3^* - \alpha^2 J_4^* = (1+\alpha^2)(T^{-1} + T)J_c \quad \text{(EQ 31)}$$

Floquet's theorem is applied to the series node, and an eigensolution to Eq. 31 is postulated based on the assumption that

$$J_1^* = -J_c e^{jk_{ez}\Delta z} \quad , \quad J_2^* = J_c e^{jk_{ex}\Delta x} \quad , \quad J_3^* = J_c e^{-jk_{ez}\Delta z} \quad \text{and} \quad J_4^* = -J_c e^{-jk_{ex}\Delta x} \tag{EQ 32}$$

By combining J_1^*, J_2^*, J_3^* and J_4^* the dispersion relation of the rectangular mesh is obtained:

$$\cos(k_{ex}\Delta x) + \alpha^2 \cos(k_{ez}\Delta z) = (1+\alpha^2)\cos(k_0\Delta l) \tag{33}$$

This equation is exactly the same as the dispersion relation of the rectangular shunt node.

The dispersion for arbitrary propagation directions is illustrated in Fig. 3. The normalized propagation vector is plotted in a polar representation. In Fig.3 the vector k_0 describes the unit circle for the infinitesimal mesh case. When a coarse discretization is selected, for example ($\Delta z/\lambda$=0.15), the wavelength can not be considered very large compared to Δz, and the velocity becomes frequency dispersive and depends on the propagation direction. The maximum dispersion occurs in the axial direction. In this example the parameter Δz is larger than Δx; thus, the propagation vector is larger along the longer mesh, and the dispersion is higher in z-direction. Checking the dispersion relation along the main axes, we know

$$\begin{cases} \cos k_{ez}\Delta z = \cos k_z\Delta z - \dfrac{1}{\alpha^2}\tan\left(k_x\dfrac{\Delta x}{2}\right)\sin k_z\Delta z \\ \cos k_{ex}\Delta x = \cos k_x\Delta x - \alpha^2\tan\left(k_z\dfrac{\Delta z}{2}\right)\sin k_x\Delta x \end{cases} \tag{EQ 34}$$

and

$$\begin{cases} k_{ez} = \dfrac{1}{\Delta z}\arccos\left(\cos k_z\Delta z - \dfrac{1}{\alpha^2}\tan\left(k_z\dfrac{\Delta z}{2}\right)\sin k_z\Delta z\right) \\ k_{ex} = \dfrac{1}{\alpha\Delta z}\arccos\left(\cos k_z\Delta z - \alpha^2\tan\left(k_z\dfrac{\Delta z}{2}\right)\sin k_z\Delta z\right) \end{cases} \tag{EQ 35}$$

The above dispersion relations are shown in Fig. 4. Compared with the reference square mesh, the higher dispersion occurs in z-direction. It is consistent with the result presented in Fig. 3.

Conclusion

In this paper the traditional square series node TLM algorithms are generalized for rectangular cells of arbitrary aspect ratio. It is shown that the anisotropic rectangular TLM networks can be conceived in such a way that the propagation vector remains independent of the direction of propagation in the infinitesimal approximation. A full dispersion analysis of the rectangular series mesh is then performed for the general case, and the results are compared to that of the traditional square mesh.

Acknowledgments

The authors thank P. So and P. Sautier for many helpful discussions and comments.

References

[1] P.B. John and R.L. Beurle: 'Numerical solution of 2-dimensional scattering problems using a transmission-line matrix', Proc. IEE, 1971, 118, (9), pp. 1203-1208

[2] J.R. Whinnery and S. Ramo: 'A new approach to the solution of high-frequency field problems', Proc. IRE,1944, 32, pp. 284-288.

[3] W.J.R. Hoefer: 'The transmission line matrix (TLM) method', in Numerical Techniques for Microwave and Millimeter Wave Passive Structures, T. Itoh, Ed. New York:Wiley, 1989.

[4] D.A. Al-Mukhtar and J.E. Sitch: 'Transmission-line matrix method with irregularly graded space', Proc. IEE, Vol 128, Pt. H, No. 6, Dec. 1981, pp.299-305.

[5] W.J.R. Hoefer and P. Sautier: 'Characteristics of the general rectangular 2D-TLM network' (to be published in International Journal of Numerical Modelling Electronic Networks, Devices and Fields).

[6] J.S. Nielsen: 'TLM analysis of microwave and millimeter wave structures with embedded nonlinear devices' Ph. D. thesis, University of Ottawa, 1992, Chapter 2.b.

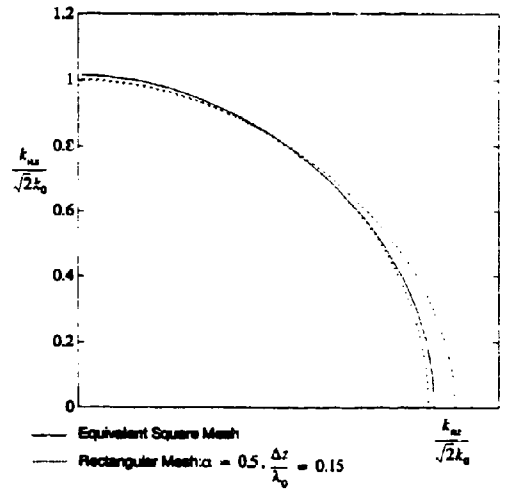

Figure 3. Dispersion of the normalized propagation vector in a bitrary direction in a rectangular series mesh.

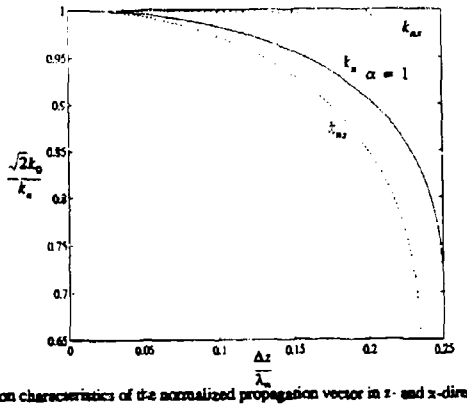

Figure 4. Dispersion characteristics of the normalized propagation vector in z- and x-directions for $\alpha = 0.5$ (Rectangular series mesh) and $\alpha = 1$ (Square mesh).

Plane-Wave Illumination for the TLM method using a partial Huygen's surface

J.F. Dawson†, D. D. Ward‡, S.J. Porter†, and S. Lawton‡
†Department of Electronics, University of York, England
‡MIRA, The Motor Industry Research Association , England

January 11, 1994

Abstract

An efficient solution to the problems associated with plane wave illumination of a scattering body in a TLM mesh, initially presented in [1] is explained. The equivalence of the solution to a partial implementation of the Huygen's surface [2] (used in the Time-Domain Finite Difference (TDFD) method) is outlined. The method allows the use of considerably smaller TLM meshes for scattering problems excited with a plane wave source than previously possible. The method uses the TLM mesh itself to generate the equivalent of retarded surface currents for the Huygen's surface. This gives automatic compensation for any dispersion in the mesh. The method is therefore suitable for problems using a graded mesh without further modification. New results are presented which demonstrate the efficacy of the solution and compare its performance with other methods of plane wave illumination.

1 Introduction

The Transmission Line Matrix (TLM) method of numerical electromagnetic analysis using the symmetrical condensed node is well known [3]. It has been widely used to determine scattering from structures under plane wave illumination [4]. However the problems of obtaining an accurate plane wave are not well reported. Here we will address these problems and provide a simple and efficient solution.

When a plane wave is excited in a finite TLM mesh with matched[1] boundaries, the sudden truncation of the mesh causes a second wavefront to be generated at each boundary. This is due mainly to the physical truncation of the wavefront at the boundaries and to a lesser extent to the fact that the boundary does not represent a true radiation boundary condition.

The problem of plane wave illumination is often overcome using problem boundaries which have a $+1$ reflection coefficient (magnetic walls) at the edge of the wave parallel to the electric field and -1 reflecting boundaries (electric walls) perpendicular to the electric field. This produces an ideal waveguide in which a plane wave can propagate. However the reflecting walls also serve to return waves scattered by the illuminated object to the observation point and thus interferes with the observation of the direct scattered waves.

[1] The transmission lines at the outer surface being terminated in a matched load.

In order to avoid this the problem space must be made large enough that reflections from the boundaries do not reach the observation point in the time span of the simulation. However this results in an excessively large problem space and may not be possible where a large number of iterations are required (e.g. when a high-Q resonant structure is present).

The implementation of asymmetric boundaries, equivalent to a partial Huygen's surface, discussed in this paper provides an efficient solution to the problems outlined above.

2 Illustration of performance

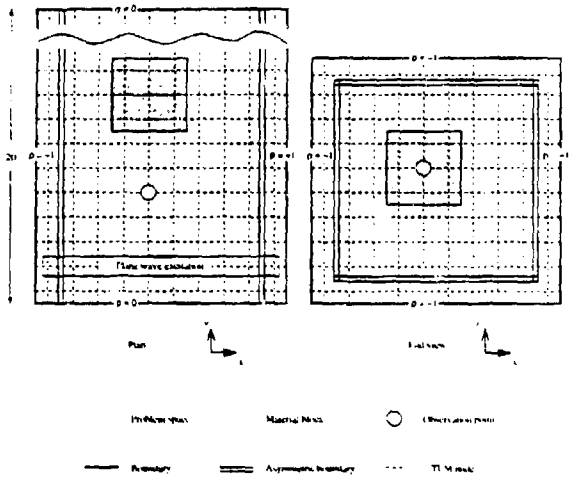

Figure 1: Arrangement of asymmetric boundaries within the TLM mesh.

In order to demonstrate this a simple Gaussian plane wave was excited in a TLM mesh, with a 10x10 node cross section (Fig. 1), and the field observed for three scenarios (Fig. 2):

1. with the wave propagating in the mesh with asymmetric boundaries as described below – the Gaussian profile is preserved;
2. with no asymmetric boundaries and matched terminations at the edges of the mesh – a considerable negative excursion occurs after the initial Gaussian pulse due to the truncation of the wavefront at the boundaries of the problem;
3. with the same 10x10 node plane wave as in 2) in a larger mesh (60x60) – a similar time response occurred showing that the negative excursion is mainly due to the truncation of the wave rather than failure of the boundary in some way.

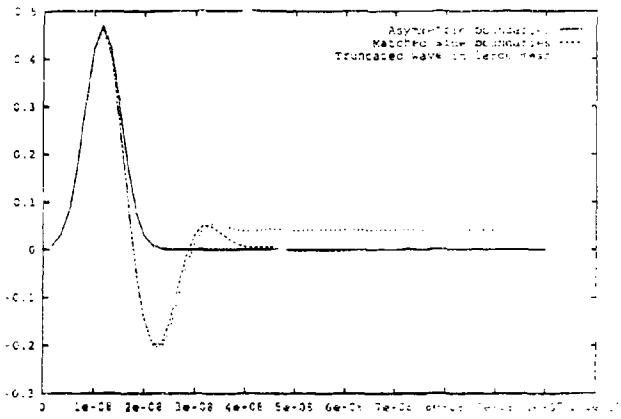

Figure 2: Comparison of a Gaussian pulse propagation with asymmetric boundaries, with matched boundaries in 10x10 cross section mesh, and a truncated 10x10 plane wave in 60x60 mesh (no scatterer).

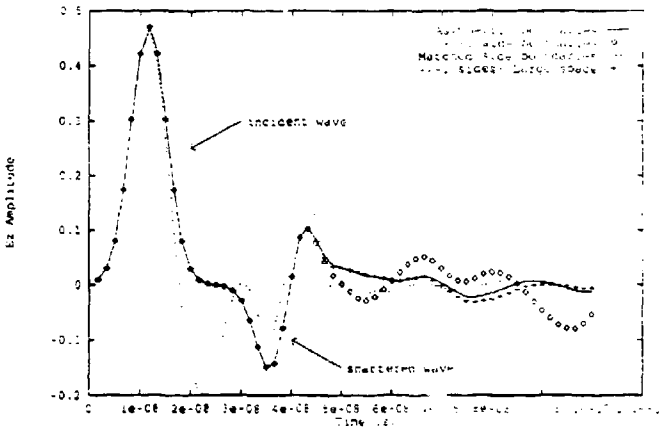

Figure 3: Comparison of Gaussian pulse plane wave in the different meshes with scattering object.

Fig. 3 show the time history at the observation point with the scattering object (Fig. 1) present. It can be seen that the use of the partial Huygen's surface gives results (solid line) which correspond very closely to the ideal case (+ points) with [illegible] boundaries used with a very large (60x20x60) mesh size but this is achieved with a small (10x20x10) mesh size. The large mesh size ensures that the reflections from the boundaries do not reach the

observation point within the observed time span. For the small mesh size $+/-1$ boundaries result (diamonds) in multiple reflections which distort the observation of the scattered field as does the additional wavefront if matched boundaries are used (broken line).

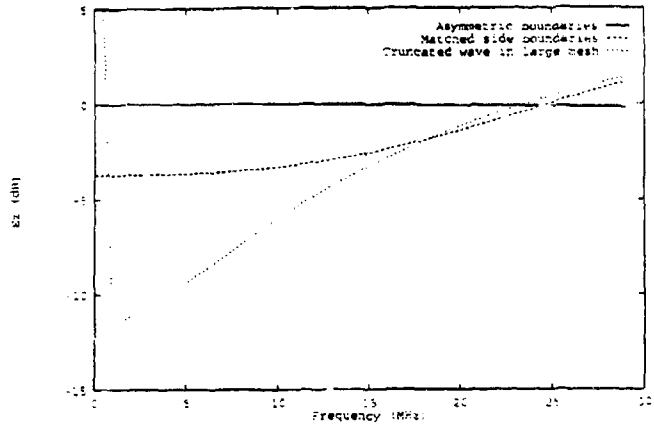

Figure 4: Comparison of the spectrum with asymmetric boundaries, with matched boundaries in 10x10 cross section mesh, and a truncated 10x10 plane wave in 60x60 mesh (impulsive excitation).

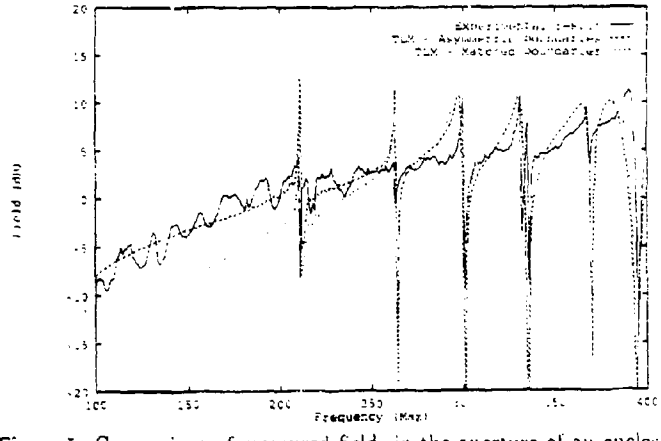

Figure 5: Comparison of measured fields in the aperture of an enclosure with TLM simulation using asymmetric and matched boundaries

Fig. 4 shows the spectrum of the wavefront incident at the observation point with impulsive excitation for the same scenarious as in Fig. 2. A 1 m node pitch is assumed. It

can be seen that the spectrum of the incident wave is flat when the partial Huygen's surface is used whilst the use of matched boundaries gives reduced energy at low frequencies. The truncated (10x10) wave in a large (60x60) mesh exhibits a large dc component but otherwise has very little energy at the low frequency end of the spectrum.

Fig. 5 compares the results obtained with asymmetric boundaries and matched boundaries with experimental results. An enclosure (Fig.6) with an aperture is placed in a semi-anechoic chamber and illuminated with a vertically polarised wave of constant amplitude. In the TLM simulation a plane wave was used, the ground plane was represented by a -1 reflecting boundary, and the walls of the semi-anechoic chamber were represented by matched or asymmetric boundaries. The field in the aperture is then plotted . In the TLM simulation it can be seen that the use of asymmetric boundaries gives a result much closer to experiment than the use of matched boundaries. However the magnitudes of first two resonant peaks, and the field minima are not predicted accurately by TLM. This may be due to the fact that the walls of the enclosure were lossless (-1 reflection coefficient) in the TLM simulation whilst the reflections from the walls of the real enclosure would not be lossless.

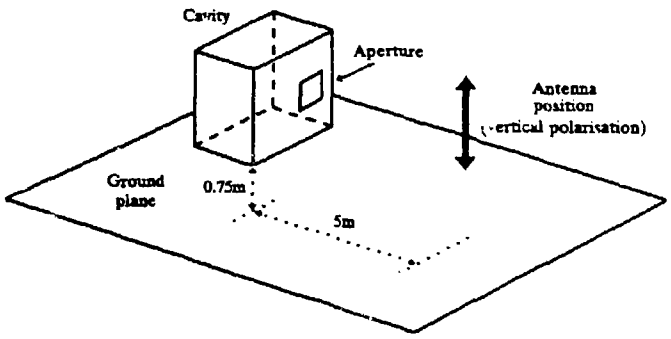

Figure 6: Experimental layout for enclosure.

3 Implementation

Using a set of simple asymmetric boundaries in the TLM mesh the distortion of the wavefront due to the discontinuity of the plane wave can be removed whilst still maintaining a matched boundary for the scattered field. As shown in Fig. 1 the TLM mesh is terminated with -1 reflection coefficient boundaries on the faces perpendicular to the electric field of the plane wave, -1 reflection boundaries parallel to the electric field, and matched boundaries on the remaining two faces. Asymmetric boundaries are constructed, as a tube, parallel to the direction of propagation of the plane wave, one mesh unit inside the TLM mesh.

The reflection coefficient of the inside faces of the asymmetric boundaries is set to zero (matched) as is the transmission coefficient. This means that the problem space appears to have matched boundaries on all sides for the scattered fields. Also no energy from the inner problem space can reach the outer region between the asymmetric boundaries and the sides of the TLM mesh. The outer faces of the asymmetric boundaries have reflection coefficients identical to the outer boundary which they face and a unity transmission coefficient. Thus a (plane) wave can propagate in the waveguide formed by the asymmetric boundaries and outer surface of the mesh undisturbed by any waves from within the problem space. However if a plane wave is excited across the entire cross section of the TLM mesh (as in Fig. 1) the parts of the wave propagating in the problem space and the outer layer are in time phase and will remain so regardless of any dispersion in the mesh. The energy transmitted from the outer layer to the problem space provides the necessary continuity so that the wave in the problem space is not truncated and thus no spurious wavefronts are generated.

Therefore, by the use of asymmetric boundaries we have achieved propagating conditions for the exciting plane wave as if we had used $+/-1$ problem space boundaries to create a waveguide capable of sustaining the wave, whilst for scattered fields the problem space has matched boundaries. The method can be shown to be equivalent to a partial implementation of a Huygen's surface as used in the TDFD method.

4 Theory

Let us consider the implications of using the reflection coefficients specified on the boundaries of the exciting surface (the asymmetric boundaries and the plane of initial excitation). In particular, let us consider three points on the surface

a) a point on the surface where the plane wave starts (minimum y coordinate);

b) a point on the right-hand surface (maximum x coordinate);

c) a point on the top surface (maximum z coordinate).

If we consider the voltage which is implicitly added in when using the appropriate reflection coefficients on these surfaces then we get for each point

a) a positive z-directed voltage, V_z, flowing in the positive y-direction (into the interior scattering region surrounded by the surface) and zero component flowing in the negative y-direction (into the exterior region of the surface);

b) a negative z-directed voltage, $-V_z/2$, flowing in the positive x-direction (out of the scattering region) and a positive z-directed voltage, $V_z/2$, flowing in the negative x-direction (into the scattering region);

c) a positive y-directed voltage, $V_y/2$, flowing in the positive z-direction (out of the scattering region) and a positive y-directed voltage, $V_y/2$, flowing in the negative z-direction (into the scattering region).

It is possible to calculate the actual fields we are creating at the boundaries of the scattering region. For the case of a boundary in the xz-plane with two voltages flowing outwards along the y-direction, the field components are

$$\mathbf{E} = E_z = \frac{V_z(\hat{y}) + V_z(-\hat{y})}{\Delta l} \tag{5}$$

$$\mathbf{H} = H_x = \frac{V_z(\hat{\mathbf{y}}) - V_z(-\hat{\mathbf{y}})}{Z_0 \Delta l} \tag{2}$$

where $V_z(\hat{\mathbf{y}})$ and $V_z(-\hat{\mathbf{y}})$ are the z-directed voltage pulses travelling in the positive and negative y directions respectively. Similar expressions can be given for the other boundaries.

Using equations 1 and 2 then allows us to calculate the fields created at the three boundaries. We get

a)

$$\mathbf{E} = E_z = \frac{V_z}{\Delta l} = \frac{V}{\Delta l} \tag{3}$$

$$\mathbf{H} = H_x = \frac{V_z}{Z_0 \Delta l} = \frac{V}{Z_0 \Delta l} \tag{4}$$

b)

$$\mathbf{E} = E_x = 0 \tag{5}$$

$$\mathbf{H} = H_y = \frac{V_z}{Z_0 \Delta l} = \frac{V}{Z_0 \Delta l} \tag{6}$$

c)

$$\mathbf{E} = E_y = \frac{V_y}{\Delta l} = \frac{V}{\Delta l} \tag{7}$$

$$\mathbf{H} = H_z = 0 \tag{8}$$

where we have used the relation $V_z = V_y = V$, say.

Using Maxwell's curl equations it is then possible to write down expressions for appropriate electric and magnetic source current densities on the surfaces which would give rise to the fields. We would need to apply the currents

a)

$$\mathbf{J} = \frac{V}{Z_0 \Delta l} \tag{9}$$

$$\mathbf{M} = \frac{V}{\Delta l} \tag{10}$$

b)

$$\mathbf{J} = 0 \tag{11}$$

$$\mathbf{M} = \frac{V}{\Delta l} \tag{12}$$

c)

$$\mathbf{J} = \frac{V}{Z_0 \Delta l} \tag{13}$$

$$\mathbf{M} = 0 \tag{14}$$

If we now consider the creation of a similar plane wave using the Huygens formalism described in [2], we see that we need to apply currents to the surface given by

$$\mathbf{M}^h = \mathbf{E}^h \times \hat{\mathbf{n}} \tag{15}$$

$$\mathbf{J}^h = \hat{\mathbf{n}} \times \mathbf{H}^h \tag{16}$$

where $\hat{\mathbf{n}}$ is a unit vector perpendicular to a particular surface and directed into the scattering region. Then, in order to create a y-directed wave with components $\mathbf{E}^i = E_y^i$ and $\mathbf{H}^i = H_x^i$ at the same three positions described earlier we need to apply the currents

a)

$$\mathbf{J}^h = -H_x^h \hat{\mathbf{z}} \tag{17}$$

$$\mathbf{M}^h = -E_z^h \hat{\mathbf{x}} \tag{18}$$

b)

$$\mathbf{J}^h = 0 \tag{19}$$

$$\mathbf{M}^h = -E_z^h \hat{\mathbf{y}} \tag{20}$$

c)

$$\mathbf{J}^h = -H_x^h \hat{\mathbf{y}} \tag{21}$$

$$\mathbf{M}^h = 0 \tag{22}$$

From an examination of the Huygen's surface currents and the currents actually applied to the surface in the new method we can see that they are equivalent with

$$E_z^h = \frac{V}{\Delta l} \tag{23}$$

$$H_x^h = \frac{V}{Z_0 \Delta l} \tag{24}$$

That is, exciting a plane wave of voltage, V, in the new method is equivalent to exciting a free space electromagnetic plane wave with fields $E = V/\Delta l$ and $H = V/Z_0\Delta l$ using a Huygen's surface.

5 Conclusions

A simple and efficient method of implementing a partial Huygen's boundary in the TLM mesh has been demonstrated. The method allows the use of considerably smaller TLM meshes for scattering problems excited with a plane wave source than previously possible. The method uses the TLM mesh itself to generate the (equivalent of) retarded surface currents for the Huygen's surface and therefore automatic compensation for any dispersion in the mesh is achieved. This also means that the method is suitable for problems using a graded mesh without further modification.

References

[1] S.J. Porter and J.F. Dawson. Improved plane wave illumination for TLM method. *Electronics Letters*, pages 1663–1664, 1992.

[2] D.E. Merewether, R. Fisher, and F.W. Smith. On implementing a numeric Huygen's source scheme in a finite difference program to illuminate scattering bodies. *IEEE Transactions on Nuclear Science*, pages 1829–1833, 1980.

[3] P.B. Johns. A symmetrical condensed node for the TLM method. *IEEE Transactions on Microwave Theory and Techniques*, pages 370–377, 1987.

[4] P. B. Johns and A. Mallik. EMP response of aircraft structures using transmission-line modelling. In *IEEE International Symposium on Electromagnetic Compatibility*, pages 387–389, Zurich, Switzerland, 5–7 March 1985.

Modeling a Resonant Length Center Driven Dipole Using the Symmetric Condensed Node (SCN) Transmission Line Matrix (TLM) Method

Michael T. Hendrick and Lloyd S. Riggs
Electrical Engineering Department
200 Broun Hall
Auburn University, Alabama 36849

Kelly Sherbondy
Belvoir Research, Development and Engineering Center
ATTN: SATBE-NTD
Fort Belvoir, VA 22060

Abstract

The transmission line matrix (TLM) method is used to analyse the balanced bridge mine detection system. These results include an examination of modeling a thin wire in a coarse TLM mesh.

I Introduction

The TLM method of electromagnetic analysis is ideally suited for modeling a balanced bridge mine detection system. This type of system requires some areas of the model to represent free space and other areas to represent a lossy earth material. Using TLM, arbitrary material parameters can be easily realised by modifying an input file. However, to use TLM to model a mine detection system, an adequate method for modeling thin linear antennas in a coarse mesh must be found.

The balanced bridge mine detection system utilises a receiving antenna located between two transmitting antennas, as shown in Figure 1. The transmitting antennas are operated 180° out of phase to create a symmetric system. Due to this symmetrical property the signal at the receive antenna is normally zero. In the presence of an anomaly, the system becomes unbalanced, and the received signal increases.

II Theory

The Transmission Line Matrix (TLM) method is a time domain analysis in which both space and time are discretised. Space is divided into discrete points, nodes, which are represented by a network of transmission lines. The transmission line equations are related to the Maxwell equations allowing the voltage pulses traveling along the lines to represent the propagation of fields.

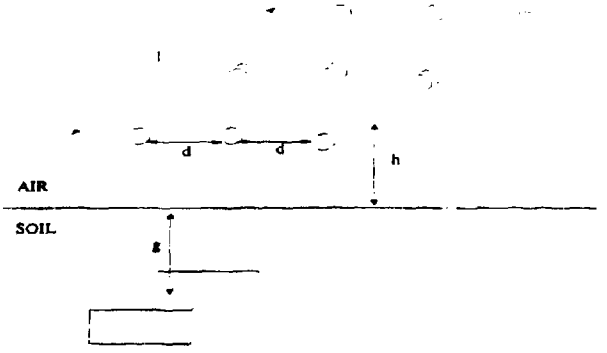

Figure 1: Geometry for a balanced bridge mine detection system as it appears in the TLM mesh.

Time progresses in discrete steps as the voltage pulses are passed from one set of transmission lines to another. The data at any node may be saved and processed. The processing may include such things as calculating the frequency response.

TLM analysis is performed in two basic steps A routine is performed which scatters all the voltage pulses (V_i) incident on a node The scattering is executed through a matrix multiplication as shown in Equation 1 with S being the scattering matrix. After scattering, the voltage pulses (V_r) are outward traveling.

$$V_r = SV_i \tag{1}$$

The outward traveling voltage pulses are then moved to the appropriate transmission lines of the surrounding nodes and are again inward traveling voltage pulses. The exchange of voltage pulses between different nodes is referred to as connecting. Every scattering and connecting process represents one discrete step in time.

The type of node we used for our analysis is called the Symmetric Condensed Node (SCN) [1] This node consist of six branches, each one composed of two uncoupled two wire transmission lines. By adding more stubs to the node, permittivity and permeability of different materials may be incorporated into the model [1]. Lossy materials may also be modeled by the use of additional stubs [2]. The scattering matrix for the SCN with permittivity, permeability, and loss stubs is

shown in Equation 2.

$$S = \begin{bmatrix}
a & b & d & 0 & 0 & 0 & 0 & 0 & b & 0 & -d & c & g & 0 & 0 & 0 & 0 & i \\
b & a & 0 & 0 & 0 & d & 0 & 0 & c & -d & 0 & b & g & 0 & 0 & 0 & -i & 0 \\
d & 0 & a & b & 0 & 0 & 0 & b & 0 & 0 & c & -d & 0 & g & 0 & 0 & 0 & -i \\
0 & 0 & b & a & d & 0 & -d & c & 0 & 0 & b & 0 & 0 & g & 0 & i & 0 & 0 \\
0 & 0 & 0 & d & a & b & c & -d & 0 & b & 0 & 0 & 0 & 0 & g & -i & 0 & 0 \\
0 & d & 0 & 0 & b & a & b & 0 & -d & c & 0 & 0 & 0 & 0 & g & 0 & i & 0 \\
0 & 0 & 0 & -d & c & b & a & d & 0 & b & 0 & 0 & 0 & 0 & g & i & 0 & 0 \\
0 & 0 & b & c & -d & 0 & d & a & 0 & 0 & b & 0 & 0 & g & 0 & -i & 0 & 0 \\
b & c & 0 & 0 & 0 & -d & 0 & 0 & a & d & 0 & b & g & 0 & 0 & 0 & i & 0 \\
0 & -d & 0 & 0 & b & c & b & 0 & d & a & 0 & 0 & 0 & g & 0 & -i & 0 & 0 \\
-d & 0 & c & b & 0 & 0 & 0 & b & 0 & 0 & a & d & 0 & g & 0 & 0 & 0 & i \\
c & b & -d & 0 & 0 & 0 & 0 & b & 0 & 0 & d & a & g & 0 & 0 & 0 & 0 & -i \\
e & e & 0 & 0 & 0 & 0 & 0 & 0 & e & 0 & 0 & e & h & 0 & 0 & 0 & 0 & 0 \\
0 & 0 & e & e & 0 & 0 & 0 & e & 0 & 0 & e & 0 & 0 & h & 0 & 0 & 0 & 0 \\
0 & 0 & 0 & 0 & e & e & e & 0 & 0 & e & 0 & 0 & 0 & 0 & h & 0 & 0 & 0 \\
0 & 0 & 0 & f & -f & 0 & f & -f & 0 & 0 & 0 & 0 & 0 & 0 & 0 & j & 0 & 0 \\
0 & -f & 0 & 0 & 0 & f & 0 & 0 & f & -f & 0 & 0 & 0 & 0 & 0 & 0 & j & 0 \\
f & 0 & -f & 0 & 0 & 0 & 0 & 0 & 0 & 0 & f & -f & 0 & 0 & 0 & 0 & 0 & j
\end{bmatrix} \quad (2)$$

The scattering is performed on every node in the system; however, the connecting cannot be done for nodes located along the edge of the mesh. At these positions, only five of the six branches have another node with which to trade voltage pulses. The five branches, which have neighboring branches, are connected using the normal process. The sixth branch, which is not abutting another branch, must be terminated so as not to disrupt the network and cause invalid data. The termination method used in this model is based on reflection coefficients. By knowing the characteristics of the material surrounding the mesh, the reflection coefficient is calculated. The inward traveling voltage pulse placed on the sixth branch is the product of the outward traveling voltage pulse and the reflection coefficient. The disadvantage of this method is that it cannot compensate for a lossy material immediately adjacent to the mesh.

For the mine detection system of Figure 1, thin linear antennas need to be modeled. The dipole, which has a diameter much less than the incremental length (Δl) of a node, is modeled by modifying the scattering matrix to represent a node that has an infinitesimally small piece of conductor located at the center. The scattering matrix is changed to reflect the negative of the inward traveling pulse back onto the same lines. A straight line of these "special" nodes can be used to represent a piece of wire. As long as no voltage pulses are impressed along the adjoining branches of the wire, no voltage pulses will ever be reflected onto these transmission lines.

III Results

Due to the fact that we are modeling this relatively small structure in a coarse mesh, the dipole cannot contain a center gap if the procedure outlined above is to be used. In our mesh the antenna is $10\Delta l$, if this model were to represent the center node of the antenna with free space then the center gap of the dipole would comprise 10% of the entire antenna. This setup is shown in Figure 2.

Therefore, our approach to the problem was based on a concept used in the moment method

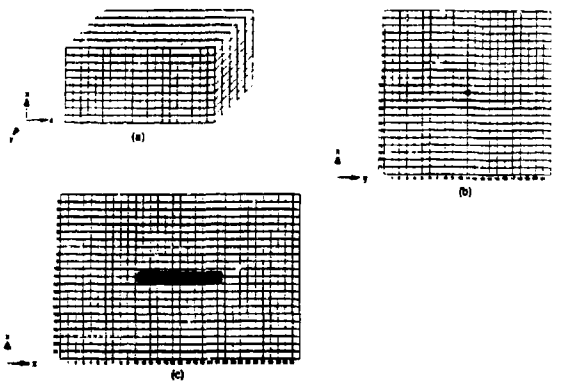

Figure 2: TLM mesh used for modeling the dipole. The dipole is located in the center of the mesh with its axis oriented in the z-direction. (a) Three-dimensional view of the mesh used to represent a block of free space. (b) Cut away view of the x-y plane. (c) Cut away view of the x-z plane.

solution of a similar type of problem. Instead of using two pieces of metal to represent the dipole, one continuous piece was used to model the entire dipole. Without a gap at the center, excitation and output must be obtained without directly using the nodes located along the antenna. The excitation is provided by exciting a magnetic current around the dipole. Voltages across the dipole are gathered indirectly, by finding the E-field around the dipole according to Equation 3

$$V = \oint E \cdot dl \tag{3}$$

The characteristic admittance of the dipole is compared to that obtained by Harrington [3] using the moment method. When the real part of the admittance peaks or the imaginary part is passing through zero, the system is resonant. From this data it can be seen that the resonant frequencies occur when the length of the antenna is approximately a multiple of half a wavelength. The resonance with which we are most concerned occurs when the antenna is approximately one half of a wavelength. The system is to be investigated in the region surrounding this frequency.

The fields are used to obtain voltages and currents at the center of the dipole. The voltage is obtained using Equation 3. The current is obtained in a similar manner using Ampere's law via Equation 4.

$$I = \oint H \cdot dl \tag{4}$$

The admittance is defined as the ratio of current to voltage.

The dipole antenna was defined as $10\Delta l$ in length with Δl defined to be 0.1 meters, thus producing an antenna with a length of 1.0 meter. The first resonance for this antenna should

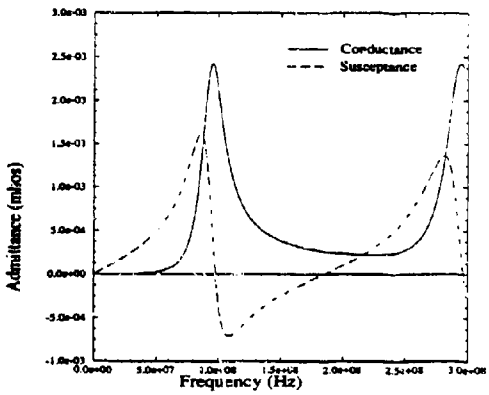

Figure 3: Input admittance of a center-fed linear antenna obtained using TLM.

theoretically occur at 150 MHz. However, the first resonant frequency for this antenna, as determined from its input admittance shown in Figure 3, occurs at 100 MHz. This difference in the theoretical and computed resonant frequencies can be explained through an examination of the TLM computed current distribution shown in Figure 4. The TLM computed current at locations between the ends of the antenna appears to be sinusoidally distributed, but the magnitude of the current at the ends of the antenna is still a large percentage of the maximum current at the antenna center. A "trailing" current occurs beyond each end of the antenna caused by the discrete nature of the TLM simulation. This trailing current continues to decrease in magnitude beyond each end of the antenna. If the antenna is increased by $2.5\Delta l$ on each end so as to include most of the trailing current, the effective length of the antenna is increased from 1.0 meter to 1.5 meters. The effective length of the antenna should therefore be used to compute the resonant frequency, which in this case is 100 MHz. Taking the extra length into consideration, Figure 3 shows the correct response for this antenna.

This technique of including the effects of the trailing current was applied to antennas of various length, but the number of Δl remained the same. The length was changed by adjusting the size of Δl, and as expected, all of these cases produced the same TLM computed current distribution with the trailing current having a length of $5\Delta l$. When the length of the antenna was held constant but the number of Δl modeling the antenna was increased, the current distribution data showed that the length of the trailing current was reduced. When a larger number of Δl was used to model the antenna the data showed the current dropped to small fraction of the maximum current in less than $5\Delta l$ beyond the ends of the antenna. This shows that the finer the discretization of the antenna the better the model approximates the actual current distribution.

The TLM model was tested by running simulations of a balance bridge mine detection system

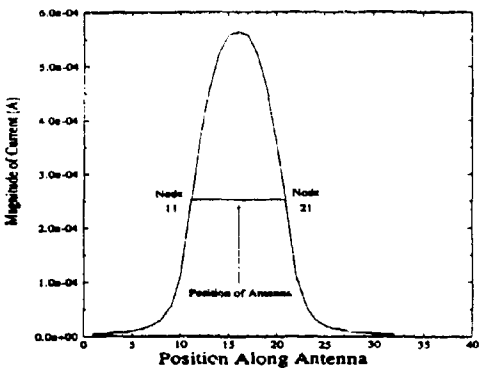

Figure 4: Current distribution along the antenna, which is being modeled as one continuous piece of wire.

examined by Hill[4]. The configuration of the mesh is shown in Figure 1. The dimensions of the setup are as given below.

$$d = 10cm$$

$$h = 8cm$$

$$l = 26cm$$

$$g = 10cm$$

$$\text{frequency} = 380\text{MHz}$$

$$\epsilon_r = 3.5 - j0.05$$

The results obtained using TLM are very close to those obtained by Hill. Figure 5 shows the comparison of the data produced by TLM and that obtained by Hill. This figure also shows the results obtained using the two-dimensional TLM. As can be seen from the results the three-dimensional TLM code shows a closer agreement with Hill's data than the results produced by the two-dimensional TLM code.

IV Conclusions

The technique presented here works well for modeling thin linear antennas. However, to use this method test need to be run to determine the amount of trailing current that must be included to

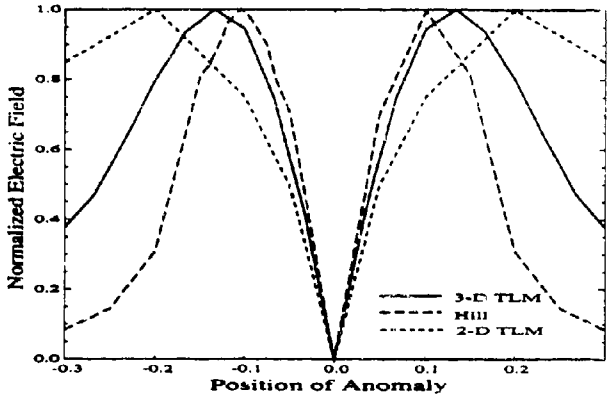

Figure 5: Normalised electric field as a function of the position of the anomaly for results obtained using T. M and by Hill

accurately model the antenna. The problem of modeling a thin wire in a course mesh has been examined by several researcher. Naylor and Christopoulos [5] developed a new TLM node and scattering matrix to treat the problem whereas Wlodarczyk and Johns [6] model the thin wire between two TLM nodes. Most recently, duffy, Benson, Christopoulos, and Herring [7] treated the problem by using a lower time ste in the immediate neighborhood surrounding the conductor. Future work will investigate the applications of these methods to the mine detection problem.

References

[1] Peter B. Johns. A symmetrical condensed node fo the tlm method. *IEEE Transactions on Microwave Theory and Techniques*, MTT-35(4):370–376, April 1987.

[2] F. J. German, G. K. Gothard, and L. S. Riggs. Modelling of materials with electric and magnetic losses with the symmetrical condensed tlm method. *Electronics Letters*, 26(16):1307,1308, August 1990.

[3] Roger F. Harrington. *Field Computation by Moment Methods*. IEEE Press, 1993.

[4] David A. Hill. Near-field detection of buried dielectric objects. *IEEE Transactions on Geoscience and Remote Sensing*, 27(4):364–368, 1989.

[5] P. Naylor and C. Christopoulos. A new wire node for modeling thin wires in electromagnetic field problems solved by transmission line modeling. *IEEE Transactions on Microwave Theory and Techniques*, 38(3):328–330, March 1990.

[6] A. J. Wlodarczyk and D. P. Johns. New wire interface for graded 3-d tlm. *Electronics Letters*, 28(8):728,729, April 1992.

[7] A. P. Duffy, T.M. Benson, C. Christopoulos, and J. L. Herring. New mehtods for accurate modelling of wires using tlm. *Electronics Letters*, 29(2):224-226, January 1993.

TLM Analysis of a Choked Circular Waveguide Antenna

Kelly W. Stricklin and Lloyd S. Riggs
Department of Electrical Engineering
Auburn University, Alabama 36849

Mike Oberhart
Jet Propulsion Laboratory
4800 Oak Grove Drive
Pasadena, California 91109

Abstract

The Transmission Line Matrix (TLM) method is used to determine the electromagnetic near-field quantities produced by the radiation from a choked circular waveguide antenna. These near-field quantities are transformed into far-field radiation patterns by use of the field equivalence principle. Numerical results are then compared to measured data provided by the Jet Propulsion Laboratory (JPL).

1 Introduction

The Jet Propulsion Laboratory (JPL) is investigating the design of the dual frequency low gain antenna for the Cassini spacecraft emergency command and low data rate link. JPL is most interested in creating an analytic tool, capable of assessing and optimizing designs based on various mission requirements (typically 7-9 GHz). In support of this investigation, an analysis has been performed on the choked circular waveguide antenna of Figure 1. This is the low gain antenna for the Mars Observer which uses a simple choke design.

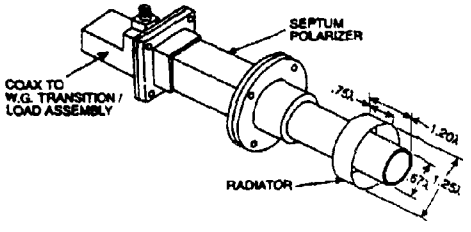

Figure 1: The GE baseline design of the Mars Observer low gain antenna showing the feed portion as a choked circular waveguide

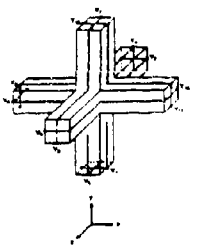

Figure 2: The symmetrical condensed node showing its 12 transmission lines and voltage pulses

A numerical technique known as the "Transmission Line Matrix" (TLM) method is used to model the propagation of waves through and about the choked circular waveguide antenna. After the proper electromagnetic radiation of the antenna has been produced using TLM, the electric and magnetic field quantities are saved over a surface surrounding the antenna. These field quantities are used to determine the far-field radiation patterns by use of the field equivalence principle.

2 Theoretical Foundations

2.1 3-D TLM method and the symmetrical condensed node

In order to implement the scattering of waves through space on a digital computer, the formulation of this wave model needs to be in discretized form. Therefore, both space and time are represented in terms of finite, elementary units, Δl and Δt. Electromagnetic fields are modeled with a network of transmission lines comprising the field space. The behavior of voltage pulses traveling on this network of transmission lines is analogous to the behavior of electromagnetic fields traveling in a homogeneous medium. Equations associated with voltage pulses on transmission lines can be related to Maxwell's equations so that TLM can realistically model the propagation of electromagnetic fields [1].

The network of transmission lines intersect at nodes which represent points in space separated by a distance Δl. Voltage pulses launched on the network scatter from point to point in space in a fixed time-step Δt. One of the more recently developed node models is the symmetrical condensed node created by Johns [?]. His symmetrical condensed node for modeling free space is depicted in Figure 2. Two-wire transmission lines connect the ports of the node on the sides of square ducts made of insulating material. In all six directions of propagation, two polarizations are carried on two pairs of transmission lines which are completely separated throughout the network of transmission lines.

Each transmission line has a characteristic impedance equal to the characteristic impedance of free space, η_0. These transmission lines link the mesh of nodes together in Cartesian fashion. Twelve voltage pulses incident upon the twelve pairs of transmission lines produce scattering into twelve reflected pulses. These incident and reflected voltage pulses appear on the terminals of the transmission lines at each of the twelve ports on the node. The voltage pulses are numbered and directed according to the arrows on Figure 2 [2].

The scattering at each node is defined by

$$\mathbf{V}^r = \mathbf{S}\mathbf{V}^i \tag{1}$$

where S is a 12×12 scattering matrix in the case with no stubs. $\mathbf{V}^r$ is the column vector of reflected pulses, and $\mathbf{V}^i$ is the column vector of incident pulses on each node. A voltage pulse V_1^i of unit amplitude incident upon port 1 of the node in Figure 2 proceeds toward the center with field quantities E_x and H_z. Likewise, the other eleven ports have field quantities associated with them. By applying the conservation of current, voltage, and energy to the symmetrical condensed node of Figure 2, the scattering matrix becomes

$$\mathbf{S} = \frac{1}{2}\begin{bmatrix} 0 & 1 & 1 & 0 & 0 & 0 & 0 & 0 & 1 & 0 & -1 & 0 \\ 1 & 0 & 0 & 0 & 0 & 1 & 0 & 0 & 0 & -1 & 0 & 1 \\ 1 & 0 & 0 & 1 & 0 & 0 & 0 & 1 & 0 & 0 & 0 & -1 \\ 0 & 0 & 1 & 0 & 1 & 0 & -1 & 0 & 0 & 0 & 1 & 0 \\ 0 & 0 & 0 & 1 & 0 & 1 & 0 & -1 & 0 & 1 & 0 & 0 \\ 0 & 1 & 0 & 0 & 1 & 0 & 1 & 0 & -1 & 0 & 0 & 0 \\ 0 & 0 & 0 & -1 & 0 & 1 & 0 & 1 & 0 & 1 & 0 & 0 \\ 0 & 0 & 1 & 0 & -1 & 0 & 1 & 0 & 0 & 0 & 1 & 0 \\ 1 & 0 & 0 & 0 & 0 & -1 & 0 & 0 & 0 & 1 & 0 & 1 \\ 0 & -1 & 0 & 0 & 1 & 0 & 1 & 0 & 1 & 0 & 0 & 0 \\ -1 & 0 & 0 & 1 & 0 & 0 & 0 & 1 & 0 & 0 & 0 & 1 \\ 0 & 1 & -1 & 0 & 0 & 0 & 0 & 0 & 1 & 0 & 1 & 0 \end{bmatrix} \tag{2}$$

which provides the basis for scattering in TLM programming [2].

After the scattering process has been carried out on every node in the transmission line mesh, a connection process must take place. This connection process takes all twelve output voltage pulses on each node, and transfers them to the corresponding ports on adjacent nodes. At the same time a node outputs its twelve voltage pulses, it receives twelve input voltage pulses from the six neighboring nodes, assuming the node is not on the boundary of the transmission line mesh.

The six field quantities can be calculated at any node from the following equations [2]:

$$\begin{aligned} E_x &= \frac{1}{2}(V_1^i + V_2^i + V_9^i + V_{12}^i) \\ E_y &= \frac{1}{2}(V_3^i + V_4^i + V_8^i + V_{11}^i) \\ E_z &= \frac{1}{2}(V_5^i + V_6^i + V_7^i + V_{10}^i) \\ H_x &= \frac{1}{2\eta_0}(-V_4^i + V_6^i - V_7^i + V_8^i) \\ H_y &= \frac{1}{2\eta_0}(V_2^i - V_6^i - V_9^i + V_{10}^i) \\ H_z &= \frac{1}{2\eta_0}(-V_1^i + V_3^i - V_{11}^i + V_{12}^i). \end{aligned} \tag{3}$$

To implement boundaries and surfaces, output voltage pulses incident upon a boundary are multiplied by the proper reflection coefficient, Γ, and injected back into the same node as input voltage pulses. In the following analysis, three types of reflection coefficients are used. For the case of a perfect electric conductor like the surface of an antenna, $\Gamma = -1$. At the edges of the TLM network, $\Gamma = 0$ so that the fields are completely absorbed. For the third case, an infinitely long waveguide is modeled using a frequency dependent reflection coefficient. An expression for this reflection coefficient is derived by using the waveguide impedence at the termination; the individual transmission lines have an impedance equal to the impedance of free space.

2.2 Near- to far-field transformations

For many antenna configurations, such as aperture antennas, it is possible to take the field quantities near the antenna and transform them into a far-field radiation pattern. One such technique is a mathematical technique based on the *field equivalence principle* [3]

The field equivalence principle allows actual sources, such as an antenna, to be replaced by equivalent sources. The fictitious sources are said to be equivalent within a region because they produce the same fields within that region [3].

The fields outside an imaginary closed surface are obtained by placing over the closed surface suitable electric and magnetic current densities which satisfy the boundary conditions. Proper current densities are selected so that the fields inside the closed surface are zero and outside they are equal to the radiation produced by the actual sources. If the fields outside of the closed surface are represented by $\mathbf{E}_1$ and $\mathbf{H}_1$ and the fields inside are made to be zero, then the surface current densities become

$$\mathbf{J}_s = \hat{\mathbf{n}} \times \mathbf{H}_1 \tag{4}$$

$$\mathbf{M}_s = -\hat{\mathbf{n}} \times \mathbf{E}_1 \tag{5}$$

where $\hat{\mathbf{n}}$ is the outward normal of S. These current densities are then used to determine the true fields radiated outside the closed surface by the sources within it [3].

After the current densities on S have been determined, the electric and magnetic vector potentials, $\mathbf{A}$ and $\mathbf{F}$, respectively, can be calculated from

$$\mathbf{A} = \frac{\mu}{4\pi} \iiint_V \mathbf{J} \frac{e^{-jkR}}{R} dv' \tag{6}$$

$$\mathbf{F} = \frac{\epsilon}{4\pi} \iiint_V \mathbf{M} \frac{e^{-jkR}}{R} dv' \tag{7}$$

where $k = \frac{2\pi}{\lambda}$ (λ is the wavelength), and R is the distance from the source point (x', y', z') to the observation point (x, y, z). The total fields are then given by

$$\mathbf{E} = -j\omega\mathbf{A} - j\frac{1}{\omega\mu\epsilon} \nabla(\nabla \cdot \mathbf{A}) - \frac{1}{\epsilon} \nabla \times \mathbf{F} \tag{8}$$

$$\mathbf{H} = -j\omega\mathbf{F} - j\frac{1}{\omega\mu\epsilon} \nabla(\nabla \cdot \mathbf{F}) + \frac{1}{\mu} \nabla \times \mathbf{A}. \tag{9}$$

However, these formulations are complex, and the integrals are difficult to evaluate. Therefore, some approximations which are valid for far-field observations will be introduced [3].

Referring to Figure 3, for *far-field observations*, R can be approximated by

$$R \simeq r - r' \cos\psi \tag{10}$$

for phase variations, and

$$R \simeq r \tag{11}$$

for amplitude variations [3].

In Equation 10, ψ is the angle between the vectors $\mathbf{r}$ and $\mathbf{r}'$. The primed coordinates (x', y', z') indicate the space occupied by the sources $\mathbf{J}_s$ and $\mathbf{M}_s$, over which integration must be performed. The unprimed coordinates (x, y, z) represent the observation point [3].

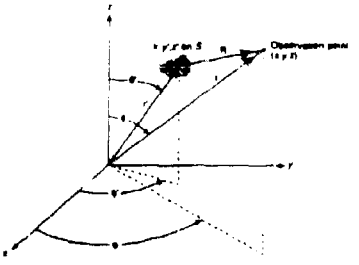

Figure 3: Coordinate system for aperture antenna analysis

Equations 6 and 7 can now be written as

$$\mathbf{A} = \frac{\mu}{4\pi}\iint_S \mathbf{J}_s \frac{e^{-jkR}}{R} ds' \simeq \frac{\mu e^{-jkr}}{4\pi r}\mathbf{N} \tag{12}$$

$$\mathbf{N} = \iint_S \mathbf{J}_s e^{+jkr'\cos\psi} ds' \tag{13}$$

$$\mathbf{F} = \frac{\epsilon}{4\pi}\iint_S \mathbf{M}_s \frac{e^{-jkR}}{R} ds' \simeq \frac{\epsilon e^{-jkr}}{4\pi r}\mathbf{L} \tag{14}$$

$$\mathbf{L} = \iint_S \mathbf{M}_s e^{+jkr'\cos\psi} ds'. \tag{15}$$

Equations 13 and 15 can be simplified by separating them into their x, y, and z components and then using a rectangular-to-spherical component transformation, to give [3]

$$N_\theta = \iint_S (J_x\cos\theta\cos\phi + J_y\cos\theta\sin\phi - J_z\sin\theta)e^{+jkr'\cos\psi} ds' \tag{16}$$

$$N_\phi = \iint_S (-J_x\sin\phi + J_y\cos\phi)e^{+jkr'\cos\psi} ds' \tag{17}$$

$$L_\theta = \iint_S (M_x\cos\theta\cos\phi + M_y\cos\theta\sin\phi - M_z\sin\theta)e^{+jkr'\cos\psi} ds' \tag{18}$$

$$L_\phi = \iint_S (-M_x\sin\phi + M_y\cos\phi)e^{+jkr'\cos\psi} ds' \tag{19}$$

where

$$r'\cos\psi = x'\sin\theta\cos\phi + y'\sin\theta\sin\phi + z'\cos\theta. \tag{20}$$

After substituting Equations 16-19 into Equations 8 and 9, and separating the fields into spherical components, the total E- and H-fields can be written as [3]

$$E_r \simeq 0 \tag{21}$$

$$E_\theta \simeq -\frac{jke^{-jkr}}{4\pi r}(L_\phi + \eta N_\theta) \tag{22}$$

$$E_\phi \simeq \frac{jke^{-jkr}}{4\pi r}(L_\theta - \eta N_\phi) \tag{23}$$

$$H_r \simeq 0 \tag{24}$$

$$H_\theta \simeq \frac{jke^{-jkr}}{4\pi r}\left(N_\phi - \frac{L_\theta}{\eta}\right) \tag{25}$$

$$H_\phi \simeq -\frac{jke^{-jkr}}{4\pi r}\left(N_\theta + \frac{L_\phi}{\eta}\right) \tag{26}$$

To implement these formulations in a computer program, discrete versions of these equations are used. After the TLM algorithm has run for several thousand iterations, the Fourier-transformed field quantities are saved on a virtual surface just inside the outer boundary of the TLM network. This virtual surface is the surface to which the equivalence principle is applied. An algorithm incorporating the above formulations, in discrete form, is used to calculate the radiated E- and H-fields.

2.3 Obtaining circular polarization patterns

The measured data provided for the Mars Observer low gain antenna was obtained for circular polarisation. Therefore, it was necessary to convert the linearly polarised far-field data produced by TLM to circularly polarised patterns.

In order to compute circular polarisation, it is convenient to define a new pair of unit vectors,

$$\hat{\mathbf{a}}_R = \hat{\mathbf{a}}_u - j\hat{\mathbf{a}}_v \tag{27}$$

$$\hat{\mathbf{a}}_L = \hat{\mathbf{a}}_u + j\hat{\mathbf{a}}_v. \tag{28}$$

These vectors correspond to time-varying unit vectors rotating in the right-handed and left-handed senses, respectively, where the thumb points in the direction of propagation [4]. Thus, any wave field can be written in one of the two following forms:

$$\mathbf{E} = E_u\hat{\mathbf{a}}_u + E_v\hat{\mathbf{a}}_v \tag{29}$$

or

$$\mathbf{E} = E_R\hat{\mathbf{a}}_R + E_L\hat{\mathbf{a}}_L. \tag{30}$$

From these two equations it can be shown that

$$E_R = \frac{1}{2}(E_u + jE_v) \tag{31}$$

$$E_L = \frac{1}{2}(E_u - jE_v). \tag{32}$$

Circular polarisation, can be thought of as a superposition of two spacially orthogonal linear polarisations separated by a 90° phase difference. Therefore, in circular coordinates, E_u becomes E_ϕ of the first polarisation. Likewise, E_v becomes E_θ of the second polarisation which is jE_θ of the first polarisation. After making these substitutions, Equations 31-32 become

$$E_R = \frac{1}{2}(E_\phi - E_\theta) \tag{33}$$

$$E_L = \frac{1}{2}(E_\phi + E_\theta) \tag{34}$$

in spherical coordinates.

3 Numerical results

A case was run to determine the radiation characteristics of the Mars Observer antenna design of Figure 1. A cross-section of the TLM model for this design is shown in Figure 4. Each node in the TLM network is 1 mm on each side. The diameter of the waveguide is 22 mm. At a frequency of 9.13 GHz, this diameter is 0.764 λ. The choke has a diameter of 42 mm, a depth of 25 mm, and the mouth of the choke is recessed 15 mm back from the aperture of the waveguide. A TLM network of 100 mm on each side surrounds this arrangement. The dominant TE_{11} mode was allowed to propagate down the waveguide and waves radiated into the surrounding TLM network modeling free space. After 15,000 iterations, the tangential electric and magnetic fields were saved on a virtual surface 90 nodes on each side. The near- to far-field transformation algorithm produced Figure 5. Measured data for circular polarization was provided by JPL for comparison. This figure shows the measured pattern for circular polarization plotted from $-90°$ to $90°$, the E_θ and E_ϕ patterns, and the right- and left-hand circular polarisation plots.

4 Limitations and conclusions

This particular case was run on the cray supercomputer to take advantage of the cray's memory and to speed up run-time. However, even the cray has a limit on the size of TLM networks it can handle. This limit seems to be on the order of 10^6 nodes. Therefore, the size and resolution of the structure being modeled are also limited. Likewise, the amount of space surrounding the antenna is limited. Enough free space in front of the antenna should be modeled so that an accurate representation of the near-field quantities on the virtual surface can be generated. For the Mars Observer antenna design with a simple choke, 1×10^6 nodes were used in the TLM analysis. Antenna designs with larger chokes can be analyzed using TLM. However, for designs using very large chokes, some resolution may need to be sacrificed.

An analysis of a circular waveguide antenna with a simple choke has been made using a TLM algorithm and a near- to far-field transformation algorithm. Initial runs produced radiation patterns that agree quite favorably with measured data. Better resolution by using larger TLM network sizes will increase the accuracy of the radiation characteristics analysis.

References

[1] Wolfgang J. R. Hoefer and Poman P. M. So. *The Electromagnetic Wave Simulator*. John Wiley and Sons, 1991.

[2] Peter B. Johns. A symmetrical condensed node for the TLM method. *IEEE Transactions on Microwave Theory and Techniques*, MTT-35(4):370–377, April 1987.

[3] Constantine A. Balanis. *Antenna Theory Analysis and Design*. Harper and Row, 1982.

[4] Edward C. Jordan and Keith G. Balmain. *Electromagnetic Waves and Radiating Systems*. Prentice-Hall, Inc., 1968.

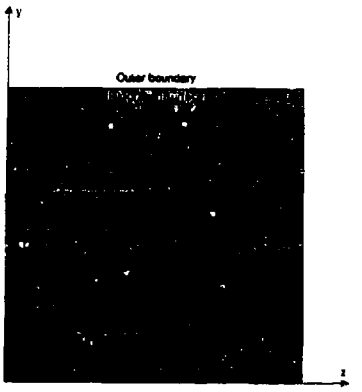

Figure 4: A $y - z$ cross-section of the TLM model for the Mars Observer choked circular waveguide antenna

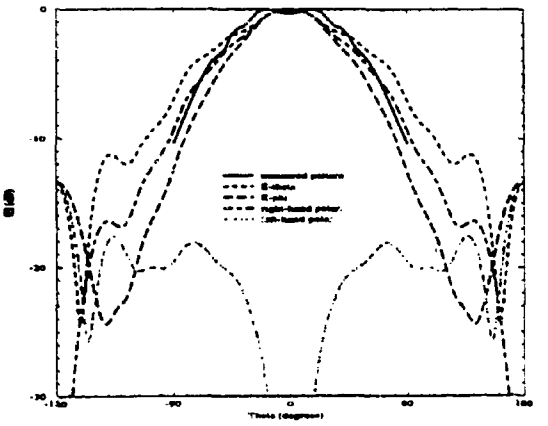

Figure 5: Far-field patterns for a choked circular waveguide including the circular polarization patterns and measured pattern, the waveguide's diameter is 22 mm and its length is 50 mm, the choke's diameter is 42 mm, its depth is 25 mm and it is recessed 15 mm from the aperture of the waveguide

COMPUTATION OF S-PARAMETERS OF A MICROSTRIP MEANDER LINE ON GaAs SUBSTRATE USING TLM METHOD

Channabasappa Eswarappa and Wolfgang J. R. Hoefer

NSERC/MPR Teltech Research Chair in RF Engineering, Department of Electrical and Computer Engineering, University of Victoria, Victoria, B.C., CANADA V8W 3P6

ABSTRACT

In this paper, a field based three-dimensional time domain Transmission Line Matrix (TLM) method has been applied to analyze a microstrip meander line configuration on GaAs substrate. Both regular and variable TLM meshes have been employed. The scattering parameters obtained have been compared with those of Sonnet em software and measurements (available data). The results agree well indicating that the TLM method, which is a fullwave electromagnetic solver, can properly account for the strong interaction between various parts of the meander line.

1. INTRODUCTION

The Transmission Line Matrix (TLM) method is a numerical technique in which both space and time are discretized [1]. The simulation of propagation of electromagnetic waves is done through scattering of impulses in a 3-D meshed network of transmission lines. This powerful and versatile technique is suitable for microwave and millimeter-wave circuit simulation, especially when the circuit geometry is highly irregular. Also since it is a fullwave electromagnetic solver, it can account for electromagnetic interaction between various parts of the circuit.

The meander lines [2] are used in monolithic microwave integrated circuits (MMICs) as delay lines as well as planar inductors. As a meander line consists of a uniform transmission line laid out in a such a way as to minimize the space required, there will be strong electromagnetic interaction between various parts of the transmission line. It will be very difficult to take care of such interaction using analytical methods. The TLM method is ideal for analysis of such structures. Also, the time domain responses obtained from the TLM method are very useful when using them as delay lines. In the following, we report a detailed analysis of a microstrip meander line configuration on GaAs substrate.

There are some difficulties associated with the TLM analysis of such large structures. The regular uniform mesh TLM leads to large computer memory and large coarseness and dispersion errors. We have applied a variable mesh scheme based on Al-Mukhtar's and Sitch's [3] approach to

reduce these errors. Also, the variable mesh allows fitting of the exact dimensions of the structure into the TLM mesh. Excitation of the circuit with a Gaussian pulse (containing narrow band frequency components) facilitates reaching the steady state faster.

This paper also compares the scattering parameters obtained from the TLM method with those obtained using Sonnet em software and measurements.

2. THEORY

The symmetrical condensed TLM node [4] (shown in Fig.1) has been used for our study. The advantages of this node when compared to the expanded TLM node are the following: Boundary description is easier, all six field components can be defined at single point in space, i.e. there is no dispersion in axial directions. It has six branches, each branch consisting of four uncoupled two-wire transmission lines. The 12 transmission lines linking the Cartesian mesh of nodes together have the characteristic impedance of free space. To compute the scattering parameters of meander lines, we need the incident and reflected fields at the input port, and the transmitted field at the output port. To compute the incident field, we discretize a length of uniform microstrip line with absorbing boundaries placed on all sides of the computational domain. Then, we include the meander line in the computational domain, and compute the transmitted field at the output port and the total field at the input port. The reflected field is obtained by subtracting the incident field

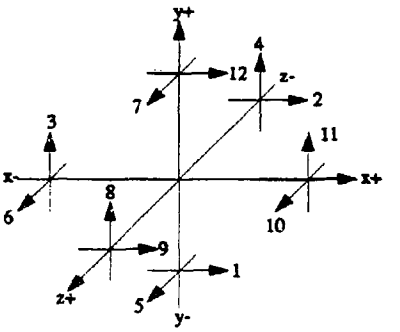

Fig. 1: The Symmetrical Condensed Node

from the total field. The scattering parameters are then determined by Fourier transforming these time domain waveforms. Good quality absorbing boundaries must be used for accurate extraction of scattering parameters. We have used the second-order one-way equation absorbing boundaries [5] in the main propagation direction of the microstrip. A voltage impulse reflected from the absorbing boundary can be computed from the knowledge of impulses in the cells in front of the boundary using the following equation:

$$\begin{aligned} V^n(m,j,k) = {} & (\alpha_1+\alpha_2)V^{n-1}(m,j,k) - \alpha_1\alpha_2 V^{n-2}(m,j,k) + (\beta_1+\beta_2)V^n(m-1,j,k) \\ & + (\gamma_1+\gamma_2-\alpha_1\beta_2-\beta_1\alpha_2)V^{n-1}(m-1,j,k) - (\alpha_1\gamma_2+\gamma_1\alpha_2)V^{n-2}(m-1,j,k) \\ & -\beta_1\beta_2 V^n(m-2,j,k) - (\beta_1\gamma_2+\gamma_1\beta_2)V^{n-1}(m-2,j,k) - \gamma_1\gamma_2 V^{n-2}(m-2,j,k) \end{aligned} \tag{1}$$

The interpolation coefficients are:

$$\alpha_i = \frac{(a-g_i(1-b))}{(a-1-g_i(1-b)-\varepsilon_i\Delta l)},\ \beta_i = \frac{(a-1+g_i b)}{(a-1-g_i(1-b)-\varepsilon_i\Delta l)},\ \gamma_i = \frac{(-a-bg_i)}{(a-1-g_i(1-b)-\varepsilon_i\Delta l)} \tag{2}$$

where coefficients a and b are weighted time and space averages of the space and time differences, respectively. ε_1 and ε_2 are damping factors. The parameter g_i for the uniform mesh is

$$g_i = 2\sqrt{\varepsilon_{eff}(f_i)} \tag{3}$$

while for the variable mesh, it can be written as

$$g_i = 2\sqrt{\varepsilon_{eff}(f_i)}\,\frac{\Delta l^{local}}{\Delta l^{min}} \tag{4}$$

where Δl^{min} is the unit length of the mesh. This is determined after scanning the entire variable mesh so that no stub impedances or admittances are negative. Δl^{local} is the space resolution at the absorbing boundaries. The absorbing boundaries on the sides and top of the meander line structure are implemented by means of a simple zero reflection coefficient.

3. NUMERICAL RESULTS

The meander line configuration is shown in Fig. 2. This line has been studied earlier by W. Pribble using Sonnet em software and measurements [6,7]. The microstrip line width and substrate thickness are 50 and 75 μm respectively. The dielectric constant of the substrate is 12.9. First, the

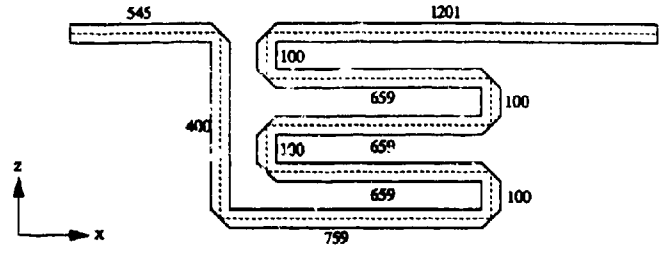

Fig. 2: The microstrip meander line configuration. Dimensions are in μm measured along the center line.

structure was discretized with a uniform TLM mesh of size (195x20x76) with the space resolution and time step of 10 μm and 0.016666 ps, respectively. The chamfers at the microstrip bends were approximated by staircasing. The excitation Gaussian pulse width (corresponding to -34 dB) was 25.45 ps. The values of the effective dielectric constants used in the design of the absorbing boundaries were 8.5 and 9.5. The coefficients *a* and *b* were taken as 0.25. The damping factors used were 0.1 and 0.0. The time-domain responses obtained at the input and output ports are plotted in Fig. 3. The scattering parameters obtained have been compared with those of W. Pribble in Figs. 4a, 4b, and 4c. The major difference between the TLM and Sonnet results is the shift in frequency of the former towards the lower end, which may be attributed to the coarseness error of the TLM analysis. Note that only five nodes were taken across the width of the microstrip. Next, a variable TLM mesh of size (170x18x100) with the following element sizes was used.

The element sizes along x: (49x14.54 + 40x6.25 + 35x14.54 + 24x6.25 + 22x14.54) μm
The element sizes along y: (11x12.5 + 7x14.54) μm
The element sizes along z: (7x14.54 + 86x6.25 + 7x14.54) μm

Eight nodes were taken across the width of the microstrip. The unit length (Δl^{min}) and time step Δt were 2.686 μm and 0.004476, respectively. The exact dimensions of the structure were fitted into the above variable TLM mesh. The scattering parameters computed have been plotted also in Figs. 4a, 4b, and 4c. This time, results agree better with those of Sonnet and measurements. The results could be further improved by employing a very fine mesh, keeping a larger distance

between the excitation and sampling points (at the input port), and placing absorbing boundaries (on the sides and top of the structure) at larger distances from the strip. IBM RISC System/6000-model 350 and HP 9000-model 755 computers have been used for computation. The computational time for the uniform TLM algorithm was about twelve hours.

4. CONCLUSIONS

A microstrip meander line configuration has been studied using the 3D-TLM method. The results seem to agree well with the available data except for a shift in frequency. Application of the variable mesh (based on Al-Mukhtar's and Sitch's approach) leads to better results, but it takes more computational time. The coarseness error, which is due to imperfect resolution of fields in the vicinity of sharp edges, has been the major source of error in the TLM analysis. This could not be reduced considerably for the meander line structure because of its large size, and limited computer resources.

REFERENCES

[1] W. J. R. Hoefer, "The Transmission Line Matrix (TLM) Method", in T. Itoh: *Numerical Techniques for Microwave and Millimeter Wave Passive Structures*, John Wiley & Sons, New York (1989).

[2] I. J. Bahl, "MIC Simulation Column" in *International Journal of Microwave and Millimeter-Wave Computer-Aided Engineering*, vol. 3, no. 2, pp. 156-157, 1993.

[3] D. A. Al-Mukhtar and J. E. Sitch, "Transmission-line matrix method with irregularly graded space," *IEE Proc., part H: Microwaves, Optics and Antennas*, vol. 128, pp. 299-305, Dec. 1981.

[4] P. B. Johns, "Symmetrical condensed node for the TLM method", *IEEE Trans. Microwave Theory Tech.*, vol. MTT-35, no. 4, pp. 370-377, April 1987.

[5] C. Eswarappa and W.J.R. Hoefer, "One-Way Equation Absorbing Boundary Conditions for 3-D TLM Analysis of Planar and Quasi-planar Structures", to be published in *IEEE Trans. Microwave Theory Techniques*.

[6] William Pribble, "MIC Simulation Column" in *International Journal of Microwave and Millimeter-Wave Computer-Aided Engineering*, vol. 3, no.4, pp. 460 - 461, 1993

[7] William Pribble, ITT-GTC, USA, private communications.

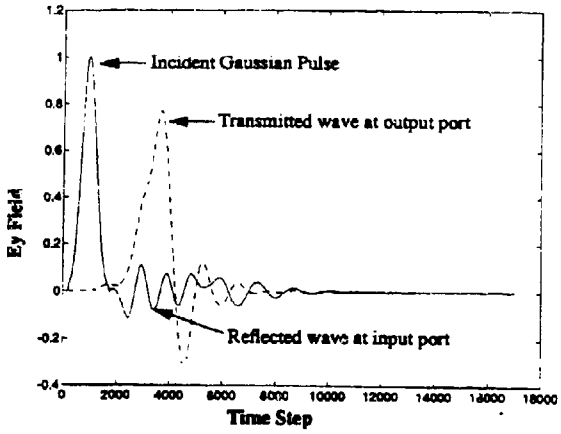

Fig. 3: Time responses for meander line

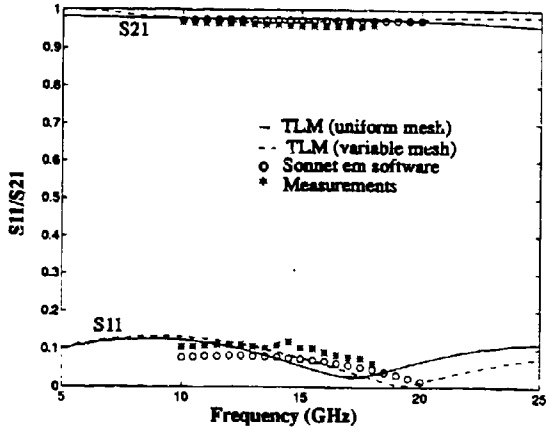

Fig. 4a: Magnitude of S-parameters for meander line

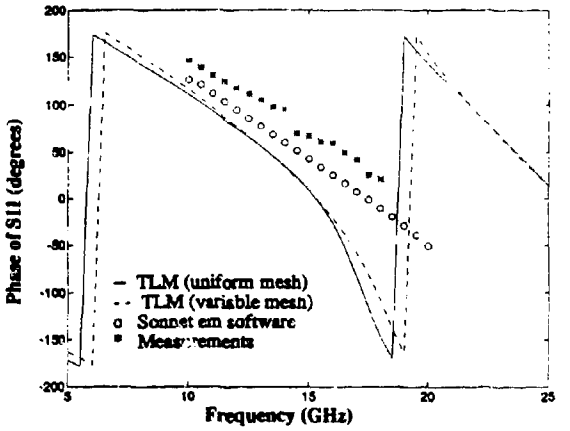

Fig. 4b: Phase of S-parameters for meander line

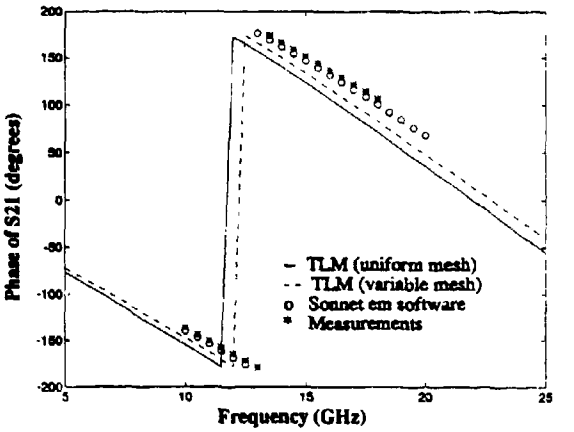

Fig. 4c: Phase of S-parameters for meander line

COMPUTATIONAL STUDIES OF FACTORS AFFECTING

LASER DOPPLER VELOCIMETER MEASUREMENTS

Dr. Joseph E. Whalen
3115 E. Navaho Street
Sierra Vista, Arizona 85635

Abstract

This paper discusses a Laser Doppler Velocimeter (LDV) Simulation (LDVSIM). Representative results include time histories of photocurrents, distribution of photocurrents showing their Gaussian behavior, effects of varying scatterer size, effects of velocity variations within the measurement volume (mv), and the effects of fluid mean flow through the mv. Emphasis is on the fluid characteristics as opposed to hardware characteristics.

1.0 Introduction

LDVs are devices for determining velocities of solid objects and fluids containing particulates. Fluid applications involve several physical phenomena that are of interest, e.g., convective flow, Brownian motion. Brownian motion limits the ability of the LDVs to measure low velocities. LDVSIM was designed to be simple and provides an alternative to more sophisticated models. Despite its simplicity, LDVSIM has provided significant insight into LDV behavior. Also, LDVSIM provides a means of validating more complicated models. Simplicity in modeling is achieved by considering the problem as an electromagnetic scattering problem. Each scatterer in the mv is considered to be a source of a spherical wave that is reflected from the scatterers onto the photo detector. The total field at the detector is the sum of the fields from the individual scatterers. Obviously, if one needs to model the millions of scatterers typically encountered, the LDVSIM approach is impractical from a computational perspective; however, as is shown later, as few as 32 scatterers are sufficient to obtain the Gaussian behavior for photocurrents that is expected in the limit of a large number of scatterers.

2.0 Laser Doppler Velocimeter (LDV) Operating Principles

Because of the Doppler effect, the frequency of light scattered from a moving object is shifted with respect to the incident light [1,2]. Since the velocity of the scatterers of interest is considerably less than the speed of light, the Doppler frequency shift is only a small fraction of the optical frequency. Since measurements at optical frequencies are impractical, "down mixing" to lower frequencies is employed to translate to a measurable frequency range. A common approach to frequency shifting is illustrated in Figure 1. The laser beam is split into two components: the reference beam and the incident beam. The reference beam is shifted in frequency by Bragg cells. The incident beam is reflected from scatterers in the fluid medium and returns as the scattered beam. Both scattered and reference beams are directed to a photo detector. For stationary scatterers, the photocurrent from the photo detector will oscillate at the frequency difference between the scattered and reference beams. A shift in frequency of the scattered beam caused by scatterer motion will appear as a shift in frequency of the photocurrent power spectra.

The output of the photo detector is amplified, filtered to remove noise outside the frequency band of interest, and demodulated. The shift in the spectrum of the demodulated photocurrent is proportional to the velocity of the scatterers. In typical laboratory applications, provision is made to extract the photocurrent time histories in a complex envelope representation. One way of achieving this is illustrated by the electronic components appearing in Figure 1. Other LDV configurations are presented in References [3,4].

3.0 Overview of the LDV Simulation (LDVSIM)

Functional flow within LDVSIM is provided in Figure 2. There are three major components: an Interactive Setup Procedure (SETUP), a batch oriented Computational Procedure (COMPUT), and a Post Processing Procedure (POSTPR). POSTPR contains spectrum analysis modules, signal processing modules including phase-locked loops, statistical analysis modules, and graphics modules. POSTPR was developed first and used as a tool to develop the algorithms in other portions of LDVSIM. In addition to obtaining inputs from the user required to run COMPUT, SETUP provides management services for input parameters and for output results, control options for COMPUT and POSTPR, and archival services.

LDVSIM is a combination of time-step processing and event processing. Photocurrents are computed at a uniform time step specified by the user. Events can occur at arbitrary times, but are assumed to fall on the uniform time step boundaries. Events include computer-program control options, e.g., time at which to turn data collection on/off, conditions under which termination is to occur, physical events such as platform accelerations, and many other events corresponding to physical phenomena.

LDVSIM is highly modular, with major modules for each of the items listed in center of Figure 2. Thus, it is relatively easy to replace a module, such as the model for the mv flow field. Although not a true "plug and play" capability since a compile step is required, the capability proved adequate in supporting a large number of investigations in a timely manner.

4.0 Mathematical Formulations

Assumptions and overview. The key sensing element in the LDV is a photo detector; the output of which is a photocurrent. To obtain the velocity, the electronic portion of the LDV determines the phase rate spectrum for the photocurrent. The magnitude of the frequency shift of the phase rate spectra is proportional to the relative velocity between the LDV and the scatterers in the mv. The following assumptions are made: (1) The beam incident on the scatterer is a plane wave. (2) The scattered beam incident on the photo detector is an outgoing, spherical wave having its origin at the scatterer. (3) The total scattered electric field incident on the photo detector is the sum of the electric fields from each scatterer. (4) The reference beam incident on the photo detector is a plane wave. An overview of the mathematical model implemented in LDVSIM follows.

Photocurrents and Phase Rate Expressions. The photocurrent is given by [3,4]:

$$(E_r+\sum_{m=1}^{N} E_{sm})\,(E_r+\sum_{m=1}^{N} E_{sm})^{*}=E_rE_r^{*}+J, \tag{1}$$

where E_r= electric field of reference (r) beam represented by a plane wave, E_{sm}= electric field from scatterer (s) beam represented by a spherical wave, N = number of scatterers, * = complex conjugate

The first term on the right-hand side of the above equation is a constant bias term that is assumed removed by the processing system. Also, the variability of the above expression across the face of the photo detector is ignored. Carrying out the multiplication leads to the following expression for the photocurrent:

$$J=\sum_{m=1}^{N} J_m+1/2\sum_{m=1}^{N}\sum_{n=1}^{N} A_mB_nG_mG_n\cos(\phi_{mn}+\eta_{mn})+\eta_J, \tag{2}$$

$$J_m=A_mG_m\cos(\omega' t+\phi_m+\eta_I-\eta_J-\eta_s), \tag{3}$$

where ω' = difference frequency between reference beam and the incident beam; A_m, B_m = terms containing wave number, laser intensity, and geometrical parameters; σ_m = scattering cross section for the mth scatterer; η = various noise sources, e.g., shot noise (J), reference (r), incident (i), scattered (s) beam noise.

The complex envelope representation for J_m is given by,

$$J_m = I_m + iQ_m, \tag{4}$$

where the I and Q are referred to as the "inphase" and "quadrature" components. To obtain expressions for I_m and Q_m, J_m is mixed with $\cos(\omega't)$ and $\sin(\omega't)$ terms. The inphase component is given by,

$$I_m = (1/2) A_m \sigma_m (\cos(2\omega' t + \phi_m + \eta_{ris}) + \cos(\phi_m + \eta_{ris})) + A_m \sigma_m \cos(\omega' t) \sum_{n=1}^{N} A_n \sigma_n \cos(\phi_{mn} + \eta_{sn}) . \tag{5}$$

A similar expression is obtained for the quadrature component; however, cosine terms are replaced by sine terms and the second sine term is negative.

The required phase rate from which velocities can be determined is obtained by differentiating the arc tangent of the ratio of quadrature to inphase components:

$$\dot{\phi} = (I\dot{Q} - Q\dot{I}) / (I^2 + Q^2) . \tag{6}$$

After taking the time derivative of appropriate terms, a messy job, an expression for the time rate of change of phase can be obtained in terms of the time rates of change of geometrical factors, scatterer velocities, propagation media characteristics, scatterer mass, and noise sources.

Scatterer Positions and Velocities. The simulation computes the value for the phase rate at time intervals specified by the user. At any particular time, the particles will have a velocity caused by Brownian effects and by the fluid velocity. The velocity distribution associated with Brownian motion is given by,

$$P_u(u_o, u, t) = \left(\frac{m}{2\pi kT(1-\exp(-2\gamma t))}\right)^{1/2} \exp(-m(u - u_o\exp(-\gamma t))^2 / 2kT(1-\exp(-2\gamma t))) , \tag{7}$$

where u_o = velocity at $t = 0$; u = instantaneous velocity of a scatterer; t = time; m = scatterer mass; k = Boltzmann's constant; T = temperature; $\gamma = 6\pi\nu r/m$; ν = viscosity, kg/(sec-m); r = scatterer radius.

The above expression is Gaussian with standard deviation and mean given by:

$$\sigma = (kT(1-\exp(-2\gamma t))/m)^{1/2},$$

$$u = u_o\exp(-\gamma t) .$$

Module BROWN computes Brownian velocities using a Gaussian distribution using the above parameters.

Between times at which the photocurrent and phase rate are computed, the scatterers are subject to collisions with surrounding molecules. As a result, the scatterers diffuse in and out of the rm. To capture these effects, new positions are computed for each time step using the distribution for particle diffusion [5]:

$$P_x(x_o, x, t) = (m\gamma^2/2\pi kT(2\gamma t - 3 + 4\exp(-\gamma t) - \exp(-2\gamma t)))^{1/2}$$
$$\exp[-m\gamma^2(x - x_o - u_o(1-\exp(-\gamma t))/\gamma)^2 /$$
$$(2kT(2\gamma t - 3 + 4\exp(-\gamma t) - \exp(-2\gamma t)))], \quad (8)$$

where x_o = initial particle position, x = particle position at time t

The above form is Gaussian with standard deviation and mean given by:

$$\sigma_x = (kT(2\gamma t - 3 + 4\exp(-\gamma t) - \exp(-2\gamma t))/(m\gamma^2))^{1/2},$$

$$\langle x \rangle = x_o + u_o(1-\exp(-\gamma t))/\gamma.$$

Module BROWN computes changes in position caused by Brownian effects using a Gaussian distribution having the above parameters. These changes are added to position changes associated with other fluid-flow elements.

Appropriate models for other velocity effects can be incorporated into LDVSIM by replacing the particle velocity module (VELINT) with an appropriate velocity field model. One model used for this paper represents fluid flow in a convection cell [8]. The required scatterer velocities are obtained by a two dimensional interpolation within measured velocity fields. LDVSIM has an option to superimpose a linear flow field on the mv so that transit broadening effects can be investigated. One other velocity component that is modeled is LDV platform motions.

5.0 Representative Results

Results are presented in the figures that follow the text.

Photocurrent Time History Characteristics. Figure 3 contains inphase and quadrature time series for Brownian motion. In addition to rapid fluctuations, the data exhibit low frequency behavior caused by Brownian diffusion of particles in and out of the mv. The average number of scatterers is 32.

Photocurrent Statistical Characteristics. In many analytic derivations the number of particles is assumed large. Typically, a mv contains thousands of scatterers, often millions. Simulation runs involving large number of particles for long periods of simulated time are prohibitive because of long computational times. Thus, it is worth determining how many scatterers need to be included in the simulation to obtain reasonable statistical agreement with the many-scatterer case. Histograms of the inphase component of photocurrent for a single scatterer (line) are compared with a 32-scatterer case (shaded portion) in Figure 4. The 32-scatterer case passes the Kolmogorov-Smirnoff test for Gaussianity at the 95% confidence level.

Photocurrent Power Spectra. If scatterer inertial effects are ignored, the power spectra of the photocurrents for Brownian motion will be Lorentzian. As inertial effects are introduced, the spectra will have a lower value. A comparison of the output from the simulation which contains inertial effects (See Eqs. 7 and 8) with the corresponding Lorentzian profile is presented in Figure 5. Note that the trend is as expected.

Brownian Motion. For these runs all effects except Brownian motion were turned off. Five different simulations were conducted corresponding to five different scatterer masses. As mass increases, the Brownian-velocity distribution peaks at lower velocities. Thus, power at high frequencies will decrease as scatterer mass increases. These effects are illustrated in Figure 6, which contains a power spectra for the photocurrents. Ultimately, the velocity of the fluid is determined by the shift in the power spectra of the photocurrent phase rate. Power spectra for photocurrent phase rates for five different particle sizes are illustrated in Figure 7. The noise floor for the 1 micron scatterers is significant.

Velocity Variability within the mv. Velocity diversity effects were investigated by introducing a convective flow pattern consisting of two eddies. The eddies are assumed generated by placing a temperature gradient across a 3x2x1 cm cell containing the ellipsoid mv with its long axis at a 10-15 degree angle with respect to the 3x2 cm face. Fluid flow is up in the center of the mv and down at either end. Placing scatterers in two groups at the ends of the mv results in a velocity component toward the detector for one group and away from the detector for the other group. The phase spectrum has two peaks corresponding to the two groups of scatterers as illustrated in Figure 8. As time passes, the scatterers migrate throughout the mv because of the convective flow. After several minutes, the resulting spectrum is as illustrated in Figure 9. Note the broad nature of the spectrum. The lack of power outside of 250 Hz reflects the maximum velocities in the cell for the thermal gradient applied. The narrow isolated peak at the left may represent trapped particles, however, this hasn't been rigorously confirmed.

A comparison of phase rate spectra for three different thermal gradients across the convection cell is illustrated in Figure 10. As the temperature increases, convective patterns are established and the scatterers velocities are no longer zero. Increasing the temperature provides a greater concentration of high speed scatterers, which increases the spectral spreading.

Transit Broadening. Transit broadening effects were investigated by introducing a mean flow in the mv. Two cases were simulated corresponding to two different velocities. These results are provided in Figure 11. The dotted line represents the higher speed. The higher speed case, line (b), is significantly broader.

6.0 Conclusions

The basic elements of Laser Doppler Velocimeter (LDV) operations as applied to fluid velocity measurements have been discussed and re-enforced with computational results. The LDV aspects illustrated in this paper represent only a small fraction of the total problem. Additional phenomena that may be of interest for future investigations include: scatterer shape, scatterer optical reflectance characteristics, scatterer internal dynamics, platform vibrations, turbulence in the vicinity of the platform, and signal processing refinements.

Developing models and investigating LDV systems provided a convenient means to investigate fundamental physical phenomena, such as Brownian motion, wave propagation through random media, optical systems, fluid flow, thermal dynamics, and electronic systems. Establishing LDV experiments at academic institutes for the purpose of investigating LDV systems is recommended as a basic research endeavor and as a teaching aid to illustrate modern aspects of laser systems as well as fundamental physical phenomena.

References.

1. Born, M., and Wolf, E., 1959, Principles of Optics, Pergamon Press, New York, New York.
2. Jackson, David J., 1962, Classical Electrodynamics, John Wiley and Sons, Inc., New York, New York.
3. Adrian, Ronald J., 1983, "Laser Velocimetry," Chapter 5, Fluid Mechanics Measurement, edited by Richard J. Goldstein, Hemisphere Publishing Corporation, Washington, D.C.
4. George, W. K., and Lumley, J. L., 1973, "The Laser-Doppler Velocimeter and its Application to the Measurement of Turbulence," J. Fluid Mech., Vol. 4, p. 1220.
5. Nelson Max, editor, "Selected Papers on Noise and Stochastic Processes," Dover Publications, p 99.
6. Busse, F. H., 1967, "On the Stability of Two-Dimensional Convection in a Layer Heated from Below," J. Math. and Physics, Vol. 46, p 140

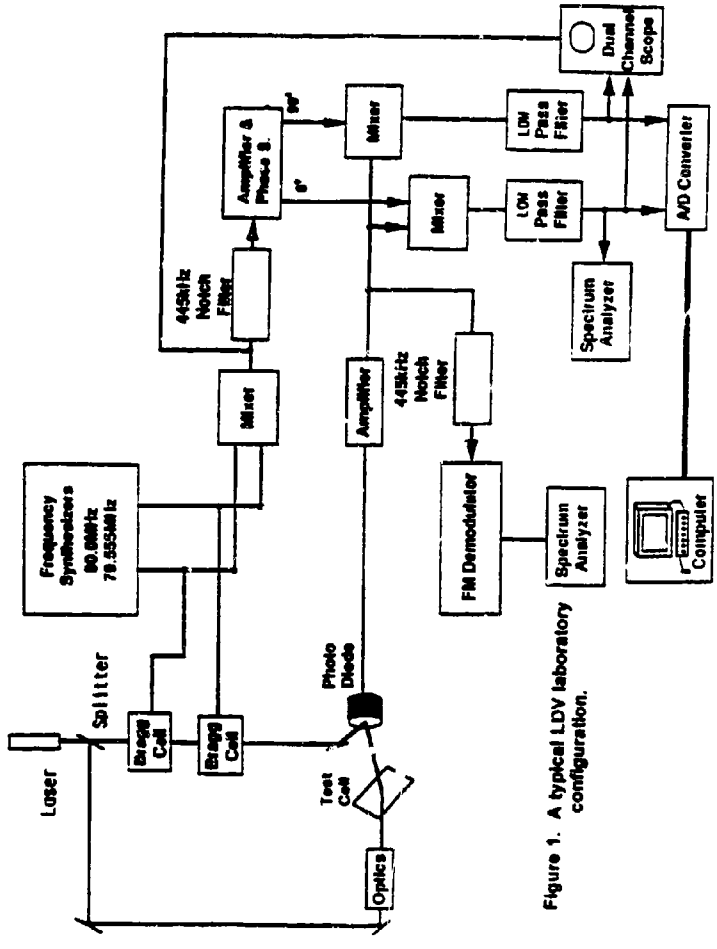

Figure 1. A typical LDV laboratory configuration.

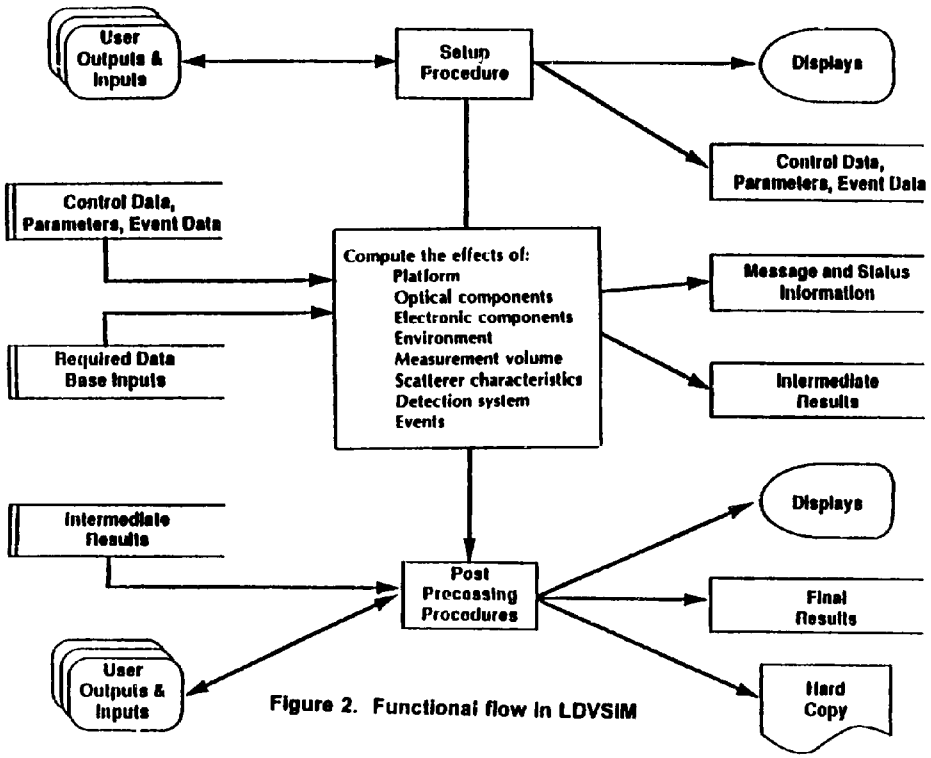

Figure 2. Functional flow in LDVSIM

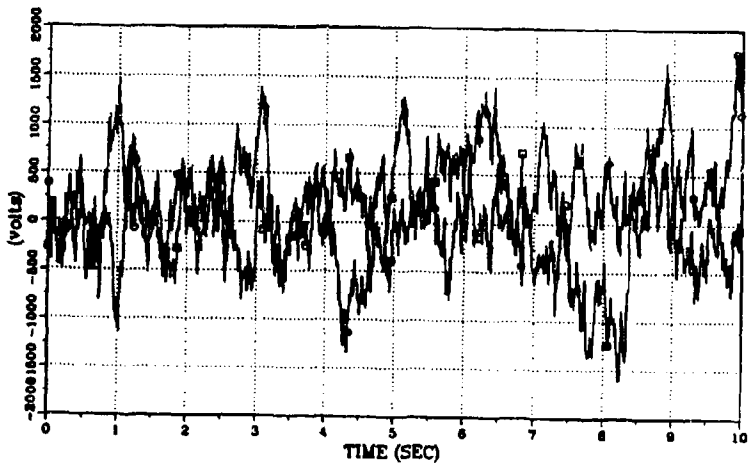

Figure 3. Inphase and quadrature components for Brownian motion.

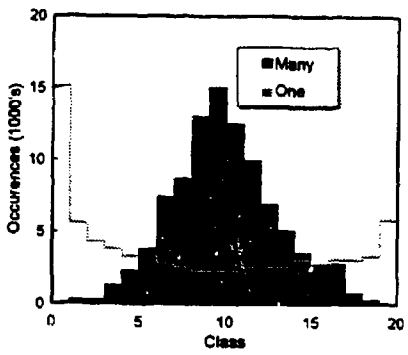

Figure 4. Photocurrent distributions.

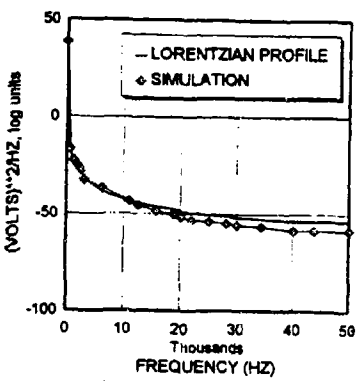

Figure 5. Comparison of simulated photocurrent with theoretical prediction.

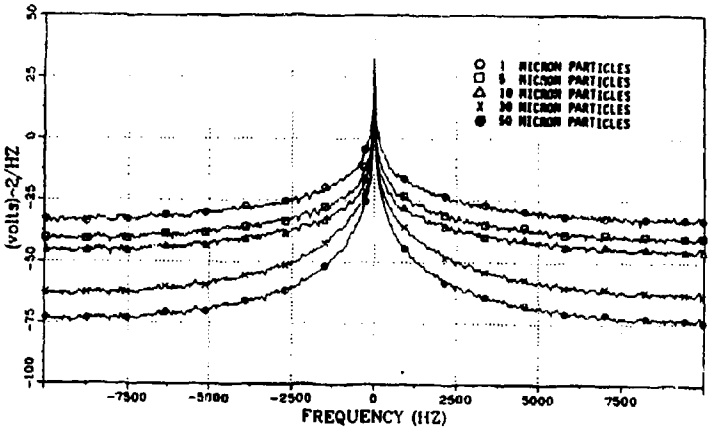

Figure 6. Comparison of photocurrent spectra for five different scatterer masses.

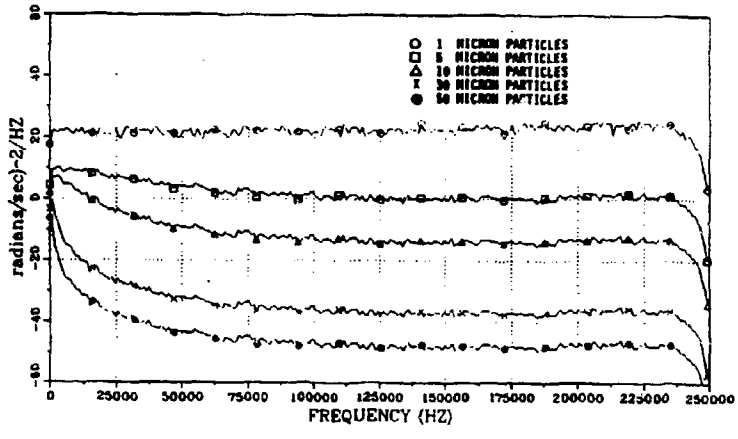

Figure 7. Comparison of phase rate spectra for five different scatterer masses.

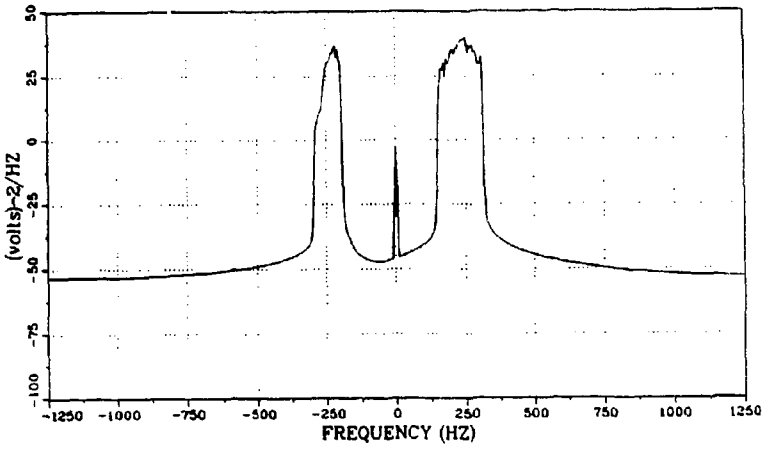

Figure 8. Photocurrent spectra for non-uniform distribution of scatterer location at the beginning of the simulation run.

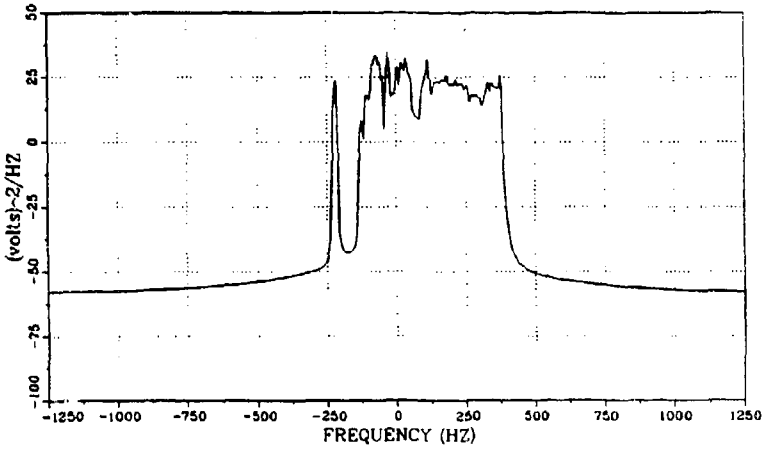

Figure 9. Photocurrent spectra after scatterers have distributed themselves throughout the measurement volume at end of simulation run.

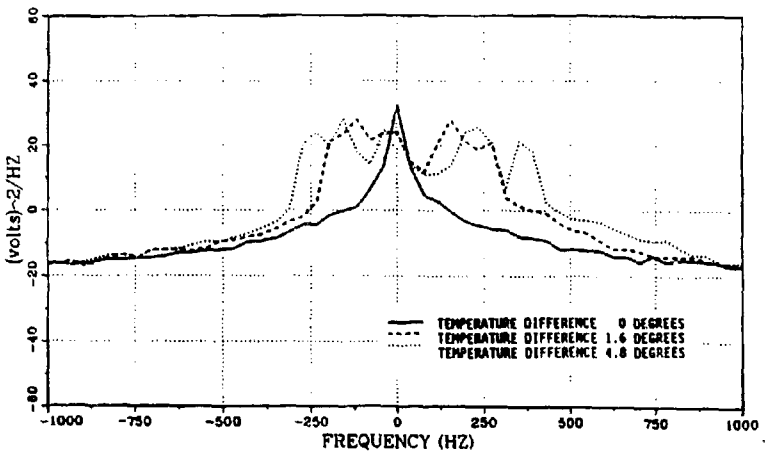

Figure 10. Photocurrent spectra for convection-cell mv at three different temperature gradients resulting in three levels of convective flow.

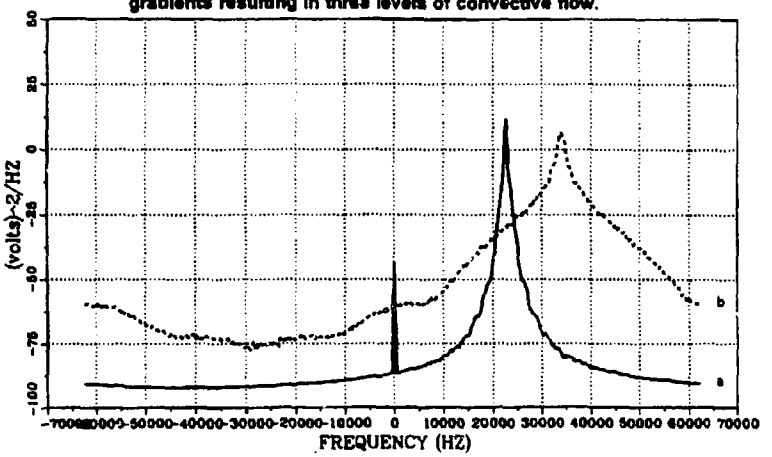

Figure 11. Photocurrent spectra at two different mean flows. (a) Mean flow = 10 cm/sec. (b) Mean flow = 15 cm/sec.

Analysis of a Cavity-Backed Slot Antenna Mounted on an Infinite Ground Plane Using the 2-D TLM Method

John B. Erwin and Stuart M. Wentworth
Dept. of Electrical Engineering
200 Broun Hall
Auburn University, AL 36849

Introduction

The transmission line matrix (TLM) method is a very powerful technique for solving electromagnetic problems. A single computer algorithm can be used to analyze a wide variety of electromagnetic interaction problems since arbitrary media parameters and boundary conditions can be changed simply by modifying an input file. The model simulates waves propagating in the time domain within a space that has been discretized into transmission line sections, called TLM 'nodes'. Voltages and currents on these nodes correspond to electric and magnetic field quantities. Two dimensional space is discretized into four-port nodes, and three dimensional space may be discretized into 12-port symmetrical condensed nodes [1]. A pulse entering one port of a node is scattered to the other ports based upon a scattering matrix which can be derived for either the 2D or the 3D node and can include the effects of material parameters such as permittivity, permeability, and conductive losses. The scattered or reflected pulse leaving one port of a node becomes an incident pulse on the appropriate port of an adjacent node. The TLM method is then a two-step iterative procedure that first involves scattering of incident pulses at every node followed by a connection step to pass the reflected pulses to adjacent nodes. Repeated application of this scattering-connection process results in an output function at some observation point (output node) which consists of a train of pulses in time which may be Fourier transformed to obtain a frequency response or convolved with an arbitrary time domain input sequence to get a corresponding output.

The TLM method can be used to calculate the fields scattered from arbitrary bodies. By exciting a particular group of nodes (a line of nodes in the 2-D model or a plane of nodes in the 3-D model), a plane wave will begin propagating through the mesh. If the bistatic RCS is desired, the scattered fields resulting from this plane wave encountering the body are determined along a virtual surface surrounding the body. One way to calculate these fields is to obtain the total fields with the scatterer in place, and the incident fields with the scatterer removed. The scattered fields are simply the difference between the total and the incident fields. The resulting fields are then used to determine the far-field pattern [2,3].

One of the difficulties in obtaining RCS through numerical modeling is that the incident plane wave must appear infinite. This requirement is often met by making the mesh very large along the wavefront. However, a large mesh containing many nodes will require a lengthy computation time. One way to simulate an infinite plane wave with a more manageable mesh size is to implement "magnetic walls" that guide the plane wave. These magnetic walls are perfectly reflecting boundaries of infinite impedance. This approach is inadequate for obtaining the incident fields (since there is no scatterer), but the magnetic walls would interfere with waves reflected off the scatterer. Ideally, scattered fields see only absorbing boundaries, which in the 2-D TLM model can be realized by using a reflection coefficient of -0.1716.

An approach to this problem is to run a total fields case, which includes the scatterer along with absorbing boundaries, concurrently with the incident fields case, which omits the scatterer and has magnetic boundaries to make the plane wave appear infinite. During each iteration, a scaled portion of the pulses reflected at the magnetic boundaries for the incident fields case are injected into the boundaries for the total fields case. The details of this approach are described in a previous work [4].

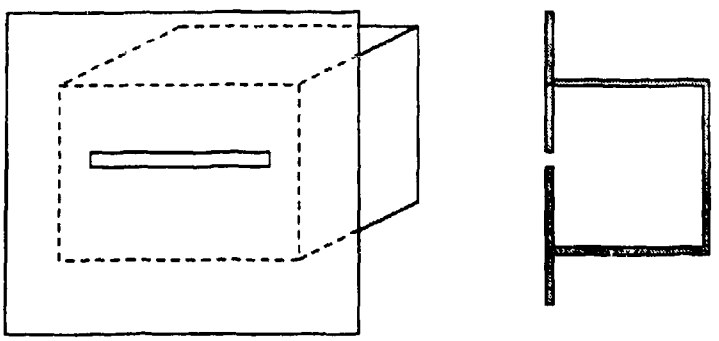

Fig. 1: 3-D depiction and side view of a cavity-backed slot antenna mounted on an infinite ground plane.

The situation is more complicated when the scatterer consists of an element mounted on an infinite ground plane. When a plane wave is incident upon an infinite ground plane, it is reflected (or scattered) as a plane wave. For a normally incident plane wave, the incident fields and those scattered from the ground plane may be maintained along the boundary by using magnetic walls with reflection coefficient +1. However, there would also be scattering from an element mounted in the ground plane which would require an absorbing boundary to prevent re-scattering. Thus, the problem of simultaneously maintaining the incident plane wave, and the two scattered fields (from the ground plane and from the mounted element) arises. This paper will discuss a solution to this problem using a cavity-backed slot antenna mounted on the infinite ground plane in a 2-D TLM mesh, as shown in Fig. 1 as an example. These antennas are commonly used in aircraft and space applications because of their conformal mounting abilities [5].

Approach

Determination of the scattered fields from a cavity-backed slot antenna mounted on an infinite ground plane requires an adequate model of the infinite ground plane in only a finite TLM mesh. One method is to truncate the ground plane, but allow it to remain excessively large compared to the mounted element. This method raises several questions: How much larger than the mounted element does the ground plane need to be? Is the size of the ground plane dependent upon the number of iterations run? In addition, how lengthy a run time can be tolerated for a large mesh? A second method, and one we will describe in this paper, is to employ a pulse injection technique to handle the reflected plane wave. This approach is similar to one taken in modeling an incident plane wave [4]. This approach, a plane wave injection technique for the incident plane wave, will be reviewed. Then we will show how a similar method can be used to model the plane wave reflected off of an infinite ground plane. Figure 2 shows the actual TLM model of a cavity mounted in a ground plane. This is an approximation of the cavity-backed slot antenna case where now the slot dimensions are actually equal to the cross-section of the cavity.

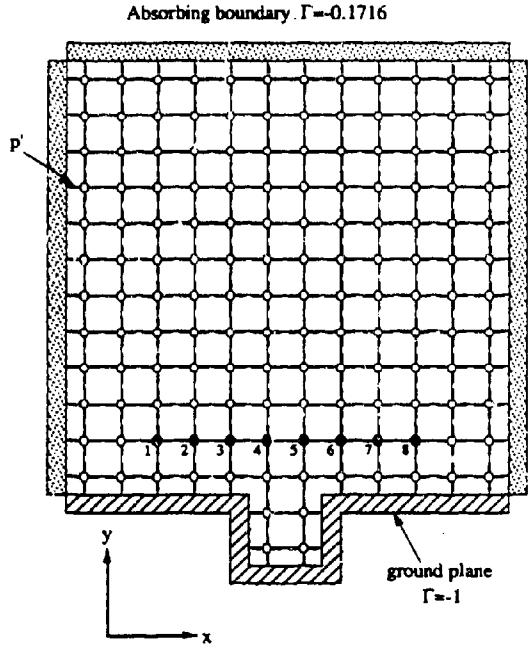

Fig. 2: A representation of the 2D model for the cavity mounted on an infinite appearing ground plane. The plane wave would be normally incident from the top, and the field points are determined at the indicated nodes 1-8.

Pulse Injection

Our problem requires simulation of both an incident plane wave and a plane wave reflected from an infinite ground plane while simultaneously absorbing the field scattered from the cavity. An accurate and time-efficient method to model an incident plane wave is to maintain the absorbing boundaries while injecting pulses previously calculated [4]. These injections maintain the integrity of the plane wave by allowing it to appear to be non-attenuating. Since the absorbing walls cannot distinguish between incident and scattered waves in the total fields case, -0.1716 times the incident field is also reflected at the boundary. Therefore, the incident field pulse at a port next to the magnetic wall is multiplied by 1.1716 and then added to the total field pulse at the corresponding port next to the absorbing wall. The pulses to be injected may be determined by running a one-dimensional string of nodes, as shown in Fig. 3a. For example, during each iteration, the pulse at port p in Fig. 3a is scaled and injected into port p' in Fig. 2. This technique works well for normally incident plane waves and may be modified for oblique incidence cases using a timed pulse injection technique for both the initial excitation and the maintenance of the plane wave [6].

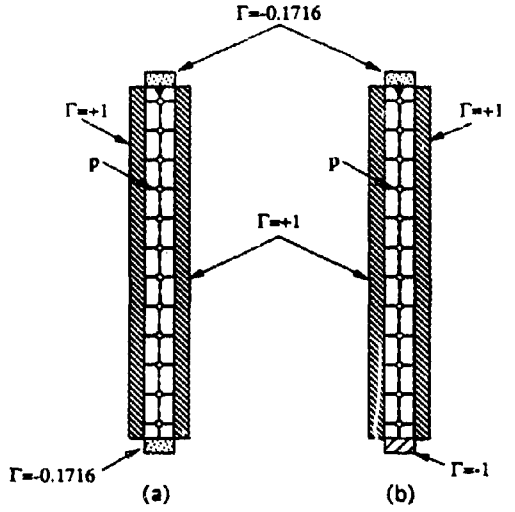

Fig. 3: One dimensional plane wave injection models. In both cases, the waves are guided by PMC walls. (a) For the incident wave case, the wave terminates in an absorbing boundary. (b) For the reflected wave case, the wave is reflected by a PEC.

For our problem, we must incorporate a unique scatterer, the infinite ground plane, to which the cavity is mounted. The technique discussed above works well for maintaining the incident plane wave while absorbing the scattered field from the cavity, but some further action must be taken to account for the scattered field from the ground plane. The field scattered from the ground plane would be a plane wave except for the presence of the cavity. It therefore should not be allowed to attenuate when propagating through the mesh. Since the absorbing boundaries used to absorb the fields scattered from the cavity would give rise to attenuation of the plane wave, an approach similar to the one used to maintain the incident plane wave may be taken to maintain the reflected plane wave.

Similar to the incident case, pulses are pre-calculated and injected into the mesh every iteration to maintain the scattered plane wave from the ground plane. The pulses are calculated by using a one-dimensional set of nodes, as shown in Fig. 3b. Note that the left and right boundaries are PMC and the bottom boundary is a PEC, representing the ground plane. Because of the normally incident field's symmetry, this accurately represents the infinite ground plane without the cavity. When the pulse is injected at the top of Fig. 3b (as shown by the arrow), a one dimensional wave, representing a plane wave, propagates through the mesh. During each iteration, the voltage pulses on the ports next to the magnetic boundaries are increased by 17.16% and injected into their corresponding ports of the 2-D mesh. In Fig. 3b, once the wave reflects from the PEC, the total fields become present in the mesh. Therefore, the reflected pulses along the PMCs represent both the incident wave and the scattered wave. Consequently, the pulses injected from Fig. 3b into Fig. 2 simultaneously maintain the integrity of *both* the incident plane wave and the scattered plane wave from the infinite ground plane.

Verification

The electric field calculated at selected points using our injection technique was compared to the field using a very large ground plane. The large ground plane extended 1249 nodes on each side of a 2 x 2 node cavity, and the mesh reached 10 nodes above this ground plane. The injection technique was used to simulate the incident plane wave, but no injection was used to simulate the reflected plane wave. The extreme size of this mesh was sufficient to calculate the field in the vicinity of the cavity as though it were mounted on an infinite ground plane. Using 1500 iterations, an accurate E-field distribution was calculated over a line of 8 nodes parallel to the ground plane. These nodes were selected 2 nodes directly above the cavity and were symmetrical to the cavity's center (the node location relative to the cavity is shown in Fig. 2).

In the mesh including the injection technique for the reflected wave, the ground plane extended only 5 nodes on either side of the 2 x 2 node cavity. Again, the mesh reached 10 nodes above the ground plane, the field was calculated over the 8 nodes indicated in Fig. 2, and 1500 iterations were run. As shown in Fig. 4, we achieved very close agreement with the large mesh case. The maximum deviation was less than 0.4%. A comparison of the phase showed similar agreement. For an additional comparison, Fig. 4 also shows the field obtained when the smaller mesh was run without the injection technique for the reflected wave (injection was still used to simulate an incident plane wave). This case deviates from the large ground plane case by as much as 16%.

There is a limit to how close the side walls can be brought in using our technique. With the walls moved to within one node of the cavity, the field deviated from the very large ground plane case (the maximum deviation was 4.0%). However, with the walls only 2 nodes from the cavity, the maximum deviation dropped to 2.0%.

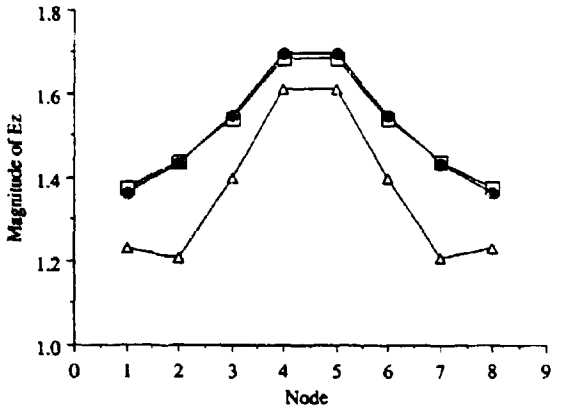

Fig. 4: Comparison among calculated electric fields for three cases:

(i) (□) a large mesh, 1500 nodes in length, used without the injection technique

(ii) (●) a small mesh, 12 nodes in length, incorporating the injection technique

(iii) (Δ) a small mesh, 12 nodes in length, without the injection technique

Conclusions

By injecting pulses at the boundaries, our 2-D TLM network can simulate a plane wave normally incident on a cavity which has been mounted on an infinite ground plane. Since a relatively small ground plane in the mesh can be made to appear infinite, a significant savings in memory and run time is realized over the large mesh approach. We are now developing a timed pulse injection technique to accurately model plane waves obliquely incident on an infinite ground plane. Further, these techniques will be adapted for the 3-D TLM network.

Acknowledgments

This work has been supported by the Antennas Laboratory of Texas Instruments, Inc., McKinney, Texas.

References

1. P. B. Johns, "A symmetrical condensed node for the TLM method," *IEEE Trans. Microwave Theory Tech.*, Vol. MTT-35, No. 4, pp. 370-377, 1987.

2. K. Umashankar and A. Taflove, "A Novel Method to Analyze Electromagnetic Scattering of Complex Objects," *IEEE Trans. on Electromagnetic Compatibility*, EMS-24, No. 4, pp. 397-405, 1982.

3. F. J. German, G. K. Gothard, L. S. Riggs, and P. M. Goggans, "The Calculation of Radar Cross-Section (RCS) Using the TLM Method," *International Journal of Numerical Modelling: Electronic Networks, Devices and Fields*, Vol. 2, pp. 267-278, 1989.

4. J. B. Erwin and S. M. Wentworth, "Plane Wave Injection Technique to Calculate RCS in a 2-D TLM Network," *Electronics Letters*, Vol. 29, No. 14, pp. 1241-1243, 8th July 1993.

5. S. Hashemi-Yeganeh and C. Eircher, "Theoretical and Experimental Studies of Cavity-Backed Slot Antenna Excited by a Narrow Strip," *IEEE Trans. Antennas Prop.*, Vol. 41, No. 2, pp. 236-241, Feb. 1993.

6. F. J. German, Personal communication, Texas Instruments, Inc., December 1993.

SESSION 3:

MULTIPOLE

Chair: Dan Reuster

Curved Line Multipoles for the MMP-Code

P. Leuchtmann and M. Gnos
Lab. of El.-mag. Fields and Microwave Electronics, ETH Zurich
CH-8092 Zurich, Switzerland

Abstract

The expansion of the electromagnetic field used in MMP (Multiple Multipole Program) may be simplified in particular cases. Depending on the set of expansion functions a significant reduction of the number of unknowns is possible. The paper describes a new set of expansion functions (the 'curved line multipoles') which may be flexibly adapted to any curved long structure including edges. Curved line multipoles have two independent parameters (order N and degree M) to predefine the maximum possible variation of the field to be expanded. N steers the variation along a curved line of finite length while M steers the field variation around this line. The calculation of the line multipoles is discussed and the application to particular scattering problems shows their advantage versus the conventional multipoles.

1. Introduction

This paper deals with a particular subset of expansion functions for the MMP-code, the line multipoles. First let us briefly describe the basic ideas of MMP (Multiple Multipole Program) in order to see what the line multipoles are good for.

The basic problem is finding an unknown electromagnetic field function f where $f = (\vec{E}, \vec{H})$ has six components, the components of the electric field $\vec{E}$ and the components of the magnetic field $\vec{H}$. In a domain D (with boundary ∂D) f has to satisfy Maxwell's equations in the stationary case ($\sim e^{-i\omega t}$): $\operatorname{curl}\vec{E} = i\omega\mu\vec{H}$ and $\operatorname{curl}\vec{H} = -i\omega\varepsilon\vec{E}$ where ω: angular frequency, μ, ε: constant (complex) permeability, permittivity in D, i: imaginary unit, t: time. On ∂D, f must satisfy some boundary conditions. MMP starts with the series expansion

$$f \approx \sum_{j=1}^{J} a_j f_j \tag{1}$$

where each expansion function f_j fulfils Maxwell's equations, but not necessarily the boundary conditions. The unknown coefficients a_j are used to satisfy the latter in a least squares sense. Obviously, the choice of the expansion functions f_j has significant influence on the convergence of the expansion (1). If the solution f has a particular behavior — e.g., f is the scattered field and radiates energy away from the scatterer — it makes sense to use only expansion functions f_j with the same behavior. On the other hand the set of expansion functions should span a wide variety of possible solutions. Let us consider a special case: scattering at an ideally conducting sphere (see fig. 1). The optimum set of expansion functions for modeling the scattered field is a series of multipole functions. Assume that the sphere is electrically large and the incident field is a linearly polarized plane wave traveling in z-direction. In this particular case, N must be large, but $M = 1$ is sufficient. Since a full multipole expansion has $N^2 - 1$ parameters while the adapted set (all orders but only terms of first degree) has only N parameters, the number of unknowns is significantly reduced without any lack of accuracy. This example shows how an intelligent choice of the expansion functions may dramatically reduce both the amount of calculation ($\sim N^3$) and

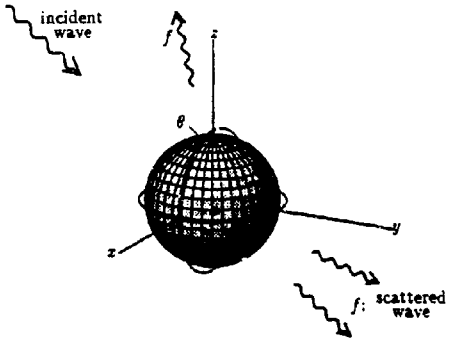

Figure 1 For any incident field, the scattered field f may be written as a sum of multipole functions, starting with a dipole and ending up with functions of higher order and degree. With the set of all multipoles up to the maximum order N any variation of f along $\theta \in [0, \pi]$ describable by an N-th order polynomial in $\cos\theta$ may be represented exactly. Similarly, with the set of all multipoles up to the maximum degree M any variation of f along $\varphi \in [0, 2\pi]$ describable by an M-th degree Fourier series in φ may be represented exactly. Note that M and N may be chosen independently, but it is always $M \leq N$. For $N, M \to \infty$ the functions form a mathematically complete set of expansion functions.

the amount of computer memory ($\sim N^2$). The line multipoles to be discussed in this paper offer a similar possibility for reducing the total number of unknowns not only for spheres but for any 'long structures'.

2. Curved Line Multipoles: Qualitative Description

The set of expansion functions to be presented in this paper may be looked as distributed multipoles along an arbitrary curved line L of finite length L. We define a longitudinal coordinate z *along* L and an azimuthal coordinate ϕ *around* the line L (see fig. 2). The field of the curved line multipoles is singular on the finite line L and fulfils Maxwell's equations anywhere else. The strength of the singularity varies along L in a polynomial way, i.e., line multipoles up to order N model any variation along $z \in [0, L]$ describable by an N-th order polynomial in z. For a given z-variation of a curved line multipole function there are various ϕ-variations available, namely any trigonometric function in ϕ. More precisely: Line multipoles up to M-th degree model any variation along $\phi \in [0, 2\pi]$ describable by an M-th degree Fourier series in ϕ. Note that M and N may be chosen independently from each other. For $N, M \to \infty$ the resulting set forms a complete set of expansion functions in the space outside the line L.

Physically, the zero degree term is the field of a line current $I(z)$ along L. Very close to L this field does not depend on ϕ. However, for a curved L the ϕ-independency is lost away from the line. This is due to the fact that ϕ- and z-values are not uniquely defined for such points. Nevertheless, the curved line multipole function gives exactly the correct field.

Curved line multipoles are useful not only for modeling the field around long thin structures like wires but also for edges. The important point is that the user may predefine the maximum variation along z and ϕ independently from each other just by specifying maximum order N and maximum degree M. Note that this is exactly what is requested in practice: E.g., the field *along* an edge varies most often much less than *around* the edge.

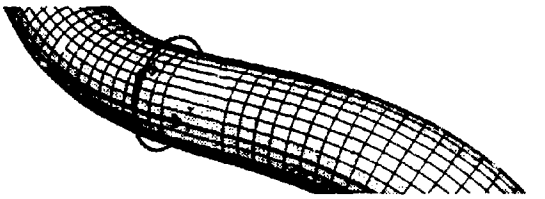

Figure 2 Curved line multipoles are singular on a line L of *finite* length, vary sinusoidally along ϕ and like a polynomial along z. This behavior is strictly true only close to L since the coordinates z and ϕ are not unique away from the curved line L.

3. The Computation of the Curved Line Multipole Fields

It is well known that the electromagnetic field of a thin *straight* line current $I(z)$ (nonzero only on the finite length) may be given in closed form if $I(z) = I_c \cos kz + I_s \sin kz$, where k is the wave number of the surrounding medium and I_c, I_s are constant [1]. Based on this formula the field of an equally segmented long straight wire with n free parameters (the currents at the segment joints) has been given [2]. Sine and cosine shaped currents on each segment were combined in such a way that the current is continuous along the whole wire. For segment lengths $\Delta l \ll \lambda = (2\pi)/k$ (λ = wave length) we have $\cos kz \approx 1$ and $\sin kz \approx kz$ on the whole segment and the mentioned combination results essentially in a polygonial approximation of an arbitrary current distribution $I(z)$.

In order to reduce the number of free parameters on a long wire the values at the segment joints may be given, e.g. equal to a polynomial $p_n(z)$ of degree n. A series $\sum_{n=0}^{N} a_n p_n$ allows the representation of any current distribution $I(z)$. Note that the field of one segment has to be calculated only once but it is part of the contribution of all p_n. The main advantage of such a procedure is that the number of segments may be chosen independently from the number of unknowns [4].

A generalization of the single segment current field has been described in [3]. While a line current has an electromagnetic field with rotational symmetry the mentioned generalization (called 'line multipoles') yields an azimuthal field behavior (along ϕ) proportional to $\sin m\phi$ or $\cos m\phi$ respectively. For $m = 0$ it is equal to the common wire current. Since the m-th degree line multipole is built up using $2m$ single currents[1], there are line multipoles of the same degree both with $\sin kz$ and with $\cos kz$ behavior. Thus it it possible to consider a segmented line and to combine the field functions of each degree to a long multipole in the same way as it has been done for the long wire in [2] and, as a next step, as in [4]. This is essentially what has been done for this paper.

Other than in the previous versions the line may be curved and segmented in an arbitrary way. The user must specify a number of points (the segment joints) and — due to the lack of rotational symmetry — for each segment an additional vector specifying the zero-ϕ direction of this particular segment. This information is stored in an extra file. The graphical MMP preprocessor 'mmptool' (or 'xmmptool') [5] allows the efficient generation of the data.

Two different types of curved line multipoles are available. The difference between the two lies in the treatment of the longitudinal behavior of the fields. The first version is essentially analogous to MMP's thin wire feature [1]. Since an N-segment wire has $N+1$ joints (including the end points) there are $N+1$ parameters. If M is the maximum degree, there are $2M+1$ functions with different ϕ-dependency for each single segment function. Thus, the total number of parameters is $P_{\mathrm{tot}}^{\mathrm{seg}} = (N+1)(2M+1)$. In the second version the number of segments is decoupled from the number of parameters in a similar way as in MMP's long wire expansions [4]. The longitudinal behavior is modeled using Legendre polynomials

[1] The actual calculation is recursive with respect to m and includes a limit (shifting all currents together on the same place) in order to have a single line with singular field values [3].

of order n and the maximum order N may be specified. Thus, the total number of parameters becomes again $P_{\rm tot}^{\rm segs} = (N+1)(2M+1)$, but N is now the maximum order of the longitudinal polynomial expansion rather than the number of segments. Of course the latter should be larger.

A second set of field functions may be obtained using non physical magnetic currents rather than electric currents. For a single segment the electric current fields are TM with respect to z while the magnetic current fields are TE. For simplicity's sake we call the respective curved multipole fields also TE and TM respectively, in spite of the fact that the longitudinal direction varies from segment to segment. A 'complete curved line multipole' has now $P_{\rm tot}^{\rm segs} = 2(N+1)(2M+1)$ free parameters. Note that the calculation of the dual field is very easy and cheap: only the final field values have to be 'dualized', i.e., interchanging $\vec{E}$ and $\vec{H}$ and multiplying by the (negative) wave impedance.

Another set of $P_{\rm tot}^{\rm segs}$ field functions may be obtained using the ingoing Greens function rather than outwards radiating Greens functions for the calculation of the field of a single current segment. This gives non physical fields in free space. Nevertheless, in bounded domains such functions are useful.

The following table gives the exact MMP data needed for all possible variants of curved line multipole expansions. Remember: an MMP expansion has 6 integer parameters (IE1–IE6) among other parameters which are not used for curved line multipoles.

IE1: 131...134 (version 1) or 141...144 (version 2)
IE2: 3 (outgoing waves) or 4 (ingoing waves)
IE3: minimum ϕ-degree or maximum degree
IE4: maximum ϕ-degree
IE5: maximum (longitudinal) order (only version 2)
IE6: 1yy or yy (2)

The parameter IE1 is 131/141, if both TE- and TM-fields are requested. In this case, all ϕ-degrees from 0 to IE3 are computed. If IE1 is 132/142, only ϕ-degrees from IE3 to IE4 are computed. Finally, IE1 = 133/143, only TM-fields are computed and for IE1 = 134/144, only TE-fields are computed, in both cases only ϕ-degrees from IE3 to IE4. The parameter IE6 is used for specifying the file with the geometric data of the line. It it named **mmp_**1yy.xxx where yy is the (two digit) number of the line and xxx is the (three digit) number of the problem to be solved. The zero order term of the TE-fields (a single magnetic current) is only computed if IE6 > 99. For the IE1 = 131...134, $P_{\rm tot} = P_{\rm tot}^{\rm segs}$ is proportional to the number of segment joints $(N+1)$ while for IE1 = 141...144, the longitudinal behavior is modeled using Legendre polynomials up to order IE5.

4. Examples

In order to show the advantage of the curved line multipoles compared to the conventional multipoles, we calculate problems where the line multipoles seem to be useful. In a first example the scattering at a banana shaped object is investigated. The geometrical situation is shown in fig. 3 giving also the time mean value of the power flux (Poynting vector), while in fig. 4, some details of the near field are represented.

The same situation has been modeled in different manners using either line multipoles or conventional multipoles. Further on, the number of parameters (i.e., the orders and degrees of the multipoles) has been varied as well as the number of matching points. Finally, the field has been computed at two different frequencies resulting in a overall 'banana' length of half a wave length λ (low frequency) and 3λ (high frequency). Field plots of the different computations look almost identical. This is due to the fact that the errors are very small: all versions deliver good results but at very different amounts of both calculation time and computer memory.

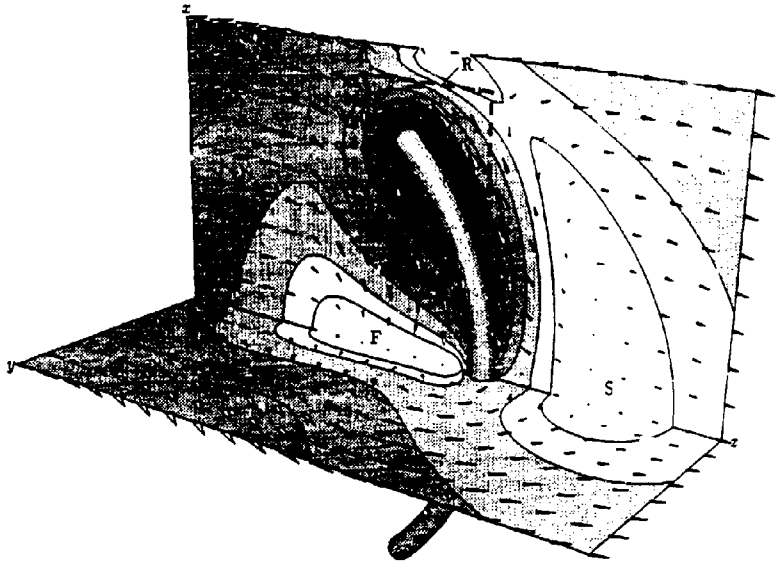

Figure 3 The banana shaped object (ideal conductor in air, half a wavelength (λ) long and 0.027λ thick, bent along a quarter of a full circle) is illuminated by an x-polarized plane wave traveling in z-direction. The picture shows the time mean value of the Poynting vector of the total near field. There is a shadow region S with low field values and a 'standing wave area' F where the fields are high but only the time mean value of the power flux is low. See also fig. 4 for more details of the field in the rectangle R.

The geometry of the situation is symmetrical with respect to two planes. This symmetry may be used to simplify the expansion. Due to the fact that the line multipoles may be curved in a three dimensional way there is no built in symmetry for these functions while conventional multipoles have built in symmetry. This has the consequence that the models are different for the two cases: Using line multipoles, one half of the 'banana' has to be modeled while using conventional multipoles only a quarter of the 'banana' must be modeled. On the other hand, more matching points per unit surface are necessary for the conventional multipoles. The following *geometrical* models are used:

I:	Rough model for conventional multipoles,	686 matching points
II:	Fine model for conventional multipoles,	1295 matching points
III:	Thick model for line multipoles,	854 matching points
IV:	Thin model for line multipoles.	840 matching points (3)

Note that model IV is a three times thinner 'banana' of the same length (diameter = 0.009λ). The following expansions have been used for the same geometrical model where all line multipoles are along the axis of the 'banana' and have 28 (internal) segments of equal length for a half of the 'banana'. In most cases an additional (point-)multipole has been used for modeling the field at the end cap. Table

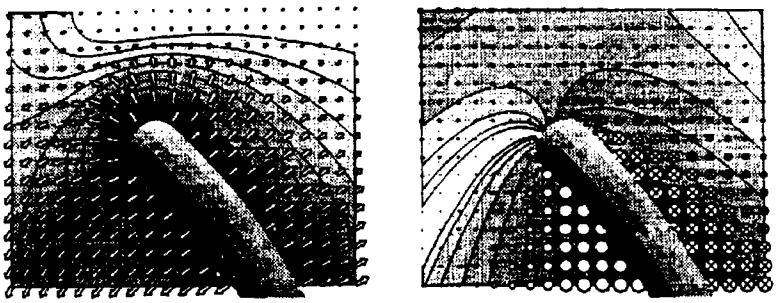

Figure 4 A more detailed view of the instantaneous value of the electric field (left) and of the magnetic field (right) respectively within the rectangle R (see fig. 3). Arrows and octagons (for vectors perpendicular to the drawing plane) show the direction of the field while the underlaid contour lines give the magnitude of the field strength.

(4) gives the integer parameters IE1 and IE5 of the line multipole, its related number of parameters N_L, the number of conventional multipoles n_{con} and its related number of parameters N_M as well as the total number of parameters $N_{tot} = N_L + n_{con} \cdot N_M$ for the different *expansion models*. For the line multipole it is IE2 = 3 (outgoing waves), IE3 = 0, IE4 = 2 (ϕ-degree) and IE6 < 100 (no magnetic current).

model:	a	b	c	d	e	f	g	h	i	k	l	m
IE1:	142	142	142	142	142	142	132	142	142	142	–	–
IE5:	5	3	5	5	8	12	–	5	8	12	–	–
N_L:	54	36	54	54	81	117	261	54	81	117	–	–
n_{con}:	–	1	1	1	1	1	1	1	1	1	19	19
N_M:	–	66	66	96	66	66	66	56	56	56	±18	±42
N_{tot}:	54	102	120	150	147	183	327	110	137	173	342	802

(4)

The local z-axes of the conventional multipoles are oriented along the 'banana' axis and its degrees are 2, i.e., equal to the ϕ-degree of the line multipoles. The multipoles in models l and m are found automatically using [5]. The number of parameters varies slightly from multipole to multipole. Note that the models using conventional multipoles are symmetry adapted. An '3D curved banana' would require both twice as many matching points and twice as many parameters for the conventional multipoles but the same numbers for the line multipole models.

Combining the geometrical models I–VI with the expansion models a–m and running the computer at low and high frequency, different results are obtained. We list the mean percentage error (mean mismatching divided by mean value of field values on the matching points times 100%) and the cpu time (in seconds) for computing the parameters and the errors on a Sun SPARC 2 machine.

model	IIIa	IIIb	IIIc	IIId	IIIe	IIIg	IIIc	IIIe	IIIf	IVh	IVi	IVk	II	IIm	II	IIm
frequency	low	low	low	low	low	low	high	high	high	low	low	low	low	low	high	high
error [%]	16.9	0.4	0.1	0.1	0.1	0.1	0.6	0.4	0.5	0.4	0.1	0.1	2.9	0.1	0.8	0.3
cpu (par)	98	122	149	181	195	447	150	195	262	137	179	243	361	3404	361	3404
cpu (err)	88	86	97	101	117	84	99	118	143	94	114	139	49	195	48	195

(5)

Figure 5 shows the distribution of the errors for some particular cases.

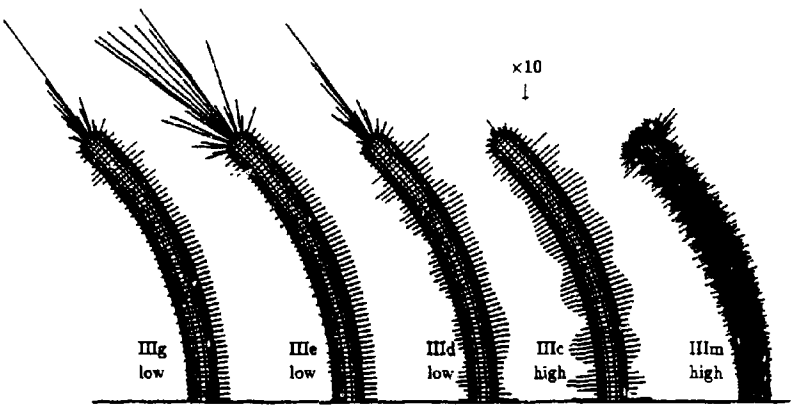

Figure 5 The error varies along the surface of the scatterer. The 'hedgehog' pictures give the distribution of the errors for three low frequency calculations (left) and two high frequency calculations (right). Note that the scaling of the errors is the same for all cases except *in case* IIIc: The actual errors are more than ten times larger in this case. The 'reference' at the very right has not significantly smaller errors, in spite of the fact that almost ten times more parameters are used. This shows the power of the curved line multipoles.

In fig. 6, a more complicated example is shown: the scattering at a four turn helix. The helix is half a wavelength λ high, the total length of the wire is almost 2λ and its thickness is $\lambda/20$. It is modeled using 3472 matching points (each rectangle on the surface in fig. 6 is one matching point).

The scattered field is modeled using four line multipoles (one for each turn) of longitudinal order 12 and a ϕ-degree of four (→884 Parameters). Additionally, two conventional multipoles have been used to model the field at the wire ends (→132 parameters). Hence the field model has 1016 degrees of freedom. The computer (a Sparc 2 workstation) needs about 6 hours to solve the problem end ends up with an average error of 2.2%. The maximum error occurs at the end of the wire and is only 26.3% (see fig. 6 left).

Note that this example brought the computer to its limit if it would be calculated using only conventional multipoles. It had to be discretized with at least 7000 matching points and 60 multipoles with 36 parameters each. This results into approximately 2200 parameters resulting in about 50 MBytes of computer memory and 11 hours cpu time on a Sparc 2 machine. The given numbers refer to the rough model of the 'banana' in our previous example. A finer model would have to double both the number of matching points and the number of parameters — and came (with 200 MBytes required memory and 88 hours cpu time on a Sparc 2 without speaking about numerical problems) definitely out of the scope of 'normal' computers.

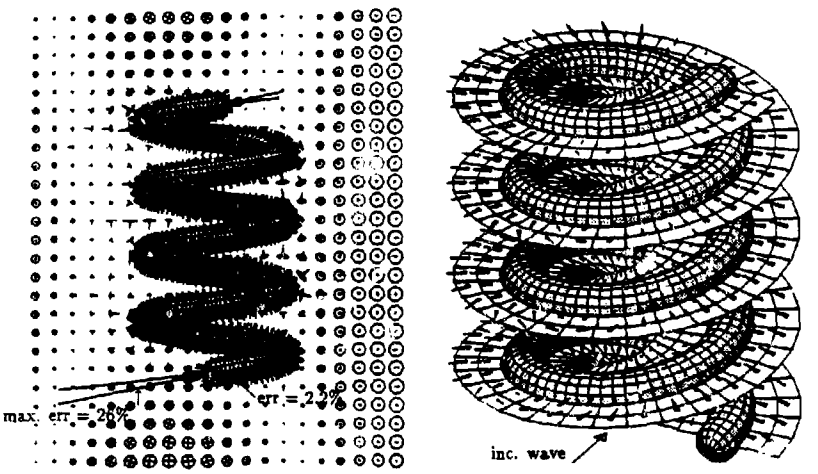

Figure 6 **Left:** The helix (ideal conductor in air, height: $\lambda/2$) is illuminated by a plane wave coming from left. The picture shows the instanstantaneous value of the $\vec{E}$-field in the $\vec{H}$-plane (the incident $\vec{H}$ is vertical while the incident $\vec{E}$-field is perpendicular to the drawing plane). The needles on the surface of the scatterer represent the local mismatching, i.e., the tangential electric field and the normal magnetic field in this case. Mean error: 2.2%.
Right: The same field on a helical surface (white). Note that the electric field is always perpendicular to the scatterer's surface. The direction of the incident wave is indicated. See also fig. 7 for the power flux of the same field.

Summary

The curved line multipoles allow the exact calculation of the near (and far) field of thin structures. Compared to conventional multipoles the number of parameters is — at comparable errors — reduced by a factor 5 ... 10 (at least!), where the reduction is increased when the wires become thinner. The scope of MMP calculable situations is significantly enlarged. The curved line multipoles are useful to take into account a priori knowledges, since the maximum field variations in two directions (along and around the line) may be chosen independently from each other.

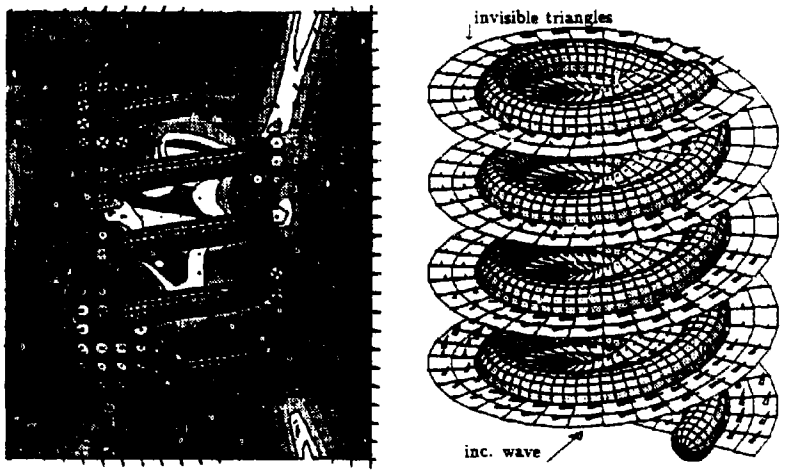

Figure 7 This picture shows the instantaneous value (left) and the time mean value (right) of the Poynting vector $\vec{S} = \vec{E} \times \vec{H}$ of the same situation as in fig. 6. The contour lines at the left represent the absolute value of $\vec{S}$. Note the 'screening effect' of the helix. Some of the vectors at the left point below the white helical surface and are not visible for this reason. The local time mean energy flux is always along the wire and may have different directions inside and outside the helix. N.B.: The same effect occurs with the 'banana' example (see fig. 3).

References

[1] G. J. Burke and A. J. Poggio, "Numerical electromagnetics code (NEC) — Method of Moments", NOSC Technical Document 116, Vol. 1, Lawrence Livermore Laboratory, Livermore, CA, January 1981.

[2] P. Leuchtmann and L. Bomholt, "Thin wire feature for the MMP-code,"in *6th Annual Review of Progress in Applied Computational Electromagnetics (ACES), Conference Proceedings*, (Monterey), Mar. 1990.

[3] P. Leuchtmann, "New expansion functions for long structures in the MMP-code," in *7th Annual Review of Progress in Applied Computational Electromagnetics (ACES), Conference Proceedings*. (Monterey), Ma. . 1991.

[4] P. Leuchtmann and M. Gnos, "New thin wire expansions for long wires in the MMP-code," in *9th Annual Review of Progress in Applied Computational Electromagnetics (ACES), Conference Proceedings*. (Monterey), Mar. 1993.

[5] P. Regli, 'mmptool', public domain program, available through ftp anonymous on sirius.ethz.ch (129.132.41.1), directory mmp, Zürich, Nov. 1993.

COMPARISON OF THE MULTIPOLE TECHNIQUE WITH THE METHOD OF MOMENTS

Daniel D. Reuster*
Department of Electrical Engineering
University of Dayton
Dayton, OH 45469-0227

Patricia A. Ryan
Georgia Tech. Research Institute
Atlanta, GA 30332-0800

Abstract

This paper presents a comparison of the multipole technique with the method of moments as applied to the problem of electromagnetic scattering by perfectly conducting cylinders. Comparisons are made on the performances of the two techniques with respect to variations of the cylinder's cross section. Theoretical development is given for both techniques, along with comments regarding the uniqueness of each technique. Comparisons are made with respect to run time, number of special function calls, matrix sizes required for convergence, and numerical stability. Bistatic scattering patterns are presented for perfectly conducting cylinders of various cross sections. Conclusions and general rules of thumb are given for the use of each technique.

1. Introduction

The method of moments (MoM) has been used for numerous years to solve various electromagnetic scattering and propagation problems where the object under study is on the order of the wavelength of interest. The method is well documented [1,2] and shown to produce reliable results for a large class of problems. However, in recent years interest has grown in the use of the multipole technique (MPT) [3,4] as an alterative method for solving many of the classical MoM problems. In response to questions regarding the efficiently and reliability of the newer MPT, two Fortran based computer codes were developed (one MoM and the other MPT) to run a direct comparison between the two techniques. The two codes both use the same subroutine (CROUT reduction) to invert their respective reaction matrices and both codes use standard IMSL libraries for all of their special function calls. Thus, the two computer codes allow for a direct comparison of the two methods and provide insight into the abilities of the newer MPT with respect to the traditional used MoM technique.

2. Mathematical Development

Figure 1 shows the cross section of three infinitely long perfectly conducting cylinders (PEC), with their axis along the z direction. The region surrounding the cylinder is free space with permeability μ_0 and permittivity ϵ_0. It will be assumed that the cylinder is illuminated by a transverse magnetic (TM) plane wave, of unit amplitude, propagating in the x-y plane.

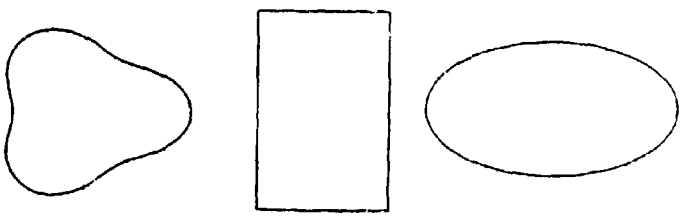

Periodic $r=0.6\lambda$ $\Delta=0.2\lambda$ | *Rectangle* $w=0.3\lambda$ $h=0.6\lambda$ | *Ellipse* $x=0.6\lambda$ $y=0.3\lambda$

Figure 1 Scattering Test Bodies.

A) Multipole Technique

Let the scattered electric field at an observation point external to the PEC cylinder be given by :

$$\vec{E}_{scat} = \sum_{n=-\infty}^{\infty} b_n H_n^{(2)}(k_0 \rho)\, e^{jn\phi}\, \hat{z} \tag{1}$$

where, k_0 and $H_n^{(2)}$ are, respectively, the wavenumber of free space and the Hankel function of the second kind of order n.

From the PEC boundary condition, the tangential components of the electric field must vanish along the contour of the cylinder. This leads to the following equation relating the incident electric field to the scattered electric field:

$$-\vec{E}_{inc} = \sum_{n=-\infty}^{\infty} a_n H_n^{(2)}(k_0 R(\phi)) e^{jn\phi} \hat{z} \quad . \tag{2}$$

where $\rho = R(\phi)$ is the parametric contour of the cylinder.

Approximating the above series by the first 2N+1 terms and enforcing the resulting equations at 2N+1 matching points on the contour results in the following matrix equation:

$$[Z_{mn}]\,[a_n] = [E_{inc}] \quad . \tag{3}$$

Solving equation (3) provides the series expansion coefficients for the scattered fields outside the cylinder.

B) Method of Moments

Let the scattered electric field at an observation point external to the PEC cylinder be given by:

$$\vec{E}_{scat} = -\frac{k\eta}{4} \int_c \vec{J}(\rho') H_o^{(2)}(k|\rho - \rho'|)\, dl' \tag{4}$$

where, η and $J(\rho')$ are, respectively, the intrinsic impedance of free space and the surface current along the contour of the cylinder.

From the PEC boundary condition, the tangential components of the electric field must vanish along the contour of the cylinder. This leads to the following equation relating the incident electric field to the surface currents along the contour of the body:

$$\vec{E}_{inc} = \frac{k\eta}{4} \int_c \vec{J}(R(\phi))\, H_o^{(2)}(k|\rho - R(\phi)|)\, dl' \tag{5}$$

where $\rho = R(\phi)$ is the parametric contour of the cylinder.

Approximating the surface current by N pulse basis functions and choosing N matching points along the contour of the cylinder, allows equation 5 to be approximated by the following matrix equation:

$$[Z_{mn}]\,[J_n] = [E_{inc}] \quad . \tag{6}$$

Solving equation 6 provides the surface currents along the contour of the body which in turn can then be integrated to produce the desired scattered fields.

3. Comparisons

Table I presents the run time and matrix sizes required to produce converged bistatic radar cross section (RCS) plots for each of the scattering bodies excited by a TM incident plane wave. All test cases were run on an HP 9000 model 730 using double precision arithmetic, CROUT reduction, and IMSL special function calls. Figure 2 shows the converged RCS patterns of the two methods for each of the test bodies.

Comparing the performance of the two techniques, with regards to the periodically deformed cylinder, shows that while both techniques produce the identical RCS plots and require

approximately the same size reaction matrix, the MoM is approximately five times faster than the MoM. This considerable speed difference is a direct result of the larger number of special function calls required to generate the MoM reaction matrix. Similar results are obtained for the rectangular cylinder, with the MPT appearing to be slightly faster. However, a close comparison of the two RCS plots shows that the RCS plot produced by the MPT is slightly off. This error is attributed to the known problems of trying to expand a step type function with a Fourier series. The short coming of the MPT is illustrated by its converged RCS plot for the elliptical cylinder which is in error with the RCS plot produced by the MoM. The MPT is limited by the numerical problems associated with the Hankel function used in the series expansion. If the number of matching points greatly exceeds the minimum electrical dimension of the body, numerical problems associated with the behavior of the Hankel functions used in the series expansion causes the matrix to become ill-conditioned. If the desired answer has not been reached at this limit, no improvement in the answer can be obtained by using an increased number of expansion functions.

4. Conclusions

Comparison of the MPT and the MoM shows a trade off between speed and versatility. The primary difference between the two codes is the generation of their corresponding reaction matrices. The MPT's reaction matrix is developed using a cylindrical basis function approach, while the MoM's reaction matrix is developed using the traditional integral equation approach. For targets near circular, the MPT requires smaller matrix sizes than the MoM; however, as the target's cross section becomes less circular, the matrix size quickly increases. Limits on the maximum allowable matrix size for the MPT are directly related to the minimum electrical dimension of the body. While the MoM does not suffer from an upper bound on the number of matching points allowed, it is, in general, slower than the MPT. This is, in part, due to the larger number of basis functions and special function calls required to accurately approximate the needed surface current. Thus, the principle factor when choosing between the two techniques is the general shape of the body under analysis.

REFERENCES

[1] R. F. Harrington, *Field Computation by Moment Methods*, Macmillan, New York, 1968.

[2] J. Moore and R. Pizer, *Moment Methods in Electromagnetics*, Research Studies Press, Letchworth, England, 1984.

[3] E. Yamashita and K. Atsuki, "The Point Matching Method," in *Analysis Methods for Electromagnetic Wave Problems*, E. Yamashita, Ed. Norwood, MA: Artech House, 1990, ch.3.

[4] C. Hafner, *The Generalized Multipole Technique for Computational Electromagnetics*, Norwood, MA: Artech House, 1990.

Table I

Method of Moments

Cylinder cross section	Periodic	Rectangle	Ellipse
Matrix size for convergence	24	26	42
Run time in seconds	0.333	0.637	1.243
Number of Special function calls	576	676	1764

Table II

Multipole Technique

Cylinder cross section	Periodic	Rectangle	Ellipse
Matrix size for convergence	25	19	23
Run time in seconds	0.164	0.119	0.131
Number of Special function calls	100	76	92

Method of Moments

Multipole Technique

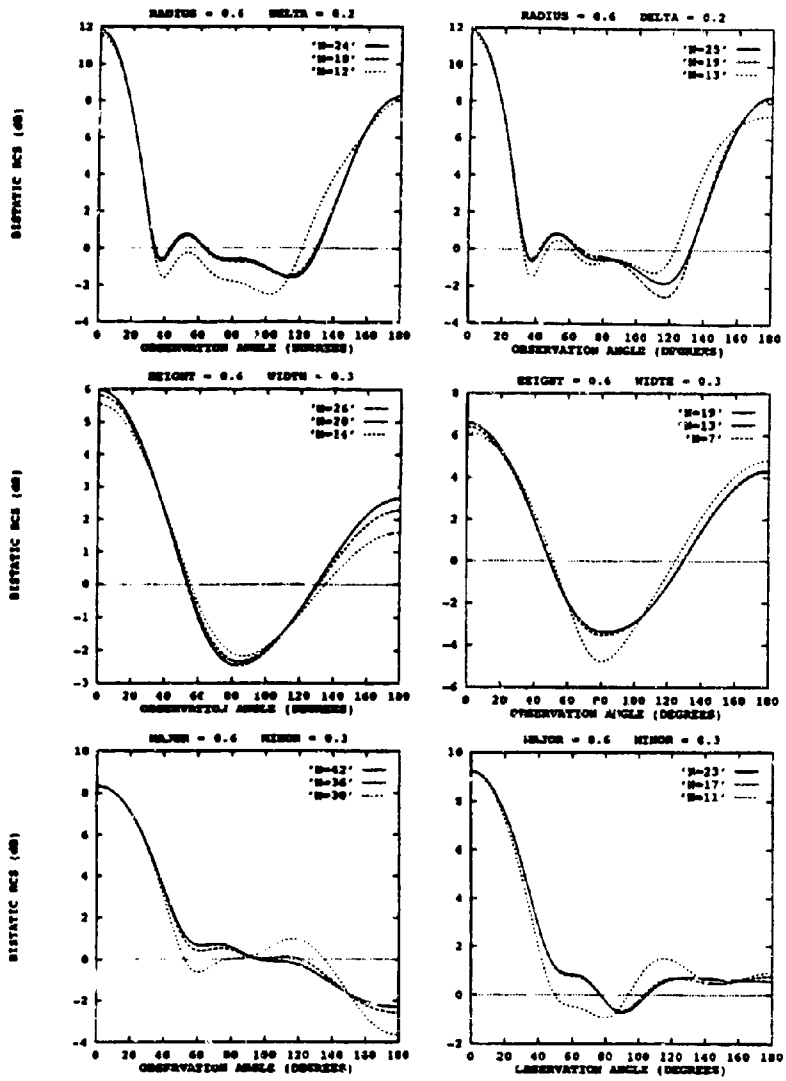

Multipoles as Metrons for the MEI-Method: A Testing Toolkit

P. Leuchtmann and N. Piller
Lab. of El.-mag. Fields and Microwave Electronics, ETH Zurich
CH-8092 Zurich, Switzerland

Abstract

The measured equations of invariance (MEI), proposed by K.K. Mei et al. [1] is compared with traditional finite difference (FD) techniques. MEI starts with the choice of the metrons which will determine the grid operator. We investigate the influence of the metrons on the operator itself, on the local errors both in inner grid points and in boundary points and the influence on the final result. As a general rule we can say that the MEI result tends to be similar to the metrons. This is both an advantage and a drawback: A good choice of the metrons yields excellent results but a bad choice turns out in real rubbish. A new MEI program has been written for this investigation. It is highly flexible, accepts input from MMP preprocessors and produces MMP compatible output files.

1. Introduction

In this paper we discuss some special details of the MEI-method (Measured Equations of Invariance) [1,2]. Since MEI is similar to the conventional FD (Finite Difference) technique we give a short description of both methods. Fig. 1 shows what type of problems we are dealing with.

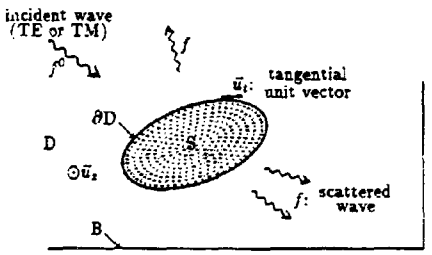

$$(\Delta + k^2)f = 0 \qquad \text{in D} \quad (1)$$

$$\left.\begin{array}{l} \text{TM}: f - f^0 = 0 \\ \text{TE}: [\bar{n}_z \times \text{grad}(f + f^0)] \cdot \bar{u}_t = 0 \end{array}\right\} \text{on } \partial\text{D} \quad (2)$$

$$\text{ABC} \qquad \text{on B} \quad (3)$$

Figure 1 A cylindrical ideally conducting structure S is embedded in a linear isotropic and homogeneous medium and is illuminated by a (time harmonic) incident plane wave f^0. The unknown scattered wave f has to satisfy both the Helmholtz equation (1) in the whole surrounding space D and the boundary condition (2) on the boundary ∂D of D. Note that f is equal to $\vec{E} \cdot \bar{u}_z$ (TM-case) or $\vec{H} \cdot \bar{u}_z$ (TE-case), and k is the wave number of the surrounding medium. The ABC (=absorbing boundary condition) on the outer boundary B (3) is necessary if the field domain D must be restricted.

For both, FD and MEI, an almost arbitrarily shaped grid is laid on D. The field value on the l-th grid point is denoted by $f(l)$. Each grid point is related to a set of N_l neighbor points with numbers l_1, l_2, ..., l_{N_l} (see fig. 2). For grid points on ∂D, the field values are given through equation (2) in fig. 2 while the values of all the other grid points are unknown. A field operator L_l gives a relation among the field value $f(l)$ and the values on the neighbor points:

$$L_l f := c_{l0} f(l) + \sum_{j=1}^{N_l} c_{lj} f(l_j) = 0 \tag{4}$$

The (complex) numbers c_{lj} fully describe the field operator L_l.

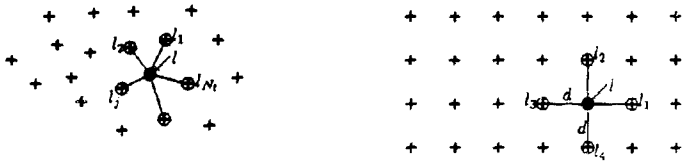

Figure 2 Part of a general grid (left) and a regular quadratic grid with grid constant d (right).

FD and MEI differ in the way how the field operators L_l are obtained. In FD, the operators are essentially first order approximations of the Helmholtz operator $(\Delta + k^2)$. E.g., in a regular quadratic grid (see fig. 2, right) we have (after multiplication with d^2)

$$c_{l0} = (kd)^2 - 4,\ c_{l1} = 1,\ c_{l2} = 1,\ c_{l3} = 1,\ c_{l4} = 1. \tag{5}$$

For non regular grids the coefficients c_{lj} depend on the relative positions of the grid points.

In general, each inner point contributes one equation to a large (but sparse) system of equations. The l-th equation contains only $N_l + 1$ unknown field values.

Points on the outer boundary B require a special treatment since the isotropy of the field operator is lost on B. So called absorbing boundary conditions (ABC) take into account some a priori knowledge on the field, e.g. the fact that the scattered wave is traveling outwards. Hence, each point on B contributes an equation to the system — and the number of unknowns is equal to the number of equations. Thus, the system may be solved. This is essentially what we refer to as FD.

Rather than approximating the Helmholtz operator, MEI finds the coefficients $\tilde{c}_{lj}$ by using field solutions m_i. The *metrons* m_i satisfy the field equation (1) in D, but not necessarily the boundary conditions (2). The i-th metron delivers the equation

$$\tilde{L}_l f := \tilde{c}_{l0} m_i(l) + \sum_{j=1}^{N_l} \tilde{c}_{lj} m_i(l_j) = 0. \tag{6}$$

In this equation, the coefficients $\tilde{c}_{lj}$ are the unknowns. They may be computed if at least N_l different metrons are chosen. If the number of metrons is larger than N_l a least squares solution may be obtained. Note that points on the outer boundary B require no special treatment. Once the coefficients $\tilde{c}_{lj}$ are determined for all grid points, the field is computed in the same way as in FD.

It is the purpose of this paper to show how different choices of metrons do (or do not) influence the final solution.

2. How Do the Metrons Influence the Field Operator?

In a first step we choose *plane waves* as metrons and consider a regular quadratic grid (see fig. 2, right). In this case, the FD field operator is given by (5). We normalize the MEI field operator in such a way that $\tilde{c}_{l0} = c_{l0} = (kd)^2 - 4$ and investigate the deviation of the other $\tilde{c}_{lj}$ from $c_{lj} = 1$ for $j = 1 \ldots 4$. The result is given in fig. 3. As a main result we find that the phase of the coefficients decreases in the main direction of the propagation of the metrons.

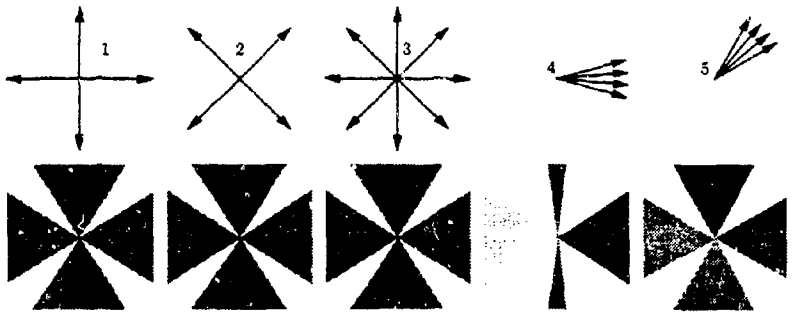

Figure 2 A quadratic grid (points 0.2λ apart) is used to show the influence of the metrons on the MEI field operator. The direction of the metron waves are given in the top, while at the bottom the resulting MEI coefficients are indicated. The shading is darker for lower phase and the triangles are narrower, if the corresponding value of $|c_{lj}|$ is smaller. Cases 1–3 are symmetrical, i.e., all four values of c_{lj} are equal. We have (here, the first index l denotes the case) $c_{1j} = 1.048$, $c_{2j} = 1.088$ and $c_{3j} = 1.068$. In case 3, eight metrons have been used ($\rightarrow$least squares for computing the coefficients c_{lj}). All these values are very close to the FD values. For cases 4 and 5 symmetry is lost since all four metrons propagate mainly in one direction. If the second index j varies from 1 to 4 in correspondance to fig. 2 right, the values of the coefficients are $c_{41} = 1.08\angle{-31}^\circ$, $c_{42} = c_{44} = 0.2\angle 0^\circ$, $c_{43} = 1.08\angle 31^\circ$ and $c_{51} = c_{52} = 0.93\angle{-8.6}^\circ$, $c_{53} = c_{54} = 0.93\angle 8.6^\circ$.

The influence of the propagation direction decreases with a finer grid. Figure 4 gives an example using TM-multipoles as metrons. These multipole functions radiate energy originating from the center of the picture towards all directions. In spite of this behavior the MEI operators are almost symmetrical as long as the grid constant d is small compared with the wave length λ.

For ingoing multipoles, i.e., the energy propagates from far away towards the singularity, the coefficients become conjugate complex to that of outgoing waves. (See fig. 5)

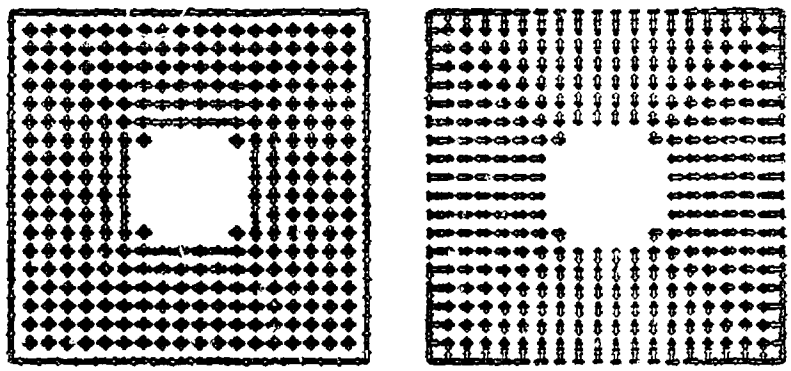

Figure 4 The first four TM-multipoles (monopole, dipoles etc.) placed in the center of the picture are used as metrons. At the left the wave length is ten times larger than at the right — $\lambda/d = 40$ and $\lambda/d = 4$ respectively. As in fig. 3 a similar graphical representation of the coefficients using arrows rather than triangles is used here.

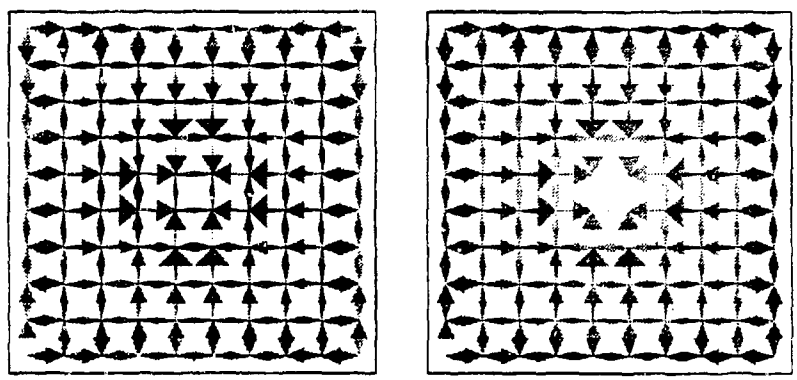

Figure 5 The first four TE-multipoles (monopole, dipoles etc.) placed in the center of the picture are used as metrons. Outgoing waves (left) are compared to ingoing waves (right). ($\lambda/d = 5$)

3. The Local Error of MEI Field Operators

We define the following local error of the MEI field operator: Given an analytical solution f of the

Helmholtz equation. (For us, f is a plane wave with a given propagation direction.) f may be evaluated on all grid points, in particular on the grid points involved in the equation of L_l. If the exact field values on the neighbors are taken the operator equation (4) may be solved with respect to the (approximate) value $f_{ap}(l)$. The difference of this value and the exact value $f(l)$ is defined as the local error η_l. For the relative error $\eta_l^{\%}$, we divide by $f(l)$.

$$\eta_l := |f_{ap}(l) - f(l)|. \qquad \eta_l^{\%} := \frac{|f_{ap}(l) - f(l)|}{|f(l)|} \cdot 100\%. \tag{7}$$

Figure 6 shows the relative local error due to the metrons of case 2, fig. 2 when the analytical solution f is a plane wave traveling in direction α. Note that the error becomes zero when f coincides with one of the metrons. This is still true for points on the outer boundary B: MEI automatically produces in this case a perfectly absorbing boundary condition.

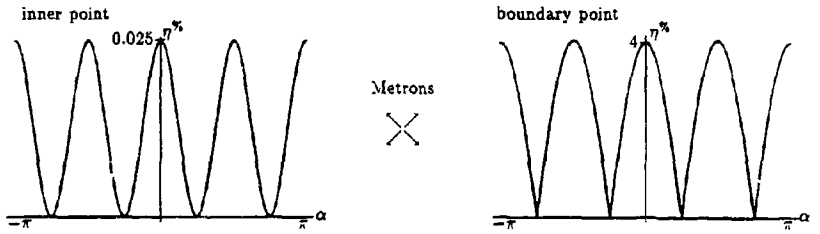

Figure 6 The relative local error $\eta^{\%}$ on an inner point (left) and on a boundary point (right) becomes zero as soon as the exact solution is used as a metron. $\eta^{\%}$ is shown as a function of the angle α between the propagation direction of the exact solution f and the horizontal direction. Here $\lambda/d = 15.7$.

Figure 7 gives the same information as fig. 6, but now for the metrons of case 4 in fig. 2. Both the inner equation and the ABS on the outer boundary B produce very accurate solutions, if the metrons are close to the exact solution.

In all cases considered up to now the local error is at least one order of magnitude smaller for inner points than for points on the outer boundary B. However, the error is small as long as the metrons are close to the solution. The choice of the metrons has a strong influence, particularly on boundary points.

4. The Global Interaction Between Metrons and Solution

As a first example we intentionally take poor metrons. A circular cylindre is illuminated by a plane wave coming from left. The scattered field to be computed using MEI is a wave traveling away from the scatterer. In spite of this knowledge we use metrons like in case 4, fig. 2, but propagating to right rather than to left. The solution is real rubbish: The scattered wave travels from right to left — just as the metrons — with an amplitude even larger than that of the incident field. Figure 8 gives a plot of this (wrong!) scattered field.

Next we solve the same problem using outgoing multipoles as metrons and find a correct solution. But if we use ingoing multipoles we find again a rather strange solution. See fig. 9.

Provided that good metrons are used MEI delivers quite accurate results. This is shown in fig. 10. As a general result we found that the use of more metrons than necessary — the coefficients c_{lj} are then

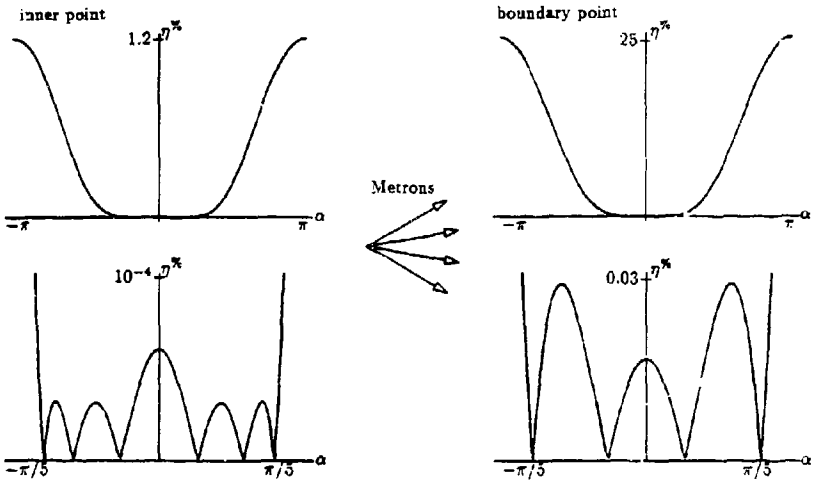

Figure 7 The relative local error $\eta^{\%}$ becomes very small, if the metrons and the exact solution are close together. On the other hand the error is increased as soon as the metrons are really different from the exact solution. Note that boundary points produce higher errors than inner points. Here $\lambda/d = 15.7$.

obtained by solving an overdetermined system of equations using least squares techniques — turns out in better results, particularly in the near field.

The fact that the choice of the metrons has an influence onto the result may be seen either as an advantage or as a drawback. It is possible to take into account a priori knowledge about the solution by an 'intelligent' choice of the metrons. E.g., K. K. Mei et al. [1] has used a specific type of metrons (outwards radiating fields of arbitrary (non physical) current distributions on the scatterer) and found reasonable ABC's from these metrons.

5. The Program

A 2D electromagnetic TE- or TM-scattering code has been written. It uses the nmptool [3,4] for the data input as well as for the representation of the results. This is advantageous at preprocessing in the sense that almost arbitrarily complex shapes of scatterers may be constructed in very short time, any regular or nonregular grid may be used and any MMP expansion function may be declared as a metron. The advantage at output time is that all features of field representation — $\vec{E}$-, $\vec{H}$- and $\vec{S}$ field plots including animation, densitity plots etc. are possible.

The only new written part is a MEI module performing the calculation of the MEI coefficients and the setup of the MEI matrix. A Linpack solver is used for the solution of the (sparse) MEI matrix. Data exchange between MEI and MMP goes through files which have appropriate MMP formats. Finally a high level 'manager program' has been written to handle the data exchange between MMP and the MEI module. This manager program includes 'macro features' (to shorten several steps to a single one) and

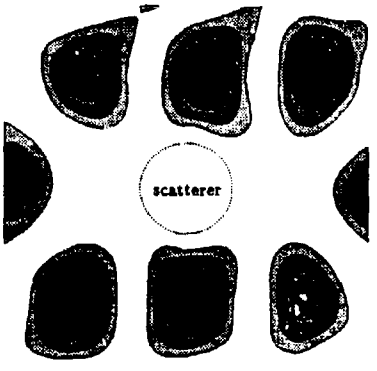

Figure 8 The scatterer is illuminated from left (TM-case). The plot shows the (wrong!) instantaneous value of the total electromagnetic field energy obtained by MEI with a poor set of metrons. Note that the patches are traveling from right to left, just as the metrons. Here $\lambda/d = 30$, diameter of the scattering cylindre: $\lambda/2$.

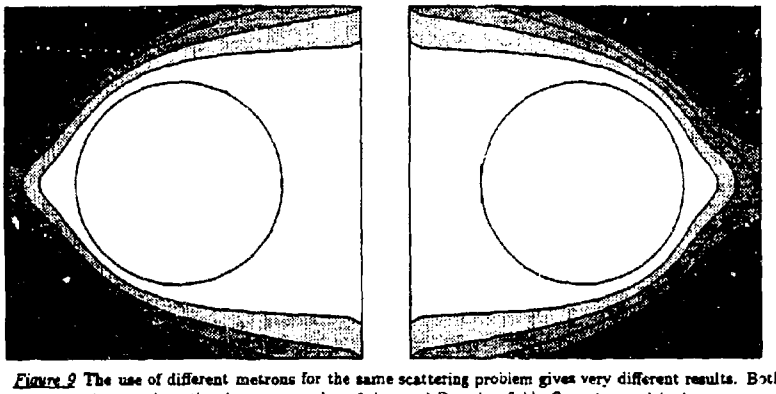

Figure 9 The use of different metrons for the same scattering problem gives very different results. Both pictures show the time mean value of the total Poynting field. Outgoing multipoles as metrons yield a correct solution (left) while ingoing multipoles as metrons yield a totally wrong power flux looking as if it came from the opposite side than the incident field but the power flux is from left to right in both cases. Here $\lambda/d = 30$, diameter of the scattering cylindre: $\lambda/2$.

automatic file generation and file naming. The program runs on Sun workstations (UNIX). It is available

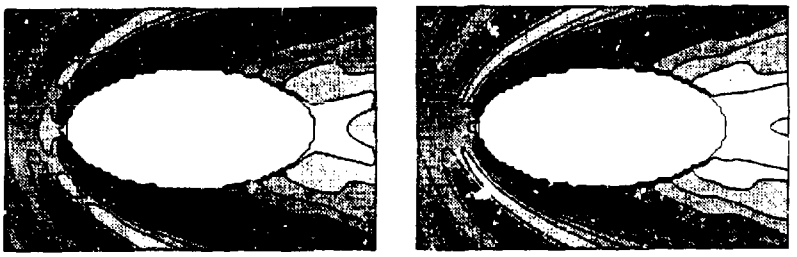

Figure 10 Comparison of MEI (left) and MMP (right). The time mean value of the Poynting vector (total field) is shown in the nearfield. The accuracy of the MMP solution is better than 1% and may be taken as a reference. For the MEI 9 metrons (outgoing multipoles) have been used (→least squares for computing the coefficients c_{ij}). Note that the MMP solution has no problems at the outer boundary. Dimension of the whole picture: $6\lambda \times 4\lambda$. $\lambda/d = 15$.

from the authors.

6. Summary

We have shown that the quality of MEI solutions does depend on the choice of the metrons. In general the solution tends to become similar to the metrons. This may be seen as an advantage since a priori knowledge about the solution may be brought in by a particular choice of the metrons. Using more metrons than necessary and computing the grid operator by least squares techniques yields better results particularly in the near field. This is at least true for the example in fig. 10. However, poor metrons deliver rubbish rather than results. The presented program allows it to play with different choices of metrons and to represent the results in many different ways.

References

[1] K. K. Mei, R. Pous, Z. Chen and Y. W. Liu, "Measured equation of invariance — a lean and fast method for field computation," in *Proceedings fo the 1992 URSI Int. Symp. on electromagnetic theory*, (Sydney) Aug. 1992.

[2] D. B Wright and A. C. Cangellaris, "Performance evaluation of MEI-based mesh truncation conditions for finite element modelling of electromagnetic scattering by penetrable bodies," in *9th Annual Review of Progress in Applied Computational Electromagnetics (ACES). Conference Proceedings*. (Monterey), Mar. 1993.

[3] L. Bomholt, P. Regli, Ch. Hafner, and P. Leuchtmann, "MMP-3D: A package for computation of 3D electromagnetic fields on PC's and workstations," in *6th Annual Review of Progress in Applied Computational Electromagnetics (ACES), Conference Proceedings*, (Monterey), Mar. 1990.

[4] P. Regli, 'mmptool', public domain program, available through ftp anonymous on sirius.ethz.ch (129.132.41.1), directory mmp, Zürich, Nov. 1993.

SESSION 4:

FINITE ELEMENT METHOD (I)

Chair: Jin-Fa Lee
Co-Chair: John Volakis

Analysis of Dielectric-Loaded Waveguides Using Covariant Projection Vector Finite Elements

Bruce R. Cr in and Andrew F. Peterson
School of Electrical and Computer Engineering
Georgia Institute of Technology
Atlanta, GA 30332-0250

Abstract

Over the years, a large number of procedures have been proposed for the analysis of dielectric-loaded waveguiding structures. Most of these approaches are unreliable because of the appearance of spurious modes. Recent research demonstrates that mixed-order covariant projection finite elements eliminate difficulties with spurious modes in vector waveguide formulations [1] Furthermore, the functions introduced in [1] can be extended to higher polynomial orders and allow parametric mappings to cells with curved sides.

This presentation describes approaches for finite element analysis of open and closed dielectric-loaded waveguiding structures using mixed-order covariant projection finite elements. Details of the element matrix calculations will be presented. Efficient sparse eigensolvers based on iterative methods will be described which can handle both non-linear as well as linear eigenvalue equations. The treatment of open geometries using local absorbing boundary conditions will be discussed. Analysis results will be presented that demonstrate the ability of the formulations to solve for the propagating modes of boxed and open microstrip lines, without the appearance of spurious modes.

Introduction

The finite element method is a useful technique for analyzing propagating modes in waveguiding structures. A scalar formulation in terms of the longitudinal component of either the electric or magnetic field is normally used when analyzing homogeneous structures loaded with isotropic material. However, the scalar formulation is inadequate (except as an approximation) for analyzing waveguides with inhomogeneous cross section or anisotropic materials [2].

To analyze waveguides inhomogeneously loaded with dielectric material, the finite element formulation must consider at least 2 vector field components. Most vector formulations are plagued by the occurrence of spurious solutions mixed in with the true ones. Many techniques have been proposed to deal with the problem of spurious solutions [1-5].

One approach that effectively eliminates spurious solutions uses mixed-order covariant projection finite elements in a standard problem formulation [1]. This presentation discusses the application of these elements to the solution of dielectric loaded waveguiding structures.

The waveguiding structure under consideration is assumed to be uniform along the longitudinal axis ($\hat{z}$) and, in general, non-uniform across the transverse plane ($\hat{x}-\hat{y}$). The structure is assumed to be filled with a source-free, inhomogeneous, isotropic, lossless dielectric material, with permitivity

$\epsilon(x,y) = \epsilon_r(x,y)\,\epsilon_o$ and permeability $\mu(x,y) = \mu_r(x,y)\,\mu_o$ (typically $\mu_r(x,y) = 1$). The time-dependent electromagnetic fields in the waveguide at the frequency ω are assumed to have the form:

$$\vec{H}(x,y,z,t) = \mathrm{Re}\,\{\bar{H}(x,y)\ \exp j(\omega t - \beta z)\} \tag{1}$$

$$\vec{E}(x,y,x,t) = \mathrm{Re}\,\{\bar{E}(x,y)\ \exp j(\omega t - \beta z)\} \tag{2}$$

where β is the propagation constant in the $\hat{z}$ direction.

Mixed-Order Covariant Projection Finite Elements

Mixed-order covariant projection finite elements were proposed by Crowley in [1]. These finite elements have been demonstrated to not allow spurious solutions in standard vector formulations. These elements fall into the general category of "edge" or "tangential" elements. In the global mesh, continuity of tangential fields between elements is maintained but normal continuity is not.

A general curvilinear quadrilateral element in the $\hat{x}-\hat{y}$ plane is mapped into the standard quadrilateral element in the $\hat{\eta}-\hat{\xi}$ plane as shown in Figure 1. In the standard element, the six $\hat{\xi}$ directed basis functions vary linearly with ξ and quadratically with η (hence the term "mixed-order"). Likewise, the six $\hat{\eta}$ directed basis functions vary linearly with η and quadratically with ξ. These twelve functions represent the transverse field components. As suggested by [6-7], the longitudinal ($\hat{z}$) components are represented by nine Lagrangian basis functions with quadratic dependence in both ξ and η. In total, there are 12 transverse and 9 longitudinal basis functions per element.

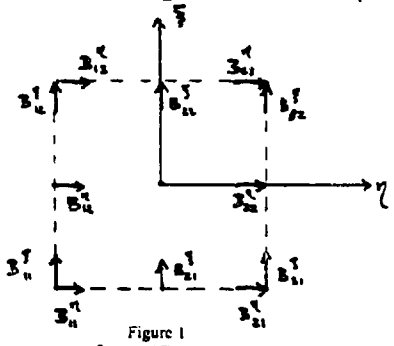

Figure 1
Standard Element

Derivation of Finite Element Eigenvalue Equations

The finite element formulation is based on the vector Helmholtz equation:

$$\nabla \times \left(\frac{1}{\epsilon_r} \nabla \times \vec{H}\right) = k_o^2\,\mu_r\,\vec{H} \tag{3}$$

$$\text{where } k_o^2 = \omega^2\,\epsilon_o\,\mu_o \tag{4}$$

Assuming the general form of (1), the transverse components can be separated from the longitudinal components according to:

$$\bar{H}(x,y,z) = \left\{\bar{H}_t(x,y) + \hat{z}\,H_z(x,y)\right\}\exp(-j\beta z) \tag{5}$$

It follows from (5) that the vector Helmholtz equation can be separated into two parts, a vector equation that is entirely transverse to $\hat{z}$:

$$\nabla_t \times \left\{ \frac{1}{\varepsilon_r} \nabla_t \times \bar{H}_t \right\} - \frac{1}{\varepsilon_r} \left(j\beta \nabla_t H_z - \beta^2 \bar{H}_t \right) = k_o^2 \mu_r \bar{H}_t \tag{6}$$

and a scalar equation that has only $\hat{z}$ components:

$$-\nabla_t \cdot \left\{ \frac{1}{\varepsilon_r} \left(\nabla_t H_z + j\beta \bar{H}_t \right) \right\} = k_o^2 \mu_r H_z \tag{7}$$

At this point, one can proceed to derive an eigenvalue equation with either k_o^2 or β^2 as the unknown eigenvalue. The derivation that follows considers k_o^2 to be the eigenvalue, with β^2 given.

For convenience, the following scaling is introduced [6]:

$$\bar{h}_t = \beta \bar{H}_t \tag{8}$$

$$h_z = -j H_z \tag{9}$$

Using (8) and (9), equations (6) and (7) can be rewritten as:

$$\nabla_t \times \left\{ \frac{1}{\varepsilon_r} \nabla_t \times \bar{h}_t \right\} + \frac{1}{\varepsilon_r} \left(\beta^2 \nabla_t h_z + \beta^2 \bar{h}_t \right) = k_o^2 \mu_r \bar{h}_t \tag{10}$$

$$-\nabla_t \cdot \left\{ \frac{1}{\varepsilon_r} \left(\nabla_t h_z + \bar{h}_t \right) \right\} = k_o^2 \mu_r h_z \tag{11}$$

Coupled weak equations are constructed by "testing" the vector equation (10) with a transverse vector testing function $\bar{T}(x,y)$ and testing the scalar equation (11) with a scalar testing function $T(x,y)$. After using some vector identities and manipulating, the following equations are obtained:

$$\iint_\Gamma \frac{1}{\varepsilon_r} \left\{ \nabla \times \bar{T} \cdot \nabla \times \bar{h}_t + \beta^2 \bar{T} \cdot \bar{h}_t + \beta^2 \bar{T} \cdot \nabla h_z \right\} = k_o^2 \iint_\Gamma \mu_r \bar{T} \cdot \bar{h}_t - \int_{\partial\Gamma} \frac{1}{\varepsilon_r} \bar{T} \cdot \hat{n} \times \nabla \times \bar{h}_t \tag{12}$$

$$\iint_\Gamma \frac{1}{\varepsilon_r} \left\{ \nabla T \cdot \nabla h_z + \nabla T \cdot \bar{h}_t \right\} = k_o^2 \iint_\Gamma \mu_r T h_z - \int_{\partial\Gamma} \frac{1}{\varepsilon_r} \left\{ T \frac{\partial h_z}{\partial n} + T \hat{n} \cdot \bar{h}_t \right\} \tag{13}$$

where $\partial\Gamma$ is the outer boundary of the region Γ and $\hat{n}$ is the outward normal on $\partial\Gamma$.

Employing the covariant projection elements for the field and testing functions produces the following matrix eigenvalue equation:

$$\begin{bmatrix} A^{tt} & A^{tz} \\ A^{zt} & A^{zz} \end{bmatrix} \begin{bmatrix} h_t \\ h_z \end{bmatrix} = k_o^2 \begin{bmatrix} B^{tt} & 0 \\ 0 & B^{zz} \end{bmatrix} \begin{bmatrix} h_t \\ h_z \end{bmatrix} \tag{14}$$

where: $A^{tt}_{mn} = \iint \frac{1}{\varepsilon_r} \left\{ \nabla \times \bar{T}_m \cdot \nabla \times \bar{B}_n + \beta^2 \bar{T}_m \cdot \bar{B}_n \right\} + \int_{\partial\Gamma} \frac{1}{\varepsilon_r} \bar{T}_m \cdot \hat{n} \times \nabla \times \bar{B}_n$ (15)

$$A^{tz}_{mn} = \beta^2 \iint \frac{1}{\varepsilon_r} \bar{T}_m \cdot \nabla B_n \tag{16}$$

$$A^{zt}_{mn} = \iint \frac{1}{\varepsilon_r} \nabla T_m \cdot \bar{B}_n - \int_{\partial\Gamma} T_m \hat{n} \cdot \bar{B}_n \tag{17}$$

$$A^{zz}_{mn} = \iint \frac{1}{\varepsilon_r} \nabla T_m \cdot \nabla B_n - \int_{\partial\Gamma} \frac{1}{\varepsilon_r} T_m \frac{\partial B_n}{\partial n} \tag{18}$$

$$B^{tt}_{mn} = \iint \mu_r \bar{T}_m \cdot \bar{B}_n \tag{19}$$

$$B^{zz}_{mn} = \iint \mu_r T_m B_n \tag{20}$$

If the problem is formulated to solve for β^2 as the eigenvalue, with k_o^2 given, a similar derivation leads to the following global matrix eigenvalue equation:

$$\begin{bmatrix} A^{tt} & A^{tz} \\ 0 & A^{zz} \end{bmatrix} \begin{bmatrix} h_t \\ h_z \end{bmatrix} = \beta^2 \begin{bmatrix} B^{tt} & 0 \\ B^{zt} & 0 \end{bmatrix} \begin{bmatrix} h_t \\ h_z \end{bmatrix} \tag{21}$$

where $A^{tt}_{mn} = \iint \left\{ \frac{1}{\varepsilon_r} \left(\nabla \times \bar{T}_m \cdot \nabla \times \bar{B}_n \right) - k_o^2 \mu_r \bar{T}_m \cdot \bar{B}_n \right\} + \int_{\partial\Gamma} \bar{T}_m \cdot \hat{n} \times \nabla \times \bar{B}_n$ (22)

$$A^{tz}_{mn} = \iint \frac{1}{\varepsilon_r} \bar{T}_m \cdot \nabla B_n \tag{23}$$

$$A^{zz}_{mn} = \iint \left\{ \frac{1}{\varepsilon_r} (\nabla T_m \cdot \nabla B_n) - k_o^2 \mu_r T_m B_n \right\} - \int_{\partial\Gamma} \frac{1}{\varepsilon_r} T_m \frac{\partial B_n}{\partial n} \tag{24}$$

$$B^{tt}_{mn} = -\iint \frac{1}{\varepsilon_r} \bar{T}_m \cdot \bar{B}_n \tag{25}$$

$$B^{zt}_{mn} = -\iint \frac{1}{\varepsilon_r} \nabla T_m \cdot \bar{B}_n + \int_{\partial\Gamma} \frac{1}{\varepsilon_r} T_m \hat{n} \cdot \bar{B}_n \tag{26}$$

In the case of a perfect electric conductor (PEC) or perfect magnetic conductor (PMC) boundary condition, it can be shown that all line integrals along $\partial\Gamma$ go to zero. For open region problems, special treatment of the boundary integrals must be considered. One such approach is addressed in the discussion of the open microstrip problem.

The PEC boundary condition is the natural boundary condition for the $\bar{H}$ formulation. The PMC boundary condition is an essential boundary condition which is imposed by enforcing that the magnetic fields tangential to the boundary are equal to zero.

Iterative Solver Method

The matrix eigenvalue equations of (14) and (21) can be written in the general form:

$$[A]\,\bar{x} = \lambda\,[B]\,\bar{x} \tag{27}$$

Because there are 21 unknowns per element, the global matrices $[A]$ and $[B]$ are large and very sparse. It has been observed by various researchers (e.g. [7]) that in edge element formulations using k_o^2 as the eigenvalue, there are as many zero eigenvalues calculated as there are free longitudinal components. It has been observed by the authors that in the present formulation using β^2 as the eigenvalue, there are as many eigenvalues that approach infinity as there are free longitudinal components.

In order not to waste computational resources on calculation of zero or infinite eigenvalues, and to allow analysis of medium sized problems (~500 unknowns) on a personal computer, the authors have developed an iterative solver using sparse matrix storage techniques. This solver is based on the shifted inverse power method which converges to the eigenvalue closest to a selected input parameter.

Choosing an arbitrary parameter μ, the generalized eigenvalue equation of (27) can be manipulated as follows:

$$[[A] - \mu[B]]\,\bar{x} = (\lambda - \mu)\,[B]\,\bar{x} \tag{28}$$

$$\left(\frac{1}{\lambda - \mu}\right)\bar{x} = [[A] - \mu[B]]^{-1}\,[B]\,\bar{x} \tag{29}$$

When equation (29) is iteratively solved, λ and $\bar{x}$ will converge to the eigenvalue and eigenvector corresponding to the eigenvalue closest to μ, provided that the initial "seed" vector $\bar{x}$ does not closely resemble another solution eigenvector.

In order to avoid performing an explicit matrix inversion, the algorithm actually iterates using the following variation of equation (29)

$$[[A]-\mu[B]]\,\bar{x}^{i+1} = [B]\,\frac{\bar{x}^{i}}{\|\bar{x}^{i}\|} \tag{30}$$

where $\bar{x}^{i+1}$ is the unknown vector, $\bar{x}^{i}$ is the value of the unknown vector calculated in the previous iteration, and $\|\cdot\|$ represents the Euclidean norm. After each iteration, $\|\bar{x}^{i+1}\|$ is computed and compared to its value in the previous iteration. When $\|\bar{x}^{i+1}\|$ converges to a stable value, the eigenvalue λ is found from

$$\frac{1}{\lambda-\mu} = \|\bar{x}^{i+1}\|\ \mathrm{sgn}\{\bar{x}^{i+1}\cdot\bar{x}^{i}\} \tag{31}$$

where $\mathrm{sgn}\{\cdot\}$ is the Signum function. The initial seed vector $\bar{x}$ is created using a random number generator in an attempt to avoid possible resemblence to a particular eigenvector and ensure that the algorithm converges to the eigenvalue closest to λ.

In the solver implemented by the authors, the shifted inverse power method is extended to calculate the set of eigenvalues $\{\lambda_i\}$ that are closest to μ. This is accomplished by working with a set of eigenvectors $\{\bar{x}_i\}$ which are orthogonalized after each solver iteration using a Gram-Schmidt orthonormalization procedure. Experimental trials show that the resulting set of eigenvalues and eigenvectors correspond to the set of eigenvalues closest to the input parameter μ.

The solver is based on a sparse matrix storage scheme and uses the Y12M subroutine library to solve the set of linear equations represented by (30) [8]. The user can vary the desired number of eigenvalues. The required number of iterations increases with both the distance between μ and the target eigenvalues and the number of desired eigenvalues. For a selection of 1 or 2 eigenvalues, the solver typically converges to six digits of accuracy within 10-40 iterations. The practical maximum number of eigenvalues that can be solved at a time is about 4. Beyond this point, the accuracy of the outer eigenvalues suffers and the convergence rate stagnates.

Application to Boxed Microstrip

A finite element analysis tool, based on equation (21) and the previously discussed eigensolver, has been written in FORTRAN 77. This tool can analyze geometries bounded by either PEC or PMC. A useful application of this tool is to analyze the propagating modes in boxed microstrip. The covariant projection vector finite elements have been recommended for this type of problem because edge elements can better handle the singularities that occur at the strip edges [7].

The geometry of the problem is shown in Figure 2. Because of the symmetry in the problem, only the right half plane of the geometry was analyzed. A PMC was used as a boundary condition in the plane of symmetry. Thirty six elements were used, and after imposition of essential boundary conditions, 463 unknowns remained. Using an HP/Apollo 720 RISC workstation, construction of the global matrices required about 100 seconds, and the solver iteration time was around 0.05 seconds per eigenvalue iteration.

The results of the analysis are in close agreement with those of [7] (obtained using an alternate covariant projection finite element formulation) and [9] (obtained using a formulation based on an integral equation method with the microstrip currents as the unknown functions). No spurious modes were observed. Figure 3 shows a comparison between the first six modes calculated using this method and that of [9].

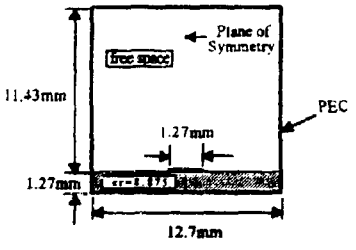

Figure 2
Boxed Microstrip Geometry

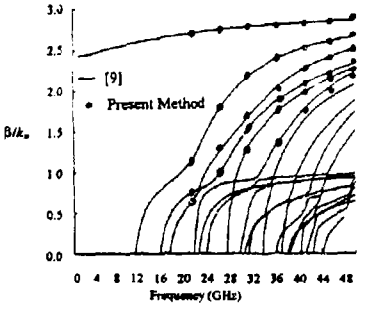

Figure 3
Comparison of Results for Boxed Microstrip

Application to Open Microstrip Problem

In order to analyze open problems, a boundary condition that mimics infinite space must be imposed along the outer boundary. In general, this type of boundary condition is a non-linear function of the eigenvalue and complicates the eigensolution procedure.

To analyze the problem of open microstrip line, an approach adapted from [10] was used. This approach differs from [10] and other similar methods in that the desired field behavior is enforced using an "absorbing boundary condition" rather than some type of "infinite element".

Along the boundary to the open region of the problem, it is assumed that the magnetic fields exhibit exponential decay in the open region according to:

$$H(x_o, y_o, z) = \bar{H}(x_o, y_o) \exp\{-\alpha_x(x - x_o) - \alpha_y(y - y_o)\} \tag{32}$$

where: $\alpha_x = \alpha\,(\hat{n} \cdot \hat{x})$ (33)

$$\alpha_y = \alpha\,(\hat{n} \cdot \hat{y}) \tag{34}$$

$$\alpha = \sqrt{\beta^2 - \varepsilon_r k_o^2} \tag{35}$$

and where $\hat{n}$ is outward normal to the boundary, and x_o and y_o are points along the boundary $\partial\Gamma$. The parameter $j\alpha$ is in effect the propagation constant of the transverse wave in the $\hat{n}$ direction. The field will exhibit exponential decay in the open region (e.g α is real positive) as long as β^2 is greater than $\varepsilon_r k_o^2$. By selecting the geometry of the finite element mesh so that all $\hat{n}$ of the boundaries to the open region are directed approximately radially outward, the fields at these boundaries can be forced to exhibit exponential radial decay. This effectively creates a type of absorbing boundary condition. The desired field behavior is embedded in the global meshes via the boundary line integrals using the basis functions modified as shown in equation (32). The resulting eigenvalue problem, however, is non-linear and special solution techniques must be used.

The finite element code used to analyze the boxed microstrip problem was modified to perform analysis of open boundary problems with fields exhibiting exponential decay in the open region. The iterative nature of the existing solver allowed solution of the non-linear eigenvalue problem with only minor modification of the algorithm. The solver was modified such that for each iteration, the boundary

line integrals of the element matrices were recalculated using the value of β^2 obtained in the previous iteration. The present version of the software can process only real valued data. Thus, in the case that α for a particular element is complex (e.g. β^2 is less than $\varepsilon_r k_0^2$), the algorithm sets the value of α equal to zero to avoid generating complex matrix entries. Since the value of α depends on the particular propagating mode of the wave, the non-linear solver can process only one eigenvalue at a time for a particular input μ.

The modified code was used to analyze the propagating modes of the open microstrip geometry shown in Figure 4. The finite element mesh is sketched in this figure, and the boundary to the open region was approximately coincident on a circle of radius 3.0 mm about the origin (straight-edged cells rather than curvilinear cells were used). Because of the symmetry of the problem, only the right half plane of the geometry was modeled. A PEC or PMC was used as a boundary condition in the plane of symmetry, varying with different propagating modes. Nineteen elements were used, and depending whether a PMC or PEC was used for the plane of symmetry, the number of unknowns was either 252 or 268. Using an HP/Apollo 720 RISC workstation, construction of the global matrices took about 50 seconds, and the solver iteration time was around 1.0 seconds/iteration. The increase in the iteration time is attributed to the fact that L-U decomposition of the matrix $[[A] - \mu[B]]$ was performed at each iteration, whereas in the previous solver, this was performed only once for each selection of μ.

The results of the analysis are in close agreement with those of [11] (obtained using an integral equation technique) and [12] (obtained using an EFIE method). No spurious modes were observed. Figure 5 shows a comparison of the various results.

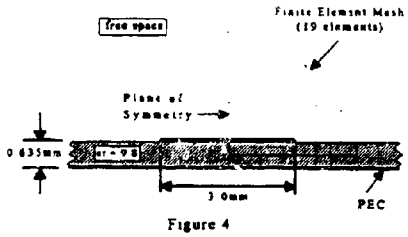

Figure 4
Open Microstrip Geometry

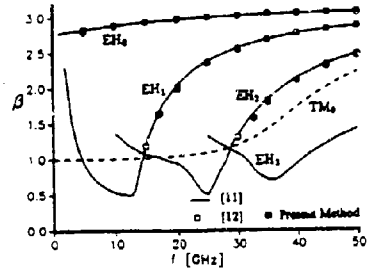

Figure 5
Comparison of Results for Open Microstrip

Conclusions

The application of mixed-order covariant projection elements to the finite element analysis of propagating modes of dielectric-loaded waveguiding structures has been presented. Approaches have been developed which can treat both closed and open waveguide problems. Details have been presented for sparse eigensolver algorithms that can solve the traditional linear eigenvalue matrix

equation as well as the non-linear eigenvalue equation that results during the analysis of the open region problem. The formulations avoid the calculation of spurious modes and sample results show good agreement with other published data.

References

[1] C. W. Crowley, "Mixed Order Covariant Projection Finite Elements for Vector Fields," Ph.D. Dissertation, McGill University, Ottawa, 1988.

[2] B. M. A. Rahman, F. A. Fernandez and J. B. Davies, "Review of Finite Element Methods for Microwave and Optical Waveguides," *Proceedings of the IEEE*, vol. 79, no. 10, pp. 1442-1448, Oct. 1991.

[3] M. Koshiba, K. Hayata and M. Suzuki, "Finite-Element Method Analysis of Microwave and Optical Waveguides - Trends in Countermeasures to Spurious Solutions," *Elect. and Comm. Japan*, part 2, vol. 70, no. 9, pp. 96-107, 1987.

[4] A. Konrad, "A Direct Three-Dimensional Finite Element Method for the Solution of Electromagnetic Fields in Cavities," *IEEE Trans. Magn.*, vol. 21, no 6, pp. 2276-2279, Nov. 1985.

[5] E. T. Moyer Jr. and E. A. Schroeder, "Finite Element Formulations of Maxwell's Equations - Advantages and Comparisons Between Available Approaches," *IEEE Trans. Magn.*, vol. 27, no. 5, pp. 4217-4220, Sept. 1991.

[6] J. F. Lee, D. K. Sun and Z. J. Cendes, "Full-Wave Analysis of Dielectric Waveguides Using Tangential Vector Finite Elements," *IEEE Trans. Microwave Theory Tech.*, vol. 39, no. 8, pp. 1262-1271, Aug. 1991.

[7] R. Miniowitz and J. P. Webb, "Covariant-Projection Quadrilateral Elements for the Analysis of Waveguides with Sharp Edges," *IEEE Trans. Microwave Theory Tech.*, vol. 39, no. 3, pp. 501-505, March 1991.

[8] Z. Zlatev, J. Wasniewski and K. Schaumburg, *Y12M*, Springer-Verlag, New York, 1981.

[9] C. J. Railton and T. Rozzi, "Complex Modes in Boxed Microstrip," *IEEE Trans. Microwave Theory Tech*, vol. 36, no. 5, pp. 865-874, May 1988.

[10] K. Hayata, M. Eguchi and M. Koshiba, "Self-Consistent Finite/Infinite Element Scheme for Unbounded Guided Wave Problems," *IEEE Trans. Microwave Theory Tech.*, vol. 36, no. 3, pp. 614-616, March 1988.

[11] K. A. Michalski and D. Zheng, "Rigorous Analysis of Open Microstrip Lines of Arbitrary Cross Section in Bound and Leaky Regimes," *IEEE Trans. Microwave Theory Tech.*, vol. 37, no. 12, pp. 2005-2010, Dec. 1989.

[12] C.H. Lee and J. S. Bagby, "The Analysis of Coupled Microstrip Transmission Lines with EFIE Method," in *Dig. URSI Radio Sci. Meeting* (Syracuse, NY), June 1988, p. 318.

A Finite Element Formulation for Multipole Modes in Axisymmetric Structures*

E. M. Nelson
Stanford Linear Accelerator Center
Stanford University, Stanford, CA 94309

Abstract

finite element field solver for multipole modes in axisymmetric structures has been written and tested. The solver is based on a weak version of the curl-curl formulation of Maxwell's equations in cylindrical coordinates. A combination of mixed-order (edge) and lagrange-type basis functions are used to avoid spurious modes. Second-order triangular elements are employed to obtain very accurate mode frequencies. Elements which touch the axis use special basis functions.

Tests on analytically soluble structures demonstrate the accuracy of the computed mode frequencies and the avoidance of spurious modes. A disk-loaded waveguide example demonstrates not only the accuracy of the solver but also boundary conditions for periodic and/or symmetric structures. The solver has been applied to the design of detuned accelerator structures for the next generation of linear colliders. A precise distribution of dipole modes is required to minimize the effect of wakefields. An overmoded 90° waveguide bend example demonstrates the applicability of the solver to curved waveguide.

Finite Element Formulation

Consider an axisymmetric structure represented by the two-dimensional region $\tilde{\Omega}$ and various types of boundaries in the z-ρ plane. The boundary Γ_{metal} is a perfectly conducting metal boundary and $\Gamma_{\text{sym(cond)}}$ and $\Gamma_{\text{sym(ins)}}$ are symmetry planes of the structure with electric and magnetic boundary conditions, respectively. For periodic structures, $\tilde{\Omega}$ is one cell bounded by Γ_{left} and Γ_{right} as shown in figure 1(a), and for symmetric periodic structures, $\tilde{\Omega}$ is a half cell bounded by $\Gamma_{\text{sym-left}}$ and $\Gamma_{\text{sym-right}}$ as shown in figure 1(b).

Writing the problem in cylindrical coordinates z, ρ and ϕ with field components E_ρ, E_ϕ and E_z, the solutions can be decomposed into multipole modes with azimuthal dependence $e^{im\phi}$. A weak formulation of Maxwell's equations for this problem in the gaussian system of units is: given the region $\tilde{\Omega}$, its material properties ϵ and μ, an azimuthal symmetry number m, and possibly a phase advance ψ (for periodic structures), find the eigenmode fields $\mathbf{E} \in \tilde{\mathcal{U}}_E$ and the corresponding eigenvalues ω^2/c^2 such that for all test functions $\mathbf{F} \in \tilde{\mathcal{U}}_E$,

$$\Re\mathrm{e} \int_{\tilde{\Omega}} \left((\nabla \times \mathbf{F}^*) \cdot \mu^{-1} (\nabla \times \mathbf{E}) - \frac{\omega^2}{c^2} \mathbf{F}^* \cdot \epsilon \mathbf{E} \right) 2\pi\rho \, d\rho \, dz = 0 \tag{1a}$$

where the space $\tilde{\mathcal{U}}_E$ of test and trial functions is

$$\begin{aligned} \tilde{\mathcal{U}}_E = \{ \mathbf{E} \in \mathcal{H}_{\text{curl}}(\tilde{\Omega}) : \\ & \hat{n} \times \mathbf{E} = 0 \quad \text{on } \Gamma_{\text{metal}} \text{ and } \Gamma_{\text{sym(cond)}}, \\ & \hat{n} \times \mathbf{E}|_{\mathbf{x}_R} = -\hat{n} \times \mathbf{E}|_{\mathbf{x}} \, e^{i\psi} \quad \forall \mathbf{x} \in \Gamma_{\text{left}}, \\ & \Im\mathrm{m} \{ \hat{n} \times \mathbf{E} \} = 0 \quad \text{on } \Gamma_{\text{sym-left}} \quad \text{and} \\ & \Im\mathrm{m} \{ \hat{n} \times \mathbf{E} e^{-i\psi/2} \} = 0 \quad \text{on } \Gamma_{\text{sym-right}} \} \end{aligned} \tag{1b}$$

and

* Work supported by Department of Energy, contract DE-AC03-76SF00515

Figure 1. The shaded region $\hat{\Omega}$ (a) is one cell of a periodic structure. The dashed lines are periodic boundaries. The arrow shows the rigid motion $\hat{\mathbf{R}}$ translating a point from the boundary Γ_{left} to the boundary Γ_{right}. The shaded region $\hat{\Omega}$ (b) represents one half-cell of a symmetric periodic structure. The dashed lines are symmetry planes.

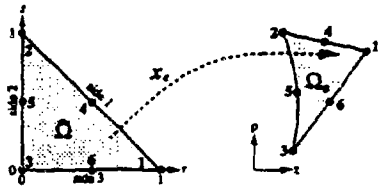

Figure 2. The map $\boldsymbol{x}_e$ from the master element $\hat{\Omega}$ to the eth element Ω_e is quadratic in the local coordinates r and s. The map is defined by coordinates (z, ρ) of six nodes.

$$\mathcal{H}_{\text{curl}}(\hat{\Omega}) = \{\mathbf{E}: \hat{\Omega} \to \mathbf{C}^3 : \int_{\hat{\Omega}} \left((\nabla \times \mathbf{E}^*) \cdot (\nabla \times \mathbf{E}) + \mathbf{E}^* \cdot \mathbf{E}\right) 2\pi\rho \, d\rho \, dz \text{ exists and is finite}\}. \tag{1c}$$

The unit normal $\hat{\mathbf{n}}$ is directed into the region $\hat{\Omega}$. Boundary conditions on the axis are implicit in condition (1c). For periodic problems, the modes have phase advance ψ across one cell of the structure. A similar formulation is available for the magnetic field $\mathbf{H}$. The dependence on m in (1a) is embedded in the curl operator. In terms of the field components,

$$\begin{aligned} \nabla \times \mathbf{E} &= \hat{\rho}\left(\frac{im}{\rho}E_z - \frac{\partial E_\phi}{\partial z}\right) + \hat{\phi}\left(\frac{\partial E_\rho}{\partial z} - \frac{\partial E_z}{\partial \rho}\right) + \hat{\mathbf{z}}\left(\frac{1}{\rho}\frac{\partial}{\partial \rho}(\rho E_\phi) - \frac{im}{\rho}E_\rho\right) \\ &= \frac{i\hat{\phi}}{\rho}\left(mE_z - \frac{\partial \tilde{E}_\phi}{\partial z}\right) + \hat{\phi}\left(\frac{\partial E_\rho}{\partial z} - \frac{\partial E_z}{\partial \rho}\right) + \frac{i\hat{\mathbf{z}}}{\rho}\left(\frac{\partial \tilde{E}_\phi}{\partial \rho} - mE_\rho\right) \\ &= \nabla_\perp \times \mathbf{E}_t + \frac{i\hat{\phi}}{\rho} \times \left(m\mathbf{E}_t - \nabla_\perp \tilde{E}_\phi\right), \end{aligned} \tag{2}$$

where $\tilde{E}_\phi = -i\rho E_\phi$, $\mathbf{E}_t = \hat{\mathbf{z}}E_z + \hat{\rho}E_\rho$ and $\nabla_\perp = \hat{\mathbf{z}}\frac{\partial}{\partial z} + \hat{\rho}\frac{\partial}{\partial \rho}$. Some insight can be gained by considering a problem with no media (vacuum). Then equation (1a) becomes

$$\begin{aligned} \Re e \int_{\hat{\Omega}} \rho(\nabla_\perp \times \mathbf{F}_t)^* \cdot (\nabla_\perp \times \mathbf{E}_t) + \frac{1}{\rho}(m\mathbf{F}_t - \nabla_\perp \tilde{F}_\phi)^* \cdot (m\mathbf{E}_t - \nabla_\perp \tilde{E}_\phi) \\ - \frac{\omega^2}{c^2}(\rho \mathbf{F}_t^* \cdot \mathbf{E}_t + \frac{1}{\rho}\tilde{F}_\phi^* \cdot \tilde{E}_\phi) \, d\rho \, dz = 0. \end{aligned} \tag{3}$$

The finite element formulation in this work is based on quadratic triangular elements. Let $\boldsymbol{x}_e : \hat{\Omega} \to \Omega_e$ be the map from the master element $\hat{\Omega}$ to the eth element Ω_e as shown in figure 2. For an element not touching the

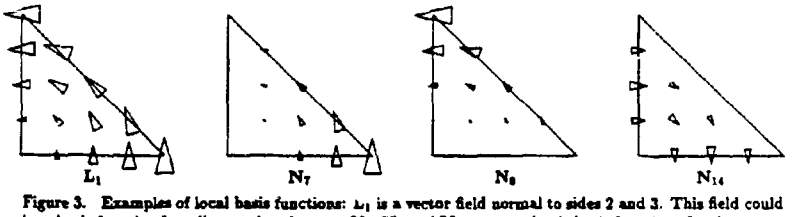

Figure 3. Examples of local basis functions: $\mathbf{L}_1$ is a vector field normal to sides 2 and 3. This field could be a basis function for a linear edge element. $\mathbf{N}_7$, $\mathbf{N}_8$ and $\mathbf{N}_{14}$ are quadratic basis functions for the vector field $\mathbf{E}_t$ constructed from $\mathbf{L}_1$. $\mathbf{N}_7$ and $\mathbf{N}_8$ have non-zero tangential field on side 1. The size and direction of the triangles indicate the magnitude and direction of the vector basis function.

axis, the scalar field $\hat{E}_\phi$ is modelled by second-order lagrange-type basis functions N_i:

$$\begin{array}{lll} N_1 = r(2r-1) & N_2 = s(2s-1) & N_3 = t(2t-1) \\ N_4 = 4rs & N_5 = 4st & N_6 = 4rt, \end{array} \tag{4}$$

where $t = 1 - r - s$. Note that the map $\boldsymbol{x}_e$ is a linear combination of the N_i listed above:

$$\boldsymbol{x}_e(r,s) = \sum_{i=1}^{6} \mathbf{x}_i^e N_i(r,s), \tag{5}$$

where $\mathbf{x}_i^e$ are the (z,ρ) coordinates of the ith node of the eth element.

The basis functions below for the vector field $\mathbf{E}_t$ were inspired by the covariant projection elements[1]–[5] of Crowley and the work of Nedelec[6]. They are similar to the basis functions described in [7] and [8]. Starting with vector fields $\mathbf{V}_i$ tangential to side i and directed counterclockwise,

$$\mathbf{V}_1 = -(\mathbf{V}_2 + \mathbf{V}_3), \quad \mathbf{V}_2 = -\frac{\partial \boldsymbol{x}_e}{\partial s} \quad \text{and} \quad \mathbf{V}_3 = \frac{\partial \boldsymbol{x}_e}{\partial r}, \tag{6}$$

construct reciprocal vector fields $\mathbf{R}_i$ normal to side i and directed inward,

$$\mathbf{R}_1 = -(\mathbf{R}_2 + \mathbf{R}_3), \quad \mathbf{R}_2 = \frac{\hat{\boldsymbol{\phi}} \times \mathbf{V}_3}{\hat{\boldsymbol{\phi}} \cdot (\mathbf{V}_2 \times \mathbf{V}_3)} \quad \text{and} \quad \mathbf{R}_3 = \frac{\hat{\boldsymbol{\phi}} \times \mathbf{V}_3}{\hat{\boldsymbol{\phi}} \cdot (\mathbf{V}_2 \times \mathbf{V}_3)}. \tag{7}$$

The reciprocal vectors can also be written as

$$\mathbf{R}_1 = \left(\frac{\partial t}{\partial z}, \frac{\partial t}{\partial \rho}\right), \qquad \mathbf{R}_2 = \left(\frac{\partial r}{\partial z}, \frac{\partial r}{\partial \rho}\right) \quad \text{and} \quad \mathbf{R}_3 = \left(\frac{\partial s}{\partial z}, \frac{\partial s}{\partial \rho}\right), \tag{8}$$

which states that the reciprocal vectors are derivatives of $\boldsymbol{x}_e^{-1}$, the inverse of the element transformation. Now construct vector functions $\mathbf{L}_i$ which satisfy $\mathbf{L}_i \cdot \mathbf{V}_j = \delta_{ij}$ on side j of the element:

$$\mathbf{L}_1 = r\mathbf{R}_3 - s\mathbf{R}_2, \qquad \mathbf{L}_2 = s\mathbf{R}_1 - t\mathbf{R}_3 \quad \text{and} \quad \mathbf{L}_3 = t\mathbf{R}_2 - r\mathbf{R}_1. \tag{9}$$

The vector fields $\mathbf{L}_i$ are suitable basis functions for a linear edge element. However, quadratic basis functions are employed in this work:

$$\begin{array}{lll} \mathbf{N}_7 = r\mathbf{L}_1 & \mathbf{N}_{10} = t\mathbf{L}_2 & \mathbf{N}_{13} = -2s\mathbf{L}_2 \\ \mathbf{N}_8 = s\mathbf{L}_1 & \mathbf{N}_{11} = t\mathbf{L}_2 & \mathbf{N}_{14} = -2t\mathbf{L}_1. \\ \mathbf{N}_9 = s\mathbf{L}_2 & \mathbf{N}_{12} = r\mathbf{L}_2 & \end{array} \tag{10}$$

The first six vector basis functions, $\mathbf{N}_7$ to $\mathbf{N}_{12}$, have non-zero tangential field on one side of the element. This field must match the tangential field of the adjacent element, if there is one, in order to construct valid global basis functions. The last two vector basis functions, $\mathbf{N}_{13}$ and $\mathbf{N}_{14}$, have no tangential field on the element sides. Each of the local vector basis functions $\mathbf{N}_{13}$ and $\mathbf{N}_{14}$ by themselves constitute valid global basis functions, thus they are internal degrees of freedom for the element. Figure 3 shows some of these local basis functions.

Elements which touch the axis are restricted so that the global basis functions satisfy condition (1c). The important terms are those weighted by $1/\rho$, hence

$$\dot{E}_\phi = 0 \quad \text{and} \quad m\mathbf{E}_t - \nabla_\perp \dot{E}_\phi = 0 \tag{11}$$

is required of each basis function. This is accomplished by using linear combinations of the basis functions above. First consider the $m \neq 0$ case. For an element with an edge (edge 3) on axis there are 6 local basis functions. Written as $(\mathbf{E}_t, \dot{E}_\phi)$ they are:

$$\begin{array}{lll} \mathbf{N}_1 = (0, s^2) & \mathbf{N}_3 = (\frac{t}{m}\mathbf{R}_3, st) & \mathbf{N}_5 = (s\mathbf{L}_2, 0) \\ \mathbf{N}_2 = (\frac{r}{m}\mathbf{R}_3, rs) & \mathbf{N}_4 = (s\mathbf{L}_1, 0) & \mathbf{N}_6 = (-2s\mathbf{L}_3, 0). \end{array} \tag{12}$$

An element with exactly one node (node 2) on axis has 11 local basis functions:

$$\begin{array}{lll} \mathbf{N}_1 = (0, r(2r-1)+rs) & \mathbf{N}_5 = (\frac{s}{m}\mathbf{L}_3, st) & \\ \mathbf{N}_2 = (0, t(2t-1)+st) & & \mathbf{N}_9 = (r\mathbf{L}_3, 0) \\ \mathbf{N}_3 = (0, 4rt) & \mathbf{N}_6 = (r\mathbf{L}_1, 0) & \mathbf{N}_{10} = (-2s\mathbf{L}_3, 0) \\ & \mathbf{N}_7 = (t\mathbf{L}_2, 0) & \mathbf{N}_{11} = (-2t\mathbf{L}_1, 0). \\ \mathbf{N}_4 = (\frac{-s}{m}\mathbf{L}_1, rs) & \mathbf{N}_8 = (t\mathbf{L}_3, 0) & \end{array} \tag{13}$$

For the special case $m = 0$ the fields $\mathbf{E}_t$ and $\dot{E}_\phi$ are uncoupled and can be separated if desired. A quadratic element with edge 3 on axis has one basis function,

$$N_1 = s^2, \tag{14}$$

for $\dot{E}_\phi$, and all 8 basis functions, $\mathbf{N}_2$ through $\mathbf{N}_9$, for $\mathbf{E}_t$. A quadratic element with only node 2 on axis has three basis functions,

$$N_1 = r(2r-1)+rs \qquad N_2 = t(2t-1)+st \quad \text{and} \quad N_3 = 4rt, \tag{15}$$

for $\dot{E}_\phi$ and all 8 basis functions, $\mathbf{N}_4$ through $\mathbf{N}_{11}$, for $\mathbf{E}_t$.

Tests

The formulation has been tested on some analytically soluble problems: an annular ring (i.e., a length of coaxial cable shorted at the two ends), a pillbox and a sphere. For the annular ring the eigenvalue error is $\mathcal{O}(h^4)$ where h is the size of the elements. For the pillbox and the sphere the eigenvalue error is $\mathcal{O}(h^{3.5})$. Examples of meshes for a sphere are shown in figure 4 and the error of the computed eigenvalue for the 10 lowest $m = 1$ modes as the mesh is refined is shown in figure 5(a). The formulation converges smoothly to the exact eigenvalue as the mesh is refined, which allows extrapolation of the computed eigenvalues to an infinitely refined mesh to obtain a better estimate of the exact eigenvalues. In figure 5(b) the error of the computed eigenvalues in a pillbox is shown as a function of m. The relative error of the computed eigenvalue increases slowly as m increases beyond $m = 2$. Hence, the formulation is suitable for large m. In addition to integer m, tests on an annular ring show the formulation works well for non-integer m as well. For more details of these tests, see [9].

Measurements[10] of the dimensions and resonant frequencies of a stack of six cells of disk-loaded waveguide were used to further test this formulation. The stack consists of five cells with a shorted half-cell at each end. A mesh is shown in figure 7(a). The measured dimensions are: cell diameter 2.159 cm, disk aperture diameter 0.8574 cm, disk thickness 0.1464 cm and period 0.8751 cm. The dispersion diagram for this structure is shown in figure 7(b). The measured frequencies in the second band agree with the computed frequencies to better than 0.1%. The estimated error of the computed frequencies is less than 0.01%, so the discrepancies are probably due to fabrication and measurement errors of the six cell stack.

Applications

The motivation for this work was the design of detuned accelerator structures[11]. A precise distribution of dipole modes is required to minimize the effect of wakefields. This solver was used to compute the dipole

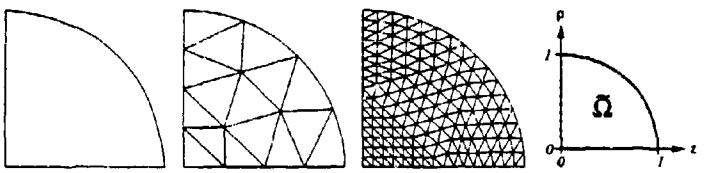

Figure 4. A course mesh (one element) and two refined meshes for the sphere problem. Each mesh covers the shaded region $\hat{\Omega}$. The dashed line is a symmetry plane.

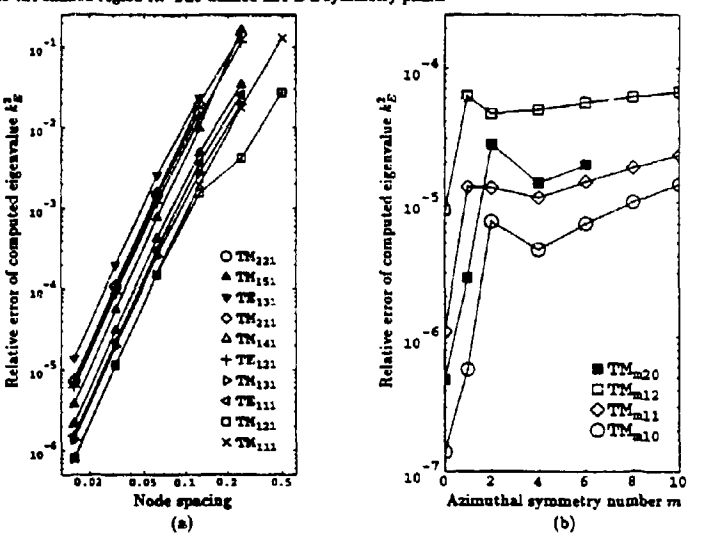

Figure 5. Relative error of the computed eigenvalue vs (a) mesh refinement and (b) m. In (a) the electric field is computed for the $m = 1$ modes of a sphere with radius 1. In (b) the electric field is computed on a 512 element mesh for a pillbox with length 1 and radius 1.

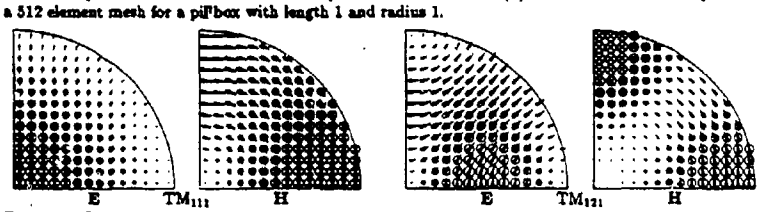

Figure 6. Field plots of the two lowest $m = 1$ modes of a sphere based on the 256 element mesh in figure 4. The triangles represent the magnitude and direction of the fields $\mathbf{E}_t$ and $\mathbf{H}_t$. The size of the circles represent the magnitude of the (imaginary) fields E_ϕ and H_ϕ. A crossed circle indicates the field is negative.

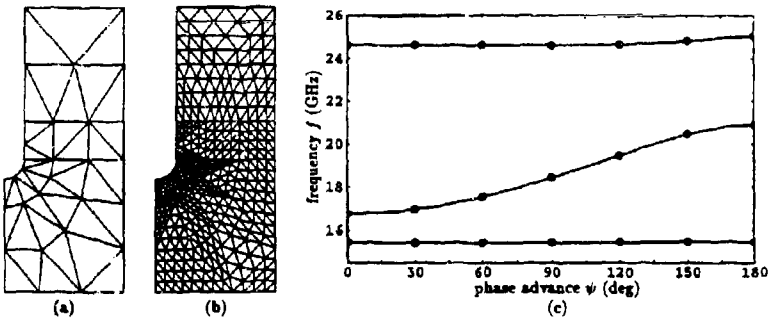

Figure 7. A coarse mesh (a) and a fine mesh (b) for one half-cell of disk-loaded waveguide. The left and right edges are symmetry planes. The bottom edge is the axis. The dispersion diagram (c) for this structure was generated from calculations at seven phase advances.

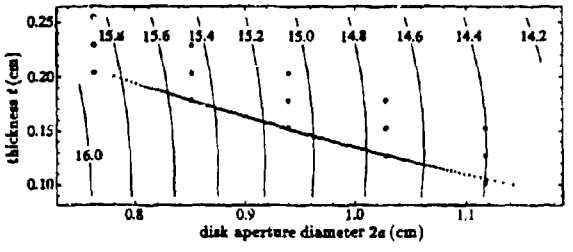

Figure 8. The lowest synchronous dipole mode frequency f_1 (in GHz) for periodic disk-loaded waveguide. The cell diameter $2b$ is determined from the synchronism condition for the 11.424 GHz accelerating mode: phase velocity $v_{ph} = c$ at phase advance $\psi = 2\pi/3$. The open circles are the dimensions at which f_1 was computed. The dots are the 206 cells of the detuned accelerator structure.

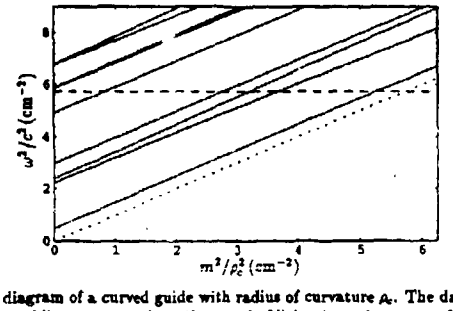

Figure 9. Dispersion diagram of a curved guide with radius of curvature ρ_c. The dashed line is the drive frequency, and the dotted line corresponds to the speed of light along the center of the guide.

mode frequencies synchronous with the beam in periodic disk-loaded waveguide, as shown in figure 8. Then cell parameters of an accelerator structure were chosen to obtain the desired dipole mode distribution.

Another application of this solver was the design of a 90° overmoded waveguide bend[12]. It is useful to consider modes propagating along ϕ in the curved guide with phase factor $e^{im\phi}$. This is analagous to modes propagating along z with phase factor e^{ikz} in straight guide. Since the bend is only over 90°, not a full circle, there is no condition that m be an integer. This solver was used to compute dispersion diagrams for the curved guide. An example is shown in figure 9. Note that the curves are not parallel as one would expect in straight homogeneous guide.

Conclusion

The finite element formulation described above computes modes in periodic structures with excellent accuracy.

References

[1] C. W. Crowley, P. P. Silvester and H. Hurwitz Jr., "Covariant Projections Elements for 3D Vector Field Problem," *IEEE Trans. Magnetics*, vol. MAG-24, pp. 397–400, Jan. 1988.

[2] A. R. Pinchuk, C. W. Crowley and P. P. Silvester, "Spurious Solutions to Vector Diffusion and Wave Field Problems," *IEEE Trans. Magnetics*, vol. MAG-24, pp. 158–161, Jan. 1988.

[3] J. P. Webb and Ruth Miniowitz, "Analysis of 3-D Microwave Resonators using Covariant-Projection Elements," *IEEE Trans. Microwave Theory Tech.*, vol. MTT-39, pp. 1895-1899, Nov. 1991.

[4] Ruth Miniowitz and J. P. Webb, "Covariant-Projection Quadrilateral Elements for the Analysis of Waveguides with Sharp Edges," *IEEE Trans. Microwave Theory Tech.*, vol. MTT-39, pp. 501–505, Mar. 1991.

[5] C. W. Crowley, "Mixed Order Covariant Projection Finite Elements for Vector Fields," Ph.D. dissertation, McGill University, Montreal, PQ, Canada, 1988.

[6] J. C. Nedelec, "Mixed Finite Elements in R^3," *Num. Math.*, vol. 35, pp. 315–341, 1980.

[7] Jin-Fa Lee, Din-Kow Sun and Zoltan J. Cendes, "Full-Wave Analysis of Dielectric Waveguides Using Tangential Vector Finite Elements," *IEEE Trans. Microwave Theory Tech.*, vol. MTT-39, pp. 1262–1271, Aug. 1991.

[8] Jin-Fa Lee, Gregory M. Wilkins and Raj Mittra, "Finite-Element Analysis of Axisymmetric Cavity Resonator Using a Hybrid Edge Element Technique," *IEEE Trans Microwave Theory Tech.*, vol. MTT-41, pp. 1981–1987, Nov. 1993.

[9] E. M. Nelson, "High Accuracy Electromagnetic Field Solvers for Cylindrical Waveguides and Axisymmetric Structures Using the Finite Element Method," Ph.D. dissertation, Stanford University, Stanford, CA, 1993; also SLAC-431.

[10] H. Deruyter and H. Hoag, private communication.

[11] J.W. Wang and E.M. Nelson, "Design of the Detuned Accelerator Structure," *Proc. 1993 IEEE Particle Accelerator Conf.*, pp. 1086–1088; also SLAC-PUB-6142.

[12] C. Nantista, N.M. Kroll and E.M. Nelson, "Design of a 90° Overmoded Waveguide Bend," in *Proc. 1993 IEEE Particle Accelerator Conf.*, pp. 983–985; also SLAC-PUB-6141.

AZIMUTHALLY-DEPENDENT FINITE ELEMENT SOLUTION TO THE CYLINDRICAL RESONATOR*

Roberto A. Osegueda, Joseph H. Pierluissi, Luis M. Gil,
Arturo Revilla and Gustavo J. Villalva
The University of Texas at El Paso
College of Engineering
El Paso, TX 79958

and

G. John Dick, David G. Santiago and Rabi T. Wang
Jet Propulsion Laboratory
California Institute of Technology
Pasadena, CA 91009

Abstract: The cylindrical cavity resonator loaded with an anisotropic dielectric is analyzed as a two-dimensional problem using a finite element approach that assumes sinusoidal dependance in azimuth. This methodology allows the first finite element treatment of the technically important case of a resonator containing a sapphire element with a cylindrically aligned c axis. Second order trial functions together with quadrilateral elements are adopted in the calculations. The method was validated through comparisons with the analytical solutions for the hollow metal cavity and a coaxial cavity, as well as through measurements on a shielded sapphire resonator.

I. Introduction

Although the analytical determination of resonant modes and frequencies of the metallic cylindrical cavity has a well established history, a solution for the cavity partially filled with an anisotropic dielectric generally requires computationally complex, three-dimensional numerical analyses. Approximate analytical means of analyzing the dielectric resonator have been proposed throughout the years [1, 2], and with some degree of accuracy the theoretical estimates have agreed well with experimental results. However, because of the inherent shortcomings of the approximate analytical models, numerical methods have continued to receive a great deal of attention during the past years [3, 4].

Recently, so called "whispering gallery" resonators consisting of a sapphire dielectric element in a metallic container have made possible new capabilities for microwave oscillator phase noise and frequency stability [5,6]. With high azimuthal mode numbers,

* This work was sponsored by and carried out in part at Jet Propulsion Laboratory, California Institute of Technology, under a contract with the National Aeronautics and Space Administration.

these resonators isolate radio-frequency energy to the dielectric element and away from the metallic container, thus providing extraordinary low losses and high quality factors (Q's). However, these widely disparate field magnitudes pose a challenge for any methodology to accurately calculate (e.g.) conductive losses due to small evanescent fields at the wall of the containing can. In particular, a three-dimensional finite element method allowing full treatment of sapphire's anisotropic dielectric constant, would require such a large number of nodes as to become impractical. Analytical methods are unattractive, with new approaches required for every geometrical configuration change. A two-dimensional finite element approach, however, would allow easy treatment of any cylindrically symmetric resonator geometry.

Because the dielectric constant for sapphire shows cylindrical symmetry, a two dimensional treatment is allowed for the important case where its crystal c axis is aligned with a physical axis of axisymmetry. In terms of the field intensities, the problem is governed by the three-component vector Helmholtz equation which can be treated as an axisymmetric problem only for modes with no azimuthal (or ϕ) dependence. Such zero-order modes can be obtained from a two-dimensional approach to the cavity in the r-z plane using a variety of techniques which yield reasonable accuracy. Higher order solution for isotropic dielectrics are still obtainable in two dimensions if the azimuthal dependence of the modes is assumed *a priori* [7]. In the work presented here, the authors reduce the finite element analysis of the anisotropic dielectric resonator to two dimensions by assuming an exponential ϕ-dependence, and limiting the permittivity tensor to posses longitudinal and transverse components only. While ruling out most anisotropic dielectric configurations, this approach makes possible the first two-dimensional finite element treatment for sapphire "whispering gallery" resonators.

II. Fundamental Equations

In terms of the magnetic field intensity H, the vector Helmholtz equation with the penalty term included is given by [8]

$$\nabla \times [k]^{-1} \nabla \times H - \alpha \nabla (\nabla \cdot H) - k_o^2 H = 0 \qquad (1)$$

in which $[k]$ is the tensor dielectric constant, α is an empirical coefficient of the penalty term $\nabla (\nabla \cdot H)$, and k_o is the free-space propagation constant. The variational energy functional associated with (1) is given by [8]

$$F\{H\} = \int_{\Omega} \{ (\nabla \times H)^* \cdot ([k]^{-1} \nabla \times H) - k_o^2 H^* \cdot H + \alpha (\nabla \cdot H)^* \cdot (\nabla \cdot H) \} \, d\Omega \qquad (2)$$

where Ω is the volume of the resonator. In a finite element solution, H is normally chosen instead of E because of the discontinuity of the latter at dielectric interfaces.

At the interface between a perfect conductor and a lossless dielectric with a unit normal vector a_n the use of (2) implies that

$$a_n \times [k]^{-1} (\nabla \times H) = 0 \quad , \tag{3}$$

as a naturally satisfied condition, while the condition

$$a_n \cdot H = 0 \quad , \tag{4}$$

needs to be enforced. There is no axis of axisymmetry for the higher order modes ($n > 0$) and, hence, no perfect magnetic conductor with its associated boundary condition needs to be invoked along the z axis.

III. Finite Element Analysis

Inside the volume of the cylindrical resonator the magnetic field vector may be described as

$$\{ H(r,\phi,z) \} = \begin{Bmatrix} H_r(r,\phi,z) \\ H_\phi(r,\phi,z) \\ H_z(r,\phi,z) \end{Bmatrix} = \{ H(r,z) \} e^{jn\phi} \quad , \tag{5}$$

where

$$\{ H(r,z) \}^T = \lfloor H_r(r,z) \quad j H_\phi(r,z) \quad H_z(r,z) \rfloor \quad , \tag{6}$$

and $H_r(r,z)$, $H_\phi(r,z)$ and $H_z(r,z)$ are functions describing the variations of the components of the field vectors in the r-z plane. The n in (5) denotes the azimuthal mode number (1, 2, 3,. . .) while j is used to establish the component H_ϕ to be in phase quadrature with the transverse components H_r and H_z. In this manner, $H_r(r,z)$, $H_\phi(r,z)$ and $H_z(r,z)$ are real functions.

This finite element formulation considers the use of general ring elements to solve for the magnetic field vectors. These elements are defined in the r-z plane and have m nodes. Within each finite element, $H(r,z)$ is approximated in terms of the standard shape function matrix $[N]$ as

$$\{ H(r,\phi,z) \} = [N(r,z)]^T \{ H \}_e \, e^{jn\phi} \quad , \tag{7}$$

in which

$$\{ N(r,z) \}^T = \lfloor N_1(r,z) \quad N_2(r,z) \quad \ldots \quad N_m(r,z) \rfloor \quad , \tag{9}$$

$$[\,N(r,z)\,] = \begin{bmatrix} \{N(r,z)\} & \{0\} & \{0\} \\ \{0\} & j\{N(r,z)\} & \{0\} \\ \{0\} & \{0\} & \{N(r,z)\} \end{bmatrix} , \tag{8}$$

and

$$\{H\}_e^T = \lfloor \{H_i\}_e^T \quad \{H_j\}_e^T \quad \{H_k\}_e^T \rfloor \quad . \tag{10}$$

Here, $\{H\}_e$ is a collection matrix of order 3m by 1 containing the unknown nodal values of the field arranged as in (10), and $N_i(r,z)$ is the shape function associated with the i^{th} node of the element. The specification of the azimuthal dependence in (7) allows for a trivial analytical integration of the functional in (2) from $\phi = 0$ to $\phi = 2\pi$ when the dielectric properties are ϕ-independent.

The substitution of the field approximation in (7) into the functional expression (2) leads to the element matrix equation

$$F_e = \{\,H\,\}_e^T \left[\,[S]_e + [U]_e - k_o^2\,[T]_e\right] \{\,H\,\}_e \quad . \tag{11}$$

where

$$[S]_e = \int_\Omega [A]^*\,[K]^{-1}\,[A]^T\,d\Omega \quad , \tag{12}$$

$$[U]_e = \int_\Omega [C]\,[C]^T\,d\Omega \quad , \tag{13}$$

$$[T]_e = \int_\Omega [N]^*\,[N]^T\,d\Omega \quad , \tag{14}$$

$$[A] = e^{jn\phi} \begin{bmatrix} \{0\} & \{\frac{\partial N}{\partial z}\} & -j\frac{n}{r}\{N\} \\ -j\{\frac{\partial N}{\partial z}\} & \{0\} & j\frac{1}{r}\{N\} + j\{\frac{\partial N}{\partial r}\} \\ j\frac{n}{r}\{N\} & -\{\frac{\partial N}{\partial r}\} & \{0\} \end{bmatrix} , \tag{15}$$

and

$$[C] = e^{jn\phi}\begin{bmatrix} (\frac{1}{r}+\frac{\partial}{\partial r})\{N\} \\ -\frac{n}{r}\{N\} \\ \frac{\partial}{\partial z}\{N\} \end{bmatrix} \tag{16}$$

The integrations of (12), (13) and (14) over the azimuthal direction are done analytically, requiring that the dielectric properties $[K]$ in (12) be ϕ-independent. This is satisfied when $[K]$ has zero value off diagonal coefficients, and when the radial permittivity is equal to the azimuthal permittivity. The integrations of (12), (13) and (14) over the element area in the r-z plane are evaluated numerically using the standard Gauss-quadrature technique generally used for isoparametric elements with non-rectangular and curved shapes [9].

The global form of the functional in (11) may be expressed symbolically as

$$F = \{H\}^T\left[[S] + [U] - k_0^2[T]\right]\{H\} \ , \tag{17}$$

where $[S]$, $[U]$ and $[T]$ are global matrices resulting from the superposition of the corresponding element matrices, and $\{H\}$ contains all the unknown nodal values of the magnetic field vector.

Applying the Rayleigh-Ritz criterion, (17) yields the eigenvalue equation

$$[[S] + [U]]\{H\} - k_0^2[T]\{H\} = 0 \ , \tag{18}$$

which needs to be solved for the resonant frequencies $\omega_r = ck_0$ and for the nodal values of the corresponding mode intensities $\{H\}$. The parameter c is the velocity of light in free space.

IV. Comparison to Analytical Solution

The proposed method was tested by solving for the resonant frequencies and modes of a metallic hollow, cylindrical cavity resonator with a radius of 3.8 cm and a height of 4.5 cm since the exact analytical solution is well-known. The resonator was modeled using rectangular ring elements with four corner nodes and bilinear shape functions. Solutions were obtained using 16, 36, 64 and 100 elements. A penalty factor of $\alpha = 1$ was assumed in (1) throughout the calculations. The identification of the modes and the removal of spurious modes was assisted by computations of the cosine of the angle β between the eigenvectors from the finite element solution and the exact eigenvectors. The cosine of this angle is given by [8] as:

$$\cos \beta = \frac{\{H\}^T \{H_e\}}{\| \{H\}^T \|_2 \| \{H_e\} \|_2} \quad , \tag{19}$$

where $\{H\}$ is the eigenvector solution of (18), $\{H_e\}$ are the nodal values calculated from the exact analytical expressions, and the factors in the denominator are Euclidian norms. If the value of $\cos \beta$ in (19) is close to one or minus one, then the field vectors $\{H\}$ and $\{H_e\}$ are the same. Equation (19) was evaluated using each $\{H_e\}$ and all $\{H\}$ vectors to find the correspondence between each analytical vector and the numerical eigenvector.

Figure 1 shows convergence curves for ω, obtained from the finite element solution for the transverse magnetic TM_{0ml} series modes, where the subscripts represent the number of oscillations in ϕ, r, and z, respectively. The abscissa corresponds to the order of mode extraction in the finite element solution. For 100 elements the resonant frequencies converged to about 0.12% from the exact values for both the TE and TM modes. Fig. 2 shows a sample of the results obtained through the use of the cosine of the angle between vectors in (19) for mode identification. The true TE_{0ml} modes are shown on the top of the figure, with a cosine close to one, while the spurious modes have values much lower than one. Fig. 3 shows the frequencies of various families of TE and TM modes of the cavity resonator as functions of the azimuthal index.

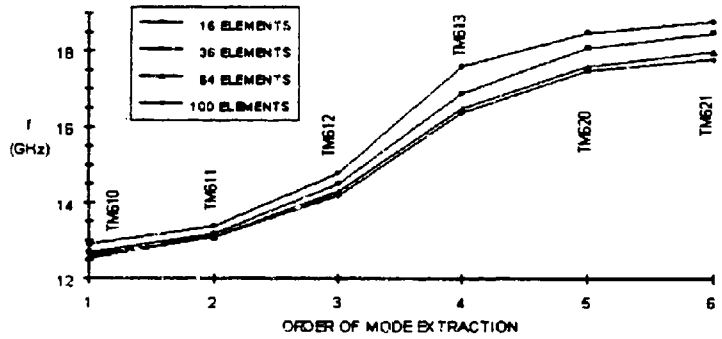

Figure 1. Convergence curves of the finite element frequencies for the first six modes of the hollow cavity with $r_c = 6$.

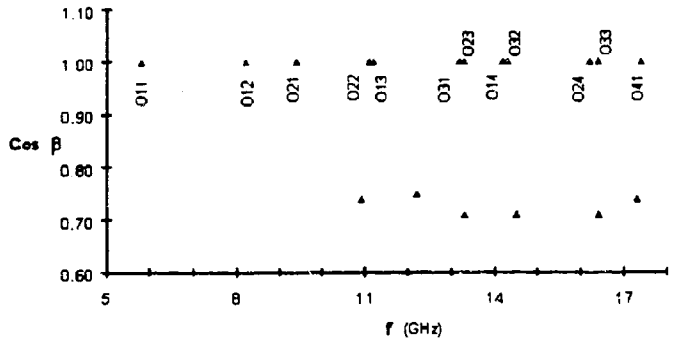

Figure 2. Finite element frequencies of modes obtained for the hollow cavity. The modes with cosines close to unity are physical, while those with smaller values are spurious.

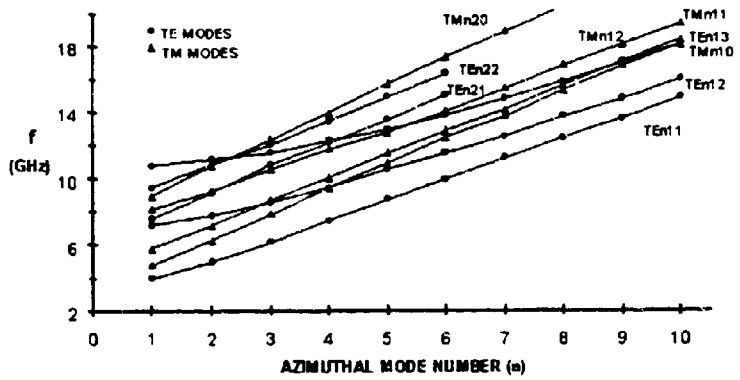

Figure 3. Sample families of modes obtained from the finite element analysis of the hollow cavity with 100 quadrilateral elements.

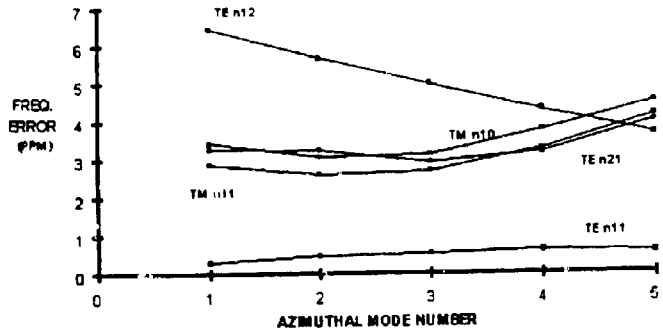

Figure 4. Frequency error for several mode families of coaxial resonator.

Somewhat higher accuracy was found when the method was applied to a coaxial cavity, where a more uniform geometry is obtained for elements near its geometrical center. The coaxial resonator had an outer radius of 5 cm, an inner radius of 2.5 cm, and a height of 5 cm. Figure 4 shows the difference in parts per million (PPM) between the finite element solution using 220 elements and the analytic solutions for various mode families. Frequency errors for the first five mode families are all less than 7 parts per million, with errors for the fundamental TE_{n11} mode family being less than 1 PPM.

V. Comparison to Measurements

The proposed finite element approach was also tested by solving for the resonant frequencies and modes of a cylindrical sapphire resonator experimentally studied by the Jet Propulsion Laboratory. Reference [5] includes details of the experimentation and of the measured frequencies for different families of modes.

Figure 5 illustrates the geometrical axisymmetric plane of the resonator tested. The sapphire material was held together by a copper core in the center and encapsulated inside a copper cylinder. The resonator was modeled using three finite

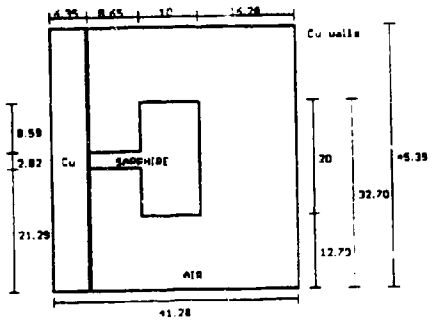

Figure 5. Dimensions (in mm) of sapphire resonator.

element meshes comprising of eight-node elements of sapphire and air materials. The dielectric properties of the sapphire material were taken from Ref. [2] as $\epsilon_{rr} = \epsilon_{\theta\theta} = 9.407$ and $\epsilon_{zz} = 11.62$. The coarse mesh consisted of 62 nodes and 15 elements, the medium mesh of 193 nodes and 54 elements, and the finest mesh has 709 nodes and 216 elements. The perfect electric conductor boundary condition reflected in (4) was enforced at all metal boundaries of the finite element meshes. The eigenvalue solution of (18) was obtained for azimuthal order values ranging from 3 to 12. Each solution yielded a set of resonant frequencies with associated eigenvectors. The lowest frequency solution corresponded to the fundamental mode for that n^{th} azimuthal order.

Figure 6 shows the resonant frequencies of the fundamental family of modes WGH_{n11} for the three meshes with n values ranging from 3 to 12, illustrating convergence of the solutions as the finite element mesh was refined. The mode classification shown is based on the notation of Jiao, et al. [6] for whispering-gallery modes. A finer mesh was not considered feasible due to computer memory limitations.

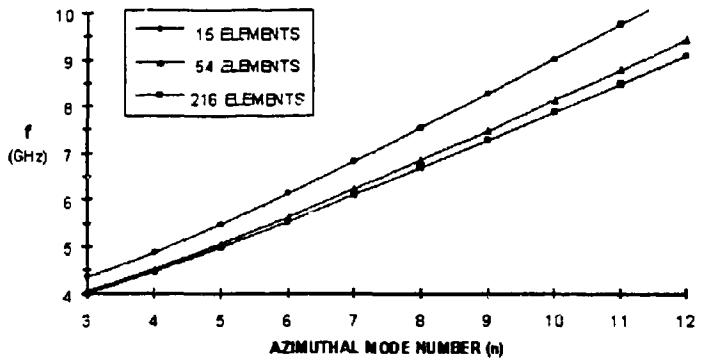

Figure 6. Convergence curves of the finite element frequency for the fundamental WGH_{n11} family in the sapphire resonator using different mesh sizes.

Figure 7 shows the frequencies of the families of modes that were identified and that matched with the frequency measurements made at the Jet Propulsion Laboratory [5]. The solid lines of the figure correspond to the finite element results and the dots are the measured values. From this figure it is observed that the finite element results agree well with the measurements. The errors in the resonant frequencies of fundamental family WGH_{n11} modes, obtained from the three meshes, with respect to the measurements are listed in Table 1. Errors of the resonant frequencies of the rest of the families shown in Fig. 7, including uncertainties in ϵ, were all less than one percent.

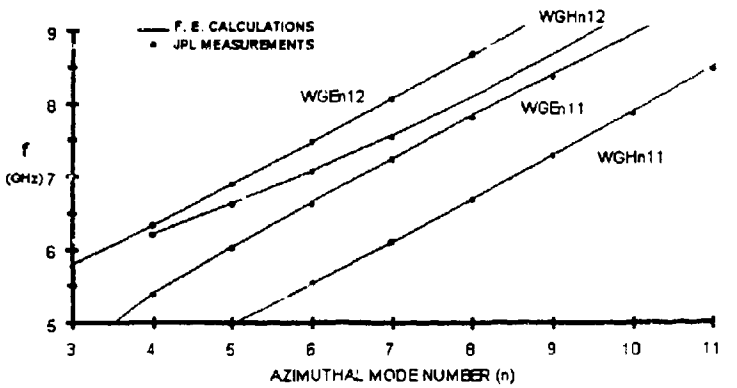

Figure 7. Comparison of resonant frequencies obtained from finite element analyses with measurements made on a cylindrical sapphire resonator.

Table 1. Error of Resonant Frequency of Fundamental Family WGH_{n11} with Respect to Experimental Measurements

Azimuthal Number n	Error (%)		
	Coarse Mesh	Medium Mesh	Fine Mesh
6	11.0	1.9	0.15
7	12.0	2.3	0.16
8	13.1	2.7	0.22
9	14.0	3.1	0.26
10	14.9	3.6	0.28
11	15.7	4.1	0.55

VI. Conclusions

A finite element method has been presented for treating a cylindrical resonator partially filled with an anisotropic dielectric as a two-dimensional finite element problem assuming harmonic oscillation for the field dependence in azimuth. This technique allows the first treatment of the technically interesting case of an anisotropic but axisymmetric dielectric mounted in a cylindrical conducting container. The method was first validated with a hollow, metallic, cylindrical resonator and with a coaxial cavity by comparing the numerically-obtained results with the exact analytical expressions. The method was then tested with a cylindrical sapphire resonator for which there are no exact solutions available. The numerical results obtained from the method were grouped by families of modes and the frequencies compared to experimental values obtained at the Jet Propulsion Laboratory. Excellent agreement was found for all the cases, thus indicating that the method is valid.

Acknowledgements

The authors wish to acknowledge the technical comments and discussions provided by Alfred R. Paiz and Lute Maleki from the Jet Propulsion Laboratory during the course of this research.

REFERENCES

[1]. Kajfez, D. and P. Gillon, Eds., Dielectric Resonators, Artech House, Boston, 1986.

[2]. Tobar, M.E. and A.G. Mann, Resonant Frequencies of Higher-Order Modes in Cylindrical Anisotropic Dielectric Resonators, IEEE MTT-S International Microwave Symposium Digest, pp. 495-498, 1991.

[3]. Konrad, A., Vector Variational Formulation of Electromagnetic Fields in Anisotropic Media, IEEE Trans. Microwave Theory and Techniques, Vol. MTT-24, No 9, pp. 553-559, 1976.

[4]. Wang, J.S. and N. Ida, Eigenvalue Analysis in Anisotropically Loaded Electromagnetic Cavities Using "Edge" Finite Elements, IEEE Trans. on Magnetics, Vol. 28,, No. 2, pp. 1438-1441, 1992.

[5]. Dick, G.J. and J. Saunders, Measurements and Analysis of a Microwave Oscillator Stabilized by a Sapphire Dielectric Resonator for Ultra-Low Noise, IEEE Trans. on Ultrasonics, Ferroelectrics, and Frequency Control, Vol. 37, No. 5, pp.339-346, 1990.

[6]. Jiao, X., P. Guillon, and L.S. Bermudez, Resonant Frequencies of Whispering-Gallery Dielectric Resonator Modes, IEEE Proceedings, Vol. 134, Pt. H. No. 6, pp 497-501, 1987.

[7]. Davies, J.B., F.A. Fernandez, and G.Y. Phileppou, Finite Element Analysis of All Modes in Cavities with Circular Symmetry, IEEE Trans. Microwave Theory & Techniques, Vol. MTT-30, No. 11, pp. 1975-1980, 1982.

[8]. Koshiba, M., K. Hayata, and M. Suzuki, Improved Finite Element Formulation in Terms of the Magnetic Field Vector for Dielectric Waveguides, IEEE Trans. on Microwave Theory and Techniques, Vol. MTT-33, No. 3, pp. 227-233, 1985.

[9]. Zienkiewicz, O.C. and Taylor, R.L., The Finite Element Method, 4th Ed., Vol. 1 Basic Formulation and Linear Problems, McGraw-Hill, London, 1989.

[10]. Conte, S.D. and C. De Boor, Elementary Numerical Analysis: an Algorithm Approach, 3rd. Ed., McGraw-Hill, NY, 1980.

ON THE "METRON" IN THE METHOD OF MEASURED EQUATION OF INVARIANCE

Wei Hong
Dept. of Radio Eng., Southeast University
Nanjing 210018, P.R. China

Kenneth K. Mei and Yao W. Liu
Dept. of Electrical Engineering and Computer Science
University of California, Berkeley, CA94720

ABSTRACT: The measured equation of invariance (MEI) is a new concept for electromagnetic field computation, and the "metron" is an important concept in the method of MEI, but people still have different opinions on the meaning of metrons up to now. Many people think metrons to be basis functions just like ones in the method of moments (MoM). In fact, metrons are quite different from the basis functions. The coefficients in MEI are determined by metrons based on the postulate: "The MEI is invariant to the field of excitation", and the current distribution or scattered field etc. are determined by the final field values at nodes other than the metrons. Previously, the metrons are usually choosed as global functions which are defined on the whole object surface. For some problems, especially for 3-D problems, the definition and calculation of global metron functions are very difficult. Therefore, in this paper we proposed several kinds of piecewise metron functions which are flexible for fitting arbitrarily shaped objects and no more computation time increased. Many numerical results are presented for comparing the different kinds of metrons.

I. Introduction

The measured equation of invariance (MEI) is a simple technique used to derive finite difference type local equation at mesh boundaries, where the conventional finite difference approach fails [1]. Convertionally, finite difference or finite element meshes span from boundary to boundary, or to any surface where an absorbing boundary condition can be simulated. It is demonstrated that the MEI technique can be used to terminate meshes very close to the object boundary and still strictly preserves the sparsity of the finite difference equations. It results in dramatic savings in computing time and memory needs.

In the first paper of MEI [1], this new method successfully applied to the scattering problems of general boundary geometries including both convex and concave metal surfaces. Lately, the authors extended this technique to the scattering problems involving penetrable medium [2] and anisotropic medium [3], where the electric metrons and the magnetic metrons are successfully decoupled by a novel concept. In this paper, a generalized FD equation for inhomogeneous anisotropic ferrite medium is derived, then the method of MEI is first extended to the scattering problems of anisotropic medium cylinders.

The coefficients in MEI are determined by metrons based on the postulate: "The MEI is invariant to the field of excitation". Previously, the metrons are usually choosed as global functions which are defined on the whole object surface. For some problems, especially for 3-D problems, the definition and calculation of global metron functions are very difficult. Therefore, in this paper we proposed several kinds of piecewise metron functions which are flexible for fitting arbitrarily shaped objects and no more computation time increased. Many numerical results are presented for comparing the different kinds of metrons.

II. The Principle of MEI

Let's consider the electromagnetic scattering problem of a conducting cylinder with arbitrarily shaped cross-section as shown in Fig.1, where several layers meshes are drawed around the surface of the cylinder.

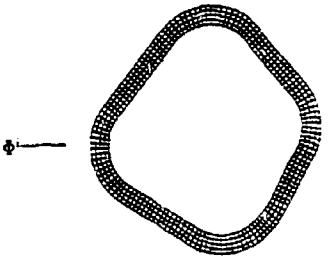

Fig.1 2D scattering problem and the meshes

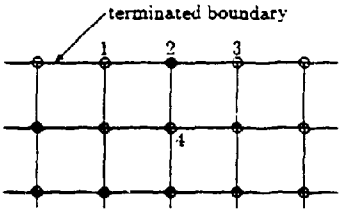

Fig.2 Nodes at terminated boundary for MEI

In the earlier paper [1], Mei postulated that the finite difference/element equations at the mesh boundary may be represented by a local linear equation of the type

$$\sum_{i=1}^{4} C_i \phi_i = 0 \tag{1}$$

where the node configuration is shown in Fig.2, and the coefficients C's are (i) location depen-

dent, (ii) geometry specific, (iii) invariant to the field of excitation.

It is known that the scattered fields at MEI nodes shown in Fig.2 can be determined by the current on the surface of the conducting cylinder as

$$\phi(\bar{r}_i) = \begin{cases} \int_\Gamma J(l')G(\bar{r}_i,\bar{r}')dl' & \text{for TM or E-wave} \\ \int_\Gamma M(l')\frac{\partial}{\partial n'}G(\bar{r}_i,\bar{r}')dl' & \text{for TM or E-wave} \end{cases} \tag{2}$$

where $G(\bar{r},\bar{r}')$ is the 2D Green's function of free space, n stands for the outward normal direction of the cylinder surface, the superscript $'$ denotes source point, $J(l')$ and $M(l')$ are electrical and magnetic currents on the cylinder surface respectively, l is the distance measured along the circumference of the cylinder and L is the total circumferential dimension of the cylinder.

If the current $J(l)$ or $M(l)$ are given, the scattered field values at the four MEI nodes are then determined by Eq.(2). However, the currents on the surface of the cylinder are unknown which are also what we want to calculate. On the other hand, the MEI Eq.(1) should be independent of the incident wave, that means the MEI should be independent of the current distribution on the surface of the cylinder for different excitation produces different current. Therefore, our MEI must be valid for various kinds of current distribution on the cylinder surface other than some special one. In other words, we should find a set of MEI coefficients $C_i, i = \overline{1,4}$ which are suitable for all kinds of currents distribution on the surface of the cylinder.

Assuming that $\{\psi_n, n = 1,2,\cdots\cdots\}$ is a complete set of functions defined on the surface of the cylinder, then any current distribution on it can be expanded with the functions set as

$$J_s(l) = \sum_{n=1}^{\infty} a_n\psi_n(l) \tag{3}$$

$$M_s(l) = \sum_{n=1}^{\infty} b_n\psi_n(l) \tag{4}$$

If the MEI Eq.(1) is valid for each expansion function ψ_n, it can be obviously seen from Eqs.(3)(4) that the MEI is valid for any current distribution on the surface of the cylinder, this also means the MEI is independent of the excitation. For this reason, we can determine the MEI coefficients $C_i, i = \overline{1,4}$ by forcing the MEI to be valid for each expansion function ψ_i. That results in the following linear algebraic equations

$$\sum_{i=1}^{4} C_i \int_\Gamma \psi_n(l')G(\bar{r}',\bar{r}_i)dl' = 0, \qquad n = 1,2,\cdots, \quad \text{for E-wave} \tag{5}$$

$$\sum_{i=1}^{4} C_i \int_\Gamma \psi_n(l')\frac{\partial}{\partial n'}G(\bar{r}',\bar{r}_i)dl' = 0, \quad n = 1,2,\cdots, \quad \text{for H-wave} \tag{6}$$

Substituting the field values at boundary nodes produced by each ψ_n into the MEI Eq.(1), a linear algebraic equation (5) or (6) with respect to the MEI coefficients $C_i, i = \overline{1,4}$ is then followed. This process just like measuring the MEI by function ψ_n, so we call ψ_n "metron".

Since the limitation of computer memory, only finite metrons $\psi_n, n = \overline{1,M}$ are used for determining the MEI coefficients, and if the number of equations M is greater than 3 (the number of MEI coefficients to be determined, C_2 is assumed to be 1), we can solve Eq.(5) or Eq.(6) by least square technique.

Generally, several metrons are enough. In our program, for instance, increasing the number of metrons (sine and cosine functions) more than 5, the results will have practically no change. The conclusion also verified the postulate of that the MEI is invariant to the excitation.

At interior nodes of the mesh, finite difference (FD) equations are valid. Coupling the MEI equations at boundary nodes to the FD equations at interior nodes and considering the incident field, a system of linear algebraic equations with respect to the scattered field values at boundary nodes and the total field values at all the interior nodes is obtained, and then the current on the surface of the cylinder is determined from its solution. Finally, the scattered fields at any point out of the cylinder can be determined by the current.

III. On the Metrons

From the discussion above, we know that the constraints on the choice of metron is rather relaxed. Usually the the following functions

$$\psi_n(l) = 1, \sin\frac{2\pi l}{L}, \cos\frac{2\pi l}{L}, \cdots \qquad l \in [0, L] \tag{7}$$

are used as metrons. In fact, many other functions, such as the following constant piecewise functions

$$\psi_n(l) = \begin{cases} 1, & \text{for } l \in [l_n, l_{n+1}] \\ 0, & \text{for } l \in [l_n, l_{n+1}] \end{cases} \tag{8}$$

where $[l_1, l_2, \cdots, l_N]$ is a partition of $[0, L]$, the piecewise linear functions

$$\psi_n(l) = \begin{cases} \frac{l-l_{n-1}}{l_n-l_{n-1}}, & \text{for } l \in [l_{n-1}, l_n] \\ \frac{l_{n+1}-l}{l_{n+1}-l_n}, & \text{for } l \in [l_n, l_{n+1}] \end{cases} \tag{9}$$

and the piecewise sine functions

$$\psi_n(l) = \begin{cases} \sin[\frac{\pi}{2} \cdot \frac{l-l_{n-1}}{l_n-l_{n-1}}], & \text{for } l \in [l_{n-1}, l_n] \\ \sin[\frac{\pi}{2} \cdot \frac{l_{n+1}-l}{l_{n+1}-l_n}], & \text{for } l \in [l_n, l_{n+1}] \end{cases} \tag{10}$$

etc., may also be effeciently used as metrons. Using the global metrons like sine and cosine functions in Eq.(7) cost nearly the same CPU time as using the piecewise constant pulses in Eq.(8), the piecewise linear functions in Eq.(9) or the piecewise sine functions in Eq.(10). When choosing piecewise functions as metrons, the number of metrons must be far greater than the number of MEI coefficients, but the integrals in Eq.(5) or Eq.(6) need only to be carried out on a small segment of the cylinder boundary. When choosing the global functions as metrons, a few metrons are enough but the integrals should be carried out on the whole boundary of the cylinder.

Fig.3 shows the RCS results of an elliptic dielectric cylinder with E-wave incidence, where the permittivity $\varepsilon_r = 4$, permeability $\mu_r = 1$, the incident angle $\theta^{inc} = 45°$, the lengths of the principal semiaxis of the ellipse are $a = 1\lambda$(wavelength), $b = 0.5\lambda$, the mesh steps $h_x = h_y = 0.025\lambda$, and global sine and cosine functions are choosed as metrons. It can be seen the results obtained by MEI are in good agreement with that obtained by MoM, and when the number of metrons is equal to or greater than 3, the results are almost the same. Besides, in Fig.3 the incident angle is 45°, if we change the incident angle, the coefficients of MEI not change, that means the MEI is independent of the excitation. For this problem, any linear combination of the three metrons is great different from the real currents. Therefore, the metron is fully different from the basis functions in MoM.

A 4:1 aspect ratio rectangular cylinder of 20λ circumferential dimension is shown in Fig.4. The surface current distributions with H-wave incidence and constant piecewise metrons are shown in Fig.5, and that with piecewise linear metrons are shown in Fig.6, where the mesh step $h = 0.04\lambda$ or 25 nodes per wavelength. The integrals in Eq.(4) or Eq.(5) are calculated by an approximate mid-point formular when constant piecewise functions as metrons, which is equivalent to using many point sources on the surface of the cylinder to measuring the MEI. It can be seen that both piecewise constant and linear metrons can get good results, but the piecewise linear metrons seem something better. For this problem and piecewise linear metrons, enough accurate results can be obtained with 30 or more metrons. It is known that, 10 segments per wavelength are basically requirement in MoM. For this problem, therefore, at least 200 piecewise basis functions are necessary for guaranteing the accuracy of the solution. Thus, it also shows the difference between metrons and basis functions.

The RCS of a 4:1 rectangular conducting cylinder with H-wave incidence and 12.5 circumferential dimension is shown in Fig.7, where piecewise sine functions are chosen as metrons. It can be seen that piecewise sine metrons can also get very good results. On our experience, piecewise sine metrons is a little better than piecewise metrons.

REFERENCES

[1] K.K. Mei, R. Pous, Z.Q. Chen and Y.W. Liu: "The measured equation of invariance: A new concept in field computation", IEEE AP-S, Digest pp.2047-2050, Chicago, July, 1992.

[2] Wei Hong, Y.W. Liu and K.K. Mei: "Application of the measured equation of invariance to solve scattering problems involving penetrable medium", Submitted to Radio Science.

[3] Wei Hong, K.K. Mei: "Application of the method of MEI to the scattering problems of anisotropic medium cylinders", Submitted to IEEE AP-S, 1994.

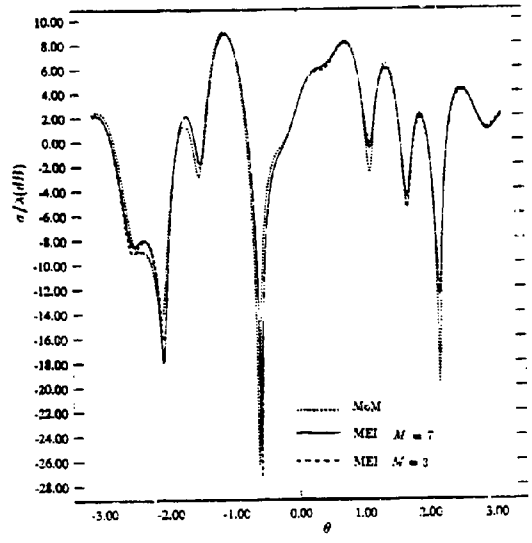

Fig.3 RCS of a elliptic dielectric cylinder

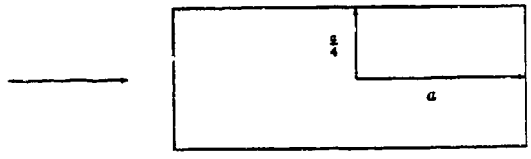

Fig.4 A 4:1 aspect rectangular conducting cylinder

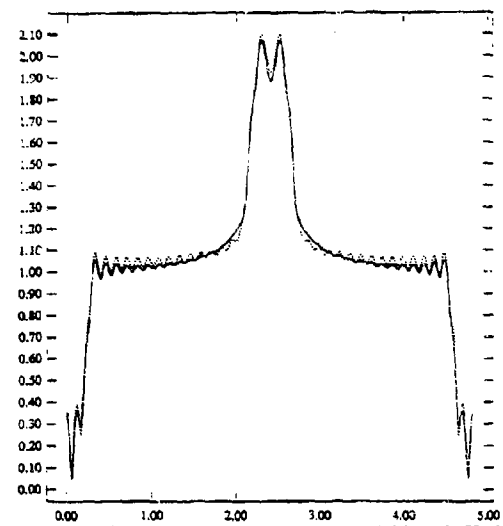

Fig.5 Current results with constant piecewise metrons, solid line: MEI, dash line: MoM

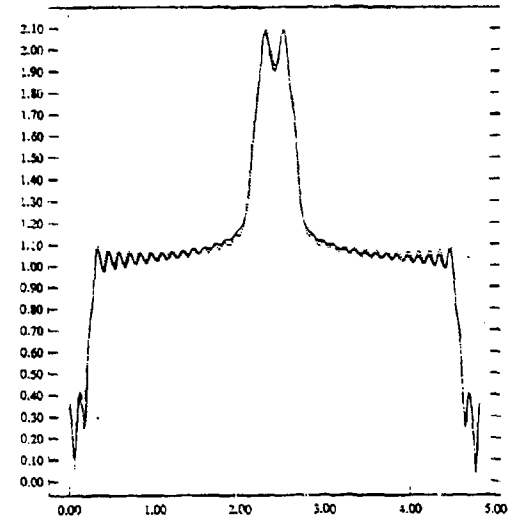

Fig.6 Current results with 50 piecewise linear metrons, solid line: MEI, dash line: MoM

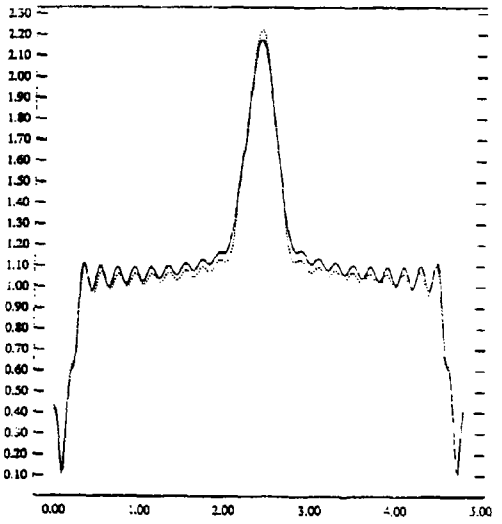

Fig.7 Current results with 30 piecewise sine metrons, solid line: MEI, dash line: MoM

THREE-DIMENSIONAL FINITE ELEMENT TIME DOMAIN APPROACH WITH AUTOMATIC MESH GENERATION FOR MICROWAVE CAVITIES

Surender Mohan and Jin-Fa Lee
ECE Dept.
Worcester Polytechnic Institute
100 Institute Rd.
Worcester, MA 01609

January 28, 1994

Abstract

The finite difference time domain (FDTD) [1] algorithm has been used widely in solving the transient responses of electromagnetic problems. However, it is difficult to model complex EM problems with curved surfaces using the FDTD method in its original form. Many variants have been proposed in the past with the aim to circumvent this difficulty with varying degrees of success. Almost all of these approaches are based upon, one form or the other, the use of finite difference approximation in both spatial and temporal domains. It is the purpose of this paper to show a finite element time domain formulation, which uses Whitney 1-forms in the spatial domain and the finite difference in the time domain, respectively, for solving Maxwell's equations. In this way, the proposed WETD method can be used on a tetrahedral finite element mesh generated by an automatic mesh generation program, TETRA.

1 Automatic Mesh Generation

Due to recent improvements in computer technology, in particular the massively parallel machines, the size of engineering problems which it is practical to analyze using finite element method is dramatically larger than before. This makes it increasingly important to automate the mesh generation process, so that creation of a mesh does not become a bottleneck in the analysis of a product design. Furthermore, if mesh generation can be fully

automated, then it becomes feasible to embed the entire finite element analysis (including the mesh generation) in a feedback loop in which the mesh can be selectively refined to ensure accurate numerical solutions.

The current implementation for meshing multiple objects, based upon the use of Delaunay tessellation [2] algorithm, comprises of three major modules. These three major modules are: surface meshing, initial Delaunay tessellation, and mesh refinements and quality improvements. The major tasks involved in each module are outlined in Fig. 1.

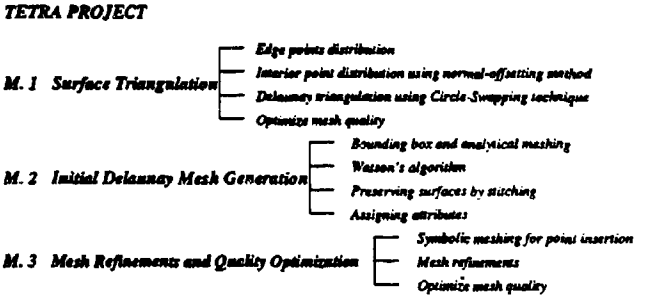

Figure 1: Three modules in current Delaunay mesh generation.

1.1 Three-Dimensional Delaunay Mesh Generation

In the Delaunay mesh generation, originally all the mesh points are generated via the surface triangulation. Except in the case of adding points to preserve the surfaces of the solid objects, no additional points should be generated.

Watson Algorithm

One method of forming Delaunay tessellation of a given set of points P is the Watson's algorithm. The basic approach as shown in Fig. 2 for a two-dimensional case, is based upon the incremental point insertion into a pre-existing mesh.

The extension of the algorithm to three dimensions can be briefly described as follows:

- Start with an initial tetrahedral mesh D_0 containing all the points to be added; new internal tetrahedra are formed as the points are entered one at a time.
- At any typical stage of the process, a new point is tested to determine which circumsphere of the existing tetrahedra contains the point. The associated tetrahedra are removed, leaving an insertion polyhedron containing the new point.
- Edges connecting the new point to all triangular faces of surface of the insertion polyhedron are created, defining tetrahedra that fill the insertion polyhedron. Combining

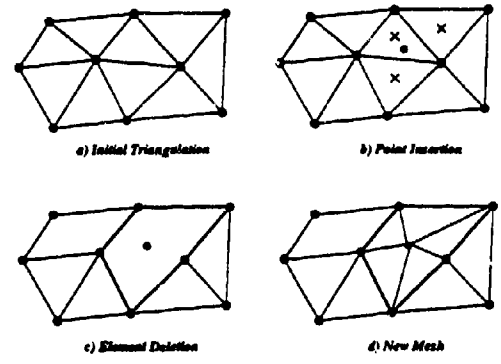

Figure 2: Watson's algorithm

these with the tetrahedra outside the insertion polyhedron produces a new Delaunay triangulation that contains the newly added point.

Watson's algorithm, although conceptually straightforward, suffers from three major difficulties in practical application. First, improper resolution in dealing with the degenerate cases can yield an invalid mesh; Secondly, due to the finite-precision calculation, the application of Watson's algorithm may result in structural inconsistencies and ultimately fail to construct a valid mesh; and, Thirdly, for real-life problems with high degrees of complexity, the algorithm will take prohibitive computation time. Therefore, methods implementing Watson's algorithm need to resolve the degenerate problems, enforce strict point convexity condition, and provide a vehicle to localize the use of Watson's algorithm.

Localize the Action

In its original form, the Watson's algorithm requires a scan through all the tetrahedra, consequently, it is inefficient and undesirable. A modification in the Watson's algorithm which localizes the action and provides a significant speed-up is proposed herein. The idea is to employ a *multi-zone* search method: First divide the bounding box into $M_x \times M_y \times M_z$ zones, and for each zone construct a directed tree with tetrahedra whose centroids are within the zone. Furthermore, by noticing that once the tetrahedron which contains the new point is located, the creation of the insertion polyhedron may not go beyond two layers of it. Hence, it is possible to form a localized *action region* centered at the tetrahedron with the new point inside it.

Finally, the modified Watson's algorithm in the present implementation works as follows:

1. First find the zone, Z_o, to which the new point belongs. Consequently, find the tetrahedron, T_o, which contains the new point. This tetrahedron should be found in 27 zones centered at Z_o, if not check all the zones (this case happens only in the early stages of the process when the number of tetrahedra is few).

2. Form a localized action region which is centered at T_e and extend no more than a few layers (we choose 3 in our program). Also, mark all the tetrahedra inside this action region.

3. Perform the circumsphere checking for all the tetrahedra inside the action region and form the insertion polyhedron.

4. Perform the point convexity checking and construct the final insertion polyhedron.

5. Connect the new point to the faces of the insertion polyhedron.

After step 5 has been completed, the new point has been successfully added to the set of tetrahedra and the process is complete.

2 FINITE ELEMENT TIME DOMAIN METHODS

2.1 FAEDO-GALERKIN FORMULATION

Let us consider the following vector wave equation for the electric field, $\vec{E}$, which is derived from Maxwell's equations:

$$\begin{aligned} \nabla \times \frac{1}{\mu} \nabla \times \vec{E} + \epsilon \frac{\partial^2 \vec{E}}{\partial t^2} &= -\frac{\partial \vec{J}}{\partial t} \quad \text{in} \quad \Omega \\ \hat{n} \times \vec{E} &= 0 \quad \text{on} \quad \Gamma_e \\ \hat{n} \times \nabla \times \vec{E} &= 0 \quad \text{on} \quad \Gamma_h \end{aligned} \tag{1}$$

where Γ_e, Γ_h are electric and magnetic walls, respectively. The weak form, or the Galerkin form, of Eq. (1) is just

$$\int_\Omega \left(\vec{v} \bullet \epsilon \frac{\partial^2 \vec{E}}{\partial t^2} + \vec{v} \bullet \nabla \times \frac{1}{\mu} \nabla \times \vec{E} \right) d\Omega = - \int_\Omega \vec{v} \bullet \frac{\partial \vec{J}}{\partial t} d\Omega \tag{2}$$

where $\vec{v}$ is a test vector function. To achieve a greater symmetry between trial and test vector functions, we apply vector identities to result in (assuming either PEC or PMC condition on the boundary Γ)

$$\int_\Omega \left[\vec{v} \bullet \epsilon \frac{\partial^2 \vec{E}}{\partial t^2} + \frac{1}{\mu} (\nabla \times \vec{v}) \bullet \left(\nabla \times \vec{E} \right) \right] d\Omega = - \int_\Omega \vec{v} \bullet \frac{\partial \vec{J}}{\partial t} d\Omega \tag{3}$$

To make this formulation operational, we use the Whitney 1-forms as the bases for the trial space S^h and expand the trial and test vector functions as

$$\vec{E}^h(\vec{r}, t) = \vec{W}_i(\vec{r})\, e^i(t) \tag{4}$$

where $e^i, \vec{W}_i$ are the circulation of the electric field and the vector basis function associated with edge i, respectively. Also, in Eq.(4) we have used the Einstein notation for the summation over index i.

Finally, the optimal weights e^i are determined by the Galerkin principle

$$\int_\Omega \left(\epsilon \vec{W}^j \bullet \vec{W}_i\right) d\Omega \;\; \frac{d^2 e^i}{dt^2} + \int_\Omega \left(\frac{1}{\mu} \nabla \times \vec{W}^j \bullet \nabla \times \vec{W}_i\right) d\Omega \;\; e^i = -\int_\Omega \left(\vec{W}^j \bullet \frac{\partial \vec{J}^h}{\partial t}\right) d\Omega \quad (5)$$

$$\text{for all } j$$

Now we put the Galerkin equation into vector notation, with $\mathcal{E}$ as the coefficient vector, the result is an ordinary differential equation (ODE) as:

$$[T] \frac{d^2 \mathcal{E}}{dt^2} + c^2 [S] \mathcal{E} = -\mathcal{F} \quad (6)$$

2.2 FINITE DIFFERENCES IN TIME

A. Central Difference

By applying the central difference to the time derivative in Eq. (6), we obtain:

$$[T] \frac{1}{\delta t^2} \left(\mathcal{E}^{n+1} - 2\mathcal{E}^n + \mathcal{E}^{n-1}\right) + c^2 [S] \mathcal{E}^n = 0 \quad (7)$$

The above equation can be rearranged to result in a matrix equation which can be used to update the coefficient vector, $\mathcal{E}$, as

$$[T] \mathcal{E}^{n+1} = -[T] \mathcal{E}^{n-1} + \left(2[T] - c^2 \delta t^2 [S]\right) \mathcal{E}^n \quad (8)$$

As evidenced in Eq. (8), the updating of the electric field, for each time step, requires solving a matrix equation of the form

$$[T] x = y \quad (9)$$

However, since the matrix $[T]$ is positive-definite, equation (9) can be solved efficiently by, for example, the Pre-Conditioned Conjugate Gradient (PCCG) method [3].

From Eq. (8), it can be shown that it will be stable if and only if the following condition holds

$$\rho\left(\left\{2[T] - c^2 \delta t^2 [S]\right\}^2\right) \leq 4\rho\left([T]^2\right) \quad (10)$$

where $\rho(A)$ is the spectral radius of the matrix A. Finally, with algebraic operations, the final stability condition can be deduced as

$$c\delta t \leq 2\sqrt{\frac{\lambda^T_{min}}{\lambda^S_{max}}} \quad (11)$$

where λ^T_{min} and λ^S_{max} are the minimum and the maximum eigenvalues of matrices $[T]$ and $[S]$, respectively.

B. Forward Difference

Applying the forward difference to the ODE in Eq. (6) results in the following procedure to update the E field in time:

$$\mathcal{E}^{n+1} = -\mathcal{E}^{n-1} + 2\mathcal{E}^n - \frac{c^2\delta t^2[S]}{[T]}\mathcal{E}^{n-1} \tag{12}$$

However, it can be shown that the numerical scheme proposed in Eq. (12) is unstable regardless of the time step δt that is used in the computation.

C. Backward Difference

When the O.D.E. (6) is approximated by backward difference, the following equation is obtained

$$\left([T] + c^2\delta t^2[S]\right)\mathcal{E}^{n+1} = 2[T]\mathcal{E}^n - [T]\mathcal{E}^{n-1} \tag{13}$$

The nice feature of Eq. (13) is that it is unconditionally stable, viz. it is stable regardless of the time step δt. The bad feature is that the numerical solution will always decay even for lossless problems.

D. Mixed Difference

As evidenced from above discussions that both forward and backward differences suffer serious drawbacks: in the forward difference scheme, the numerical solution always grows; whereas, in the backward difference case, it always decays. Consequently, in their original forms, neither one of them is practical. To eliminate these numerical artifacts, we propose here a mixed difference scheme. Namely,

$$\text{mixed difference} = \frac{1}{2}\text{forward difference} + \frac{1}{2}\text{backward difference} \tag{14}$$

Applying this mixed difference to the ODE in Eq. (6) results in

$$\mathcal{E}^{n+1} = -\mathcal{E}^{n-1} + \frac{4[T]}{(2[T] + c^2\delta t^2[S])}\mathcal{E}^n \tag{15}$$

It can be shown that equation (15) is not only unconditionally stable but also the energy of the numerical solution remains a constant, as is required for lossless problems.

3 NUMERICAL RESULTS

A. Rectangular Cavity

A rectangular cavity with dimensions $2m \times 3m \times 4m$ has been analyzed by using the three WETD methods described in this paper. The cavity is first discretized into tetrahedra with the average element size $h = 0.378m$, furthermore the constant σ for the excitation is chosen as $\sigma = 1/(\pi f)$ and $f = 500MHz$. The CPU time, number of iterations, and the computed resonant frequencies are summarized in Table 1. We note that WETD1 provides the best

accuracy with the longest computation time. Whereas, the WETD3 offers reasonably good results with much less computation time.

B. Spherical Cavity

Shown in Fig. 3 is a finite element mesh for an air-filled spherical cavity with radius $r = 1m$. The mesh corresponds to an average element size $h = 0.15m$. This cavity will be difficult to model using the conventional FDTD algorithm, however, it presents no problem for the current finite element time domain methods. The time step used in the simulation is $c\delta t = 0.07618607$ and the simulation runs for 500 iterations. The numerical results computed by WETD3 is summarized in Table 2. As can be seen from the Table, the comparison of the first three computed resonant frequencies to the exact ones are excellent.

	Exact Soln	*WETD1*	*WETD2*	*WETD3*
c δ t		*0.06209*	*0.1891125*	*0.1891125*
Iterations		*9137*	*3000*	*3000*
CPU		*20379.7*	*11626.7*	*9669.2*
Mode1 (MHz)	*62.5*	*61.9298*	*61.193*	*61.58*
Mode2 (MHz)	*83.853*	*82.5751*	*80.557*	*81.719*
Mode3 (MHz)	*90.139*	*88.7661*	*86.367*	*87.916*

Table 1: Numerical results for a rectangular cavity.

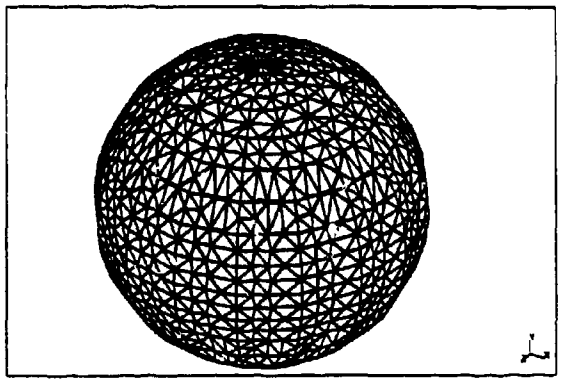

Figure 3: Tetrahedral mesh for a sphere by using the Delaunay mesh generation.

$h = 0.15$ $c\,\delta t = 0.07618607$

Exact (MHz)	*Computed (WETD 3) (MHz)*	*error (%)*
131.016	*130.745*	*0.207*
184.7789	*184.581*	*0.107*
214.5279	*215.345*	*0.382*

Table 2: Numerical results for a sphere cavity.

References

[1] K. S. Yee, "Numerical solution of initial boundary value problems involving Maxwell's equations in isotropic media," IEEE Trans. Antennas Prop., vol. AP-14, pp. 302-307, 1966.

[2] A. Bowyer, "Computing Dirichlet tessellations," The Computer Journal, vol. 24, no. 2, pp 162-166, 1981.

[3] G. H. Golub and C. F. Van Loan, "Matrix computations," second edition, Baltimore, MD: The Johns Hopkins Press, 1991.

Time stepping methods for transient analysis of magnetodynamic problems

F. Delincé*, A. Nicolet, F. Henrotte, A. Genon, W. Legros
University of Liège - Institut Montefiore - Sart Tilman B28
B-4000 Liège - Belgium
tel: +32-41-56373,
fax: +32-41-562910
nicolet@montefiore.ulg.ac.be

* This author is a Research Assistant with the Belgian National Fund for Scientific Research.
This work presents research results of the Belgian programme on Interuniversity Poles of attraction initiated by the Belgian State, Prime Minister's Office, Science Policy Programming. The scientific responsibility is assumed by its authors.

Abstract

The most widespread method used to solve transient magnetodynamic problems is the Crank-Nicolson (CN) method. For linear differential equations, the CN method is unconditionally stable. The behaviour of pure magnetodynamic systems is a simple damping even for non linear problems and the CN method is often stable and accurate enough. Nevertheless when the non-linear electromagnetic model is coupled to another model e.g. a mechanical model for moving parts or circuit equations for the feeding of conductors, it may exhibit a much more complicated behaviour. In this case, the CN method may become unstable. Another possibility is the more stable backward Euler method but it is less accurate and tends to overdamp waveforms. In this paper, alternative methods are presented.
An important point is that the finite element discretization of magnetodynamic problems leads to systems of differential algebraic equations that can not be treated numerically like regular ordinary differential equations [1]. They are index 1 systems, i.e. with the coefficient matrix of the differential terms singular, and can only be treated by implicit methods. Candidate methods are the backward differentiation formulas, the implicit Runge-Kutta methods and the methods based on repeated Richardson extrapolation.
A numerical example of two-dimensional magnetodynamic problem coupled with electric circuits and hysteresis models is presented with an emphasis on energy conservation.

Introduction: magnetodynamics and differential/algebraic systems

The equation for the two-dimensional magnetostatics is [2]:

$$\mathrm{div}(\nu \,\mathrm{grad}\, A) = -J \tag{1}$$

where ν is the magnetic reluctivity and A and J are respectively the vector potential and the current density. These vectors have only the z component different from zero. Using Ohm's law, the case of eddy currents can be dealt with by introducing (2) as the expression for the current density in (1):

$$J = \sigma E = -\left(\frac{\partial A}{\partial t} + U\right) \tag{2}$$

The conductor is characterized by its electrical conductivity σ, and U can be interpreted as the terminal voltage of the conductor (per unit of length). The finite element formulation is based on the usual discrete Galerkin method. Weighted residuals (3) for the domain Ω of boundary Γ are constructed, where w is a weighting function (depending on space variables).

$$\iint_{\Omega}\left[\nu \,\mathrm{grad} A.\,\mathrm{grad} w + \sigma\left(\frac{\partial A}{\partial t} + U\right)w\right]d\Omega - \oint_{\Gamma} w\nu\frac{\partial A}{\partial n}d\Gamma = 0 \tag{3}$$

The space discretization of (3) using the functions w leads to a differential system of equations. For a classical choice of the weight functions, the unknowns of the problem are the nodal value of the vector potential. In a non conducting region, the conductivity is equal to zero and the concerned equations reduce to algebraic ones.

In the rest of the paper, the reference to electromagnetic quantities is given up and the general system of differential/algebraic equations (DAE) (4) is considered:

$$A\ \dot{y}(t) + B\ y(t) = b(t) \tag{4}$$

where A and B are coefficient matrices, b is the right hand member vector, y is the unknown vector, t is the time and the dot indicates the time derivative. Note that A and B may depend on y in the case of a non linear system e.g. B depends on y in the case of ferromagnetic saturation and one has B(y(t)).
The numerical solution of system (4) requires a time discretization. A simple scheme is given by (5):

$$A\ \frac{y_{n+1}-y_n}{\Delta t} + B\ (\alpha y_{n+1} + (1-\alpha)y_n) = \alpha b_{n+1} + (1-\alpha)b_n \tag{5}$$

Indices n and n+1 refer to quantities at time t_n and $t_{n+1} = t_n + \Delta t$ respectively. Various choices of the parameter α lead to classical methods (α=1. is implicit (backward) Euler, α=0. is explicit (forward) Euler, α=1/2 is Crank-Nicolson, α=2/3 is Galerkin).
The matrix $A/\Delta t + \alpha B$ is involved in the solution of system (5). One obvious condition is that it must be invertible i.e. non singular. The study of DAE systems such as (5) involves the matrix pencil $A + \lambda B$ of matrices A and B where λ is an arbitrary parameter [1,3]. It must be regular i.e. $\det(A + \lambda B)$ must not vanish identically. If it is not the case, it is impossible to find a Δt and an α such that $A/\Delta t + \alpha B$ is not singular and the system is meaningless. On the other hand, if $A + \lambda B$ is a regular pencil, matrices E, F exist such that:

$$A^e = E\ A\ F = \mathrm{diag}(I, J) \tag{6}$$

$$B^e = E\ B\ F = \mathrm{diag}(W, J) \tag{7}$$

where diag denotes a square matrix constructed with the argument square matrices placed on its diagonal, I are unit matrices of the suitable dimension, W is a regular square matrix, and J is a nilpotent Jordan block matrix with blocks of the form:

$$\begin{bmatrix} 0 & & 0 \\ 1 & 0 & \\ & \ddots & \ddots \\ 0 & & 1\ \ 0 \end{bmatrix} \tag{8}$$

The size of the largest of these blocks is m, the nilpotency or index of the system (The nilpotency of a matrix J may alternatively be defined as the integer m such that $J^m = 0$ and $J^{m-1} \neq 0$). With $y^e = F^{-1}y$ and $b^e = E\ b$, the DAE system (4) is in his Kronecker normal form (KNF)[1]:

$$\begin{cases} \dot{u} + W u = q \\ J\dot{v} + v = r \end{cases} \quad \text{with} \quad y^e = \begin{pmatrix} u \\ v \end{pmatrix} \quad b^e = \begin{pmatrix} q \\ r \end{pmatrix} \tag{9}$$

The numerical behaviour of a DAE system depends strongly on its nilpotency. On the one hand, if the nilpotency is greater than one, the system is very difficult to solve and special techniques must be used. On the other hand, if the nilpotency is equal to one (J is identically equal to zero), the system is much easier to solve and some classical methods for ODE may work.
In the case of the magnetodynamic system (4), two kinds of equations must be considered. The first kind are the equations corresponding to nodes belonging to at least one conducting region. The time derivative of the corresponding nodal value of the vector potential gives a non zero term on the diagonal of A. Such equations do not influence the nilpotency of the system. The second kind are the equations corresponding to nodes belonging only to non conducting regions. Those equations do not have any differential term, they are purely algebraic and their contributions to the matrix A are null lines. They obviously lead to a system of nilpotency 1. Therefore, classical methods such as the scheme (5) may be used. Nevertheless, if the explicit Euler method is tried, the singular matrix $A/\Delta t$ is involved and the solution is impossible. In general, purely explicit methods may not be applied to solve (4) because they involve singular matrices and implicit methods must be used. Some of these methods are presented in the following sections.

Multistep methods: backward difference formulae

The general differential system (10) is considered:

$$\dot{y} = f(y, t) \tag{10}$$

To solve it by a backward difference formulae (BDF) method [4], the following replacements are made:

$$\dot{y} \rightarrow \frac{1}{\Delta t}\sum_{j=0}^{p}\alpha_j \; y_{n+1-j} \tag{11}$$

$$f \rightarrow \sum_{j=0}^{q}\beta_j \; f_{n+1-j} \tag{12}$$

Indices i refer to quantities at times t_i , e.g. $y_i = y(t_i)$ and $f_i = f(y_i,t_i)$, all the times t_i being spaced by a constant time step Δt. The solution being known up to time t_n , the solution at time t_{n+1} is computed by solving for y_{n+1} the system obtained by doing the replacements (11) and (12) in (10). A particular method is defined by giving p+1 coefficients α_i and q+1 coefficients β_i. Table 1 shows some classical methods. Adams Moulton and Gear methods appear as higher order generalisation of the scheme (5).

method	p	α_0	α_1	α_2	α_3	q	β_0	β_1	β_2
Implicit Euler	1	1	-1			0	1		
Crank Nicolson	1	1	-1			1	1/2	1/2	
Adams Moulton	1	1	-1			2	5/12	8/12	-1/12
two step Gear	2	3/2	-4/2	1/2		0	1		
three step Gear	3	11/6	-18/6	9/6	-2/6	0	1		

Table 1: Backward difference methods

In the case of the DAE system (4), with the following notations:

$$y_\alpha = \sum_{j=0}^{p}\alpha_j \; y_{n+1-j} \tag{13}$$

$$B(y)y'_\beta = \sum_{j=0}^{q}\beta_j \; B(y_{n+1-j})y_{n+1-j} \tag{14}$$

$$b_\beta = \sum_{j=0}^{q}\beta_j \; b_{n+1-j} \tag{15}$$

the computation of the next time step is the solution of the system (16):

$$A\frac{y_\alpha}{\Delta t} + B(y)y'_\beta = b_\beta \tag{16}$$

for y_{n+1}, where the dependence of B on y has been made explicit.

<u>One step methods: Runge Kutta methods</u>

The general differential system (10) is considered again. An approximation of the solution from the values y_n of the solution at the previous time step may be obtained by solving the following relations [5]:
<u>form 1</u>

$$\begin{cases} Y_i = y_n + \Delta t\sum_{j=1}^{s}\beta_{ij} \; f(Y_j, t_n + \alpha_i\Delta t) \quad i = 1\ldots s \\ y_{n+1} = y_n + \Delta t\sum_{i=1}^{s}\mu_i \; f(Y_i, t_n + \alpha_i\Delta t) \end{cases} \tag{17}$$

or form 2

$$\begin{cases} k_i = \Delta t\ f(y_n + \sum_{j=1}^{s} \beta_{ij}\ k_j,\ t_n + \alpha_i \Delta t) \quad i = 1...s \\ y_{n+1} = y_n + \sum_{i=1}^{s} \mu_i\ k_i \end{cases} \tag{18}$$

The equivalence of both forms may be shown by remarking that $k_i = \Delta t\ f(Y_i,\ t_n + \alpha_i \Delta t)$. A s-step method is characterised by the coefficients α_i, β_{ij} and μ_i given in its Runge-Kutta tableau or Butcher diagram:

α_1	β_{11}	β_{12}	...	β_{1s}
α_2	β_{21}	β_{22}	...	β_{2s}
...	...	...		...
α_s	β_{s1}	β_{s2}	...	β_{ss}
	μ_1	μ_2	–	μ_s

with $\alpha_i = \sum_{j=1}^{s} \beta_{ij}$.

The Runge Kutta methods may be sorted according to the structure of their diagram. The classical explicit methods are the methods for which $\beta_{ij} = 0$ for $j \geq i$. If this condition is not fulfilled (if $\beta_{ij} \neq 0$ for $j \geq i$), the methods are called the implicit Runge Kutta methods (IRK). Special cases of IRK are the diagonally implicit Runge Kutta (DIRK) methods (if $\beta_{ij} = 0$ for $j > i$), a sub category of which are the singly diagonally implicit Runge Kutta (SDIRK) methods (if $\beta_{ij} = 0$ for $j > i$ and if $\beta_{ii} = \beta$ for all i).
The IRK methods may be applied to the DAE system (4). Nevertheless, only form 2 may be used because form 1 would involve the inverse of A in its last step. The adaptation of form 2 to the DAE systems gives the following relations [6]:

$$\begin{cases} Ak_i = \Delta t \left[b(t_n + \alpha_i \Delta t) - B(y_n + \sum_{j=1}^{s} \beta_{ij}\ k_j)\ (y_n + \sum_{j=1}^{s} \beta_{ij}\ k_j) \right] \quad \text{for } i = 1...s \\ y_{n+1} = y_n + \sum_{i=1}^{s} \mu_i\ k_i \end{cases} \tag{19}$$

In this case, a (s.n) x (s.n) system has to be solved to find the k_i. Nevertheless, in the case of DIRK, k_1 depends only on y_n, k_2 only on y_n and k_1, etc... and the relations (19) reduce to a set of s successive systems of size n x n.
Here are some examples of DIRK:

• one step method [7]

λ	λ	
	1	

In the case of linear problems, this method reduces to scheme (5) excepted for the independent term b which is discretised as $b(t_n+\lambda\Delta t)$ instead of $(1-\lambda)b(t_n)+\lambda\, b(t_{n+1})$.

• two step method [7]

λ	λ	0
$1-\lambda$	$1-2\lambda$	λ
	1/2	1/2

• three step method [8]

$\alpha/2$	$\alpha/2$	0	0
1/2	α	$1/2-\alpha$	0
$1-\alpha/2$	α	$1-2\alpha$	$\alpha/2$
	α	$1-2\alpha$	α

with $\omega = \sqrt[3]{2}$ and $\alpha = \frac{1+\omega+\omega^{-1}}{3}$.

Note that this method is symplectic i.e. for Hamiltonian systems, it conserves the symplectic two form. The weaker properties of volume conservation in phase space (Liouville's theorem) and of conservation of energy are a consequence of this symplectiness. Unfortunately the problems considered in this paper are not Hamiltonian and this scheme does not conserve energy.
The following algorithm may be used to implement the DIRK method to solve (4) and to keep the form of the non linear systems to be solved as close as possible to the ones involved in the other methods:

For i = 1 to s-1

- To find K_i, solve the system:

$$\left(\frac{A}{\Delta t\,\beta_{ii}} + B(K_i)\right) K_i = b(t_n + \alpha_i \Delta t) + \frac{A}{b\beta_{ii}} \left(y_n + \sum_{j=1}^{i-1} \beta_{ij} k_j\right)$$

- Compute $$k_i = \frac{K_i - y_n - \sum_{j=1}^{i-1} \beta_{ij} k_j}{\beta_{ii}}$$

Compute $$y_{n+1} = y_n + \sum_{i=1}^{s} \mu_i k_i$$

One step methods: extrapolation methods

The principle of extrapolation methods is to perform computations with a basic scheme for a sequence of decreasing time steps and to extrapolate to zero time step (Richardson's deferred approach to the limit) [9]. This is made by considering the asymptotic development of the error of the basic scheme in powers of the time step and by annulling the successive terms. The following algorithm has been used for the computations performed in this paper: The chosen basic scheme is the implicit Euler method. Although the Crank Nicolson method is more accurate, small oscillations due to its weaker stability jeopardise the convergence of the extrapolation process. The implicit Euler method is very stable and its error development includes all the powers of the time step from the first one. The error development of CN includes the same terms excepted the first order one. The following sequence of time steps is considered [9]:

$$\{\Delta t,\ \Delta t/2,\ \Delta t/4,\ \Delta t/6,\ \Delta t/8,\ \Delta t/12,\ \ldots,\ \Delta t/n_i\ \ldots\}\ ,\quad n_i = 2n_{i-2}\ \text{ for } i > 4 \tag{20}$$

Starting at time t_n with solution y_n, a solution T_{i1} at time $t_n+\Delta t$ is obtained by performing n_i steps of implicit Euler method with the time step $\Delta t/n_i$. The following sequence of approximations is obtained:

$$\{T_{11},\ T_{21},\ T_{31},\ T_{41},\ T_{51},\ T_{61},\ T_{71},\ \ldots,\ T_{i1}\ \ldots\} \tag{21}$$

The higher order approximations are obtained by constructing the following diagram:

$$\begin{array}{llll} T_{11} & & & \\ T_{21} & T_{22} & & \\ T_{31} & T_{32} & T_{33} & \\ \vdots & & \ddots & \\ T_{n1} & & \cdots & T_{nn} \end{array} \tag{22}$$

The first column is given by (21) and the other ones are computed using the following recurrence formula (polynomial extrapolation):

$$T_{i,k} = T_{i,k-1} + \frac{(T_{i,k-1} - T_{i-1,k-1})}{\left(\frac{a_i}{a_{i-k+1}}\right) - 1} \qquad (23)$$

In practice, the diagram is constructed line by line by computing a new T_{i1} and performing the extrapolations. The process is stopped when T_{ii} and $T_{i,i-1}$ agree up to the required accuracy. The rational extrapolation may also give good results and is advised by some authors [9]. It requires only the use of (24) instead of (23):

$$T_{i,k} = T_{i,k-1} + \frac{(T_{i,k-1} - T_{i-1,k-1})}{\frac{a_i}{a_{i-k+1}}\left[1 - \frac{T_{i,k-1} - T_{i-1,k-1}}{T_{i,k-2} - T_{i-1,k-2}}\right] - 1} \qquad (24)$$

In practice, both extrapolations are performed and the best is chosen. In numerical tests, the polynomial extrapolation seems to better converge.

Numerical examples

As an application, the discharge of a capacitor in a series RLC circuit is considered, where the inductive effects are computed by the finite element method [10]. This is a free oscillation problem, which is more sensitive to time integration method than forced oscillation ones. First, the linear case ($\mu_r = 1000$) is considered in order to study the behaviour of the various schemes. The reference solution is computed with the Crank-Nicolson method and with a very small stepsize $h = 4.10^{-4}$ sec. For comparing the various methods, a constant stepsize of $h = 4.10^{-3}$ sec is considered, which corresponds approximately to 20 stepsizes in one period. In figure 1, the multistep methods are compared. It appears that the implicit Euler method has a too important damping effect. The Crank-Nicolson scheme is very accurate (the energy of the system is approximately conserved), but a small frequency error is introduced. The more precise scheme is the Adams Moulton one, but it becomes unstable after a few periods. Finally, two step Gear is not of great interest because frequency error as well as numerical damping effect are present. It must be noticed that all these methods are similar in computation time. Higher order methods (such as two step Gear and Adams Moulton) only require the storage of intermediate vectors.

The one step methods are compared in figure 2. It appears that the symplectic DIRK method as well as the extrapolation method give excellent results. Convergence of the extrapolation process is generally reached after 3 subdivisions of the stepsize. This means that this method is more expensive that Crank-Nicolson scheme. Larger stepsizes have been tried. For the largest stepsize (4h), the extrapolation process converges after 4 subdivisions. The solution is still excellent, but seems discontinuous. This can explain why the Crank-Nicolson method is preferred for linear problems.

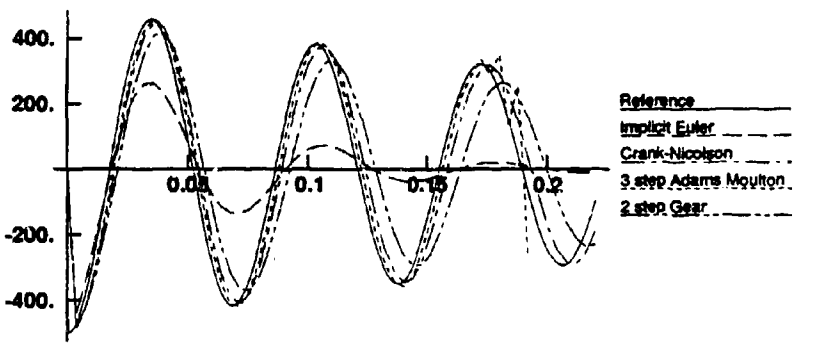

Figure 1 : Time evolution (s) of capacitor voltage (V) - Multistep methods.

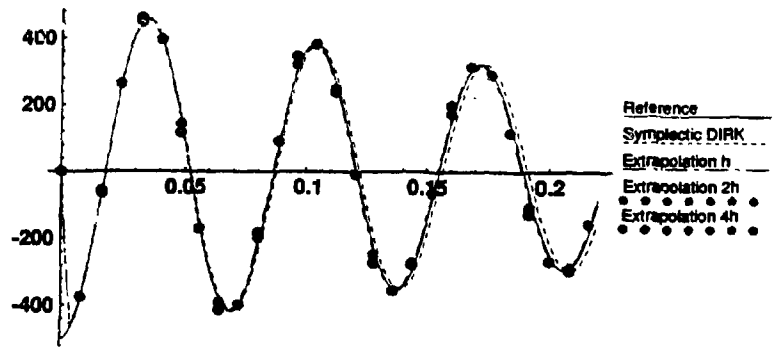

Figure 2 : Time evolution (s) of capacitor voltage (V) - One step methods.

As a non linear test, the same problem with a hysteretic core is considered. As a criterion of quality of the solution, the energy balance is checked. In the beginning, only electrostatic energy is present. This energy is converted to magnetostatic energy and dissipated into Joule and hysteretic losses. The summation of these four types of energy must give the total energy of the system and must stay constant. The implementation of the Preisach hysteresis model in the finite element equations with the computation of hysteretic losses and of magnetostatic energy is given in reference [10].
In this case, it is shown that Crank-Nicolson method does not conserve the total energy of the system (figure 3), the opposite of the extrapolated solution (figure 4). Further developments will concern the application of IRK methods to non linear problems.

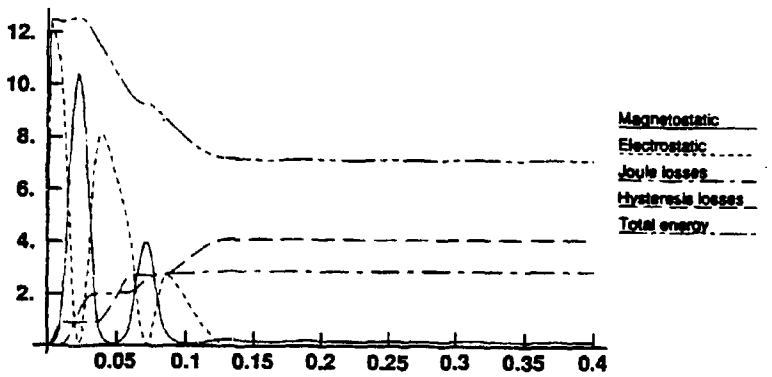

Figure 3 : Time evolution (s) of the energies (J) computed with Crank-Nicolson scheme.

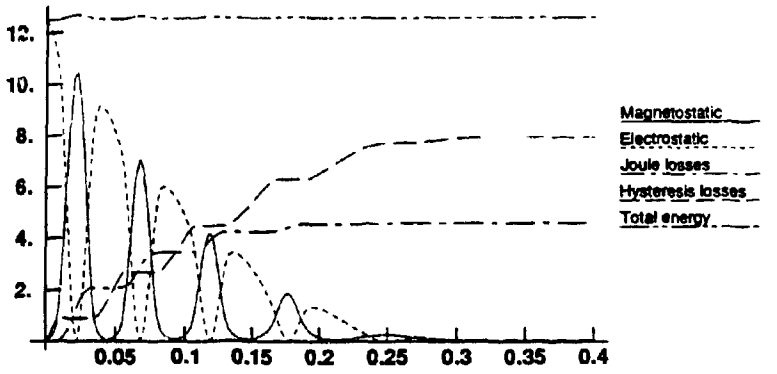

Figure 4 : Time evolution (s) of the energies (J) computed with extrapolation method.

Conclusion

The Crank-Nicolson method appears to be a simple and accurate method. Nevertheless it may fail in some problems. An interesting alternative are the extrapolation methods. Although they are time consuming, extrapolation methods are very robust and provide a natural mechanism of step control. Energy conservation appears to be a good test of the validity of the method for very complex problems.

References

[1] R. Marz, *Numerical Methods for Differential Algebraic Equations*, Acta Numerica 1992, Cambridge University Press, Cambridge, 1992 pp. 141-198.

[2] P.P. Silvester, R. L. Ferrari, *Finite Elements for Electrical Engineers*, Cambridge University Press, Cambridge 1986.

[3] C. W. Gear, L. R. Petzold, *Differential/Algebraic Systems and Matrix Pencils*, Matrix Pencils Proceedings, Pite Havsbad 1982, Lecture Notes in Mathematics 973, Springer Verlag, New York, 1983, pp. 75-89.

[4] C. W. Gear, *Numerical Initial Value Problems in Ordinary Differential Equations*, Prentice-Hall series in Automatic Computations, Englewood Cliffs, N.J., 1971.

[5] S. P. Norsett, P. G. Thomsen, *Local Error Control in SDIRK-Methods*, BIT 26 (1986), pp. 100-113.

[6] K. E. Brenan, S. L. Campbell, L. R. Petzold, *Numerical Solution of Initial-Value Problems in Differential-Algebraic Equations*, North Holland, New York, 1989.

[7] K. Burrage, *A Special Family of Runge-Kutta Methods for Solving Stiff Differential Equations*, BIT 18 (1978), pp. 22-41.

[8] J. M. Sanz-Serna, *Symplectic Integrators for Hamiltonian Problems: an Overview*, Acta Numerica 1992, Cambridge University Press, Cambridge, 1992 pp. 243-286.

[9] J. Stoer, R. Bulirsch, *Introduction to Numerical Analysis*, Springer Verlag, New-York, 1980.

[10] F. Delincé, A. Nicolet, F. Henrotte, A. Genon, W. Legros, *Influence of Hysteresis on the Behaviour of Coupled FE-Electric Circuit Models*, Compumag'93, Miami, Florida, Oct. 31-Nov. 4, 1993, to appear in the IEEE Transaction on Magnetics.

COMPLEX PERIODIC BOUNDARY CONDITIONS FOR AC FINITE ELEMENT MODELS

A. Frenkel
RAFAEL
P.O.Box 2250
Haifa, ISRAEL

J. R. Brauer and M. A. Gockel
The MacNeal–Schwendler Corporation
4300 W. Brown Deer Road
Milwaukee, WI 53223 USA
Email: j_brauer@macsch.com

Abstract

This paper describes for the first time new *complex* periodic boundary conditions that enable efficient finite element modeling of periodic alternating current electromagnetic devices. These boundary conditions are shown to be a special form of multipoint constraint. Applications are made to low frequency electrical machinery and to high frequency phased array antennas. Computed results are verified by their agreement with those of much larger models.

INTRODUCTION

Periodic boundary conditions are commonly used to reduce the size of finite element models to only one portion of an entire device [1]. Conventional periodic boundary conditions constrain the potentials and fields on one boundary to be equal or opposite to those on a boundary one period away. Thus in alternating current electromagnetic problems, these periodic boundary conditions specify a phase shift that is an integer multiple of 180 degrees.

This paper describes and applies new *complex* phasor periodic boundary conditions that enable smaller phase shifts and therefore smaller ac models to be used. While similar boundary conditions have recently been mentioned for a hybrid method [2], this paper is the first to describe the theory of complex boundary conditions for finite elements.

The first application of the new boundary conditions is to low frequency apparatus. Results obtained for a one–third pole model of an induction motor with the new boundary conditions are compared to those of an entire pole model using conventional boundary conditions.

The second application of the new boundary conditions is to high frequency antennas. An infinitely periodic phased array is analyzed with the new boundary conditions for comparison with results obtained by a much larger finite element model having conventional boundary conditions. The new complex periodic boundary conditions are also used for antenna scan angles that cannot be analyzed using conventional boundary conditions.

COMPLEX MULTIPOINT CONSTRAINTS

The finite element analysis software used here, MSC/EMAS™[3], based upon the potential vector $\{u\}$ made up of magnetic vector potential $\overline{A}$ and time–integrated electric scalar potential ψ, has three matrices making up its equation:

$$[M]\{\ddot{u}\} + [B]\{\dot{u}\} + [K]\{u\} = \{P\} \tag{1}$$

where $[M]$ is proportional to permittivity, $[B]$ is proportional to conductivity, and $[K]$ is proportional to reluctivity. $\{P\}$ is the excitation and is assumed known. In this paper we assume sinusoidal ac excitation, so that u is a complex phasor, and so are its first and second time derivatives. Thus for an angular frequency $\omega = 2\pi f$, (1) becomes:

$$[-\omega^2 M + j\omega B + K]\{u\} = [F]\{u\} = \{P\} \tag{2}$$

Boundary conditions that relate a potential u on one boundary m to those on another boundary n can be expressed as a *multipoint constraint*. This constraint obeys a matrix relation between nodal values:

$$\{u_m\} = [G_{mn}]\{u_n\} \tag{3}$$

One way of enforcing such a constraint is the *Lagrange multiplier technique* (LMT). It can be expressed as:

$$\begin{bmatrix} F_{ss} & F_{sm} & G_{ms}^{\dagger} \\ F_{sm}^{\dagger} & F_{mm} & -I \\ G_{ms} & -I & O \end{bmatrix} \begin{Bmatrix} u_s \\ u_m \\ q_m \end{Bmatrix} = \begin{Bmatrix} P_s \\ P_m \\ O \end{Bmatrix} \tag{4}$$

where the vector partition q_m contains the Lagrange multipliers and where † indicates the adjoint.

Another way of enforcing the constraint of (3) is the *constraint variable elimination technique* (CVET). It can be expressed as:

$$[F_{ss}']\{u_s\} = \{P_s'\} \tag{5}$$

where

$$[F_{ss}'] = [F_{ss}] + [F_{sm}][G_{ms}] + [G_{ms}^{\dagger}][F_{sm}^{\dagger}] + [G_{ms}^{\dagger}][K_{mm}][G_{ms}] \tag{6}$$

$$\{P_s'\} = \{P_s\} + [G_{ms}^{\dagger}]\{P_m\} \tag{7}$$

If [F] is a real symmetric matrix, then [F'] is Hermitian; otherwise [F'] is a complex unsymmetric matrix. Open boundaries [4],[5] might produce an unsymmetric [F'] matrix.

The two constraint techniques are compared as follows. The LMT enlarges the size of the matrix, but makes it more sparse. The CVET reduces the size of the matrix, and was chosen for the computations of this paper.

APPLICATION TO LOW FREQUENCY APPARATUS

The low frequency device to be analyzed is a 60 Hz polyphase AC induction motor that has two poles. Figure 1 shows the geometry of the induction motor, including the stator windings of phases A, B, and C. There are 24 stator slots and teeth, and 36 rotor bars and teeth. These numbers of stator and rotor teeth are quite common for induction motors. Because of the three – phase stator windings, the number of stator slots is usually a multiple of 3 times the number of poles, and hence 24 stator slots are often used. To minimize torque variation and acoustic noise, the number of rotor teeth is usually significantly greater than the number of stator teeth, and hence 36 aluminum rotor bars are often used [6].

The minimum model size with conventional real periodic boundary conditions is one pole pitch, or 180 degrees. Figure 2 shows the 180 degree finite element model developed for the motor of Figure 1. The model consists of 444 two–dimensional quadrilateral finite elements and 414 triangular finite elements. There are 697 grid points (nodes), each with only one degree of freedom, the component of magnetic vector potential A that is in the z direction normal to the 2D finite elements. The boundary conditions consist of setting A to zero at the inner and outer diameters, plus periodic boundary conditions. The periodic boundary conditions are [1]:

$$A(r, 180^{\circ}) = (-1)\, A(r, 0^{\circ}) \tag{8}$$

which are enforced at the grid points of radius r between the inner and outer motor radii. Because (8) involves a coefficient that is a real number, most finite element codes are able to enforce it.

The ac magnetic field can be computed for the 180° model of Figure 2 at various slip frequencies. Figure 2 shows the computed magnetic flux lines at a typical instant and a typical slip frequency of 3 Hz (5% of 60 Hz). The computed values of stored energy and induced power for the 180° model are listed in Table 1.

Figure 3 shows a new 60° model of the motor of Figure 1. It has one third the number of finite elements of the 180° model, and has only 241 grid points. Figure 4 requires the complex periodic boundary conditions:

$$A(r, 60^{\circ}) = (\cos 60^{\circ} + j \sin 60^{\circ})\, A(r, 0^{\circ}) \tag{9}$$

which are enforced at the grid points of radius r between the inner and outer motor radii.

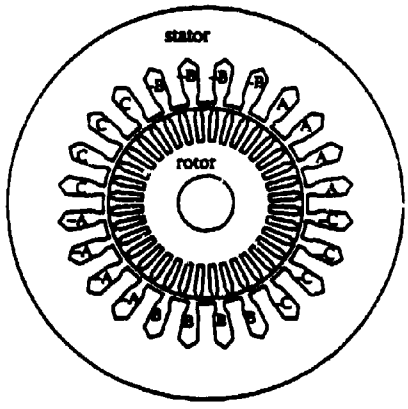

Figure 1. Induction motor with stator windings of phases A, B, and C.

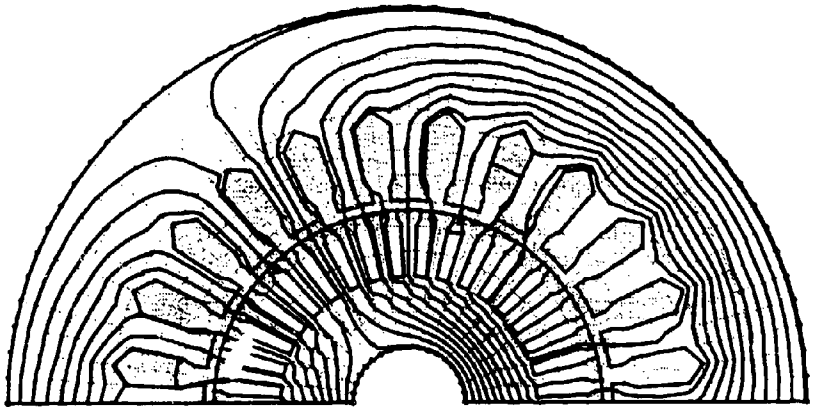

Figure 2. One-pole (180°) finite element model of Figure 1, showing computed instantaneous fluxlines.

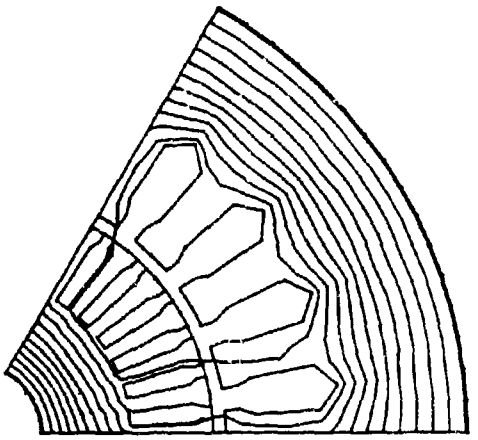

Figure 3. One-third pole (60°) model of Figure 1, showing computed instantaneous fluxlines.

The ac magnetic field was computed for the 60° model of Figure 3 at various slip frequencies. Figure 3 shows the computed magnetic flux lines at a typical instant at slip frequency of 3 Hz; the flux lines agree with those of the 180° model of Figure 3. The computed energy and power for the 60° model are listed in Table 1, and are seen to be exactly one third those of the 180° model. Hence the complex periodic boundary conditions are obtaining the correct answers. Because the complex conditions reduce the model size, the overall CPU time is reduced from 60.7 seconds to 40.9 seconds on an HP 9000 workstation. This reduction is expected to be even more dramatic for larger models such as 3D models. In addition to CPU reductions, disk storage and memory requirements are also greatly reduced by the complex periodic boundary conditions.

Table 1. COMPUTED ENERGY & POWER IN INDUCTION MOTOR MODELS

Parameter	180° model	60° model
Magnetic energy (joules)	2.074543E-2	6.915143E-3
Power (watts)	7.229740E-2	2.409915E-2

APPLICATION TO PHASED ARRAY ANTENNAS

The high frequency device to be analyzed is a phased array microwave antenna. Figure 4 shows the finite element model of four antennas of the phased array, which are fed by rectangular metal waveguides operating in the fundamental TE10 mode with electric field in the y direction. The frequency is 3 GHz. The waveguide width in the x direction is 5.714 cm and its length in the z direction is 12 cm. Note that a radome of relative permittivity 3.0625 and thickness 2.857 cm covers the waveguide opening to free space [7].

The four antenna cells of Figure 4 are assumed to be members of an infinite array of geometrically identical cells placed along the x axis. The identical waveguides are all assumed to have excitations of identical amplitude, but with phase angles that are proportional to their positions along the x axis. There are also identical waveguide antennas arrayed in the y direction, but the excitation magnitudes and phases are invariant in the y direction. By varying the phase shift in the x direction, the antenna beam can be scanned (pointed) at various angles in the xz plane. Hence this phased array antenna can be analyzed using two-dimensional finite elements in the xz plane. To absorb the power leaving the finite element model at the maximum x boundary of Figure 4, special planewave ABCs (Absorbing Boundary Conditions) are used at that boundary [5].

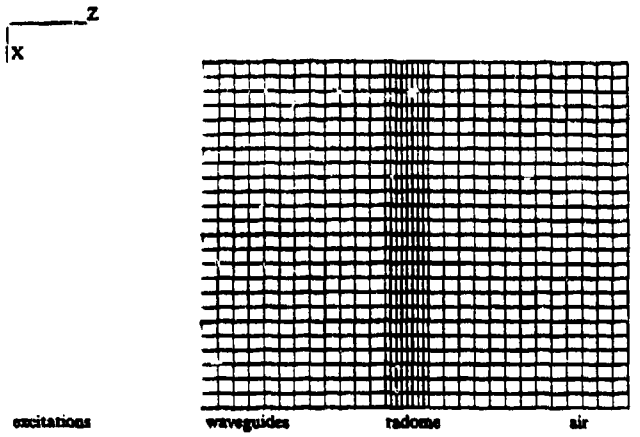

Figure 4. Finite element model of four antenna cells of a phased array along the x axis.

In the case of a phase shift per cell that is an integer divisor n of 180 degrees, a model of the infinite array can be made with real multipoint constraints. These constraints must be placed on a model that contains n antennas. For example, the finite element model of Figure 4 with four antenna cells has real multipoint constraints for 180 degree total phase shift, or 45 degrees phase shift per cell. Figure 5 shows the Poynting vector computed by MSC/EMAS for the model of Figure 4, showing that the energy is directed at a scan angle of 12.64 degrees. This obeys the well-

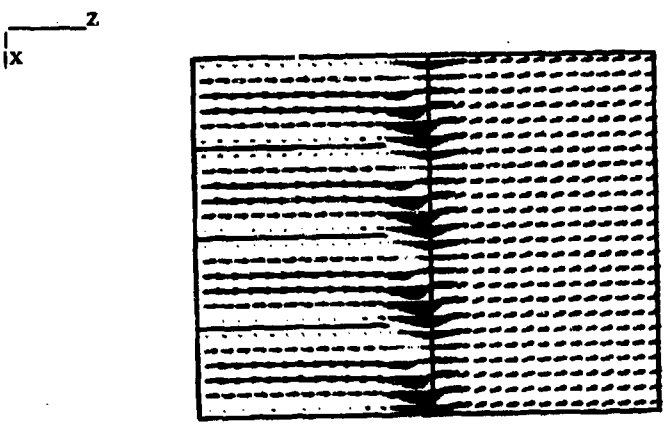

Figure 5. Computed Poynting vectors for the four cell model of Figure 4, for phase shift Φ_x = 45 degrees.

known relation [7] between phase shift angle Φ_s (in degrees) and scan angle θ_s:

$$\sin \theta_s = \Phi_s \lambda/(360^{\circ} d) \tag{10}$$

where λ is the wavelength and d is the cell width, which is 5.714 cm in this case.

Figure 6 shows the phase fronts computed for the four cell model. The phase fronts have the same angle as the Poynting vectors of Figure 5, that is, 12.64 degrees.

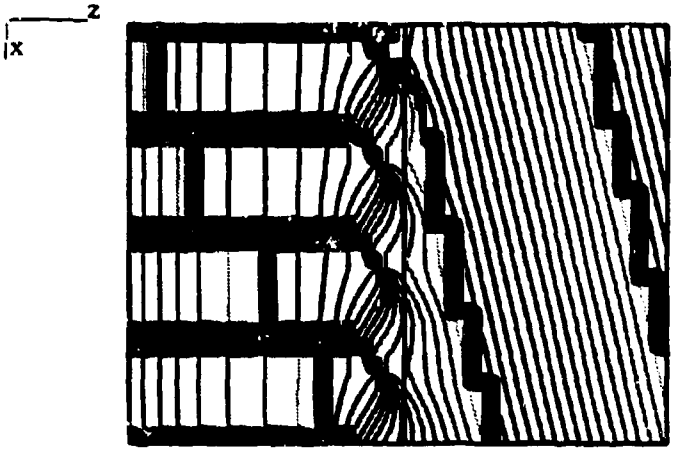

Figure 6. Computed phase fronts of four cells of phased array.

Complex multipoint constraints can be used to analyze the entire antenna array with a model of only one of its antennas. For example, Figure 7a shows the Poynting vector computed by MSC/EMAS with a one cell model with complex constraints of phase shift 45 degrees. The results agree with those of the four cell model of Figure 5, even though the number of finite elements is reduced by a factor of four.

Figure 7b shows the phase angles of the electric field computed for the one cell model. The phase fronts have the same angle as Figure 6, that is, 12.64 degrees. The complex periodic boundary conditions are properly imposing a phase difference of 45 degrees from one boundary of the model to the opposite side of the model.

Another key advantage of the complex periodic constraints is that the one cell model of Figure 7 can be used to analyze the array with *any phase shift angle, not just an integer divisor of 180 degrees*. Figure 8a shows the computed Poynting vectors for a phase shift of 20 degrees, and Figure 8b shows the computed phase angles. Note that again the phase angle boundary conditions are obeyed, and that the scan angle is reduced according to (10).

Figure 9 shows the computed results for a phase shift of 70 degrees. Note in Figure 9a that the scan angle is increased according to (10). Figure 9b shows that the boundary conditions of 70 degree phase shift are obeyed.

The above phased array antenna has been modeled with two-dimensional finite elements and with only one component of magnetic vector potential $\overline{A}$, in the same direction y as the electric field. The reflection coefficients computed by MSC/EMAS will be compared with those of the method of moments [7] in a future paper [5].

Complex periodic boundary conditions have also been implemented in MSC/EMAS for three dimensional finite element models. In such cases, up to three components of $\overline{A}$, as well as scalar potential ψ, are all given phase constraints. Phased arrays that scan in two directions require three dimensional finite element models with such multi-degree-of-freedom complex multipoint constraints.

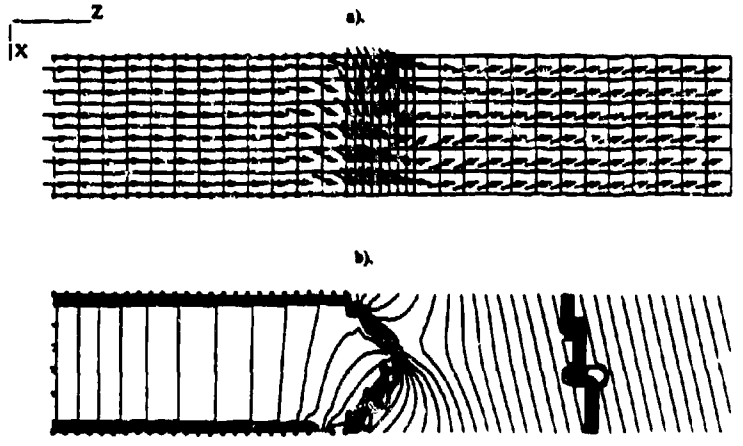

Figure 7. One cell model of phased array with complex periodic constraints of 45 degree phase shift. a). computed Poynting vectors, b). computed phase angles (20 degrees per contour line).

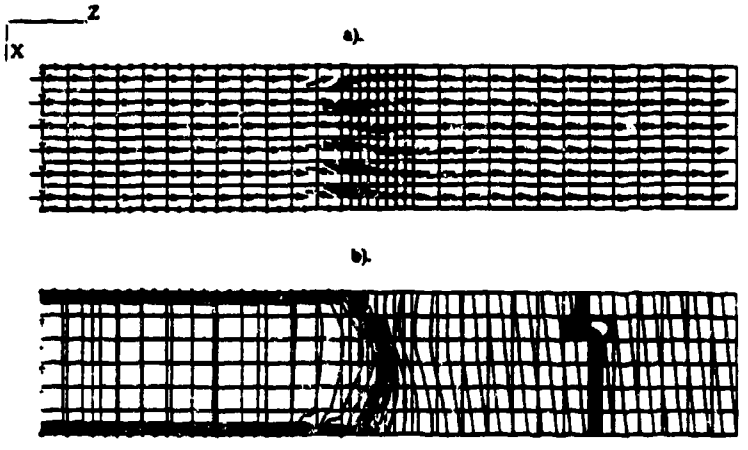

Figure 8. Computed results for one cell model with phase shift of 20 degrees a).Poynting vectors, b). phase angles of electric field (20 degrees per contour line).

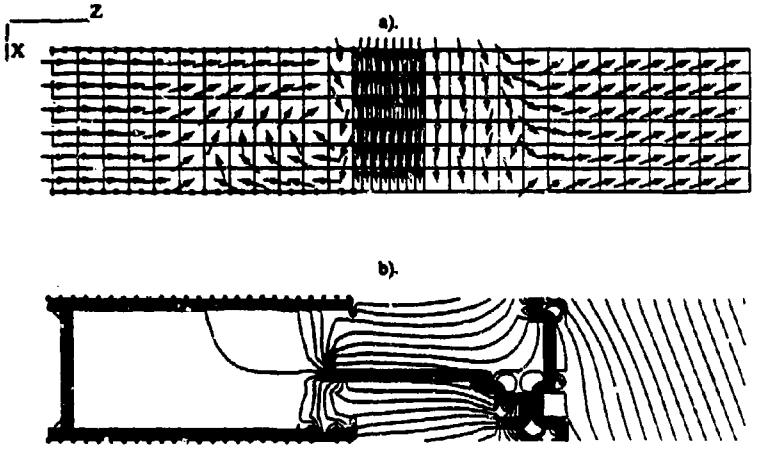

Figure 9. Computed results for one cell model with phase shift of 70 degrees
a).Poynting vectors, b). phase angles of electric field (20 degrees per contour line).

CONCLUSIONS

Complex periodic boundary conditions have been shown to be special forms of multipoint constraints that are enforcable by finite element matrix operations such as the Lagrange multiplier technique or the constraint variable elimination technique. These complex constraints enable a finite element model of only one geometric cell to represent an array of such cells excited with varying phase angles. Computed fields for a 60 Hz induction motor and a 3 GHz phased array antenna show that the complex periodic boundary conditions on one cell models produce the same results as those obtained with much larger models without the new boundary conditions. The new boundary conditions are especially helpful in modeling phased array antennas, where they are required for analyzing arbitrary phase shift and scan angles.

REFERENCES

[1] John R. Brauer (ed.), *What Every Engineer Should Know About Finite Element Analysis (2nd ed.)*, New York: Marcel Dekker, Inc., 1993, pp. 136–141.

[2] Eric Lucas and Thomas Fontana, "3D Vector Finite Element Analysis for Infinite Doubly Periodic Radiating Arrays," *URSI Radio Science Meeting Abstracts*, Ann Arbor, MI, 1993, page 193.

[3] J. R. Brauer, B. S. Brown, and M. M. Jenich, "ABC Finite Elements for Open Boundary Electromagnetic Problems of Frequencies from DC to GHz,", *Proc. of ACES Symposium*, 1993, pp. 830–837.

[4] A. Prenkel, M. Gockel, and E. Nakamoto, "Finite Element Analysis of Infinite Periodic Antenna Arrays," *URSI XXIVth General Assembly Abstracts*, Kyoto, Japan, 1993, p. 49.

[5] A. Prenkel and J. R. Brauer, "Absorbing Boundary Conditions For Finite Element Modeling Of Phased Array Antennas," *Proc. of IEEE Antenna & Prop. Society Symposium*, Seattle, June 1994, in press.

[6] Philip L. Alger, *Induction Machines (2nd ed.)*, New York: Gordon and Breach Science Publishers, 1970, Chapter 10.

[7] N. Amity, V. Galindo, and C. P. Wu, *Theory and Analysis of Phased Array Antennas*, New York: Wiley--Interscience, 1972, p. 238.

Computer Codes for the Analysis of Planar and Cylindrically Conformal Printed Antennas

Jian Gong, Leo C. Kempel and John L. Volakis
Radiation Laboratory
Department of Electrical Engineering and Computer Science
University of Michigan
1301 Beal Ave.
Ann Arbor, MI 48109-2122

Introduction

The hybrid finite element-boundary integral (FE-BI) method has been found particularly attractive for simulating patch antennas/arrays, printed spirals and nonplanar cavity-backed antennas. The analysis of such a diverse collection of antennas and arrays can be readily analyzed using a single computer code while taking into consideration feeding lines and antenna geometry substructure. Because the exact boundary integral is used for terminating the finite element mesh on the aperture surface, there is no compromise in accuracy and furthermore use of the Fast Fourier Transform (FFT) in evaluating the boundary integral contribution leads to a minimal $\mathcal{O}(N)$ memory requirement and a substantial increase in the efficiency of the solution method.

After a brief overview of the formulation, in this paper we will describe the characteristics and capabilities of a new computer code which uses tetrahedral elements for discretizing antenna cavity and triangular patches for zoning the aperture. The geometrical interface of the code will be addressed. The accuracy of this FE-BI code will also be described in comparison to other finite element formulations which employ absorbing boundary conditions or artificial absorbers for terminating the mesh. Several calculation examples involving different antenna geometries will be presented. Radar cross section (RCS) and radiation patterns as well as input impedance computations will be compared to measured or reference data.

A second code for cylindrically conformal patch antennas will also be described. This code employs shell elements for meshing the antenna cavity. Since these elements are analogous to bricks, the code incorporates its own mesh generation algorithm for rapid geometry specification. Attention will be focused on the validation of this code for wraparound patch antennas and accurate feed modeling using measured or reference data. In addition, antenna performance results will be presented as a function of radius for a typical configuration.

Formulation

The FE-BI system for cavities embedded in a metallic surface (planar or cylindrical) may be written as a matrix equation

$$\left[\mathcal{A}\right]\begin{Bmatrix} E_j^{sp} \\ E_j^{int} \end{Bmatrix} + \begin{bmatrix} [\mathcal{G}] & [0] \\ [0] & [0] \end{bmatrix}\begin{Bmatrix} E_j^{sp} \\ E_j^{int} \end{Bmatrix} = \begin{Bmatrix} f_i^{ext} \\ f_i^{int} \end{Bmatrix} \qquad (1)$$

where the entries of $[\mathcal{A}]$ are due to the finite element portion of the formulation and $[\mathcal{G}]$ is attributed to the boundary integral. The coefficients E_j^{sp} and E_j^{int} denote unknowns associated with the aperture and interior fields, respectively, whereas f_i^{ext} is the excitation function due to exterior sources, such as a plane wave, and f_i^{int} is the excitation function due to interior sources. In this paper the source is an infinitesimally thin probe feed normal to the patch and cavity base. This formulation may be readily modified to include the effect of lumped impedance posts, shorting pins or resistive cards as reported by Jin and Volakis [1].

Solution Methodology

For both planar and cylindrical geometries, the unknown electric fields are found by solving (1) using a Biconjugate Gradient-Fast Fourier Transform (BiCG-FFT) solver. Since the system is symmetric, only one matrix-vector product is required for each iteration of the BiCG algorithm. This product comprises the bulk of the computational effort in the solution and it is therefore advantageous to minimize its execution time. In our implementation, substantial CPU reduction time is achieved by using a sparse matrix-vector product for the finite element matrix term $[\mathcal{A}]$ and a discrete convolution product for the boundary integral term $[\mathcal{G}]$. The resulting product imposes both low computational and memory load.

Having determined the electric fields within the cavity and on its aperture, engineering quantities such as RCS, radiation pattern and input impedance may be determined. Both the RCS and antenna pattern are computed using the aperture fields while the input impedance calculation requires the interior fields near the probe feed.

Planar Code

Consider the printed conformal antenna configuration shown in figure 1 where a cavity is recessed in a perfectly conducting ground plane. Printed on the cavity's aperture is a radiation element of arbitrary shape. In order to simulate the geometrical irregularities as well as the dielectric inhomogeneities of these antennas, we choose tetrahedral elements for the FE volume discretization because of their geometrical adaptability. The expansion of the unknown electric field in this implementation is then carried out by using linear edge-based shape functions [2] since these elements are well suited for vector field representation. The boundary integral portion of the system is formulated on the basis of the equivalence principle which requires an integral equation in terms of the free space Green's function and a magnetic current over the aperture surface which relates the magnetic field $\bar{H}$ to the tangential component of the electric field $\bar{E}$. This leads to an exact boundary condition for the FE volume termination as opposed to other truncation schemes such as absorbing boundary conditions or artificial absorbers. The tetrahedral elements in the cavity reduce to triangle patches on the aperture surface which results in triangular zoning. Linear edge-based shape functions associated with a pair of triangular patches are introduced for the electric field expansion. Again, the surface basis functions just like their volume counterparts are divergence free and well suited for the vector field representation.

Since a geometry of arbitrary composition is to be analyzed, a commercial meshing package such as SDRC I-DEAS is employed for preprocessing so that a tedious

geometric data input is avoided. An interface between the main program and the mesh generator is provided as the second stage of preprocess. To reduce the memory requirement, only nonzero elements for the FE system are stored and the BiCG solver is utilized. If the geometry of the radiating elements is regular and uniform zoning on the aperture is physically accessible, then the boundary integral system becomes a discrete convolution (provided the unknown edges are appropriately ordered) and the efficient BiCG-FFT solver is used.

Since tetrahedral/triangular elements are chosen for the cavity/aperture discretization, a particular feature of this program is its capability to simulate planar/nonplanar antennas, dielectric substrate inhomogeneities and diverse feeding schemes. Several numerical examples are shown to illustrate the code's capability. Figure 2(a) displays a square Archimedean spiral. A square rather than a circular spiral was selected because it allowed comparisons with reference data. The complementary square spiral consists of strip arms, each of width 0.09375 cm, placed (free-standing) on the aperture of a square air-filled cavity which measures 2.812 cm per side and 0.9375 cm deep. Figure 2(b) illustrates the $\phi = 45°$ plane $\sigma_{\theta\theta}$ and $\sigma_{\phi\phi}$ bistatic patterns for this structure where the plane wave was incident from 30° off normal. The $\sigma_{\theta\theta}$ pattern compares well with corresponding data based on the finite difference-time domain (FD-TD) method [4]. No FD-TD data were available for the $\sigma_{\phi\phi}$ pattern but as expected, the $\sigma_{\phi\phi}$ return is much lower and vanishes at grazing. Figure 3(a) illustrates a circular patch residing on the surface of a 0.406 cm thick substrate having a relative dielectric constant of $\epsilon_r = 2.9$. The patch's diameter is 2.6 cm and the substrate is enclosed in a circular cavity 6.292 cm wide. This cavity was recessed in a low cross section test body for measurements. A comparison of the measured and calculated input impedance is displayed in figure 3(b). For brevity, the excellent RCS data comparison is not shown. The feed in this case was placed 0.8 cm from the patch's center and it is again seen that the measurements and calculations are in good agreement. We considered next the modeling of a one-arm conical spiral to demonstrate the geometrical versatility of the tetrahedral code. A configuration of the spiral radiator and surface mesh is illustrated in figure 4(a) from a side view. The top and bottom edges of the strip forming the spiral follow the lines $\rho = 0.0503\lambda \exp[0.221(\phi \pm 2.66)]$, $z = a_{\pm} \exp(0.221\phi)$, where (ρ, ϕ, z) denote the standard cylindrical coordinates, $a_{\pm}$ are equal to 0.0832λ and 0.0257λ, respectively, and $0 < \phi < 2\pi$. This spiral arm resides on an inverted cone (9.24 cm tall) whose bottom cross section has a diameter of 1.68 cm and the top cross section has a diameter of 21.78 cm. For our calculations $\lambda = 30$ cm and the spiral was situated in a circular cavity 10.01 cm deep. The computed E_ϕ radiation pattern, using a probe feed at the cavity base, is given in figure 4(b). It is seen that the E_ϕ principal plane pattern is in good agreement with the data given in [5]. However, the E_θ pattern differs from the measured data primarily because of the circular cavity included in the analytical model. The latter was not part of the measurement configuration which consisted of the spiral antenna on a large circular plate.

Cylindrical Code

The cylindrical code differs from the tetrahedral code primarily in terms of its elements and dyadic Green's function. The elements are circular shell elements such as the one shown in figure 5. These elements, like their tetrahedral counterparts, are

divergence free in accordance with the requirements of the vector wave equation and hence no penalty function is required. They are also edge-based elements and are therefore well suited for electromagnetics applications since they avoid specification of a field at geometry corners where a singularity might exist. The cylindrical shell element shown in figure 5 is most closely related to the brick element and is in fact a member of the general class of curvilinear brick elements. The dyadic Green's function used in this code eliminates the presence of the magnetic field on the mesh boundary and requires a magnetic current with support only over the aperture. Thus, the unknowns are associated with the electric field within the cavity and on the aperture. Although use of such a Green's function is typically associated with a large computational burden for large radius cylinders, we have found that by employing a high frequency asymptotic evaluation, we can maintain a highly efficient code.

The cylindrical code currently allows the calculation of the RCS, the antenna pattern and the input impedance for cylindrical-rectangular and wraparound antenna elements. Of principal concern are the radiation and scattering properties of wraparound antenna arrays. Two types of arrays may be constructed: discrete cylindrical-rectangular cavities and cylindrical-rectangular patches printed atop a continuous substrate ring. These two types of wraparound arrays are illustrated in figure 6. The scattering and radiation behavior of each of these arrays are of interest to a low observable antenna designer and are the subject of a series of papers [6,7]. Evidently, continuous wraparound cavities support substrate modes which dramatically affect the back lobe RCS and radiation patterns.

An interesting application of this code is to investigate the effect of curvature on the resonance behavior of printed antennas. The resonance characteristics of an axially polarized 3.5 cm × 3.5 cm patch antenna which is placed within a 14 cm × 14 cm × 0.3175 cm cavity filled with a dielectric substrate ($\epsilon_r = 2.17$) is shown in figure 7. The input impedance is also strongly affected by curvature for axially polarized elements as shown in figure 8.

This code can currently model continuous and discrete wraparound arrays, two-dimensional arrays on a cylinder face, planar arrays and elements which contain lumped impedance/shorting posts. In the near future, resistive card overlays will be added to the code for RCS vs. gain trade-off studies involving curvature.

References

1. J-M Jin and J.L. Volakis, "A hybrid finite element method for scattering and radiation by microstrip patch antennas and arrays residing in a cavity," *IEEE Trans. Antennas Propagat.*, Vol. 39, pp. 1598-1604, Nov. 1991.

2. M.L. Barton and Z.J. Cendes, "New vector finite elements for three dimensional magnetic field computations," *J. Appl. Phys.*, Vol 61, pp 3919-3921, 1987.

3. C.W. Penney and R.J. Luebbers, "Radiation and scattering form a square Archimedean spiral antenna using FD-TD," *Electromagnetics*, 1994 (to appear).

4. D.W. Smith and P.E. Mayes, "Numerical and experimental analysis of circularly polarized radiating line antennas," *Electromagnetics Lab Report N0. 90-4*, University of Illinois, 1990.

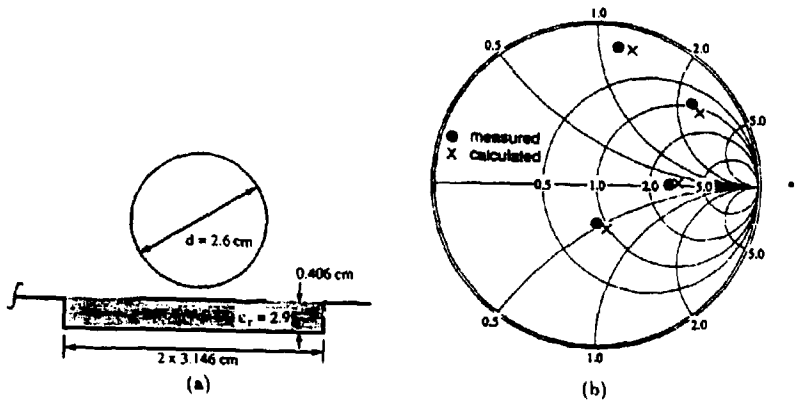

Figure 3: Circular patch antenna: (a) geometry; (b) input impedance.

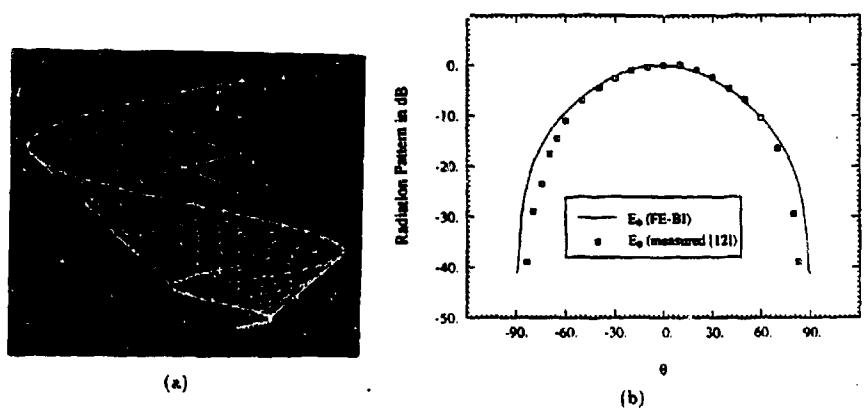

Figure 4: Spiral antenna: (a) geometry; (b) principal plane antenna patterns.

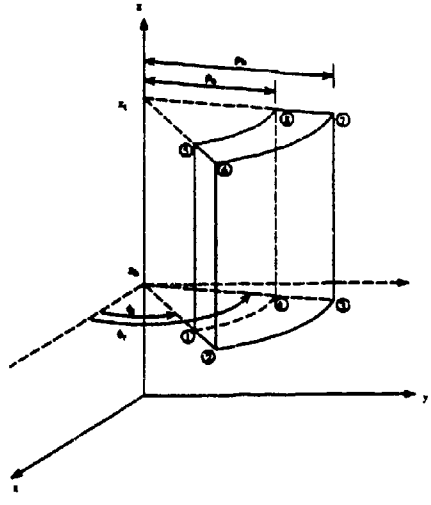

Figure 5: Cylindrical shell element.

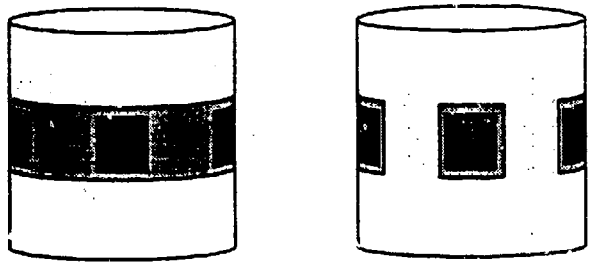

(a) (b)

Figure 6: Illustration of two types of arrays: (a) wraparound array; (b) discrete cavity array

5. L.C. Kempel and J.L. Volakis, "Scattering by cavity-backed antennas on a circular cylinder using the FE-BI method," *1994 IEEE Antennas and Propagat. Soc. Int. Symp.*

6. L.C. Kempel and J.L. Volakis, "Radiation by patch antennas on a circular cylinder using the FE-BI method," *1994 IEEE Antennas and Propagat. Soc. Int. Symp.*

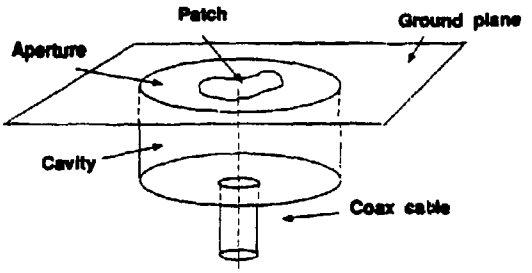

Figure 1: Arbitrary cavity-backed antenna element recessed in a ground plane.

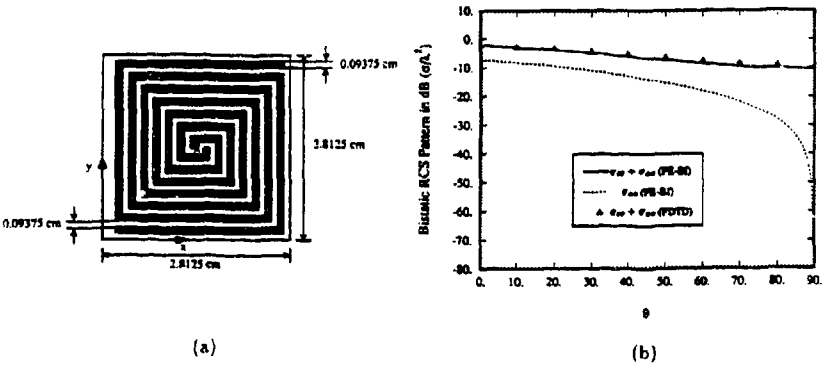

(a) (b)

Figure 2: Archimedean spiral: (a) geometry; (b) bistatic patterns.

5. L.C. Kempel and J.L. Volakis, "Scattering by cavity-backed antennas on a circular cylinder using the FE-BI method," *1994 IEEE Antennas and Propagat. Soc. Int. Symp.*

6. L.C. Kempel and J.L. Volakis, "Radiation by patch antennas on a circular cylinder using the FE-BI method," *1994 IEEE Antennas and Propagat. Soc. Int. Symp.*

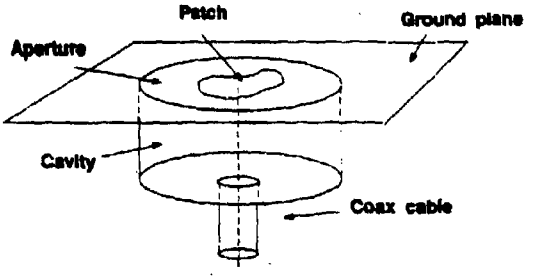

Figure 1: Arbitrary cavity-backed antenna element recessed in a ground plane.

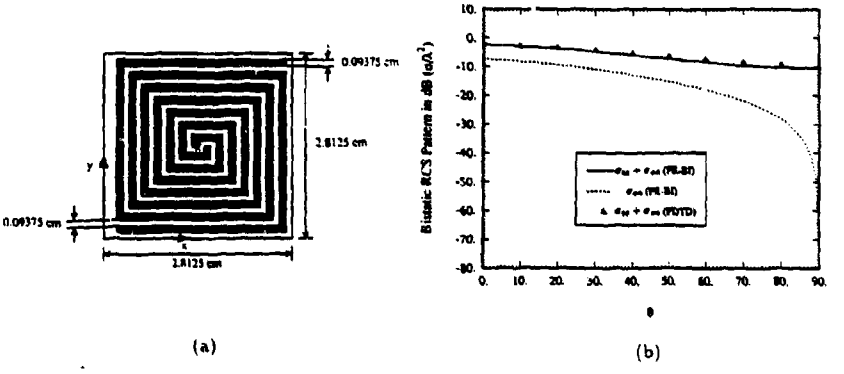

(a) (b)

Figure 2: Archimedean spiral: (a) geometry; (b) bistatic patterns.

SESSION 5:

BOUNDARY CONDITIONS

Chair: Carey Rappaport

COMPARISON AND GENERATION

OF

HIGHER ORDER FDTD ABSORBING BOUNDARIES

David Steich and Raymond Luebbers*
Department of Electrical Engineering
The Pennsylvania State University
University Park, PA 16802

ABSTRACT

For application to radiation and scattering problems the Finite Difference Time Domain (FDTD) method requires the limits of the computation space to approximate unbounded free space. Poor performance of this absorbing boundary limits the accuracy which can be obtained by FDTD, and may be a source of instability. When making an FDTD calculation an important decision is the number of cells to use in the boundary layer. In this paper convergence tests made by varying the size of this boundary will be reported for popular outer boundary conditions. Further, a new approach for expressing these and other boundary conditions and for obtaining higher order boundary conditions from lower order ones will be presented.

I. INTRODUCTION

When the Finite Difference Time Domain (FDTD) method as proposed by Yee [1] is applied to scattering and radiation problem, the surfaces formed by the truncation of the FDTD cell space must absorb the scattered or radiated fields for accurate results. This absorption is not perfect, and the fields reflected back into the FDTD space introduce errors. Better absorption reduces these errors. Absorbing boundary conditions in common use provide better absorption as they are moved farther from the scatterer or radiator since the fields impinging on the outer boundary more closely approximate plane waves incident at angles nearer to the surface normal. In addition, the fields reflected back to the radiator or scatterer will be of lower amplitude due to the spatial spreading of the waves. As a practical matter, any of the popular absorbing boundary conditions will provide accurate results if the outer boundaries are moved far enough away from the radiator or scatterer. But this requires relatively more computer memory and time.

Many absorbing boundaries have been proposed in the literature. The most popular ones are based on the one-way wave equation. This assumes a wave incident on the outer boundary surface, then attempts to predict values of this wave just outside the FDTD space based on present and past values of the wave at various locations near the outer boundary.

A survey of various boundary conditions is given in [2]. A more recent comparison of boundary conditions is contained in [3].

In [4] the Mur condition is compared with other boundary conditions relative to the distance from the source to the outer boundary. In [5] it is shown that increasing the order of the absorbing boundary, while improving performance for a surface at infinity, may actually degrade performance when the absorbing surface is close to the scatterer. But the results given in [4,5] of absorption error relative to distance again are difficult to relate to actual FDTD performance, since no correspondence is given between the boundary reflections and their effect on quantities of actual interest, such as scattering cross section or antenna currents.

There has been discussion of the relative stability of different boundary conditions. Most of these have been for two-dimensional geometries, and have used an analytical approach. In [6] it was shown that some boundary conditions are inherently unstable. In [7] it was analytically shown that some boundary conditions may be unstable even if the Courant condition is satisfied. A more complete discussion of stability was given in [8]. In [8] it was demonstrated that the choice of discretization has a strong effect on stability.

Here we have chosen to evaluate several representative outer boundary conditions using methods that relate directly to practical applications in electromagnetics. Four popular FDTD absorbing boundary conditions will be compared for representative geometries in both two and three dimensions. The comparison will be made by observing convergence of FDTD results while increasing the distance from the scatterer or radiator to the outer boundary. This method provides information on the most important criteria in comparing absorbing boundaries, that is, how far must the boundary be removed from the geometry in order to obtain accurate results.

The four boundary conditions to be compared are second order Mur [9], Superabsorption [10] (sometimes here referred to as "Super") applied to first order Mur, the second order Liao [11] absorbing boundary modified for increased stability [12], and second order Higdon [13, 14] modified for increased stability. Applying Superabsorption to first order Mur results in a second order boundary. The stabilized forms of Liao and Higdon were used since it was found that the unstabilized forms were likely to become unstable before typical FDTD radiation or scattering calculations were completed. All results labeled Liao and Higdon are computed with stabilized forms.

Higher order Liao and Higdon boundary conditions are generated by forming products of lower order conditions. In this paper we show how to express the boundary conditions in a coefficient matrix. The coefficient matrix clearly shows which field values are being used to estimate the boundary field. The coefficient matrices for lower order outer boundaries may then be combined to form higher order outer boundary conditions. The combination operation is straightforward and simple to implement. It allows lower order boundary conditions optimized for different incidence angles or with different stabilizing loss terms to be combined. Even different boundary conditions of different order may be combined. For example, order P Higdon could be combined with order Q Liao to produce a combined outer boundary condition of order P+Q. Another advantage of the coefficient matrix notation is that the analytical plane wave reflection coefficients are easily obtained using the same procedure regardless of the particular boundary condition being considered.

The notation of Yee is used, with $E^n(I,J,K)$ corresponding to the electric field at location $x=I\Delta x$, $y=J\Delta y$, $z=K\Delta z$ at time $t=n\Delta t$. The absorbing boundary equations are for a z component of electric field on the x=0 plane, that is, an $E^n(I=0,J,K)$ component is understood to be E_z at

x=0. If the J and K indices are unchanged in any given equation they may be omitted for clarity. All three-dimensional calculations use $\Delta x=\Delta y=\Delta z=1$ cm cubic FDTD cells with time step $\Delta t=0.01926$ ns which is at the Courant limit. All two-dimensional calculations use $\Delta x=\Delta y=0.5$ cm with time step 0.0236 ns, also at the Courant limit.

The far zone fields and scattering cross sections used in some of the convergence tests were obtained from the near zone fields using the methods described in [15,16]. The FDTD equations were implemented in single precision, while all absorbing boundary calculations were performed in double precision. No difference between single and double precision calculation of the boundaries was noted. For scattering calculations with an incident plane wave, the scattered field formulation of FDTD was used [17,18], and only scattered fields were incident on the outer boundaries for absorption. However, for radiation calculations, total fields were to be absorbed.

II MUR BOUNDARY

The second order Mur absorbing condition at the boundary x=0 used in these comparisons is given in (16) of [9]. Since this absorbing boundary utilizes electric field values at different y and z (J and K) locations, it cannot be used for field values at locations adjacent to the other outer surfaces. At these locations first order Mur as given in (15) of [9], is used.

III. SUPERABSORPTION

For these comparisons Superabsorption as described in [10] is applied to first order Mur so that a direct comparison between it and second order Mur can be made. Superabsorption can be applied to other boundary conditions, so that the results of its application to first order Mur presented here should not be taken, and is not presented, as a general evaluation of the method.

IV. LIAO BOUNDARY

Since we will be modifying the Liao boundary to increase stability, it will be discussed in more detail. The Nth order Liao absorbing boundary condition for an electric field component located on the $x=I\Delta x=0$ surface is given by [11]

$$E^{n+1}(I=0) = \sum_{j=1}^{N} \sum_{k=1}^{2j-1} T_{jk} E^{n+1-j}(I=k-1) \tag{1}$$

where the first order (N=1) T_{jk} coefficients are given by

$$T_{11} = \frac{(2-s)(1-s)}{2} \tag{2}$$

with

$$T_{12} = s(2-s) \tag{3}$$

$$T_{13} = \frac{s(s-1)}{2} \tag{4}$$

$$s = \alpha \frac{c\Delta t}{\Delta x} = \frac{1}{\cos(\theta_i)} \frac{c\Delta t}{\Delta x} \tag{5}$$

where α is a constant. To include effects of different incidence angles for waves striking the outer boundary α may be taken as the reciprocal of the cosine of the incidence angle θ_i, where θ_i is the incidence angle on the outer boundary (θ_i=0 for normal incidence). For uniformity in the comparisons, and to limit the number of plots, α=1 is used for all calculations in this paper.

For higher order implementations the additional T_{jk} coefficients can be obtained from the recursion relation

$$T_{jk} = \sum_{i=\max(1,k-Q(j-2))}^{\min(j,2k)} T_{(j-1)(k-i+1)} T_{1i} (-1)^{j-1} \frac{N!}{j!(N-j)!} \tag{6}$$

The form of the Liao boundary given here is slightly different than in [11], and is simpler to implement. An excellent discussion of the Liao absorbing boundary is given in [19]. There is no difficulty at edges and in corners since the J,K values are unchanged for all terms.

The major difficulty with applying the Liao absorbing boundary as given above is that it tends to be unstable in many situations. Conditions that may cause instability include locating the outer boundary close to the geometry, calculating many time steps, and including dielectric or magnetic materials in the geometry. For this reason a modification to the original Liao absorbing boundary has been proposed [12]. In this modification equation (2) becomes

$$T_{11}^{*} = \frac{(2-2d-s)(1-s)}{2} \tag{7}$$

where increasing d from zero corresponds to introducing energy loss in the calculation. Larger values of d provide increased stability, but at the expense of increasing reflections from the boundary. For all calculations in this paper a value of d=0.0075 was used. This value was obtained empirically from calculations for a variety of different geometries and total time steps. These indicate that for calculations involving relatively few time steps, or with the outer boundary relatively far from the object, d can be decreased without losing stability. Conversely, calculations with large number of time steps or with the outer boundary close to the object tend to require larger values of d for stability.

V. HIGDON BOUNDARY

Higdon's boundary condition has been given in a lossless form [13]

$$\left[\prod_{j=1}^{N}\left(\cos\theta_j\frac{\partial}{\partial t}-c\frac{\partial}{\partial x}\right)\right]E=0 \tag{8}$$

and with added loss [14]

$$\left[\prod_{j=1}^{N}\left(\cos\theta_j\frac{\partial}{\partial t}-c\frac{\partial}{\partial x}+\zeta_j\right)\right]E=0 \tag{9}$$

where N is the order, the θ_j are the plane wave incidence angles, and the $\zeta_j \geq 0$ are loss terms that may be used to increase stability. They may also be used to increase absorption of reactive fields [20].

Equations (8) and (9) can be discretized in different ways. With θ_j=0 and N=1, (8) is equivalent to (10) of [9] which yields the first order Mur absorbing boundary. We can thus discretize (8) to be identical with first order Mur. Adding the incidence angle dependence and stabilizing loss we obtain first order stabilized Higdon as

$$E^{n+1}(I=0,J,K)=(1-d)E^{n}(1,J,K)$$

$$+\frac{\alpha c\Delta t-\Delta x}{\alpha c\Delta t+\Delta x}\left(E^{n+1}(1,J,K)-E^{n}(0,J,K)\right) \tag{10}$$

where d is a small positive number which corresponds (as with the Liao boundary) to an energy loss and α is a constant related to the assumed incidence angle on the outer boundary as defined in (5). Again, there are various ways of adding the stabilizing loss. The approach used here is simple, and provides good stability and absorption. For all calculations stabilized Higdon is used with d=0.005. The parameter α remains equal to one in all cases.

The next step is to extend (10) to higher orders based on (8). In order to do this efficiently we introduce a coefficient matrix notation in the following section.

VI. COEFFICIENT MATRIX METHOD

Implementing some types of higher order boundary conditions is greatly simplified by use of a coefficient matrix which relates each multiplying coefficient to the particular electric (or magnetic) field term it multiplies. It is a matrix notation, but to generate higher order boundary conditions the matrices combine in a operational way, not by usual matrix multiplication. The combination process is straightforward.

To start we consider locating electric (or magnetic) field quantities in space and time in the vicinity of the outer boundary field location of interest in the following matrix arrangement:

$$(E) = \begin{pmatrix} E^{n+1}(0,J,K) & E^{n+1}(1,J,K) & E^{n+1}(2,J,K) & . & . \\ E^{n} & (0,J,K) & E^{n} & (1,J,K) & E^{n} & (2,J,K) & . & . \\ E^{n-1}(0,J,K) & E^{n-1}(1,J,K) & E^{n-1}(2,J,K) & . & . \\ . & . & . & . & . \\ . & . & . & . & . \end{pmatrix} \tag{11}$$

The electric (or magnetic) fields are arranged in position horizontally, and in time vertically.

An analogy exists with a system of linear equations, but instead of the unknown linear equation variables, we have the known values of electric fields plus the one unknown boundary field in the upper left corner of the matrix. The matrix will be large enough to contain all the electric field terms included in a given boundary condition, which will depend on the particular boundary condition and its order. For example, for first order Mur only the four terms in the upper left corner are included in the matrix, since first order Mur does not involve any other electric fields.

Any absorbing boundary condition that operates on field terms with the same J,K positional locations can be put in this form very easily. This includes all the boundary conditions considered here except for second order Mur. Forms such as second order Mur which operate on multiple spatial dimensions can also be put in coefficient matrix notation, but the coefficient matrix will have additional dimensions corresponding to transverse field variations. This can be quite simply accommodated in calculations by declaring an array with sufficient dimensions for each spatial variation plus one for the time variation.

First order Liao has a coefficient matrix given by

$$\begin{pmatrix} -1 & 0 & 0 \\ T_{11} & T_{12} & T_{13} \end{pmatrix} (E) = 0 \tag{12}$$

The stabilized form of first order Liao is obtained merely by substituting T_{11}^{*} for T_{11}.

First order stabilized Higdon has a coefficient matrix

$$\begin{pmatrix} -1 & b_1 \\ -b_1 & (1-d_1) \end{pmatrix} (E) = 0 \tag{13}$$

where $b_1 = \dfrac{\alpha_1 c\Delta t - \Delta x}{\alpha_1 c\Delta t + \Delta x}$ and d_1 is the stabilizing factor. With α_1=1 and d_1=0 first order Higdon as implemented here is identical with first order Mur.

One advantage of this coefficient matrix notation is that the terms being used to estimate the outer boundary electric field are clearly shown. For example, both first order Mur

and first order Higdon operate on the current time electric field one position into the space, plus past time electric fields at the boundary and at one position in. First order Liao operates only on past values of electric field, but goes one field location further into the FDTD space.

While useful in this way, the real advantage of this coefficient matrix notation is in generating higher order boundary conditions from lower order ones. This is most clearly seen from considering the product notation equations (8) and (9). These equations clearly state that higher order absorbing boundary conditions are to be obtained by forming products of lower order ones. The combination process involves multiplying and shifting. A general definition of this operation process on the coefficient matrices can be given as follows. Consider two different coefficient matrices for two different outer boundary conditions. The first is given by

$$A_1(p_1,q_1) = \begin{pmatrix} a^1_{00} & a^1_{01} & .. & .. & a^1_{0Q_1} \\ a^1_{10} & a^1_{11} & .. & .. & a^1_{1Q_1} \\ .. & .. & a^1_{p_1q_1} & .. & .. \\ .. & .. & .. & .. & .. \\ a^1_{P_1 0} & a^1_{P_1 1} & .. & .. & a^1_{P_1Q_1} \end{pmatrix} \tag{14}$$

and a corresponding matrix $A_2(p_2,q_2)$ is defined similarly. Each by itself defines an outer boundary condition. We wish to obtain the combined higher order boundary condition. Let the resulting coefficient matrix be defined as $A(p,q)$. The combination process will yield terms in $A(p,q)$ with indices p=0,1,2,...(P_1+P_2) and q=0,1,2,...(Q_1+Q_2). Each term in this coefficient matrix is given by

$$A(p,q) = -\sum_{p_1=0}^{P_1}\sum_{q_1=0}^{Q_1}\sum_{p_2=0}^{P_2}\sum_{q_2=0}^{Q_2} \delta_{(p_1+p_2)p}\,\delta_{(q_1+q_2)q}\,A_1(p_1,q_1)\,A_2(p_2,q_2) \tag{15}$$

where the Kronecker delta is defined as

$$\delta_{\mu\nu} = \begin{cases} 0, & \mu \neq \nu \\ 1, & \mu = \nu \end{cases}$$

Equation (15) provides the shift combinations necessary to generate each term of the combined coefficient matrix. This process corresponds to the product combinations given in equations (8) and (9).

For example, consider generating second order Higdon from two first order Higdon coefficient matrices as given in (13). Each of the first order Higdon coefficient matrices could have different α and d terms, which is allowed for by having subscripts 1 and 2. Applying (15), the coefficient matrix for second order Higdon is

$$\begin{pmatrix} -1 & b_1+b_2 & -b_1b_2 \\ -b_1-b_2 & (1-d_1)+(1-d_2)+2b_1b_2 & -b_1(1-d_2)-b_2(1-d_1) \\ -b_1b_2 & b_2(1-d_1)+b_1(1-d_2) & -(1-d_1)(1-d_2) \end{pmatrix} \tag{17}$$

Third order Higdon can be generated by applying (15) to combine (17) with first order Higdon of (13). The process can be repeated to generate Higdon boundary conditions of arbitrary order.

While not explicitly clear from the statement of the Liao boundary condition, higher order Liao boundary conditions can also be generated using this approach. For example, by applying (15) with both coefficient matrices A_1 and A_2 given by (12), the coefficient matrix for second order Liao is obtained as

$$\begin{pmatrix} -1 & 0 & 0 & 0 & 0 \\ T_{11}+T_{11} & T_{12}+T_{12} & T_{13}+T_{13} & 0 & 0 \\ -T_{11}T_{11} & -2T_{11}T_{12} & -2T_{11}T_{13}-T_{12}T_{12} & -2T_{12}T_{13} & -T_{13}T_{13} \end{pmatrix} \tag{18}$$

While different in appearance, this result is exactly equivalent to the Liao boundary condition expressions given in Section IV for N=2. Note that equation (6) is not needed to generate higher order Liao boundary conditions when using the coefficient matrix approach. First order Liao is directly extended to second order Liao, and then to third or higher order by combining coefficient matrices.

The result given in (18) assumes that both first order Liao coefficient matrices use the same values of α (and d if the stablized form is used). But the coefficient matrix combination operations used to obtain (18) will work just as well if the T_{pq} terms for the different first order Liao coefficient matrices use different values of α and/or d. So that designing higher order absorbing boundary conditions with different contributing orders optimized for different incidence angles used to compute the α parameter and with different loss factors d is quite simple using this approach.

Furthermore, Liao and Higdon (or any other boundary condition that can be expressed in coefficient matrix notation) can be combined together. For example, coefficient matrices for first order Liao and first order Higdon could be combined to give a second order boundary condition that would combine the features of both. If transverse directions are included in the coefficient matrix by adding additional dimensions, this procedure allows boundary conditions involving transverse directions to be combined. For example, a second order Mur boundary could be combined with an order P Liao boundary to create a (P+2) order Mur-Liao boundary condition.

VII. THREE-DIMENSIONAL CONVERGENCE

In this section an example comparison between the boundary conditions is made for three-dimensional calculations. This example is wide band scattering from a flat conducting plate.

The plate is 40 x 40 cm, and is centered in the FDTD space and perpendicular to the z coordinate axis. The incidence angle is θ=45, φ=0, which puts the back and forward scatter into an edge of the FDTD space, but not into a corner. Results are shown in Figures 1-4. Mur has not converged even with a 40 cell border, Super has converged with a 30 cell border and almost converged with 20 cells, and Liao and Higdon have very nearly converged with a 20 cell border.

This three dimensional example is chosen as a representative set from a large collection of similar calculations. They indicate that for three dimensions the Super, Liao and Higdon boundaries perform much better than Mur, with Liao and Higdon perhaps slightly better than Super for close boundaries, and with Liao and Higdon providing almost identical convergence results. While not included here, all boundary conditions converged to identical results for all test cases if the outer boundary was located at a sufficient distance from the geometry. Mur was the only exception, and only for geometries where convergence still had not been obtained for boundary distances at the limit of available computer memory. We now proceed to a comparison in two dimensions.

VIII. TWO-DIMENSIONAL CONVERGENCE

While two-dimensional FDTD calculations have somewhat limited application, they may be useful in certain situations. We therefore include one two-dimensional comparison, a perfectly conducting circular cylinder. For this calculation the cylinder has a 0.25 m radius, so that with 0.5 cm square FDTD cells the cylinder diameter is 100 cells. Staircase errors are not a factor in the comparison, since they will be the same for all four boundary conditions. The excitation is a pulsed plane wave incident from φ=45 degrees.

Figures 5-8 show the far zone backscatter for the four boundary conditions for various borders between the cylinder and outer boundary. The advantages of Super, Liao and Higdon over Mur are even more striking than for the three dimensional calculations considered in the previous section. This may be due to the necessity of using first order Mur in corners, but there may also be more fundamental shortcomings with Mur in two dimensions. While Super, Liao and Higdon have converged reasonably well with a 30 cell border, the Mur results have not converged even with a 250 cell border. The Liao and Higdon results for small borders are slightly better than Super, especially at low frequencies.

IX. ANALYTICAL REFLECTION COEFFICIENTS

Additional insight into the performance of these outer boundary conditions may be gained by consideration of analytically-determined reflection coefficients. Following the approach of [22], it is very simple to determine the analytical reflection coefficients using the coefficient matrices presented in Section VI. For simplicity we assume that the boundary condition can be specified using a two-dimensional coefficient matrix operating on time and one spatial dimension. For a general coefficient matrix $A(p,q)$ with indices p=0,1,2,...P and q=0,1,2,...Q, we can express the operation of this matrix on the electric field quantities of (11) explicitly as

$$\sum_{p=0}^{P}\sum_{q=0}^{Q} A(p,q)\,E^{n+1-p}(I-q,J,K) = 0 \tag{19}$$

Equation (19) specifies a particular absorbing outer boundary as determined by the coefficients of the $A(p,q)$ matrix. If different J or K values of electric fields are used in the boundary conditions, as in second order Mur for example, this can be included by adding additional dimensions to the $A(p,q)$ matrix and adding more summations.

Following the approach in [22] we can then obtain the reflection coefficient R as

$$R = \frac{1 - S_i}{1 - S_r} \tag{20}$$

where

$$S_i = \sum_{p=0}^{P}\sum_{q=0}^{Q} A(p,q)\,e^{j(\omega p\Delta t - \beta_x q\Delta x)} \tag{21}$$

and

$$S_r = \sum_{p=0}^{P}\sum_{q=0}^{Q} A(p,q)\,e^{j(\omega p\Delta t - \beta_x q\Delta x)} \tag{22}$$

and where in (21) and (22) the term corresponding to p and q simultaneously equal 0 is not included. Once the coefficient matrix for a particular absorbing boundary is determined, the plane wave reflection coefficient can be obtained easily. Additional summations can be added to (21) and (22) to include electric field values with different J or K indices.

Using this result, calculations of analytical reflection coefficients for the boundary conditions considered in the previous comparisons have been made. These calculations are made for the same outer boundary parameters used in the convergence comparisons. The incidence parameter α=1, and the loss term remains d=0.0075 for stabilized Liao and d=0.005 for stabilized Higdon. The calculations are for a three-dimensional FDTD space. Example results are shown in Figure 9 for FDTD cells size corresponding to 10 per wavelength. The behavior of the stabilized and unstabilized Liao and Higdon boundaries are quite similar. The deep null in the unstabilized versions is softened with stabilization. Both Liao and Higdon are significantly better than Mur and Super at incidence angles near normal. Other calculations of analytical reflection coefficients indicate that they are a reasonable indication of performance at high frequencies, where there are many cells per wavelength. But at lower frequencies, where the outer boundaries are near the target (as measured in wavelengths) are are interacting with reactive fields, the analytical reflection coefficients do not provide a reliable indication of absorbing boundary performance.

X. SUMMARY AND CONCLUSIONS

Four absorbing outer boundary conditions popular among FDTD users have been compared. The four boundary conditions are second order Mur, Superabsorption applied to first order Mur (which is then of second order), and stabilized forms of the second order Liao and Higdon boundary condition. The three-dimensional comparisons indicate that Superabsorption, stabilized Liao and stabilized Higdon provided significant improvement over the Mur condition. In most three-dimensional comparisons stabilized Liao and Higdon performed nearly identically, with both of these converging somewhat faster than Superabsorption. The two-dimensional comparison indicate that Superabsorption, stabilized Liao and stabilized Higdon provide even more of an improvement over the Mur condition than for three dimensions, again with Liao and Higdon providing slightly better performance.

Analytical calculations of plane wave reflection coefficients for the outer boundary conditions, including stabilization loss, were presented. These showed the effects of adding stabilizing loss to Liao and Higdon boundary conditions.

These results are presented to provide information for FDTD users faced with choosing an outer boundary condition and determining the size of the free space border region. They are not an exhaustive evaluation of the Superabsorption method or of the stabilized Liao and Higdon conditions. Superabsorption may be applied to many different boundary conditions, and our results are specific to its application to first order Mur as described. These results strongly indicate that the Superabsorption method is valuable, since applying Superabsorption to first order Mur provided much more absorption than second order Mur.

Similarly, Liao and Higdon may be stabilized using different values of the stabilizing factor or using different values of α. However, unless extreme stability is required for calculations which include unusually large numbers of time steps (hundreds of thousands or more) the second order Mur absorbing boundary is not the optimum choice. It requires significantly more border space in three dimensions than other boundary conditions, and performs very poorly in two-dimensional applications.

To aid in the generation of higher order boundary conditions, a coefficient matrix notation was introduced. The coefficient matrix notation also allows a general implementation of absorbing boundaries, so that changing from Liao to Higdon, for example, requires only changing the first order coefficient matrix entries. The analytical reflection coefficients are also obtained in a simple and straightforward way from the coefficient matrix.

XII ACKNOWLEDGEMENT

The second author would like to acknowledge helpful discussions with Dr. Richard Holland who has long been aware of the shortcomings of the Mur boundary condition in two dimensions. Discussions with Dr. Brian Zook have also been very helpful to the second author in developing an understanding the operation of the Higdon boundary condition.

XIII REFERENCES

1. K. S. Yee, "Numerical solution of initial boundary value problems involving Maxwell's equations in isotropic media," IEEE Trans. Antennas and Propagat., vol. AP-14, pp 302-307, May 1966.
2. T. G. Moore, J. Blaschak, A. Taflove, and G. Kriegsman, "Theory and applications of radiation boundary operators," IEEE Trans. Antennas and Propagat., vol. AP-36, No. 12, pp 1797-1812, December 1988
3. P. Tirkas, C. Balanis, and R. Renaut, "Higher Order Absorbing Boundary Conditions for the Finite-Difference Time-Domain Method," IEEE Trans. Antennas and Propagat., vol. AP-40, No. 10, pp 1215-1222, October 1992.
4. F. X. Canning, "On the Application of Some Radiation Boundary Conditions," IEEE Trans. Antennas and Propagat., vol. AP-38, pp 740-745, May 1990.
5. F. X. Canning, "Are Higher Order Radiation Boundary Conditions More Accurate?", Proceedings of the IEEE AP-S International Symposium (Dallas, TX), pp 1364-1367, 1990.
6. L. H. Howell and L. N. Trefethan, "Ill-posedness of absorbing boundary conditions for migration," Geophysics, vol. 53, pp 593-603, May 1988.
7. R. A. Renaut and J. Petersen, "Stability of wide-angle absorbing boundary conditions for the wave equation," Geophysics, vol. 54, pp 1153-1163, Sep. 1989.
8. R. A. Renaut, "Absorbing Boundary Conditions, Difference Operators, Stability," Journal of Computational Physics, vol 102, pp 236-251, 1992.
9. G. Mur, "Absorbing boundary conditions for finite-difference approximation of the time-domain electromagnetic-field equations," IEEE Trans. Electromagn. Compat., vol. EMC-23, pp 1073-1077, Nov. 1981.
10. K. K. Mei and J. Fang, "Superabsorption—A Method to Improve Absorbing Boundary Conditions", IEEE Trans. Antennas and Propagat., vol. AP-40, pp 1001-1010, Sep. 1992.
11. Z. P. Liao, H. L. Wong, G. P. Yang, and Y. F. Yuan, "A transmitting boundary for transient wave analysis," Scientia Sinica, vol. 28, no. 10, pp 1063-1076, Oct. 1984.
12. M. Moghaddam and W. C. Chew, "Stabilizing Liao's Absorbing Boundary Conditions using Single Precision Arithmetic," Proceedings of the IEEE AP-S International Symposium (London, Ontario), pp 430-433, 1991.
13. R. L. Higdon, "Absorbing Boundary Conditions for Difference Approximations to the Multi-Dimensional Wave Equation," Mathematics of Computation, vol. 47, No. 176, pp 437-459, October 1986.
14. R. L. Higdon, "Numerical Absorbing Boundary Conditions for the Wave Equation," Mathematics of Computation, vol. 49, No. 179, pp 65-91, July 1987.
15. R. Luebbers, K. Kunz, M. Schneider, F. Hunsberger, "A Finite Difference Time Domain Near-Zone to Far-Zone Transformation", IEEE Transactions on Antennas and Propagation, vol 39, no 4, pp 429-433, April 1991.
16. R. Luebbers, D. Ryan, J. Beggs, "A Two-Dimensional Time Domain Near Zone to Far Zone Transformation," IEEE Transactions on Antennas and Propagation, vol 40, no 7, pp 848-851, July 1992.
17. R. Holland, L. Simpson, and K. Kunz, "Finite difference analysis of EMP coupling to lossy dielectric structures," IEEE Trans. EEMC, vol. EMC-22, pp 203-209, Aug. 1980.

18. K. Kunz, R. Luebbers, The Finite Difference Time Domain Method for Electromagnetics, CRC Press, 1993.
19. W. C. Chew, Waves and Fields in Inhomogeneous Media, Van Nostrand Reinhold, 1990.
20. J. Fang, "Absorbing Boundary Treatments in the Simulation of Wave Propagation in Microwave Integrated Circuits," Conference Proceedings of the 9th Annual Review of Progress in Applied Computational Electromagnetics, Naval Postgraduate School, Monterey, CA, pp 322-329, March 22-26, 1993.
21. R. Luebbers, K. Kunz, "Finite Difference Time Domain Calculations of Antenna Mutual Coupling", IEEE Transactions on Electromagnetic Compatibility, vol 34, no 3, pp 357-360, August 1992.
22. S. Ray, "Characterization of Radiation Boundary Conditions used in the Finite-Difference Time-Domain Method," Proceedings of the IEEE AP-S International Symposium, San Jose, California, June 26-30, 1989.

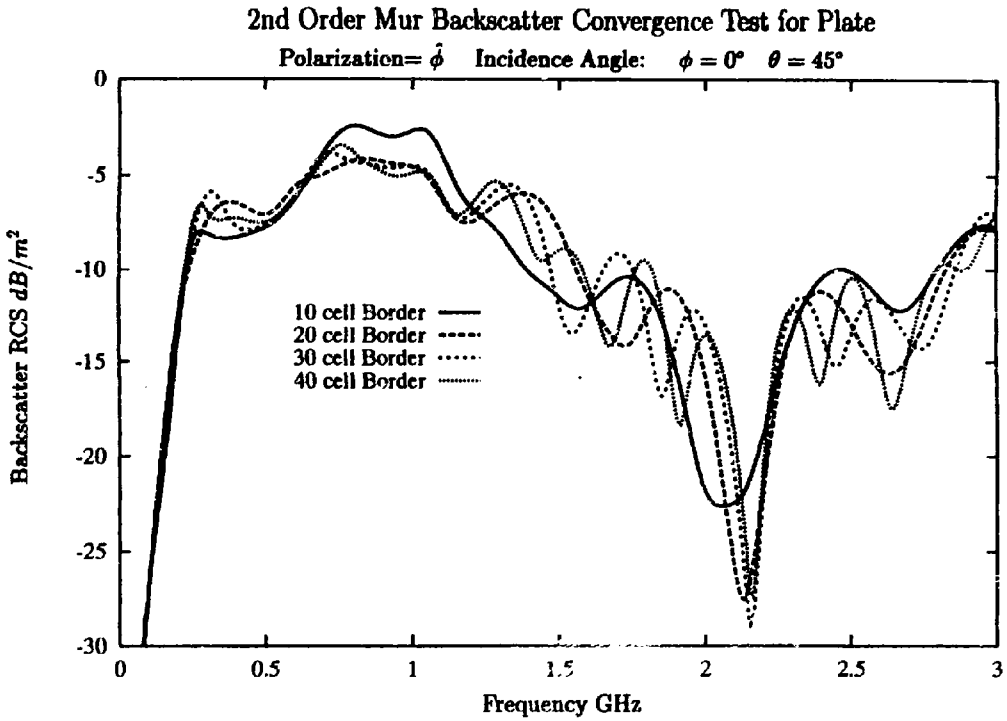

Figure 1: Farzone backscatter convergence for 40cm x 40cm conducting plate using 2nd Order Mur ORBC.

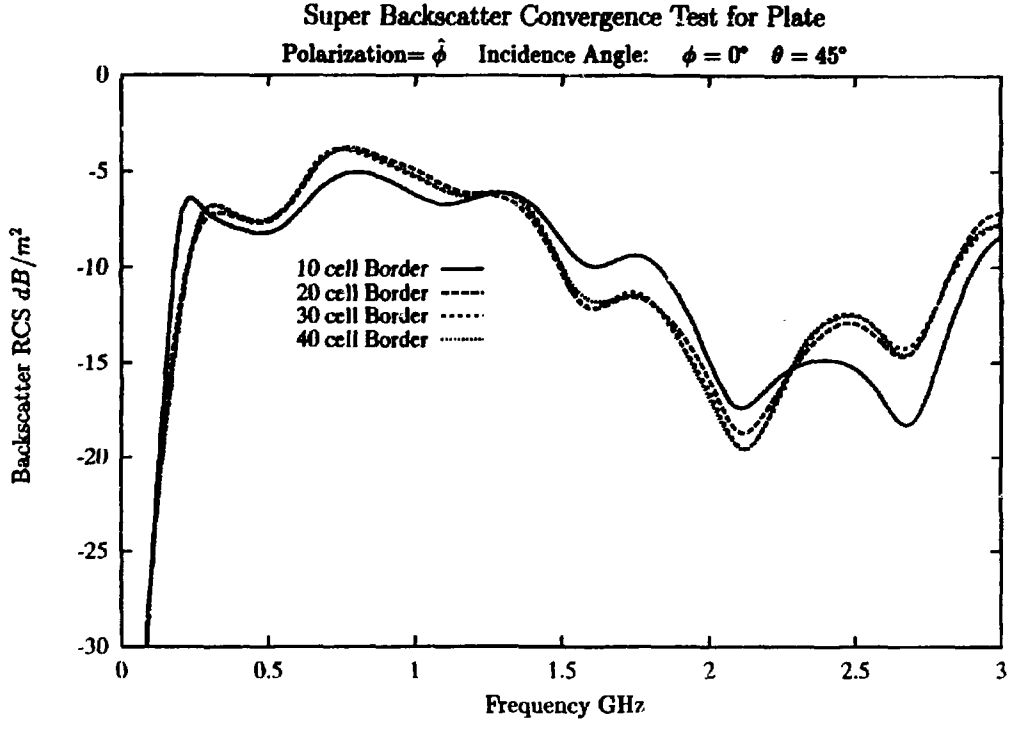

Figure 2: Farzone backscatter convergence for 40cm × 40cm conducting plate using Super GRBC.

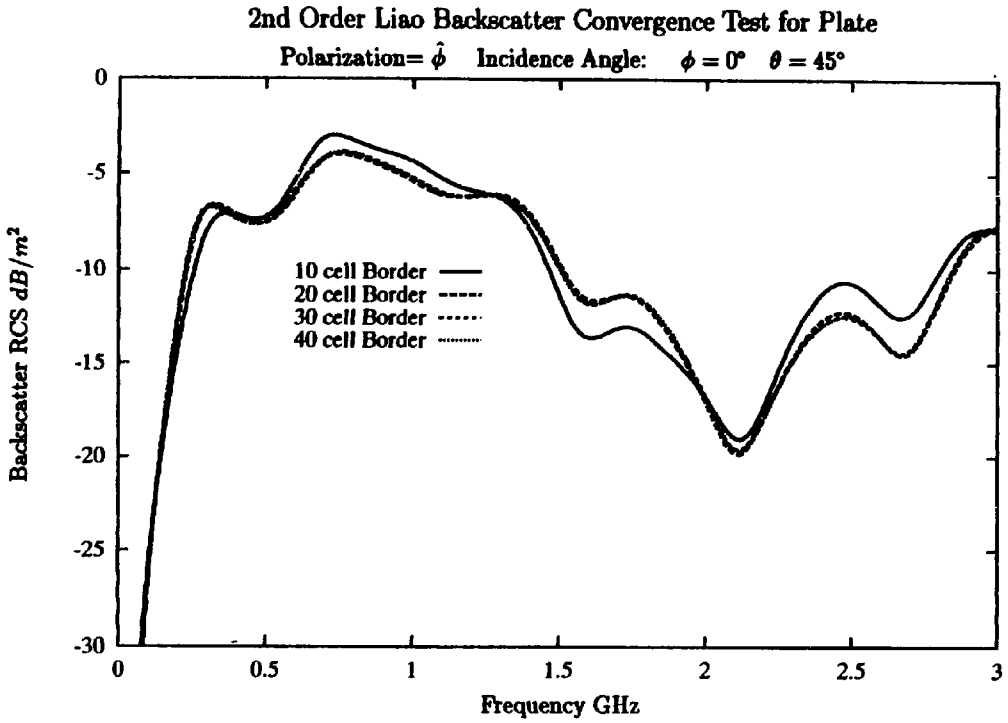

Figure 3: Farzone backscatter convergence for 40cm x 40cm conducting plate using stablized 2nd Order Liao ORBC.

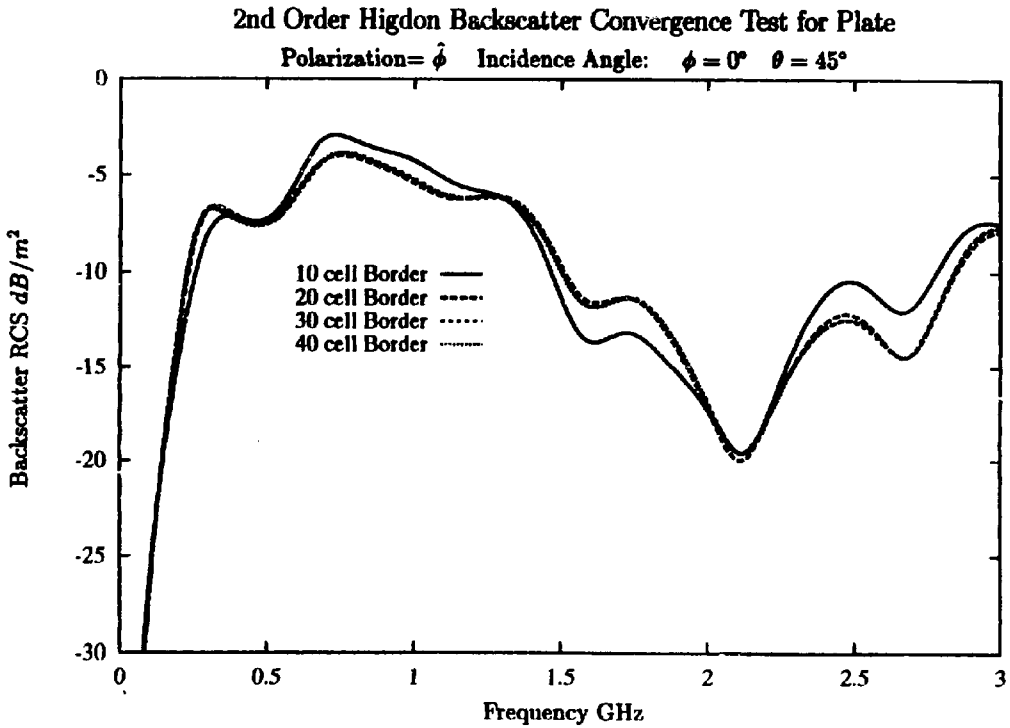

Figure 4: Farzone backscatter convergence for $40cm \times 40cm$ conducting plate using stablized 2nd Order Higdon ORBC.

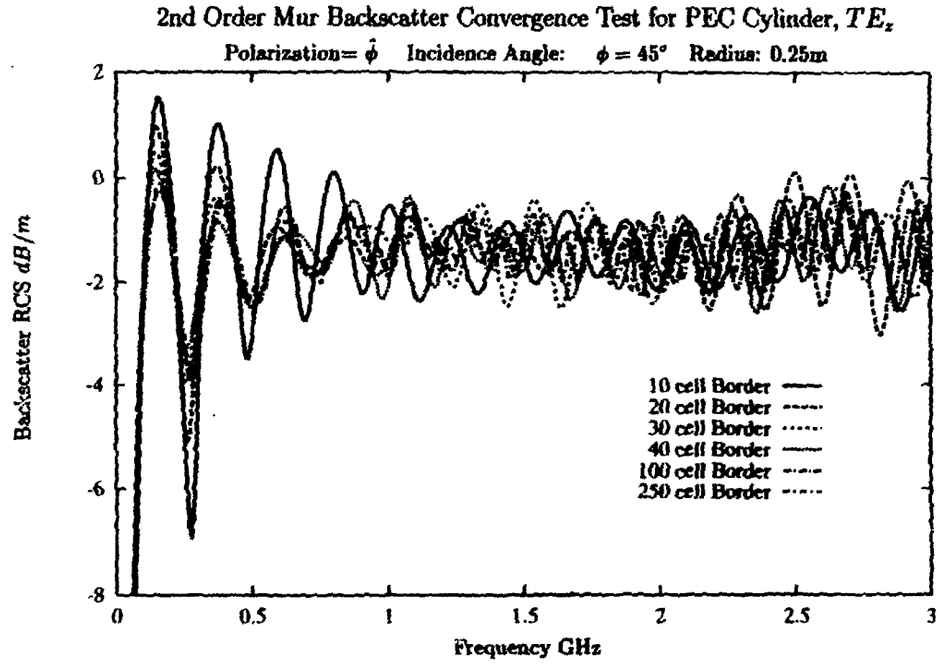

Figure 5: Farzone backscatter convergence for 40cm × 40cm conducting plate using stabilized 2nd Order Higdon ORBC.

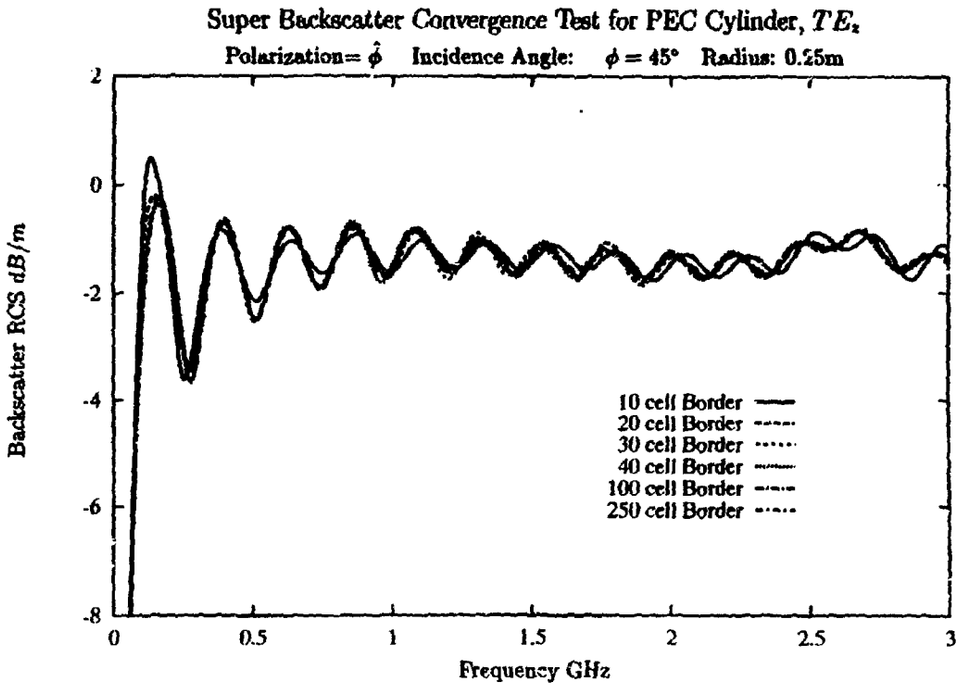

Figure 6: Farzone backscatter convergence for 40cm×40cm conducting plate using stablized 2nd Order Higdon ORBC.

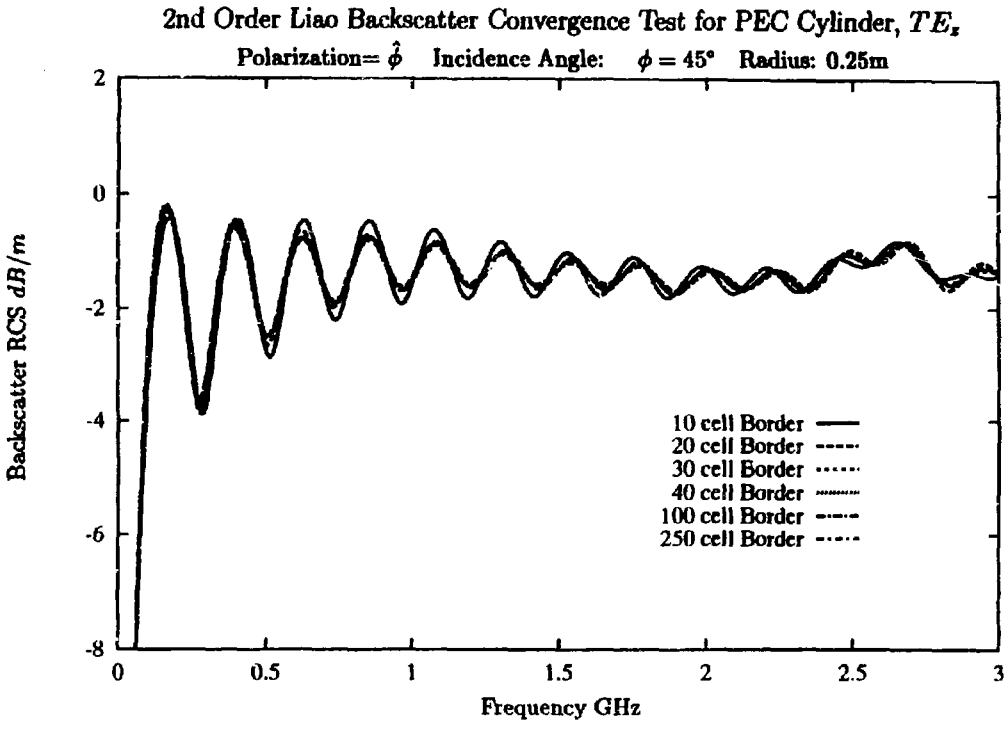

Figure 7: Farzone backscatter convergence for $40cm \times 40cm$ conducting plate using stablized 2nd Order Higdon ORBC.

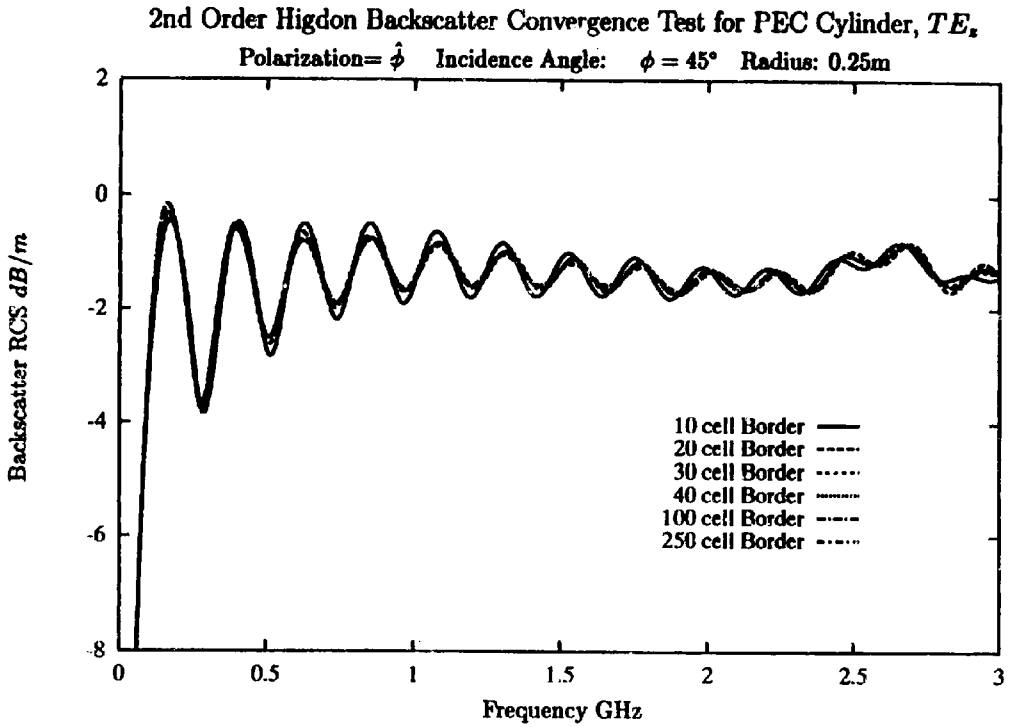

Figure 8: Farzone backscatter convergence for $40cm \times 40cm$ conducting plate using stabilized 2nd Order Higdon ORBC.

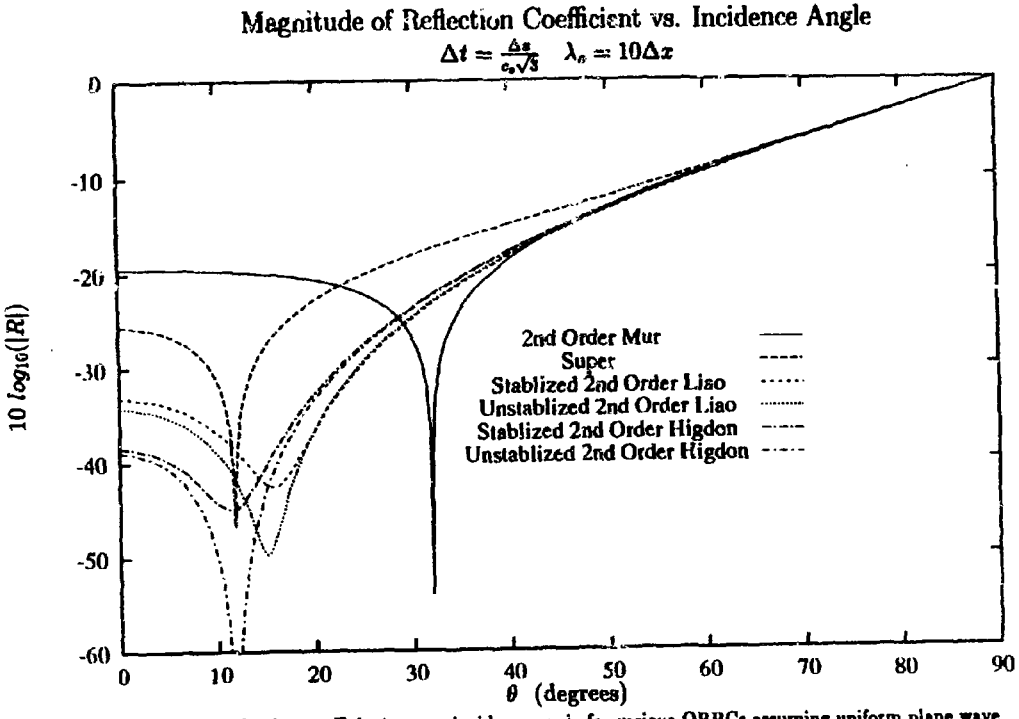

Figure 9: Magnitude of reflection coefficient versus incidence angle for various ORBCs assuming uniform plane wave illumination. All the ORBC coefficients are set for $\theta = 0°$. The stablized Liao reflection coefficient has been stablized with a loss term $d = 0.0075$ applied to T_{11} and the stablized Higdon reflection coefficient has been stablized with $d = 0.005$ applied to T_{11}.

Adaptive Absorbing Boundary Conditions in Finite Difference Time Domain Applications for EMI Simulations

Bruce Archambeault and Omar M. Ramahi
Digital Equipment Corporation
Maynard, MA 01754

ABSTRACT

Absorbing boundary conditions (ABC) are typically constructed to annihilate waves impinging on the mesh truncating boundary at, or close to, normal incidence. These ABCs give sufficient accuracy provided that the truncation boundary is chosen far from the source or scatterer, making the computation (using finite element or finite difference methods) very expensive. This paper presents an alternative formulation to ABCs by optimizing the boundary condition at each boundary cell for the highest likely direction of incidence. The adaptation of the new ABC to the Finite Difference Time Domain (FDTD) solution is simple and effective.

INTRODUCTION

Absorbing Boundary Conditions (ABCs) have been widely used in Finite Difference Time Domain (FDTD) and Finite Element (FE) modeling of open region scattering problems and microwave circuits. Several papers have been published explaining and comparing the performance of a number of different ABCs. The basic operation of these absorbing boundary conditions is to simulate free space, that is, absorb all electromagnetic waves as if there was an infinite amount of free space in place of the ABC. These boundary conditions are enforced along the boundary of the computational domain that is used to truncate the finite difference grid and are usually derived with the assumption that waves impinge on the boundary at angles equal to or close to normal incidence.

To construct the perfect absorbing boundary condition, two major considerations are in order: (1) The boundary condition has to absorb waves impinging on the boundary from all directions simultaneously, and (2) The boundary operator must absorb waves that are both evanescent and traveling at the same time (evanescent waves typically exist in the near field.) To construct a boundary operator that addresses (1) is theoretically possible but would require extensive computer memory and calculations to be performed at each boundary cell, not to mention the possibility of unstable solutions. The construction of boundary operators to accommodate (2) is possible but comes at a considerable cost and complexity in code development time and code execution time. To the knowledge of the authors, the Lindman absorbing boundary condition [1] is the only ABC that has the potential of effectively dealing with evanescent and traveling waves, but involves considerable computational complexity and can be very expensive to implement.

For an important class of electromagnetic radiation problems such as those arising in Electromagnetic Interference (EMI) applications, a large dynamic range is critical to allow accurate prediction of radiation from shielded structures. Typical ABCs can produce reflections on the order of -60 dB relative to the incident pulse amplitude. This level of accuracy in the boundary conditions is usually sufficient for classical scattering applications. However, for EMI applications higher accuracy is needed. It is important to note that this limitation on the accuracy cannot be lifted even if the outer boundary is receded further by increasing the computational domain, since waves still impinge on the boundary at angles that deviate appreciably from normal incidence.

In this work, we made use of the flexibility inherent in the FDTD method to minimize the reflections arising from the use of the ABC. This was possible by adapting the ABC to the wave's most likely direction of incidence at each of the boundary cells. For the special class of radiation problems such as in EMI, the source is typically localized which allows a good prediction of the angles the incident waves make with the boundary. Since the ABC is adapted to a *single* wave (at each boundary cell,) one can get optimal results by using an *exact* boundary condition, or more accurately, an adaptive absorbing boundary condition (AABC).

FORMULATION

There are several ways in which one can construct an adaptive absorbing boundary condition. In this work, the formulation is based on the Liao's absorbing boundary condition [2] which has the advantages that, first, it is readily adaptable to the FDTD grid, and, second, it guarantees stability for a wide range of incident angles.

The Liao's N^{th} absorbing boundary condition can be written as [3]

$$\phi(x,t+\Delta t) = \sum_{j=1}^{N}(-1)^{j+1}C_j^N\,\phi(x-jc\Delta t, t-(j-1)\Delta t)$$

where

$$C_j^N = N!/[j!\,(N-j)!]$$

ϕ is the field value and Δt is the time step used in the FDTD solution. Notice that the field values involved in the absorbing boundary condition are not necessarily evaluated at the FDTD grid. To express the boundary condition in terms of field values available at the FDTD grid, quadratic interpolation is used. For instance, $\phi(x - c\Delta t, t)$ is expressed in terms of the field at the boundary point x as

$$\phi(x-c\Delta t,t) = \frac{(2-s)(1-s)}{2}\phi_1^1(x) + s(2-s)\phi_2^1(x) + \frac{s(s-1)}{2}\phi_3^1(x)$$

where

$$\phi_i^m(x) = \phi[x-(i-1)\Delta x, t-(m-1)\Delta t]$$
$$s = \frac{c\Delta t}{\Delta x}$$

The Liao's ABC as given above is optimized for normal incidence, in the sense that rays hitting the boundary at normal incidence would be completely absorbed. To optimize the Liao's ABC for each cell lying on the lattice truncation boundary, we will make the assumption that only one ray hits the boundary. Define θ to be the angle the assumed incident ray makes with the normal direction at a particular boundary cell. To optimize the boundary condition for each boundary cell, the wave speed is modified by the assumed angle of incidence θ as

$$c_\theta = \frac{c}{\cos(\theta)}$$

The absorbing boundary condition applied at each boundary cell will then be

$$\phi(x, t + \Delta t) = \sum_{j=1}^{N} (-1)^{j+1} C_j^N \phi(x - j c_\theta \Delta t, t - (j-1)\Delta t)$$

It is important to keep in mind that the full strength of the adaptive absorbing boundary condition is realized when the source is localized in space which gives rise to a single ray hitting each boundary cell (assuming the truncation boundary is outside the near field region.) In EMI problems involving radiation through a single slot, the slot width or area is typically small compared to the size of the computational boundary and to the distance from the slot to the lattice truncation boundary. In such problems, the most appropriate choice for the center of the localized source, for the purpose of enforcing the adaptive absorbing boundary condition, will be the geometric center of the slot. For problems where multiple slots of equal or similar widths/area exist, it was found, as can be seen from the numerical results presented below, that if the center of the localized source was taken as the geometric center of the points defining the centers of the slots, then the AABC still gives an appreciable improvement over ABC. Finally, for cases where some slots are larger in size than others, it is recommended that the choice for the center of the localized source should be made such that it will bias the slots with larger sizes.

NUMERICAL RESULTS

Two representative examples were studied to show the effectiveness of using the adaptive absorbing boundary conditions in FDTD solutions. In the first example, we considered the two-dimensional problem of radiation through an 0.01m wide aperture in an infinite perfectly conducting ground screen. The geometry of the problem is shown in Fig. 1. The time step used in the FDTD solution is $\Delta t = 2.36$ ps and the grid size used was $\Delta x = \Delta y = 0.001$m. The source excitation function is the derivative of a Gaussian pulse of width 32 Δt. Since the interest lies in finding the radiation levels outside the source region, the optimal choice for the localized source for the purpose of applying the AABC, is chosen to be the center of the aperture as shown in Fig. 1. The electric field (E_z) at the observation point is shown in Fig. 2 as calculated using the FDTD method for both cases using the ABC and AABC. Since the field contribution at the observation point is coming from two ray-like waves, the first coming through a direct path from the localized source, and the second is the reflec-

tion from the side truncation boundaries. The results shown in Fig. 2 clearly demonstrate that the AABC has significantly reduced the effect of the second ray.

The second example employed the geometry and FDTD parameters used above, but two apertures were added. Each of the three apertures has a width of 0.01m, and the separation between them is 0.01m, as shown in Fig. 3. In this case, the field contribution at the observation point is expected to come from several ray-like waves emanating from the three apertures, thus resulting in an effective source which is more distributed over the conducting screen than what was experienced in the first example (see Fig. 1.) The optimal choice for the localized source will be again at the center of the three apertures as shown in Fig. 3. Numerical results using the FDTD method are shown in Fig. 4, which, despite the existence of a distributed source, i.e., the three huygens' sources at the three apertures, the AABC performed appreciably better than the ABC.

CONCLUSION

This work presented an alternative formulation to ABCs for certain class of radiation problems having localized sources or sources distributed over a small region. By optimizing the boundary condition at each boundary cell for the highest likely direction of incidence, spurious reflections can be reduced significantly resulting in more accurate solutions. The new numerical formulation, or the adaptive absorbing boundary condition is especially well-suited for implementation into the FDTD method.

REFERENCES

[1] E. L. Lindman, "Free space boundary conditions for the time dependent wave equation," *J. Comp. Phys.*, No. 18, pp. 66-78, 1975.

[2] Z. P. Liao, H. L. Wong, B. P. Yang and Y. F. Yuan, "A transmitting boundary for transient wave analysis," *Scientia Sinica* (series A.), No. 27(10), pp 1063-1076, 1984.

[3] W. C. Chew, *Waves and Field in Inhomogeneous Media*. New York: Van Nostrand Reinhold, 1990.

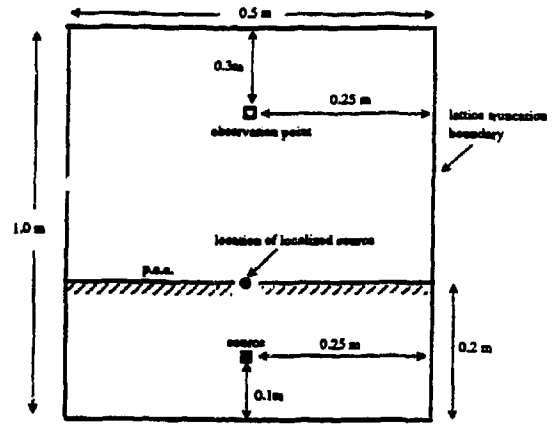

Fig. 1. Geometry for radiation through a single aperture in an infinite ground plane Aperture width is 0.01m.

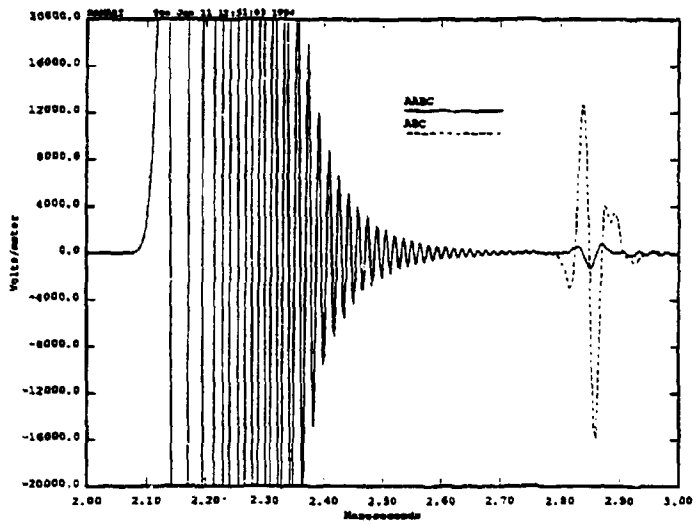

Fig. 2. Electric Field (Ex) at observation point for the single aperture case as obtained using the FDTD method with ABC and AABC.

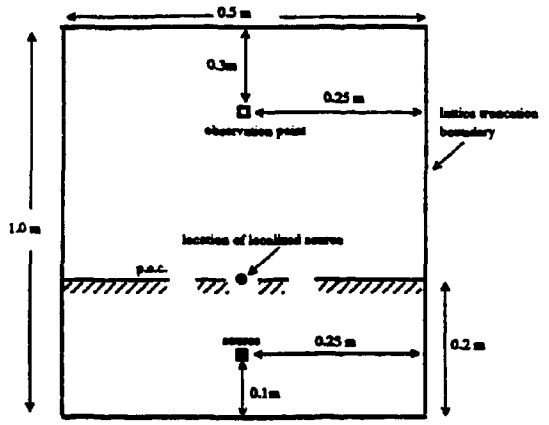

Fig. 3. Geometry for radiation through three apertures in an infinite ground plane. Apertures are 0.01m in width and are separated by 0.01m.

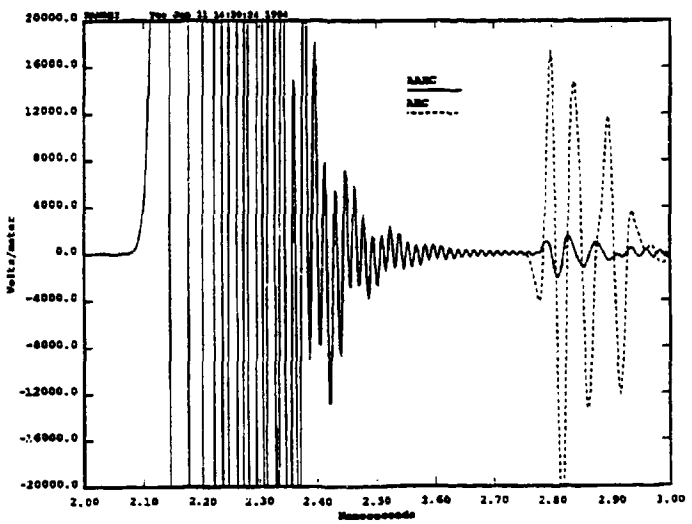

Fig. 4. Electric Field (Ez) at observation point for the three apertures case as obtained using the FDTD method with ABC and AABC.

A Dispersive Outer Radiation Boundary Condition for FDTD Calculations

Brian J. Zook
Southwest Research Institute
P.O. Drawer 28510
San Antonio, TX 77228-0510

Introduction

Outer radiation boundary conditions (ORBCs) in the Finite-Difference Time-Domain (FDTD) method are usually applied to free-space computational boundaries. This is satisfactory for Radar Cross Section and similar problems where the modeled object is suspended in free space. There are a number of applications, however, where the computational boundaries are located in dissipative media which may or may not be dispersive. Examples of such media include soil and plasmas. In these cases, a free-space ORBC results in unacceptable reflections, motivating the development of a dispersive ORBC.

Higdon's Outer Radiation Boundary Condition

Higdon's ORBC has the flexibility to be adapted for use in dispersive media [1]. Not only is it able to handle different wave velocities, but Fang astutely observed the method is able to absorb evanescent waves by including attenuation terms in the ORBC [2]. Higdon originally introduced small attenuation terms to stabilize the ORBC. We wish to emphasize that the attenuation terms are even more general and can be used to account for other forms of attenuation, in particular, to absorb a wave propagating through a dissipative medium. For a wavefield $u(x,t)$ approaching the boundary $x = 0$ from $x > 0$, the Nth-order ORBC can be written as

$$\left[\prod_{i=1}^{N}\left(\frac{1}{v_i}\frac{\partial}{\partial t} + \alpha_i - \frac{1}{\cos\theta_i}\frac{\partial}{\partial x}\right)\right] u(0,t) = 0 . \qquad (1)$$

Each term of this ORBC annihilates plane waves traveling at velocity v_i impinging at an incidence angle of θ_i through a medium with attenuation coefficient α_i.

Higdon discretizes this differential operator by introducing a mixing parameter h, used to mix time and space derivatives. This parameter affects both stability and accuracy. The discrete form of the ORBC can then be written as:

$$\left[\prod_{i=1}^{N} \hat{B}_i\right] u(0, t+\Delta t) = 0 \qquad (2)$$

where

$$\hat{B}_i = s_{xi} \frac{\left(\hat{1} - \hat{z}_t^-\right)\left[(1-h)\hat{1} + h\hat{z}_x\right]}{\Delta t} + \alpha_{xi} - \frac{\left(\hat{z}_x - \hat{1}\right)\left[(1-h)\hat{1} + h\hat{z}_t^-\right]}{\Delta x}. \quad (3)$$

The slowness and attenuation in the x-direction are given by

$$s_{xi} = \frac{\cos\theta_i}{v_i}$$
$$\alpha_{xi} = \alpha \cos\theta_i \quad (4)$$

The differencing operators are defined as: $\hat{1}$, the identity operator; $\hat{z}_x$, which is the spatial projection operator (distance Δx); and $\hat{z}_t^-$, which is the time projection operator (time Δt). The mixing parameter h goes from 0 to 1; typically a value of 0.5 is used.

The discretized boundary condition (2) can be implemented in a convenient "loop" form:

$$\sum_{m=0}^{N} \sum_{n=0}^{N} T_{mn} u_{mn} = 0 \quad (5)$$

where

$$u_{mn} \equiv u(n\Delta x, t + \Delta t - m\Delta t).$$

The T_{mn} matrix elements are coefficients determined from the ORBC parameters by expanding (2); this expansion only needs to be done during ORBC initialization. The matrix elements are found to be convolutions of the first-order operator coefficients in (3). This is a convenient computational form for use in the FDTD program, allowing the ORBC parameters, including order, to be adjusted without reprogramming.

Reflection Coefficient

The reflection coefficient of this ORBC can be determined by assuming the total wavefield $u(x,t)$ is the sum of an outgoing plane wave and (reflected) incoming plane wave, which is then substituted into (5). The reflection coefficient depends upon the ORBC parameters, the incidence angle of the plane wave, and the frequency and complex wavenumber of the plane wave.

The importance of ORBC attenuation coefficients is illustrated in Figure 1, which shows the amplitude reflection coefficient as a function of incidence angle. The medium is a Debye medium with $\varepsilon_s = 9$, $\varepsilon_\infty = 4$, $\sigma = 0.01$ S/m, and $f_0 = 500$ MHz, where the relative dielectric constant is given by:

$$\varepsilon_r = \varepsilon_\infty + \frac{\varepsilon_s - \varepsilon_\infty}{1 + jf/f_0} + \frac{\sigma}{j2\pi f\varepsilon_0} \quad (6)$$

The figure shows the magnitude of the reflection coefficient for 500 MHz plane waves. If no attenuation is included in the ORBC, the reflection is unacceptably large. Including attenuation in the ORBC reduces the reflection significantly.

Figure 2 shows the reflection coefficient as a function of frequency, for plane waves at normal incidence. Again, ORBC attenuation reduces the reflection coefficient significantly. The figure shows that the reflection coefficient goes to unity at zero-frequency; this can also be shown analytically. This suggests that source signals, such as an incident pulse, should not contain significant energy at very low frequencies.

The low-frequency reflection phenomenon is particularly problematic when the computational domain is mostly filled with a dissipative or dispersive medium. In such media, low frequencies experience much less attenuation than high frequencies. This means any low-frequency energy that is reflected from the ORBC is able to travel large distances in the simulation resulting in a low-frequency "ringing" effect, which we have observed. Furthermore, since high-frequency energy may be largely attenuated by the medium before reaching the boundary, the high-frequency reflection coefficient is not as important. This means the ORBC design should be skewed such that a small low-frequency coefficient is favored.

We would like to have an ORBC that has a small reflection coefficient over a broad range of both frequency and incident angle. A simple choice of ORBC parameters would be to choose velocities and attenuation coefficients that correspond to the medium at frequencies within the range of the source spectrum. But as we have seen, a small low-frequency coefficient needs to be favored. Also, ORBC stability, discussed below, is another consideration. We find it useful to examine the reflection coefficient as a function of both frequency and angle by using a contour plot, such as in Figure 3.

Stability of the ORBC

Material and ORBC parameters also affect the stability properties of the ORBC. The analytic differential ORBC (1) is unstable unless the ORBC attenuation is larger than the attenuation of the medium. We have derived a stability criterion for this ORBC. It is based on requiring the roots of the Z-transform to lie inside the unit circle [3]. The stability can be analyzed for each order separately. The root for the i^{th}-order is found to be:

$$z_{i,\mathrm{root}} = \left[1 + \frac{\rho_i (b_i - jc_i)}{d_i + j a_i c_i}\right]^{-1} \tag{7}$$

where

$$\rho_i = \frac{v_i \Delta t}{\Delta x}$$

$$a_i = h(\rho_i + \cos\theta_i)$$

$$b_i = \alpha_i \Delta x \cos\theta_i - \mathrm{Re}\{K - 1\}$$

$$c_i = \mathrm{Im}\{K - 1\}$$

$$d_i = \cos\theta_i + a_i \mathrm{Re}\{K - 1\}$$

$$K = e^{j\tilde{k}_x \Delta x} = e^{j(k - j\alpha)\Delta x \cos\theta}$$

The Z-transform root gives us a stability criterion:

$$c_i^2(2a_i - \rho_i) - b_i(2d_i + b_i\rho_i) < 0 \qquad (8)$$

This expression shows there are two main ways to increase stability: 1) reduce the mixing parameter h, or 2) increase the ORBC attenuation coefficient. Because of the sensitivity of the reflection coefficient frequency response to the ORBC attenuation, we find it convenient to adjust the mixing parameter.

Figure 4 shows a stabilized reflection coefficient, created by adjusting the ORBC parameters for Figure 3. The reflection coefficient is now both larger and smoother, which seems to be characteristics of the stabilization process.

FDTD Implementation

We have implemented this ORBC in an FDTD code. Instead of applying the ORBC to the E-field, as is usually done, we apply it to the H-field, allowing the adjacent E-fields to be updated with the usual interior dispersive update equations. For the interior calculations, we are using the recursive convolution method developed by Luebbers [4].

As an example of the ORBC implementation, we show the results of TE polarization calculations. The configuration is shown in Figure 5. Two calculations are done — one on the small domain Ω_1 and one on the larger domain Ω_2. Both calculations are stopped before reflections from Ω_2 can reach Ω_1. Thus, any differences between the two runs at all field points inside Ω_1 are only affected by reflections from Ω_1. Samples are taken at the two indicated points, just inside Ω_1. The source is an infinitesimal H-field source located at the center of the domains.

Figure 6 shows such a run. Notice the pulse is dispersed but decays nicely to zero showing no instability. The reflections from the edge and the corner were approximately -55 dB and -30 dB, respectively. The source function used was a pulse that has a center frequency near 500 MHz, with energy ranging from 70-2100 MHz (60 dB points).

Figure 7 shows a run with a source function that produces more low-frequency energy. The reflections from the edge and the corner were about -50 dB and -40 dB, respectively. When comparisons are done between the two domain calculations, a low-frequency difference is seen that is slowly dissipated.

Conclusions

We have shown how Higdon's ORBC can be adapted for use in dissipative and dispersive media. A stability criterion and contour plots (frequency vs. angle) of the plane wave reflection coefficient can be used to design an optimal ORBC. Results show a complex relationship between ORBC parameters, material properties, reflection coefficient, and stability. Yet, properly applied, this ORBC allows calculations inside an infinite dispersive medium.

References

[1] Robert L. Higdon, "Numerical Absorbing Boundary Conditions for the Wave Equation," *Math. Comput.*, vol. 49, no. 179, pp. 65-90, July 1987.

[2] Jiayuan Fang, "Absorbing Boundary Treatments in the Simulation of Wave Propagation in Microwave Integrated-Circuits," in *Proc. 9th Annual Review of Progress in Applied Computational Electromagnetics*, Monterey, CA, pp. 322-329, March 22-26, 1994.

[3] M. Moghaddam and W.C. Chew, "Stabilizing Liao's Absorbing Boundary Conditions Using Single-Precision Arithmetic," in *Proc. 1991 IEEE Antennas and Propagation Society Symposium*, Ontario, Canada, pp. 430-433, June 24-28, 1991.

[4] Raymond Luebbers, Forrest P. Hunsberger, Karl S. Kunz, Ronald B. Standler, and Michael Schneider, "A Frequency-Dependent Finite-Difference Time-Domain Formulation for Dispersive Materials," *IEEE Trans. Electromagnetic Compat.*, vol. 32, no. 3, pp. 222-227, Aug. 1990.

i	v_i (m/s)	θ_i	Figure 3 α_i (m^{-1})	Figure 4 α_i (m^{-1})
1	$8.00 \cdot 10^7$	20°	0.60	0.66
2	$1.00 \cdot 10^8$	20°	1.0	1.1
3	$1.23 \cdot 10^8$	20°	7.8	8.6

Table I: ORBC Parameters for Figures 3 and 4

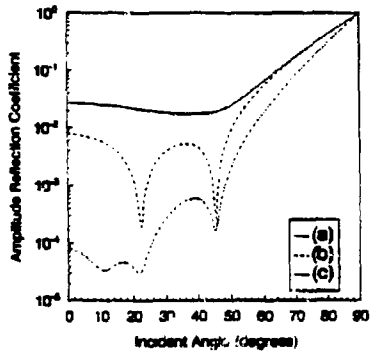

Figure 1: REFLECTION COEFFICIENT VERSUS ANGLE. a) 2nd-order, no ORBC attenuation, θ_i = 20° and 45°; b) 2nd-order, with α_i = 5.8 m^{-1}, θ_i = 20° and 45°; c) 3rd-order, with α_i = 5.8 m^{-1}, θ_i = 0°, 20° and 45°.

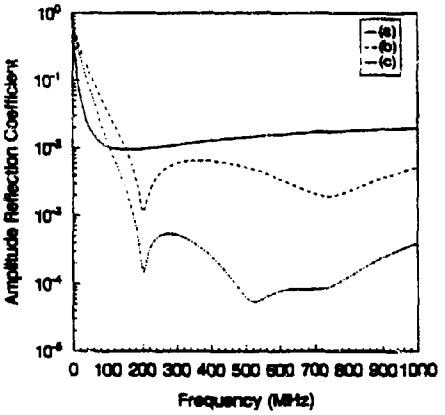

Figure 2: REFLECTION COEFFICIENT VERSUS FREQUENCY. a) 2nd-order, no ORBC attenuation, using 200 MHz and 700 MHz velocities; b) 2nd-order, with attenuation and velocities at 200 MHz and 700 MHz; d) 3rd-order, with velocities and attenuation at 200 MHz, 500 MHz, and 700 MHz.

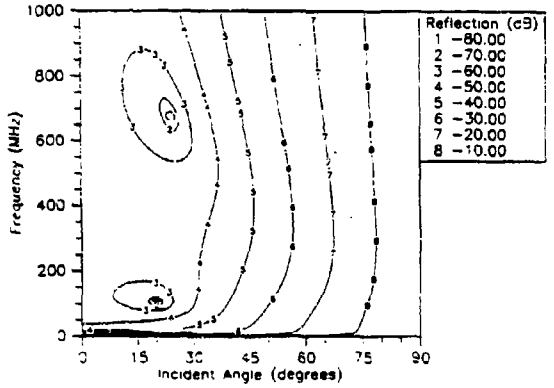

Figure 3: REFLECTION COEFFICIENT VERSUS FREQUENCY AND ANGLE. 3rd-order, using h = 0.5 and parameters shown in Table I.

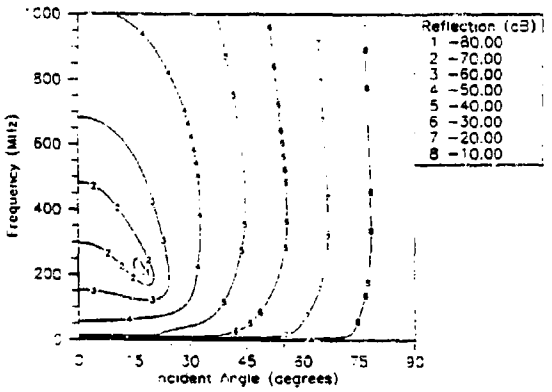

Figure 4: REFLECTION COEFFICIENT VERSUS FREQUENCY AND ANGLE. 3rd-order, using h = 0.1 parameters shown in Table I.

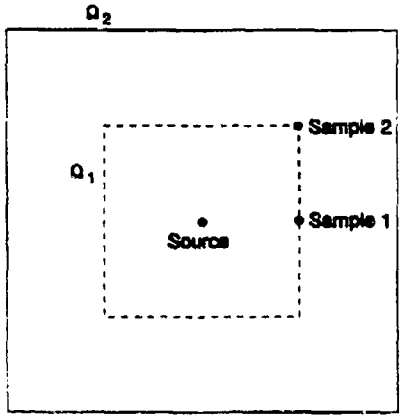

Figure 5: FDTD TESTING GEOMETRY.

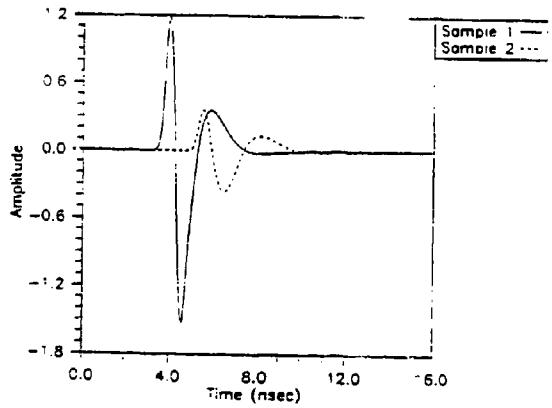

Figure 6: TEST 1 TIME-DOMAIN RESULTS. Uses ORBC parameters from Figure 4, with a source function producing little low-frequency energy.

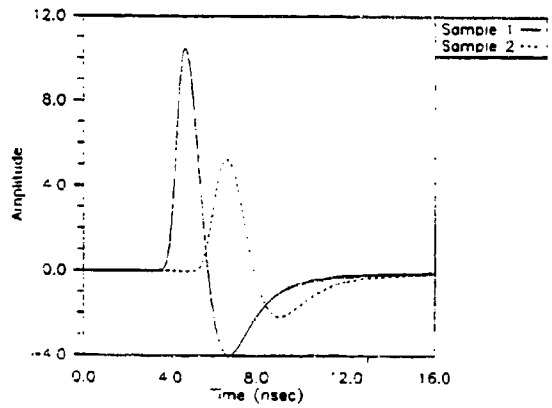

Figure 7: TEST 2 TIME-DOMAIN RESULTS. Uses ORBC parameters from Figure 4, with a source function producing some low-frequency energy.

FDTD ANALYSIS OF A CURVED SAW-TOOTH ANECHOIC CHAMBER ABSORBING BOUNDARY CONDITION

Carey M. Rappaport and Tolga Gürel
Center for Electromagnetics Research
Northeastern University
Boston, MA 02115

Abstract A new type of lattice termination algorithm, based on anechoic chamber absorber foam geometry, with specially simulated electric and magnetic conductivity, chosen to prevent reflections and simulate infinite, open free space, is described and analyzed. The advantage of this ABC over currently used ones is that it prevents reflections from much wider incident angles. Since incident waves need not be normal to this boundary for absorption, the boundary can be placed much closer than previously possible.

When this ABC is implemented using FDTD, a similar but relatively simple operation is performed over each element in the computational grid, making EM field simulation particularly well-suited to massively parallel supercomputer platforms, and enormous computational speed-ups are expected.

INTRODUCTION

Minimizing the amount of computational space between the scatterer and the mesh termination has long been a difficulty in numerical electromagnetics. Since the equivalence principle allows the computation of the electromagnetic field everywhere given the current on a closed surface, all that is required to solve scattering problems is to find the induced current on the scattering object. Finding the field distribution in the region surrounding the object is unnecessary except to give the correct current on the object. It is not possible in general, however, to ignore this field, since it is not known *a priori* what form it will take.

Several types of absorbing boundary conditions (ABCs), with a variety of outer boundary geometries have been reported[1-5]. There are different advantages to the various shapes of this boundary. While a circular boundary is computationally simplest, it is difficult to approximate with rectangular cells, and for long, thin scatterers, large amounts of empty, uninteresting space must be included within the computation domain. A rectangular boundary may pose problems at its corners and edges.

More general ABCs which cancel wave incident from angles other than normally incident to the boundary have been proposed [3-5]. These apply approximate solutions to the wave equation at the radiation boundary, with annihilation for multiple discrete angles. Unfortunately, for each additional angle of annihilation, the order of the differential operator increases. The number of elements in the vicinity of the boundary which must be included in the higher-order difference operation thus increases. Although a wide range of incident angles can be absorbed with these ABCs, the resulting complexity at the boundary may become prohibitive. Also, placing a higher order ABC close to an irregularly shaped scatterer presents difficulties on curved arcs or corners.

SAWTOOTH ANECHOIC CHAMBER-BASED ABC

The idea behind the sawtooth anechoic chamber ABC was first described in the *Journal of Elec. Waves and Appl.* [6]. This presentation analyzed the anechoic chamber ABC using the Finite Difference Frequency Domain method of computing scattered field. However, the Finite Difference Time Domain (FDTD) formulation is more useful when considering a finite wave pulse with a continuous spectrum of frequency components, incident from a single angle [7,8,9]. The sawtooth ABC can easily be applied to FDTD simulation.

The fundamental principle of the new ABC is that used with the carbon-loaded absorber foam pyramids lining the interior walls of anechoic antenna test chambers. The steeply slanted lossy material faces absorb some of the incident energy and tend to redirect any reflected waves into other pyramids for additional absorption. The net effect of the wall of pyramids is to absorb all incident waves. And since incident waves from all directions will be absorbed, the lossy pyramids work very well at preventing wall reflections in antenna test chambers. In a two dimensional analysis, which was considered in this project, the pyramids become triangular saw teeth.

With computer modeling, the material characteristics of the absorbing layer need not be those of real dielectric com-

pounds. Instead, the material can be modeled as being lossy by having both electric and magnetic conductivity σ, σ_M, and with values of permittivity ϵ and permeability μ selected for a perfect match at the second bounce of the normally incident wave. If the vertex angles of these triangles are equilateral, the angle the reflected ray makes with the second triangle face is 90° (0° local incidence angle). This geometry is shown in Figure 1.

As long as $\mu/\epsilon = \sigma_M/\sigma = \mu_0/\epsilon_0$ (which corresponds to maintaining constant frequency domain wave impedance across the boundary), there will be no reflections for normal incidence to a triangle face.

This requirement is difficult to attain with real materials, but quite easy to specify by computer. It is important to make the conductivities large enough so that the wave quickly decays as it propagates into the absorber medium, but not so large that the decaying field is inadequately sampled on the mesh.

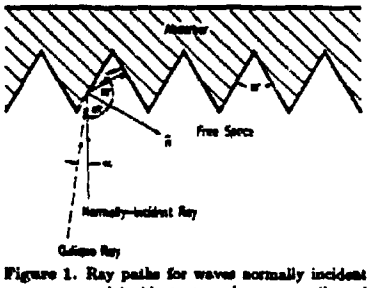

Figure 1. Ray paths for waves normally incident and incident at angle α on equilateral triangular absorbing boundary, showing multiple bounces into medium.

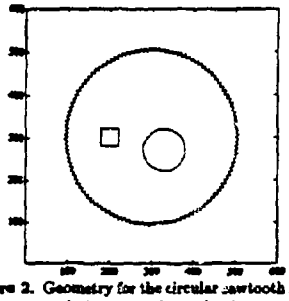

Figure 2. Geometry for the circular sawtooth ABC enclosing perfectly conducting square (to the left) and showing the circular cylindrical pulse maximum level at $t = 0$.

FDTD SIMULATION

Two dimensional FDTD simulation of this equilateral triangle saw-tooth absorbing layer is examined using an excitation pulse which simulates a cylindrical wave, emanating from a point source. Unfortunately, there is no closed form solution, in the time-domain, to the cylindrical wave equation. The standard Hankel function solutions only work in the frequency domain. Therefore, the asymptotic form, with a radial gaussian envelope and a modulating carrier is used:

$$\overline{E}(x) = \hat{z}E_0 \frac{e^{-\left(\frac{\rho-ct}{W}\right)^2}}{\sqrt{\rho/\rho_0}} \cos\frac{\pi}{\delta}(\rho - ct), \qquad \rho = \sqrt{(x-x_0)^2 + (y-y_0)^2}$$

For large radii, this form approximates the wave equation well. For lesser radii, however, a small but noticeable inward-propagating wave is generated. To eliminate spurious effects of this artifact, a small disk of matched, lossy ABC media is inserted at the center of the cylindrical wave. Being small enough to not interact with the out-going wave, this disk is kept in place until the artifact is reduced to insignificant levels, and then removed. The above equation is discretized by using $x \rightarrow i\Delta, y \rightarrow j\Delta, t \rightarrow n\Delta t$. The computational domain is chosen as a rectangular grid of points (i, j), $0 < i \leq i_{max}$, $0 < j \leq j_{max}$.

The magnetic field components, which follow directly from Faraday's law, have the exact same space and time dependence, but are orthogonal to $\overline{E}$ and are reduced in magnitude by the material impedance $\eta = 377\Omega$.

The ultimate use of the sawtooth ABC is in the form of a contour enclosing the scatterer. Figure 2 shows this geometry, with an off-center square scatterer. The source center is at $(x_0, y_0) = (270, 330)$ or 30 by 30 grid points away from the center of the computational domain. The pulse half-width, $W = 15$.

To save computation time, and reduce the strongly oblique incident pulse interaction with the ABC, the total fields are calculated only in a reduced square region immediately surrounding the diamond-shaped scatterer[10]. Scattered fields are calculated outside the total field region. The boundary between the two field regions is specified in terms of the total field minus the calculated incident field for the external (scattered field) calculation, and in terms of the scattered field plus the same calculated incident field for the internal (total field) calculation. With this procedure, the incident field never encounters the ABC, so no severe oblique angle illumination occurs.

The calculations are performed with normalized electrical parameters, μ and ϵ, with the only requirements being that $\sqrt{\mu/\epsilon} = \eta = |E|/|H|$, and normalization $\sqrt{\mu\epsilon} = c = 1$ for simplicity. Since this is a time-domain simulation, the time scale is arbitrary, and there is no frequency scale. The only physical scale is the relative lengths of the sawtooth edge and the half-width, W of the gaussian envelope. The conductivity is specified in terms of the dielectric relaxation time $\tau = \epsilon/\sigma$. Thus, for a wave to decay by a factor of e in 20 time steps, $\sigma = \epsilon/20$. Also, the Courant condition, which specifies the relative sizes of time and space steps in the FDTD algorithm, $c\Delta t/\Delta z$ is chosen to be 0.5, implying that the wave advances $n/2$ steps in space in an interval of n time steps.

GRAPHICAL DATA PRESENTATION

For FDTD simulations in which modulated incident fields are simulated, a great deal of data must be calculated and displayed. There are certainly concerns of the limited dynamic core memory needed for each time calculation step, and with massive amounts of disk storage to record the results at the required intervals. The most debilitating aspect of complicated FDTD simulation analysis, however, is in the accurate graphical display of the computed fields.

The most descriptive means of presenting field data is by using three-dimensional and contour plot graphics. There are many graphical software packages available, but none can intelligibly plot the complete behavior of a wave which oscillates 100 times across the computational frame. The problem comes from displaying all the data, resulting in an impossibly dense grid with 600 by 600 crossing lines. The overabundance of data is usually dealt with by under-sampling. The field data can be sampled every 12 points to yield a 50 by 50 point graphical 3-D surface (as is presented in this report, see figure 3a). These mesh plots are quite readable, but because of the undersampling of the modulation, the field appears quite discontinuous.

A valuable alternative was developed to illustrate the gross behavior of the scattered fields without resorting to changing the scale or resolution of the plots. The alternative is to numerically low-pass filter the field data. This is the same well-established technique sometimes used in AM radio signal demodulation. In the current application, the wave signal field data is available for spatial points rather than as a function of time, so the smoothing involves low-pass spatial filtering.

Rather than using a formal Fourier transform or convolution to filter the spatial data, the envelope can be simply detected by finding the absolute values of the modulation peaks, and then connecting these values with straight line segments. As long as the modulation is fast enough so that the changes between peaks are small relative to the peak values, using straight segments to join the peaks does not introduce much error. There are about 3 peaks within the full gaussian pulse width, $2W$, so the error is minimal. The line segments are found in both x- and y-directions, yielding first-order finite element patches covering the absolute value of the modulated 2-dimensional spatial waveform.

Once the surface patches are found, the intermediate sample points are easy to find using the bi-linear interpolation. The result of smoothing and interpolating the data of Figure 3a is shown in Figure 3b. Note that the wave is now circular, continuous, and entirely positive. This plot does not depict the modulation at all, but shows the overall envelope shape. Used in conjunction with Figure 3a, the smoothed data gives considerable information about this highly modulated extremely numerically dense wave.

COMPUTATIONAL RESULTS

FDTD results have been obtained for the cylindrical source illuminating a square scatterer. For each of Figures 3 through 6, the first figure on the page presents the actual data values, the second shows the smoothed bulk field behavior. These figures give the total electric field in the presence of the square perfectly conducting scatterer shown in Figure 2. The ABC is positioned on the circle with radius 200 grid units, 100 units in from each edge of the domain.

Figure 3 gives the total field at 150 time steps, where the first scattering from the square is visible in the middle of the bottom part of the plot. The smoothed plot (Figure 3b) obscures the scatterer by interpolating right over it. It is for smaller effects, such as this scatterer, that the actual data plot (Figure 3a) is essential. Figure 4 gives the pulse at $t = 250\Delta t$, when interaction with the circular sawtooth ABC becomes visible. Examining the upper right corner, at the point on the ABC closest to the pulse center, the amplitude begins to decrease. The smoothed plot, Figure 4b shows this effect of the wave penetrating the ABC most clearly. At 400 time steps, Figure 5 demonstrates that almost all the incident pulse has entered the upper right corner, and been attenuated. Some of the incident pulse is still present in the lower left corner, not having completely reached the ABC yet. The final plot in the incident wave sequence, Figure 6, occurs for $t = 600\Delta t$.

The absorption of the incident pulse is clearly visible in this sequence. Also, the scattering from the square dominates the fields in the center of the computational domain. The specular reflection from the scatterer and its shadow are

clearly seen in Figure 5. Figure 6 indicates that only the scattered field remains at 600 time steps, with no reflections of the incident wave from the ABC circle.

CONCLUSIONS

An improved absorbing boundary condition based on anechoic chamber absorber foam prevents reflections from a wide range of incidence angles, and hence could be positioned very close to electromagnetic scatterers. The reduction of unimportant computational space leads to savings of computer memory and CPU time. In the test cases considered, the novel ABC absorbs almost all of the incident field, regardless of the dominant frequency components and incident angles of the scattered waves. Based on the results presented, this novel ABC is effective at terminating the lattice.

One particular advantage of this novel saw-tooth ABC is that it "parallelizes" very efficiently. While other higher-order pseudo-annihilation operator ABCs require matrix inversion or other special handling of boundary grid points, the saw-tooth ABC can be treated just like the rest of the computational grid. The only difference with calculations in the lossy ABC layer is the use of electric and magnetic conductivity. Since the same operations are performed inside the layer as outside, the code is particularly simple and efficient for SIMD computers, and less error-prone on conventional computers. Numerical experiments on massively parallel supercomputers, indicate that for very large FDTD simulations, 90% of the total computational CPU time is spent on calculating the necessary coefficients for the third-order Liao ABC at the grid perimeter. For a 4000 by 4000 point grid, there are about one-thousand times as many points in the interior as on the perimeter, yet the bulk of the calculation was spent on the ABC.

Furthermore, the ABC can be closely positioned around a scatterer of any shape by merely specifying the boundary location. Other ABC methods may only work on planes parallel to grid axes or on circular boundaries. The extra savings of using the sawtooth ABC on a piecewise-straight-with-elliptical-arc grid termination could be considerable.

REFERENCES

1. Bayliss, A., Gunzburger, M., and Turkel, E., "Boundary Conditions for the Numerical Solution of Elliptic Equations in Exterior Regions," *SIAM Journal of Applied Mathematics*, vol. 42, 1982, pp. 430-451.

2. Engquist, B., and Majda, A., "Absorbing Boundary Conditions for the Numerical Simulation of Waves," *Mathematics Computation*, vol. 31, 1977, pp. 629-651.

3. Lee, C., Shin, R., Kong, J., and McCartin, B.J., "Absorbing Boundary Conditions on Circular and Elliptic Boundaries," *PIERS Symposium Proceedings*, July 1989, pp. 317-318.

4. Lindman, E., "Free-Space Boundary Conditions for the Time Dependent Wave Equation," *Journal of Computational Physics*, vol. 18, 1975, pp. 66-78.

5. Rigdon, R., "Numerical Absorbing Boundary Conditions for the Wave Equation," *Math. Comp.*, vol. 49, 1987, pp.65-90.

6. Rappaport, C. and Bahrmasel, L., "An Absorbing Boundary Condition Based on Anechoic Absorber for EM Scattering Computation," *Journal of Electromagnetic Waves and Applications*, vol 6, no.12, Dec. 1992, pp. 1621-1634.

7. Yee, K.S., "Numerical Solution of Initial Boundary Value Problems Involving Maxwell's Equations in Isotropic Media", *IEEE Transactions on Antennas and Propagation*, vol. AP-14, 1966, pp. 302-307.

8. Taflove, A., Umashankar, K., "The Finite-Difference Time-Domain (FDTD) Method for Electromagnetic Scattering and Interaction Problems," *Journal of Electromagnetic Waves and Applications*, vol. 1, 1987, pp. 243-267.

9 Rappaport, C., "Preliminary FDTD Results form the Anechoic Absorber Absorbing Boundary Condition," *1992 IEEE AP-S Symposium Digest*, July 1992, pp. 544-547.

10. Mur, G., "Absorbing Boundary Conditions for the Finite-Difference Approximation of the Time-Domain Electromagnetic-Field Equations," *IEEE Transactions on Electromagnetic Compatibility*, vol. EMC-23, no. 4, Nov. 1966, pp. 377-382.

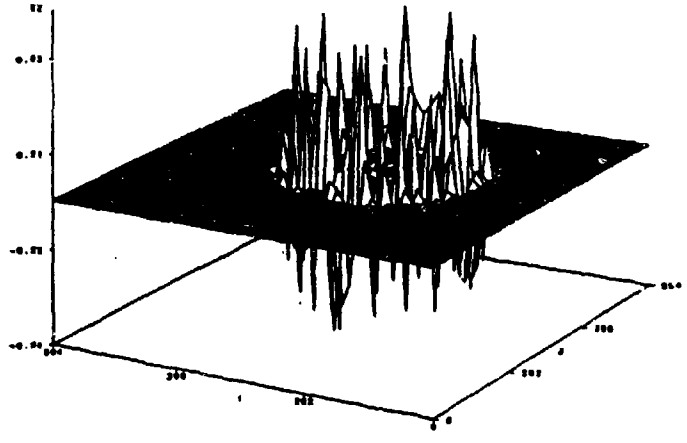

Figure 3a: Actual computed data for total field due to cylindrical pulse, $t = 150$.

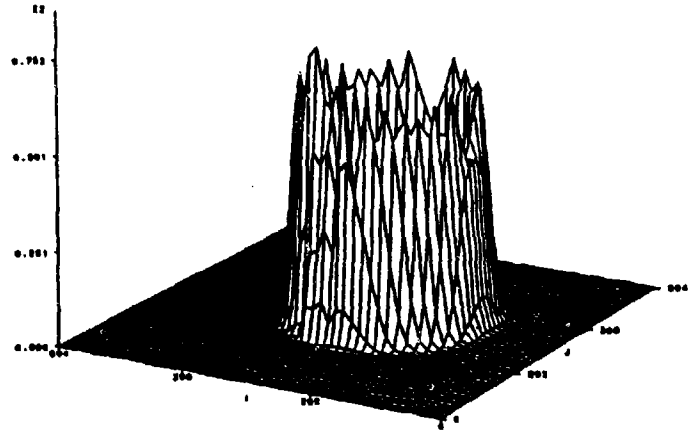

Figure 3b: Smoothed data at $t = 150$.

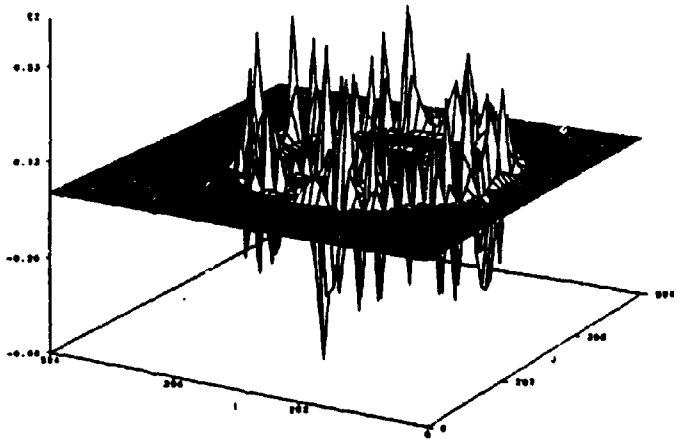

Figure 4a: Actual computed data for total field due to cylindrical pulse, $t = 250$.

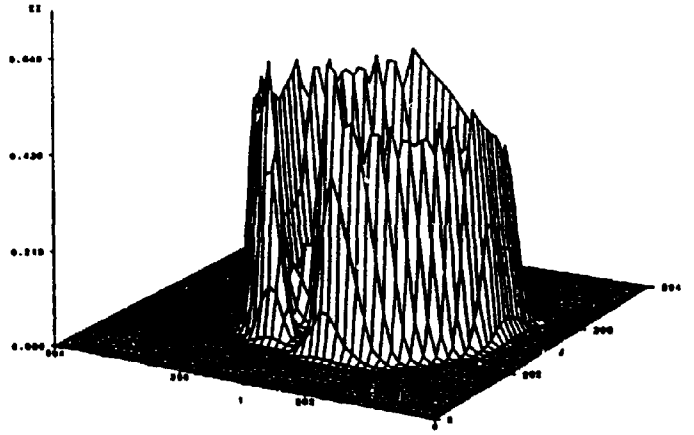

Figure 4b: Smoothed data at $t = 250$.

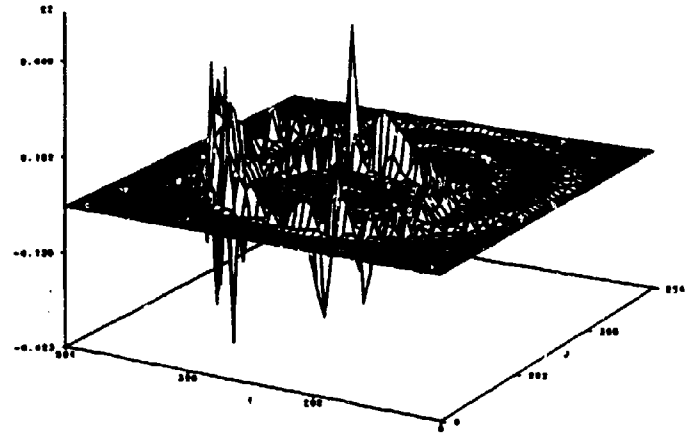

Figure 5a: Actual computed data for total field due to cylindrical pulse, $t = 400$.

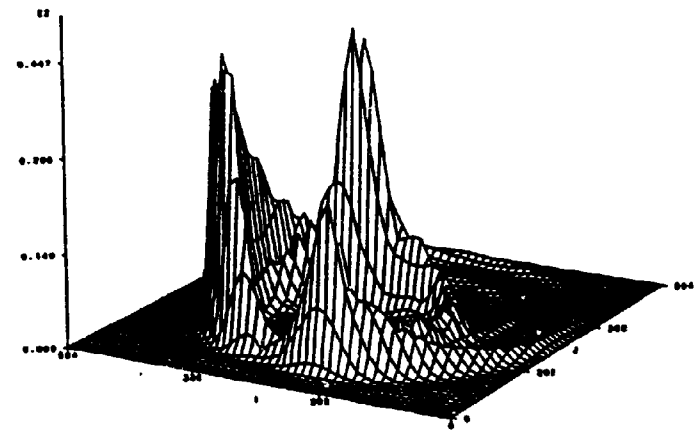

Figure 5b: Smoothed data at $t = 400$.

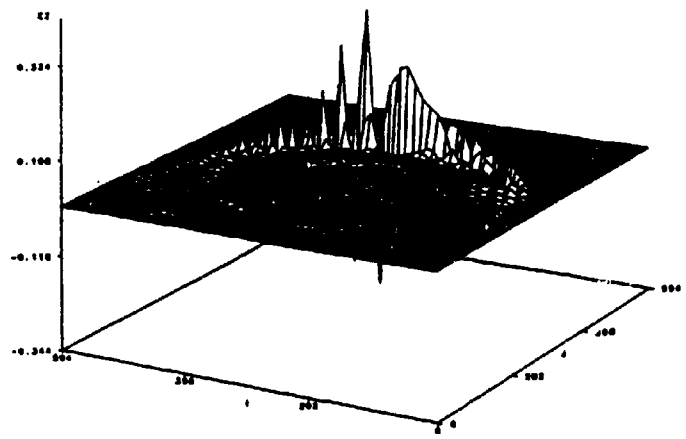

Figure 6a: Actual computed data for total field due to cylindrical pulse, $t = 600$.

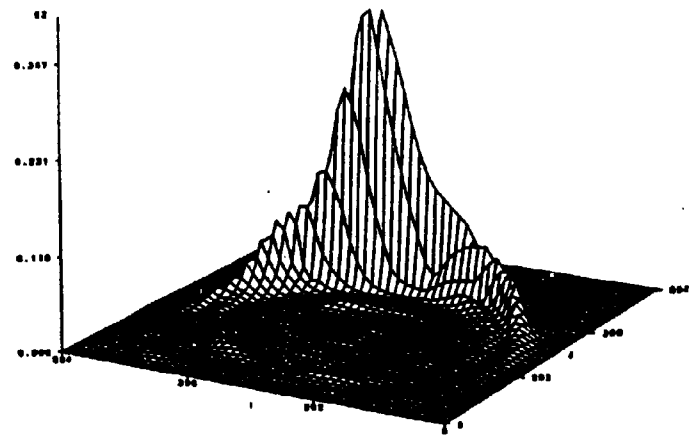

Figure 6b: Smoothed data at $t = 600$.

SUPERIMPOSED MAGNETIC FIELD IN FORCED CONVECTION LAMINAR BOUNDARY LAYER

by

Alexandru M. Morega and Mihaela Morega

Department of Electrical Engineering
POLITEHNICA UNIVERSITY of BUCHAREST
Bucharest, ROMANIA

ABSTRACT. The Blasius problem for the laminar boundary layer is reformulated for the case of an electroconductive fluid. The impact of an external magnetic field is observed through the similitude (Blasius) function $f(\eta)$. Further more, the associated thermal (Pohlhausen) problem is solved for this class of flows and the temperature profile is obtained. Finally, the true path of convection as well as the effect of the external magnetic field are found to be better witnessed by the *heatfunction*, a novel physical quantity.

1. Introduction

Electroconductive fluids convecting in external (imposed) magnetic fields are the siege of supplementary (thermal, mechanical, etc.) phenomena. When the incident magnetic field is steady (time independent) and the flow is slow (such as moderate free stream velocity or natural convection) the main effect is an increase of the drag force produced through electrodynamic (Lorenz) forces.

If the electroconductive fluid is a heat carrier as well, as it is the case of forced convection processes, the heat transfer pattern is influenced too.

In many situations (crystal growth, electrometallurgy, magnetohydrodynamics, etc.) this is a side effect and it is important to know in what sense it acts - improving or not the process under control. Chandrasekhar [1] studied the modification and the stability of the flow pattern of a fluid under the influence of a magnetic field. Oreper [2,3] analyzed this effect in a crystal growth natural convection context while Morega [4,5] showed the corresponding modification of the thermal structure of the apparatus. The hydrodynamic analysis of fully developed internal flows (Hagen - Poiseuille) in a magnetic field (Hartmann's problem) is reported by Mocanu [7].

Less attention was devoted to the changes induced in forced convection boundary layers (the slender transitional region, in the fluid, leaning the solid wall bathed by the flow) and specifically in conjunction with the heat transfer. The interesting features of such an interaction can be investigated through simple, basic models. Therefor, we focus on the heat transfer problem of a steady, laminar forced convection boundary layer flow - the Blasius and Pohlhausen problems. The viscous flow under study leans a thermally constrained (isothermal), solid flat wall. The objective of our work is to evaluate the effects of an imposed magnetic field, transverse to the flow direction. It will be seen that for the specific magnetic field assumed, the main features of the convecting flow are preserved - the velocity and temperature profiles are still self - similar. Further to completing the classical (Blasius) model, by including terms to account for the magnetic field contribution and solving the combined flow and temperature problems, we use the *heatfunction* - a novel physical quantity - to show the modification which occurs in the true path of convection by the presence of the magnetic field. Introduced a decade ago by Bejan [6], the heatfunction imposed itself in the heat transfer community, at least as a powerful visual means in convection processes [8,9,10].

2. Formulation of the problem and analysis

The equations that govern the mass, momentum and energy in the constant property forced convection laminar boundary layer flow of Fig. 1 are [11]:

$$\frac{\partial u}{\partial x} + \frac{\partial v}{\partial y} = 0 , \tag{1}$$

$$u\frac{\partial u}{\partial x} + v\frac{\partial u}{\partial y} = \nu\frac{\partial^2 u}{\partial y^2} - \frac{\sigma B^2}{\rho}u , \tag{2}$$

$$\rho C_p\left(u\frac{\partial T}{\partial x} + v\frac{\partial T}{\partial y}\right) = k\frac{\partial^2 T}{\partial y^2} . \tag{3}$$

Here ν is the kinematic viscosity, σ is the electric conductivity, ρ is the mass density, C_p is the heat capacity, k is the thermal conductivity and T is the absolute thermodynamic temperature. It is assumed that the external (imposed) magnetic field is time-independent and oriented in the k-direction (oz axis). Its presence (and, hence, influence) is limited to a slender region inside the boundary layer. Further to the scale analysis [6] the (Oy) projection of the momentum equation, as compared to the (Ox) one, is a balance between second-order (small) terms and, thus, not relevant.

The specific form of the magnetic flux density is considered to be the principal part (first order) of a Laurent expansion for a more general field $B = B(y) = B_o\frac{L}{y}$ (L is a characteristic length, typically the length of the plate in the flow direction). This definition for B satisfies the divergence-free restriction and preserves the similarity features of Blasius - Pohlhausen velocity and temperature boundary layers. The difficulty that this quantity diverges for $y \to 0$ is alleviated through the observation that the flow is assumed viscous and, hence, on the plate: $u = 0$ and $v = 0$. The (electroconductive) fluid is then motionless and the quantity $\sigma B^2 u$ (Lorenz force) vanishes in this limit.

Further more, the reaction of the induced electric field upon the incident magnetic field is neglected.

In general (3-D), the steady state form of the energy equation can be written as:

$$\mathrm{div}\left(w\,T - \alpha\,\mathrm{grad}\,T\right) = 0 , \tag{4}$$

where $\alpha = k / (\rho C_p)$ is the thermal diffusivity and w is the 3-D velocity field. It is possible to introduce a vector potential, H(x,y,z) through its curl:

$$\mathrm{curl}\,H = w\,T - \alpha\,\mathrm{grad}\,T . \tag{5}$$

This quantity, labeled "heatfunction" was introduced by Bejan [6] for the 2-D flows in Cartesian coordinates and used thereafter to evidence the heat transfer process in convective media. When $w = 0$ (i.e. pure conduction) H reduces to the classical heat flux. The heatfunction, as a visual aid, is recognized to be superior to the isothermal representation in convection heat transfer [8, 9, 10].

From the point of view of *the fundamental theorem of vector fields* [7] in 2-D problems H is completely defined through (5) since (one can easily check) $\mathrm{div}\,H = 0$. In the special case of the 2-D boundary layer (eqs. 1-3), eq. (5) reduces to:

$$\frac{\partial H}{\partial y} = \rho C_p u \left(T - T_{ref} \right), \tag{6}$$

$$-\frac{\partial H}{\partial x} = \rho C_p v \left(T - T_{ref} \right) - k \frac{\partial T}{\partial y}. \tag{7}$$

For conciseness we shall present only the cold isothermal plate (T_o) washed by a warm fluid whose free stream temperature is T_∞ (warm). The reference T_{ref} is set to T_o, the lowest temperature in the boundary layer. All other existing similarity thermal boundary layers (imposed heat flux, etc. [12]) can be treated analogously.

Following the classical (similarity) Blasius solution [11]:

$$u = U_\infty f', \tag{8}$$

$$v = \frac{1}{2}\left(\frac{\nu U_\infty}{x} \right)^{1/2} \left(\eta f' - f \right), \tag{9}$$

where, $f' = df / d\eta$ U_∞ is the free stream velocity of the fluid, U_∞ is the free stream velocity and

$$\eta = \frac{y}{x} Re_x^{1/2}, \quad Re_x = \frac{U_\infty x}{\nu}. \tag{10}$$

After some manipulations, eqs. (1) and (2) produce the ordinary differential equation:

$$-\frac{1}{2} f f'' = f''' - \frac{f'}{\eta^2} Ha_L^2, \tag{11}$$

where $Ha_L = B_o L \sqrt{\frac{\sigma}{\mu}}$ is the Hartmann number [7]. Eq. (11) differs from the classical Blasius equation through the second term in the right hand side. The boundary conditions for this (Cauchy) problem (1), are [11]:

$$f(0) = 0, \quad f'(0) = 0, \tag{12}$$

$$f'(\eta_{inf}) = 1. \tag{13}$$

It is worth noting that eq. (11) preserves the same property of invariance to the transformations:

$$f \to b f, \quad \eta \to \frac{\eta}{b}, \tag{14}$$

as the initial (Blasius) equation [6] which greatly reduces the trial-and-error shooting procedure of finding $f''(0)$ - the missing boundary condition.

Following Pohlhausen's (similarity) analysis, the nondimensional temperature $\theta(\eta) = (T - T_o)/(T_\infty - T_o)$ satisfies [11]:

$$\theta'' + \frac{Pr}{2} f \theta' = 0, \tag{15}$$

where $Pr = \nu / \alpha$ is the Prandtl group, subject to the boundary conditions:

$$\theta(0) = 0, \quad \theta'(\eta_{inf}) = 1. \tag{16}$$

For the similarity boundary layers, [13] an analytic solution for $\widetilde{H}$ is available:

$$\widetilde{H}(\bar{x}, \bar{y}) = \bar{x}^{1/2}\, g[\eta(\bar{x}, \bar{y})], \tag{17}$$

where,

$$\widetilde{H} = \frac{H}{\rho C_p U_\infty (T_\infty - T_0) L\, Re_L^{1/2}}, \tag{18}$$

is the nondimensional heat function and

$$g(\eta) = f(\eta)\,\theta(\eta) + \frac{2}{Pr}\,\theta'(\eta). \tag{19}$$

is the *similarity heat function*.

The first part of the problem, eqs.(11), (12), (13) was written as an autonomous system of ODEs and solved using a 4^{th} / 5^{th} order adaptive η-step Runge Kutta algorithm with error control per η-step (tolerance set to 10^{-6}). A first run was carried out with $f''(0)=1$ (assumed value) and a second (final) run with $f''(0) = f''(\eta_{inf})^{-3/2}$, based on the invariance property of eq. (11) mentioned before. Since classically, $\eta_{inf} > 5$ we set $\eta_{inf} = 20$ (a safe limit) and kept it throughout the analysis.

The second part of the problem, the temperature field, was then solved. Again, the Runge Kutta algorithm and the trial-and-error scheme was used to integrate eqs. (15) and (16), written as an autonomous system of ODEs and to pin point the appropriate initial condition, $\theta'(0)$. The needed $f(\eta)$ function was obtained through a locally parabolic interpolation scheme of the tabulated output for the flow phase. At this stage $\widetilde{H}(\bar{x}, \bar{y})$ can be computed using $f(\eta)$, $\theta(\eta)$, $\theta'(\eta)$ (locally parabolic interpolations) and the analytic formula (17).

3. Results

Figure 2 shows the influence of the magnetic field on the convection system via $f'(\eta)$ (the u-component of the velocity) for Ha = 0.; 0.5; 1.; 1.5; 2.

For a fluid such as silicon, with $\rho = 2330$ kg m^{-3}, $\nu = 4.3\cdot10^{-6}$ m^2 s^{-1}, and $U_\infty = 1$ cm s^{-1}, L = 1 cm this would mean B_0 = 0; 5; 10; 15; 20 mT. Figure 3 shows the corresponding $\theta(\eta)$ profiles when Ha = 0.; 0.5; 1.; 1.5; 2., for silicon (Pr = 1.48).

Nusselt number, defined [6] through $Nu = -k\,(\partial T/\partial y)_{y=0} / (T_0 - T_\infty)$ and plotted in Fig. 4, evidences a clear reduction in the heat absorbed by the cold wall. One can speculate that in the limit when $B_0 \to \infty$ there will be only a conduction region in the boundary layer and, hence, the Nu number (ratio convection / conduction) will reach an asymptotic value - this trend is apparent in Fig. 4 too.

Figures 5 and 6 show $\vartheta(\bar{x}, \bar{y})$ and $\widetilde{H}(\bar{x}, \bar{y})$ for the Ha = 0 and 2 cases under investigation. The temperature contour plots indicate an increasingly cold boundary layer region for increasing values of the Ha number. No other trend is readily distinguishable from these plots (Figs. 5b and 6b) while the contour plots for the heatfunction offer some more subtle insights in the true path of convection. First, they are orthogonal to the wall indicating that at this surface the heat transfer is only through conduction. For increasing Ha numbers, this orthogonality is extended to a larger domain - conduction is predominant over the transport component in the energy equation. The heatlines density is decreasing with the Ha number indicating a colder boundary layer, as the constant temperature lines suggest too. The effect of the imposition of a magnetic field is, for short, equivalent to a shift (decrease) in the Pr number for the fluid - an apparent increasing of the conduction part in the overall heat transfer process.

4. Conclusions

In this study we reported the modified Blasius equation to include the presence of a specific (fast decaying) external magnetic field. The resulting profiles (velocity and temperature) maintain the self similarity property.

Although in this work we addressed only the cold isothermal wall (Pohlhausen problem), it is clear that this approach is applicable to all other thermal cases (based on Blasius flow solutions) known to preserve this property - heat flux walls, etc. [12].

The degree of departure from the velocity and temperature master profiles (no magnetic field) can be monitored through the variation of the Ha (Hartmann) group. Qualitatively, a second "knee" appears when Ha ≠ 0 in the velocity profile, while the temperature profile keeps the same shape.

The heatlines prove to be more sensitive than the isotherms to the changes in the flow structures. The orthogonality to the isothermal plate is consistent with the hypothesis of viscous flow (adherent to the wall). This shows that the heat transfer is only through diffusion (no temperature convection) at the plate level. When Ha > 0 the heat lines "orthogonality" is apparent in a larger zone and their density decreases - it is a stem that the magnetic drag of the flow reduces also the temperature convection. The diffusion counterpart in the overall heat transfer is larger in the presence of the magnetic field. This features are not easily distinguishable in the classical isothermal charts.

The decrease in the overall heat transfer process is confirmed through the decay experienced by the Nu (Nusselt) group too. The effect of an external magnetic field can be sought as an artificial decrease of the Pr (Prandtl) number of the fluid.

5. References

1. Chandrasekhar, S., *Hydrodynamics and hydromagnetic stability*, Clarendon (1962).
2. Oreper, G., M. and Szekely, J., "The effect of an externally imposed magnetic field on buoyancy driven flow in a rectangular cavity", J. Cryst. Growth, 64, pp. 505 - 515 (1983).
3. Oreper, G., M. and Szekely, J., " The effect of a magnetic field on transport phenomena in Bridgman- Stockberger crystal growth", J. Cryst. Growth, 67, pp. 405-419 (1984).
4. Morega, Al., M., "Magnetic field influence on the convective heat transfer in the solidification processes", Part. I, Rev. Roum. Sci. Techn., Electr. Energ., 33, 1, pp. 33-39 (1988).
5. Morega, Al., M., "Magnetic field influence on the convective heat transfer in the solidification processes", Part. II, Rev. Roum. Sci. Techn., Electr. Energ., 33, 2, pp. 155 -166 (1988).
6. Bejan, A., *Convection heat transfer*, John Wiley and Sons, New York, 1984.
7. Mocanu, C., I., *Electromagnetic field theory*, 2nd edition, Ed. Didactica si Pedagogica, Bucharest (1992).
8. Littlefield, D. and Desai, P., "Buoyant laminar convection in a vertical cylindrical annulus", J. Heat Transfer, 108, pp. 814 - 821 (1986).
9. Aggarwal, S., K. and Manhapra, A., "Use of heatlines for unsteady bouyancy-driven flow in a cylindrical enclosure", J. Heat Transfer 111, pp. 576 - 578 (1989).
10. Ho, C., J. and Lin, Y., H., "Natural convection of cold water in a vertical annulus with constant heat flux on the inner wall", J. Heat Transfer 112, pp. 117 - 123 (1990).
11. Incropera, F., P. and De Witt, D., P., *Fundamentals of heat and mass transfer*, 3rd edition, John Wiley & Sons, New York (1990).
12. Sparrow, E., M. and Lin, H., S., "Boundary layers with prescribed heat flux - application to simultaneous convection and radiation", Int. J. Heat Mass Transfer 8, pp. 437 - 448 (1965).
13. Morega, Al., M., *Optimal geometries of electronic packages cooled by forced convection*, Ph. D. Thesis, Duke University (1993).

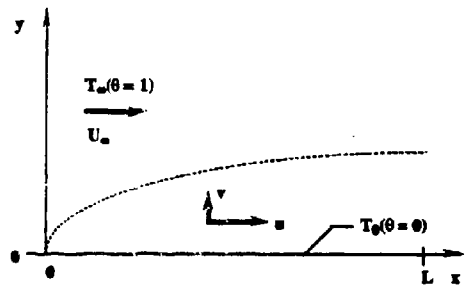

Figure 1

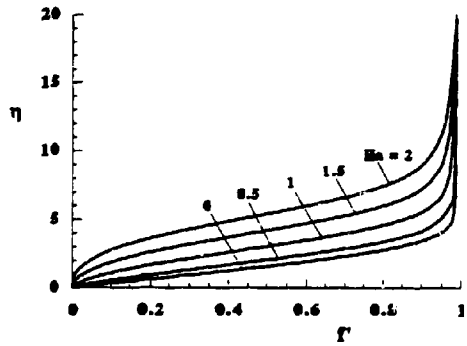

Figure 2

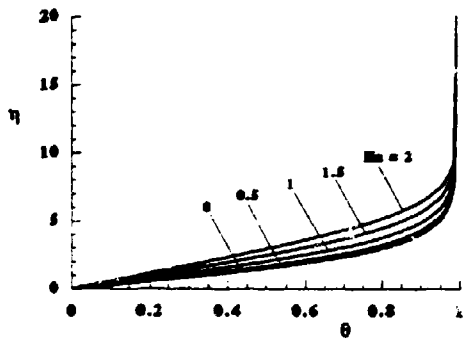

Figure 3

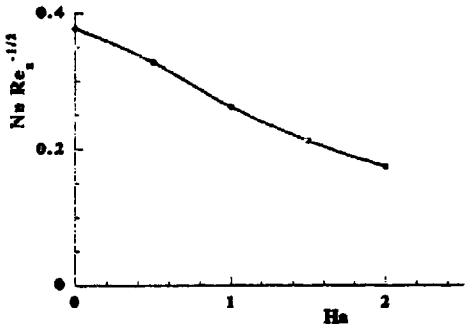

Figure 4

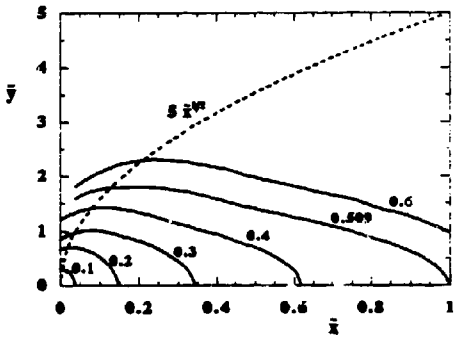

Ha = 0

$\bar{H}(\bar{x},\bar{y})$

Figure 5a

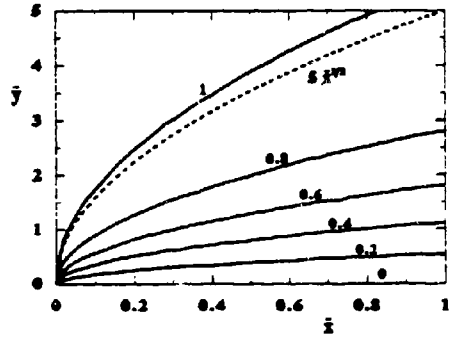

Ha = 0

$\theta(\bar{x},\bar{y})$

Figure 5b

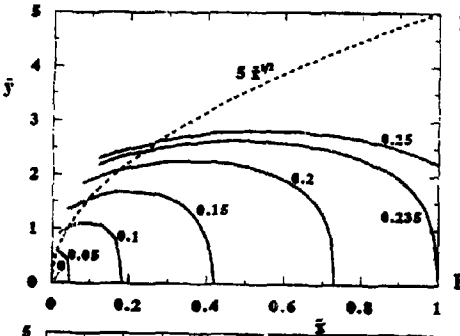

Figure 6a

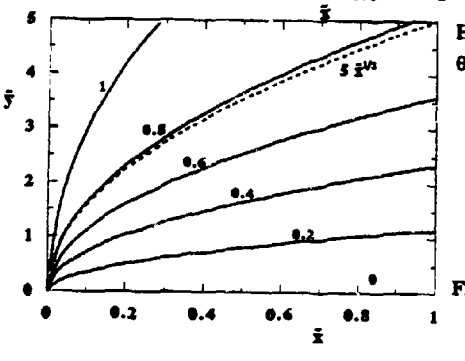

Figure 6b

SESSION 6:

OPTIMIZATION

Chair: Richard Gordon

OPTIMIZED BACKSCATTERING SIDELOBES FROM AN ARRAY OF STRIPS USING A GENETIC ALGORITHM

Randy Haupt and Azar Ali*
Department of Electrical Engineering
2354 Fairchild Dr Suite 2F6
United States Air Force Academy, CO 80840

Abstract - A uniform array of closely spaced perfectly conducting thin strips has a backscattering pattern with a maximum relative sidelobe level of about -13 dB. We present a method of using a genetic algorithm to strategically remove some of the strips in this array to yield the lowest backscattering sidelobe level possible.

INTRODUCTION

A closely spaced grid of thin strips has a backscattering pattern very similar to that of a perfectly conducting plate of the same size. Increasing the spacing between the srtips increases the resistivity of this structure as seen by the incident wave. Consequently, the peak scattering return is reduced but the relative sidelobe levels remain fairly constant. Once the spacing between the strips gets too big, the backscattering pattern no longer resembles that of a flat plate.

One possible method of reducing the backscattering sidelobe levels is to nonuniformly space the strips in the grid. The nonuniform spacing spatially tapers the current distribution across the grid. If the distribution of strips is most dense in the center and gradually thins towards the edges, then certain strip geometries may lower the backscattering sidelobes.

This paper investigates options to lower the sidelobes of an array of thin strips by thinning the population, in other words by removing some of the strips in a uniform grid. Thinning is used in antenna arrays to lower the sidelobe levels in the far field pattern of the array. Usually, however, a statistical method is used to thin the array. Here, we apply a genetic optimization algorithm [1] to arrive at an ideally thinned distribution of strips that results in the lowest backscattering sidelobe level.

FORMULATION

Consider an array of uniformly spaced strips as shown in Figure 1. The strips are infinitely long in the z-direction and have a center-of-strip to center-of-strip separation of d and each strip has a width of 2w. Only backscattering is considered, so the direction of the incident wave and the direction of scattering are given by ϕ. The incident plane wave has an electric field polarized in the z-direction and has a magnetic field normalized to one. The currents induced on the strips are found

from an integral equation formulation given by

$$e^{j2\pi x_m \cos\phi} = \frac{\pi}{2}\int_{-w}^{w} \sum_{n=1}^{N} J_n(x')\, H_0^{(2)}(2\pi\,|x_m - x'|)\, dx'$$

where

- x' = distance in wavelengths
- $J_n(x')$ = current density on strip n
- $2w$ = strip width in wavelengths
- $H_0^{(2)}$ = zeroth order Hankel function of the second kind
- x_m = distance in wavelengths to center of strip
- ϕ = angle of incidence

The current density is found using point matching with pulse basis functions. Excellent results were obtained with three pulses per strip. Once the current is found, the backscattering RCS is calculated from

$$\sigma(\phi) = \frac{\pi}{2}\left|\sum_{n=1}^{N} (2w)\, J_n(x_m)\, e^{j2\pi x_m \cos\phi}\right|^2$$

Figure 2 is an example of a backscattering pattern of a fully-populated array of strips. The strip width is $2w=0.037\lambda$ and the spacing between strip centers is $d=0.1\lambda$, where λ is the wavelength. Its maximum relative sidelobe level is -13.3 dB. Our goal is to reduce the maximum sidelobe in this backscattering pattern by removing strips from the array. The new thinned array of strips has a tapered current density across the array.

OPTIMIZING THE GRID USING A GENETIC ALGORITHM

We begin with the uniform grid having the backscattering pattern shown in Figure 2. The idea is to lower the relative backscattering sidelobe levels by removing strips from the grid. Thus, the width of the strips and spacing between strips is an integer multiple of d . The grid is encoded into a string of binary bits that is called a gene. A "1" in the gene indicates the strip is present, while a "0" indicates the strip is gone (Figure 3). Each gene has a unique backscattering pattern. The objective function to be minimized is the lowest maximum relative sidelobe level in the backscattering pattern.

The genetic algorithm starts with a random set of M genes [2]. Each gene contains the information for whether a strip is present in the array or not and has an associated maximum relative sidelobe level. The genes are ranked from the minimum sidelobe (genetically superior) to the maximum relative sidelobe level (genetically inferior). Genes in the bottom half of this list are discarded. The remaining genetically superior genes mate and form new offspring. Mating takes place between two genes when the genes swap genetic material and form two new genes. A random bit is selected for each set of parents. The parents exchange the bits to the right of the selected bit to form two offsprings. Now, there are M genes of which M/2 are genetically superior from the previous list and M/2 are the offspring from these genes. One final step is to randomly mutate a

small percentage of the bits. A mutation just changes a "1" to a "0" or a "0" to a "1". This mutation is an important step in the algorithm, because it helps the algorithm avoid local minima.

Genetic algorithms are slow. On the other hand, they search for a global minimum and can handle a large number of unknowns. In addition, they are well suited to optimizing problems with discrete parameters.

OPTIMIZED GRID OF STRIPS

The genetic algorithm is applied to the uniform array of 40 strips. Starting with 80 genes and optimizing over 8 generations produces a genetically superior gene given by [1 0 0 0 0 1 1 1 1 0 1 0 1 1 0 1 1 1 0 1 1 1 0 1 1 0 1 1 0 1 0 1 1 1 1 0 0 0 0 1]. The thinned array represented by this gene now consists of only 24 strips but has a relative sidelobe level of -17.1 dB. Figure 4 shows the backscattering pattern of the optimized array. Note that the peak RCS is also reduced, because 40% of the strips were removed from the grid.

REFERENCES

1. J.H. Holland, "Genetic algorithms", Scientific American, July, 1992, pp. 66-72.
2. Goldberg, David E. **Genetic Algorithms.** Addison-Wesley, New York: 1989.

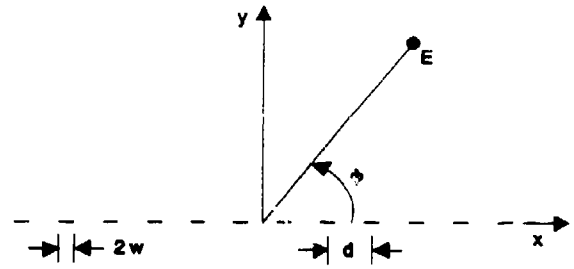

Figure 1 Diagram of an array of perfectly conducting thin strips.

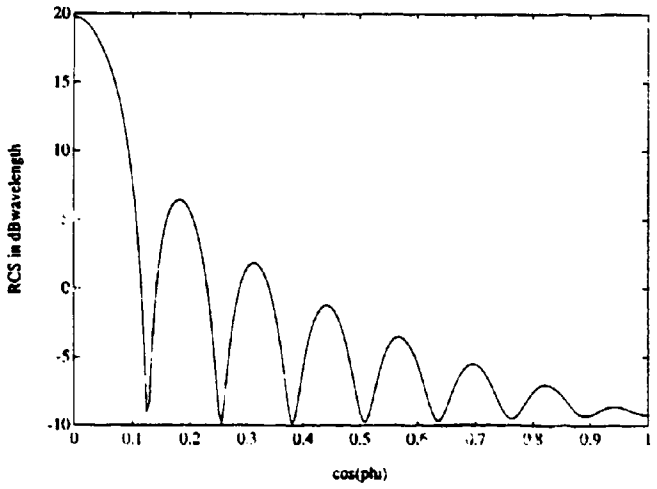

Figure 2 Backscattering pattern of a fully-populated array of 40 strips with d=0.1 λ and 2w=0.037λ. The maximum relative sidelobe level is -13.3 dB.

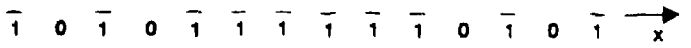

Figure 3 Gene associated with an array of uniformly spaced strips. A "1" indicates the strip is present, and a "0" indicates a strip is absent.

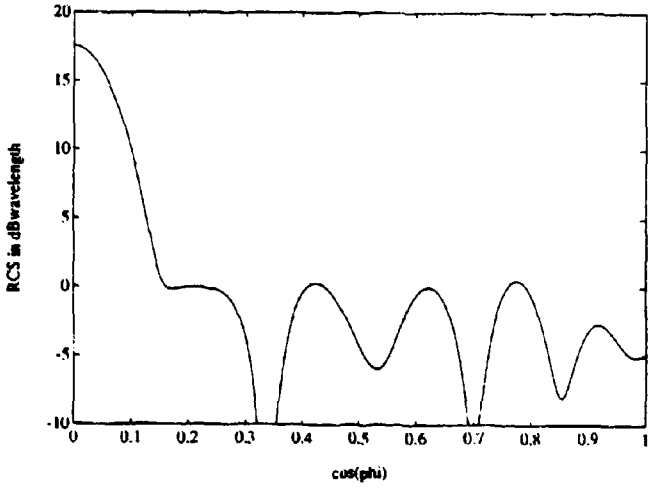

Figure 4 Backscattering pattern of a thinned array of 40 strips with d=0.1λ and 2w=0.037λ. There are 24 strips present and 16 removed. The relative sidelobe level is -17.1 dB.

NUMERICAL ELECTROMAGNETICS CODE OPTIMIZATION DESIGN SOFTWARE (NECOPT)

James K. Breakall, Joel S. Young,
Robert J. Bauerle, Athena I. McDowell
Department of Electrical Engineering
The Pennsylvania State University
University Park, PA 16802

Todd A. Erdley
Paragon Technology, Inc.
200 Innovation Blvd., Suite 240
State College, PA 16803

This paper discusses a new antenna optimization software package developed for personal computer based workstations. The Numerical Electromagnetics Code OPTimization design software package (NECOPT) is a new and innovative approach for designing antennas. Most previous antenna modeling software has been only concerned with the analysis of antennas where the user could test or determine the performance characteristics. For designing antennas, one still needed to either test different designs by trial and error, or apply "handbook" approaches. The computer is an extremely powerful tool which is utilized to dramatically accelerate the optimization process in NECOPT.

Circuit analysis codes use the same methods that we now apply to antenna analysis software to produce a package that can optimize the design of antennas. The circuit analysis tools have been very useful over the traditional methods of circuit design and have made a major impact in analog,digital and microwave circuit design. We have incorporated the powerful techniques used in circuit design codes and have produced antenna design software which works with the well tested NEC antenna analysis package. Using this package, the user can provide design goals for the antenna and the computer will perform an iterative adjustment of user selected parameters on the antenna to achieve the final results.

The implementation of this package has been achieved using highly accurate, fast and flexible optimization techniques which act as a driver for the NEC analysis software. The user creates a data input file very similar to the standard NEC data file and indicates which parts of the file are to be considered the variables for the computer to iteratively adjust in order to achieve a desired performance goal. The user can set limits for the variables in order to maintain "realism" for the final design. After the desired performance characteristics have been established, the computer will begin an iterative adjustment of the parameters until the goals are realized.

DESCRIPTION

The NECOPT software package consists of a quasi-Newton optimizer integrated with a double precision version of NEC2 and the required interfaces to provide the necessary communication between the two sections. Both constrained and unconstrained optimization is provided by the optimizer. User input is provided by a series of command lines similar to standard NEC input which are appended to a standard NEC input file. The input section defines all the desired design goals, variables, and optimization parameters. In addition to optimization the NECOPT package has the ability to sequence any variable defined in the NEC input file over a specified range of values. This may be useful for developing design curves or performing a worst case analysis. The intermediate values of the variables and goals may be output to a plot file for further processing or graphical analysis.

GOALS

Goals in the NECOPT system define what parameters the user is interested in optimizing or examining. Four different NEC output types may be sampled and processed with the NECOPT package, far-field patterns, near-field patterns, source impedance, and segment currents. For each goal there are many options which select specific parts of the desired NEC output data or define the processing to be performed on it. The many options provide a generic and versatile interface to nearly every type of NEC output data. High level characteristics such as gain, pattern beamwidth, VSWR, front-to-back ratio, and many others may be chosen for optimization and output processing.

Multiple goals may be specified for the same run of the NECOPT package. Each goal may be separately weighted to allow the user to balance the significance of each goal to meet the specific needs of the problem at hand.

VARIABLES

Variables identify which parameters of the NEC input file are to be optimized or changed. Three types of variables are available to the user, optimization variables, function variables, and step variables. Variables may specify any non-integer quantity in a NEC input file. Items such as geometry position and length, loading, excitation, and frequency, may be defined by variables.

Optimization variables are controlled by the optimizer and are automatically adjusted to meet the defined goals. The range of optimizer variables may be limited by user input bounds.

Function variables are used to define one variable in terms of other previously defined variables. They are not part of the optimization process. They only serve as an aid in defining the user's input structure. Function variables are particularly useful for varying the size of symmetric input structures, or other structures where relative proportions must be maintained. They allow non-physical parameters to be optimized or scanned.

Step variables are simply sequenced from an initial value to an end value by the optimizer. They are useful for sweeping a parameter and observing the corresponding output. When combined with an appropriate output selection they may be used to determine worst/best case performance over a given range of one or more parameters.

EXAMPLE

This example demonstrates the use of the NECOPT package in the design of an optimum 3-element Yagi antenna. The only design goal was to maximize the front-to-back ratio by changing the lengths of the director and reflector elements. The element spacing was fixed as was the length of the driven element. The element radius was fixed at 1.0E-4 wavelengths. Table 1 contains a summary of the Yagi parameters, and Figure 1 contains a diagram of the structure.

Figure 2 contains a surface plot of the problem space. Step variables in the NECOPT package were used to step the reflector and director lengths over the complete matrix of values. Reflector length is shown on the Y-axis; director length is shown on the X-axis; and the front-to-back ratio is shown as the surface value or the Z-axis. The optimum front-to-back ratio of 22.4 dB is obtained with a reflector length of 0.499λ and a director length of 0.457λ. From the figure it is apparent that there are several other local maximum points on the surface.

The optimizer was used to find the optimum location from several different starting points. Because there is more than one local maximum in the problem space, the optimizer will find different solutions depending on the choice of starting point. Figure 2 shows the optimization paths taken when the variables were constrained between the specified bounds. The paths shown in Figure 2 start with a circle and terminate with an X. The paths are overlaid on a contour map of the surface shown in Figure 1. The optimizer is very well behaved in this mode. When the optimizer reaches a local maximum point on a boundary it terminates without wasting computation time searching for solutions which are not desired.

Figure 4 shows the optimization paths when the variables are not constrained. For the unconstrained case, depending on the initial starting point, the optimizer may waste valuable computation time searching for undesired solutions which are out of bounds. This situation will depend on the initial starting point.

CONCLUSIONS

This software package represents a major breakthrough as compared to the antenna design methods currently available. The NECOPT package brings the proven analysis power of NEC together with optimization to create a powerful new design tool for antenna engineering. The NECOPT package significantly expands the users ability to develop an optimum antenna design in a timely fashion.

Table 1

3-Element YAGI parameters		
Element	Length (λ)	Spacing (λ)
Reflector	0.4 - 0.6	0.182
Driven	0.5	NA
Director	0.4 - 0.6	0.182

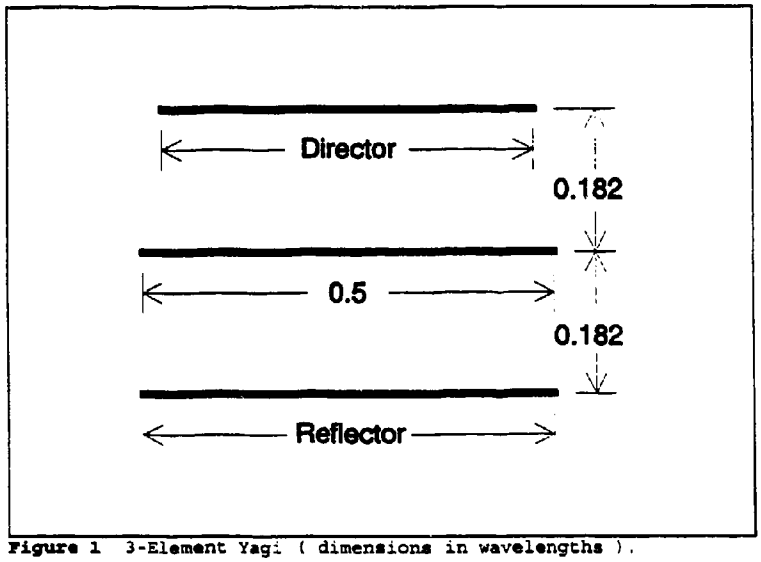

Figure 1 3-Element Yagi (dimensions in wavelengths).

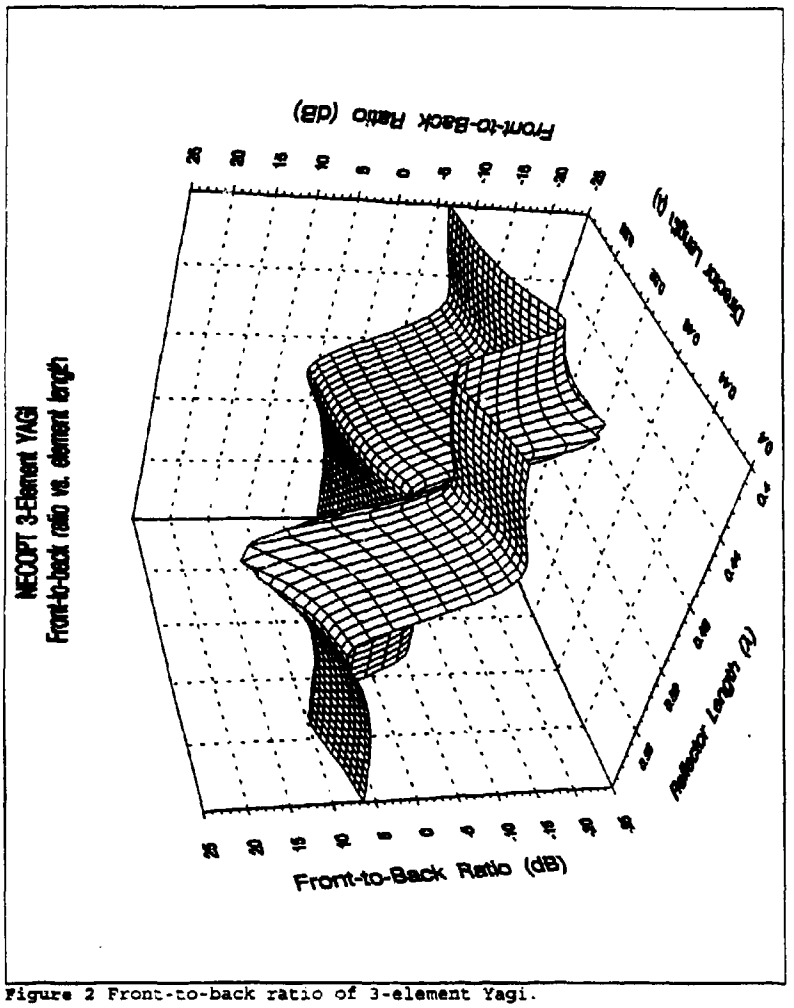

Figure 2 Front-to-back ratio of 3-element Yagi.

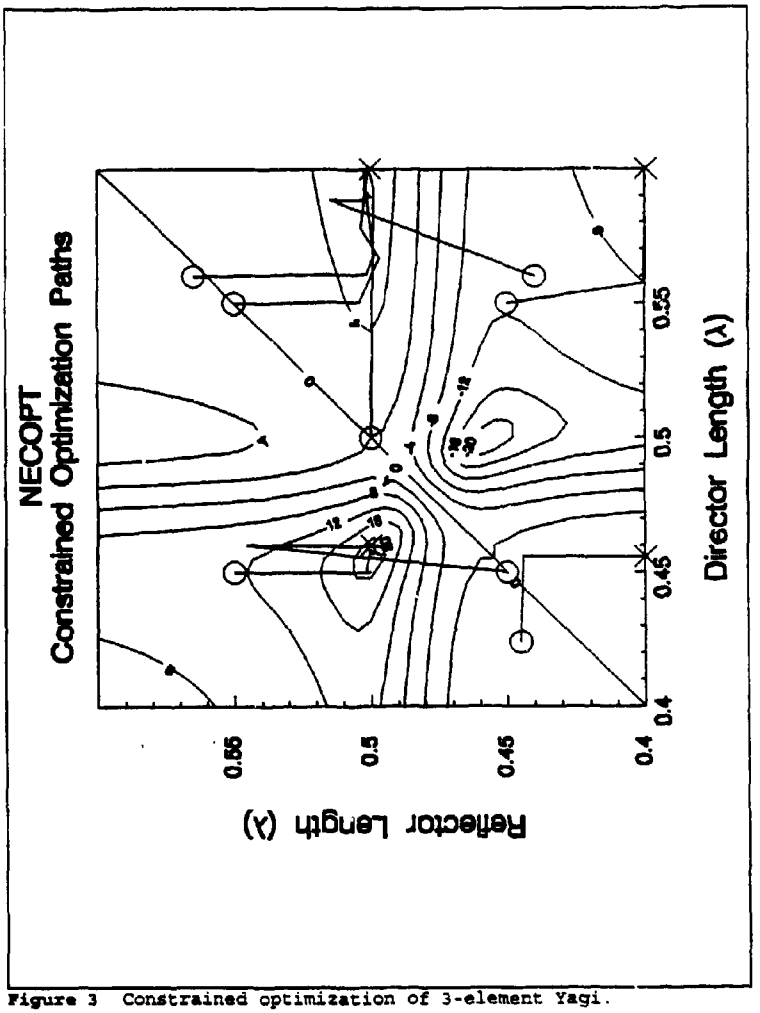

Figure 3 Constrained optimization of 3-element Yagi.

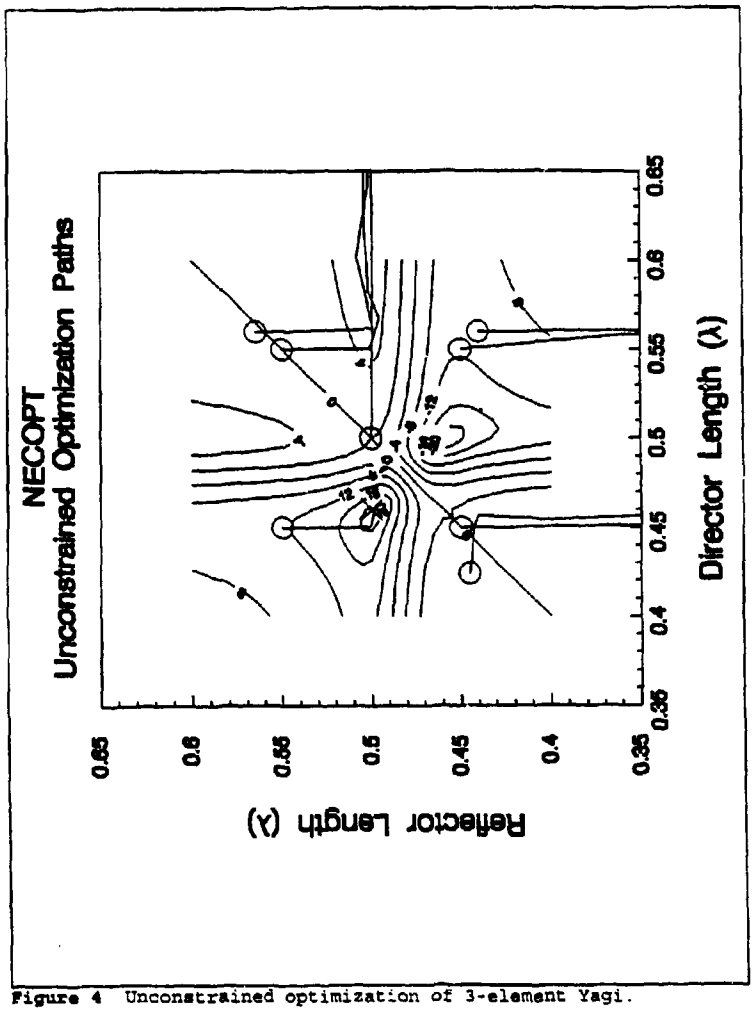

Figure 4 Unconstrained optimization of 3-element Yagi.

On the Computation of an Optimised Interference Adaptive Radar Signal

by
Heiner Kuschel
FGAN-FHP
Forschungsinstitut für Hochfrequenzphysik
Neuenahrer Str. 20
53343 Wachtberg-Werthhoven

1.Introduction

One of the research projects of FGAN-FHP is an experimental VHF-radar which is used to study specific problems of low frequency radar. Since the VHF-band is mainly used for radio communications, the problem of mutual interference of radio services and radars has to be solved if the benefits of low frequency radar are to be exploited. Here, a method has been developed to avoid mutual interference by spectrally shaping the basic radar signal waveform in order not to transmit radar energy at frequency ranges, within the radar signal bandwidth, where a narrow band radio transmission has been detected. The basic radar signal is a linear frequency modulated pulse (chirp) of 2 MHz bandwidth.
The basic chirp pulse is spectrally shaped so that spectral notches occur at frequencies of radio services. Thus, by receiving the radar signal echo with a matched filter, shaped in the same manner, neither the radar is affected by radio transmissions, nor radio services suffer from radar interferences.
The detection properties of the radar, however, are strongly affected by this pulse shaping. Unwanted sidelobes occur and can mask weaker targets. To counter this effect, further shaping of the signal spectrum is applied.

2. Spectral Signal Shaping

The basic radar signal is a linear frequency modulated pulse (chirp) of 2 MHz bandwidth and a duration of 16.4 µsec, yielding a pulse compression factor of 32. The radar pulse is sampled at 3.9 MHz resulting in 64 samples per pulse. In the frequency domain, the spectrum of the sampled signal consists of 64 frequency samples. The 2 MHz bandwidth of the pulse is represented by 32 frequency samples with a spectral resolution of 60 kHz.
To adapt the radar signal to the present interference situation, a spectral analysis of the electromagnetic environment is conducted using a fast Fourier transform (FFT) algorithm. This spectrum is compared to a given threshold, resulting in a weighting vector w(f) which is set to zero at those spectral samples, where the interference exceeds the threshold and which is set one elsewhere. The vector w(f) is multiplied with the signal spectrum, producing spectral notches at the frequencies of interference. Fig.1 shows the low pass representation of an interference spectrum (a) and the shaped spectrum of the basic chirp pulse (b), adapted to the interference situation. In the time domain, the spectral shaping can be regarded as an amplitude and phase modulation of the radar pulse. Fig 2 shows a block diagram of the spectral shaping process.

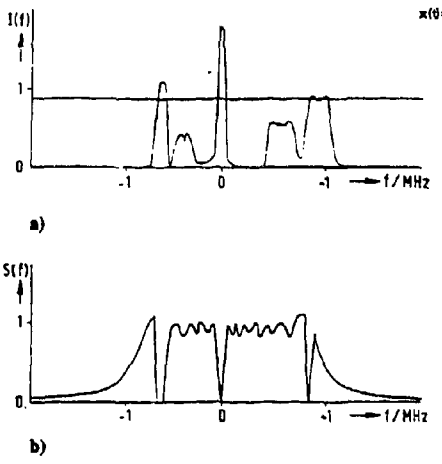

Fig. 1 a) interference spectrum, b) shaped signal spectrum

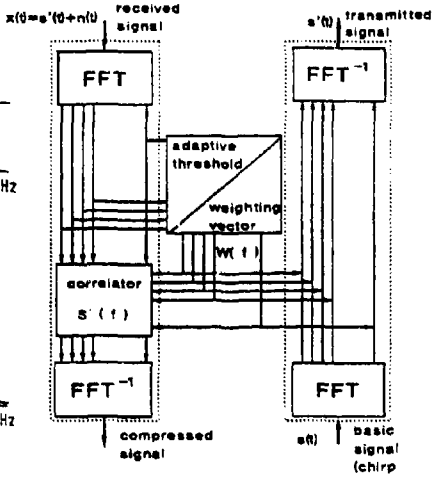

Fig. 2 block diagram of spectral shaping process.

3. Distortion by Shaping

The choice of the radar waveform is subject to several requirements, one the most vital is a point target response with narrow a peak and low sidelobes after compression. Here, the Doppler tolerant chirp waveform was chosen as a starting point. The signal properties, like a narrow main peak, low sidelobes and Doppler tolerance can be displayed in the so called ambiguity function. It is defined as /1/

$$A(t_d, f_d) = |\chi_0(t_d, f_d)|^2$$

where χ_0 is the cross-correlation function of the radar signal and its dopplershifted version, t_d denoting the time delay and f_d denoting the Doppler shift frequency. Fig 3 shows the ambiguity function of a chirp signal of 5 MHz bandwidth and 10 µsec duration for different Doppler shifts f_d, as an example.If an interference situation is assumed and the radar signal is spectrally shaped to avoid transmission in disturbed areas, the ambiguity function is subject to changes, too. Depending on the spectral location and bandwidth of the interferences within the radar signal bandwidth, the Doppler tolerance of the radar signal is affected, as well as the time sidelobe structure of the ambiguity function. Since at VHF-radar frequencies Doppler frequency shifts are small, even for fast targets, all interesting Doppler frequencies are within the mainlobe of the ambiguity function. Fig 4 shows a small section of the ambiguity function for a spectrally shaped radar signal with +- 3kHz Doppler shift region, indicating a negligible distortion of the main peak due to spectral shaping.

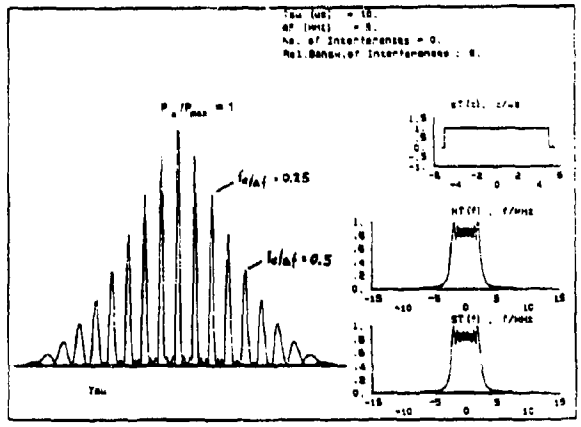

Fig.3 Ambiguity function of the basic chirp signal for different Doppler shifts with respect to the signal bandwidth $f_d/\Delta f$.

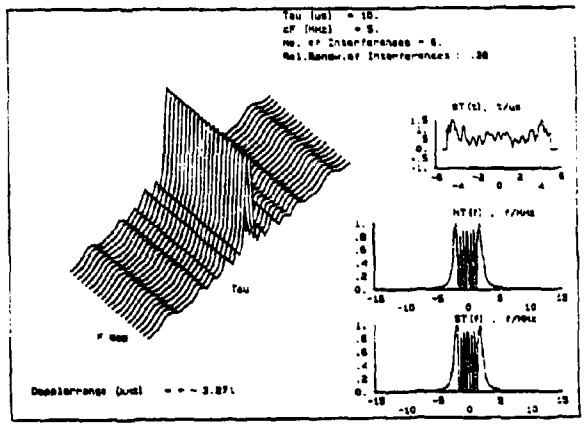

Fig. 4 Main peak section of the ambiguity function of a shaped chirp signal.

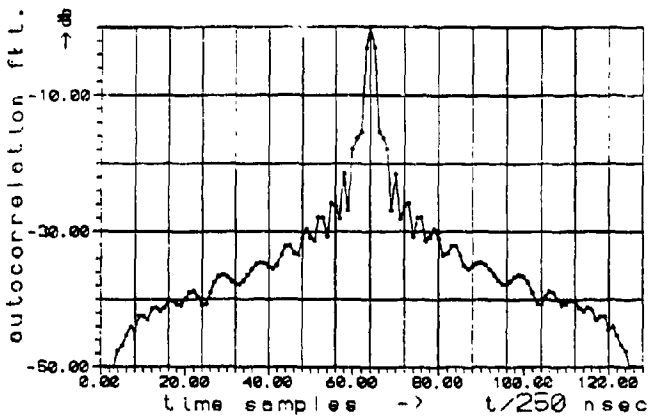

Fig. 5 a) Autocorrelation function of original chirp signal with transient.

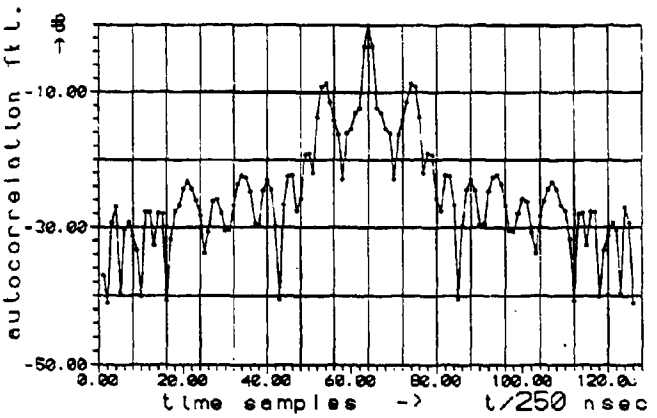

Fig 5 b) Autocorrelation function of shaped chirp signal.
Interferences: 0.3-0.4, 0.6-0.7, 1.0-1.1, 1.4-1.5 MHz

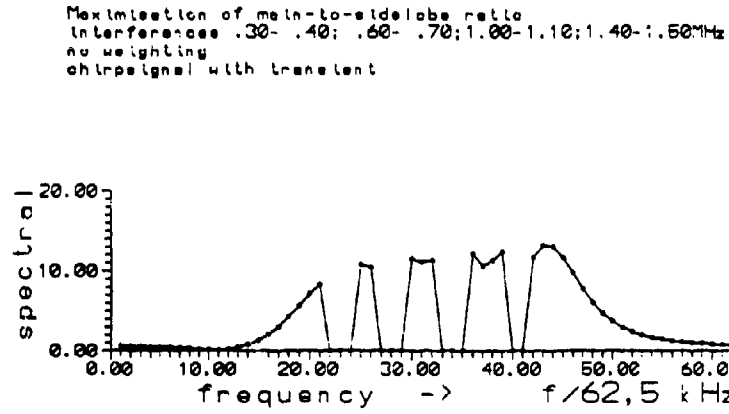

Fig 5 c) Spectrum of the shaped signal.

Serious radar performance degradation, however, can be expected from increased sidelobes of the compressed pulse. In figure 5, the autocorrelation function of the original chirp signal (a) is compared to that of a signal spectrally shaped to avoid interference (b). Since in the discussed system, the transmitter is switched with every pulse, the transient of the transmitter has the effect of a weighting function on the signal, smoothing the leading and trailing edges of the pulse. The adaptation to four interfering sources covering 20 % of the signal bandwidth causes an unacceptably high sidelobe level. Figure 5.c gives the spectrum of the shaped signal, showing 4 notches. The sidelobes would mask weaker targets in the adjacent range cells. Hence, the radar signal has to be modified in a way that the sidelobes of the autocorrelation function are reduced to a reasonable level without loosing its spectral notch structure.

4.Signal Optimisation

The problem of optimal shaping of the radar signal under the constraints of interference avoidance and a reduced sidelobe level could not be solved analytically, yet. Though, a reasonable approach to solve the problem is the so called random walk method which is known from evolution.

The method is based on the random mutation of one of the 32 complex spectral samples, representing the signal bandwidth, at a time. For the mutation, first a maximum mutation stepwidth δ is set and a complex number c_m is generated. The real and the imaginary part of c_m are randomly distributed between $-\delta/2$ and $+\delta/2$. Another call of the random generator yields the random position of the sample to be mutated under the constraint that a mutation within the predefined notches is rejected and a new trial is conducted. The chosen spectral sample $S(f_n)$ is added to the mutation step c_m, forming the new sample $S(f_n)$. To check the new signal waveform s(t), a 64 step FFT (Fast Fourier Transform) is applied to the spectrum S(f).

The autocorrelation function $\chi_0(t_d)$ is calculated as the integral

$$\chi_0(t_d) = \int_{-\infty}^{\infty} S^*(f)\, S(f)\, e^{j2\pi f t_d}\, df$$

using the equivalent sum

$$\chi_0(t_d) \approx \Delta f \sum_{n=-64}^{64} |S(f_n)|^2\, e^{j2\pi f_n t_d}$$

The resulting autocorrelation function $\chi_0^{(n)}(t_d)$ is then compared to the autocorrelation function $\chi_0^{(n-1)}(t_d)$ prior to the mutation, according to the chosen optimisation criterion. Mutations, leading to deteriorations are neglected, those leading to improvements are retained. After an improving mutation, the sequence starts over again with the new spectrum S(f) as the basic signal. During the optimisation run, no FFT is used for the calculation of the new signal waveform, instead it is sufficient to replace only that term of the sum $\chi_0(t_d)$ containing the mutated sample $S(f_n)$. After the final mutation step, the signal waveform is calculated again, using an FFT algorithm. It is then used as the present radar pulse, adapted to the interference situation and opimised for reduced sidelobes. The optimisation criterion that is used within the random walk sequence is dependent on the desired properties of the autocorrelation function.

5. Optimisation criteria

Three optimisation criteria have been examined for the reduction of the sidelobes of the autocorrelation function of a spectrally shaped radar pulse.

1. Maximisation of main-to-sidelobe-ratio
2. Maximum similarity with a sample function
3. Maximum similarity with an ideal generic model function.

For all of the optimisation criteria, the optimisation is conducted under the constraint of not affecting the transient phase of the pulse. The criterion of "maximisation of the main-to-sidelobe-ratio", first of all, requires a definition of the extension of the mainlobe. Here, the mainlobe is defined to strech from the center of the maximum to the center of the first local minumum, symmetrically to the center of the maximum. All samples of the autocorrelation function beyond the first local minimum are regarded as sidelobes. Since a general effect with the reduction of sidelobes is the broadening of the mainlobe, the mainlobe area has to be updated with every improving mutation. The second and third optimisation criteria are based on a different principle. The difference between the autocorrelation function of the mutated signal and that of the model function is calculated and diminuations of the difference after a mutation are regarded as improvements. Deviant shapes of the mainlobes of the two compared functions normally yield larger difference or error values than a lack of similarity in the sidelobes. Hence, since reduced sidelobes are a desired property, the errors in the sidelobes are assessed higher

than those in the mainlobe. The sample function chosen for the optimisation was the autocorrelation function of an unshaped chirp pulse with transient, having low sidelobes. In the case of using a generic modal function, an autocorrelation function resembling a Dirac impulse was applied for comparison.

6. Parameter Sensitivity

Random walk methods are , in general, sensitive to the choice of parameters like starting value and step width. The number of iterations is of less importance , though there is a threshold, depending on the choice of the other parameters, limiting the cost effectiveness of further improvements. Little influence can be recognized from the choice of different starting values, too. It is insignificant, which of the spectral samples is mutated first. The mutation step width, however, has a deciding factor for the success of the random walk signal optimisation. It is hardly predictable, if the starting position - before the first mutation - is in the vicinity of the global maximum or a local one. Hence, the mutation step width has to be high enough so that the vicinity of a local maximum can be left and it should, on the other hand, be low enough to avoid stepping from one local maximum area to the next with every mutation, and to stay in the vicinity of the global maximum, once this area is reached. Several mutation step widths have been tried, as well as different strategies to alter the sample which is to be mutated.

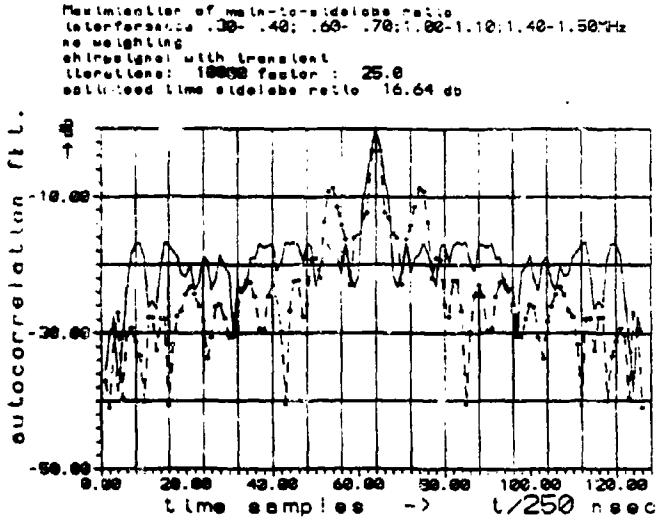

Fig. 6 a Autocorrelation function of shaped signal after 10000 iterations δ = 25.

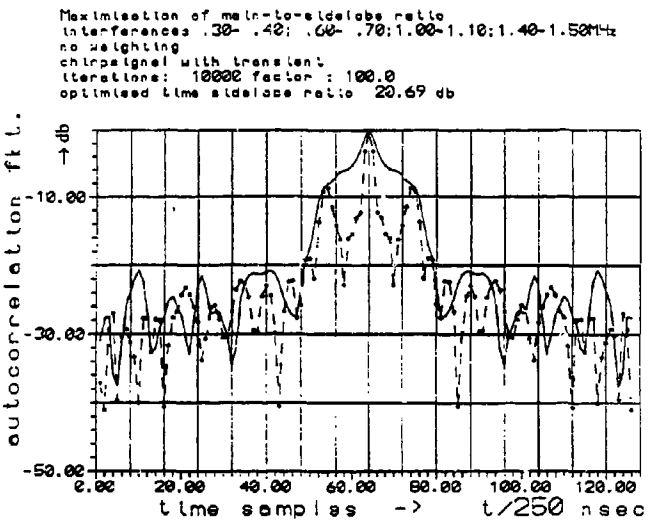

Fig. 6 b Autocorrelation function of shaped signal after 10000 iterations $\delta = 100$.

Some mutation strategies have been rejected as not being successfull. Among them were the multiplication with a random factor or changing the real and imaginary component by the same factor, as well as changing only one of the complex components. The choice of a maximum mutation step width, given by an empirically determined value has proven to be a good compromise since large mutation steps, enabling significant changes, are possible as well as small variations for a closer approach of a maximum. The principle influence of the mutation step width is demonstrated in figure 6 for the two values $\delta_1 = 25$ and $\delta_2 = 100$, when the criterion of maximum main-to-sidelobe ratio is applied. With $0.5\,\delta_1$ being equal to the maximum spectral sample of the unweighted pulse, the mutation steps are in the order of magnitude of the real and imaginary part of the spectral samples, while δ_2 allows mutation steps larger than the spectral signal amplitude which requires more flexibility in the signal generation. Figure 6a shows the autocorrelation function (akf) of the shaped signal after 10000 iterations with $\delta = 25$ (solid line) compared to the akf without signal optimisation (dashed line). Figure 6b shows the akf before (dashed) and after (solid) optimisation for $\delta = 100$. The larger mutation step width achieves a better sidelobe suppression at the expense of a broader mainlobe and higher signal amplitudes.

7. Results and Conclusions

Numerous simulations have been made with different interference scenarios. Here, one typical scenario with 4 interferences, covering 20% of the signal bandwidth, shall be regarded to compare the different optimisation criteria. In figure 7, the result of the optimisation after 10000 iterations with $\delta = 100$ is displayed for the case that the deviation of the akf of the shaped signal from the akf of an unshaped chirp with transient is minimised. Figure 8 shows the result of the minimisation of the deviation from an ideal, Dirac-like akf. The reference functions are represented by the dashed lines. These criteria may be successfully applied, if a narrow mainlobe is the most important demand. The maximisation of the main-

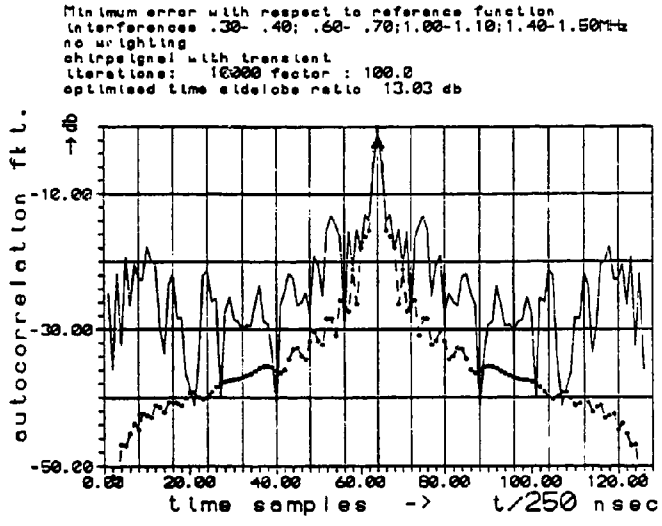

Fig. 7 Autocorrelation function of shaped signal after 10000 iterations.
Criterion: Minimisation of deviation from reference function.

to-sidelobe ratio always tends to lower the sidelobes at the expense of a broadened mainlobe, as shown in figure 6. Using the latter criterion, after 50000 iterations, a sidelobe level of -24.63 db compared to -22 db for the unshaped pulse with transient can be reached. The signal shape has significantly changed, both in the spectral and time domain but the notch structure is still maintained, as shown in figure 9.The width of the mainlobe has increased by a factor of 3, reducing the range resolution of the radar by 1/3. This is shown in figure 10. In table 1, three stepwidths $\delta = 25$, 50 and 100 are compared for iterations ranging from 1 to 50000.

Table 1: Main-to-sidelobe ratio in db as fuction of stepwidth and number of iterations

iterations .	1	50	100	500	1000	5000	10000	50000
stepwidth.								
δ=25 .	8.52	10.76	11.73	14.53	15.14	16.38	16.64	17.01
δ=50 .	8.52	9.33	9.97	13.53	14.73	15.60	16.55	18.91
δ=100 .	8.52	10.52	11.14	18.46	19.34	20.40	20.69	24.63

A further approach to the optimisation was made using a weighting function on the shaped signal before starting the mutations. The first trial was conducted on a Hamming weighted chirp signal. The result given in figure 11 does not seem to be too promising, but further work using other weighting functions and stepwidths will be done in the future. Regarding the implementation in the experimental radar processor, the iteration time is an important aspect. The cpu-time for the calculation of the optimised signal with 50000 iteration is about 12 seconds on a 486 processor. For real time optimisation of a radar signal, a specialized DSP type signal processor would take 1 second, so that the adaptation of the radar signal to the present interference situation could be done within one update period of a search radar.

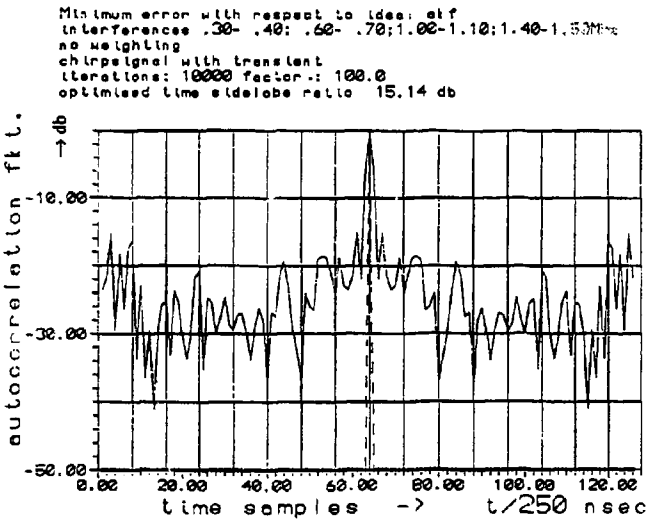

Fig. 8 Autocorrelation function of shaped signal after 10000 iterations.
Criterion: Minimisation of deviation from Dirac-like akf.

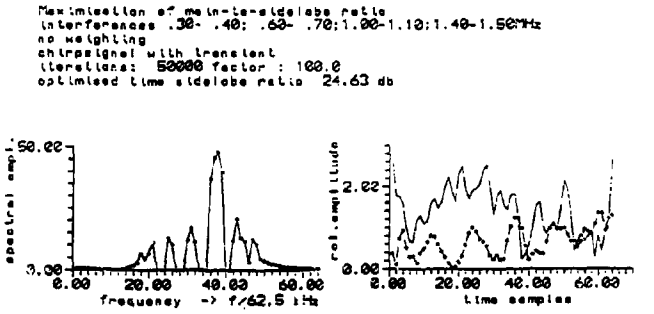

Fig.9 Signal spectrum and envelope after 50000 iterations $\delta = 100$.

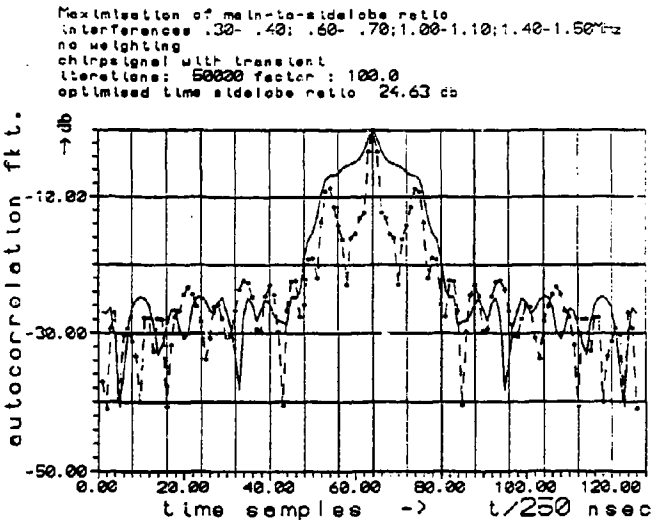

Fig.10 Autocorrelation function of shaped signal after 50000 iterations $\delta = 100$.

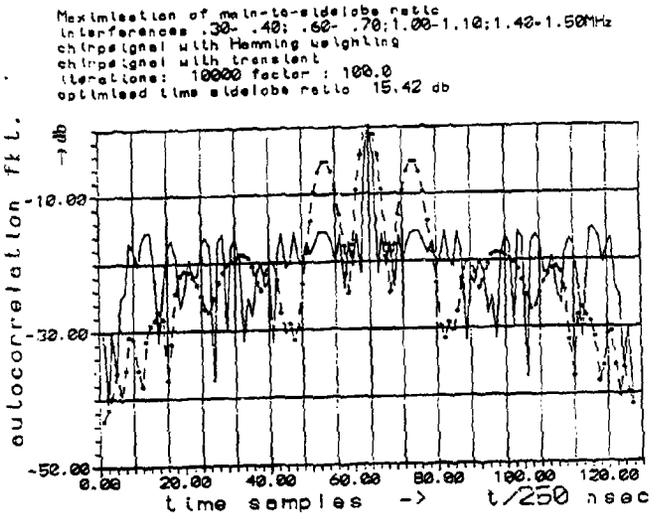

Fig.11 Autocorrelation function of Hamming weighted chirp after 10000 iterations $\delta = 100$.

8. References

/1/ D.K.Barton — Modern Radar System Analysis, Artech House

/2/ S.Davidovici, E.G.Kanterakis — Narrow Band Interference Rejection Using Real-Time Fourier Transforms. IEEE Trans. on Comm. Vol 37, No. 7. 1989

/3/ L.E.Garth, H.V.Poor — Narrowband Interference Suppression in Impulsive Channels, IEEE Trans. AES Vol. 28, No. 1 1992

/4/ Y.S.N. Murty, A.Bhagavathi Rao — Design of Waveform Agile Radar Systems ICOMM-90, New Delhi 1990

/5/ B. Honary, M. Darnell, T. Ng, G. Markarian — Spectral Shaping Codes for Co-Channel InterferenceSuppression. 5th Int. Conf. on HF-Radio, Edinburgh,UK No. 339 1991

Optimization Techniques Applied to Electromagnetics

F. M. Landstorfer
Institut für Hochfrequenztechnik,
University of Stuttgart, Germany

1 Introduction

The history of electrical engineering is strongly connected with the discovery of the basic laws of electromagnetic field theory by Ampère and Faraday. This development found its climax and preliminary end by the contributions of J.C. Maxwell and H. Hertz at the end of the 19th century.

While the theory of electromagnetic fields and waves has been well understood since this time, its application to engineering problems remains a challenge. Contrary to the ambitions of natural sciences such as physics, it is synthesis rather than analysis that is required for solving typical engineering problems. Out of many possible solutions we are looking for the optimum, either by applying our professional experience or by using mathematical optimization techniques or – most likely to succeed – by a combination of both.

In the following, some examples will be given to demonstrate the potential of mathematical optimization methods for solving electromagnetic problems in an – at least partially – new way.

2 Mathematical Optimization Routines

The overwhelming majority of electromagnetic engineering problems can be characterized by a number of parameters, which can be arranged in a vector

$$\vec{x} = (x_1, x_2, x_3 \dots x_n) \tag{1}$$

and have to be chosen in such a way that a certain function

$$F(\vec{x}),$$

which depends on these parameters and acts as a quality criterion, will become a global minimum or maximum depending on the situation given. Generally this optimization process will have to be performed under consideration of certain side constraints. It should be noted that there is presently no method available to yield a global extremum with any certainty and that only when

arriving at the same solution from different starting points some confidence can be placed into its global nature.

If $\vec{x}$ has only two parameters x_1 and x_2, $F(\vec{x})$ can be represented in a 3-D-plot as given in Fig. 1 and the optimization process consists in finding those values of x_1 and x_2 for which $F(\vec{x})$ becomes a minimum. With the majority of examples to follow, a *conjugate gradient method with line search* was used as it showed faster convergence compared to other methods such as conventional gradient techniques or the *Simplex*- method.

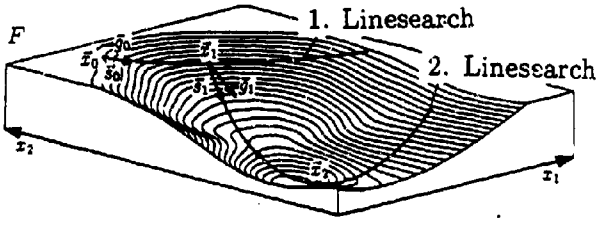

Figure 1: Minimizing a function of two variables with the *conjugate gradient method*

3 Coaxial Resonator Shaped for Maximum Unloaded Q

Conventional coaxial line resonators as shown in Fig. 2a have constant inner and outer diameters and a length of $\lambda/2$. By properly shaping the inner conductor while the outer conductor and the resonance frequency remain constant (Fig. 2b), it should be possible to obtain a higher value of the unloaded Q. For the analysis of this problem a variational technique is utilized [1]. For any coaxial line resonator with rotational symmetry the resonant wave number can be given by

$$k^2 = \frac{\int\int_L [\frac{\partial H_\varphi}{\partial z} + (\frac{1}{\rho}\frac{\partial}{\partial z}(\rho H_\varphi))^2]\,\rho\,d\rho\,dz}{\int\int_L H_\varphi^2\,\rho\,d\rho\,dz} \quad . \tag{2}$$

Equation (2) contains the magnetic fieldstrength H_φ only. L is the area in the longitudinal section of the resonator between inner and outer conductor. As k^2 at resonance corresponds to an eigenvalue, equation (2) is stationary and H_φ can be found by means of the *Rayleigh-Ritz* variational technique. For a given shape of the longitudinal section of the inner conductor (the outer conductor remains unchanged) H_φ can be approximated by

$$H_\varphi = \rho \sum_{i=1}^{N} c_i H_i \quad , \tag{3}$$

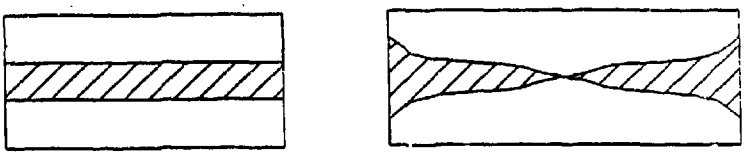

Figure 2: a) Conventional resonator b) Resonator shaped for maximum Q

where H_i denotes N different basis functions and c_i N different unknown constants. For basis functions monomes of the conveniently standardized coordinates ρ' and z' are chosen. Inserting equation (3) into (2) and setting the partial derivatives of this expression with respect to c_i equal to zero, a set of linear equations is obtained whose solutions give the unknown constants c_i and consequently the magnetic field from which the unloaded quality factor Q of the resonator can be computed.

For the optimization process the shape of the inner conductor is approximated by straight-lined segments whose boundary coordinates form the parameter vector $\vec{x}$ to be varied for maximum Q. In order to simultaneously fulfil the side constraint of constant resonance frequency, the length of the resonator is considered a variable as well.

The final resonator as given in Fig. 2b offers an almost 10 % increase in unloaded Q as compared to a conventional one.

4 Shaped Dipole Reflector Antenna

Shaping wire antennas for optimum performance has been dealt with in [2]. Here, as an example for broadband problems, optimization of the UHF reflector-antenna as shown in Fig. 3a will be discussed. Its E- and H- plane radiation patterns are given in Fig. 4a. By a proper shaping of reflector and dipole of this antenna it should be possible to reduce the considerable frequency sensitivity particularly in the H-plane. For this purpose the reflector is modelled by a wire grid and the computations are done with NEC [4]. For the numerical optimization, a quality criterion has to be defined, which helps to decide wether an actual antenna shape is better or worse than another. The squared deviation of the radiation pattern C from a desired pattern C_d defines error functions F_E and F_H for the E- and H-planes.

$$F_E = \frac{1}{mn} \sum_{i=1}^{n} \sum_{j=1}^{m} [C_d(\varphi_j) - C(\vartheta_i, \varphi_j)]^2 \qquad (4)$$

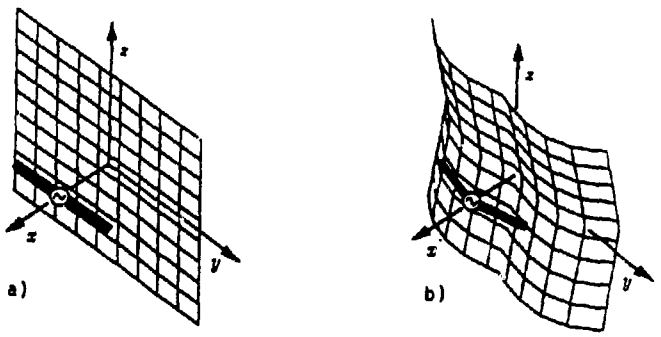

Figure 3: Conventional (a) and shaped (b) reflector antenna

$$F_H = \frac{1}{mn} \sum_{i=1}^{n} \sum_{k=1}^{p} [C_d(\vartheta_k) - C(f_i, \vartheta_k)]^2 \tag{5}$$

Frequency is sampled at n different points, the radiation patterns at m or p different angles, respectively. The two given error functions F_E and F_H are combined via the weighting factors w_1 and w_2, which balance the different sensitivities of the error functions.

In order to avoid nonphysical solutions during the optimization, a so-called penalty concept is applied. The penalty function P_s becomes active (i.e. large) when the side lobe level exceeds a certain level and thus turns the optimization procedure away from the "prohibited area". A further penalty function P_p ensures that the parameters do not assume values that would lead to weird geometries. The whole quality criterion function is now given by the weighted sum

$$F = w_1 F_E + w_2 F_H + w_3 P_s + w_4 P_p \tag{6}$$

and will be minimized in the course of the shaping process.

The shape of the dipole in the coordinate system of Fig. 3 is given by a spatial vector-function of the form

$$\vec{r}_s(\xi_i) = \hat{e}_x (\xi_1 y^0 + \xi_2 y^1) + \hat{e}_y y^1 + \hat{e}_z 0, \tag{7}$$

with half the dipole length

$$l = \sqrt{(x_1 - x_2)^2 + (y_1 - \quad)^2} = \frac{\lambda_m}{4} = \text{const.} \tag{8}$$

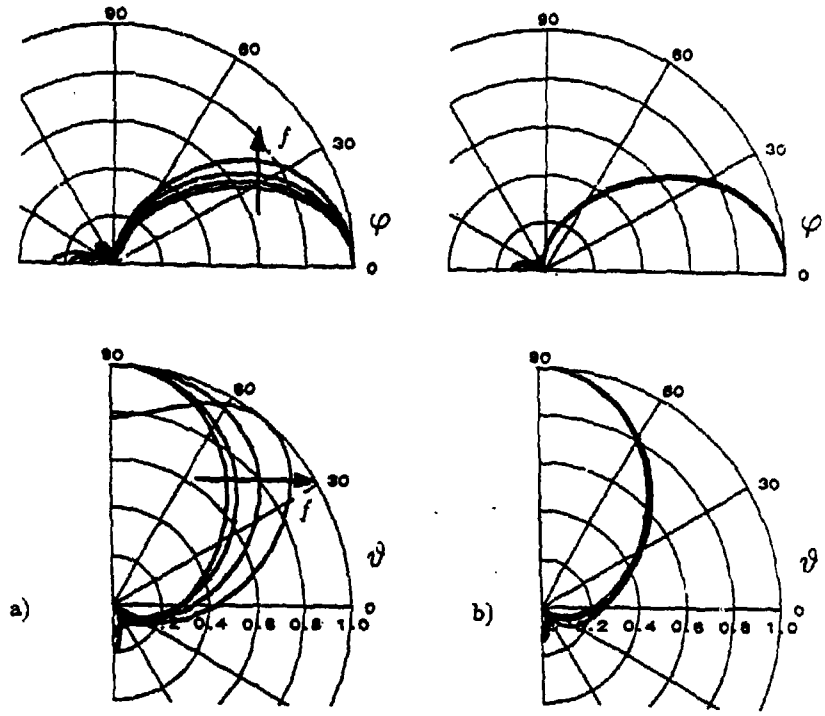

Figure 4: Radiation patterns over one octave for the antennas of Fig. 3a (a) and Fig. 3b (b)

Assuming symmetry to the planes $y = 0$ and $x = 0$, the shape of one quarter of the reflector is given by a spatial vector–function of the form:

$$\vec{r}_r(\xi_i) = \hat{e}_z p(y, x, \xi_i) + \hat{e}_y y^1 + \hat{e}_x x^1. \tag{9}$$

The chosen polynomial is

$$p(y, x, \xi_i) = \xi_3 y^1 + \xi_4 y^2 + \xi_5 y^3 + \xi_6 y^4 + \xi_7 y^5 + \xi_8 x^1 + \xi_9 x^2 + \xi_{10} x^3 + \xi_{11} x^4 + \xi_{12} x^5 \tag{10}$$

$\hat{e}_x, \hat{e}_y, \hat{e}_z$	:	unit vectors in the directions of the cartesian coordinates,
ξ_i	:	parameters of the shaping function,
x_1, y_1	:	location of the dipole center,
x_2, y_2	:	location of the dipole end,
$p(y, x, \xi_i)$	:	polynomial that gives the shape of the reflector.

The result of the optimization process is shown in Fig. 3b and Fig. 4b. It is possible to obtain nearly frequency-independent radiation patterns over a one octave bandwidth with the optimized shape of dipole and reflector. This holds not only in the E- and H-plane but also in three dimensional space.

5 Omnidirectional Array

Antennas consisting of dipoles in front of a reflecting screen are often arranged in arrays around a central mast in order to provide omnidirectional radiation for FM- and TV-stations (Fig. 5). On the assumption of proper individual radiation characteristics, the overall radiation pattern of the array would be omnidirectional, only if the phase centers of the different array elements were located in the center of the mast. As this is not possible with this type of antennas, the radiations of the different elements of the array superimpose in a frequency-dependent way. The resulting deviation from the ideal omnidirectional pattern is the "ripple", which is measured in dB. For an antenna of the type shown in Fig. 5, which consists of a flat straight broadband dipole

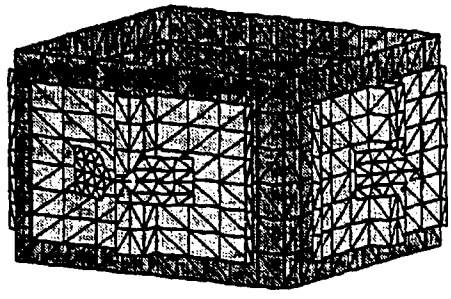

Figure 5: Array of 4 reflector antennas with flat V-dipoles arranged round a central mast

in front of a reflecting screen with a central ridge, the maximum ripple over an octave bandwidth is around 5 dB with a mast diameter in the order of 2λ at center frequency. As this antenna is already in practical use, only small variations of its geometry, such as a tilt between the two halves of the dipole and a change of the distance dipole-reflector could be contemplated in order to optimize the omnidirectional pattern. The analysis was carried out using a computer program developed by Jakobus [6], based on the method of moments [3], modelling dipole and reflector with triangular patches as shown in Fig. 5 and using basis functions for the surface currents according to Rao et al. [5].

Fig. 6 shows that by proper choice of tilt or bend angle and distance of the flat dipole to the reflecting screen, the maximum ripple within an octave bandwidth can be reduced by a factor greater than two.

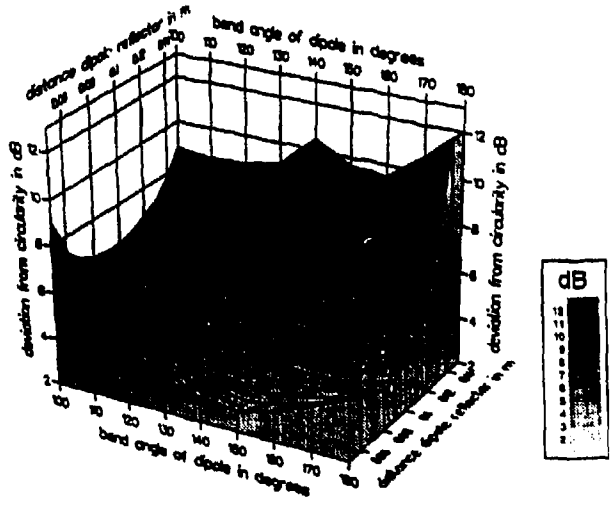

Figure 6: Ripple of omnidirectional pattern over dipole bend angle and distance from reflector

6 ILS–Glidepath

Fig. 7 shows the 3D–modelling by triangular patches of the approach area of an airport with instrument landing system (ILS). Greatly simplified, the interference between an antenna array installed abeam the intended touchdown zone and its mirror image with respect to the ground produces a null of the electrical fieldstrength, which acts as a guiding line (instrument glide path) for landing aircraft. With uneven terrain in the approach area the mirror image becomes blurred and the glidepath will show deviations from the ideal straight line, which until now could only be compensated by changes in antenna position and phase after lengthy trial and error procedures. With a new optimization technique [7] based on an extended UTD, all antenna parameters can now be determined in advance and intermediate calibration flights have become dispensable.

References

[1] N. Y. Zhu and F. M. Landstorfer, "Quality factor optimisation of coaxial resonators," *Electronics Letters*, vol. 24, pp. 862–863, 1988.

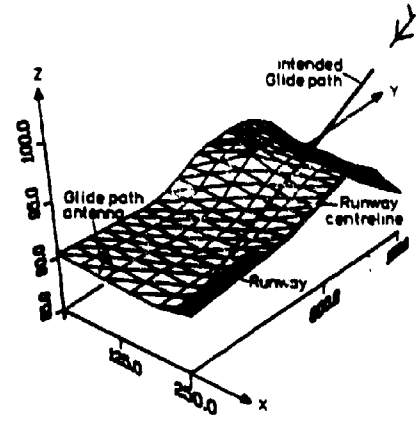

Figure 7: Modelling of 3D-terrain by triangles for UTD optimization of ILS-glidepath

[2] F. M. Landstorfer and R. R. Sacher, *Optimisation of Wire Antennas*. Research Studies Press (J. Wiley), Chichester, England, 1984.

[3] R. F. Harrington, *Field Computation by Moment Methods*. Macmillan Company, New York, 1968.

[4] G. J. Burke and A. J. Poggio, *Numerical Electromagnetics Code*. Lawrence Livermore National Laboratory, 1981.

[5] S. M. Rao, D. R. Wilton, and A. W. Glisson, "Electromagnetic scattering by surfaces of arbitrary shape," *IEEE Transactions on Antennas and Propagation*, vol. 30, pp. 409–418, 1982.

[6] U. Jakobus, J. Christ, and F. M. Landstorfer, "PO-MoM analysis of cavity backed antennas," *Proceedings of the 8th International Conference on Antennas and Propagation*, IEE Conference Publication Number 370, pp. 111–114, 1993.

[7] N. Zhu, F M. Landstorfer, and G. Greving, "Three-dimensional terrain effects on high frequency elctromagnetic wave propagation," *Proceedings 21st Europ. Microwave conference*, pp. 1205–1210, 1991.

SESSION 7:

FINITE ELEMENT METHODS (II)

Chair: Jin-Fa Lee
Co-Chair: John Volakis

Hybrid Finite Element-Modal Analysis of Jet Engine Inlet Scattering

Daniel C. Ross, John L. Volakis and Hristos T. Anastassiu

Radiation Laboratory
University of Michigan
Ann Arbor MI 48109-2122

abstract – Accurate numerical simulation of radar scattering from jet engine inlets is of vital importance for target identification. High frequency techniques fail due to the complexity of the engine face. A hybrid finite element-modal method is presented. Only the region of the inlet directly adjacent to the engine face is considered for the finite element portion of the solution, which is assumed to have a circular cross section. The finite element method is used to find a generalized scattering matrix for an N-port representation of the engine face, where N is the number of traveling cylindrical waveguide modes in the inlet. Important implementation issues are addressed including: the use of an optimized, fictitious, material absorber to truncate the FEM mesh, and an examination of the suitability of node-based or edge-based elements. Results are shown for some benchmark configurations.

1.0 Introduction

The simulation of radar scattering from jet engine inlets is an important step towards the characterization of aircraft structures. While high frequency techniques can accurately simulate many scattering mechanisms on a typical aircraft, these techniques are not suitable for resonant or guiding structures such as antennas/radomes and jet engine inlets. The engine face is an intricate target, possessing complex geometrical features at the wavelength level or less, and is therefore inappropriate for high frequency analysis. By comparison, the finite element method (FEM) [1][2] is well suited for the analysis of geometrically complex, inhomogeneous volumetric targets such as the engine face. However, in spite of its inherent O(n) storage demand, the FEM analysis would still require prohibitive computational resources were it to be also used for modeling the volume enclosed by the inlet leading to the engine. By coupling the finite element method (applied at the engine face), to a high frequency ray or modal technique (to propagate the fields in and out of the inlet), an efficient method is developed for analyzing the inlet and engine configuration.

Of importance in this analysis is the interface between the ray/modal and FEM methods, and the truncation of the finite element mesh. Given that the inlet cross section near and at the engine location is circular, and our desire to propose an efficient and flexible coupling scheme, the coupling of the FEM and ray fields in this paper is accomplished via the generalized modal scattering matrix. That is, the FEM analysis generates the modal scattering matrix which can then be interfaced with any high frequency technique for computing the engine scattered fields without reference to the geometry of the jet engine. Regarding the truncation of the FEM mesh, several schemes are considered including absorbing boundary conditions, the unimoment method and a new artificial broadband absorber, with the later found most effective for this application. The suitability of edge-based and node-based elements for this application is also presented.

2.0 Finite Element-Modal Formulation

Consider the three-dimensional cavity configuration shown in Figure 1. The cavity is excited by an arbitrary field (typically a plane wave) through its opening at the left side and is assumed to have a complex geometrical configuration (an engine) at its right end. We are interested in computing the field scattered by this complex cavity termination due to a given excitation which is assumed to be specified at the left pinioning of the cavity. In our analysis, the cross section of the cavity is assumed to be arbitrary and of diameter greater than a free space wavelength up to the connectivity boundary as shown in Figure 1. Beyond this connectivity boundary, the cavity's outer perimeter is assumed to be circular but may enclose complex geometrical configurations such as an engine. Since the cavity is circular at the connectivity boundary, the incident and scattered fields can be decomposed into cylindrical waveguide modes and a generalized scattering matrix can be found to replace the entire portion of the geometry to the right of the connectivity boundary.

The generalized scattering matrix $[S]$ of a given termination relates the coefficients of the incoming modes to the coefficients of the corresponding outgoing modes. That is

$$[S]\{a\} = \{b\} \tag{1}$$

where the elements of the vectors $\{a\}$ and $\{b\}$ are simply the coefficients of the incoming and outgoing modes respectively. We remark that if the connectivity boundary is placed a distance $\frac{1}{4}\lambda$ from the cavity termination, only propagating modes need be considered without compromising accuracy.

3.0 Finite Element Analysis

The traditional FEM analysis involves the solution of the time harmonic, weak form of the wave equation in a bounded volumetric region of space. Being a partial differential equation method, the FEM analysis leads to sparse matrices (with about 10 to 50 nonzero entries per row) and permits the modeling of complex inhomogeneous regions without a need for special care and considerations. For our problem at hand, the FEM analysis region is shown in Figure 2 and is seen to extend a bit beyond the connectivity boundary Γ to a mesh termination boundary Γ'. On Γ' it is necessary to enforce an absorbing boundary condition (ABC) or some other mesh termination scheme which ensures the outgoing nature of the waves. That is, Γ' must be a non-reflecting boundary and this will be discussed later in more detail. We remark that the cross section between Γ and Γ' is again assumed circular for this analysis but this assumption has no bearing on the actual cavity of Figure 1.

On the basis of the FEM-modal formulation, we are interested in computing the fields scattered by the cavity termination due to the modal excitation

$$\bar{E}^{inc} = \bar{\Psi}_q \tag{2}$$

The total field in the FEM region is then given by

$$\bar{E} = \bar{E}^{inc} + \bar{E}^{s} \tag{3}$$

and the unknown scattered electric field satisfies the weak wave equation (see for example [1],[2] and [4])

$$\iiint_{\Omega}\left\{\frac{1}{\mu_r}(\nabla\times\bar{E}^s\cdot\nabla\times\bar{T})-\bar{T}\cdot k_0^2\varepsilon_r\bar{E}^s\right\}dv-\iint_{\Gamma}\{jk_0\eta\bar{T}\cdot(\hat{n}\times\bar{H}^s)\}ds+$$

$$\iiint_{\Omega}\left\{\frac{1}{\mu_r}(\nabla\cdot\bar{E}^s)(\nabla\cdot\bar{T})\right\}dv= \tag{4}$$

$$-\int_{\Gamma_d}\left\{\left[\frac{1}{\mu_{r2}}-\frac{1}{\mu_{r1}}\right]\bar{T}\cdot(\hat{n}_d\times(\nabla\times\bar{E}^{inc}))\right\}ds-\iint_{\Gamma}\left\{\frac{1}{\mu_r}\bar{T}\cdot(\hat{n}\times(\nabla\times\bar{E}^{inc}))\right\}ds$$

in which Γ_d represents the surface over dielectric boundary discontinuities between regions of different magnetic permeability. Note that $\hat{n}_d$ points from μ_{r2} to μ_{r1} and only material discontinuities within the scatterer, not the fictitious absorber contribute to the boundary integral on Γ_d. Also, the third term on the left hand side of (4) is the usual penalty term which ensures that the divergence condition be satisfied in the Galerkin least squares sense.

4.0 Implementation of the FEM Solution

Creating user-oriented and efficient software to implement the above FEM formulation requires that a number of issues be addressed. First, the most appropriate shape and elements must be chosen. Also, since the problems will be large, efficient pre-processing software must be created to extract (from a given mesh) information needed to enforce the boundary conditions. This includes finding metal surfaces and edges, corners, normals, material discontinuities and the elements on the connectivity boundary. It is also crucial to develop preprocessing algorithms that run in O(n) time for a general mesh. To this end, an efficient preprocessor has been created for extracting relevant information from an arbitrary three-dimensional tetrahedral mesh [3].

Elements and Field Expansions

There are two classes of field expansions that could be used with tetrahedral elements: node based and edge based expansions. Edge-based elements are a better choice than node-based elements for the eigenvalue problem because standard node-based elements cannot accurately represent the eigenvectors (fields) that correspond to zero eigenvalues. All of the eigenvalues that should be zero (one for each internal degree of freedom) have some small non-zero value when using standard node-based elements. This large scale degeneracy causes considerable numerical problems when computing the eigenvalues especially for large systems. When using edge-based elements, the eigenvalues are cleanly split into zero and non-zero groups thus alleviating much of the numerical problems [5]. (That is, the zero eigenvalues are identically zero.)

Although edge-based elements are indeed better for eigenvalue problems, the best choice of elements for three-dimensional scattering analysis is not clear. Both classes of elements were considered (node-based and edge-based) for this problem.

Node-based elements

When using linear node based elements, the scattered field is given by

$$\bar{E}^s = \sum_{a=1}^{4} (\hat{x}N_x^a E_x^a + \hat{y}N_y^a E_y^a + \hat{z}N_z^a E_z^a)$$

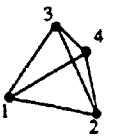

where

$$N_x^a = N_y^a = N_z^a = N^a(x, y, z)$$

are the standard scalar shape functions [1] and E_x^a, E_y^a and E_z^a are the components of the vector degrees of freedom associated with each of the four nodes.

By numerical experimentation was found that boundary conditions for these elements must be implemented carefully to avoid deterioration the system condition. For a node lying on a conductor, two tangent vectors can be defined from the surface normal, such that

$$\begin{aligned} \hat{t}_1 \cdot \bar{E}^s &= -\hat{t}_1 \cdot \bar{E}^{inc} \\ \hat{t}_2 \cdot \bar{E}^s &= -\hat{t}_2 \cdot \bar{E}^{inc} \end{aligned} \tag{5}$$

where $\hat{t}_{1,2}$ denote the orthonormal unit vectors tangent to the metallic surface. There are many possible ways of coupling the global equations to enforce the boundary conditions (5), but there is always a best way which preserves the system's condition. If the boundary conditions are enforced arbitrarily, it is possible to completely destroy the condition of the system and to generate wrong results. The following procedure will guarantee a well conditioned final system:

Given the metal surface normal $\hat{n}$ at the node, find the two tangent vectors $\hat{t}_1$ and $\hat{t}_2$ as follows

- if $|\hat{y} \times \hat{n}| > 0.15$ then set $\hat{t}_1 = \dfrac{\hat{y} \times \hat{n}}{|\hat{y} \times \hat{n}|}$

  else set $\hat{t}_1 = \dfrac{\hat{x} \times \hat{n}}{|\hat{x} \times \hat{n}|}$

- $\hat{t}_2 = \dfrac{\hat{t}_1 \times \hat{n}}{|\hat{t}_1 \times \hat{n}|}$

- Given the three global equations for E_x^a, E_y^a and E_z^a at the node

  - find the largest component of $\hat{t}_1$ (x, y or z) and replace the corresponding global equation with $\hat{t}_1 \cdot \bar{E}^s = -\hat{t}_1 \cdot \bar{E}^{inc}$

  - find the largest component of $\hat{t}_2$ (x, y or z) and replace the corresponding global equation with $\hat{t}_2 \cdot \bar{E}^s = -\hat{t}_2 \cdot \bar{E}^{inc}$

Edge-based elements

The first order, vector, edge based, tetrahedral elements given in Figure 5 expand the unknown field as

$$\bar{E}^s = \sum_{a=1}^{6} \bar{N}_a E_a$$

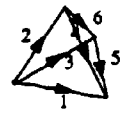

where $\bar{N}_a$ is the vector shape function associated with the a'th edge. The scalar degrees of freedom E_a refer to the component of the scattered field directed along the a'th edge.

These elements were implemented for the inlet termination scattering problem and were found to break down when the scattered field was purely TE (no z component of the scattered electric field). This breakdown is highly mesh dependant and is manifested in a poorly conditioned global system. Clearly, if a vector field at the center of a given edge of an element is orthogonal to that edge, edge-based elements cannot represent that field and yield a singular system. When a large volume is filled with a free tetrahedral mesh and the solution is purely TE, apparently a nearly singular system may result.

Since it is the job of the FEM to find the modal coupling, and since this coupling may in some cases be pure TE, the elements must be able to accurately represent a pure TE field while at the same time represent other types of fields. Because of the above difficulties for edge-based elements in modeling pure TE fields, we resorted to the node-based elements for this application.

Mesh Termination Schemes

At the open end of the mesh, the fields radiate into an infinite, cylindrical waveguide. The boundary condition at this open end must absorb all traveling modes in the guide. The most obvious choice is to expand the scattered field as a sum of all traveling modes and couple this expansion directly to the FEM equations.

Let the tangential electric field at the open end be given by

$$\bar{e}^s = \sum_{m=1}^{M} b_m \bar{\Psi}^s_m \tag{6}$$

where b_m ar unknown coefficients and $\bar{\Psi}^s_m$ is a cylindrical waveguide mode. Substitution of this expansion into the second term of (4) yields

$$\iint_S \{ jk_0\eta \bar{T} \cdot (\hat{n} \times \bar{H}^s) \}\, ds \rightarrow \iint_S \{ \frac{1}{\mu_r} \bar{T} \cdot \left(\sum_{m=1}^{M} b_m \hat{n} \times (\nabla \times \bar{\Psi}^s_m) \right) \}\, ds \tag{7}$$

With the introduction of the new coefficients b_m, to solve the system, resulting form (4), it is necessary to construct additional equations. These are given by

$$b_m = \frac{\int_S \bar{e}^s(x, y, z_0) \cdot \bar{\Psi}^{s^*}_m(x, y, z_0)\, ds}{\int_S \bar{\Psi}^s_m(x, y, z_0) \cdot \bar{\Psi}^{s^*}_m(x, y, z_0)\, ds} \tag{8}$$

and couple each unknown coefficient b_m to the fields associated with nodes on Γ. This leads to a sparse, square (FEM) system coupled to a dense, rectangular (modal expansion) system. While this scheme worked for shorted inlets, it was found to be unstable for the stub terminated inlet.

The design of a fictitious material absorber to absorb all traveling modes is complicated because the impedance and propagation constants of these modes vary greatly. The eight traveling modes in a guide of radius 0.66λ were used to design an optimized absorber. Clearly, if the absorber were allowed to be very long, a nearly perfect absorber could be constructed. However, since the absorber will be part of the FEM mesh, as a design constraint, it should be no more than about a half of a free space wavelength long to be practical.

A Monte Carlo optimization scheme based on [6] was used that has the desirable property of finding not only the best performing but also the most stable design. A five section, metal backed absorber was used as a starting point with ε_r and μ_r set to unity in each section. The length of each section was set initially to $.1\lambda$. The 15 parameters (material constants and lengths of each section) were varied randomly, independent of one another. Transmission line theory was used to calculate the reflection coefficient for each mode (see Figure 3), and the algebraic sum of reflection coefficients (the sum of absolute values) was used as the global optimization parameter. A pass/fail criterion on the global parameter was set to give about a 50% yield. For each random design, a pass or fail was noted for each parameter and after a number of designs have been sampled, a pattern begins to emerge. Some parameters indicate a tightening up is in order since most of the 'good' designs were centered about a certain value. Other parameters indicate a don't care condition as all values worked equally well. A new set of initial values and ranges is chosen and the process is restarted. Again, the global parameter threshold is chosen to give about a 50% yield. This global threshold continues to drop each iteration until a stable design is found. The final design and its performance is shown in Figure 4. Note that the reflection coefficient for all modes is less than .1 (-10 dB).

Example: Circular stub termination

A circular stub terminated inlet was analyzed because this geometry also possesses a reference mode matching solution [7]. The absorber was placed 0.33λ from the stub and the scattering matrix was computed at a distance of 0.25λ in front of the stub. Figure 5 shows a cut of the volume mesh for this configuration and the co-polarized backscatter patterns are given in Figure 6.

It was found that the proper handling of the boundary conditions at the inner edge (the rim of the stub) was critical. If the total field were set to zero at this inner edge, the results were quite wrong. However, if only the component tangential to the edge (E_ϕ) was set to zero, whereas E_z was allowed to float, the results were much improved and this is shown in Figure 6.

While the shown results are in good agreement for horizontal polarization, there is some discrepancy in the vertical polarization. Finer sampling around the rim does improve the comparisons slightly but with very slow convergence. The result shown were obtained using a global element size of $\frac{1}{12}\lambda$ and an element size of $\frac{1}{20}\lambda$ around the rim

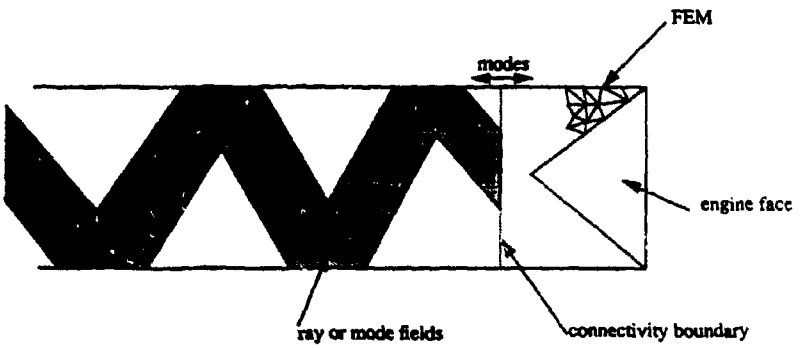

FIGURE 1. Hybrid jet engine inlet analysis.

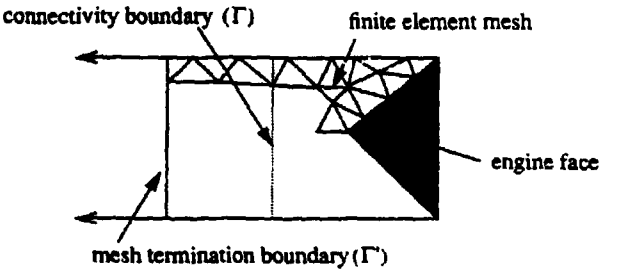

FIGURE 2. Engine face region where finite element analysis is applied

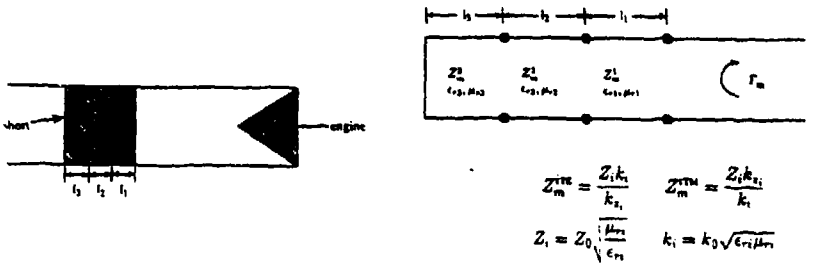

FIGURE 3. Transmission line model of cylindrical waveguide absorber

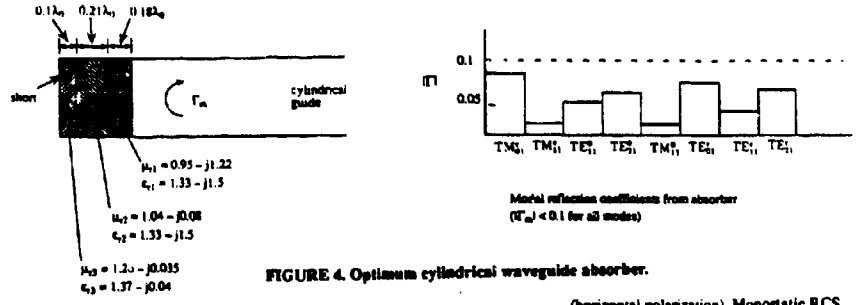

FIGURE 4. Optimum cylindrical waveguide absorber.

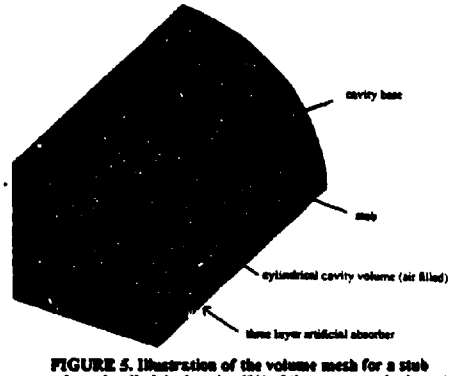

FIGURE 5. Illustration of the volume mesh for a stub terminated cylindrical cavity (1/4 of the geometry is shown)

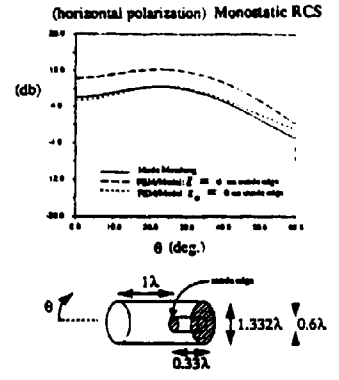

FIGURE 6. Results for a stub terminated inlet

References

[1]P. P. Silvester and R. L. Ferrari, *Finite Elements for Electrical Engineers*, Cambridge, 1986.

[2]J. L. Volakis, A. Chaterjee and L. C. Kempel, "A review of the finite element method for three-dimensional electromagnetic scattering," *J. Opt. Soc. Am.-A*, April 1994 (to appear)

[3]D. C. Ross, "Some Finite-Element Preprocessing Algorithms for Electromagnetic Scattering", *IEEE Antennas and Propagation Magazine*, Vol. 35, No. 3, pp. 68-72, June 1993.

[4]K. D. Paulsen, D. R. Lynch and J. W. Strohbehn, "Three-dimensional finite, boundary and hybrid element solutions of the Maxwell equations for lossy dielectric media," *IEEE Trans. Microwave Theory Tech.*, vol. 36, no. 4, pp 682-693, Apr. 1988.

[5]Z. J. Cendes, "Vector Finite Elements for Electromagnetic Field Computation", *IEEE Trans. on Magnetics*, Vol. 27, No. 5, pp. 3953-3966, Sept. 1991.

[6]A. B. MacFarland, "Parameter Centering and Tolerancing", Master's Thesis, Electrical Engineering Graduate School, Univ. of Idaho, Aug. 86.

[7]H. T. Anastassiu and J. L. Volakis, "The Mode Matching Technique for Electromagnetic Scattering by Inlets with Complex Terminations", Technical Report 030395-3-T, The University of Michigan, EECS Radiation Laboratory, Ann Arbor MI, October 1993.

Three-Dimensional Finite Element Analysis on a Parallel Computer

Richard K. Gordon
Department of Electrical Engineering
University of Mississippi
University, MS 38677

I. Introduction

In the recent past, a number of researchers have investigated the use of parallel computers for the solution of problems in computational electromagnetics. For instance, in [1], Calalo, Cwik, Imbriale, Jacobi, Liewer, Lockhart, Lyzenga, and Patterson discuss the implementation of an FDTD code and the NEC code on the Mark III Hypercube. Barkeshli and Volakis present the parallelization of the CGFFT algorithm in [ ]. In [3], Bedrosian, D'Angelo, and deBlois review the implementation of the T-matrix method and an integral equation technique on parallel computers. And Chatterjee, Volakis, and Windheiser discuss the parallelization of a finite element algorithm in [4].

In the present paper, a three-dimensional finite element algorithm that employs edge elements is used in the analysis of complex cavities. The cavities may have arbitrary shape and loading. A three-dimensional finite element formulation [5] is used to determine the cutoff frequencies of the cavity. Edge elements are used in order to eliminate the possibility of spurious modes.

Because the number of unknowns needed to model a three-dimensional region grows so rapidly as the size or complexity of the region increases, there is a strong motivation to try to implement the numerical analysis of such regions on parallel computers. The use of a parallel computer permits the analysis of significantly larger cavities than those that could be conveniently studied using most sequential computers. Furthermore, in some cases it can also result in a significant speedup in the numerical solution process.

In this paper, the parallelization of the three-dimensional finite element algorithm is discussed in detail. Results obtained on the 400 node Paragon parallel computer at the San Diego Supercomputer Center are compared to those generated on the Cray X-MP2/216 at the University of Mississippi. Computation times are presented and the advantages and disadvantages of using either kind of computer are discussed.

II. Finite Element Formulation

A three-dimensional finite element algorithm is employed in this analysis. The derivation of the equation that is implemented in the numerical procedure begins with Maxwell's equations for a source-free region:

$$\nabla \times \vec{E} = -j\omega\mu\vec{H} \tag{1}$$

and

$$\nabla \times \vec{H} = j\omega\varepsilon\vec{E}. \tag{2}$$

If each side of (2) is multiplied by $\frac{1}{\varepsilon}$, the curl of each side of the resulting equation is taken, and (1) is used to eliminate the curl of $\vec{E}$ on the right hand side, the resulting equation is:

$$\nabla \times (\frac{1}{\varepsilon}\nabla \times \vec{H}) = \omega^2\mu\vec{H}. \tag{3}$$

It is the weak form of this equation that is implemented in the numerical procedure. The next step in the derivation of this weak form is to multiply each side of (3) by a testing function $\vec{T}_i$ and then to use the vector identity $\nabla \cdot (\vec{a} \times \vec{b}) = \vec{b} \cdot \nabla \times \vec{a} - \vec{a} \cdot \nabla \times \vec{b}$ to obtain:

$$\frac{1}{\varepsilon}(\nabla \times \vec{H}) \cdot (\nabla \times \vec{T}_i) - \omega^2\mu\vec{T}_i \cdot \vec{H} = \nabla \cdot \left[\frac{1}{\varepsilon}\vec{T}_i \times (\nabla \times \vec{H})\right]. \tag{4}$$

In the method used here, the region of interest is divided into a number of parallelepipeds. With each edge of a parallelepiped there are an associated vector basis function and vector testing function. $\vec{T}_i$ is the vector testing function associated with edge #i. If we integrate (4) over ΔV, the region occupied by a single parallelepiped, and use the divergence theorem on the right hand side, we obtain:

$$\iiint_{\Delta V}\left[\frac{1}{\varepsilon}(\nabla \times \vec{H}) \cdot (\nabla \times \vec{T}_i) - \omega^2\mu\vec{T}_i \cdot \vec{H}\right]dV = \oiint_{\partial(\Delta V)}\left[\frac{1}{\varepsilon}\vec{T}_i \times (\nabla \times \vec{H}) \cdot \hat{n}\right]dS \tag{5}$$

where $\partial(\Delta V)$ is the surface bounding ΔV.

If (2) is used on the right hand side, the resulting equation is:

$$\iiint_{\Delta V}\left[\frac{1}{\varepsilon}(\nabla \times \vec{H}) \cdot (\nabla \times \vec{T}_i) - \omega^2\mu\vec{T}_i \cdot \vec{H}\right]dV = \oiint_{\partial(\Delta V)}\left[j\omega\left(\vec{T}_i \times \vec{E}\right) \cdot \hat{n}\right]dS. \tag{6}$$

This equation is valid over the region ΔV enclosed by a single parallelepiped. The goal is to find the equation that is appropriate for the entire meshed region Γ, the boundary of which is $\partial\Gamma$. This is done by summing the equations (6) that result from all of the parallelepipeds. When this summation is done on the left hand side, it is clear that the result is simply an integral of exactly the same form over the entire region Γ. To determine what happens on the right hand side, consider a

face shared by two adjacent parallelepipeds. We note that since no source is present, the tangential component of $\vec{E}$ is continuous across this face and that the normal vector pointing out of one of the parallelepipeds will be the negative of the normal vector pointing out of the other. So, the contributions from the right hand sides of the equations (6) of these two adjacent parallelepipeds will exactly cancel. Since no sources are present in the cavity, this same cancellation will occur along any interior face in the mesh. So, when the contributions from all of the parallelepipeds are added, the result on the right hand side is an integral of exactly the same form over $\partial\Gamma$, the surface of the entire meshed region. Thus, the desired weak form of (3) can be written as:

$$\iiint_{\Gamma}\left[\frac{1}{\epsilon}(\nabla\times\vec{H})\cdot(\nabla\times\vec{T}_i)-\omega^2\mu\vec{T}_i\cdot\vec{H}\right]dV=\oiint_{\partial\Gamma}\left[j\omega\vec{T}_i\cdot(\vec{E}\times\hat{n})\right]dS. \tag{7}$$

In this work, the goal is to determine the cutoff frequencies of a cavity that is enclosed by either pmc or pec walls. If the walls are pmc, the value of the tangential component of $\vec{H}$ along the walls is known; thus, for any edge i that lies along the wall, there is no need for the use of a testing function; $\vec{T}_i$ can be taken to be zero. Thus, if the walls are pmc, the right hand side of this equation is zero. If, on the other hand, the walls are pec, then $\vec{E}\times\hat{n}$ is zero along the walls. So, again, the right hand side of (7) vanishes. So, for either pmc or pec walls, we have:

$$\iiint_{\Gamma}\left[\frac{1}{\epsilon}(\nabla\times\vec{H})\cdot(\nabla\times\vec{T}_i)-\omega^2\mu\vec{T}_i\cdot\vec{H}\right]dV=0. \tag{8}$$

As was mentioned above, with each edge of a parallelepiped there are an associated vector basis function and vector testing function. The vector basis function at edge j is $\vec{B}_j$. In the finite element procedure, $\vec{H}$ is expressed in terms of these basis functions as:

$$\vec{H}(x,y,z)=\sum_{j=1}^{N}h_j\vec{B}_j(x,y,z) \tag{9}$$

where N is the total number of edges in the mesh. If this expression is substituted into (8), we obtain:

$$\sum_{j=1}^{N}\left[\left(\iiint_{\Gamma}\left[\frac{1}{\epsilon}(\nabla\times\vec{B}_j)\cdot(\nabla\times\vec{T}_i)-\omega^2\mu\vec{T}_i\cdot\vec{B}_j\right]dV\right)h_j\right]=0. \tag{10}$$

This is one equation in the N unknowns h_1 through h_N. If we now let i vary from 1 to N, i.e., we test over each edge, we obtain a system of N equations in N unknowns that can be written in matrix form as:

$$\overline{M}\bar{h} = \bar{0} \tag{11}$$

where

$$M_{i,j} = \iiint_V \left[\frac{1}{\varepsilon} (\nabla \times \bar{B}_j) \cdot (\nabla \times \bar{T}_i) - \omega^2 \mu \bar{T}_i \cdot \bar{B}_j \right] dV. \tag{12}$$

The only way that (11) can be satisfied for non-trivial $\bar{h}$, i.e., the only way there will be non-trivial source-free solutions, is for the determinant of $\overline{M}$ to be zero. This observation leads us to the technique that is used to determine the cutoff frequencies of the cavity.

III. Procedure for Finding Cutoff Frequencies

We note from (12) that the entries of $\overline{M}$ depend on the frequency, f, where $f = \frac{\omega}{2\pi}$. The technique for determining the cutoff frequencies begins with a choice of an initial frequency, f_o, and frequency increment, Δf. Once the initial frequency, f_o, is chosen, all the terms in the matrix are determined and the determinant of the matrix can be calculated. This is done and then the frequency is incremented by the amount Δf. The determinant is then calculated again. This process of calculating the determinant as the frequency is scanned continues until the determinant changes sign, thereby indicating that a cutoff frequency has just been passed. At this point, it is known that a cutoff frequency lies between the last two frequencies considered; a more precise value for this frequency can be obtained either by interpolation or by choosing a smaller frequency increment and scanning between the last two frequencies considered.

IV. Parallelization of the Technique

This algorithm was parallelized in three respects. Parallelization was incorporated into the assembly and storage of the matrix, the evaluation of the determinant, and the frequency scanning. The idea is as follows. After the finite element mesh has been generated for the geometry of interest, the size of the system matrix is known. In order to save memory, this matrix is stored in banded storage mode. Still, it is generally too large to fit on one node. So, the minimum number of nodes that will accommodate this matrix is next calculated; this number is called *nmin*. The next step is to choose the number of nodes over which the matrix is distributed for a single calculation of the determinant, keeping in mind that this number must be greater than or equal to *nmin*. This number is called *nopergr*. The next step is to decide the total number of nodes that will be used. This total number is divided by *nopergr* to obtain the number *groups*. The idea is that all of the nodes are divided into a number of groups of nodes. Each group has *nopergr* nodes. The total number of groups is *groups*. Since each group is capable of accommodating the matrix, it can work independently of all the other groups. So, frequency scanning is achieved by assigning different frequencies to different groups. Within each group, the filling of the matrix and the evaluation of the determinant is

distributed over all *nopergr* nodes in the group. Thus, the assembling and storage of the matrix, the evaluation of the determinant, and the scanning of the frequency have all been parallelized.

V. Numerical Results

Although this technique is suitable for the determination of the cutoff frequencies of an arbitrarily shaped and arbitrarily filled cavity, in order to be able to obtain a comparison with analytical values for the cutoff frequencies, an empty cavity having the shape of a parallelepiped was chosen for the sample numerical results. This cavity had lengths in the x, y, and z directions of 5 cm., 7 cm., and 11 cm., respectively. The walls were pec. The technique described above was implemented on the 400 node Paragon computer at San Diego Supercomputer Center (SDSC). For the sake of comparison, the unparallelized version of this algorithm was implemented on the Cray X-MP2/216 at the Mississippi Center for Supercomputing Research (MCSR). A frequency range of 2.3-5.4 GHz and frequency increment of 0.1 GHz were chosen and a finite element mesh with 5 divisions in the x-direction, 7 divisions in the y-direction, and 11 divisions in the z-direction was used. The total number of edges in the mesh was 1,512. The numerically determined values for the cutoff frequencies were the same on both computers; these values are shown in the right hand column of Table 1. Note that two of the first ten cutoff frequencies were not detected. The reason for this is that each of these two frequencies is the cutoff frequency for two modes. Thus, the determinant goes to zero at this frequency but does not change sign; so, the cutoff frequency cannot be detected using the procedure described above. For the other cutoff frequencies, the agreement between the numerical and analytical values is quite good.

The time required to run this program on the Cray X-MP2/216 was 97.044 s. The time required on the Paragon depended on the number of nodes used as shown in Table 2 and Fig. 1. In this case, the goal was to determine the effect of the frequency scanning. So, the calculation of the determinant at a single frequency was assigned to a single node; that is, *nopergr* was chosen to be 1 and *groups* was equal to the total number of nodes employed. As can be seen from Fig. 1, there was essentially linear speed-up over the entire range. The reason for this is that the frequency scanning is embarrassingly parallel; the calculations of the determinant at different frequencies are completely independent of each other.

The next goal was to investigate the effect of the parallelization of the calculation of the determinant. So, a single frequency was chosen. The determinant at this frequency was calculated using 1, 2, 4, 8, 16, and 32 nodes. The results are shown in Table 3 and Fig. 2. The speed-up is not even close to linear in this case. There is some benefit in using 2, 4, 8, or 16 nodes rather than just 1; in fact, the best choice of those tested is 4 nodes. Note that if 32 nodes are used the elapsed time is longer than if a single node is employed. The reason for this and for the failure to achieve linear speed-up in this case is that when the matrix is distributed over several nodes, a considerable amount of inter-node communication is necessary in the calculation of the determinant; this communication slows down the technique.

VI. Conclusions

A three-dimensional finite element algorithm that employs edge elements in the determination of the cutoff frequencies of an arbitrarily shaped and arbitrarily filled cavity has been discussed. A method for parallelizing this technique has also been presented. This method includes parallelization of both the frequency scanning and the calculation of the determinant of the finite element matrix. It was found that the frequency scanning was an embarrassingly parallel procedure; essentially linear speed-up was obtained for this part of the parallelization. On the other hand, if the matrix is distributed over several nodes, the calculation of the determinant requires considerable communication between these nodes; thus, the speed-up obtained for this part of the parallelization fell considerably short of being linear.

The computation time on the Cray X-MP2/216 was less than for any of the cases attempted on the Paragon. Furthermore, the development of the code for the Cray X-MP2/216 required less effort than did the development of the code for the Paragon. But it is important to recall the simplicity of the cavity that was under investigation. For a cavity of more complicated shape and/or filling, the discretization process can easily lead to a mesh that will be too large for convenient analysis on the Cray X-MP2/216; this is the kind of case for which the technique described is suitable.

Acknowledgments

The author would like to express his sincere appreciation to the National Science Foundation for affording him the opportunity to participate in the Metacenter Computational Science Institute in Parallel Computing, the San Diego Supercomputer Center for the use of their Paragon computer and their expert advice, and the Mississippi Center for Supercomputing Research for their expert help and the use of the Cray X-MP2/216.

REFERENCES

[1] R. H. Calalo, T. A. Cwik, W. A. Imbriale, N. Jacobi, P. C. Liewer, T. G. Lockhart, G. A. Lyzenga, and J. E. Patterson, "Hypercube parallel architecture applied to electromagnetic scattering analysis," *IEEE Transactions on Magnetics*, vol. 25, num. 4, pp. 2898-2900, July 1989.

[2] K. Barkeshli and J. L. Volakis, "A vector-concurrent application of a conjugate gradient FFT algorithm to electromagnetic radiation and scattering problems," *IEEE Transactions on Magnetics*, vol. 25, num. 4, pp. 2892-2894, July 1989.

[3] G. Bedrosian, J. D'Angelo, and A. deBlois, "Parallel computing for RF scattering calculations," *IEEE Transactions on Magnetics*, vol. 25, num. 4, pp. 2884-2889, July 1989.

[4] A. Chatterjee, J. L. Volakis, and D. Windheiser, "Parallel computation of 3D electromagnetic scattering using finite elements," submitted to *International Journal of Numerical Modeling*.

[5] K. Ise, K. Inoue, and M. Koshiba, "Three-dimensional finite-element method with edge elements for electromagnetic waveguide discontinuities," *IEEE Transactions on Microwave Theory and Techniques*, vol. 39, num. 8, pp. 1289-1295, August 1991.

Analytical Value for Cutoff Frequency (GHz)	Numerical Value for Cutoff Frequency (GHz)
2.54	2.50
3.29	3.30
3.47	3.50
3.69	3.70
3.93	not detected
4.05	4.10
4.50	4.60
4.59	not detected
4.62	4.70
5.23	5.30

Table 1. Comparison of analytical and numerical values for cutoff frequencies

Total Number of Nodes	Elapsed Time (s)
1	12,953.847
2	6,631.990
4	3,212.869
8	1,626.152
16	834.421
32	432.927

Table 2. Elapsed time for calculation of determinant at 32 frequencies

Total Number of Nodes	Elapsed Time (s)
1	421.812
2	270.178
4	199.148
8	222.546
16	351.279
32	693.090

Table 3. Elapsed time for calculation of determinant at 1 frequency

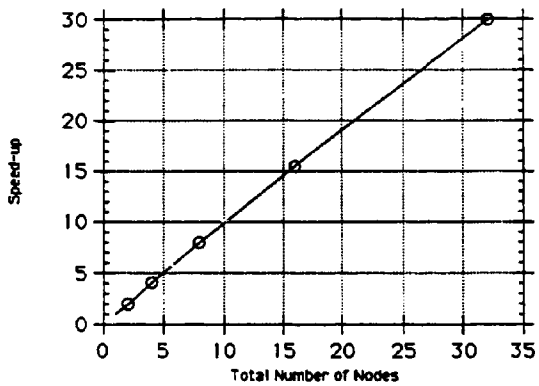

Figure 1. Speed-up for scanning of frequencies

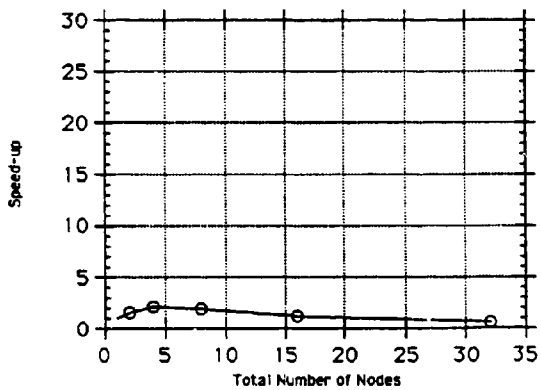

Figure 2. Speed-up for calculation of determinant

THE PERFORMANCE OF A PARTITIONING FINITE ELEMENT METHOD ON THE TOUCHSTONE DELTA

Yung Shirley Choi-Grogan and Robert Lee*
ElectroScience Laboratory
Dept. of Electrical Engineering
The Ohio State University
1320 Kinnear Rd.
Columbus, OH 43212

Kalluri Eswar and P. Sadayappan
Dept of Computer and Info. Science
The Ohio State University
2036 Neil Ave.
Columbus, OH 43210

I. Introduction

The finite element modeling of electrically large structures has always been a difficult problem in electromagnetics because the number of unknowns increases dramatically as the electrical size of the structure increases. One of the ways to increase the efficiency of the finite element method is to use a "divide and conquer" strategy. This idea has been applied to integral equation methods in which the computation domain is partitioned into many smaller sections. The solution is then generated in each section independent of the other sections. The coupling between the sections is then performed in either an iterative manner [1] or by employing a more rigorous and computationally expensive procedure [2,3]. The concept of partitioning has also been used for the finite element method [4,5]. However, in all these methods except [2], the partitioning has only been performed along one dimension. In this paper, we consider an extension of [4] for two-dimensional (2-D) geometries, where the computation domain is partitioned along both dimensions. In [4], the problem of electromagnetic scattering from a 2-D cylinder is considered where the bymoment method [6] is used for the boundary truncation. The bymoment method requires the solution of multiple finite element problems with known Neumann boundary conditions. Since the purpose of this paper is to consider the improvement in efficiency of the finite element solution, we will only consider finite element problems with known Neumann boundary conditions. Another major advantage of the partitioning method is its inherent adaptablity to massively parallel multiprocessors. Since much of the calculations for each section are done independent of the other sections, each processor can perform the operations associated with its own sections without communicating with the other other processors. The performance of the method on a MIMD (multiple input multiple data) architecture is shown here.

II. Formulation

The 2-D problem considered here is an infinitely long cylinder of arbitrary shape and arbitrary material properties in free space. In this paper, only the TM_z polarization is described. Let us consider a partitioning of a representative cylinder (Figure 1) A known Neumann boundary condition is applied to the outer boundary which is represented by $\delta\Omega$. The inter-section boundaries are denoted by δS_n.

The Neumann boundary condition can be defined in terms of the tangential magnetic field along the boundaries of each section. Although the Neumann boundary condition is given on $\delta\Omega$, it is not known a priori on δS_n. However, we can approximate the values on each inter-section boundary in terms of a sum of known basis functions multiplied by unknown coefficients. The Neumann boundary condition on the inter-section boundary is defined to be:

$$\frac{1}{\mu}\frac{\partial E}{\partial n} = \sum_{i=1}^{\infty} a_i \Psi_i(t), \qquad t \in [0, d] \tag{1}$$

where t represents the points on the inter-section boundary δS_n which has a length of d. The variable a_i represents a set of the unknown coefficient to be determined. The function $\Psi_i(t)$ is a set of linearly independent basis functions. In the numerical implementation of (1), the infinite sum is truncated to I.

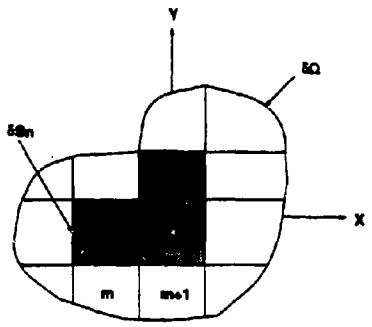

Figure 1: The partitioned solution domain

Let us consider the interior n^{th} section (not touching $\delta\Omega$) with the Neumann boundary conditions applied on each of the four inter-section boundaries. Based on the property of linearity, the total electric field solution on the n^{th} interior section can be determined from the superposition of the four boundary value problems. The total solution on the section is expressed as a sum of four boundary value solutions:

$$E_n^{total}(x,y) = E_n^U(x,y) + E_n^D(x,y) + E_n^R(x,y) + E_n^L(x,y) \tag{2}$$

where the four field solutions are defined to be,

$$E_n^L(x,y) = \sum_{i=1}^{I} p_{i,n}\Lambda_{i,n}^L(x,y) \quad ; \quad E_n^D(x,y) = \sum_{i=1}^{I} q_{i,n}\Lambda_{i,n}^D(x,y)$$
$$E_n^R(x,y) = \sum_{i=1}^{I} r_{i,n}\Lambda_{i,n}^R(x,y) \quad ; \quad E_n^U(x,y) = \sum_{i=1}^{I} s_{i,n}\Lambda_{i,n}^U(x,y) \tag{3}$$

The subscripts i,n refer to the i^{th} term in the sum and the n^{th} section respectively. The superscripts, L (left), D (down), R (right), and U (up), refer to the side of the section on which the Neumann boundary condition is applied, with its corresponding unknown coefficient vectors (p_n, q_n, r_n, and s_n). The finite element solution $\Lambda_{i,n}(x,y)$ is obtained from the use of the corresponding basis function $\Psi_i(t)$ as the Neumann boundary condition.

To evaluate the unknown coefficients on each inter-section boundary, the finite element solutions of each section are coupled to the adjacent sections by enforcing the continuity of the tangential electric and magnetic fields on the inter-section boundary. The continuity of the tangential magnetic field is enforced explicitly. However, the continuity of the tangential electric field is enforced in an integral sense. The application of field continuity results in a sparse matrix equation, which we call the *coupling matrix*. A general sparse Cholesky LU factorization and

Table 1: Time comparison for solving the entire body vs the partitioned body

solution	traditional method		partition technique	
domain	time(sec)		subregion	time(sec)
	banded	sparse		
4λ sq	5.10	1.01	.5λ sq	1.21
			1λ sq	1.71
8λ sq	106.89	5.77	.5λ sq	5.65
			1λ sq	7.97
12λ sq		16.27	.5λ sq	14.18
			1λ sq	19.36

solve algorithm [7] is used to solve the coupling matrix. In order to minimize the fill-ins during the LU factorization , a nested dissection reordering of the matrix is done. It is expected that the computation time will be proportional to $N^{1.5}$ and the storage will be proportional to N where N represents the size of the coupling matrix.

III. Performance for the Sequential Partitioning Technique

To demonstrate the efficiency of the partitioning technique, we study the results of the method on a plane wave incident on a rectangular region of free space of varying sizes. The main reason that we consider free space is that the boundary conditions are known for this case. The efficiency should be the same for more complex geometries. The three problems considered here are free space square regions with sides of length 4λ, 8λ, and 12λ. Eight-node quadrilateral elements are used to discretize the computation domain. For the traditional method, the number of nodes in the three computation domains is 4,961 (4λ), 19,521 (8λ), and 43,681 (12λ). Each geometry is partitioned into either 0.5λ square sections or 1λ square sections. Triangular subdomain basis functions have been used for Ψ_i in (1). For the cases presented below, the solutions from the partitioning method and the traditional method have been compared to verify that they have the same degree of accuracy.

A. Time Performance

Table 1 shows the computation time for the traditional method and the partitioning technique on a Cray YMP. The first two time columns in Table 1 represent the time required to solve the corresponding problems with the traditional finite element method by the use of either the a banded solver algorithm or a general sparse solver algorithm. The latter algorithm has a smaller number of non-zeros and thus requires a smaller operation count to factorize the matrix.

The data for the 4λ geometry show that the partitioning technique is more computationally expensive than the traditional method. This difference in time is due to the overhead time required in coupling the partitioned sections and in calculating and solving the coupling matrix. The geometry is not large enough to take advantage of the partitioning technique with the given sizes of the partitioned sections. However, as the size of the solution domain increases (and the partitioned sections are of a relatively smaller size), the computation time becomes smaller than that required for the traditional method. As the size of the computation domain increases, we expect the difference in efficiency between the partitioning method and the traditional method to increase. Unfortunately, a larger size could not be tested because the memory requirements for the traditional method exceeded the available memory on the Cray.

Table 2: Memory comparison for solving the entire body vs partitioned body

solution	traditional method		partition technique	
domain	Memory(Mword)		subregion	Memory(Mword)
	banded	sparse		
4λ sq	0.63	0.56	.5λ sq	0.06
			1λ sq	0.03
8λ sq	4.80	2.81	.5λ sq	0.39
			1λ sq	0.18
12λ sq	15.99	7.07	.5λ sq	1.12
			1λ sq	0.54

B. Memory Requirements

The reduction in memory requirements is one of the major advantages of the partitioning technique over the traditional method. Table 2 shows the memory requirements for both the traditional and the partitioning technique on the same solution domains as discussed in Table 1. The first two "memory" columns in Table 2 represent the memory requirements for the traditional method with either a banded solver algorithm or a general sparse solver algorithm. For the sparse solver algorithm only the nonzero values of the matrix under consideration need to be stored, whereas, the banded solver stores all the terms within the entire half bandwidth. The last column is for the memory requirements of the partitioning technique.

IV. Parallel Implementation of the Partitioning Technique

The MIMD architecture of the Intel machines allows each processor to execute different instructions on different data. It is noted that concurrency of operations is greatly utilized before generating and solving the coupling matrix; no communication is required for solving the finite element solutions for the appropriate sections. Communication between processors starts during the calculation of the coupling matrix.

A. Mapping the Coupling Matrix

The sparse Gaussian elimination algorithm operates on units of the matrix that we will call *row-columns*. There are as many row-columns as there are unknowns in the coupling system. Row-column i consists of the following matrix elements: (i) the diagonal element in row/column i (C_{ii}), (ii) the upper triangular elements in row i ($C_{ij}, j > i$), (iii) the right hand side element in row i ($C_{i,N+1}$), and (iv) the lower triangular elements in column i ($C_{ji}, j > i$). The forward elimination phase of the sparse Gaussian elimination consists of two kinds of operations: (i) *normalize*: the scaling of the upper triangular and right hand side elements of a row-column by its diagonal element, and (ii) *update*: the modification of the elements of a row-column i using the elements of a row-column k, where $i > k$ and C_{ki} is a nonzero. The time required for the back substitution phase is much smaller than that the forward elimination phase. The mapping algorithm therefore concentrates on making the forward elimination process efficient.

The mapping of the row-columns to processors should be done so as to simultaneously have low communication and good dynamic load balancing. A simple data structure, called the *elimination tree* helps in achieving this. This tree has N nodes, one for each of the row-columns of the matrix, and the parent of each node i is defined by $parent(i) = \min \{j : j > i \text{ and } C_{ij} \text{ is a nonzero}\}$. It can be shown that a row-column updates only a subset of its ancestors in the elimination tree and in turn is updated only by a subset of its descendants. In general, therefore, if a mapping

is chosen so that nodes which are in the same subtree are mapped onto the same processor or among a small subset of the processors, reduction in communication can be expected.

A heuristic algorithm, called *recursive partitioning* [8], which takes the amount of work at each node of the elimination tree into consideration to produce a load-balanced mapping, is used. The amount of work at each node is considered to be the sum of the number of update operations *onto* the row-column corresponding to the node and the number of normalization operations for the row-column corresponding to the node. The algorithm performs a breadth-first traversal of the elimination tree assigning nodes in wrap fashion to all processors. This continues until two sets of subtrees having approximately equal total work are found. At this point, the set of processors is split into two subsets, each of them assigned one subset of subtrees, and the algorithm is recursively applied to each of them.

B. Mapping Sections

The mapping of sections to processors is performed by using a simple heuristic algorithm. The results of the FEM computations on a section are needed to determine the values in the row-columns whose unknowns are represented by the expansion terms on the boundaries of the section. Call these row-columns the *relevant* row-columns of the section. Therefore, each section is mapped onto one of the set of processors that have at least one of its relevant row-columns mapped onto them. The processor chosen out of this set is the one that has the maximum number of the relevant row-columns mapped onto it. If there are ties, the section remains unmapped at that point. After attempting to map all sections using the above method, all remaining sections are mapped to processors using a greedy algorithm as follows. Each unmapped sections is considered in turn and mapped onto the processor that has the least number of sections mapped onto it at that point.

C. Solving the Coupling System in Parallel

The parallel algorithm used for the computationally dominant forward elimination phase maps the update and normalize computations as follows. The updating operation of a row-column i (the target row-column) using a row-column k (the source row-column) can be considered to happen in two stages. The first is a set of multiplications to form the contribution of row-column k to row-column i. The second is the subtraction of the contribution to the corresponding elements in row-column i. The multiplication operations are mapped onto the processor that owns the source row-column. If the processor owns other source row-columns that update the same target row-column, all their contributions are *added* together on the processor. This combined contribution is then sent to the processor that owns the target row-column, where it is *subtracted* from the target row-column's elements. The normalizing operations for a row-column are mapped onto the processor that owns it.

The next issue to consider after deciding on the computation mapping is the order in which each processor carries out its computations. One approach is for each processor to consider each target row-column in turn. The combined contribution for this target (using the source row-columns that the processor owns) is formed and then sent to the processor owning the target, if it is a different processor, or subtracted locally if it is the same processor. If a row-column is owned, the processor also waits for all combined contributions destined for it to arrive from other processors. These combined contributions are subracted from the row-column, and it is then normalized. By considering the targets in increasing order of their index in the matrix, all the locally owned sources that update it are guaranteed to have been normalized by the time the target is considered. This approach is based on the fan-in algorithm for parallel sparse Cholesky factorization [9]. The primary advantage of this approach over the one to be considered next is that the working storage required on each processor consists mainly of the storage required for one

combined contribution. This storage, which need be only as large as the largest row-column, is reused for each target row-column. The primary drawback of the approach is the problem of idling processors due to the fact that updates onto subsequent target row-columns are not performed by a processor until all combined contributions are received for earlier owned row-columns, even though the source row-columns that update the later target have been normalized and ready to be used.

Another approach to the ordering of the computations on each processor is based on the *kji-agg-sup* algorithm [10]. In this approach, a normalized source row-column can be used to update any of its target row-columns. These updates are added together to form a combined contribution as before. Instead of considering the target row-columns in turn, this approach maintains a queue of normalized locally owned sources, and considers sources from this queue as they become available. If the queue is empty, the processor waits for combined contributions to arrive from other processors. This approach has been found, in the Cholesky factorization case, to have better dynamic load balancing than the fan-in approach. It also has the advantage of making better use of the data cache, if one exists, on each processor. However, its main drawback is the amount of working storage required on each processor. There will be many partially formed combined contributions existing on each processor at any instant. Therefore, working storage is required on each processor that could potentially be as large as the sum of the sizes of the target row-columns for which combined contributions originate from the processor. This is quite unsatisfactory, especially for large problems. The approach presented next, which is the one used here, addresses this problem.

Each processor participating in a forward elimination computation based on row-columns needs space for the row-columns that it owns. In addition, space is needed for keeping the nonzero structure of the matrix (in compressed form, and thus usually taking up considerably less space than the matrix), and for some auxiliary information such as row-column-to-processor mapping information. The new approach uses all the remaining memory on each processor for storing combined contributions formed on that processor. The parallel algorithm can thus adapt to the amount of available memory. Updates to any target row-column are done whenever possible.

The computation on each processor is driven by a queue of locally owned source row-columns that have been completely updated. When this queue is empty, the processors waits for messages from other processors containing combined contributions to be applied to its owned row-columns. A source that is deleted from the queue is normalized and then used to update its targets in succession. If a target is owned, it is directly updated in the matrix structure. if this is the last update onto the target, it is added to the queue. If a target is not owned, then a combined contribution for the target needs to be updated. If this is the first update onto that target, space for its combined contribution is allocated from the available memory. In any case, if this is the last owned source to update this target, the combined contribution is sent to the target's owner, and the space used by it is freed. If memory is unavailable for the combined contribution of a target that is being updated for the first time, it is added to a queue of pending targets. The source which attempted to update the target is placed on a list of failed sources associated with that target. When space is freed, a target from the pending queue is allocated space, and it is updated by the sources that had been placed on its list.

V. Results for the Parallel Partitioning Technique

In this section, we will show the benefits of parallelization of the partitioning technique for further reducing the computation time. The parallel computers used for collecting the data is the 547-node 2D mesh architecture Intel Touchstone Delta machine. The problems considered here

are the 8λ and 12λ cases from the sequential results. A square region with sides of length 20λ (120,801 unknowns) is also considered.

The total execution time consists of four dominant components: generating the boundary conditions for each partitioned sections, solving the finite element solutions on the sections for each boundary condition, generating the coupling matrix, and finally, solving the unknown coefficients from the coupling matrix. The finite element solutions are calculated for various sections on different processors concurrently. From the "bdry" and "FEM" columns in Table 3, we can see that the time reduction in generating the boundary conditions and solving the finite element solutions is approximately a linear function with respect to the number of processors used. As the number of processors increases, the section mapping algorithm will distribute all sections to balance the work load on each processor.

Message passing starts when the finite element solutions are used to generate the coupling matrix. The "set coup" column in Table 3 represents the time spent in sending and receiving the finite element solutions and to generate the coupling matrix. There is a decrease in the time required for generating the coupling matrix as the number of processors increases. This is due to the fact that fewer row/column pairs are owned by one processor as the matrix is distributed among more processors. However, the time spent on passing messages is dependent on the coupling and the section mapping algorithms. It also depends on the volume of the messages and the number of initiated communications.

The final stage of the parallelized partitioning technique is the solution of a coupling matrix by the use of a parallel Gaussian elimination algorithm. The column "solver" in Table 3 shows the time required in solving the coupling matrix. The total computation time in Table 3 shows a significant reduction in the time required for solving the electrically large solution domain by

Table 3: Execution time on the Touchstone Delta

entire	# secs.	# Γs	sect. size	# procs.	total time	bdry	FEM matrix	set coup.	solver
8 λsq	256	2880	.5 λ sq	4	34.76	10.59	10.43	4.00	9.63
				8	18.93	5.34	5.25	1.6	6.63
				16	10.59	2.75	2.69	.74	4.30
				32	6.36	1.44	1.31	.38	3.14
				64	4.28	0.66	0.61	.21	2.70
12 λsq	144	2904	1 λ sq	4	133.02	37.18	67.36	7.90	19.77
				8	71.36	18.18	34.11	4.03	14.24
				16	40.45	9.31	17.28	2.18	10.88
				32	22.96	4.86	8.96	0.90	7.44
				64	13.79	2.11	4.75	.512	5.61
12 λsq	576	6624	.5λ sq	16	29.52	6.34	5.86	2.40	14.82
				32	16.35	3.07	2.94	0.83	9.39
				64	10.97	1.58	1.57	0.67	7.04
				128	8.27	0.88	.871	0.58	5.83
				256	6.98	0.49	.486	0.51	5.38
20 λsq	400	8360	1λ sq	32	80.08	12.42	23.46	2.91	40.50
				64	51.89	6.26	12.32	2.46	30.05
				128	34.16	3.22	6.63	1.86	21.65
				256	27.39	1.61	3.31	0.81	20.86

using the partitioning finite element technique. In Table 3, we see that a speed-up factor of approximately 1.85 is achieved when 8 processors are used instead of 4. The speed-up factor is approximately 5.73 as we increase the number of processors from 4 to 32. The latter two cases represent two larger problems which require more processors for the field solution. The smaller value of the speed-up factor for the larger problems is due to the larger number of processors used and the dominance of the the Gaussian elimination algorithm as the size of the coupling matrix increases.

VI. Summary

The two major concerns for the efficiency in solving an electrically large electromagnetic problem are the computation time and memory requirements. The partitioning technique was discussed and the numerical results summarized to show the benefits of the paritioning technique over the traditional finite element method. The fact that the partitioned sections can be solved independently is ideal for a parallel implementation of the method. Algorithms such as nested dissection ordering and parallel Gaussian elimination were carefully implemented to reduce the operation counts and the communication time on each processor.

VII. References

[1] K. R. Umashankar and A. Taflove, "Numerical analysis of electromagnetic scattering from electrically large objects using spatial decomposition techniques," *IEEE Trans. Antennas and Propagat.*, AP-40,pp. 867-877,August,1992.

[2] W. C. Chew and C. C. Lu, "NEPAL–An $N^{1.5}$ algorithm for solving volume integral equations," *IEEE Antennas and Propagat. Soc. Int. Sym. Dig.*, vol. 1,pp. 184-187, July, 1992.

[3] T. M. Wang and H. Ling, "Electromagnetic Scattering from three-dimensional cavities via a connection scheme," *IEEE Trans. Antennas and Propagat.*, AP-39,pp. 1505-1513, Oct.,1991.

[4] R. Lee and V. Chupongstimun, "A partitioning technique for the finite element solution of electromagnetic scattering from electrically large dielectric cylinders," to appear in *IEEE Trans. Antennas and Propagat.*

[5] C. T. Spring and A. C. Cangellaris, "A Partitioning Approach to the Electromagnetic Characterization of Large Two and Three Dimensional Structures," *1992 URSI Radio Science Meeting Digest*, p. 230.

[6] A. C. Cangellaris and R. Lee, "The bymoment method for two-dimensional electromagnetic scattering, *IEEE Trans. Antennas and Propagat.*, AP-38,pp. 1429-1437,Sept.,1990

[7] A. George and J. W. Liu, *Computer Solution of Large Sparse Positive Definite Systems*, Prentice-Hall, Englewood Cliffs, NJ, 1981.

[8] K. Eswar, P. Sadayappan, and V. Visvanathan, "Parallel direct solution of sparse linear systems," in *Parallel Computing on Distributed Memory Multiprocessors*, F. Özgüner and F. Erçal (eds.), Springer Verlag, Berlin Heidelberg New York, 1993.

[9] C. Ashcraft, S. Eisenstat, and J. W.-H. Liu, "A fan-in algorithm for distributed sparse numerical factorization," *SIAM J. Sci. Statist. Comput.*, Vol. 11, pp. 593-599, 1990.

[10] K. Eswar, P. Sadayappan, C.-H. Huang, V. Visvanathan, "Supernodal sparse Cholesky factorization on distributed-memory multiprocessors," *Proceedings of the Twenty-second International Conference on Parallel Processing*, St. Charles, IL, Vol. III, pp. 18-22, 1993.

SESSION 8:

VALIDATION

Chair: Patricia Foster
Co-Chair: Mike Hazlett

A DATABASE OF MEASURED DATA FOR RCS CODE VALIDATION

S. R. Mishra, C. L. Larose, M. Flynn
David Florida Laboratory
Canadian Space Agency
Ottawa, Canada

C. W. Trueman
Concordia University
Montreal, Canada

SUMMARY

The Canadian Space Agency's David Florida Laboratory (DFL) has measured the radar cross section (RCS) of a large number of targets over the past few years. The objective of this measurement program was to create a database of measured data expressly for the purpose of validating and developing modeling guidelines for various computational codes. Targets measured vary in their complexity from simple geometrical shapes such as cubes, cylinders, pyramids, cones, rods, and more complicated objects like models of generic aircraft and ships. The RCS database program was conceived to help organize this large collection of RCS measurements. It was the intention of the program developers to enhance the accessibility of the RCS data and provide some simple tools for plotting and viewing the measurements. The database program and some of the measured data will be made available for public distribution.

Although developed for distributing RCS data the software is suitable for use with any information that can be stored in discrete data files. The program employs a hierarchical organizational system. Each experiment (or data file) is categorized by a series of labels that are arranged in a 'tree'. This is similar to the MS-DOS hierarchical system of directories and subdirectories. For example the path

Single/cube/dielectric/10cm/face on/VVpol/Sept 23, 1993

could represent a single angle RCS measurement of a 10cm dielectric cube, vertical transmit, vertical receive polarization (VV). This path would be associated with a corresponding data file, say "CUBE.RPL" stored somewhere on a connected mass storage system. This methodology is sufficiently generalized so that any kind of data files can be organized using the database.

Once entered into the database, the data files can be manipulated in several ways. There are options for moving, compressing and decompressing, editing, viewing, and plotting data files. Compression and decompression is accomplished using Gnu's freely distributable GnuZIP compression code. It typically compressed files at a ratio of 5 to 1 saving large amounts of disk space. Although the database has its own algorithms for plotting multiple data files on the same graph (in a Window), the program is bundled with RPLOT software developed at Concordia University. RPLOT is a complete plotting package providing options like zooming and axes-scaling.

One of the themes for database development is easy access. For this reason, the database has been written under the Microsoft Windows 3.1 OS. This facilitates the implementation of a friendly point-and-click interface, and allows for a wide distribution of the database software and measured data.

The DFL's RCS database file currently contains nearly 1100 experiments representing 32 megabytes (uncompressed) of single angle RCS measurements. Once the full-angle measurements are included, the database will represent several hundred megabytes of measured data. However, only part of this data is released for public distribution. This includes all published data and data independently verified by comparison with computational codes.

VALIDATION OF TARGET MEASUREMENTS IN MULTIPATH ENVIRONMENT

A. J. Stoyanov, K. M. Wilson and Y. J. Stoyanov

Carderock Division, Naval Surface Warfare Center
Bethesda, MD 20084-5000

Abstract

Computer models provide the flexibility and insight into the relationship among the basic parameters that may be difficult to obtain from measured data. Improvements in the computational techniques permit exploring wider ranges of natural phenomena influencing radar signature. In this paper we present comparison of calculated and experimental results of radar backscattering from a trihedral corner reflector at different altitudes above the sea surface. The presence of the sea surface may substantially influence target radar cross section (RCS) since the electromagnetic wave propagation is dominated by two-path coherent interference between direct and surface-reflected waves. The target RCS may vary considerably as a function of radar and target height above the sea surface due to different propagation path lengths. Relative variations in the RCS of the corner reflector are calculated for different radar and target heights above the sea surface at different ranges and validated using measured data. Influence of the multipath lobing on the RCS measurements of radar targets in the marine environment is also considered.

Introduction

The growing interest in the radar cross-section of Navy targets calls for accurate modeling of natural phenomena. In many cases the radar signature of a marine target includes effects of clutter, multipath and target motion. Analysis of the target RCS requires accurate determination of all the effects influencing radar returns. The two basic methods of determining radar reflectivity of full scale targets are static and dynamic measurements. The static measurements when correctly implemented are inherently accurate and repeatable, but limited to target sizes which can be handled conveniently. For those cases where the target cannot be positioned for static measurements, dynamic measurements are used. The major advantage of the dynamic RCS measurements is that "real world" data are obtained. While dynamic RCS data are very practical, one must be careful about concluding that the measured data include all major scattering centers of the target. Environmental influence and limitations on the viewing angles and ranges at which good measurements can be made encourage repetitious measurements which, however, can easily produce high costs. Analytic techniques become valuable for analysis of different conditions and trade-offs that may influence radar scattering from a target.

Considerable research has been conducted on low-elevation angle RCS measurements of marine targets.[1,2] Since the target is located on the sea surface, part of the transmitted signal from the radar and the return signals from the individual scatterers on the target are reflected off the sea surface. The surface reflected signal and the desired signal from the target form a composite signal that enters the main beam of the radar and may seriously degrade its performance. The direct path and multipath return signals sum constructively or destructively so that energy illuminating the target may increase or decrease as compared with free space measurements.

It was shown earlier that the lobing structure due to the interference of the direct and reflected signals creates problems for radars operating at low elevation angles because severe fading and distortions in measured RCS can occur[1]. To quantify fading and distortions in measured RCS, a series of experiments was conducted at Santa Cruz Radar Imaging Facility (SCRIF). Measurements were made of radar returns from a trihedral corner reflector of known free space radar echoing area. A helicopter with the mounted trihedral descended from high altitude to the ocean surface and then ascended at the same range to determine the sea influence on a scatterer along the vertical direction. Measurements of the multipath effects have been performed at different ranges. A computer model was

used in predicting RCS returns from the trihedral at various elevations above the sea surface. Results of the measurements and computer calculations are presented below.

2. Multipath Measurements

To investigate the multipath phenomenon under controlled conditions, a series of measurements were conducted at Santa Cruz Island located west of Los Angeles in October 1992. The SCRIF antennas are positioned at two different sites located at the edge of a high cliff above the Pacific Ocean. The high elevation site antennas are mounted 1550 ft. above sea level. The low elevation site antenna is mounted further down the cliff only 110 ft above the sea surface. The low-elevation site antenna is connected to the high site using optical fiber cables. The RF signals are converted to light signals and shipped back and forth to the low site on a single mode fiber optic cable. Two fiber optic transmit-receive links are used.

Calibration of the high-elevation site radar is performed using a 24- by 24 in. dihedral corner reflector mounted on a cliff some 1500 ft from the antenna. The RCS of the dihedral corner reflector at 10 GHz is 35.8 dBsm. For the low site a 35.875 in. trihedral corner reflector is used some 2500 feet from the antenna. The RCS of the trihedral corner reflector at 10 GHz is 35.1 dBsm. A complete calibration of the radar system is performed immediately before and after the test. Periodic system checks are performed during the test.

All RCS measurements were taken using a step-chirp waveform. Each burst consists of a series of pulsed sinusoids the frequencies of which increase in equal increments from some minimum value to a maximum value over the duration of the burst. The base frequency of 9 GHz is increased in 256 steps so that the total band-width is 256 MHz. The radar return from an illuminated patch at a specific downrange location is measured by means of range gating. The down-range dimension is one-half the pulse length expressed in units of length, or one-half the pulse-width times the speed of light. Range resolution of 0.59 m is achieved. Both vertical and horizontal polarizations are available.

Figure 1 shows the calculated RCS of the triangular trihedral corner reflector versus elevation angle at two different azimuth angles when one of the triangular faces is horizontal. The RCS of a corner reflector provides strong and relatively steady signal return over a wide range of aspect angles. The RCS of a triangular corner reflector as a function of spherical angles θ (elevation) and φ (azimuth) is[3]:

$$\sigma(\theta,\varphi) = \frac{4\pi}{\lambda^2} a^4 [\cos\theta + \sin\theta(\sin\varphi + \cos\varphi) - 2[\cos\theta + \sin\theta(\sin\varphi + \cos\varphi]^{-1}]^2 \qquad (1)$$

where a is the dimension of the orthogonal edge of the triangular corner reflector. Note that the RCS of the trihedral corner reflector changes only 0.5 dB from its maximum value within 8 degrees in elevation and 10 degrees in azimuth. Such stability over a wide range of aspect angles is more than sufficient for the trihedral to be mounted in the helicopter.

The first measurement run was executed with the trihedral mounted in a helicopter making a 360 degree turn at about 800 ft above the sea surface to avoid any multipath effects. Figure 2 shows target altitude and the RCS returns for H-polarization from the helicopter and the trihedral that indicate a consistently higher RCS when the radar is looking directly into the trihedral than the return from the helicopter. Relative returns from the trihedral corner reflector and the helicopter were measured from the high site some 3 nmi away. Measured median RCS values for H-polarization are about 32.0 dBsm that corresponds to the predicted maximum RCS of the trihedral. It is interesting to note that the maximum RCS of the helicopter does not exceed 25 dBsm except for a few bursts. The median return from the helicopter is about 14.2 dBsm for H-polarization. The median RCS of the trihedral is greater than the radar return from the helicopter by more than 10 dB. Clearly, median RCS contributions from the helicopter are an order of magnitude smaller than the median RCS of the trihedral.

The RCS measurements of the trihedral corner reflector in the helicopter were performed from the high- and low-elevation radar sites at three different ranges. Each run consisted of measuring RCS returns from the trihedral when the helicopter was descending from some 300 ft above the sea surface as low as possible and then ascending again to the initial altitude.

Position of the scatterer relative to the sea surface was obtained using a digital altimeter. The altimeter provides digital output and interfaces directly to data acquisition. The altimeter is calibrated and has a dual-diaphragm pressure sensor which has extremely low sensitivity to shock, vibration, acceleration, and changes in orientation or temperature. Calibration data are stored in ROM memory, and groups of readings can be averaged before storing on a hard disk. According to manufacturer specifications, the accuracy of the altimeter is ± 8 ft and the altitude resolution is one foot. Altitude is recorded every second.

To ensure the maximum radar scattering from the trihedral corner reflector, a television camera was installed to guide the pilot in orienting the helicopter so that the trihedral always faced the radar antenna. Figure 3 shows the altitude and the RCS data measured at the high site as a function of burst number (alternatively, burst number can be translated into time) for the horizontal polarization. Figure 4 shows the altitude and the RCS data measured at the low site. Note the differences in the measured RCS lobing structure when the measurements are performed from the high site versus the low radar site.

Figures 5 and 6 show a portion of the measurement run with the helicopter ascending from the surface to 150 ft. at 5 nmi range for high and low radar sites, respectively. The 150 ft altitude was arbitrarily chosen to represent the highest position of a scatterer on a ship. Large fluctuations in the RCS of the trihedral corner reflector are observed for measurements performed from the low site. Note that the RCS of the reflector stabilizes when the helicopter is hovering at the same altitude. The RCS values strongly depend on the height of the scatterer relative to the sea surface and may vary as much as 20 dB when measured from the low radar site. The median RCS of the scatterer, however, varies only a few dB when all RCS measurements are included from the sea surface up to 150 ft. The following table shows median RCS values of the scatterer measured from the high and the low radar sites for both the ascending (a) and descending (d) helicopter.

Median RCS of scatterer measurements above the sea surface.

	High Radar Antenna Site		Low Radar Antenna Site	
Polarization	Median Range, nmi	Median RCS, dBsm	Median Range, nmi	Median RCS , dBsm
H-pol. (d)	2.84	32.76	2.90	35.08
H-pol. (a)	2.91	32.91	2.90	34.13
H-pol. (d)	5.19	33.98	5.06	32.83
H-pol. (a)	5.17	34.01	5.01	35.30
H-pol. (d)	8.18	30.67	8.14	29.61
H-pol. (a)	8.18	31.04	8.13	32.75

The median RCS values presented are averaged (average RCS return is calculated for all 256 frequencies in the burst) and again medianized for all bursts during the target descent from 150 ft to the sea surface or for the target ascent from the sea surface to an altitude of 150 ft. Median values are chosen to avoid target RCS dependence on the number of bursts. The median RCS measured at the high site shows stable returns for the two polarizations and are almost the same for descending or ascending periods at a given range. Differences, however, are present between the median RCS of the scatterer measured at the low radar site for the descending or ascending periods. The differences in the median RCS become progressively larger as the range increases. Such instability is due to strong multipath influence on measured RCS values of the target at low radar sites.

Figures 7 and 8 show relative variations in the RCS of the target measured at low- and high-radar sites as a function of target height at the 5- and 8 nmi range, respectively. Relative variations in the RCS of the trihedral corner reflector measured at the high and low radar sites can be calculated directly from the given height of the transmitting antenna, the target, and the distance between them.

The Multipath Phenomena.

Multipath effects occur since the sea surface can act as a good radar reflector, especially when the surface is smooth. The direct path electromagnetic wave combines with the wave reflected from the sea surface so that the target is illuminated by complex wave front. The reflection properties of the sea surface are not subject to control and depend on the roughness of the surface. If we examine the phases of the individual waves arriving at the target from the sea surface, we will generally find that a fraction of these phases will be randomly distributed (diffuse scattering) and the remainder will be strongly correlated in phase (coherent scattering). The diffuse scattering can be neglected in the first approximation for small grazing angles because the phases in the diffuse scattering signal produce a field strength that is small compared with the coherently reflected field.[4] The result of the interference effects among the various paths between radar and target is[5]:

$$\sigma = \sigma_s(\theta)\,|F|^2 \tag{1}$$

where $\sigma_s(\theta)$ is the RCS of a scatterer in free space. The factor F is the function of many parameters:

$$F = A + 2\,\mu\,B + \mu^2\,C \tag{2}$$

in which A, B, and C represent individual patterns and are functions of antenna pattern, elevation angle and frequency[6]. Each term can be traced to one of the interaction effects between the radar, target and sea surface. The first term represents the pattern that would be measured had the sea not been present and therefore, represents the free space pattern of an isolated target. The second term includes two contributions which are identical and represent the interaction of the target with the sea surface. These two single-bounce paths are identical, because of the reciprocity, hence the multiplicative factor 2 is present in Eq. (2). A multiplicative factor μ represents a single bounce mechanism and denotes a complex reflection coefficient for the sea surface. The third term in Eq. 2 represents the pattern of the image of the target in the sea except for the double bounce factor μ^2. Thus, the cumulative effect of the three scattering components (direct, single bounce and double bounce) is present in the radar echo response.

A simple theoretical model has been developed to calculate the specular reflection coefficient, μ, of rough surface[4]. The root-mean-square (RMS) value of the specular reflection coefficient is:

$$(\mu)_{RMS} = (\rho_s)_{RMS}\,G \tag{3}$$

where ρ_s is the specular scattering coefficient and G is the reflection coefficient for a smooth sea surface. For a Gaussian-model rough surface:

$$\langle\rho_s\rangle^2_{average} = \exp\{-(4\pi\,\Delta h\,\sin\psi/\lambda)^2\} \tag{4}$$

where Δh is the root-mean-squared deviation in surface height, ψ is the grazing angle, and λ is the radar wave length. The quantity in the parenthesis is just the phase difference between two rays that reflect from the rough surface: one ray reflecting from the mean surface level and other from a crest of height Δh on the surface. This simple theoretical model agrees fairly well with actual measurements over a range of grazing angles[4]. The propagation measurements with which the model can be compared permit only relatively crude estimates of Δh, and it does not appear useful to consider more elaborate models until more complete and accurate data with quantitative ground truth are obtained. A sea state description, however, can be related to the root-mean-square wave height and grazing angles. For sea

states and grazing angles exceeding about twice the critical angle, the specular component becomes insignificant, and reflection coefficient will depend upon the diffuse scattering factor[7].

Figures 9 and 10 show calculated RCS of the trihedral corner reflector for 9.2 GHz at low- and high radar sites for 5- and 8 nmi ranges, respectively. The range and positions of the reflector relative to the sea surface are measured values during each experimental run. The similarity between the calculated (Figures 9 and 10) and measured (Figures 7 and 8) RCS values for different target altitudes is remarkable considering model simplifications. The differences in the lobing structures can be attributed to a number of environmental factors among which sea swells may play important role. The agreement of the calculated and observed RCS can further be improved by considering relative changes in the antenna and target positions during the experiment.

Conclusions

It has been demonstrated that a theoretical model is capable of describing RCS measurements in the multipath environment. Differences in RCS values for a given target measured at low and high radar sites are clearly identified and explained using straightforward appmach. Future work on the multipath phenomena will be aimed at extending the range of sea conditions, target geometries and radar parameters.

Acknowledgments: The authors wish to thank all personnel in the Measurement Technology Department of the CDNSWC Signatures Directorate associated with the measurements for their contributions to the collection and processing of the data. The authors are grateful for the support by the Office of Naval Research, Surface Ship Technology Program.

References:

1. Stoyanov, A. J. et al., "Multipath Effects on Radar Cross Section Measurements", Antenna Measurement Techniques Association, 12th Annual Meeting and Symposium, Philadelphia, PA, 1990.

2. Li, M.-C., "Concurrent RCS Measurements," Antenna Measurement Techniques Association 13th Annual Meeting and Symposium, Bolder, CO, 1991.

3. Ruck, G. T., editor, "Radar Cross Section Handbook," Plenum Press 1970.

4. Beckmann, P., and A. Spizzichino, "The Scattering of Electromagnetic Waves form Rough Surfaces," Oxford, Pergammon Press, Ltd, 1963.

5. Skolnik, M. I., editor, "Radar Handbook," McGraw-Hill, 1990.

6. Kerr, D. E., editor, "Propagation of Short Radio Waves," McGraw-Hill, 1951.

7. Barton, D. K. and H. R. Ward, "Handbook of Radar Measurements," Artech House, 1984.

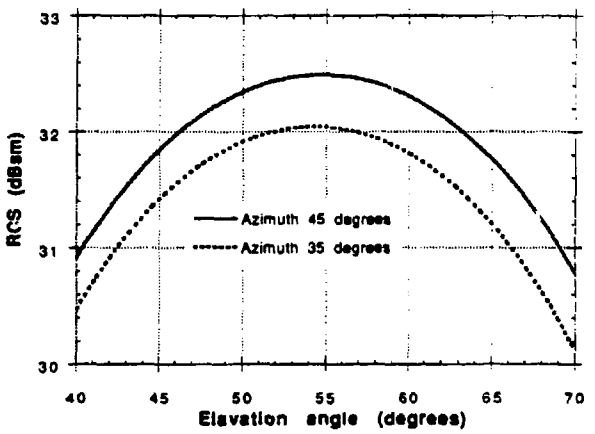

Figure 1. Calculated RCS of the triangular trihedral corner reflector.

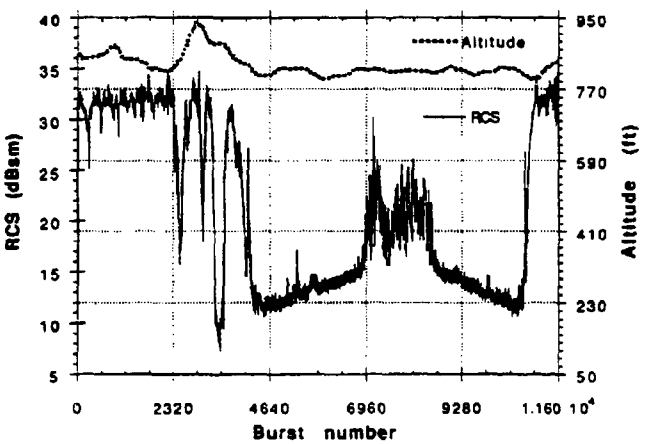

Figure 2. RCS of the trihedral mounted in a helicopter making 360 degrees turn at about 800 ft above the sea surface measured from high site.

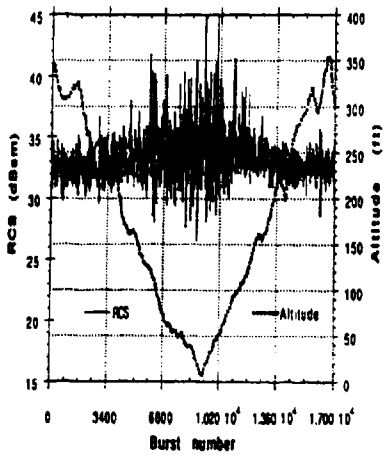

Figure 3. Altitude and RCS of the scatterer measured at 5 nmi from high radar site for H-polarization.

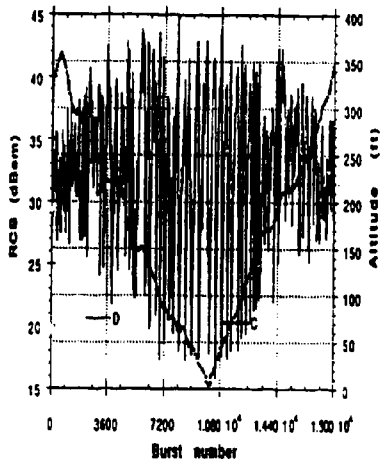

Figure 4. Altitude and RCS of the scatterer measured at 5 nmi from low radar site for H-polarization.

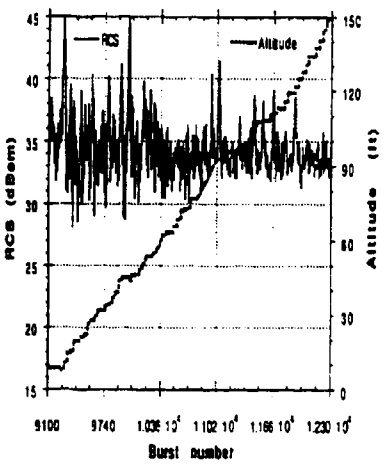

Figure 5. Partial altitude and RCS of the scatterer measured at 5 nmi from high radar site for H-polarization.

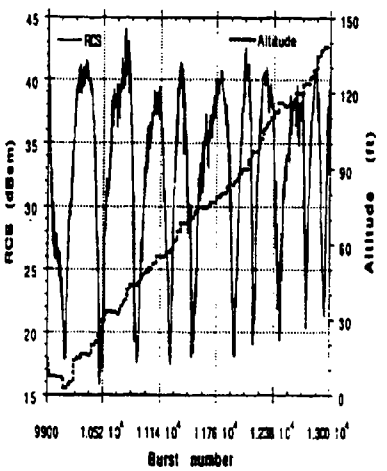

Figure 6. Partial altitude and RCS of the scatterer measured at 5 nmi from low radar site for H-polarization.

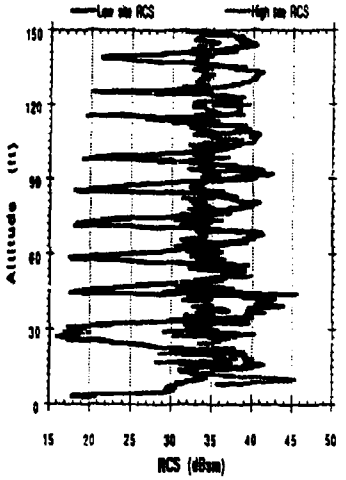

Figure 7. Comparison of the relative variations in the RCS measured at 5 nmi range from both high and low sites.

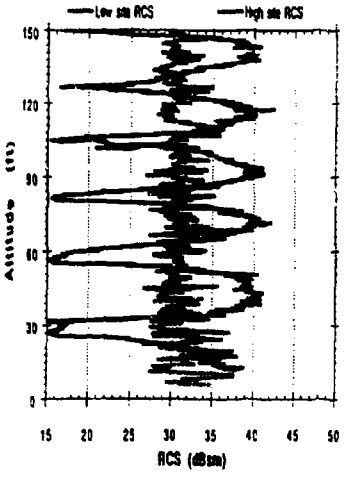

Figure 8. Comparison of the relative variations in the RCS measured at 8 nmi range from both high and low sites.

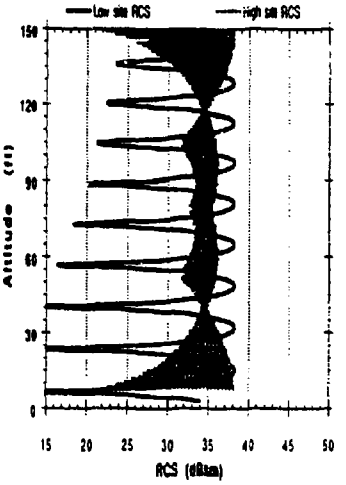

Figure 9. Comparison of the relative variations in the RCS calculated at 5 nmi range from both high and low sites.

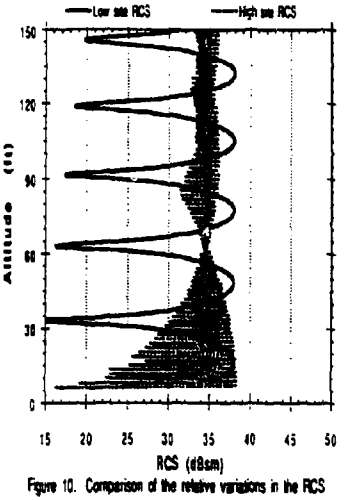

Figure 10. Comparison of the relative variations in the RCS calculated at 8 nmi range from both high and low sites.

ON THE BENCHMARK SOLUTION OF A TYPICAL ENGINEERING LOSS PROBLEM

Z. Cheng, Q. Hu, S. Cao, Z. Liu, C. Yu, M. Wu
Baoding Transformer Works, Baoding 071066, China

ABSTRACT

This paper introduces a benchmark model closed to a typical loss problem in electrical engineering, presents the testing results of eddy currents, magnetic flux densities and power losses with respect to the model, further verifies the available computer codes.

1. ENGINEERING BACKGROUND

The total stray-field loss of large power transformers caused in windings and structural parts[6] can be obtained by load-loss test, however, it is difficult to exactly determine the distribution of total loss either by experiment or by analysis, moreover, the computing results of so large engineering field problem can not be strictly verified.

It is really necessary to establish a reduced problem-oriented model which enable us to have the interested data in detail, for example, the 3-D magnetic flux densities and eddy currents including their waveforms, the distribution of the stray- field losses, the hysteresis and shielding effects, etc., and various available computer codes can be further verified through this benchmark model.

Twin stray-field loss models (A & B) [3-4] have been made in Baoding Transformer Works, Baoding, China. Fig. 1 shows the engineering background of the model.

2. BENCHMARK MODEL

2.1 Description of the model (A & B)

Model B consists of two air-core exciting coils and a steel plate with no hole was set near the coils, the exciting currents flowing in different coils are in the opposite directions.

The Model A has the same exciting coils as Model B and two steel plates being nearby the coils. In the center of one steel plate of Model A there is a hole.

2.2 Input parameters

The dimensions of the steel plates and the coils were shown in Fig. 2, the other parameters are as follows:

2.2.1 Steel plate

(a) B-H curve was shown in Fig. 3.

(b) Conductivity (S/M): 5.8751×10^6 at 20 ℃

2.2.2 Exciting coil

(a) Turn number of each coil: 300 turns.

(b) Exciting current (AC, 50 Hz): 10.0 (A) (rms).

(c) Dimension and conductivity of copper wire,

2.0 mm thickness and 6.7 mm height for bare wire.
The net sectional area of the wire , 13.04 mm ^{2}.
Conductivity (S/m) : 5.7143*10^7 at 20 ℃

2.3 Quantities to be computed and measured

2.3.1 Magnetic flux densities at specified positions, see Fig.4 and Table 1;
2.3.2 Power losses caused in the steel plates, see Table 2;
2.3.3 Total magnetic flux interlinked with steel plate at specified positions, see Fig. 5 and Table 3;
2.3.4 Total magnetic flux interlinked with the exciting coils, see Fig.6 and Table 4;
2.3.5 Eddy currents at specified positions on the surface of steel plates, see Fig.7 and Table 5;
2.3.6 Eddy current losses caused in the exciting coils with and without steel plate, see Table 6.

3. TESTING RESULTS

The 3-D eddy current codes based on the T-Ψ [1-2], the Ar-V-Ar [2] and the combination of the T-Ψ and the Ar-V-Ar [6] developed by authors were used to analyze the models in both the time harmonic and the transient cases. The brick element with 8 nodes and the PICCG solver were adopted.

The mirror-image method was used to calculate the magnetic field and eddy current losses of exciting coils for Model B. The 2-D F.E code shows a 2-D distribution of magnetic field on the symmetric plane of the models.

The Gaussmeter (made by F.W.Bell) was used to measure the magnetic flux densities at specified positions outside steel plate, while the 'interlinked coils' were used for measuring magnetic flux densities inside steel plate, as shown in Fig.13. The waveforms of the flux densities were obtained by a 'computer-aided-test' system developed by authors, as well as the waveforms of the eddy currents at specified positions on the surface of steel plates.

Since total stray-field losses were distributed in both steel plates and exciting coils, to split them a combined method of experiment and analysis was used, i.e., the total stray-field losses were measured, while both the losses of the coils and the losses of steel plate were calculated.

Some measured and computed results of magnetic flux densities, eddy currents and power losses were shown in Fig. 8-14 and Table 1-6.

4. CONCLUSIONS

The benchmark model described here is quite closed to the stray-field loss problem in power transformers. The detailed testing of the problem-oriented model to verify various possible analysis methods is necessary before solving more general practical problem. The presented results of magnetic flux densities, eddy currents and power losses with respect to the model seem to be satisfactory.

Acknowledgement

This work was supported by National Natural Science Foundation of China.

REFERENCES

[1] T. Nakata, N. Takahashi, K. Fujiwara, Y. Okada, 'Improvements of T－Ω method for 3- D eddy current analysis', IEEE., Mag-24, January, 1988, pp. 94-97
[2] O. Biro, K. Preis, ' Finite element analysis of 3-D eddy currents', IEEE., Mag-26, March, 1990, pp. 418-423
[3] Z. Cheng, S. Gao, and D. Zhang, ' An electrical engineering model for loss evaluation', proceedings of Asian TEAM workshop and international seminar on computational applied electromagnetics, Sendai, Japan, March 1991, pp. 117-123
[4] Proceedings of Asian TEAM workshop, 1000Island Lake, China, October 18-19, 1992, (Ed. Z. Cheng, K. Jiang, N. Takahashi) pp. 131-138
[5] K. Karsai, D. Kerenyi, L. Kiss, 'Large power transformers', (Book), ELSEVIER, 1987
[6] Z. Cheng, S. Gao, C. Ye, J. Wang, P. He, 'On the development of the combined eddy current code', Proceedings of 8th ACES, March 16-20, 1992, pp. 314-320

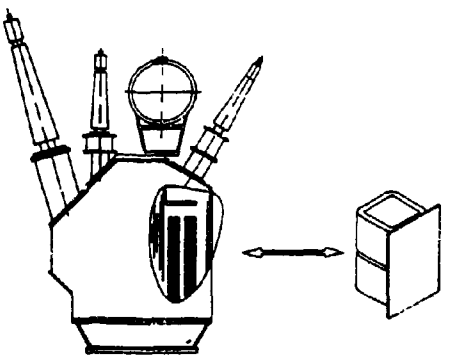

Fig. 1 Engineering background

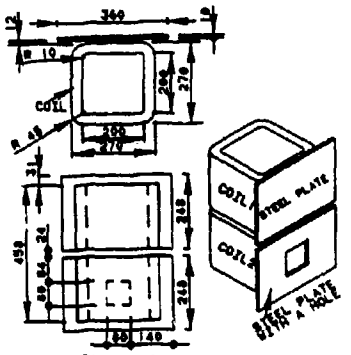

Fig.2 a) Model A

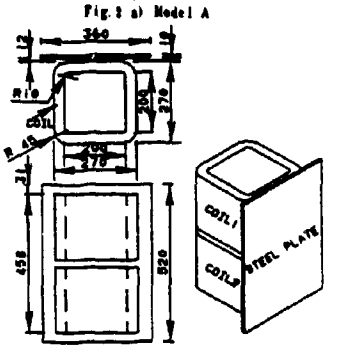

Fig.2 b) Model B

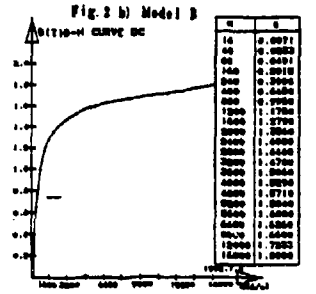

Fig.3 B-H curve of steel plate

Table.1 Flux densities Bx(T) in the air

Position	Coordinates(mm) X	Y	Z	Bx(T)
I				
II				
III				
IV				

Notes: 1) Ampere Turn(AT):3000.0
2) Positions see Fig.4.

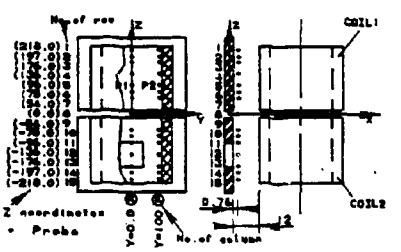

a) model A

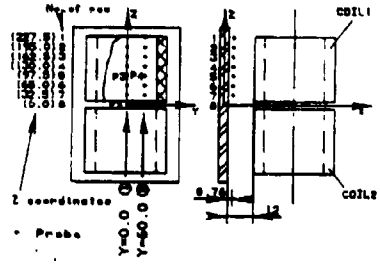

b) model B

Fig.4 Specified positions for magnetic flux densities

TABLE 2 POWER LOSS GENERATED IN PLATES(W)

MODEL A	MODEL B
9.68	12.38

At 23°C

TABLE 3

POSITIONS	Φ(Wb)	Aver. Bn(T)
A	0.18152E-3	0.068316
B	0.31468E-3	0.063980
C	0.32756E-3	0.099978

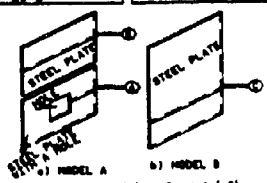

a) MODEL A b) MODEL B

Fig.5 Specified positions for total flux interlinked with steel plate

TABLE 4

POSITIONS	Φ(Wb)	Aver. Bn(T)
a	0.13538E-3	0.01540
b	0.25809E-3	0.01389
c	0.64306E-3	0.01278

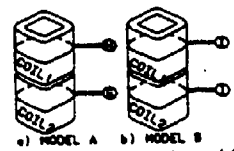

a) MODEL A b) MODEL B

Fig.6 Specified positions for total flux interlinked with exciting coils

TABLE 5 Unit:J(A/m²)

POSITIONS P (X,Y,Z)	MODEL A Jr	MODEL A Jz	MODEL B Jr	MODEL B Jz
① (-5.0,196)	80096.20	37849.89	------	------
② (-5.00, 0)	------	------	93883.15	209688.10
③ (-5.00,-130)	31187.63	78676.98	281400.30	159974.20
④ (-5.0,-195)	31935.68	16888.48	194486.10	82691.22

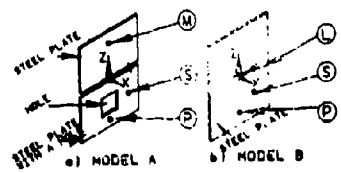

a) MODEL A b) MODEL B

Fig.7 Specified positions for eddy currents on the surface of steel plate

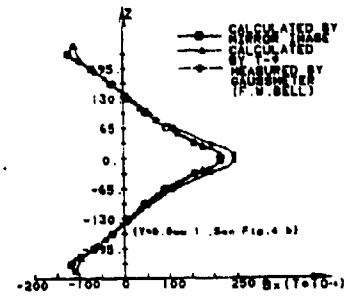

a) X=5.76, Y=0.00, Position I, see Fig.4-(b)

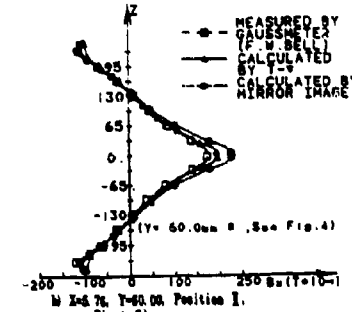

b) X=5.76, Y=60.00, Position II, see Fig.4-(b)

Fig.8 Magnetic flux densities at prescribed points for Model B

TABLE 6 EDDY LOSS GENERATED IN COILS(W)

Cases.	MODEL A	MODEL B
WITH PLATE	3.43	3.40
WITHOUT PLATE	2.44	2.44

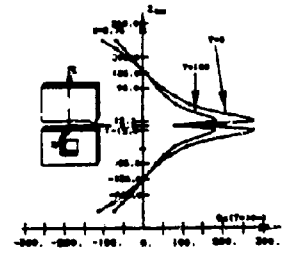

Fig. 9 Magnetic flux densities at prescribed points for Model A
Model: I=6.7A, T=0.0% Position E,
I=6.7A, T=100.0% Position F,
see Fig. 4-(a).

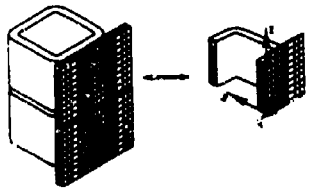

a) 3-D mesh Model B. 1/4 region was analyzed
Model: Total number of brick elements = 2808
Total number of nodes = 3468
Number of constraint nodes = 440
Number of unknowns
= 10834 for Ar-T-Ar
= 4776 for T-0
Computer: IBM 3277 (main storage 1MB)

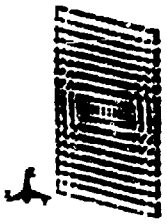

b) Eddy current plot by "EDY" (T-0)

Fig. 10 Distributions of eddy currents of Model B

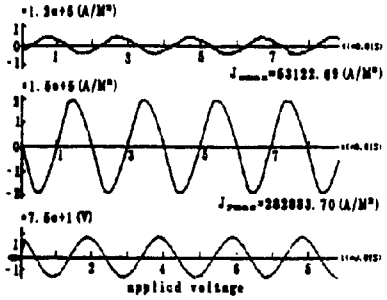

a) point M for model A. see Fig. 7

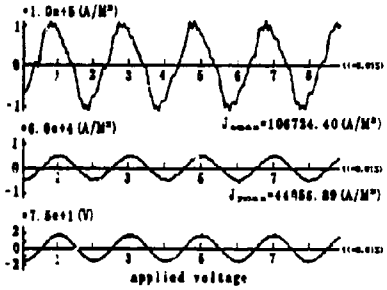

b) point S for model A. see Fig. 7

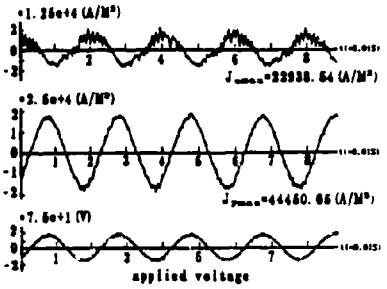

c) point P for model A. see Fig. 7

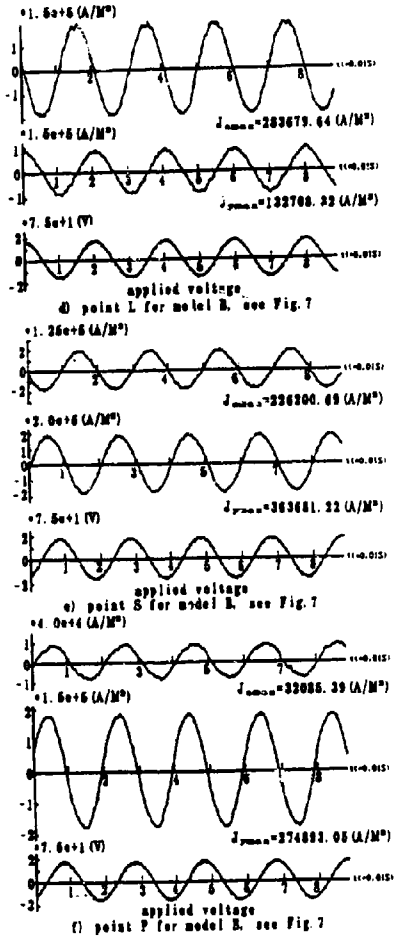

Fig. 11 Waveform of eddy currents at prescribed positions, see Fig. 7

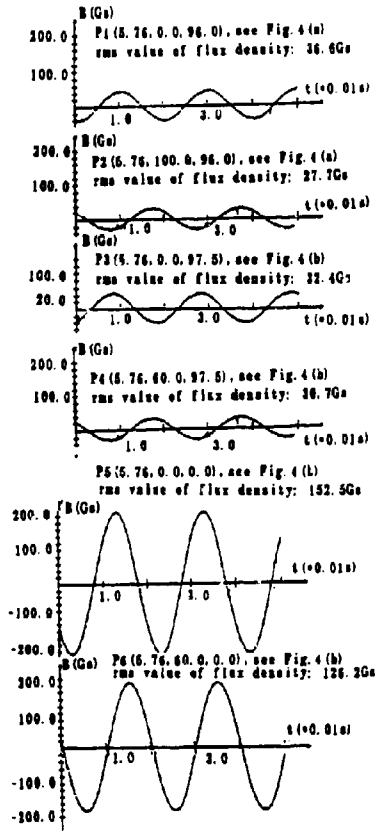

Fig. 12 Waveform of magnetic flux densities at prescribed positions. [Note]: Points P1-P6, see Fig. 4

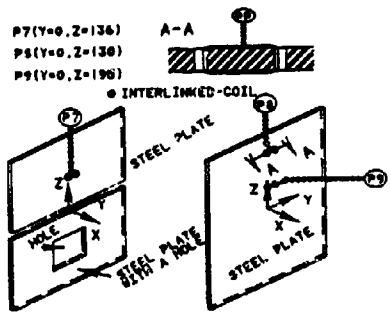

P7 (Y=0.0, z=136.0), see Fig.13(a)
rms value of interlinked flux density: 1980.0Gs

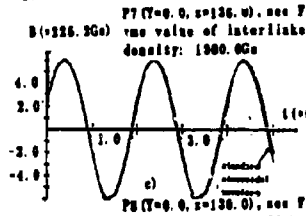

P8 (Y=0.0, z=136.0), see Fig.13(b)
rms value of interlinked flux density: 949.3Gs

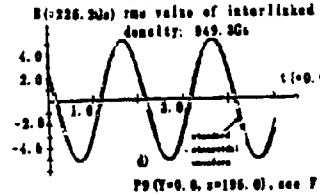

P9 (Y=0.0, z=196.0), see Fig.13(b)
rms value of interlinked flux density: 831.1Gs

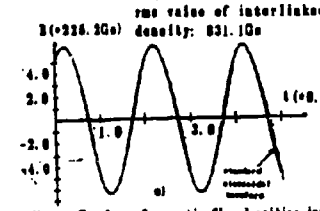

Fig.13 Waveform of magnetic flux densities inside steel plate at prescribed positions

[Note]: Fig.13-(a, d, e) show the waveforms of magnetic flux densities inside steel plate which were measured by the "interlinked-coil". Positions P7, P8, P9, see Fig.13-(a, b).

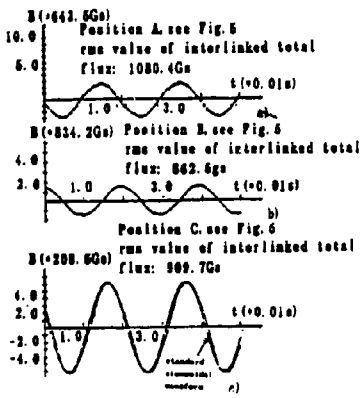

Fig.14 Waveform of total flux interlinked with steel plates at prescribed positions

[Note]: Fig.14-(a, b, c) show the waveform of total flux interlinked with steel plate at the specified positions. position A, B, C, see Fig.5

Evaluation of Radar Signature Predictions Using *XPATCH*[1]

R. O. Jernejcic, A. J. Terzuoli, Jr. • Air Force Institute of Technology
R. F. Schindel • Sverdrup Inc.

Abstract: ***The ability to accurately identify objects from their radar signatures is of continuing interest, however, to be practical a comprehensive catalogue of signatures must be generated. The radar signature prediction code XPATCH [1] is one tool used to generate such a catalogue. It is a high frequency polarimetric code based on the Shooting and Bouncing Ray (SBR) method [2], Physical Optics (PO), and the Incremental Length Diffraction Coefficient (ILDC) formulation [3]. XPATCH utilizes flat faceted representations of the objects being predicted. Using Inverse Synthetic Aperture Radar (ISAR) signatures, this paper compares XPATCH data to measured data. Two simple multibounce geometries are used in this comparison.***

Introduction: *XPATCH* has already undergone extensive validation in the frequency domain and time domain, using primitive and complex shapes [4]. As a result, it has been determined that the validity of *XPATCH* results are highly susceptible to: 1) user selected input parameters, 2) measurement error of data used in the validation process, 3) facetization levels (the number and size of the facets used in the geometry file), and 4) the electrical size (wavelength versus object size). All these factors are significant, both when selecting the test geometries, and when analyzing the results. A series of ISAR images were formed using the measured data of three slightly different loaded dihedrals and of a trophat. *XPATCH* was then used to predict data over the same set of angles and frequencies that were measured. This paper analyzes how well *XPATCH* reproduced the complex electric field data necessary to generate such high resolution radar images.

Dihedrals: Since the production of high resolution ISAR images was a goal, the geometries selected needed to have readily identifiable features. The loaded dihedral is basically a square sided metal right dihedral, each plate being 12 inches to a side. A metal cylindrical bead, or rod, is attached to the intersection of the two plates. Figure 1 shows a faceted example of one such dihedral; three different bead diameters were used. As has been noted elsewhere, the level of facetization of the CAD model plays an important role in the accuracy of the prediction. The three dihedrals' facet models were all created with the same set of facet parameters; hence all are fairly close in the number of facets in each. The dihedral bead diameters and facetizations are as follows: #1) large bead dihedral, 0.5" diameter, 7954 facets; #2) medium bead dihedral, 0.25" diameter, 6050 facets; #3) small bead dihedral, 0.125" diameter, 5098 facets. The faceted geometry files were created using the Advanced Computer Aided Design (ACAD) [5] software package.

All three dihedrals were imaged with the same parameters. Each was measured and predicted at 181 angles, from -45 deg. to 45 deg. in 0.5 deg. increments. Thus, at 0o azimuth, one plate of the dihedral will be illuminated specularly, while the other is illuminated edge on. Figure 2 shows the object mounting and orientation during measurement. The number of frequencies swept at each angle was 1601, from 2 to 18 GHz in increments of 20 MHz. Each azimuth cut was taken at an elevation of 0^{o}, at horizontal polarization.

Figures 3, 4, 5 show the (a) measured and (b) *XPATCH* predicted images of Dihedral #1, #2, #3 respectively; they are oriented so that 0 deg. is at the top of the page. Notice that any return from the front edge of the edge-on plate is completely absent, while a very bright hard line appears where the specular plate should be. Multibounce effects are evident in the fan like pattern spreading out to either side of the interior corner of the dihedrals.

The very bright line running at 45 deg. across the dihedral image appears to be an artifact of the Four Nearest Neighbor Interpolation (FNNI) scheme used to generate the image. This postulate was tested by imaging another object, at a much lower resolution, using both the FNNI method and a Full Data Set Interpolation (FDSI) method. These lines were present in the image processed using FNNI, but absent in the imaged created using FDSI. The same set of field data was used in both cases. This phenomenon seems to occur when a geometry consists of acute interior angles.

Looking further at the images based on *XPATCH* predicted data, we note the small return from the front edge of the edge-on plate. This is because the *XPATCH* faceted representation models the plates as solid volumes with a finite thickness. It does not appear in the measured images, because the measurement chamber has a noise

[1] This work was supported by the U. S. Air Force Wright Laboratories.

floor such that signals close to or below this value are masked by chamber noise; of course *XPATCH* has no such restriction. Notice also the ghost lines running somewhat diagonally behind the dihedral image, which are absent in the measured image. These are somewhat less noticeable in the *XPATCH* predicted image of dihedral #2 (Figure 4(b)), and are completely absent for dihedral #3 (Figure 5(b)). Thus it could be due to the bead running along the inside of the corner. As the bead gets smaller, the lines disappear. Notice also that the FNNI diagonal streak is nearly invisible in Figure 5(b).

Figure 6 shows an expanded image of dihedral #3. Notice how far away the multibounce signal extends from the object. Also note the faint acute angle FNNI induced line running through the corner of the dihedral's image which extends out to the limits of the image frame, with no sign of diminishing. For a very complex geometry, this phenomenon could clutter the image so as to make it unrecognizable.

Tophat: The tophat consists of a 0.5 meter long by 0.5 meter diameter metal cylinder with a 1.5 meter diameter circular metal plate attached to one end. The geometry is shown in faceted form in Figure 7. This object was measured and predicted at 701 angles, from -5 deg. to 105 deg. in increments of 0.15 deg.. The number of frequencies swept at each angle was 1601, from 2 GHz to 18 GHz in increments of 20 MHz. Each azimuth cut was taken at an elevation of 5.5 deg., at horizontal polarization. The slightly positive elevation cut was chosen to bring out more of the curved edge of the brim of the tophat. Had it been imaged at 0 deg. elevation, the brim would have been simply a straight line, similar to the broadside plates on the dihedral images. Figure 8 shows the mounting and orientation of the tophat as it was measured.

Because of the size and weight of the tophat, it was necessary to mount it permanently on a counter-weighted channel beam. This was then affixed to a metal pole that attached to the pylon rotator. The tophat ACAD model did not include the channel beam. Figure 9 shows the measured tophat image. It is much easier to see the tophat in this image than it was to see the dihedrals in their respective images. The brim is well defined, as is the interior edge where the cylinder meets the brim. In this image, the radar was swept across the upper right quadrant of the picture from 5 deg. to the left of vertical to 10 deg. past the right hand edge of the brim. Because of this, we see more detail on the right side, including specular return from the right side of the cylinder. On the right side, note the multibounce spreading at the point where the cylinder and brim meet. We can also see a small amount of edge diffraction coming from the left side of the end of the cylinder (labeled Point A).

The fairly high return coming from the back side of the tophat is the result of the channel beam bolted to the back of the tophat (indicated by Point B). Because it was permanently mounted to the tophat, vector subtraction could not be used to eliminate its return. Instead, electric Radar Absorbing Material (RAM) was wrapped around the fixture, the weights used to counter-balance the tophat, and the mounting pole affixed to the pedestal rotator. In addition, the back surface of the brim was coated with magnetic RAM, to prevent traveling waves across the back of the brim. While this did not completely mask the mounting beam, it did greatly reduce its return.

Next we look at the ISAR image as predicted by *XPATCH*. In Figure 10, we immediately notice the well defined brim of the tophat. Also apparent is the high return from the intersection of the cylinder and brim, particularly on the right side. We can see the characteristic flaring (or lobing) diagonally from this point. As with the dihedrals, this is possibly a manifestation of the multibounce effect. It is apparent in the measured image as well, though to a lesser extent. Again, this is likely the result of the finite noise floor in the measurement range. We also see a small return from the front left edge of the cylinder, just as in the measured image (point A in Figure 9).

The one major feature absent is the specular return from the right side of the cylinder. This was caused, in the measured image, by a broadside illumination of the cylinder, at an incident azimuth of 90 deg.. While *XPATCH* does not predict certain types of scattering phenomenon, such as tip diffraction and traveling/creeping waves, none of these would be dominant at this particular azimuth. Facetization is one likely reason for this anomaly. In his article on the effects of facetization level on *XPATCH* predictions, Miller [6] states that about 10,000 facets were generally needed to insure accurate results for a doubly curved objects such as the almond. It is possible that at this particular elevation of 5.5 deg., there are too few facets on the sides of the cylinder that is perpendicular to the incident wave.

Testing this hypothesis, another set of predicted data was generated, with a 100 deg. aperture covered in increments of 0.15 deg., and the frequency swept from 2 to 18 GHz in 25 MHz steps. The image created from this data is shown in Figure 11. This different set of angles and frequencies would insure that a different set of rays struck the object, with a different ray density and set of incidence angles. As one can see, the cylinder edge missing in the previous image is now there. So it could be the result of facetization error, or an artifact of the imaging process. Except for this one inconsistency, the *XPATCH* image appears to be a good match with the measured.

Conclusions: This set of simple objects was used to evaluate *XPATCH's* ability to produce high resolution ISAR images. Of particular interest was the effect of multiple bounces of the incident wave on the image. These tests highlighted the code's capabilities and limitations, as well as factors and parameters that could significantly effect

the fidelity of the prediction. They provide insight into how well *XPATCH* will perform on more complex geometries.

Acknowledgment: The authors are grateful to the following people for their suggestions: Dennis Andersh, Mike Hazlet, Paul Skinner, Joe Sacchini, Andy Lee, Lee Henderson, Jon Young, Eric Walton.

References

[1] S. W. Lee, and D. J. Andersh, *User Manual for XPATCH*, DEMACO, Inc., September 1993.

[2] H. Ling, et al. "Shooting and Bouncing Rays: Calculating the RCS of an Arbitrarily Shaped Cavity," *IEEE Transactions on Antennas and Propagation*, vol. 37(2), pp. 194-205, February 1989.

[3] R. A. Shore, and A. D. Yaghjian. "Incremental Diffraction Coefficients for Planar Surfaces," *IEEE Transactions on Antennas and Propagation*, vol. 36, pp. 55-70, January 1988.

[4] E. M. Miller, D. J. Andersh, A. J. Terzuoli, Jr., "The Effect of Model Facetization on RCS Predictions," *Digest of the 1993 IEEE/APS International Symposium*, Univ. of Mich.; Ann Arbor, MI, June 28-July 2, 1993, vol. 3, pp. 1404-1407.

[5] P. D. M. Group, *Advance Computer Aided Design (ACAD) Version 7.2 User's Manual*. MZ 2635 General Dynamics, Fort Worth Division, General Dynamics Boulevard, Fort Worth, TX 76108

[6] E. M. Miller, D. J. Andersh, A. J. Terzuoli, Jr., "Facetization Level and the Effect on XPATCH Predictions," *Proceedings of the 9th Annual Review of Progress in Applied Computational Electromagnetics*, Naval Postgraduate School, Monterey, CA, March 22-26, 1993, pp. 610-617.

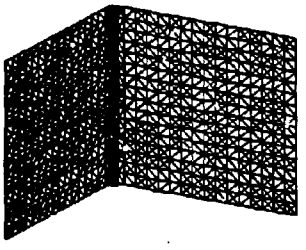

Figure 1. Dihedral Loaded with 1/2 inch rod.

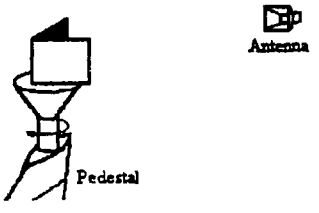

Figure 2. Dihedral measurement orientation and mounting.

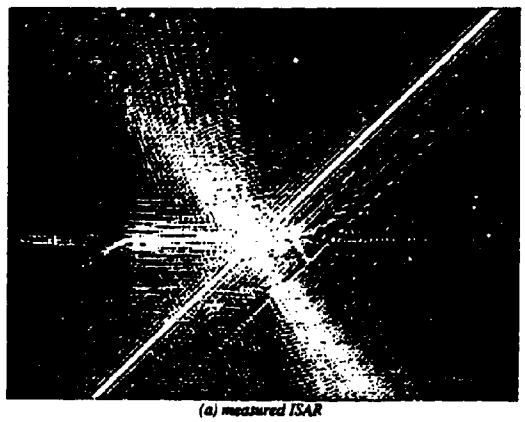

(a) measured ISAR

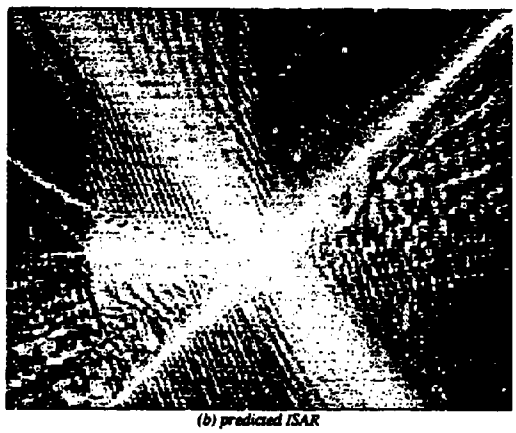

(b) predicted ISAR

Figure 3. Dihedral #1, large bead, H-pol, 2-18 GHz in 20 MHz steps, -45 to 45 deg. in 0.5 deg. steps.

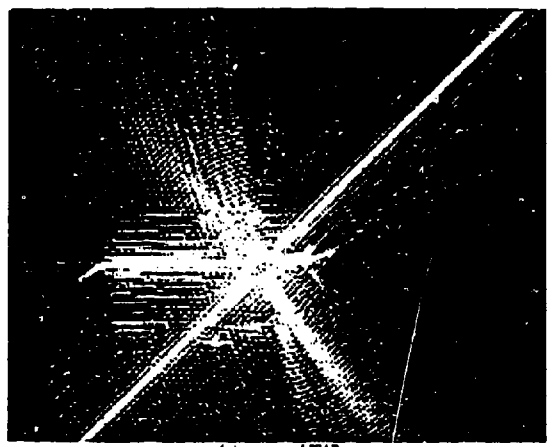

(a) measured ISAR

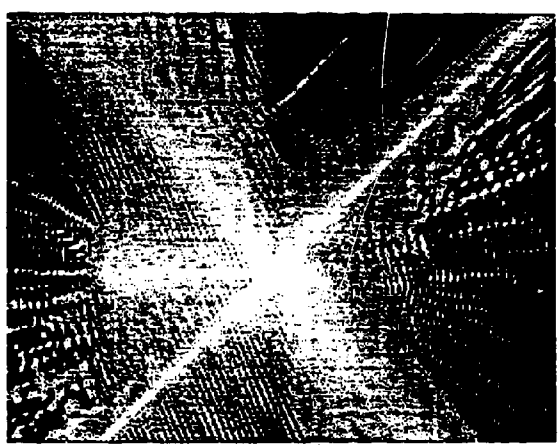

(b) predicted ISAR

Figure 4. Dihedral #2, med. bead, H-pol, 2-18 GHz in 20 MHz steps, -45 to 45 deg. in 0.5 deg. steps.

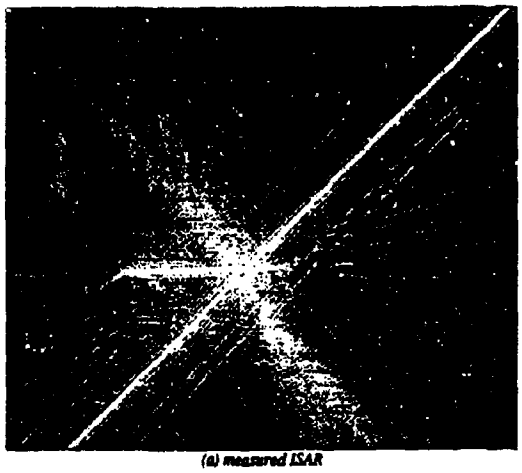

(a) measured ISAR

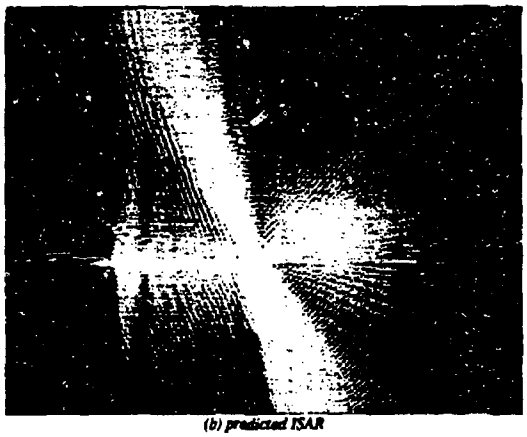

(b) predicted ISAR

Figure 5. Dihedral #3, small bead, H-pol, 2-18 GHz in 20 MHz steps, -45 to 45 deg. in 0.5 deg. steps.

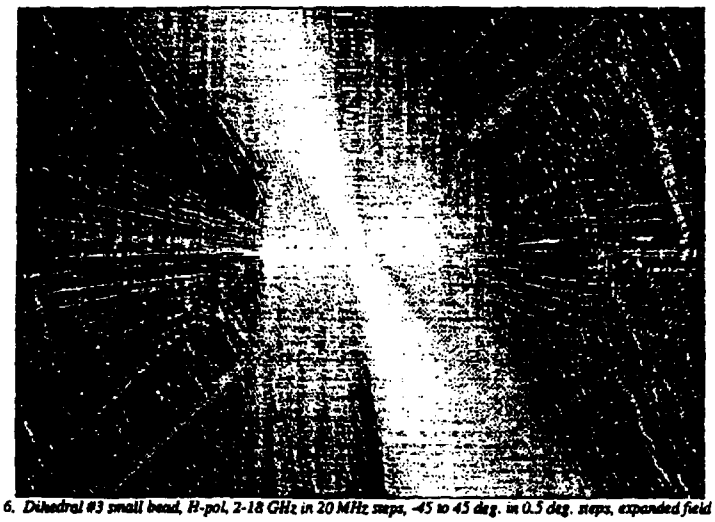

Figure 6. Dihedral #3 small head, H-pol, 2-18 GHz in 20 MHz steps, -45 to 45 deg. in 0.5 deg. steps, expanded field of view.

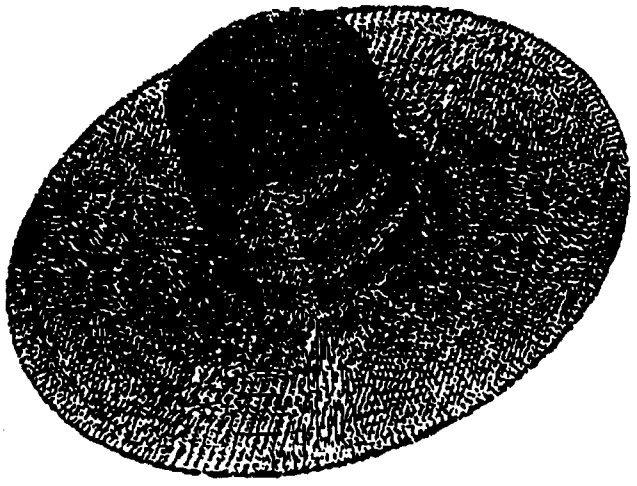

Figure 7. Faceted representation of tophat, with 5,566 facets.

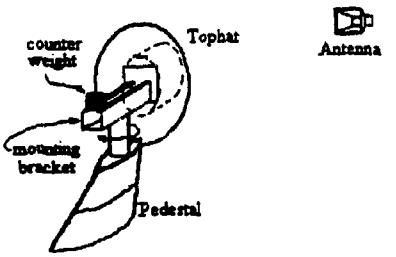

Figure 8. Tophat measurement orientation and mounting.

Figure 9. Tophat, measured ISAR, H-pol, 2-18 GHz in 20 MHz steps, -23 to 23 deg. in 0.15 deg. steps.

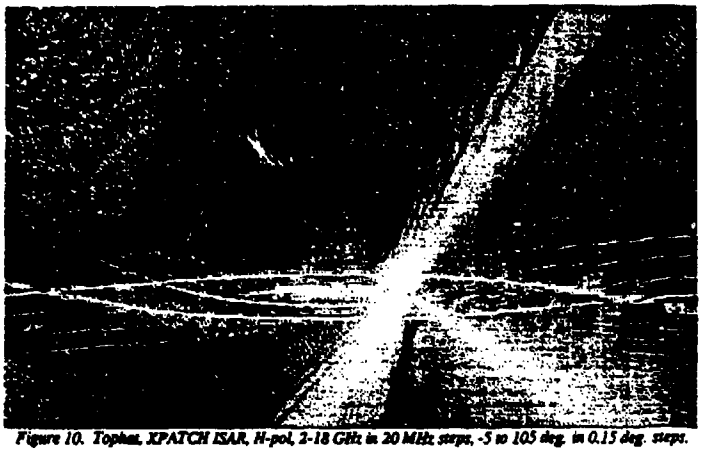

Figure 10. Tophat, XPATCH ISAR, H-pol, 2-18 GHz in 20 MHz steps, -5 to 105 deg. in 0.15 deg. steps.

Figure 11. XPATCH predicted ISAR using 640 frequencies and 666 angles, H-pol.

Transformable Scale Aircraft-Like Model For the Validation of Computational Electromagnetic Models and Algorithms

by

Donald R. Pflug and Daniel E. Warren
Rome Laboratory
525 Brooks Road
Griffiss AFB, NY 13441-4505

Abstract

A novel technique which utilizes measurements on a Transformable Scale Aircraft-Like Model (TSAM) to validate computational electromagnetics (CEM) computer codes is described. Good agreement between measured and simulated data is necessary in order to validate algorithms and models residing within large computational electromagnetics (CEM) codes. If computation and measurement errors are sufficiently small or are known, the remaining differences between simulated and measured data can be attributed to algorithm and modeling limitations within the code. The combination of these errors (simulation error) often can be estimated but not the individual errors. The novelty in the technique is to make measurements on a scale aircraft-like model that is a duplicate, in both form and substance, of the model in the code. Differences between measured and simulated data then can be attributed to algorithm error since measured and simulated aircraft models coincide. From knowledge of both algorithm and simulation errors, modeling error now can be estimated. Modeling and simulation errors can be adjusted separately as required to minimize simulation and measurement differences. Measurements as a validation tool now become more useful and helpful. Initially TSAM will be fabricated using conducting canonic shapes and simple radiation sources. Over time it is expected that the TSAM will be modified by installing new components that correspond to new CEM simulation capabilities. Measurements on the transformed TSAM then will be used to validate the improved simulation. Advanced TSAM components are expected to include nonmetallic materials, doubly curved surfaces, realistic aircraft shapes and more sophisticated radiation sources.

Introduction

During the last twenty years a large number of computational electromagnetics (CEM) codes have been developed by numerous individuals and organizations. These codes range from large, multi-purpose, widely distributed, well maintained and validated simulations employing established numerical techniques individually or in hybrid combinations to perform system level CEM analysis to smaller, specialized codes developed by individual researchers using state-of-the-art methods to attack very specialized or specific sets of problems.

A very important aspect in the development of any CEM code is validation. The problems associated with code validation are particularly acute for large codes involving numerous modules and program paths. One validation method is to compare results from different codes. The code under test analyzes standard or benchmark problems whose answers are known very accurately. Such an approach, while very useful, may provide only limited validation because a small or special part of the code may be tested and the solutions may be of practical use only over a limited frequency range. Another method, commonly used for codes distributed in the CEM community, is to analyze a wide variety of CEM problems over time which collectively test all code modules. Such analysis commonly is performed during code development but also can be provided as feedback by the user community to the code developer. This method can be used repeatedly over the life cycle of the code and provides "lessons learned" data as well as validation. As new problems are analyzed over time, code maintenance, modification and enhancements are performed and validation is accomplished by comparison to other simulation results or measurements as the code evolves and matures. Unfortunately, different simulations do not analyze a problem identically even if both use the same analysis techniques, implement the same algorithms and modeling schemes, or use the same coding practices. Also, it is usually difficult or impossible to relate the differences observed between the CEM code output and validation data to specific limitations within the code quantitatively or even qualitatively. Hopefully, trends in the results will be consistent and the collective numerical data reasonably close to measurements and other simulated data.

The best CEM code validation is good agreement between simulated results and carefully controlled measured data. Unfortunately, the differences observed between simulation and measurement are difficult to explain and are analogous to and are as difficult to quantify as the differences between simulation and simulation. A further complication is that "good agreement" depends on the sophistication of both the modeling and algorithms implemented in the code and external measurements performed for validation.

These difficulties in interpretation that are encountered when comparing simulations and measurements form a common thread running through CEM validation. In this paper, a novel test article, the Transformable Scale Aircraft-Like Model (TSAM), is described. The special configuration of the TSAM is designed to mirror the modeling capabilities of a given CEM code exactly and, as a consequence, appears to hold great promise for allowing algorithm and modeling errors within a CEM code to be assessed qualitatively and quantitatively using measurements on the TSAM as a guide. Both errors then can be adjusted as necessary to achieve a given level of code simulation accuracy. The CEM code to be used initially for simulation is the General Electromagnetic Model for the Analysis of Complex Systems (GEMACS) [1] but the TSAM validation methodology is applicable to CEM codes in general. The TSAM appears to open the door to using measurements to validate CEM codes in a more informative and useful way.

CEM Code Validation and the TSAM Concept

When the results of simulation are compared to measurement, differences are always present and ultimately place a limit on the accuracy to which CEM codes can be validated by measurements. Figure 1 shows a comparison between measured and simulated (GEMACS) radiation patterns from an aircraft antenna. There is general agreement overall but there are apparent differences in location of pattern maxima and minima as well as in pattern shape and power levels. These differences are due principally to the following factors: limitations within the code on modeling of the geometry and physics of the problem (modeling error); limitations in both the equations used by the code to describe the relevant electromagnetic phenomena and in their specific implementation within the code (algorithm error); limitations in the computational capabilities of the computer platform hosting the code (computation error), and limitations in measurement accuracy (measurement error). The combination of these errors (simulation error) can be estimated comparing the results from the code against measurements for a representative set of CEM problems. The individual errors typically are not known and may be mutually dependent. In this paper, it will be assumed that both computation error (typically computer round-off error) and measurement error either are known or are sufficiently small so as to be unimportant. Simulation error in this case then reduces to modeling and algorithm error.

The novelty in the technique is to make measurements on a scale aircraft-like model that is a duplicate, in both form and substance, of the model developed for use by the code. Differences between measured and simulated data then can be attributed only to algorithm error since measured and simulated aircraft models coincide. From knowledge of algorithm error and simulation error, modeling error can be estimated and adjusted if necessary. Differences between measurement and simulation now point to specific causes. TSAM will be composed of replaceable parts chosen to coincide with the current modeling capabilities of the code. As the CEM code evolves and matures, the TSAM parts and configuration will evolve and mature to match the simulation. Detail will be added incrementally to the TSAM to match incremental advances in code simulation capability. Measurements will be performed to validate code modifications at every step.

TSAM initially will be aircraft-like in the sense that canonic shapes such as cylinders and flat plates will be configured to resemble a wide bodied aircraft. The TSAM dimensions were chosen to represent approximately a 1/20 scaling in frequency. All measurements contemplated to date will be done in an anechoic chamber facility at Rome Laboratory.

TSAM Initial Configuration

The first TSAM design has been chosen to conform roughly to the general shape of a wide bodied airborne platform. This initial TSAM test article will be a metallic structure fabricated from highly conducting materials, such as aluminum and copper, and composed of several canonic

shapes to represent wings, fuselage, stabilizers, engine nacelles and engine pylons. Each canonic shape can be modeled exactly in principle using the GEMACS code.

The design and dimensions of the TSAM (1/20 scale model) are shown in Figure 2. This initial configuration incorporates a hollow elliptical cylinder capped at both ends as a fuselage, two thin flat plates as wings, three thin plates as the horizonal and vertical stabilizers, four uncapped circular cylinders as engine nacelles and four thin plates for pylons. The elliptical cylinder is capped in front to form a blunt model for the nose section and is capped in the rear to form a tapered tail section. All components are hinged and individually removable. The geometry of each component can be modeled exactly in principle by GEMACS and the complete metallic structure is assumed perfectly conducting. Since the wings of a wide bodied aircraft flex considerably in flight, both thin plates serving as wings will be hinged in order to vary the wing cant. Fuselage rigidity is maintained by an I-beam positioned inside the hollow elliptical cylinder as shown in Figure 3. This I-beam also serves to position and support a scale model antenna on the TSAM. The complete TSAM test article is shown in Figure 4.

TSAM Initial Excitation

The TSAM will be excited by one or more antennas mounted directly on the structure. Initially, antennas will be either thin wires or cones that serve as monopoles, the cone antennas providing a wider bandwidth. The antenna to be excited will be connected to a 50 Ohm cable threaded through the antenna mounting structure to the antenna under test. Pattern measurements will be done for all antennas, both in the absence and presence of the test article, in an anechoic chamber using standard measurement techniques. It is anticipated that coupling measurements between pairs of antennas on TSAM also will be performed using a network analyzer which will sweep over the relevant range of frequencies.

Simulation Program

The ability of GEMACS to analyze large, system level electromagnetic problems and the presence within GEMACS of a variety of analysis techniques and solution algorithms make it a logical first choice for use with the TSAM. GEMACS was developed to analyze system-level electromagnetic interactions between sources and general material bodies having a complex geometry. The analysis is performed in the frequency domain using modern numerical techniques such as the method of moments (MOM), uniform theory of diffraction (UTD), and finite differences (FD) either individually or in hybrid combination. The various regions of external problems are treated using an appropriate combination of MOM and GTD techniques while internal problems are treated using finite differences. Coupling between exterior and interior regions is achieved by matching exterior and interior solutions at apertures using appropriate boundary conditions.

A number of solution techniques exist within GEMACS to efficiently solve for the unknowns in the problem under study. Matrix techniques include a full-matrix lower-upper decomposition (LUD) algorithm, a banded-matrix iteration (BMI) algorithm and algorithms for handling rotational or planar symmetry. A model order reduction (MOR) algorithm for reducing matrix size is also is available whenever FD is used. Electromagnetic sources include incident fields, excitations on antenna structure, and specific antenna and radiator patterns. GEMACS output that is particularly useful includes radiation patterns from sources on the structure that include the distortions of the structure.

Summary and Future Directions

A novel and promising validation methodology has been described in which measurements on a specialized test article, the TSAM, are used to determine the quality of the modeling and analysis techniques residing in advanced CEM simulation programs. The use of the TSAM makes it possible to distinguish CEM modeling error from algorithm error. Deficiencies in CEM simulations are identified more specifically and measurements are better understood and thus become more useful and helpful as a validation tool. The configuration chosen for the TSAM must mirror the simulation capabilities of the CEM code being studied. Initially, the TSAM configuration will be chosen to match the capabilities of GEMACS which approximates system-level complex geometries with a set of canonic shapes (wires, cylinders and flat plates).

Because aircraft wings are a major source of multipath and the GEMACS fuselage model is rather crude, the evolution of canonic models for the TSAM will focus initially on them. The next TSAM wing design will most likely have a triangular cross section followed by a similar wing with a rounded leading edge and camber. Finally a scale model of an actual wing design will be used. The rear stabilizers will undergo a similar evolution. The current GEMACS fuselage is either a blunt truncated capped cylinder or is constructed from a series of connected plates tapered at different angles to form a nose. Both models will evolve towards an actual fuselage in several steps where geometry becomes progressively smoother and more realistic. Sources, it is hoped, can evolve to small flush mounted elements or arrays. Finally, it is planned that the TSAM will contain nonmetallic materials.

Reference

1.E. L. Coffey III and D. L. Kadlec, *General Electromagnetic Model for the Analysis of Complex Systems (GEMACS), Version 5.0,* Advanced Electromagnetics, RADC-TR-90-360, Volumes I,II,III, December 1990.

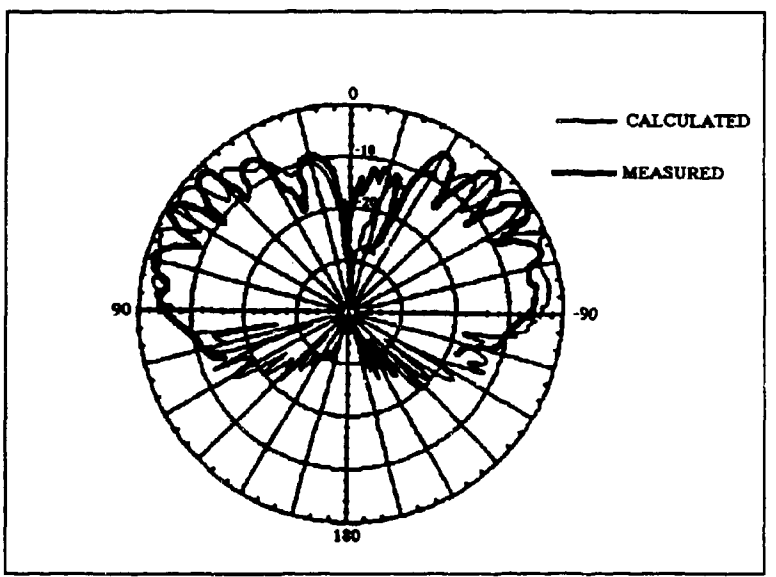

Figure 1. Antenna Pattern Measured and Simulated Data

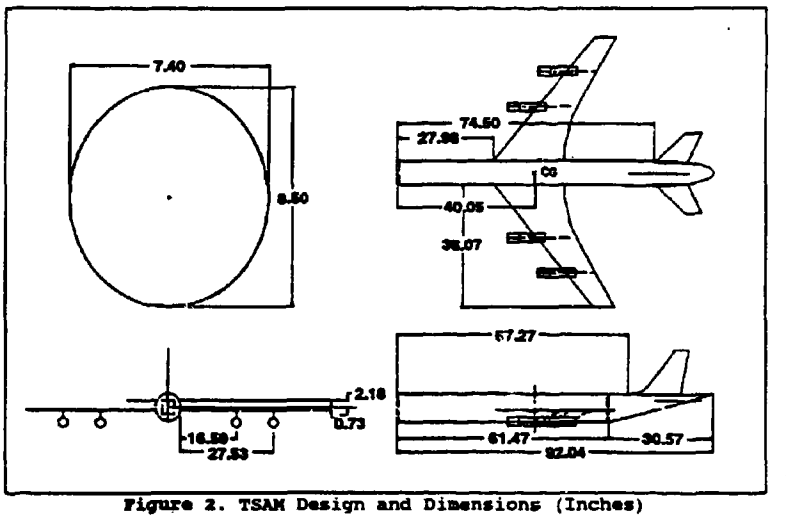

Figure 2. TSAM Design and Dimensions (Inches)

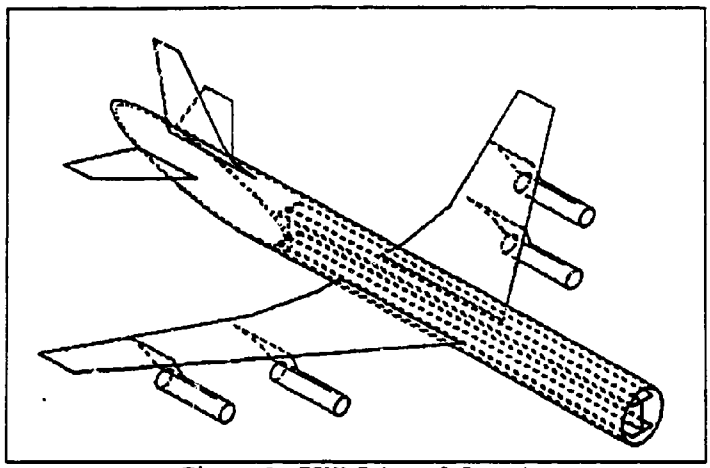

Figure 3. TSAM Internal Layout

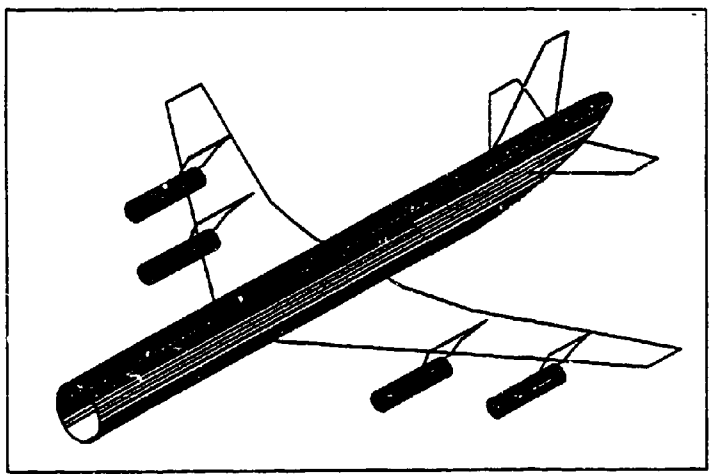

Figure 4. TSAM Complete Structure

INFRARED VERIFICATION of ELECTROMAGNETIC CODE PREDICTIONS

Sydney Blocher, John Norgard*, Joseph Sadler,
Ronald Sega**, William Prather

Microwave Research Group
USAF Phillips Laboratory (PL/WSR)
3550 Aberdeen Avenue SE
Kirtland AFB, NM 87117-5776

ABSTRACT

An infrared (IR) imaging technique has been developed to map two-dimensional electric field distributions near an emitter or a scattering body. This technique is applied to verify the time domain results of the TSAR code for the problem of scattering from and coupling into a cylinder. The cylinder has a circular cross-section and contains a long thin rectangular slot aperture centered in its side and oriented in the axial direction. The cylinder is irradiated with a pulse normally incident on the cylinder. The polarization of the incident pulse is perpendicular to the axis of the cylinder. A Fast Fourier Transform (FFT) of the pulse data is used to predict the frequency domain (CW) effects at various resonant frequencies associated with the lengths of the cylinder and the slot.

Experimentally measured IR thermograms (field images) are compared with the theoretically predicted CW results in the interior of the cylinder in a plane centered on the aperture. The field near the aperture slot is of special interest and is also mapped with the IR imaging technique.

This example illustrates the use of the IR technique to correlate theoretical data with experimental observations and to experimentally validate numerical codes which predict electric field distributions inside complicated objects.

---

* Also with the University of Colorado at Colorado Springs
** Also with NASA/JSC Houston

1. Introduction

A non-destructive, minimally perturbing infrared (IR) measurement technique [1-6] has been developed to observe electric fields. This measurement technique produces a two-dimensional IR thermogram (image) of the electric field being measured, i.e. a two-dimensional isothermal contour map or a gray scale of the intensity of the electric field.

This IR imaging technique is applied to determine the modal distributions of the electric fields induced inside a cylindrical cavity when excited through a thin slot aperture. The mode structure was measured in the cross-sectional plane at the center of the slot.

Numerical computations of the fields coupled into the cylinder also were determined using the Temporal Scattering And Response (TSAR) code from Lawrence Livermore National Laboratory (LLNL). The mode structure was determined in the same cross-sectional plane at the center of the slot.

Comparisons between the theoretical predictions and the measured IR results are made to verify the accuracy of the experimental technique and the numerical code.

The experimental setup for the IR imaging of the cavity modes and the numerical aspects of the TSAR model of the cylinder are discussed next.

2. IR Measurement Technique

The IR measurement involves the observation of microwave energy deposited in an electrically lossy detection screen placed in the plane over which the electric field is to be measured. Joule heating of the detector material results in IR emissions which can be detected by an IR imaging system. The detection screen material is calibrated such that a given temperature rise (above the ambient temperature of the material) corresponds to a particular electric field intensity level.

2.1. IR Experimental Setup

A thin, planar sheet of lossy carbon loaded paper is used to map electric fields. The carbon sheet is placed in the plane over which the electric field is to be measured. The absorbed heat energy is converted into conducted and convected heat energy and into re-radiated EM energy. The radiated EM energy is concentrated in the IR band. This "black body" energy is detected with an IR (Scanning) Array or with an IR (Starring) Focal Plane Array (FPA). The camera can detect temperature differences of approximately 0.009 °K, and has a relative accuracy of plus or minus 10% when detecting electric fields.

2.2. IR Thermograms (Images)

The measured two-dimensional temperature distribution is digitized and stored in the memory of the IR camera. The electric field can be visualized by presenting the two-dimensional temperature profile as a false color image, where cool colors (for example

shades of blue) represent weak areas of EM energy and hot colors (for example shades of red) represent strong areas of EM energy. The resulting two-dimensional false color image is called an IR thermogram, ie. an iso-temperature contour map, and is a representation of the electric field distribution passing through the screen material.

Therefore, it is possible to correlate local surface temperature variations to electric field intensities. The stored IR thermogram data represents the temperature distribution over the extent of the detector screen and is a map of the intensity of the electric field distribution absorbed in the screen.

3. Cylindrical Experiment

As an example of the IR measurement of electric fields, a right circular cylinder, containing a long, thin slot aperture in its side, was irradiated with microwave energy from a horn antenna. The experimental setup is shown in *figure 1*.

The experimental cylinder was one meter in length and had an inner diameter of approximately 10 centimeters. The rectangular slot aperture was 0.64 millimeters in width and was 10 centimeters in length. The slot was located in the middle of the cylinder and was oriented parallel to the axis of the cylinder. The cylinder was irradiated with microwave energy at 2 GHz (15 centimeter wavelength) from a pyramidal horn antenna, polarized in the circumferential direction of the cylinder. Cylindrical TE modes were predominantly excited by the wave polarization inside the cavity.

The arrangement of the IR camera and the detector screen for images of the slot aperture coupling into the cylindrical waveguide cavity is also shown is *figure 1*. To measure the interior cylindrical waveguide cavity modes, the IR camera was positioned on the axis of the cylinder and looked through a wire mesh screen which simulated a microwave shield.

4. Theory/Experiment

Measurements on a finite length cylinder and theoretical predictions for the cross-sectional electric field modes are now presented and correlated.

4.1 Measurements (IR Thermograms)

A small circular disk of carbon paper was positioned in the radial plane that intersected the middle of the slot aperture.
IR thermograms were made of the cylindrical modes excited inside the cavity in this plane. The brightness of each color in the image corresponds to the intensity of the EM field.

Thermograms of the induced modes coupled into the cylindrical waveguide cavity are shown in *figure 2*. The long, thin, horizontal slot aperture is centered on the left-hand side of the IR thermograms. Note the reflection in the waveguide walls. *Figure 2a* is an image of the electrical field coupled through the aperture for a frequency 10% below the

cutoff frequency of the cylindrical waveguide and shows the excitation of an evanescent mode. The EM energy coupled through the aperture is visible in this thermogram and, as predicted by Bethe Hole coupling models, has the radiation pattern of an electric dipole. The dominant TE_{11} waveguide modal pattern is partially developed in the center of the waveguide. *Figure 2b* is an image of the electrical field coupled through the aperture for a frequency 10% above the cutoff frequency of the cylindrical waveguide and shows the excitation of the dominant TE_{11} cylindrical waveguide mode.

Figure 3 is an image of the electrical field coupled through the aperture at a frequency of 2 GHz and shows the excitation of the dominant TE_{11} cylindrical waveguide mode. The dominant TE_{11} waveguide modal pattern is now fully developed in the center of the waveguide.

The modal patterns of the induced cylindrical cavity modes are clearly indicated in these figures.

4.2 Theory (TSAR Code)

The numerical computations on the cylinder were performed using the TSAR code from LLNL. This code utilizes the Finite Difference Time Domain (FDTD) method to calculate the electric and magnetic fields from the Maxwell curl equations[7,8].

First, the object was modeled using the MGED package from the BRL-CAD package. Then, an FDTD mesh was made using the Ana package, on which the TSAR code was run. Due to the physically small width of the axial slot, the hybrid thin slot algorithm (HTSA) in the TSAR code was used to couple the incident field into the cylinder[8].

The object was excited by a time domain gaussian function with a sinusoidal modulation of 2 GHz. This modulation was chosen since it was very close to the resonant frequency of the slot. The gaussian envelope was seventy time steps wide with its peak at 40 time steps. Second order Mur boundary conditions located eight "pad" cells from the cylinder enclosed the computational problem space. The code was run for a total of 2048 time steps to allow the excitation of the experimentally determined TE_{11} mode.

The mode structure was determined by arranging a series of point sensors across the transverse axes (y and z axes in the TSAR code) of the cylinder at the center of the slot. The total time domain electric field was calculated and a FFT was performed at each point. By plotting the resonant field values as a function of position, the familiar plot for this mode was produced and verified (figure 4).

5. Results

Comparisons between the theoretical predictions in Figure 4 and the measured IR thermograms in Figure 3 show that good correlations exist between theory and experiment. Each pair of figures show the theoretical contour plot and the experimental gray scale plot

at the frequency corresponding to the electrically equivalent theoretical result.

6. Conclusion

The IR measurement technique is a viable method to aid in the determination of EM energy coupled into complex cavity structures. This method is of particular importance in the study of coupling into complicated geometrical shapes, whose patterns of electric field modal distributions may not be found easily using theoretical methods.

The IR method allows for rapid observation of EM field activity and interference, resulting in an in-depth understanding of the EM scattering and coupling phenomena. Qualitative and quantitative comparisons can be made between the fields measured using the thermal radiation experimental approach and the fields predicted using a theoretical/numerical approach. Experimental and theoretical data, therefore, can be easily correlated with this technique.

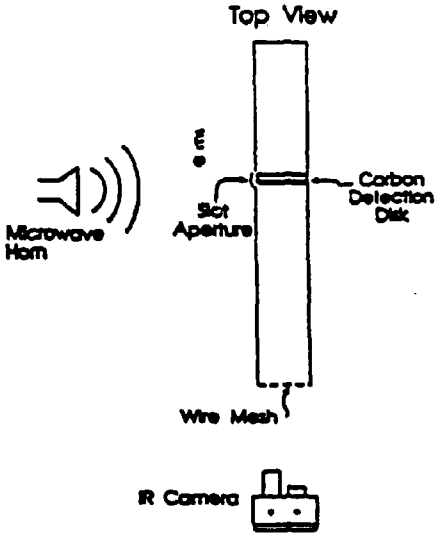

Fig. 1. - *Experimental Arrangement of IR Camera and Detector Screen*

REFERENCES

[1] D.W. Metzger, J.D. Norgard and R.M. Sega, "Near-Fields Patterns from Pyramidal Horn Antennas: Numerical Calculation & Experimental Verification" *IEEE-EMC Transactions*, Vol. 33, No. 3, August 1991, pp. 188-196.

[2] R.M. Sega and J.D. Norgard, "Infrared Measurement of Scattering and Electromagnetic Penetrations through Apertures," *IEEE-NS Transactions*, Vol. NS-33, No.6, December 1986, pp. 1658-1661.

[3] J.D. Norgard, R.M. Sega, K.J. Ianacone, M.G. Harrison, A.T. Pesta and M.A. Seifert, "Scattering Effects of Electric and Magnetic Field Probes," *IEEE-NS Transactions*, Vol. NS-36, No. 6, December 1989, pp. 2050-2057.

[4] R.M. Sega and J.D. Norgard, "An Infrared Measurement Technique for the Assessment of Electromagnetic Coupling," *IEEE-NS Transactions*, Vol. 32, No. 6, December 1985, pp. 4330-4332.

[5] R.M. Sega, J.D. Norgard and G.J. Genello, "Measured Internal Coupled Electromagnetic Fields Related to Cavity and Aperture Resonance," *IEEE-NS Transactions*, Vol. NS-34, No. 6, December 1987, pp. 1502-1507.

[6] J.D. Norgard, D.C Fromme and R.M. Sega, "Correlation of Infrared Measurement Results of Coupled Fields in Long Cylinders with a Dual Series Solution," *IEEE-NS Transactions*, Vol. NS-37, No. 6, December 1990, pp. 2138-2143.

[7] K.S. Yee, "Numerical Solution of Initial Boundary Value Problems Involving Maxwell's Equations in Isotropic Media," *IEEE-AP Transactions*, Vol. AP-14, No. 3, 1966.

[8] R.R. McLeod, "Temporal Scattering and Response Software User's Manual, Version 2.3, LLNL Report, June 1992.

[9] D.J. Riley and C.D. Turner, "Hybrid Thin-Slot Algorithm for the Analysis of Narrow Apertures in Finite-Difference Time-Domain Calculations," *IEEE-AP Transactions*, Vol. AP-38, No. 12, 1990.

VALIDATION OF A DIFFRACTION PROGRAM

P R Foster

Microwave and Antenna Systems, Malvern, UK

INTRODUCTION

The problem of validation and accuracy of a diffraction program is addressed. The program (ALDAS) deals with the radiation patterns of low directivity antennas on conducting structures such as aircraft, ships, spacecraft, masts for cellular radio. The program is based on the division of a conducting structure into elementary canonical shapes such as plates, elliptical cylinders, cones and ellipsoids [1]. Validation requires careful assessment of the program output against radiation patterns generated by other means which have included:-

- measured patterns
- patterns generated by other computer techniques - mainly Method of Moments
- patterns generated by analytical techniques.

Validation provides a check on gross errors in the algorithms and allows an estimate of the errors in the radiation patterns. Various techniques have been investigated for assessing the accuracy and the two most useful techniques have been found to be:-

- RMS errors based on point by point differences. These are obtained by taking the difference in gain level between the ALDAS computed results and the comparison results at exactly the same angle and then computing the RMS error in various gain bins (those of the ALDAS results).
- Percentage coverage plots. The percentage, P, of the total number of angles which have gain greater than G(dBi) is computed and P% plotted as a function of G.

The accuracy is dependent on the size of the structure elements in terms of wavelengths since diffraction theory, being based on ray tracing, is less accurate when the element dimensions are less than two wavelengths. The accuracy is also dependent on the complexity of the structure.

The validation exercise was approached by considering the structures in increasing order of complexity as

1) Single isolated elements

2) Simple structures consisting of three or four structure elements

3) Complex structures such as aircraft

SINGLE ISOLATED ELEMENTS

Isolated elements, such as flat plates, circular plates, cylinders and ellipsoids have been considered.

Plates

Many measured radiation patterns of a monopole (See Figure 1 for an example) on a conducting ground plane [2] or of a dipole over a ground plane [3] have been used in the program validation. Additional comparison material has been generated using NEC-3 [4], an example of which is shown in Figure 2. Convergence tests on the MoM input data was carried out using increasing numbers of segments. These are particularly required around the base of the monopole and around the edge of the conducting plate where the currents are changing very fast [5]. The slight differences between the NEC-3 and ALDAS results can be attributed to ignoring a second order double diffraction in ALDAS (ray path from the monopole, diffracted off one edge and then diffracted off the opposite edge). As the dimensions of the plate are increased, the agreement improves (compare Figure 1 and Figure 2 and see Table 1).

Table 1: Antenna above a conducting plate: RMS Error (dB)

Gain Range (dBi)	MONOPOLE				DIPOLE	
	1λ square (MoM)	5 λ square (measured)	5 λ square (MoM)	20 λ square (measured)	4.74 λ sq (measured)	4.74 λ sq (measured)
> 0.0	0.67	1.37	2.20[1]	0.71	0.83[2]	1.22[3]
-10.0 < G < 0.0	1.84	3.40	5.50	1.98	2.61	1.63
-20.0 < G < -10.0	0.67	5.08	7.92	2.39	4.96	3.99

1. The MoM results had not converged. More segments should have been used.
2. In E-plane of dipole
3. In H-plane of dipole

Cylinders

A similar exercise has been carried out for monopoles and dipoles over cylinders of circular cross-section. Few examples are available where the cylinder has a radius greater than 1 or 2 wavelengths. Some examples are tabulated in Table 2 for a cylinder of radius 1 wavelength. Cylinders require that geodesics are found for the rays diffracted round the surface but, since a cylinder is a 'developable' surface, this is a straight-forward exercise. However, the ray tracing is more difficult than for a flat plate.

Table 2: Antenna above a cylinder (Radius 1 λ): RMS Error (dB)

Gain Range (dBi)	MONOPOLE		DIPOLE
	Modal Matching[6]	Method of Moments[4]	Modal Matching [3]
G > 0.0	0.36	0.71	0.43
-10.0 < G < 0.0	1.12	1.98	0.49
-20.0 < G < -10.0	1.37	2.39	1.55

Spheres and Ellipsoids

Spheres and ellipsoids are doubly curved surfaces and require that the geodesics are found for each ray diffracted round the surface [7]. The problem is more difficult than that of an antenna over a cylinder. Radiation patterns of a monopole mounted on spheres of different radii have been published in Russian [8] and the Method of Moments has been used to model a monopole and a dipole over an ellipsoid. The results provided by Byelkina and Weinstein (using an analytical method) have radii varying from 0.477 to 15.9 λ. As the radius increases so does the agreement between ALDAS and these results. Figure 3 shows the radiation patterns for a monopole on a sphere of radius 1.5915 λ for ALDAS and Byelkina and Figure 4 shows the results for a sphere of radius 15.9 λ. Measured cross-polarisation results of a monopole on an ellipsoid at 8 Ghz also agreed well with computed results [9]. Table 3 shows the increase in agreement as the dimensions increase in wavelengths.

Table 3: Antenna above spheres and ellipsoids[1]: RMS Error (dB)

Gain Range (dBi)	Monopole								Dipole
	0.76,0.5, 0.79,0.79 λ	Sphere rad 0.477 λ	Sphere rad 0.477 λ	Sphere rad 0.80 λ	Sphere rad 0.80 λ	Sphere rad 1.59 λ	Sphere rad 2.39 λ	Sphere rad 15.9λ	0.54,0.3, 0.3,0.54 λ
G > 0.0	1.70	2.16	1.7	2.02	1.22	0.81	0.12	0.05	0.81
-10.0 < G < 0.0	3.31	2.51	2.00	2.75	1.37	1.47	0.87	0.35	1.62
-20.0 < G < -10.0	3.70	4.30	4.20	1.85	0.33	0.98	0.36	1.07	4.63
Reference	MoM	MoM	[8]	MoM	[8]	[8]	[8]	[8]	MoM

1. Ellipsoids are specified by four semi-axes, +X, Y, Z, -X

STRUCTURES

Simple Structures

The results for simple structures, such as boxes or a cylinder with attached plates, will be less than accurate than isolated single elements. There are few such examples available in the literature to use as checks. The general trend is that the RMS error is about 1.5 times that for a single isolated element.

Complex Structures

Structures are 'complex' when they consist of many structural elements. Examples are civil and military aircraft, ships, space-craft, ground vehicles and so on. Extensive data is available for several aircraft at frequencies ranging from 500 MHz to 10 GHz in which the model may contain up to 70 structural elements. Details of some examples are given in Table 4. The accuracy is influenced by the choice of the structural elements which are used to make up the structure. If the geometry is varied and the range of radiation patterns obtained is examined, the most obvious features are

1) the mean gain level does not vary very much (+/- 0.5 dB)

2) the positions of the nulls does vary by several degrees.

Since the RMS errors are based on differences between the gain levels at the same angle, any skewing of the null positions will make the numerically derived errors appear much worse than they seem to the eye. An alternative presentation is the 'Percentage Coverage Plot'. An example is shown in Figure 5 for the results of a monopole on a BOEING 747. The corresponding radiation patterns are shown in Figure 6 and Figure 7. For the systems engineer, the Percentage Coverage Plot is more appropriate because it gives a measure of the system performance. Such plots have an accuracy of +/- 0.5 dB down to -20.0 dBi even on the most complex structures.

Table 4: Antennas on complex structures: RMS Error (dB)

Structure	Frequency (Ghz)	Gain Range (dBi)		
		G > 0.0	-10.0 < G < 0.0	-20.0<G<-10.0
KC-135:monopole over wings [10]	1.4	2.15	5.17	5.62
KC-135:monopole fwd of wings [10]	1.4	1.43	8.20	8.76
BOEING 747: monopole on fuselage:(Φ = 0.0,90.0 degs) [11]	1.0	2.08	3.77	7.63
BOEING 747: monopole on fuselage:(Θ= 60 – 120 degs) [11]	1.0	2.56	4.70	8.76
Helicopter: Spirals on nose (Θ= 60-120 degs) [12]	2.0 - 8.0	0.25	0.50	-

CONCLUSIONS

The radiation patterns presented in the previous sections have shown that simple canonical structures are well modelled but that complex structures are not so accurate. This is due to the difficulty of describing a complex structure such as an aircraft in terms of the canonical shapes allowed in ALDAS. The assumption has been made in this document that all errors are due to ALDAS since it is not possible to disentangle the various error sources. However, it is clear that the errors in ALDAS will be less than those quoted.

1) For single elements, the accuracy improves as the size of the element in wavelengths increases above 2 or 3 λ. This is not surprising since diffraction theory theoretically breaks down for dimensions less than 1 λ. Much of this comparison work was carried out using MoM or other analytical techniques which are likely to be more accurate than measurements. Convergence tests on MOM models are essential.

2) When complex structures are studied, measurements must be relied upon and often no details of the measurement techniques are given. Personal experience has shown that measuring a low gain antenna on a structure requires a chamber which has a reflectivity of less than -40.0 dB and a mounting/rotation system which does not introduce spurious reflections. A reflectivity of -45.0 dB translates into a gain error of 1.0 dB at a gain level of -20.0 dBi when the peak gain is 5.0 dBi.

3) When a complex structure such as an aircraft is modelled using ALDAS, various other sources of error come in.

   - the structure of the aircraft will not be totally conducting. There will be transparent sections such as cockpits, radomes et cetera
   - an actual aircraft is not accurately modelled using flat plates and the simple curved shapes provided by ALDAS for the fuselage
   - the measurements are likely to be in error themselves
   - for accurate modelling, it is possible that the measured radiation patterns of the antenna in free space should be used rather than generic patterns. These are not generally available.

4) The use of the percentage coverage plot does seem useful as it gives an accurate indication of the gain coverage which is useful for system purposes. The accuracy of ALDAS appears much better because the null rotation effects are removed.

Table 5 summarises the RMS errors on a point by point basis. The percentage coverage plots indicate an accuracy of better than +/- 1.0 dB down to a gain level of -20.0 dBi.

Table 5 General Level of Accuracy in ALDAS: RMS Error (dB)

Gain Range (dBi)	Single Element		Simple Structure	Aircraft
	$< 2\lambda$	$>> 2\lambda$		
G >0.0	0.7	0.4	1.0	2.0
-10.0 < G < 0.0	1.4	0.8	2.0	5.0
-20.0 < G < -10.0	2.5	1.2	4.0	7.0

REFERENCES

1 P R Foster, 'Analysis of Low Directivity Antennas on Structures', 6th ACES Symposium, 1990, p362-369

2 Foster P R and Miller T, 'Radiation Patterns of a Quarterwave Monopole on a Finite Ground Plane', ICAP81, p451 - 455, York, 1981

3 P K Pathak, 'Techniques for High-frequency Problems', Chapter 4 in 'Antenna Handbook', edited by Y T Lo and S W Lee, Van Nostrand, 1988

4 G J Burke and A J Poggio, 'Numerical Electromagnetic Code - Method of Moments', Technical Doc 116, NOSC, 1977

5 C Sillence, private communication.

6 W Burnside, 'Analysis of On-aircraft Antenna Patterns', Ph D Thesis, Ohio State University, 1972

7 P R Foster, 'Accuracy and Complexity in Electromagnetic Codes as Applied to a GTD/UTD Program', CEM-91, London 1991, p404-411

8 M G Byelkina and L A Weinstein, 'Radiation Patterns of Spherical Surface Antennas', in 'Diffraction of Electromagnetic Waves by Some Bodies of Revolution', Soviet Radio, Moscow 1965 (in Russian)

9 P R Foster, Unpublished measurements. Monopole on an ellipsoid, 1992

10 W D Burnside et a., 'A study of KC-135 aircraft antenna patterns', Trans IEEE, AP-23, No 3, 1975, p309-316

11 N C Albertsen and Fl Jansen, 'Pattern predictions for L-band antennas on aircraft', TICRA Report S-77-03, November 1977

12 Results of measurement on scale model

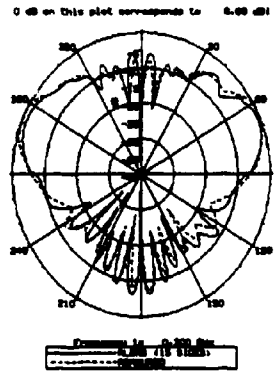

Figure 1 Patterns of a monopole on the upper side of a circular conducting plate of diameter 7 λ. Measured results from Foster and Miller [2]. Gains have not been altered.

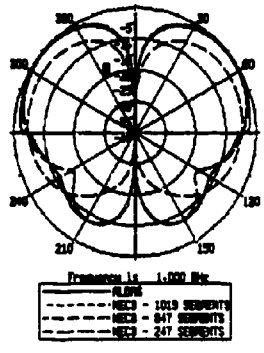

Figure 2 Patterns of monopole mounted on a square conducting plane of side 1 λ. 0.0 dB corresponds to 3.11 dBi

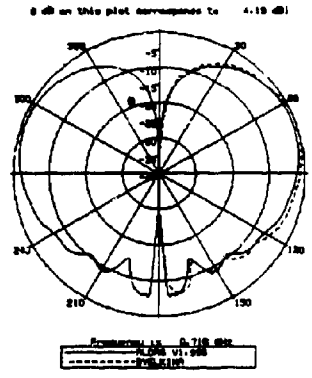

Figure 3 Radiation pattern of a monopole on a sphere radius 1.5915 λ compared with Byelkina [8].

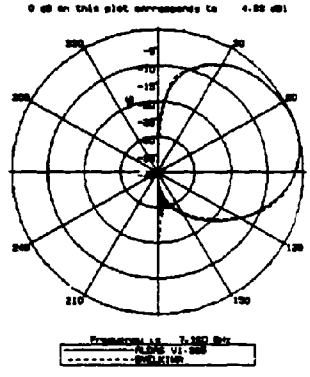

Figure 4 Radiation pattern of a monopole on a sphere radius 15.915 λ compared with [8].

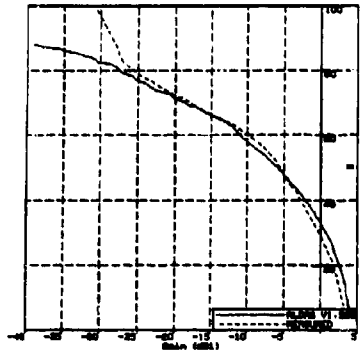

Figure 5 Percentage coverage plot for radiation patterns of a monopole on the upper fuselage of a BOEING 747 [11].

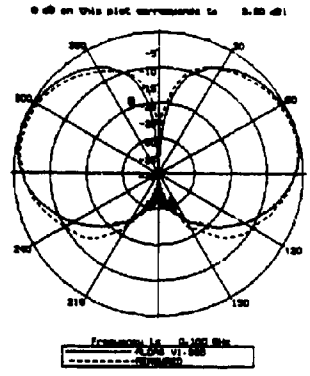

Figure 7 Radiation pattern for the configuration of Figure 5 (Roll plane)

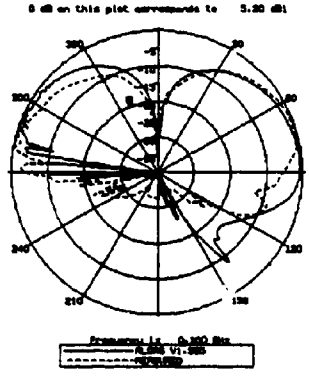

Figure 6 Radiation pattern for the configuration of Figure 5 (Pitch Plane)

SESSION 9:

ANTENNAS

Chair: Gary Theile

NEC Modeling and Testing of an

Ultra-Wideband Antenna for High-Power Operation

E.H. Lenzing, Dr. B.S. Perlman, R. Pastore, US Army Research Laboratory,
EPSD Ft. Monmouth, N.J.
Dr. C.D. Hechtman, H.F. Lenzing,
Stevens Institute of Technology, Hoboken, N.J.

In an antenna design proposed for high power, wideband operation , a tapered TEM 'horn' is terminated with a conical spiral antenna so that the small feature size associated with the high frequency operation is replaced by a structure capable of handling higher power, while maintaining minimal reflections thus producing a hybrid antenna structure capable of supporting high power over a wide frequency spectrum . The antenna can be driven with a high speed laser controlled solid-state switch or other high frequency generator.

This paper discusses the design features and the modeling and testing of this prototype conical spiral/TEM horn hybrid antenna. Issues concerning the NEC wire modeling of surfaces and problems arising from it will be discussed.

Introduction

The category of antennas generally referred to as "wideband antennas" consists of planar and conical spirals [1], log-periodic arrays [2], Vivaldi tapers [3], bowtie horns, etc. There have been recent attempts to combine two wideband antenna types in order to realize ultra-wideband operation [4,5]. In the antenna presented herein, a bowtie-horn antenna is terminated with a conical spiral antenna, thus extending the low-frequency cutoff of the structure, conceptually resulting in an ultra-wideband radiator. The intent of the present design is to drive the antenna with a high-speed, laser-controlled solid-state switch situated across the quasi-parallel bowtie horn conductors.

Antenna Design and Modeling

The smallest dimension of the bowtie horn determines the upper-frequency limit of the structure, and also determines its power-handling capability. The lower-frequency limit of the structure is determined by the largest diameter of the conical spiral. To minimize reflections at the bowtie horn to conical spiral transition, the conductors must follow a smooth and continuous path, matching the tangential derivative all
along the transition. To accomplish this, a novel structure which is actually a section of a Cornu spiral was modeled and also fabricated in the laboratory.

A representative structure (figure 1) was modeled and analyzed using the Numerical Electromagnetics Code (NEC) [6]. Figure 2 is a closer view of the bowtie horn structure. In order to be compatible with NEC, the structure was modeled with wires. The wires making up the arms of the spiral run only in the direction of the spiral curve. This has been shown to be a valid approximation by Aria and Mei in their integral equation formulation of conical spiral antennas [7]. This also was tested by simulating the antenna with and without crosshatching wires. The two different cases showed little difference in current distribution or radiation pattern. A further consideration for modeling the antenna surfaces with wires is the wire radius. The generally accepted rule for wire diameter is that the set of wires representing a square grid must have a total surface area of twice the square grid area being modeled [8]. Using this rule, the wire diameters in the spiral portion of the antenna must increase exponentially. To further test this method of conducting surface simulation

small microstrip patches were modeled using NEC and another popular MOM microstrip modeling package called Sonnet [10]. The patches were also fabricated and tested and compared with the simulation data. The wire diameters used in the NEC simulation were then scaled until the simulation matched the measurements. This scaling was then used in the antenna model.

Modeling and Testing Results

Computation of input resistance from 2 to 19 GHz is shown in figure 3. In the lower portion of the band, the input resistance varies around 180 ohms,the theoretical input resistance of a conical spiral of these dimensions predicted by Dyson [1]. At the upper portion of the band, the input resistance climbs toward 377 ohms but then begins to decrease slowly above 17 GHz. This may be explained by leakage from the parallel plate waveguide region.

Representative modeled radiation patterns are shown in figure 4. Note that the polarization is frequency dependent: at the higher frequencies where the bowtie horn is the predominant radiator, polarization is elliptical/near linear. In the lower frequency, conical spiral regime, polarization is elliptical /near circular.

The modeled antenna structure was fabricated in the laboratory, and the return loss was measured using an HP8510C network analyzer. The return loss results are shown in figure 5. A photograph of the antenna structure is shown in figure 6. It should be noted that this design was not intended to be driven by a constant or swept source, rather by a laser controlled or other switch. Work will have to be done in order to transform the parallel plate balanced mode to a coaxial unbalanced mode for connection purposes. Preliminary studies are underway to explore the use of ultra-wideband baluns [9]. It must be stressed that the fabricated antenna was only for CAD model validation to keep us on track with the modeling.

A test of the prototype antennas power capability was conducted at the EPSD pulse power center . A 250 amp 25kv pulse across a one hundred ohm load was applied to the antenna with no arcover or heating. High-power pattern measurements are not available but e-field probes were placed at various points in the lab and the risetimes of the detected field showed wideband operation. Work is underway to produce a proper method of testing the transient response of the antenna.

References

[1] J.D. Dyson, "The characteristics and design of the conical spiral antenna," IEEE Trans. on Antennas and Propagation,vol. 13, July 1965,pp 488-499.
[2] R.H. DuHamel and D.G. Isbell, "Broadband logarithmically periodic antenna structure,"IRE Nat. Conv.Rec.,part 1,1957,pp. 119-128
[3] P.J. Gibson,"The Vivaldi aerial,"Proc. 9th Europ. Mic. Conf.,1979,pp.101-105.
[4] A.K.Y. Lai,A.L.Sinopoli,and W.D. Burnside,"A novel antenna for ultra-wideband applications,"IEEE Trans. on Antennas and Propagation,vol. 40,no. 7, July 1992,pp. 755-760.
[5] A. Marvin and S.J. Porter," 30 Mhz to 1 Ghz in one sweep-the bilog,"EMC Test and Design Magazine,Aug. 1993,pp. 28-30.
[6] G.J. Burke and A.J. Poggio,"Numerical eletromagnetics code (NEC)-method of moments,"Naval Oceans Syst. Center, San Diego,CA,NOSC TECH Doc.116,Jan. 1981.
[7] A.E. Atia and K.K. Mei,"Analysis of multiple-arm conical log-spiral antennas,"IEEE Trans. on Antennas and Propagation,vol. 19,no.3,May 1971.
[8] A.C. Ludwig,"Wire grid modeling of surfaces,"IEEE Trans on Antennas and Propagation,vol. 35,no.9,Sept. 1987.

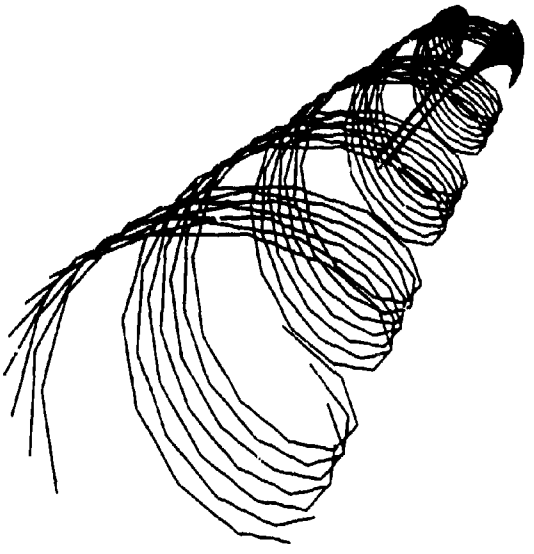

fig.1 Wire model representation of the hybrid antenna.

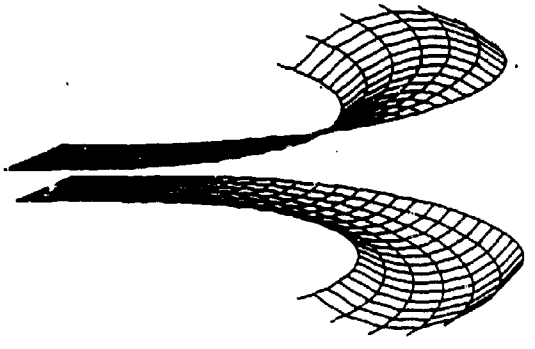

fig.2 Expanded view of tapered horn model.

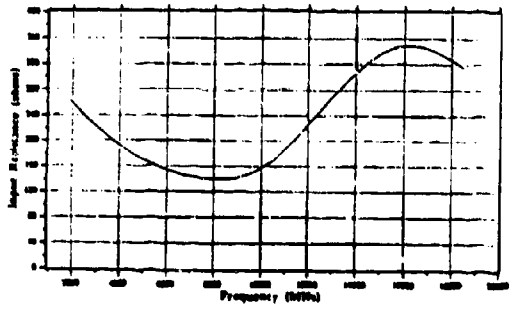

fig 3. Simulated input resistance versus frequency.

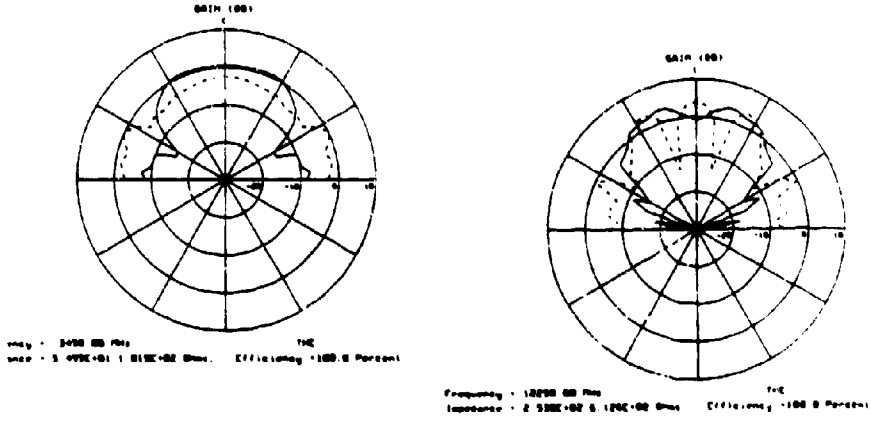

fig.4 Simulated radiation plots for 3.450 and 12.225 Ghz.

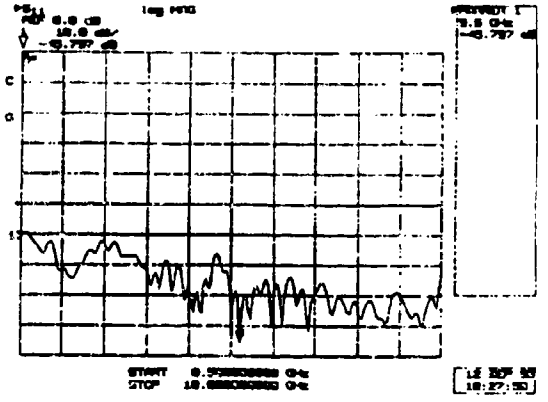

fig.5 Measured return loss over the design frequency range.

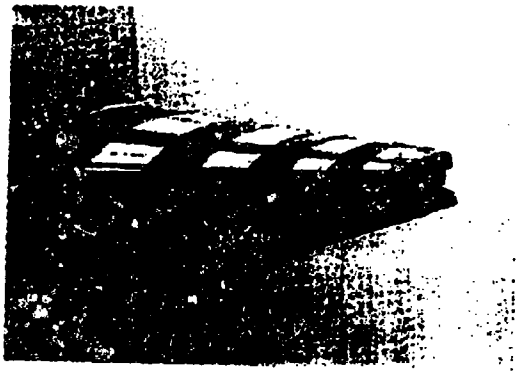

fig. 6 Photograph of the antenna prototype.

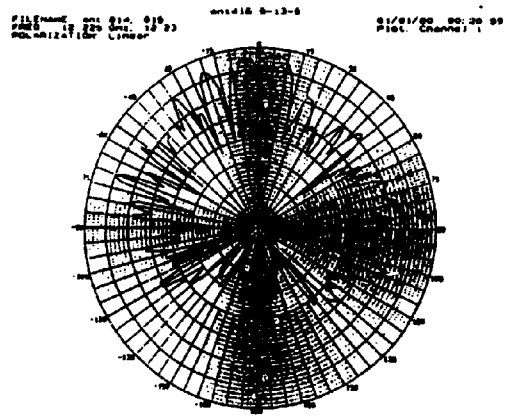

fig. 7 Measured radiation pattern for 12.250 Ghz

A Practical Application of NEC Impedance Calculations*

W. Perry Wheless, Jr., *University of Alabama*
Darko Kajfez, *University of Mississippi*

Abstract— At a given frequency, the theoretical feed-point impedance of an idealized wire antenna can be related to the measured impedance of the practical antenna through a fractional linear transformation. For many wire antenna types at frequencies through VHF, the accuracy of Numerical Electromagnetics Code (NEC) impedance calculations is sufficient that numerical results from NEC can be taken for theoretical values. It is demonstrated here that the fractional linear transformation relationship can be valid over substantial bandwidths, as well as at a fixed frequency, even when the three transform coefficients are restricted to be complex constants. Useful predictions of measured input impedances at new frequencies of interest can be made within the frequency range determined to be reliable by the impedance data analysis procedure.

I. Introduction

Fig. 1 illustrates that the theoretical wire antenna feed-point impedance Z_{ideal} is changed to actually observed impedance Z_{meas} by the feeding network associated with the antenna. The linear network shown in Fig. 1 may include insulators and supports, transmission line sections, a balun, lumped-element components of an antenna tuning unit, and stray reactances, with linearity the only assumption necessary for the network. It has been shown [1] that the theoretical impedance of a delta-gap cylindrical dipole can be related one-to-one to the actual measured impedance through a bilinear transformation at a given single frequency. The transformation is

$$Z_m = \frac{a_1 Z_i + a_2}{a_3 Z_i + 1} \qquad (1)$$

where a_1, a_2, and a_3 are complex coefficients and Z_m, Z_i are shortened names for Z_{meas} and Z_{ideal}, respectively. In [1], the independent variable is distance d of a horizontal dipole above a perfect ground plane; the ideal impedances Z_i associated with the various distances of interest, at a fixed frequency, were obtained from an integral equation approach. It is believed that the transformation applies equally well to other types of practical wire antennas.

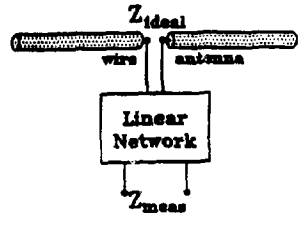

Fig. 1. Practical wire antenna equivalent.

The procedure of determining the transformation coefficients a_1 to a_3 has become known as de-embedding [2][3]. The technique in [3] includes computation of the standard deviations for the three transform coefficients directly from the measured data. Notable strengths of the methodology include only one inversion of a complex 3×3 matrix in all cases, and the ordering of data points is not important. In many applications, the number of data points greatly exceeds 3, in which case an overdetermined set of equations is solved in a least squares sense. While the impedance transformation associated with practical antennas is one class of problems amenable to treatment with the fractional linear transformation, the formulation actually relates the (complex) input to output for linear two-ports in general.

Wire antennas are nowadays analyzed reliably, even in the proximity of lossy earth, by numerical methods. Most notable among the available wire antenna codes are NEC-2 and NEC-3 [4][5], which are both based on the moment method. NEC-2 is available to the public, and is a powerful tool for the analysis of wire antennas residing in the air

*This work was partially supported by Phillips Laboratory, Kirtland AFB, NM, under an IPA agreement with The University of Alabama.

half-space. NEC-3 is required to analyze antennas involving air-to-earth 'ground stakes' or underground (buried) wires, but the distribution of NEC-3 is restricted. NEC-4 exists but is generally unavailable because its distribution is strongly restricted, so NEC-4 is not considered here. When properly applied (that is, the known inherent limitations of the codes are observed) to a broad class of wire antenna types, NEC-2 and NEC-3 can calculate feed-point impedances which are accurate and reliable to the point that they can be taken as ideal theoretical values. Similarly, network analyzers are now widespread so that reflection coefficients, or impedances, may be measured readily.

The main objective of this paper is to demonstrate application of the fractional linear transformation relationship to the new situation where the variable is frequency and the geometry is fixed, as compared to the original formulation for fixed frequency and a variable geometry dimension [1]. It is shown here that the approach can be valid over a significant bandwidth, even when the transformation coefficients are (complex) constants. A trailing-wire HF antenna, deployed from a fixed-wing aircraft, is used as a specific example to illustrate the basic characteristics of the impedance transformation when frequency is allowed to vary.

II. Procedure for Impedance Data Analysis

For convenient reference, essential points of the computer-based procedure for determination of the impedance transformation coefficients and other parameters of interest are summarized below. Additional details and considerations are in [1] and [3] where it is noted that the basic vector description which yields the curve-fitting procedure for the fractional linear transformation follows from [6].

Re-writing Eq. 1 in implicit form gives

$$a_1 Z_i + a_2 - a_3 Z_i Z_m - Z_m = 0 \qquad (2)$$

for a single ideal impedance Z_i and a single corresponding measured impedance Z_m. When multiple points are involved, a second subscript is added to denote the number of the independent variable sample. That is, at the "n"-th data frequency, measurement and NEC computation give Z_{mn} and Z_{in}, respectively, and Eq. 2 becomes

$$a_1 Z_{in} + a_2 - a_3 Z_{in} Z_{mn} = Z_{mn}. \qquad (3)$$

With just three data points, we have three equations which allow a basic solution for a_1, a_2, and a_3. An overdetermined system results from total data points $N > 3$, in which case a least squares solution may be obtained: it is usually more reliable to solve a larger, overdetermined system of equations because it reduces the influence of random errors in the measurements.

To obtain a matrix equation suitable for computer implementation, in accord with [6], the coefficients of a_1, a_2, and a_3 from the left hand side of Eq. 3 are loaded respectively into

$$|e_1\rangle = \begin{bmatrix} Z_{i1} \\ Z_{i2} \\ \vdots \\ Z_{iN} \end{bmatrix}, \qquad (4)$$

$$|e_2\rangle = \begin{bmatrix} 1 \\ 1 \\ \vdots \\ 1 \end{bmatrix}, \qquad (5)$$

and

$$|e_3\rangle = \begin{bmatrix} -Z_{i1} Z_{m1} \\ -Z_{i2} Z_{m2} \\ \vdots \\ -Z_{iN} Z_{mN} \end{bmatrix}, \qquad (6)$$

with the right hand side values packaged into the fourth vector

$$|f\rangle = \begin{bmatrix} Z_{m1} \\ Z_{m2} \\ \vdots \\ Z_{mN} \end{bmatrix} \qquad (7)$$

so that Eq. 3 can be written compactly as

$$|f\rangle = \sum_{i=1}^{3} a_i |e_i\rangle. \qquad (8)$$

The distance between $|f\rangle$ and its expansion is minimized when constants a_i are found from solving

the matrix equation

$$\begin{bmatrix} (e_1,e_1) & (e_2,e_1) & (e_3,e_1) \\ (e_1,e_2) & (e_2,e_2) & (e_3,e_2) \\ (e_1,e_3) & (e_2,e_3) & (e_3,e_3) \end{bmatrix} \begin{bmatrix} a_1 \\ a_2 \\ a_3 \end{bmatrix} = \begin{bmatrix} (e_1,f) \\ (e_2,f) \\ (e_3,f) \end{bmatrix} \tag{9}$$

through inversion of the 3×3 matrix, noting that here the weighted scalar product is defined to be complex by

$$(e_i, e_j) = \sum_{k=1}^{N} w_k e_{ik}^* e_{jk}. \tag{10}$$

In Eq. 10. w_k is a weighting factor which can be chosen so as to prevent large values of $|Z_{in}|$ or $|Z_{mn}|$ from exerting undue influence on the outcome of the calculations. When the magnitudes of Z_i and Z_m are comparable, the w_k have a minor effect, and may all be taken to be unity.

When the difference between the left hand and right hand sides of Eq. 3 is actually computed for the n-th value of the independent variable, with the three a_i known by virtue of solving Eq. 9, imperfections in Z_{in} and/or random errors in Z_{mn} will cause the result to deviate slightly from zero. If this small discrepancy is called ε_n,

$$a_1 Z_{in} + a_2 - a_3 Z_{in} Z_{mn} - Z_{mn} = \varepsilon_n. \tag{11}$$

The implications of this for judicious selection of the weighting factors w_k are considered in [1], with the conclusion that appropriate weights are

$$w_k = \frac{1}{1 + |Z_{in}|^2 \left(1 + |Z_{mn}|^2\right)}. \tag{12}$$

These are, in fact, the weights which are applied in the following example.

III. Example

A trailing-wire HF antenna, deployed to a length of approximately 16.75 meters from a fixed-wing aircraft, is shown in Fig. 2. The antenna is clearly visible, extending below the fuselage in the profile view of Fig. 2. Wire dispensing units for such trailing-wire antennas are characterized by large

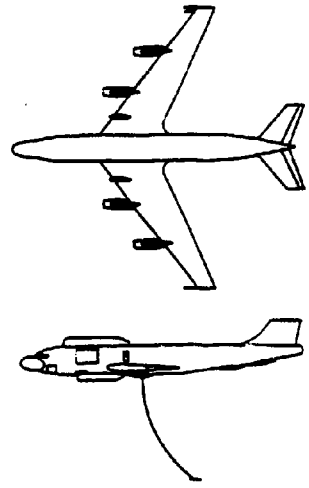

Fig. 2. Top and profile views of aircraft with trailing-wire HF antenna.

stray reactance values. A lumped-element static drain is attached to the wire. Also, a length (approximately 6 m) of 50Ω coaxial cable connects the antenna feed point to the network analyzer located in the aircraft's equipment bay. Hence, there are multiple contributions to the overall linear network of Fig. 1.

The "ideal" feed-point impedance for the antenna at each frequency of interest is computed using the wire grid model shown in Fig. 3, using the NEC-2 code on a personal computer (PC) [4] [5]. The NEC computed impedances, Z_{in}, and measured input impedances, Z_{mn}, at frequencies from 14.4 to 16.6 MHz in 0.2 MHz steps are plotted in Fig. 4. and they are also given in Table I. The relationship between the two sets of impedances is not apparent from inspection of Fig. 4.

The transformation coefficients are calculated on the basis of four frequencies: 14.4, 15.2, 15.8, and 16.6 MHz. Afterwards, input impedances Z_{mn} are predicted by applying Eq. 1 to the NEC-

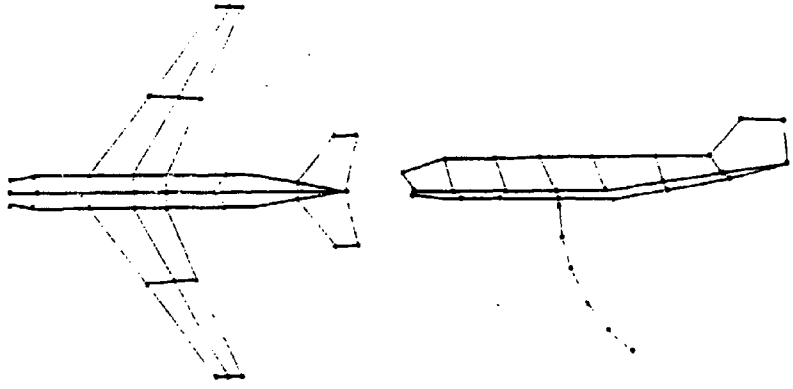

Fig. 3. Top and profile views of wire-grid model used in NEC-2 analysis.

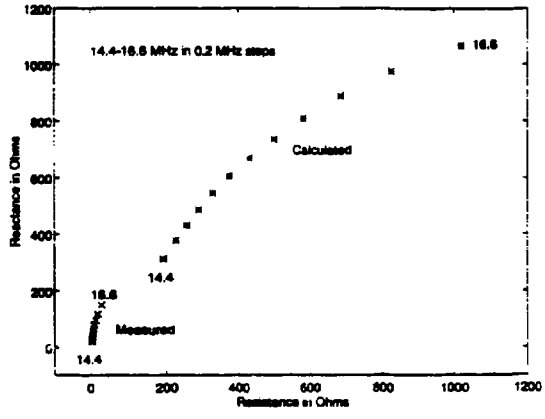

Fig. 4. Measured and NEC-computed impedances.

Table I
NEC-Computed, Measured, and Predicted Impedances for HF Trailing-Wire Antenna
Transformation Constants Based on Four Frequencies

n	Freq. (MHz)	NEC-Computed Impedance (Ω)	Measured Impedance (Ω)	Predicted Impedance (Ω)	Error %
1	14.4*	192.4-j 312.4	1.6-j 18.0	.8-j 18.0	0.0
2	14.6	228.8-j 377.3	3.8-j 22.0	.8-j 23.8	3.6
3	14.8	265.2-j 431.7	4.1-j 28.4	.1-j 28.0	2.3
4	15.0	298.6-j 487.5	4.3-j 34.3	4.3-j 34.6	1.1
5	15.2*	337.0-j 546.2	4.8-j 40.7	4.8-j 40.8	0.5
6	15.4	373.0-j 605.6	5.4-j 47.3	5.8-j 48.1	0.6
7	15.6	421.2-j 661.8	6.5-j 56.5	6.6-j 56.4	0.6
8	15.8*	468.0-j 725.9	8.0-j 67.1	8.2-j 66.4	1.0
9	16.0	501.7-j 806.2	9.9-j 79.8	10.4-j 78.7	1.5
10	16.2	600.4-j 894.1	13.5-j 96.2	12.6-j 94.9	1.4
11	16.4	626.2-j 975.8	19.0-j118.7	18.9-j117.8	0.9
12	16.6*	1019.0-j1067.0	29.4-j180.9	29.3-j182.5	1.0

Average Error = 1.2%

* = coefficient basis frequency
Reliability factor RF = 0.0012 (should be less than 1.0)

Transformation coefficients:

a_1 = 0.063871 - j 0.018938 (± 0.002242)
a_2 = -1.857386 - j 7.668350 (± 0.713291)
a_3 = -0.000293 - j 0.000138 (± 0.000031)

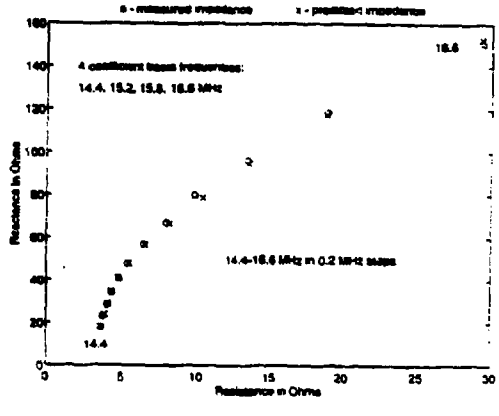

Fig. 5. Predicted and measured impedances. four coefficient basis frequencies.

computed impedances Z_m over the frequency band 14.4-16.6 MHz in 0.2 MHz steps. Consequently, the prediction capability of the transformation is tested at eight new frequencies in the band spanned by the four coefficient basis frequencies.

Measured and NEC impedances are reported in Table I. The calculated values of transformation constants a_1, a_2, and a_3 are also given there. Predicted impedances using these a_i values in Eq. 1 are listed for comparison with Z_m in Table I, and Fig. 5 is a graphical presentation of the predicted versus measured impedances. The error at each frequency, reported in the last column of the table, is the ratio of the length of the 'Error' vector in Fig. 6 to the length of the 'Measured Z' vector, expressed as a percentage. The worst case error between predicted and measured values is 3.6% at 14.6 MHz. For the four coefficient basis frequencies, the average error is only 0.6% and, for all twelve frequencies represented in Table I, the average error is just 1.2%. The excellent agreement of predicted impedances with measured values in Fig. 5 is impressive.

Because the measured impedances for this particular example contain only small random errors, the inclusion of additional basis frequencies in the calculation of the a_i values does not lead to any appreciable improvement of the final results (namely, the average error). The average error remains comparable, in fact, even when all twelve data points are included in the initial coefficient calculations. In other applications, where the measured data may be subject to larger random experimental errors, the inclusion of more data points into the calculation of transformation coefficients should yield improved agreement of predicted and measured impedances.

Fig. 6 illustrates symbolically the measured multidimensional vector, its predicted value (projected to the space spanned by the three vectors $|e_i\rangle$), and the error vector. A useful indicator, called reliability factor, is defined as follows

$$R_f = 10\sqrt{\frac{\|\epsilon\|^2}{\|Z_m\|^2}}. \qquad (13)$$

The geometrical meaning is that the magnitude of the error vector must not be greater than 10% of the magnitude of the measured vector. Thus, to have confidence in the measured data, the computed reliability factor must be smaller than unity. It can be seen in Table I that this condition is well satisfied for the example shown ($R_f \approx 10^{-3}$).

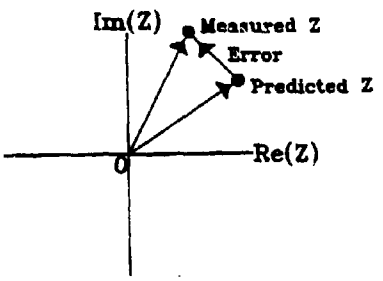

Fig. 6. Relationship of error to measured impedance on complex plane.

IV. Data Analysis Software

The first program for calculation of the fractional linear transformation coefficients and other parameters of interest from a set of measured and theoretical impedances was written in the Fortran language, and named FRALIN. The results in this paper were all obtained with a subsequent MATLAB [7] program, named FRALIN2, for use with the PC software MATLAB for Windows version 4.0. The output graphics from MATLAB were all produced on a PostScript-equipped laser printer.

Readers interested in obtaining the computer code used in this work should contact the first author at the Department of Electrical Engineering, University of Alabama, Box 870286, Tuscaloosa, AL 35487-0286.

V. Conclusions

A fractional linear transformation was used earlier [1] to relate in a one-to-one manner the ideal and measured impedances for a dipole antenna as a function of height above a ground plane. This

work provides additional evidence that other practical wire antenna types also may be modeled reliably by the same procedure. Also, the results in this paper show that the transformation may be applied over limited bandwidths, even for coefficient values which are restricted to be constants.

One possible application of this impedance transformation model is to predict the input impedance of a wire antenna at new frequencies of interest within a band spanned by a few (but > 3) sample frequencies on which calculation of the transformation coefficients is based.

The transform relationship between the ideal antenna impedance one obtains from NEC and actual remote feed-point impedance for practical wire antennas should be of particular interest to users of HF/VHF wire antennas.

Future work will attempt to extend the transformation to become frequency dependent so that wider frequency ranges, including resonant and anti-resonant regions, can be modeled with one set of coefficients.

Acknowledgment

The provision of measured impedance data by Mr. Neil Hurst is gratefully acknowledged.

References

[1] D. Kajfez and R.L. Dube, "Measurement of impedance transformation on practical dipoles," *IEEE Trans. Antennas Propagat.*, vol. AP-21, pp. 544-549, July 1973.

[2] R.F. Bauer and P. Penfield, Jr., "De-embedding and unterminating," *IEEE Trans. Microwave Theory Tech.*, vol. MTT-22, pp. 282-288, March 1974.

[3] D. Kajfez, "Numerical Determination of two-port parameters from measured unrestricted data," *IEEE Trans. Instrum. Meas.*, vol. IM-24, pp. 4-11, March 1975.

[4] G.J. Burke and A.J. Poggio, "*Numerical Electromagnetics Code ("NEC) - Method of Moments*," Lawrence Livermore National Laboratory, Report UCID-18834, January 1981.

[5] G.J. Burke, "*User's Guide Supplement for NEC-3 for Modeling Buried Wires*," Lawrence Livermore National Laboratory, Report UCID-19918, October 1983.

[6] I.M. Gel'fand, *Lectures on Linear Algebra* (translated from the Russian by A. Shenitzer), Interscience Tracts in Pure and Applied Mathematics, Number 9, New York: Interscience Publishers, Inc., 1961, ch. 1.

[7] MATLAB is a trademark of The MathWorks, Inc., Cochituate Place, 24 Prime Park Way, Natick, MA 01760.

NEC4 Analysis of a Navy VLF Antenna

C. A. Deneris, J. H. Schubartz, P. M. Hansen, J. C. Logan
Naval Command, Control, and Ocean Surveillance Center
RDT&E Division
San Diego, CA 92152-7304

ABSTRACT

NEC4 is used to evaluate proposed modifications to a Navy VLF top-loaded monopole. Charge densities are computed and used to calculate the maximum top-load gradient for two wire sizes. Although the antenna is electrically small, a large number of segments is needed to obtain the desired resolution in the charge data. Gradient values derived from the NEC4 data are shown to be in close agreement with those derived from measured data. The gradient values show that the proposed configuration does not meet the maximum gradient design limit for this antenna.

INTRODUCTION

Electrically short, top-loaded monopoles are commonly used by the U.S. Navy for Very Low Frequency (VLF) communication. Although electrically small, the operating frequency range (typically 12 kHz to 30 kHz) results in physically large antennas requiring significant maintenance. One such antenna is the Cutler VLF Antenna System located at U.S. Naval Radio Station, Washington County, Maine. The antenna is a dual array, with each array measuring over 970' in height and 6000' in diameter. This massive structure is currently scheduled for extensive wire replacement. An economical way to evaluate the proposed changes is necessary, and using numerical modeling is one solution. This paper presents a computer-aided analysis of the Cutler antenna using the Numerical Electromagnetics Code, Version 4 (NEC4) [1]. Previous work has demonstrated the applicability of NEC-GS (NEC-Ground Screen) to similar VLF antennas [2]. Here, the objective is to use NEC4 to determine the maximum surface electric field, or gradient, on the antenna top-hat. Knowing the gradient provides a means of assessing the impact of the proposed wire replacement on antenna performance.

ANTENNA DESCRIPTION

The Cutler antenna consists of two identical arrays as shown in Figure 1. Each array is essentially a base-fed, top-loaded monopole. The top-hats of each array consist of six diamond shaped panels arranged symmetrically around a central tower. The panels are supported by one center tower (T0), six inner towers, and six outer towers. The towers range in height from 800' at the outer ring to just under 1000' at the center. Each tower is supported by a system of guy wires. All towers and guy wires are grounded, and all the panels are insulated from the towers and each other. Each panel is fed using several down lead wires extending from a connection near the center tower insulator, to a helix house at the base where they are tied together.

A plan view illustration of a single top-hat panel is shown in Figure 2. Each panel in the array is approximately 3000' long, and has eight wires running from T0 to the outer towers. The four inner wires of each panel are 1" diameter solid core cables. The four outer wires of each panel consist of 1" solid core cables connected to 1.5" diameter hollow core cables. Hollow core cables were originally used to save on weight. The 1.5" diameter is necessary to avoid corona on the antenna at lower operating frequencies.

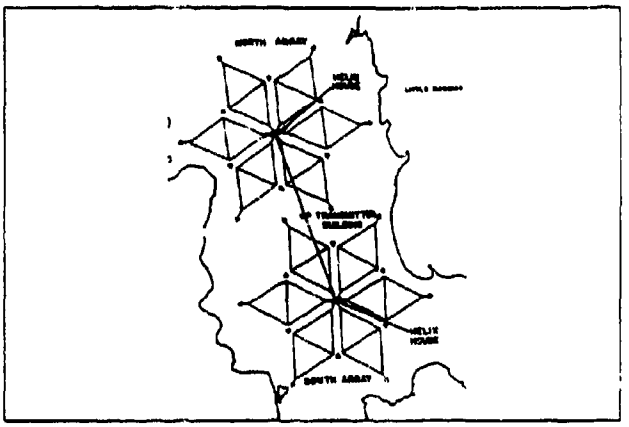

Figure 1. General layout of the Cutler antenna [3].

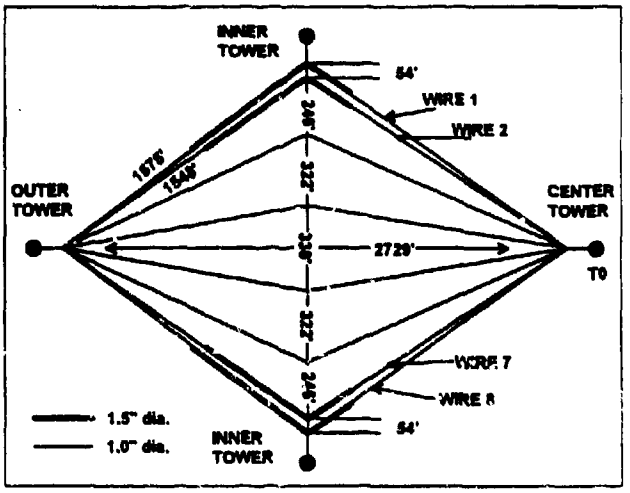

Figure 2. Plan view of a single top-hat panel of the Cutler antenna.

Corona is a discharge of electrical energy that can occur near a sharp point of a conductor raised to a high potential. Energy is discharged when the electric field strength on the conductor exceeds the breakdown voltage of the surrounding air. Since the energy is dissipated into the air, it represents a power loss in the system. Therefore, it is important to avoid corona to maintain system efficiency.

Currently, the Cutler antenna operates at 24.0 kHz. It's maximum input power is one megawatt for single array operation, and two megawatts for dual array operation. At 24.0 kHz, corona is not a problem in the 1.0" wires. However, it is desirable to operate at 17.8 kHz, and at this frequency, the 1.5" wires are needed. Unfortunately, these wires are due for replacement and the hollow core cable is no longer available. It was necessary therefore, to study different configurations to find an alternative to the 1.5" cable. Modeling the antenna using NEC4 provided a convenient way to do this.

THE NEC4 MODEL

A NEC4 model of the Cutler antenna was constructed for the computer-aided analysis. Although the antenna consists of two arrays, it is often operated using only a single array. Therefore, single array operation was assumed to simplify this analysis. Two antenna configurations were modeled. Configuration 1 models the antenna in its present state, using both 1" and 1.5" diameter top-hat wires. Configuration 2 consists entirely of 1" top-hat wires. Table 1 below gives model dimensions for both configurations. Inner panel wires refer to the panel sections from T0 to the inner towers. Outer panel refers to the sections from the inner towers to the outer towers.

Antenna Element	Configuration 1: 1" and 1.5" Wires		Configuration 2: 1" Wires Only	
	Length (ft.)	Diameter (in.)	Length (ft.)	Diameter (in.)
Center Tower	979.5	72.0	979.5	72.0
Inner Towers	875.8	72.0	875.8	72.0
Outer Towers	799.0	72.0	799.0	72.0
Downleads	550.1	1.0	550.1	1.0
Inner Panel Wires				
Wires 1 & 8	1352 223.3	1.0 1.5	1575 —	1.0 —
Wires 2 & 7	1216 224.9	1.0 1.5	1441 —	1.0 —
Outer Panel Wires				
Wires 1 & 8	800.0 774.7	1.0 1.5	1575 —	1.0 —
Wires 2 & 7	774.2 774.7	1.0 1.5	1549 —	1.0 —

Table 1. Dimensions of the NEC4 Cutler antenna model.

Since the antenna is rather complex, several approximations were made in constructing the computer models. To begin with, the top-hat elements were modeled as flat wires with no catenary. All tower guy wires were neglected and a perfect ground was assumed. Since the towers are insulated from the panels in the antenna, they were modeled as free standing monopoles in the model. On the actual antenna, several vertical feed wires fan out from the source at the base to each panel. On the computer model, each panel was fed using a single vertical lead extending from the source. Furthermore, since the center tower is not fed, the feed structure had to be made slightly asymmetric to accommodate the tower's position. That is, the distance from the source to each panel varies slightly from panel to panel. This asymmetry can clearly be seen in the center of Figure 3, which shows a view of the NEC4 wire

model. Finally, since the dual outer wires on each outer panel edge are so close to each other near the panel vertices (see Figure 2), the geometry had to be altered to allow NEC4 to recognize them as separate wires. Specifically, the outer panel wire separation at the inner tower connection was less than 10^{-3} times the length of the wire segments, thus violating the separation criteria in NEC4 [1]. To get around this limitation, the outer two wires (# 1 and #8) were modeled as a single wire near the inner vertex of each panel. At a distance of two segments (≈ 112 ft.) from the center tower, the wire splits into two separate wires. The angle between the wires was adjusted to achieve the specified separation at the inner tower ring. Modifying the geometry seems justified since the resulting difference in wire lengths is small compared to a wavelength. Thus, there will only be a small effect on the calculations. Also, it was felt that the charge around the inner tower region would be higher, and therefore more critical to the onset of corona, than the charge near the center tower. Hence, modeling accuracy at T0 was sacrificed in favor of maintaining the correct wire spacing at the inner towers.

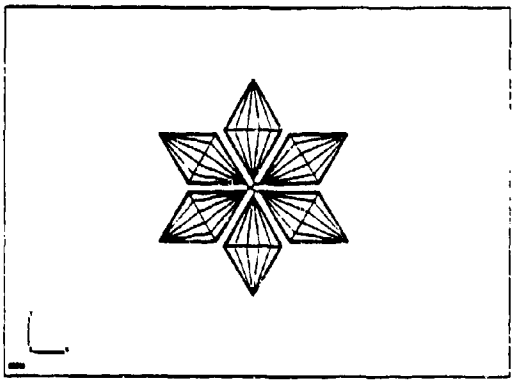

Figure 3. Plan view of the NEC4 Cutler model.

Calculations were performed using the single precision version of NEC4 on a Convex C240 Mini-supercomputer. To obtain the maximum practical resolution in the charge density, the model required approximately 3000 unknowns and five hours to run. As with all Method of Moments wire modeling, there is a trade off between model size, computation time, and the minimum segment size limit of the program. In addition, the asymmetrical feed arrangement of this particular model prevented using symmetry in the calculation. Since small segment modeling in NEC4 has been significantly improved over earlier versions [1], computation time and model size became the limiting factors for this study. Taking the factors above into account, it was decided segment lengths of approximately 55 ft. (≈ 0.001 $\lambda_{17.8\ kHz}$) would give the maximum practical resolution. Given the large physical size of the antenna, the resulting model contained 2997 segments.

Current and charge were calculated at 17.8 kHz and 24.0 kHz for both antenna configurations. Figures 4 and 5 show the calculated charge distribution, normalized to 1 amp input current, for the outer two panel wires (wires 1 and 2, or 7 and 8 in Figure 2) at each frequency. These are the only panel wires with 1.5" sections, and therefore show the greatest change between Configuration 1 and Configuration 2. Note the change in wire diameter is clearly seen in the data for Configuration 1. The results indicate the charge density is slightly less when only 1" wires are used. In the graphs, the data is plotted along the wires from the middle tower to the outer tower. Similar results were obtained for the wires extending from the middle tower to the center tower.

		17.8 kHz		24.0 kHz	
Configuration	Wire #1 Diameter (in.)	Q_{max} (C/m/A)	E_{max} (kV/mm)	Q_{max} (C/m/A)	E_{max} (kV/mm)
1	1.0 and 1.5	2.93×10^{-10}	0.685	2.24×10^{-10}	0.429
2	1.0	2.82×10^{-10}	0.999	2.15×10^{-10}	0.618
I_{max} (A)		2477		2030	

Table 2. Maximum top-hat gradients calculated using NEC4.

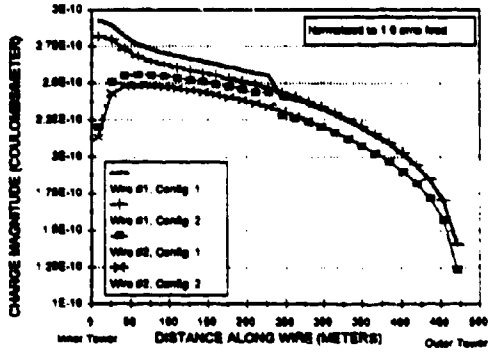

Figure 4. Calculated charge density for top-hat wires 1 and 2 at 17.8 kHz.

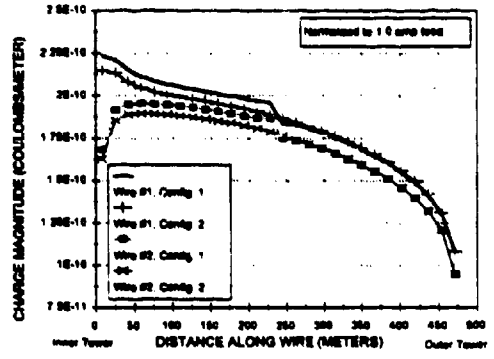

Figure 5. Calculated charge density for top-hat wires 1 and 2 at 24.0 kHz.

GRADIENT CALCULATIONS

The surface electric field, or gradient, on a conductor determines whether or not corona will occur. For this reason, it is an important parameter to consider when working with high voltage antennas like Cutler. In this case, the gradient can be used to assess the impact of replacing the 1.5" wires with 1" wires. According to [4], the maximum allowable gradient to avoid corona for the Cutler antenna is .8 kV/mm. Therefore, if the maximum gradient on the 1" replacement wires exceeds this limit they will not meet the design requirement.

For a cylindrical conductor, the gradient can be calculated from,

$$E = \frac{q_L}{2\pi\varepsilon_0 r} \tag{1}$$

where q_L is the linear charge density in coulombs per meter, ε_0 is the permittivity of free space, and r is the radius. Examination of Figures 4 and 5 shows that the maximum charge density per amp occurs on the outer wire (#1 or #8) at the inner tower connection. Multiplying these charge values by the maximum antenna input current and substitution into (1) yields the maximum gradient. The maximum antenna base currents I_{base} for single array operation are 2477 A at 17.8 kHz, and 2030 A at 24 kHz [3]. Using these currents, the maximum top-hat gradients for each configuration are calculated and shown in Table 2.

The validity of the NEC4 data was checked by comparing the results with gradients calculated from measurements. The measurements were taken during a model study of the antenna using a 100:1 scale model [4]. The model data includes the current distribution on the outer panel wires, which can be used with (1) to calculate the gradient.

To calculate the gradient from the measurements, the charge density must be derived from the current distribution. From the continuity equation, the linear charge density along a wire is related to the slope of the current distribution by,

$$Q_{Total} = \frac{\partial I}{\partial t} = \frac{I}{\omega} \tag{2}$$

and

$$q_L = \frac{\partial Q_{Total}}{\partial L} = \frac{1}{\omega}\frac{\partial I}{\partial L} \tag{3}$$

where Q_{Total} is the total charge on the wire beyond a given point, ω is the radian frequency, and q_L is the linear charge density at the point. Substituting (3) into (1) gives,

$$E_s = \frac{1}{4\pi^2\varepsilon_0 fr}\frac{\partial I}{\partial L} \tag{4}$$

where E_s is the surface electric field (*i.e.*, the gradient) on the wire. Equation (4) is a maximum when the slope of the current distribution is a maximum. From [4], the maximum slope of the measured current distribution is 0.0296 mA/m per Amp of input current. Therefore, substitution into (4) gives an equation for the maximum surface gradient as a function the antenna base current I_b:

$$E = \frac{0.0296\times10^{-3} I_b}{4\pi^2\varepsilon_0 fr} \tag{5}.$$

Measured input currents for various configurations of the antenna model are found in [3], including maximum currents for 1.0" and 1.5" wires at several frequencies. Substituting the currents into (5) resulted in the curves shown in Figure 6. The graph compares the measured data with the NEC4 results. The agreement between the two is very good, with the NEC4 values falling within 10% of the measurements. Note that both the NEC4 data and the measured data indicate 1.0" wires on the outer panel are unacceptable for operation at 17.8 kHz, as the gradient in this case exceeds the 0.8 kV/mm design limit.

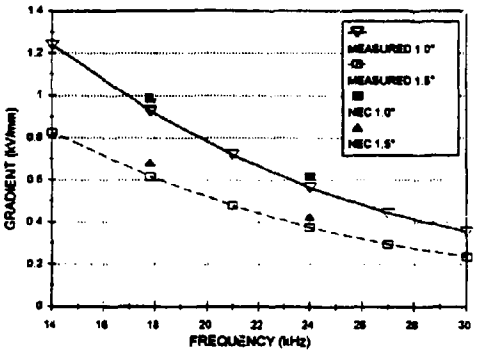

Figure 6. Measured and calculated maximum top-hat gradient for the Cutler antenna.

SUMMARY

The results of this work help demonstrate NEC4's ability to complement the antenna design process. In this particular case, it was shown NEC4 can be used to evaluate proposed changes to the Navy's Cutler, Maine VLF top-loaded monopole. Charge data from NEC4 was used to calculate the maximum top-hat gradient for the antenna. The computed results agree very well with measured model data. Both data sets indicate the gradient on the 1.0" wires exceeds the maximum design limit needed to avoid corona at 17.8 kHz.

REFERENCES

[1] G. J. Burke, "Numerical Electromagnetics Code -NEC-4 Method of Moments, Part 1: User's Manual", UCRL-MA-109338, Lawrence Livermore National Laboratory, Livermore, CA, Jan. 1992.

[2] J. P. Cahill, "Comparison of NECGS to measured design curves for VLF monopoles", *6th Annual Review of Progress in Applied Computational Electromagnetics*, pp. 308-315, Mar. 19-22, 1990.

[3] C. K. H. Tsao, L. W. Campbell, and B. Ambroseno, "Final report on proof of performance tests Cutler VLF antenna U.S. Naval radio station Washington County, Maine", P&B Publication No. 715, Pickard and Burns INC., Aug. 25, 1981.

[4] W. S. Alberts, R. E. Ankers, *et. al.*, "U.S. Naval radio station Cutler, Maine recommended radiation system design", DECO Report No. 13-s-4, Developmental Engineering Corporation, Jun. 28, 1957.

NEARLY SEVEN YEARS OF SUCCESS USING MININEC FOR ANALYSIS AND DESIGN OF STANDARD BROADCAST MEDIUM WAVE AM DIRECTIONAL ANTENNAS

JAMES B. HATFIELD, P.E.
HATFIELD & DAWSON CONSULTING ENGINEERS

INTRODUCTION

In the nineteen sixties, Robert Silliman was one of the first consulting radio engineers to use computer point matching techniques based on Hallen's integral equations to analyze broadcast antenna behavior. In succeeding decades Grant Bingeman, Jerry Westberg, Stan Kubina, G.M. Royer, Dave Pinion and others applied various moment method programs to the analysis of AM standard broadcast directional antennas. By the end of the nineteen eighties NEC, MININEC and a program from Ohio State University were in common use for AM antenna analysis.

Consulting engineers such as this writer, Ron Rackley and Karl Lahm (now at VOA) have used MININEC since the mid nineteen eighties for the analysis and adjustment ("tune up") of AM directional antennas. Advantages that MININEC offers for modeling medium wave monopoles over radial wire ground screens are ease of use, the centering of current pulses on segment junctions, and greater accuracy handling abrupt radius transitions. Good agreement with measured and FCC computed far field patterns is achieved with MININEC using just seven segments per radiator. Experience impedance curves can be duplicated with a reasonable margin of error if the base region of the tower is modeled in detail and an impedance correction is added to the computed results. Near electric and magnetic field human exposure from AM towers can also be computed using MININEC if the modeling is performed carefully. RF shock hazard estimates for workers on de-energized power lines and container loading cranes near AM stations have been computed using MININEC. Conversely the effects of power lines and cranes upon AM directional antenna patterns and Federal Communications Commission (FCC) mandated monitor points have been computed using the near field provisions of MININEC.

ADJUSTING AM DIRECTIONAL ANTENNAS

FCC directional antenna pattern computations are based upon point sources and parallel ray geometry (See Figure One). The design specifications used to determine pattern shape include the relative contribution to the far field of each radiator in terms of the field ratio and phase of the radiation from each point source. Since the horizontal plane far field of each radiator, in milliVolts per meter at one Kilometer, is $120\pi/\lambda$ times the total current moment of the radiator the relative contribution of each radiator to the far field is found by taking the ratios of the total current moments of the radiators. The MININEC drive voltages for a given set of FCC design parameters can be found by inverting a matrix whose constants, derived from MININEC computations, relate the drive voltages to the far fields. The FCC requires that directional

antenna performance be monitored. This is accomplished by measuring the relative magnitude and phase of the tower currents, usually at the base. The matrix inversion process produces the voltage drives that can be used to compute the base currents and phases for a given set of field ratios and phases.

The computed base current values are used to adjust directional antennas. After the adjustments have been made ground level measurements are performed along radials extending 30 Kilometers from the center of the array. These measurements are used to prove that the directional pattern is within the limits prescribed for it by the FCC.

Over the years we have adjusted or assisted others in adjusting nearly 100 directional antennas using the MININEC / matrix inversion technique. In all but two of the adjustments the measurements verified the accuracy of the procedure. In both of the exceptions the horizontal plane field was perturbed by nearby scatterers. In one case there was re-radiation from nearby office buildings and in the other case there were terrain irregularities. In those situations it was less expensive and time consuming to adjust the array by trial and error than it was to model complex objects in the environment in order to account for their effects.

Most AM directional antennas are used to control skywave radiation at night at some angle above the horizon. The adjustment of arrays so that horizontal plane measurements can be made in the presence of re-radiating or scattering objects to show the proper pattern can have a deleterious effect upon the performance of the antenna array at a vertical angle. Less interference would therefore be caused by simply adjusting the array to base current parameters based upon method of moments computations and not worrying about making accurate horizontal plane measurements. Such a proposal is now before the FCC.

DE-TUNING AM TOWERS

If one sets the field ratio of a tower to zero and then follows the procedure outlined above, the computed drive voltage for that tower will result in current moments that sum to zero for that tower, or at least to a value five or six orders of magnitude below the reference tower. The computed currents for the array and the de-tuned tower will show an active base impedance with a resistive component that is usually a few percent of the reactive component. This means that the conjugate of the reactance can be applied to the base of the tower for de-tuning purposes. This impedance should be trimmed by measuring the current minimum at the height where the phase reversal in the computed current distribution occurs. The base reactance is then adjusted for a minimum reading.

Since the de-tuning process reduces the field in the horizontal plane where field strength measurements are made the radiation at vertical angles increases. For nighttime operation the horizontal plane pattern is therefore within limits while the vertical angle radiation increases potentially creating greater skywave interference (See Figure Two). For this reason de-tuning unused towers in a nighttime array is not necessarily a good idea.

MITIGATING RADIO TOWER / POWER LINE INTERACTIONS

It sometimes happens that power lines are constructed near existing AM directional arrays. If the power poles or towers are 30 meters or more tall their re-radiation and mutual coupling effects can distort the far field pattern of the station. Additional problems are created when there is a "skywire" or "shield" wire running along the tops of the poles for lightning protection and electrically connected to the poles. The poles and towers used for power transmission usually provide a conductive path to ground. The RF current flowing in the loops thus created causes directional antenna pattern distortion. The meters used to measure the AM stations fields employ shielded loop antennas to measure the magnetic field component of the transmitted wave. Since the electric field is the desired measurement parameter, the magnetic field magnitude is multiplied by the impedance of free space and depicted on the meter face in terms of electric field. When measurements are made within the near field of the RF currents circulating in the loop created by the power line erroneous readings result. This effect can be predicted using the near magnetic field computation of MININEC. Re-adjustment of the array can then be made based upon MININEC computations so that the FCC monitoring points near the power line are brought into tolerance while arrangements are being made to either de-tune the power poles or float the "skywire".

When electric power transmission lines are in close proximity to AM radio towers serious RF shock hazard to electric utility linecrews can result. In one instance two AM towers were located near a 150 KV line. One of the towers was only 23 meters from the line. Several instances of RF burns were reported to the utility safety officer. The work crane, power line, and power poles were modeled in a simplified schematic fashion. Computations of the RF current that flows through an equivalent human impedance at the crane work platform at various locations were made to determine the potential shock hazard.

AM TOWER BASE IMPEDANCE

The measurements and computations of R.W.P. King and other academic workers are usually used to benchmark antenna impedances computed by moment method programs. The center conductor of a coaxial cable poked through a sheet of copper, used by King and others as a model for computations and measurements of a monopole over a ground plane, is not the same as a base insulated tower fed by a horizontal half inch pipe. When the base capacitance and the radius disjunction between the base and the feed line are carefully modelled (See Figure Three) the base impedance given by MININEC is much closer to the measured impedance of the typical AM tower. The match between the computed values and the curves showing the measured base impedance for towers of various heights is improved when one adds a correction of 5 + j43 Ohms to all computed values (See Figure Four).

COMPUTING BANDWIDTH

Programs such as WCAP (a specialized program similar to SPICE written for the analysis of directional antennas and their feed circuitry) can be used for dynamic modeling of the

combination of the directional antenna and its feed system. The frequency response of the transmitted signal can be determined in this manner. MININEC can be used to compute the self and mutual admittances for the antenna array over a specified range of frequencies. This is useful for determining why a station's sound quality varies in different directions in a directional pattern.

RF HAZARD COMPUTATIONS

The FCC requires a showing from licensees that the provisions of ANSI C95.1-1982 Standard for Safety Levels with Respect to Human Exposure to Radio Frequency Electromagnetic Fields are met. MININEC can be used for this purpose, but its accuracy decreases as one approaches the tower. The electric and magnetic near field computations provided by MININEC are useful if one is careful to check for convergence. Seven segments per wire gives a lumpy and unrealistic result. Fifty segments show a computed field that varies smoothly with distance and is a reasonable approximation of measured values. Figure Five shows the computed near fields with a measured data point for comparison. Figure Five also shows the effect of insufficient segmentation upon accuracy. Ric Tell, Bob Cleveland of the FCC, and Ed Mantiply of the EPA have explored this issue in several papers.

NIGHTTIME INTERFERENCE

The method that has been used for FCC purposes since the nineteen thirties to compute vertical angle radiation from AM towers utilizes simple trigonometric functions to represent tower current distributions. The impact of mutual coupling between towers upon the current distribution is ignored in these calculations. Nighttime interference can be affected by inaccurate computations of the antenna current distributions since the vertical angle radiation, computed from the current distribution, contributes to the increased coverage a station provides at night due to skywave propagation. The vertical angle fields computed using the more realistic MININEC current distributions provide a more accurate picture of potential skywave interference (See Figure Six).

NEAR FIELD COMPUTATIONS AND MEASUREMENTS OF ARRAY PERFORMANCE

In order to provide performance verification information for an array that is located at the shoreline of a tropical island, Ron Rackley and Ben Dawson used the nearfield computation feature of MININEC to calculate magnetic field values for specified locations very close to the array. Measurements were made at these locations using a conventional magnetic field intensity meter desensitized by shorting the loop antenna shield. The meter, with the shield shorted, was then calibrated in a known field. The same MININEC model that was used for array pattern, current distribution, and impedance calculations predicted near magnetic fields that agreed with measured values to better than 2% accuracy. The data provided by this technique was used to demonstrate proper operation of the antenna system despite the fact that complete far field measurements were virtually impossible due to open ocean on one side of the array, and dense roadless tropical jungle on the other.

CONCLUSION

Programs like NEC and MININEC have enabled the practicing radio engineer to analyze antennas in new ways to solve problems for which there was previously no exact solution. For AM medium wave directional antennas this means that the effects of coupling between antenna elements upon the antenna current distributions can be included in the design and analysis process and precise relationships between antenna currents and radiated fields can be computed. Directional antenna adjustment and pattern verification based upon NEC and MININEC computations has been successfully performed for hundreds of AM arrays all over the world by a cadre of international radio engineers. These programs have also been helpful for the analysis of the interactions of radio towers with cranes and power lines and the human exposure to electromagnetic fields. Newer versions of NEC and MININEC, such as NEC4, VLF+, and MININEC Professional have the potential to help engineers analyze finer structures in greater detail with higher accuracy.

The FCC is currently investigating whether its Rules & Regulations regarding AM pattern verification should be updated to include numerical electromagnetic modeling techniques. The burden and expense of detailed measurement and data analysis could be replaced in the future by stricter requirements for antenna current or voltage monitoring and computations using NEC, MININEC or other moment method computer programs.

We have finally reached the point where simplified directional AM antenna pattern analysis based upon trigonometric functions is about to be replaced by more exact moment method techniques. A further benefit of this change will be the ability for the AM radio engineer to analyze complex electromagnetic environments using a desk top computer. The responsibility incurred through use of these programs will be to always check for stability and convergence in the computed results and to verify that the results agree with measured data.

$$E = K\left(F_1 + F_2 \angle 5\cos(\phi_T - \phi) + \gamma_2 \right) \quad \text{FAR FIELD}$$

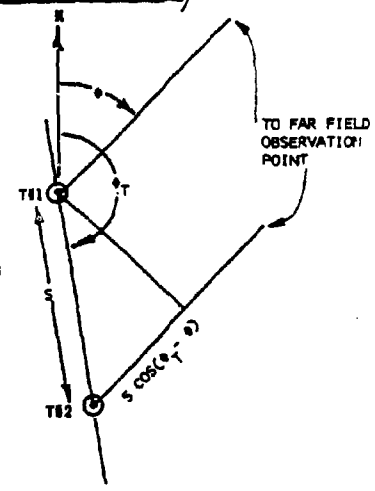

γ_1 = PHASE OF TWR#2 RELATIVE TO TWR#1

F_1, F_2, RELATIVE FIELD RATIOS OF TOWERS

ϕ = AZIMUTH FROM TRUE NORTH OF OBSERVER

ϕ_T = AZIMUTH OF TOWER #2 FROM TRUE NORTH

S = SPACING BETWEEN TOWERS

K = PATTERN SIZE CONSTANT

HATFIELD & DAWSON CONSULTING ENGINEERS	FIGURE 1 HORIZONTAL PLANE FAR FIELD CALCULATED FROM POINT SOURCES

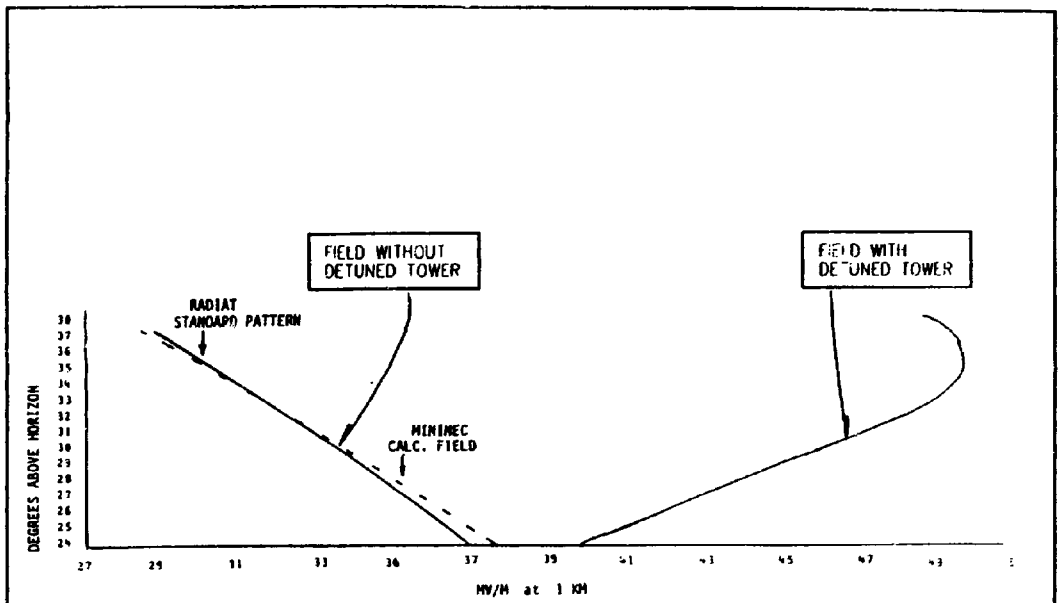

HATFIELD & DAWSON CONSULTING ENGINEERS	FIGURE 2 EFFECT OF DETUNED TOWER ON VERTICAL ANGLE RADIATION

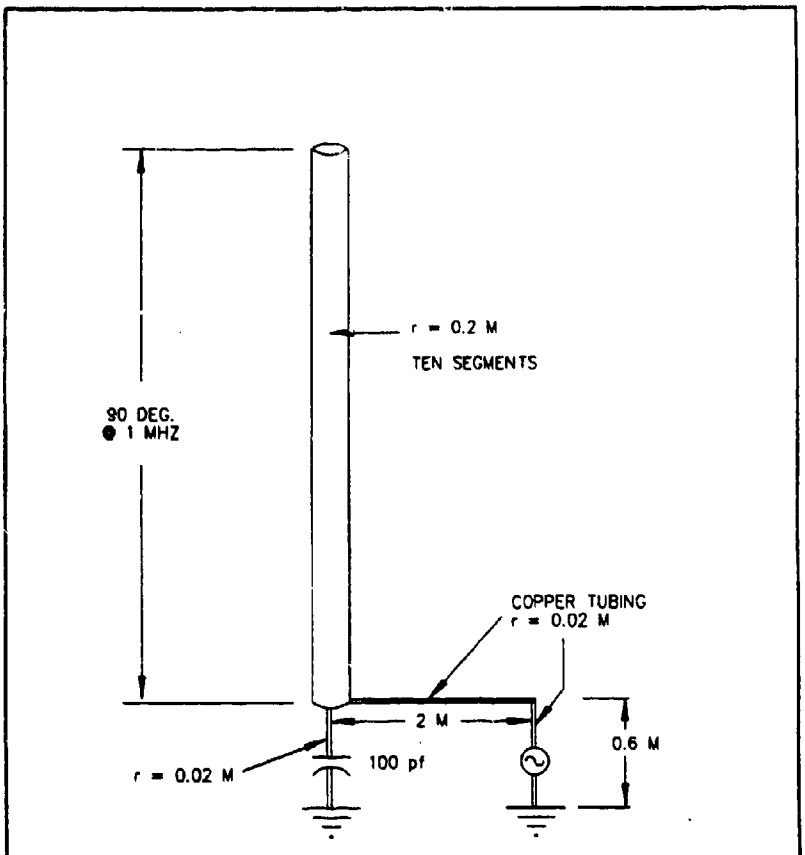

HATFIELD & DAWSON CONSULTING ENGINEERS	FIGURE 3 TOWER & FEED MODEL FOR MININEC IMPEDANCE COMPUTATIONS

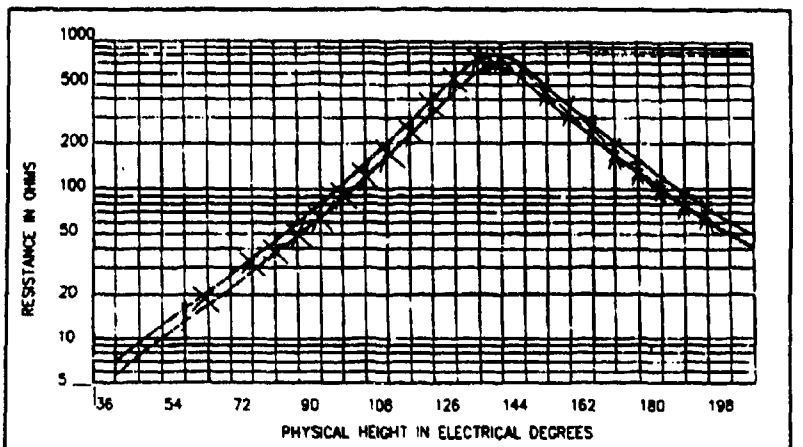

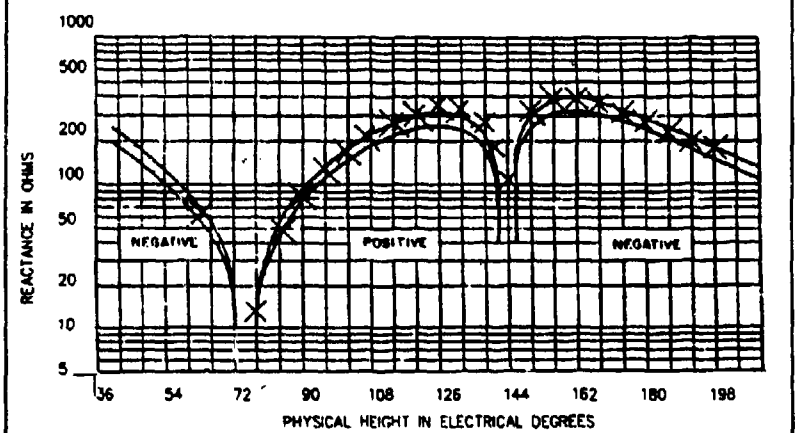

HATFIELD & DAWSON
CONSULTING ENGINEERS

FIGURE 4
SELF IMPEDANCE OF MONOPOLE OVER A RADIAL WIRE GROUND SCREEN. MODELED BY MININEC (SEE FIGURE 3) AND CORRECTED BY ADDING 5 + j43 TO COMPUTED IMPEDANCE. COMPUTED DATA POINTS PLOTTED ON EMPIRICAL CURVES FROM ELECTRONICS MAGAZINE ARTICLE (JUNE 1952 pg.143)

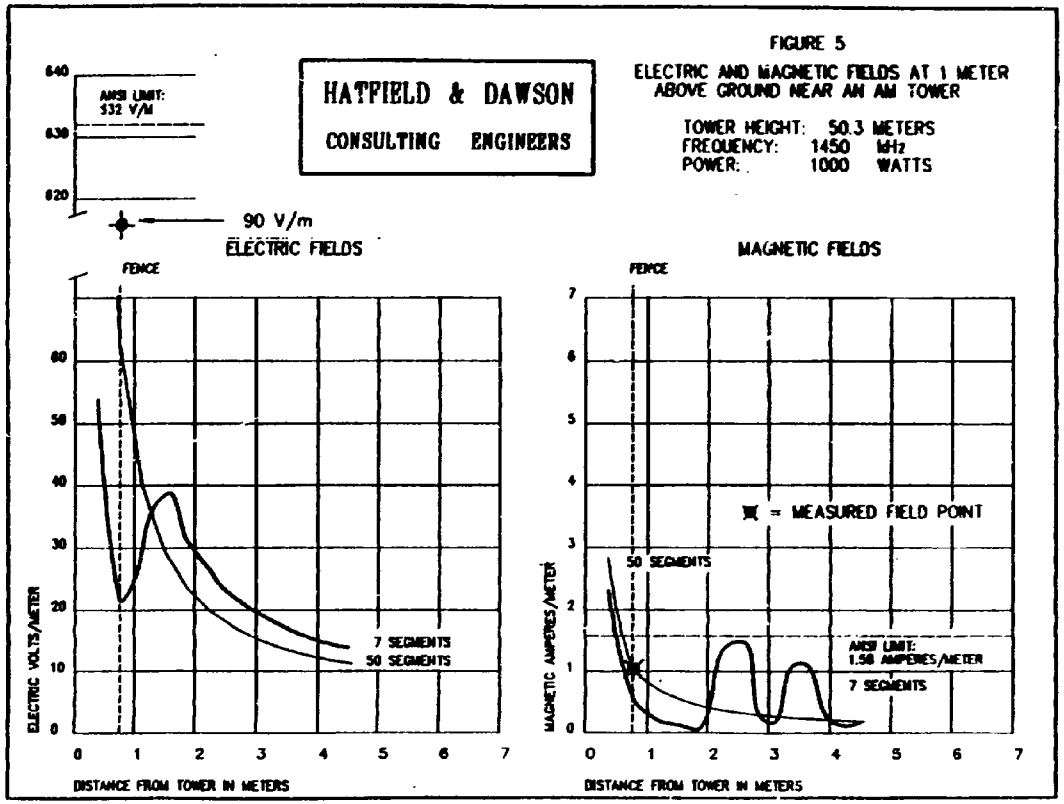
HATFIELD & DAWSON
CONSULTING ENGINEERS
FIGURE 5
ELECTRIC AND MAGNETIC FIELDS AT 1 METER ABOVE GROUND NEAR AM AM TOWER
TOWER HEIGHT: 50.3 METERS
FREQUENCY: 1450 kHz
POWER: 1000 WATTS
ANSI LIMIT: 532 V/M
90 V/m
ELECTRIC FIELDS
MAGNETIC FIELDS
FENCE
ELECTRIC VOLTS/METER
MAGNETIC AMPERES/METER
7 SEGMENTS
50 SEGMENTS
= MEASURED FIELD POINT
ANSI LIMIT: 1.58 AMPERES/METER
DISTANCE FROM TOWER IN METERS

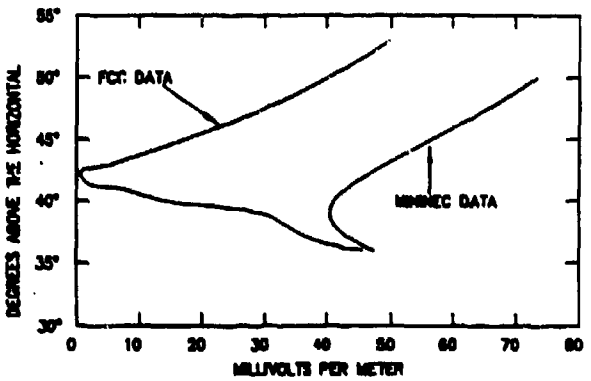

HATFIELD & DAWSON CONSULTING ENGINEERS	FIGURE 6 COMPARISON OF VERTICAL ANGLE AM FIELD FROM A 0.6 WAVELENGTH TOWER AS COMPUTED BY FCC METHODS AND MININEC

ANALYSIS OF AIRBORNE ANTENNAS WITH THE ESP, NEC-BSC, AND NEW-AIR CODES

B V Andersson, Å Johansson, U Lidvall, T Lundin
Communicator CEC AB
PO Box 1310, S-17125 Solna
Sweden

1 Abstract

Radar and communication antenna systems on an AEW-aircraft have been analysed with the use of the ESP, NEC-BSC, and NEW-AIR computer programs.

Antenna pattern coverage and antenna to antenna coupling have been computed taking the complex environment of the antennas into account. Calculated antenna patterns have been compared to measured data.

2 Introduction

On modern airborne early warning (AEW) platforms it is important to have radar and communication antenna functions with the required pattern coverage, sidelobe characteristics, and antenna to antenna isolation. Several systems with simultaneous operation are necessary in order to fulfil the AEW-task. Generally a large number of antennas have to be integrated on the aircraft carrying the AEW-radar.

It is important to have the capability to analyse and access the performance of antenna systems and combinations of antenna systems, including their complex environment, in early development phases, during system development, and in test phases of a project to accomplish a balanced design with the best overall performance. The capability to analyse antennas in their true environment makes it possible to evaluate their influence on system performance and to investigate modifications and improvements.

For this adequate computational tools are required. Such tools are the computer codes ESP, NEC-BSC, and NEW-AIR, developed at The Ohio State University, ElectroScience Laboratory. ESP, based on the method of moments (MoM), can be used for the low frequency problems and NEC-BSC and NEW-AIR, based on ray methods (UTD), can be used for the high frequency analysis.

This paper presents results from the analysis of radar and communication antennas on an AEW-aircraft using these codes. Antenna patterns and antenna to antenna coupling have been computed.

3 Analysis of a radar antenna on an AEW-aircraft

3.1 Model

Alternative antenna arrangements for an AEW-system, fig. 1, have been studied. The influence of different carrier aircraft (SAAB 340, Fairchild METRO C26) on the performance of a dorsal radar antenna have been investigated with the NEC-BSC code. One of the two side looking array antennas is modelled as an array aperture. The aircraft model is built with PEC ellipsoids, cones, cylinders, and flat plates as shown in fig. 2.

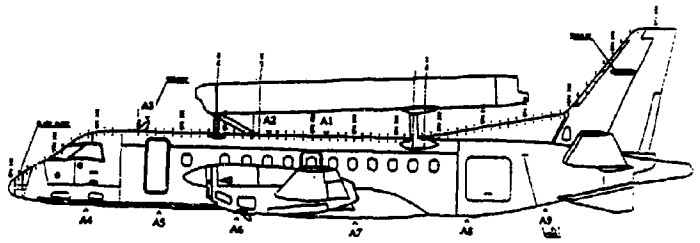

Fig. 1 AEW-aircraft (SAAB 340) with dorsal radar unit and communication antenna positions A1-A9 indicated

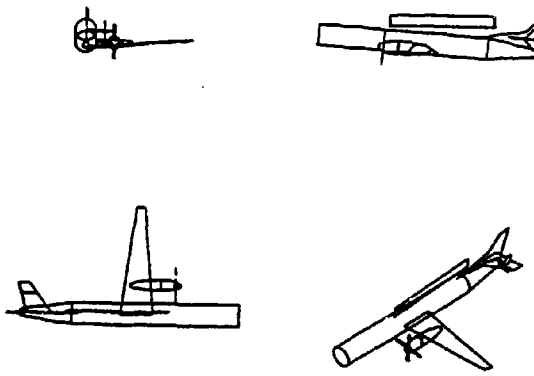

Fig. 2 NEC-BSC model of an AEW-aircraft (Fairchild METRO C26) for the analysis of the dorsal radar antenna

3.2 Computed radiation pattern

The radiation function for one side looking array antenna has been calculated with NEC-BSC at S-band. An azimuth radiation pattern, 4° below the horizontal plane, for an ideal array aperture is shown in fig. The main structural (Fairchild METRO C26) scattering contributions to he side lobe levels emanate from the wing, the engine, and the propeller blades.

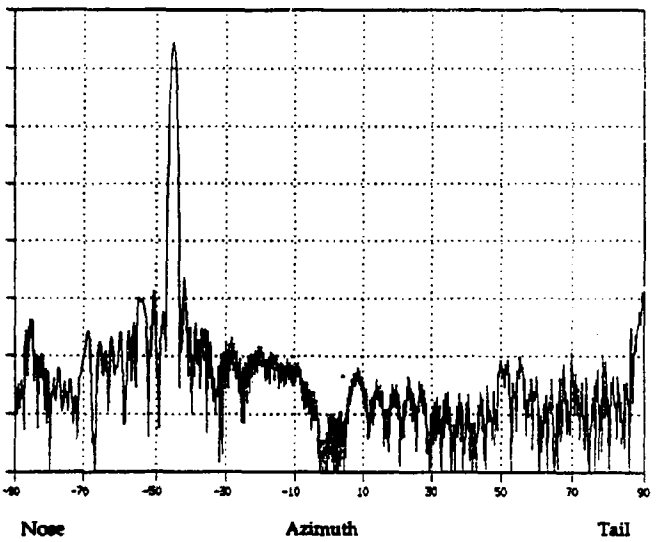

Fig. 3 Calculated azimuth radiation pattern, 4° below the horizon, with NEC-BSC for the dorsal radar antenna at S-band. Carrier aircraft Fairchild METRO C26

4 Analysis of communication antennas on an AEW-aircraft

4.1 Model

The AEW-aircraft of fig. 1 is modelled with PEC plates as shown i fig. 4 for the calculation of communication antenna patterns with the ESP-code. The model of fig. 4 has also been used for the calculation of the coupling between three antenna pairs. The communication antennas are modelled as monopoles on a ground plane.

4.2 Computed radiation patterns

The radiation function for an antenna at position A2 in fig. 1 has been computed with ESP at 130 MHz. Fig. 5 shows a calculated azimuth pattern

and a corresponding measured pattern from scale model measurements. In this case no dorsal unit was present on the aircraft. Very good agreement between calculated and measured patterns can be observed. A computed coverage pattern as function of azimuth and elevation for the A3 antenna with the dorsal radar unit on the aircraft is shown in fig. 6.

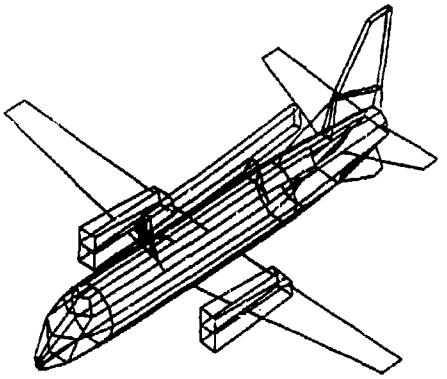

Fig. 4 PEC plate model of AEW-aircraft (SAAB 340) for ESP-analysis of communication antennas

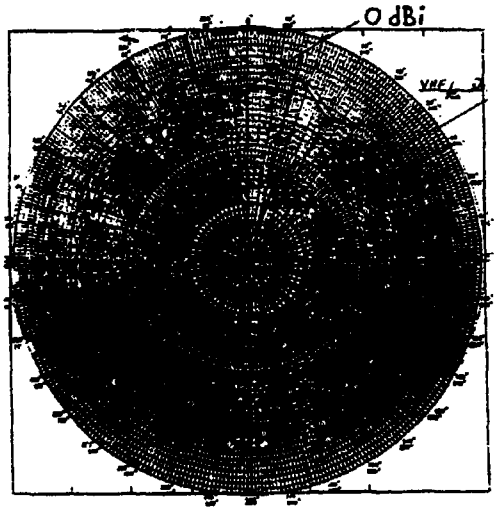

Fig. 5 Calculated and measured azimuth patterns with ESP for communication antenna A2 at 130 MHz. No dorsal radar unit on the carrier aircraft.
Calculated - - - , Measured ——

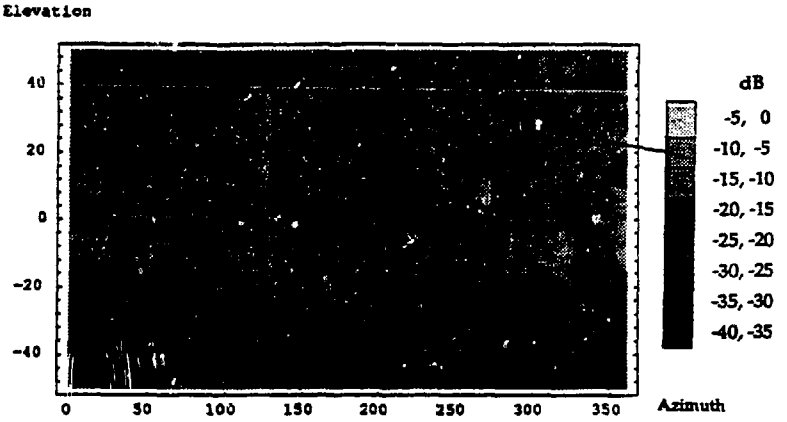

Fig. 6 Calculated coverage pattern with ESP for communication antenna A3 at 130 MHz. The dorsal radar unit placed on the carrier aircraft. Azimuth 0°, elevation 0° corresponds to the forward direction.

The coverage pattern for an antenna at position A5, fig. 1, has been calculated at UHF-band with NEW-AIR as shown in fig. 7. The model for the aircraft during these calculations consists of an ellipsoid and flat plates. A combined coverage pattern for three antennas analysed with NEW-AIR is presented in the forward and backward sectors in fig. 8. The fast rippie with angular direction is due to the many wavelengths distance between the antennas.

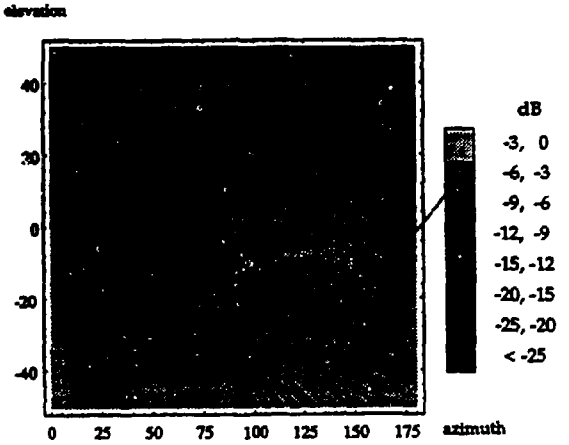

Fig. 7 Computed coverage pattern with NEW-AIR for an antenna at position A5 (fig. 1) on UHF-band. Azimuth 0°, elevation 0° corresponds to the forward direction.

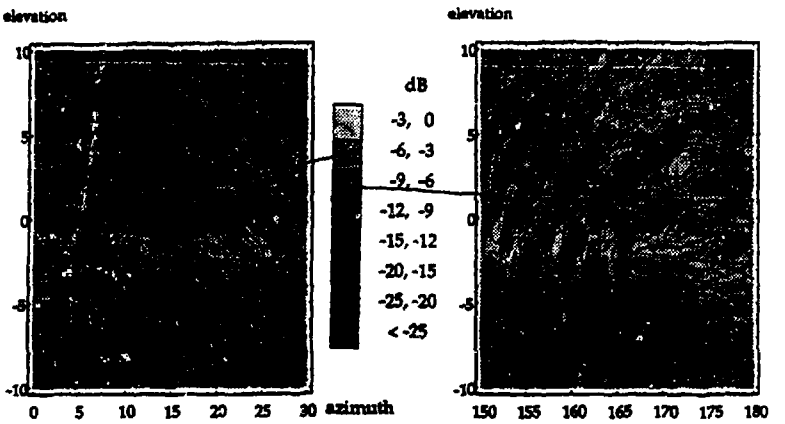

Fig. 8 Combined coverage pattern for the three antennas at positions A1, A5, and A9 (fig. 1) analysed with NEW-AIR at UHF-band
Azimuth 0°, elevation 0° corresponds to the forward direction.

4.3 Computed antenna coupling

The coupling between antennas at position A4, A6, A7, and A8 (fig. 1) has been calculated with ESP over the frequency band 100-250 MHz as shown in fig. 9. The coupling has also been calculated for the same antenna pairs

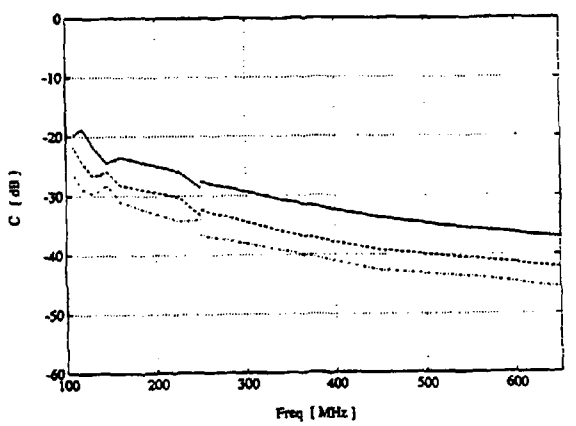

Fig. 9 Computed maximum coupling between three antenna pairs with ESP in the band 100-250 MHz and with NEW-AIR in the band 250-650 MHz
Ant pos A4 to A6 ——, ant pos A4 to A7 - - - , ant pos A4 to A8 -.-.-

and frequencies 250-650 MHz with NEW-AIR (fig. 9). The agreement between the results for the ESP and the NEW-AIR computations at the transition frequency 250 MHz is very good.

5 Conclusions

Airborne radar and communication antennas have been analysed using the ESP, NEC-BSC, and NEW-AIR computer codes. Antenna radiation patterns and antenna to antenna coupling have been calculated.

These computer programs have been shown to be useful tools in all phases of development of communication and radar systems. The performance of antenna systems including the influence of their complex environment can be calculated. The computer codes have proven to be useful when many systems are integrated on one platform and the goal is to achieve a balanced design with the best over all performance.

H-60 Helicopter Antenna Placement Evaluation: Experimental and NEC-BSC Results

J. M. Harris and M. L. Wheeler

Georgia Tech Research Institute
Georgia Institute of Technology
Sensors and Electromagnetics Applications Laboratory
Atlanta, Georgia 30332

ABSTRACT

This paper presents the details of an antenna placement evaluation that was performed for the HH/MH-60G PAVE HAWK helicopter. The antenna system is part of the AN/ARS-6 Lightweight Airborne Recovery System (LARS) and consists of two blade antennas mounted on the underside of the helicopter fuselage. The antenna outputs are supplied to a combiner network that produces the sum (Σ) and difference (Δ) patterns used by the LARS for direction finding. The antenna Σ pattern is determined for two available locations on the underside of the fuselage using two methods: scale model antenna measurements, and computer modeling. The physical model of the predominant features of the helicopter underside and nose was constructed at 1/4 scale. The computer model was constructed using the Numerical Electromagnetics Code - Basic Scattering Code (NEC-BSC) with source distributions derived from the Numerical Electromagnetics Code - Method of Moments (NEC-MOM). To overcome NEC-BSC limitations, several analytical models were constructed and the results were combined to form composite antenna patterns to compare to the measurements on the physical model. The composite and measured patterns compared very well with the antennas located further than one wavelength from any scattering structure. However, the patterns were significantly different with the antennas located within one wavelength of a scattering structure.

INTRODUCTION

The placement of antennas for a new system on an aircraft can be a difficult task. The antennas must be placed in an area where they will provide maximum performance for the system while minimizing performance degradation to and from existing systems. Often, existing structures or antennas limit the number of suitable locations for mounting the new antennas. These limitations can degrade the performance of the new antennas and their associated system. Therefore, the placement of new antennas on an aircraft requires trade-offs to optimize system performance.

The HH/MH-60G PAVE HAWK helicopter is equipped with various communication, navigation, and defense systems that utilize antennas mounted on the fuselage. In addition, the exterior of the aircraft contains lights, sensors, access doors, and other structures that limit the available locations for a new antenna system. The installation of the AN/ARS-6 Lightweight Airborne Recovery System (LARS) on the PAVE HAWK requires that two blade antennas be mounted on the underside of the fuselage. The LARS is a UHF Radio system, operating in the 225-300 MHz frequency band, used to locate and direct the aircrew to downed aviators equipped with hand-held LARS transponders. The outputs of the two aircraft-mounted antennas are provided to a combiner network that produces the sum and difference patterns used by the LARS to perform direction finding. For optimum performance the two antennas are mounted 15 inches apart on a line orthogonal to the longitudinal axis of the aircraft. The two antennas must be mounted as far forward as possible to minimize fuselage shading in the forward direction.

Figure 1 shows the underside of the PAVE HAWK. The space for locating the LARS antennas on the underside of the aircraft is limited. For this reason and because of the requirement to minimize electromagnetic interference (EMI) to other existing aircraft systems, the possible locations for mounting the LARS antennas were reduced to the two shown in Figure 1. The forward location is labeled FWD and the rear location is labeled AFT.

Two methods were utilized to evaluate the performance of the LARS antennas at the FWD and AFT locations. First, a 1/4 scale model of the forward underside of the PAVE HAWK helicopter was constructed. This model was simplified to include only the scaled radius of curvature of the aircraft fuselage and a scaled version of the AN/AAQ-16 Forward Looking Infrared (FLIR) turret. Other aircraft features, such as lights and flush-mount antennas, were not included because they were not expected (based engineering judgement and experience) to have a significant effect on the antenna performance. This simplification allowed the model to be constructed and tested quickly while producing accurate antenna performance data. Secondly, a computer model equivalent to the simplified physical model was constructed using the Numerical Electromagnetic Code - Basic Scattering Code (NEC-BSC) [1]. Several variations of the computer model were evaluated to identify the one that provided the best prediction of antenna performance relative to the scaled model measurements.

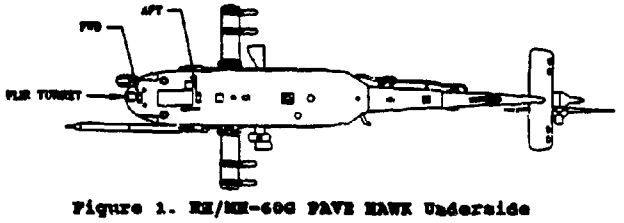

Figure 1. HH/MH-60G PAVE HAWK Underside

For both the physical and computer model evaluations, only the antenna elevation pattern along the helicopter roll axis was considered. This approach was chosen because, first, the LARS is designed as a homing system to direct the aircrew to the survivor. Therefore, the primary direction of arrival of the signal from the survivor radio is toward the nose of the aircraft. Secondly, the aircraft will fly at various altitudes depending on the threat environment and other factors. Along with the aircraft's nose down attitude in forward flight and typical range limitations, these altitudes correspond to elevation angles from a few degrees below horizon to a few degrees above horizon. Therefore, the performance of the LARS antenna system in the elevation plane is most important.

SCALE MODEL ANTENNA PATTERN MEASUREMENTS

The 1/4 scale model of the forward underside of the PAVE HAWK included the single dimension radius of curvature and AN/AAQ-16 FLIR turret shown in Figure 2. The scale factor was chosen primarily because of the availability of higher frequency blade antennas similar in construction to the LARS blade antennas and the large item size limitations of the anechoic chamber in which the antenna pattern measurements were made. Scaling the aircraft to 1/4 requires that the LARS operating frequency be scaled upward by a factor of four. Therefore, the LARS mid-band frequency of 265 MHz was multiplied by four to obtain the 1060 MHz test frequency.

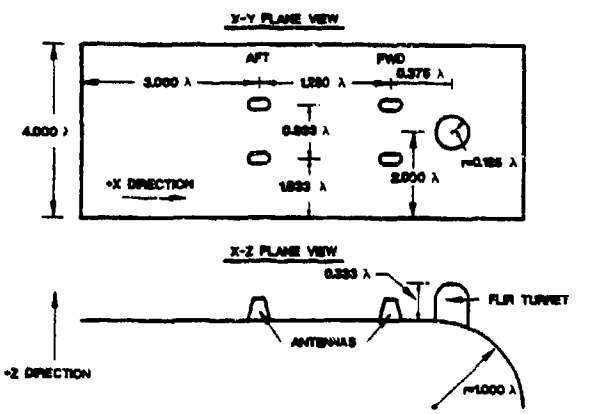

Figure 2. 1/4 Scale Model

The fuselage portion of the model was constructed of a single sheet of aluminum formed on a wood frame. A single curvature was considered sufficient for evaluating the elevation plane performance of the LARS antennas. The FLIR turret model was constructed of a cardboard cylinder and frame covered with adhesive-backed aluminum foil. The FWD and AFT positions for the antennas shown in Figure 2 correspond to the FWD and AFT positions on the aircraft shown in Figure 1. The Σ antenna pattern was formed by combining the two antenna outputs in phase. The Σ elevation pattern (in the X-Z Plane) was measured in an anechoic chamber. Absolute antenna gain measurements, in dBi, were obtained using the substitution method of normalizing the pattern data to that of a standard gain antenna located at the phase center of the antennas at the FWD and AFT positions.

Figure 3 is a plot of the X-Z Plane (elevation) antenna patterns for both antenna locations. (It should be noted that the model is mounted with the fuselage underside facing upward to simplify the measurements.) Theta (θ) is the angle measured from the positive Z (vertical) Axis. Therefore, θ=90° is equivalent to the horizon with values of θ>90° being above horizon on the actual aircraft. The primary observation from reviewing the test data is that the FLIR turret significantly decreases the LARS antenna gain when the antennas are mounted in the FWD location. This is not a surprising result due to the size of the turret and its close proximity to the antennas in the FWD position. Included on Figure 3 are lines showing the peak envelope of the two patterns. These envelopes are used later when comparing the measured data to the predicted data.

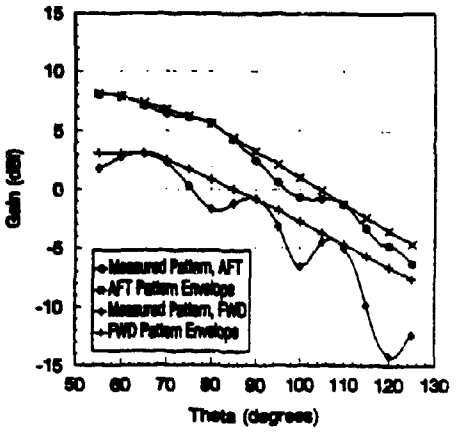

Figure 3. Antenna Patterns Measured on 1/4 Scale Model

ANTENNA PATTERN PREDICTIONS USING NEC-BSC

Computer modeling of structures for numerical electromagnetic analysis is difficult when the structure dimensions are on the order of only a few wavelengths. When structures have dimensions that are large compared to a wavelength, they can be modeled effectively using the plate and cylinder models of a Geometric Theory of Diffraction (GTD) code such as NEC-BSC. When the structures are on the order of a wavelength or smaller, they can be modeled using a Method of Moments (MOM) code such as the Numerical Electromagnetics Code - Method of Moments (NEC-MOM) code [2]. In NEC-MOM, solid surfaces are modeled using wire mesh grids. However, the number of wire mesh segments required by NEC-MOM can be excessive when the structure dimensions are several wavelengths. NEC-MOM models requiring large numbers of segments require significant computing capacity and time. For the analysis reported here, NEC-BSC was chosen because of the ease of constructing the model and the availability of sufficient computing power to analyze the model.

The NEC-BSC user's manual [1] lists several structure size limitations that should be observed to obtain accurate results. The manual states that plate edges should be at least one wavelength long and that the major and minor radii of an elliptical cylinder should be at least one wavelength. In addition, the length of the cylinder should be at least one wavelength. The manual also states that all sources should be spaced at least one wavelength from a plate edge although this spacing can be reduced to one-quarter wavelength for "engineering evaluations." The models presented here met these requirements with the exception of the radius and length of the cylinder used to model the FLIR turret.

The first NEC-BSC model, shown in Figure 4, consists of a flat rectangular plate terminated on the surface of and tangent to a large cylinder. A small cylinder, representing the FLIR turret, is orthogonal to the plate and intersects the large cylinder at the same point as the plate. The small cylinder penetrates the large cylinder to a depth of 0.07 wavelengths to insure that the code considers them connected. This model is an accurate representation of the physical 1/4 scale model. The two pairs of sources shown for the FWD and AFT locations (not modeled concurrently) are defined to have an in-phase excitation with a half dipole radiation pattern. The X-Z Plane (elevation plane) pattern predicted by NEC-BSC for the two antenna locations is shown in Figure 5. It should be noted that the antenna side of the flat plate used to model the fuselage underside faces along the positive Z Axis. Therefore, $\theta=90^{\circ}$ is equivalent to the horizon and values of $\theta>90^{\circ}$ represent the antenna response above the horizon on the actual aircraft.

The following observations are made concerning the X-Z Plane pattern shown in Figure 5 for the AFT antenna location:

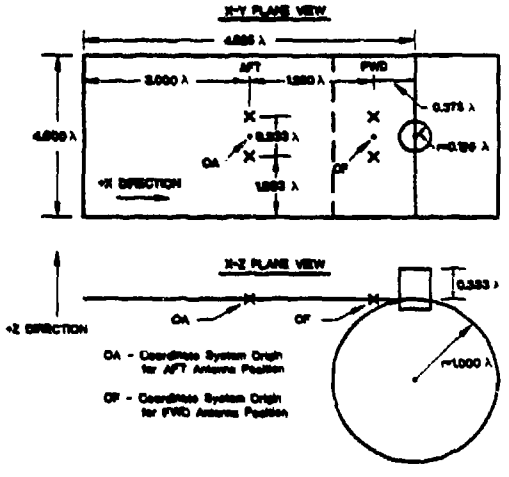

Figure 4. NEC-BSC Two Cylinder and Plate Model

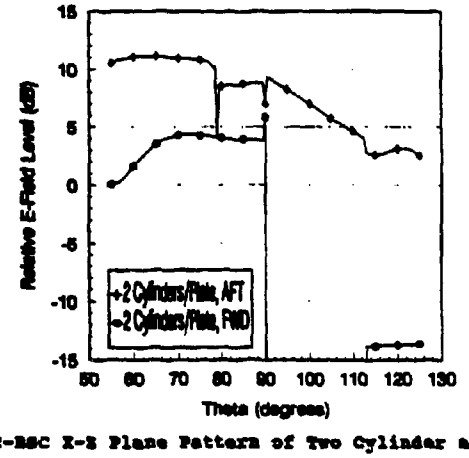

Figure 5. NEC-BSC X-Z Plane Pattern of Two Cylinder and Plate Model

(1) The discontinuity at $\theta=78^\circ$ is due to the inclusion of reflections and diffractions from the turret cylinder at $\theta>78^\circ$. For $\theta<78^\circ$, the pattern is primarily the direct signal from the sources.
(2) The discontinuity at 90° is due to the exclusion of the direct signals and diffractions/reflections from the turret cylinder. The pattern for $90^\circ<\theta<113^\circ$ is dominated by diffraction from the large cylinder.
(3) For $\theta>113^\circ$, the pattern is dominated by diffractions from the flat plate edge opposite the large cylinder.

The following observations are made concerning the X-Z Plane pattern shown in Figure 5 for the FWD antenna location:

(1) The pattern for $55^\circ<\theta<90^\circ$ is a combination of direct rays from the sources and reflections/diffractions from the turret cylinder.
(2) NEC-BSC predicts no pattern response for $90^\circ<\theta<113^\circ$. However, if the sources are moved along the flat plate away from the turret cylinder to a location outside of the radius of the large cylinder, NEC-BSC will calculate the pattern. An explanation for this anomaly cannot be given without further investigation.
(3) For $\theta>113^\circ$, the pattern is dominated by diffractions from the flat plate edge opposite the large cylinder.

In order to confirm the pattern responses for $\theta<90^\circ$ for the FWD and AFT locations, another model consisting of a large rectangular flat plate intersected by a small cylinder representing the FLIR turret was constructed. As seen in Figure 6, the location of the sources and the turret relative to the aft edge of the large plate are identical to those for the model shown in Figure 4. The long front portion of the flat plate effectively prevents front edge diffractions from distorting the pattern for $\theta<90^\circ$. The turret cylinder is imbedded in the flat plate to a sufficient depth to insure that the code considers them connected. Figure 7 shows the X-Z Plane antenna patterns predicted by NEC-BSC for this model. The patterns for $\theta<90^\circ$ are almost identical to those shown in Figure 5 thereby adding confidence to the predictions. The patterns for $\theta>90^\circ$ shown in Figure 7 should be ignored due to the model limitations.

In order to confirm the AFT location antenna pattern response and determine the FWD location antenna pattern response for $\theta>90^\circ$, a third model was constructed. This model, shown in Figure 8, consists of a large cylinder intersected by a small cylinder representing the FLIR turret. The turret cylinder penetrates the large cylinder to a sufficient depth to insure that the code considers them connected. The sources, modeled as point sources with dipole radiation patterns, are located on a plane tangent to the large cylinder at the point where the turret cylinder intersects it. The long flat plate extending from the bottom of the large cylinder is used as a baffle to prevent signals from diffracting around the bottom of the large cylinder and distorting

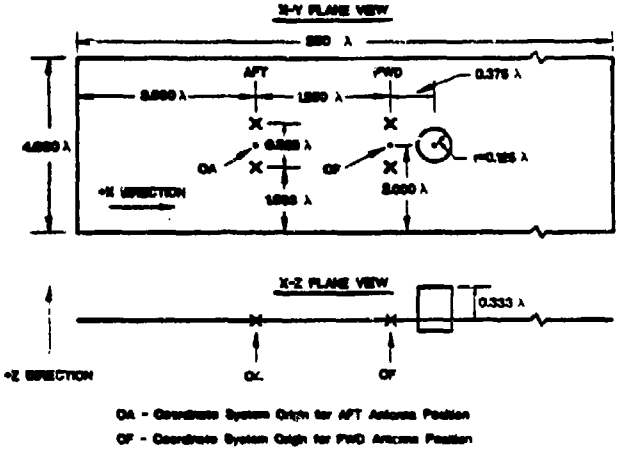

Figure 6. NEC-BSC Large Plate and Cylinder Model

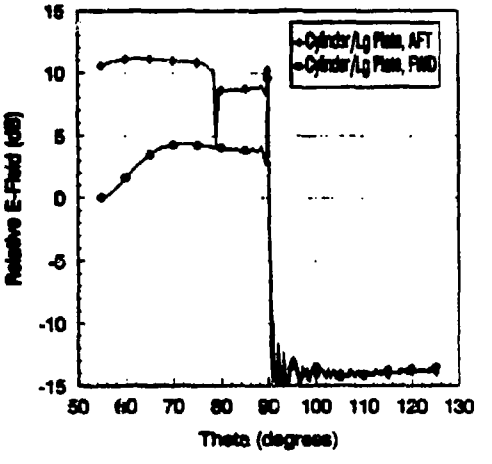

Figure 7. NEC-BSC X-Z Plane Pattern for Large Plate/Cylinder Model

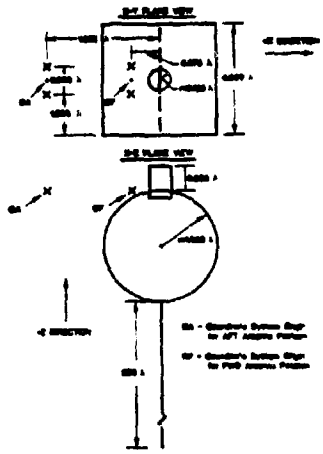

Figure 8. NEC-BSC Two Cylinder and Baffle Plate Model

the pattern response for $\theta>90^{\circ}$. Figure 9 shows the X-Z Plane antenna patterns predicted by NEC-BSC for this model. Note that NEC-BSC does calculate a response for the FWD location for $\theta>90^{\circ}$. The response for $\theta>90^{\circ}$ is considered a reasonable representation of the response for both the FWD and AFT antenna locations. The patterns for $\theta<90^{\circ}$ shown in Figure 9 can be ignored due to the model limitations.

The antenna patterns produced by NEC-BSC using single point sources are the relative E-Field levels (in dB) and not the absolute gain levels (in dBi) required for a direct comparison to the measured antenna pattern data. The method used to determine the absolute gains requires that the single point sources be replaced with a line of point sources to model the spatial distribution of the actual antennas and that the relative E-Field be normalized to the total radiated power [1]. The current distributions of the distributed point sources and the total radiated power are determined using NEC-MOM. The NEC-MOM model for this analysis consists of two monopoles mounted on an infinite ground-plane. The spacing between the monopoles is the same as the spacing between the blade antennas on the 1/4 scale model. Each monopole was modeled with five segments and driven with a 0.707 volt source (equal power split between the two monopoles). The current distributions for each of the five segments are given in Table 1. Each point source shown in Figure 4 is replaced by five point sources oriented on a line perpendicular to the positive Z side of the flat plate. The five point sources are spaced apart by 0.05λ and assigned

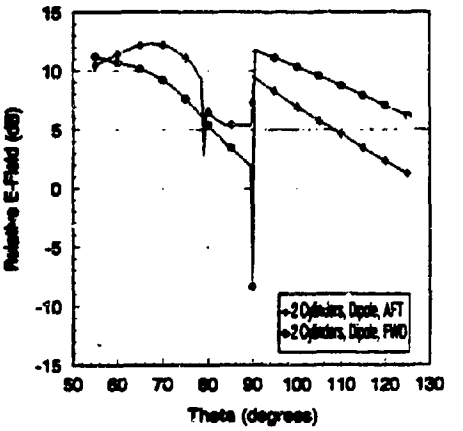

Figure 9. NEC-BSC X-Z Plane Pattern for Two Cylinder/Baffle Model

Table 1. NEC-MOM Source Distributions

Height Above Flat Plate	Current Distribution	
	Magnitude	Phase
0.025λ	0.013623	-3.636
0.075λ	0.012466	-6.227
0.125λ	0.010184	-8.422
0.175λ	0.008915	-10.142
0.225λ	0.002718	-11.589

the current weightings given in Table 1. The relative E-Field calculated using NEC-BSC with these distributed sources applied to the model shown in Figure 4 is then normalized by the total radiated power that was computed with NEC-MOM. Using this method, a maximum absolute gain of 6.9 dBi was calculated at θ=58° for the AFT antenna location and -0.8 dBi at θ=63° for the FWD antenna location.

Based on the predicted X-Z Plane patterns shown in Figures 5, 7, and 9 along with the absolute gain values determined previously, a composite X-Z Plane pattern can be constructed for comparison to the measured data. The composite patterns are constructed as follows:

(1) For $55^\circ<\theta<90^\circ$, the pattern data for the AFT and FWD antenna locations shown in Figure 5 (or equivalently Figure 9) is used with limited smoothing to remove discontinuities.
(2) For $90^\circ<\theta<125^\circ$, the pattern data for the AFT and FWD antenna locations shown in Figure 9 is used.
(3) The peak of each pattern is normalized to the absolute gain values determined using the distributed sources.

The resulting composite patterns are shown in Figure 10 along with the measured patterns and in Figure 11 along with the envelopes of the measured patterns.

CONCLUSIONS

The LARS antenna X-Z Plane (elevation) composite patterns predicted using NEC-BSC are in relatively good agreement with the patterns measured on the 1/4 scale model (see Figure 10). The absolute gains predicted by the NEC-BSC model for the FWD and AFT antenna locations at $\theta=90^\circ$ (the median of the angles of interest) are within 2 dB of the measured values. In addition, the NEC-BSC generated X-Z Plane responses for $\theta>90^\circ$ that are within 2 dB of the peak envelope of

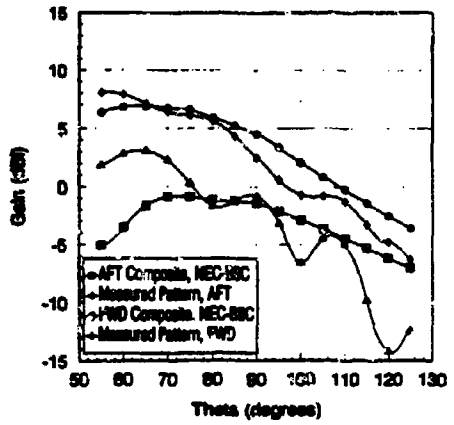

Figure 10. Composite NEC-BSC X-Z Plane Patterns and Measured Patterns

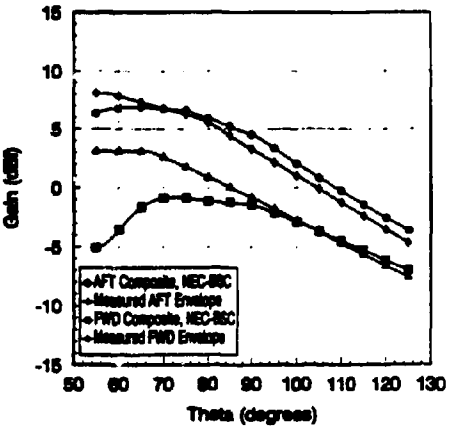

Figure 11. Composite NEC-BSC X-Z Plane Patterns and Envelopes of Measured Patterns

the test data for both antenna locations. Also, the NEC-BSC model matched within 2 dB the AFT location X-Z Plane test data for $\theta<90^{\circ}$. However, the computer model did not accurately model the X-Z Plane response or the nulls shown in the test data for the FWD antenna location. Differences up to 8 dB between the predicted and measured patterns were generated for the FWD antenna location. These errors can probably be attributed to the close spacing of the antennas to the FLIR turret and the fact that the model did not strictly conform to the dimensional restrictions required for NEC-BSC. Also, the FLIR turret was modeled with a flat top cylinder in NEC-BSC and not a hemispheric dome as in the scale model. This could significantly affect the FWD location patterns for $\theta<90^{\circ}$.

As stated earlier, NEC-BSC is most useful for analyzing structures that are large compared to a wavelength. NEC-MOM is most useful for analyzing models that are on the order of a wavelength. However, NEC-BSC models can be constructed and analyzed quickly compared to NEC-MOM models. Also, more computer processing power is required to analyze NEC-MOM models which require a large number of segments. In the case presented here, NEC-BSC produced reasonable results for a structure that is only a few wavelengths in extent with some structure dimensions and some source-to-structure spacings less than one wavelength. However, a single NEC-BSC model was not sufficient to produce the desired results and some processing was required to generate the

composite patterns. The availability of test data prior to the NEC-BSC analysis assisted in determining the model manipulations required to produce reasonable results. Unfortunately, test data is not usually available prior to a NEC-BSC analysis. Therefore, NEC-BSC should be used with caution when analyzing relatively small structures. A method-of-moments code, such as NEC-MOM, should be used for cases such as the one presented here if sufficient time to construct the model and computing power is available.

Based on the computer model and test data presented here, a recommendation was made to locate the LARS antennas at the AFT location on the PAVE HAWK. Measurements of the on-aircraft LARS antenna performance for the selected location were not possible due the difficulty and expense of executing a full scale aircraft antenna test. However, flight testing of the HH/MH-60G PAVE HAWK confirmed that the LARS met its range versus altitude requirements indicating adequate antenna performance.

ACKNOWLEDGMENTS

The work presented here was performed under U. S. Air Force Contract No. F09603-91-G-0096-0010 out of the Warner Robins Air Logistics Center at Robins AFB, Georgia.

REFERENCES

[1] "Near Zone - Basic Scattering Code User's Manual with Space Station Applications, Version 3," M. J. Marhefka and J. W. Silvestro, Ohio State University Electroscience Laboratory, March 1989.

[2] "Numerical Electromagnetics Code (NEC) - Method of Moments, Version NEC-2," G. J. Burke and A. J. Poggio, Lawrence Livermore National Laboratory, January 1981.

An Antenna Simulation Superstructure to the OSU *ESP4* Program

Kurt L. VanVoorhies
West Virginia University

Introduction

The numerical electromagnetic simulation tool described herein was one of several tools developed as a means to comprehensively investigate the nature of a particular wire wound biffilar conical and toroidal helical antenna [1]. The overall investigation incorporated both simulation and experimental techniques, both of which complimented one another. The principle utility of the simulation was in predicting both the electric current distributions on the constituent wire elements, and the radiation patterns when the antenna was operated at the resonance and band edge frequencies.

This simulation tool, hereinafter referred as *ESP4K*, was developed with sufficient generality to facilitate the study of a wide variety of related antenna geometries. The *ESP4K* tool is a superstructure to the Electromagnetic Surface Patch Version IV program, hereinafter referred as *ESP4*, developed by Ohio State University (OSU) [2]. *ESP4K* comprises a collection of programs - written in both C and FORTRAN for operation in a Unix® environment - and related data structures; and a system for data management. The *ESP4* program was selected as the kernel for *ESP4K* because of 1) its ability to simulate geometries with both wires and open plates, 2) its ready availability in source code form from OSU, and 3) its current support by OSU. The *ESP4K* tool extends the *ESP4* program with 1) an improved user interface for both pre-processing and post-processing data, 2) additional functionality, including calculation of resonance and bandwidth, and 3) the creation of five generalized parameterized geometries. While the *ESP4K* tool was specifically tailored to the *ESP4* program, many of its constituent procedures are of general utility, and would be applicable to any simulation program.

The purpose of this paper is to describe the philosophy and methodology of *ESP4K* and to discuss its specific interrelation to the *ESP4* program; considering the overall inputs and outputs, the added functionality and geometries, the modifications to the *ESP4* kernel, and some limitations of the *ESP4* kernel that were discovered by this investigation. The reader is referred to [1] for the details of the *ESP4K* constituent procedures. An *ESP4K* user's manual has not yet been written.

Overview of OSU's *ESP4* Program

ESP4 is a FORTRAN program comprising a large MAIN procedure (over 1500 lines of code), 58 subroutines, and 7 functions. *ESP4* solves the Electric Field Integral Equation (EFIE) using the Moment Method, and is applicable to both radiation and scattering problems for geometries containing wires and/or plates, the latter having either open or closed surfaces. The program is controlled with a sequential list input file containing strictly numeric data. The input and output files interface with pre-defined logical units to which the user must assign corresponding physical data files. Several of the *ESP4* output files are formatted for input to a GKS graphics post processor for plotting: 1) the problem geometry and vectorized current mode distribution on plates, 2) an elevation cross-section radiation/scattering pattern, and 3) an azimuth cross-section radiation/scattering pattern. The problem geometry is specified either as a formatted list of node coordinates and interconnections, or via a user-defined FORTRAN subroutine.

The *ESP4* MAIN procedure comprises three levels as defined by two nested control loops which successively define the problem. The actual Moment Method simulation is performed at the lowest level. These three levels are designated in order as follows: 1) MAIN procedure, 2) NRUNS: plate geometry loop, and 3) NWGS: wire geometry/feed loop. Parameters common to all simulations, such as the locations of the field point and the pattern cross-section planes; and the simulation frequency(s), are defined at the MAIN level. The plate geometry is then specified at the NRUNS level, and finally the wire geometry, wire/plate attachments, load impedances, and feed voltages are specified at the NWGS level. In a given run of the *ESP4* program, each plate geometry specified in the NRUNS loop is simulated using all wire geometries specified in the NWGS loop. The *ESP4* simulation is performed at discrete user-defined frequencies, and the system impedance matrix may be either calculated at each frequency; or for a sweep of frequencies, calculated a coarse frequency intervals and interpolated at fine frequency intervals.

ESP4K Philosophy and Methodology

The development of the *ESP4K* tool was motivated by the desire to reliably perform a large number of simulations on a variety of parametrically defined geometries, and to present the results in a readily utilized form. The related procedures were designed to improve the overall efficiency and reliability of 1) defining the problem, 2) running the simulation, and 3) accessing the results within a consistent framework; enabling the user to focus on the engineering and physics of the problem to be solved. The *ESP4K* procedures achieve this objective by using hierarchical, self-documenting, tab-delimited, structured tables as the means for both input and output, both by the user - via off-the- shelf spreadsheet based programs - and by the *ESP4K* constituent procedures -via a collection of custom written utility subroutines.

Program Input

Several ways to increase the efficiency and reliability of a simulation program are 1) by reducing the amount of input that must be entered by the user and 2) by labeling the inputs that can or must be entered by the user, and providing default values for optional inputs. This is achieved in the *ESP4K* tool with a series of hierarchical, self-documenting, tab-delimited, structured input tables which are readily created with a spread-sheet program such as Microsoft® Excel; each row of a given table representing a different data record, and each column of the table representing a different data field. A subset of the fields - normally one and by default the first - called keys, are used to designate the records. All of the fields are named, and these names are contained in the first record of the table. The *ESP4K* procedures locate a particular item in the table by the field name and key value, so the fields and records can be in any order without affecting the operation of the program. Additional fields and records can also be added to any table without affecting access to the prior table contents.

The amount of required user input for a given simulation may be reduced by structuring the input tables to group similar quantities - in the sense of all quantities being generally required at the same point in the program - together as records of separate tables. In general, these tables can be linked together either relationally or hierarchically, depending upon the nature of the data. A relational linkage is established when multiple tables share the same key value. A hierarchical relation is established when the field contents - of a field named after the corresponding child table - of the parent table contain key values of the child table. This hierarchical scheme enables a single record of a child table to be used for many different simulations without having to re-enter the information of the child table for each simulation; i.e. this enables either a many to one, or many to few relationship to be established between the parent table and its children. This also enables the information in the child table to be accessed via recognizable labels. For example, many simulations may specify the use of copper conductors. The simulation program requires a numerical value for the conductivity of the material. Rather than having to specify this value in its proper units for every simulation, as is required by *ESP4* program, the *ESP4K* procedures use a child table of material characteristics whose key values are the material names, and whose field value is the conductivity in the appropriate units. With *ESP4K*, the user need only specify the name of the material, i.e. "copper", in the field of the corresponding parent table. The value of conductivity is then found automatically from the child table by the *ESP4K* preprocessing procedure. These parent-child relationships will be evident in the specific input tables that are described later.

In addition 1) to providing a self-documenting, transparently expandable input mechanism, 2) to providing a means for reducing the user input requirements, and 3) to enabling easily remembered character string key values to be substituted for difficult to remember numerical values, these hierarchically structured input tables provide a natural and automatic way of documenting entire sets of simulations for archival purposes.

File & Data Management

Simulations or experiments begin with the specification of the conditions under which these are conducted - the design of experiment. The result of the simulation or experiment is a corresponding set of output data or measurements. Since the output data is only meaningful in the context of the conditions under which it was generated, an automatic mechanism for establishing this linkage can improve the reliability of the simulation and improve the user's efficiency in analyzing the results. All datasets generated by the *ESP4K* procedures are automatically named in a manner that maintains full traceability back to the corresponding input tables. Each execution of the *ESP4K* procedures is designated by a unique three digit simulation number. Then, within a given simulation, the iteration level of each of the MAIN procedure's primary nested control loops - already discussed for the *ESP4* program, i.e. the NRUNS loop, and the NWGS loop - is designated by a corresponding letter, beginning with "A" and sequentially incremented with each pass through the loop. The *ESP4K* tool uses an additional frequency specification loop, termed NFQS, nested below the NWGS loop, and this loop is also designated by a corresponding letter. All datasets for a given simulation are uniquely named using these designators. The various datasets are distinguished from one another by a two or three letter symbolic code, i.e. EL for elevation cross-section, or JM for current mode distribution and associated wire geometry. The simulation number and these designators are also specified as fields in the program input tables, establishing the direct correspondence between

input conditions and output results. The automatic naming of all output datasets eliminates any confusion as to the conditions under which a given set of data was generated, which is important to maintaining control and integrity of the data when performing a large number of simulations under a wide variety of conditions.

Program Output

Most output files generated by the *ESP4K* procedures are also formatted as self-documenting, tab-delimited tables, which can be parsed to a spreadsheet based program for either display, printing, or subsequent processing or analysis. The *ESP4K* tool contains a post-processing procedure with reads the collection of such output files from a specified simulation and prepares a secondary set of data tables - containing only essential data - and a corresponding grapoics command file for automatic plotting by the TriMetrix, Inc. Axum® PC based plotting and analysis program. Axum® offers a wide variety of plot types, axis types, and analysis capabilities including 2-D, 3-D, Smith chart, and polar plots. The *ESP4K* plots are coded by color, symbol shape and line type and include labeled numerical data, all designed to maximize the assimilation of information by the user.

User Interface Mechanism

Since the *ESP4K* procedures rely upon tab-delimited tables for both input and output, the principle user-interface can be off-the-shelf spreadsheet programs, which are capable of reading and writing such files. These programs provide a considerable advantage of 1) being already readily available and familiar to most users, 2) providing powerful display, formatting, and printing capabilities, 3) providing additional processing capabilities such as sorting, secondary calculations, and plotting, and 4) being separately documented, maintained, and enhanced. The *ESP4K* tool utilized the Microsoft® Excel program as the primary user interface for creating input data, and the TriMetrix, Inc. Axum® program as the primary user interface for plotting output data. The input tables can be readily created by copying and then modifying records from previous simulations. Multiple tables can be simultaneously displayed in a Windows® or Macintosh® environment enabling the user to simultaneously view all input conditions.

Adaptability

The self-documenting feature of the input and output tables enable older tables to remain transparent to the evolution of the programs. Modifications or additions to the *ESP4K* programs requiring additional input variables can be readily accommodated - without disrupting existing data or the associated programs which access that data - by simply adding columns to existing tables.

Accommodation of Objective Functions

In forming the *ESP4K* tool, the *ESP4* MAIN procedure was reformulated into 30 separate, structured procedures. The global variables used by these procedures were allocated amongst 32 separate COMMON blocks. These steps were taken 1) to improve clarity, 2) to eliminate redundancies, 2) to add specific functionality to the code including the automatic calculation of resonant frequency and bandwidth, and 4) to prepare for automatic optimization of antenna design. The last two items require the definition of an objective function, which for third item was either the reactive impedance, or the difference between the operating and target VSWR levels. This was added by modifying the *ESP4* program to make the specification of frequency, independent of the calculation and the solution of the impedance matrix so that an independent root solver could find the resonant and band edge frequencies. Other objective functions can be readily added to the *ESP4K* procedures, for example to perform a geometrically constrained optimization of antenna design parameters to maximize the radiation gain or bandwidth.

Consistency

The *ESP4K* procedures correct an inconsistency in the specification of values for the several mathematical and physical constants used amongst the various *ESP4* subroutines. Table 1 shows the various values for these constants as defined in both *ESP4* and *ESP4K*. The *ESP4K* procedures define only three constants numerically: pi, the speed of light, and Euler's constant; other constants are then defined in terms of these three variables. The numerical definitions are made in the MAIN procedure and shared with all other procedures via a COMMON data block.

Parameterized Geometry

The specific wire geometries simulated by the *ESP4K* tool are described later. Each is defined in a generalized form in terms of its relevant geometric parameters, which can be specified either in absolute measurement units, or normalized with respect to a specified design frequency. The values for the parameters are specified in the respective input tables, enabling the user perform parametric design studies directly. With the addition of an optimizer and the definition of an objective function, the values of these parameters could also be optimized automatically.

Table 1 Comparison of Physical and Mathematical Constants

Description	Name	*ESP4* Values	*ESP4KVV* Value
Speed of Light	CLIGHT	300.0 E6 299.8 E6	299.7925 E6
Free Space Impedance	ETA	376.7 376.730366239 120.0*PI	U0*CLIGHT
Euler's Constant	EULER	0.577216 0.57721566	0.5772156
Permittivity of Free Space	E0	8.85E-12 8.854E-12	1/(U0*CLIGHT^2)
Permeability of Free Space	U0	1.26 E-06	400.*PI*1. E-9
PI/2	PI2	1.57079632	PI/2
Pi	PI	3.14159 3.1415926 3.14159265 3.14159265359 4.0*ATAN(1.0)	3.14159265
2*PI	TP	2.*PI 6.28318 6.283185 6.2831853 6.28318530718	2.*PI
4*PI	FP	4.*PI 12.56637	4.*PI
Radian/Degree	DGRD	57.29578 1/0.0174533 180/PI	180/PI

Overview of E3P4K

Design of Experiment : Preparation of Input Tables

The simulation experiment is "designed" by interactively constructing input tables using a spreadsheet program. This was performed on a Macintosh® IIci computer with a large format display which enabled most tables to be simultaneously displayed on the screen. The Macintosh® operating system was well suited for this and other window-intensive operations.

Data Processing

Pre-processing: The input tables are then sent via Ethernet to a Silicon Graphics Inc. Indigo® workstation operating under the IRIX®/Unix® operating system. The Unix® operating system facilitated both the processing of data and the development of all the *ESP4K* procedures. The C- language preprocessing procedure called *esp4prepx* used a custom utility program called *genab* to extract the necessary data, corresponding to the specific simulation number, from the input tables; constructing a sequential list-formatted file that could be read by the FORTRAN simulation program, called *ESP4KVV*.

Simulation: The *ESP4KVV* program was developed from the OSU *ESP4* program and includes: 1) a completely reformulated MAIN procedure and related subroutines, as already discussed, 2) the *ESP4* subroutines and functions, some with minor modification to substitute COMMON data blocks for parameter argument lists, and to add hooks for extracting data, such as the current modes, 3) FORTRAN and C subroutines for calculating four generalized wire geometries, 4) C procedures for automatically finding resonance and band limit frequencies, and for interpolating between these points with sufficient resolution to construct reasonably smooth Smith charts of input impedance, and 5) C procedures for managing data and constructing the various output data files. In addition to those nested control loops described for the *ESP4* program, the *ESP4KVV* contains a frequency selection control loop, designated as the NFQS loop that is nested within the NWGS loop.

Post-processing: The output files from the *ESP4KVV* simulation, and the corresponding input tables, are automatically read by the C-language *preplot* program, which constructs batch processing command files for control of the PC-based, TriMetrix, Inc. Axum® plotting program. Axum® can process spreadsheet-formatted data files in a batch mode that is controlled by the above described command file, known to Axum® as a history file. All of the plots are stored in template form in a master file, and these templates are then modified to incorporate data from the specific tests to be plotted. The *preplot* program can process multiple simulations, and a DOS batch file is automatically constructed with the proper calls necessary to prepare the constituent plots for each of the selected simulations.

Preparation of Plots

The history files, data files, and the DOS batch file are transferred via Ethernet to a PC/386 running the DOS operating system. The plots are generated in a background mode with the simple execution of the DOS batch command file. The full complement of plots for each simulation comprises five pages, each page having four plots.

Input Tables

Table 2 outlines the structure of the *ESP4K* hierarchical input tables. Five root level, relational tables are defined, the name of each beginning with the string "SIM_" and each having a key field called "SIM_#" which contains the three digit simulation number. This three digit simulation number is passed into the *esp4prepx* program as an argument upon invocation, and is in turn used to find the corresponding records in each of these root level tables. The SIM_main table is read first, and has one and only one entry for each simulation. The fields NRUNS, NWGS, and NFQS specify the number of iterations in the respective nested control loops in the MAIN program, and also indicate the number of corresponding records in the SIM_runs, SIM_wires, and SIM_freq tables respectively, whereby a new record is read from the SIM_runs table with each iteration of the NRUNS loop, a new record is read from the SIM_wires table with each iteration of the NWGS loop, and a new record is read from the SIM_freq table with each iteration of the NFQS loop. The parameters NRUN, NWG, and NFQ in these tables are the identifiers used for file management, as discussed above. Normally for each simulation these are listed sequentially, A-Z. The SIM_z table is used for saving and/or retrieving a system impedance matrix. All of the *ESP4* input variables have been carried over to the *ESP4KVV* procedure without any change in name or meaning, so many of the fields in the *ESP4K* input tables will be recognizable to *ESP4* users.

Table 2 *ESP4KVV* Input Table Structure

SIM_main (SIM_# Date NGO NPRINT NRUNS NWGS NFQS IWR IWRZT INWR IRGM IFIL INTGR8 Field
THRFS PHRFS THINFS PHINFS RADPAT PHFE THFA SCPAT ISE PHSE ISA THSA THIN PHIN
Comment)
INTGR8 (id INT INTP INTD)
Field (Field RF_tar NRF RF_min RF_max RF_scale RF_norm)
RADPAT (id IPFE FNDFE IPFA IEF@A IAF@E)
SCPAT (id IPSE FNDSE IPSA FNDSA IES@A IAS@E)

SIM_runs (SIM_# NRUN Material Wire_rad Plate_Design)
Material (id CMM Resistivity(cm) Notes)
Wire_rad (id A B&S_dia_in IANORM)
Plate_Design (id Freq PLATETYPE PLATEID)

SIM_wires (SIM_# NWG Wire_Design)
Wire_Design (id Freq WIRETYPE WIREID Shape Naide2 NContra Nfilar Feed IFDTYP0 ICNNCT
Description)
DIPOLE (WIREID id HL2 INORM NM2 DHN NFLD OFFSET)
HELIX (WIREID id HL2 HD HP IHL INORM NM2 IPSNS1 IPSNS2 ROFF IROFF Alfa0 NTurns NSeg
NFLD OFFSET)
DILOOP (WIREID id HL2 HD INORM NM2 IPSNS1 IPSNS2 ROFF Alfa0 NTurns NSeg NFLD OFFSET
DZ_connect DZ_loop DA_tline DA_roll)
RNGBAR (WIREID id HL2 HD INORM NM2 Alfa0 NTurns NSeg NFLD OFFSET)
Feed (Feed node ZL_real ZL_imag V_mag V_phase_dg IF

SIM_freq (SIM_# NFQ FMC1 FMC2 FREQSWP Resonance IFQR IFQS IFQV VSWR IFQPAT)
FREQSWP (id NCalcZ NTrpltZ INDZ' DFZ: DFF IPFQ)
Resonance (id ZIRZ ZIZRRZ IZTPL8 DSMIN DSMAX DVSWR NFF_min)

SIM_z (SIM_# NRUN NWG NFQ IRDZM Z_infile IWRZM)

SIM_main : General Simulation Parameters

The SIM_main table has four child tables: INTGR8, Field, RADPAT, and SCPAT, which are correspondingly named as fields in the parent table. The INTGR8 table contains values for the Simpson's rule integration parameters. The Field table contains parameters defining the distance(s) of the field point(s) to the center of the antenna, wherein the *ESP4KVV* program can calculate the fields at a multiplicity of such distances in contrast with the *ESP4* program for which only one radial distance could be specified. The RADPAT and SCPAT tables specify the parameters for the radiation and scattering patterns. These tables contain new parameters enabling the field patterns to be calculated at a surface-defining mesh of points, extending the *ESP4* program's limitation of single elevation and azimuth cross-sections. A single record in each of the above tables are used for most simulations, demonstrating the economy of this hierarchical input table methodology - frequently used information need only be entered once, and the root level tables contain the essence of the simulation.

SIM_rems : Material Properties, Wire Size, & Plate Design

The SIM_rems table contains information about material properties and plate design, and references the following tables: Material, Wire_rad, and Plate_Design. Material names are used as key values in the Material table, and Wire gauge numbers are used as key values in the Wire_rad table. The Plate_Design table is structured with two key fields. The PLATETYPE field refers to the name of a table containing plate design parameters, while the PLATEID field refers to the key value of the corresponding record in this table. Users may easily add their own parameterized plate design subroutines to the *ESP4KVV* program, then specify and construct the corresponding input tables, and finally modify the preprocessing procedure to read and process these tables.

SIM_wires : Wire Geometry

The SIM_wires table specifies the wire geometry. The Wire_Design field designates a record in the corresponding Wire_Design table which represents a specific physical embodiment. The Wire_Design table in turn references the parameters for a specific wire geometry via two key fields, WIRETYPE and WIREID. The WIRETYPE field specifies the name of a table, while the WIREID field specifies the specific record within that table. The key values for all of these tables are typically chosen to be meaningful names or character strings. Four different WIRETYPE tables are presently defined: DIPOLE, HELIX, DILOOP, and RINGBAR. Each of these tables define a center-fed element which is oriented along a line. The DIPOLE table specifies the usual linear dipole element. The HELIX table specifies a helical element or a contrawound helical element. The DILOOP table specifies a specialized representation of a helix, or contrawound helix, comprising a series of open loop elements, normal to and concentric with the antenna axis, which are interconnected by a series of collinear elements which are parallel to the axis of the antenna. The RINGBAR table specifies a ring-bar representation of a contrawound linear helix, after the work of Birdsall and Everhart [3]. These WIRETYPE tables specify the geometric parameters in terms of either absolute or wavelength normalized units. The physical size of a normalized antenna is set by the design frequency from the Freq field of the Wire_Design table. The generalized linear elements defined in the WIRETYPE tables can be transformed into either a circle, semicircle, or polygon by specifying such in the Shape field of the Wire_Design table. The integer parameter NSide2 specifies half the number of sides in the polygon. For circular or polygonal shapes, the ICNNCT field specifies whether the wire element is closed or open. The NContra parameter specifies whether the HELIX or DILOOP antennas are bifilar contrawound, or monofilar, while the Feed field specifies the key value in the Feed table which defines the voltage and impedance at the feed point(s). Each of the generalized linear elements can be segmented, and feed points can be located at the segment boundaries.

As an illustration of the generality of these geometries and the simplicity of their specification, one record in the DIPOLE table, together with various combinations of parameters in the Wire_Design table, can be used to specify either a conventional linear dipole, a semicircular dipole, a polygonal approximation to a circular loop, or an even-sided polygonal loop. The loop configurations may be either open or closed, and may be fed at either a single point, as with a conventional dipole or loop, or at multiple points, e.g. such as at four equi-spaced points in a Smith "Cloverleaf" antenna. This same generality also applies to helix, diloop, and ring-bar embodiments.

SIM_freq : Simulation Frequency and/or Frequency Sweep

The SIM_freq table specifies the frequency or frequency range at or over which the simulation is performed. When simulating over a range of frequencies, the frequencies may either be specified at fixed frequency intervals - as in the original *ESP4* program - or the simulation may be used to automatically find resonant and band edge frequencies, using a specified VSWR as the criteria for defining the operating bandwidth. The former approach is specified by the table named FRQSWP which has the standard *ESP4* variables. Radiation patterns can be calculated at these fixed frequency points. The latter approach is specified by the table named Resonance. Radiation patterns can be calculated at resonance and band edge frequencies. The program finds the resonant and band edge frequencies using the ZBRENT algorithm from [4], and then - so as to produce data for smooth Smith Charts - successively splits the resulting frequency intervals until the generalized distance between adjacent frequency points in the complex Smith plane is less than a table-specified amount.

Output Data Files

The output files produced by the *ESP4K* procedures are listed in **Table 3**. Reference [1] lists the detailed structure of these files. The data files are written in three different formats. The *ESP4* format designates the *ESP4* program's standard files which are described in [2]. The *ESP4KVV* format designates files which result from pre-processing the input tables and which are used as direct input to the ESPKVV program. The Tab format designates self-documenting tab-delimited files whose general structure has already been described. The dataset naming convention - an integral part of the *ESP4K* data management system - comprises a two or three character functional prefix, followed by an alphanumeric simulation-identifying suffix composed from the following elements: a) SIM_#, the simulation number; b) NRUN, the character representation of the NRUNS loop counter; c) NWG, the character representation of the NWGS loop counter; d) NFQ, the character representation of the NFQS loop counter; and e) IRZ, the character representation of the resonance number. The suffixes used in **Table 3** are defined as follows:

FNAME = [SIM_#][NRUN][NWG][NFQ]
GNAME = [SIM_#][NRUN][NWG]
RZNAME = [SIM_#][NRUN][NWG][NFQ][IRZ].

Output Plots

The *preplot* program selectively reads the ESP4K output tables and constructs files of plot commands in the Axum® plotting language suitable for subsequent batch processing. **Table 4** lists *ESP4K*'s full contingent of 20 plots spanning 5 pages utilizing a variety of axes types, and annotated with sufficient numerical data for the user to - in most cases - fully comprehend the simulated embodiment without having to rely upon other output data. The wire geometry is shown in both 3-D (Plot 1) and in a generalized form (Plot 2) - the generalized variables being the azimuthal and poloidal angles for a toroidal geometry whose major axis is z-oriented. The feed locations are shown with symbols, and the corresponding voltage and phase are tabulated. *ESP4K* supports geometries with both one and two wires, and the current distributions for each wire are shown color and symbol-coded at all resonance and corresponding band edge frequencies on separate plots for each wire (Plots 3 and 4). The frequency response of impedance is shown in Plots 5 and 6 at both full scale, and at a finer scale not exceeding +/- 1000Ω, which reference lines delineating the resonance and band edge frequencies. Plot 7 shows the impedance in Smith chart format, with separate lines corresponding to normalizations with respect to each of the resonant impedances. Plot 8 shows the VSWR, separately normalized for each resonance, plotted against the corresponding normalized frequency. These plots are annotated with lists of the normalized resonant and band edge frequencies, the corresponding resonant impedances and normalized bandwidths. The radiation gain and phase are shown, in Plots 9 and 10 respectively, as a function of frequency for both polarizations at the specific field point specified in the SIM_main table. Plot 11 shows various measures for the antenna velocity factor which is the ratio of the wavelength of the guided wave to that of free space. Plot 12, useful for antennas with multiple feed points, shows a normalized impedance as a function of feed point. The plots on last two pages show the radiation gain as a function of elevation (Plots 13-16) and azimuth angle (Plots 17-20), respectively, for both theta (vertical) and phi (horizontal) polarizations on both linear and polar axes. The gain is plotted at each resonance and corresponding band edge frequency with coding by color, symbol, and line type.

ESP4 Anomaly

The *ESP4KVV* program utilized the *ESP4* solution methodology without change other than the above-described use of uniform values for the physical and mathematical constants. The velocity factor of helical and contrawound helical antenna elements was of particular interest to the investigation described in [1]. The simulated velocity factor of monofilar helical elements was consistent with experimental measurements, however the simulated velocity factor of bifilar contrawound helical elements with anti-symmetric current mode distributions - otherwise similar in pitch, diameter, and length - was a factor of about two to three times faster than that actually measured. This will be reported in greater detail in a later publication.

Summary

The *ESP4K* simulation tool is an enhancement of the OSU *ESP4* program. The hierarchical, structured input and output tables provide a consistent and easy to use interface which facilitates the simulation of a broad set of parameterized wire geometries. User inputs are kept to a minimum and are self-documenting. The procedures and tables are inherently open ended and flexible, enabling other parameterized geometries to be readily defined and simulated within the same framework. The *ESP4K* tool presently runs in a combined Unix® and DOS environment, the later being required for the plotting program. A broad set of annotated plots are automatically generated for each simulation, enabling the user to quickly understand many measures of the simulated antenna embodiment's performance. The underlying *ESP4KVV* program can automatically calculate resonant frequencies and VSWR bandwidth, and is structured to facilitate the definition of other objective functions and the incorporation of separate optimization procedures.

Table 3 List of *ESP4KVV* Output Files

Dataset Name	Format	Description
ZM[FNAME]	*ESP4*	System Impedance Matrix
PI[SIM_#]	*ESP4KVV*	Copy of *ESP4KVV* list input
ZL[GNAME]	Tab	Impedance calculation log
EL[FNAME]	Tab	Elevation Radiation Pattern
AZ[FNAME]	Tab	Azimuth Radiation Pattern
ES[FNAME]	Tab	Elevation Scattering Pattern
AS[FNAME]	Tab	Azimuth Scattering Pattern
RC[FNAME]	Tab	Near Field Radiation Pattern in Antenna Coordinates
PAT[SIM_#]	*ESP4*	*ESP4* Radiation/Scattering Pattern Data
FV[GNAME]	Tab	Radiation Frequency Response : Resonance & VSWR : All Data
RV[GNAME]	Tab	Radiation Frequency Response : Resonance & Bandwidth : Summary
SW[RZNAME]	Tab	Radiation Frequency Response : Localized w.r.t. Resonant Frequencies
FR[GNAME]	Tab	Radiation Frequency Response : Fixed Frequencies
RZ[GNAME]	Tab	Radiation Frequency Response : Resonant Frequencies
FS[GNAME]	Tab	Scattering Frequency Response : Fixed Frequencies
FRQ[SIM_#]	*ESP4*	*ESP4* Frequency Response Data
WI[Wire_Design]	*ESP4KVV*	Copy of *ESP4KVV* list input : Wire Geometry
WG[Wire_Design]	Tab	Wire Geometry
JM[FNAME]	Tab	Wire Geometry & Current Mode Distribution
GEO[SIM_#]	*ESP4*	*ESP4* Geometry Data

Table 4 *ESP4K* Output Plots

Page	Plot	Description
a	1	3-D Wire Geometry
	2	Generalized Wire Geometry
	3,4	Current Distribution - Wire 1,2
b	5, 6	Impedance Frequency Response - Full Scale, Fine Scale
	7	Smith Chart
	8	VSWR
c	9, 10	Radiation Gain/Phase vs. Frequency (Theta & Phi Polarization)
	11	Velocity Factor
	12	Relative impedance of multiple feed points.
d	13,14	Elevation Cross-Section, Theta/Phi Polarization, Linear Scale
	15,16	Elevation Cross-Section, Theta/Phi Polarization, Polar Scale
e	17,18	Azimuth Cross-Section, Theta/Phi Polarization, Linear Scale
	19,20	Azimuth Cross-Section, Theta/Phi Polarization, Polar Scale

References

1. VanVoorhies, K.L., *The Segmented Bifilar Contrawound Toroidal Helical Antenna*, Ph.D. Dissertation, West Virginia University, Dec., 1993. (To be published by University Microfilms International).
2. Newman, E.H., *A User's Manual for the Electromagnetic Surface Patch Code: ESP Version IV*, NASA Administration Center, Langley Research Center, Hampton, VA, 1988.
3. Birdsall, C.K.; Everhart, T.E., "Modified Contra-Wound Helix Circuits for High-Power Traveling Wave Tubes," *IRE Transactions on Electron Devices*, ED-3, Oct. 1956, 190-204.
4. Press, W.H.; Flannery, B.P.; Teukolsky, S.A.; Vetterling, W.T., *Numerical Recipes in C (The Art of Scientific Computing)*, Cambridge University Press, New York, 1988.

A Study of Two-Dimensional Tapered Periodic Edge Treatments for the Reduction of Diffraction[1]

R. A. Burleson, A. J. Terzuoli, Jr. • Air Force Institute of Technology
E. K. English • Mission Research Corp.
L. W. Henderson • Ohio State University

Introduction: This paper presents the results of a study using tapered periodic edge treatments to reduce wide band edge diffraction from a knife edge for the polarization parallel to the plane of incidence. The tapers were designed using the Periodic Moment Method (PMM) and the Finite Difference Time Domain (FDTD), and then experimentally verified.

The designs described herein use the capacitive properties of thin strips for parallel polarization. Other designs were built and tested for the orthogonal polarization using their inductive properties, but the results were not very promising. Since the tapers were to be ultimately used in antennas, the tapers were designed and tested at near grazing incidence; the measurements were intended to approximate a two dimensional (2D) knife edge with plane wave incidence and a far field observation point.

The Designs: The tapers were designed using the PMM Version 3.0 [1] for doubly-infinite structures hosted on a 33 MHz 486DX. To use this code, local periodicity was assumed for the taper design. By taking values along the taper and assuming local periodicity, the reflection coefficient was found as a function of position on the taper. Due to the 8:1 length to width ratio required by PMM, the reflection coefficients near free space could not be calculated for the capacitive taper.

For the capacitive taper, the ground plane edge was the most difficult, since the challenge was to develop a design that had large capacitance (low impedance) over a bandwidth of 2-18 GHz. The reflection coefficient for the ground plane side should be very close to unity (0 dB) over the bandwidth.

The tapers were photo etched on a 10 mil dielectric substrate with a 5 mil minimum line width. The dielectric substrate had a dielectric constant of 4.5 over 2-18 GHz. The capacitive taper design had a constant center to center spacing design with varying strip widths. To increase the capacitance, this design had a second array of thin strips on the bottom of the dielectric substrate. The bottom array was the same as the top array except that it was offset by half of a center-to-center spacing, as shown in Figure 1. The widest strip that had a 5 mil gap and a large reflection coefficient over the entire bandwidth was 330 mils wide, as shown in Figure 2. The strip widths were linearly tapered from 330 to 5 mils, with the center-to-center spacing for the capacitive design being 335 mils. Two tapers were built, 15 and 30 cm long.

The taper produced resonances that occurred at approximately the same position on the taper. The lower frequencies approached the resonance faster, and have a more gradual taper, as shown in Figure 3. At the resonance, the impedance approaches ∞ and the ground plane is exactly matched to free space. On the ground plane side of the resonance, the reflection coefficient (in dB) decreased from 0 to large negative values. On the free space side of the resonance, the reflection coefficient increased toward the free space edge. The reflection coefficient was still fairly low at the end of the taper over most of the frequency range. The ground plane interface was still a scattering source for low and high frequencies, due to low reflection coefficients and a second resonance, respectively. This taper displayed the best reflection and impedance characteristics of all of the designs over the frequency range.

[1] This work was supported by the U. S. Air Force Wright and Phillips Laboratories.

Measurements: Since the goal of this study was to develop better tapering mechanisms for antennas, the tapers needed to be effective at near grazing incidence. To study the effectiveness of the taper designs, a platform was designed to simulate an semi-infinite thin ground plane. To minimize edge diffraction from the sides of the ground plane, the AEL horn was mounted at the apex of a triangular plate. The triangular plate was then mounted on a 2 inch Styrofoam substrate for stability. The source antenna was then mounted by a wooden bracket to the apex of the triangle. Since the distance from the antenna to the edge is more than 5 wavelengths, the plane wave incidence approximation on the edge is valid. Figure 4 shows the setup of the antenna platform.

The total field was measured for a variety of angles and frequencies. The angles recorded were bistatic, because the source was fixed for all measurements about 4.7 deg. from grazing off the triangular ground plane. The source horn was rotated to have the E-field orthogonal to the long edge. The horn was mounted on the apex of the ground plane by a small wooden bracket. The antenna was rotated to the proper polarization and then bolted into the wooden bracket. The taper was attached to the Styrofoam substrate with masking tape. To reduce scattering, copper tape was applied to the interface between the taper and the ground plane.

The taper showed a marked improvement over a bare edge. First the hard edge diffraction from the platform with no taper was compared to the UTD prediction of a knife edge with incident angle = 4.7 deg. from the ground plane. Figure 5 shows the comparison with additional scattering in the measured data over the UTD prediction of the data knife edge, in the region less than 30^0 into the shadowed region. Marked improvement is displayed in the region greater than 30^0 into the shadow region for both the long and short tapers. Figures 7, 8, and 9 give the frequency scans of the capacitive design at the observation angles 90 deg., 120 deg., and 150 deg. respectively. The design seemed to work well over the frequency range 5-15 GHz, which agreed with the results from Figure 3. The taper did not seem to be effective in the region less than 30 deg. into the shadow region, possibly due to the additional scattering sources.

FDTD Model: A 2D TE(z) FDTD code [2, 3], hosted on a Silicon Graphics workstation, was used to calculate the capacitive taper. To ensure that the dielectric slab of 10 mils thick could be modeled by the code, the cell size was set to 0.4244 mm by 0.4244 mm which gave time steps of 1 psec. The dielectric constant for the Styrofoam was set to 1.02 and the dielectric constant for the photo etch substrate was set to 4.5. The entire grid size for the FDTD run was 4300 by 700. The runs for this model required over 50 MB of RAM and several hours. The observation angles measured were 90, 60, 30, 0, -30, -60, and -90 deg.. The time domain results were then Fourier Transformed to echo width using a companion program; see Figure 10.

FDTD supported the measurements since no noticeable reduction was made in diffraction until the observation was greater than 30 deg. into the shadow region in both the FDTD model and the measurements. The FDTD results showed improvement for the long over the short taper only at frequencies less than 6 GHz. This result agreed with the measurements. The type of taper used (linear, binomial, triangular, etc.) should only be significant when the taper is electrically shorter. The FDTD results suggested that the capacitive taper was effective in the range of 2-13 GHz. This result tended to support the experimental data, where the capacitive taper was effective in reducing deep shadow fields in the frequency range of 6-16 GHz.

Further, the FDTD results showed additional scattering for the no taper design in the shallow shadow region. FDTD was then used to isolate the sources of additional scattering. First, slope diffraction was considered, but since the source was a simple source, no slope diffraction could occur. Second, the scattering from the 2 inch thick Styrofoam was considered; FDTD was used to determine the scattering as a function of the dielectric constant from the 2 inch thick Styrofoam alone, without the ground plane or taper design. The FDTD results from the dielectric substrate alone showed considerable scattering in the region less than 30 deg. into the shadow region. Therefore, at least part of the additional scattering was due to scattering from the Styrofoam substrate.

Conclusions: The taper was highly effective over a frequency range of 6-16 GHz. The taper did have resonances which would produce dispersion for a signal in the time domain. This property, while unwanted for time domain applications, is tolerable for continuous frequency applications.

One improvement to the taper would be to change from constant center-to-center spacing to constant gap size i.e. the length of the gap between strips. This change would provide a more continuous taper design and increase the bandwidth of the taper. Another improvement to the first taper would be to load the free space edge of the taper. This would reduce the scattering from the free space end of the taper. Another taper improvement would be to try different periodic geometries that create capacitive impedance. Discrete capacitive elements would be better for bandwidth and continuous tapers; however, these discrete elements would resonate and degrade time domain applications. Therefore, depending upon the application, the taper could be improved in a variety of ways.

The measurements in this study were bistatic measurements. Monostatic or backscatter measurements would also be of interest especially for RCS reduction. Monostatic measurements would be much easier to perform and would not require such a large structure for measurements. Also monostatic measurements would not require the assumptions that were needed in a bistatic study. If a similar antenna platform was to be used in a future study, the dielectric constant of the Styrofoam must be measured for proper modeling. For a dielectric constant so close to unity, a cavity resonance method of measuring the dielectric constant would be needed instead of the waveguide method. Other future work would be to attach the tapers directly to antennas, much like edge cards. Another major area of study for these periodic tapers would be the reduction in edge scattering from a finite size radome. For better modeling of the tapers, singly-periodic PMM codes could be used instead of Henderson's PMM code. This would allow the tapers to be designed without having to assume local periodicity. To improve the modeling of the platform using FDTD, the entire structure, including the source antenna, should be modeled using a 3D total field FDTD code. This would eliminate the plane wave incidence and the 2D approximations. By modeling the entire structure, the additional sources of scattering would be easier to determine.

Acknowledgment: The authors are grateful to the following people for their suggestions: Carl Baum, Jerry Buchenaur, Raley Marek, Dave Schriner, Paul Skinner, Joe Sacchini, Bill Baker, Leo Felsen, Carey Rappaport, Larry Carin, Ray Luebbers, Jon Young, Eric Walton, Jim Maloney, Allen Taflove.

References

[1] L. W. Henderson, *Introduction to PMM*, Technical Report 715582-5, The Ohio State University ElectroScience Laboratory, Department of Electrical Engineering; prepared under Contract F33615-83-C-1013 for Avionics Laboratory (AFWAL/AAWP-3), Air Force Wright Aeronautical Systems Command, Wright-Patterson Air Force Base, OH, Feb. 1986.

[2] J. Beggs, R. Luebbers, and H. Langdon, *User's Manual for TEC: PSU FDTD Code Version C for Two-Dimensional Transverse Electric (TE) Transient Scattering from Frequency-Independent Dielectric and Magnetic Materials*, University Park, PA, June 1993.

[3] K. S. Kunz, R. J. Luebbers, *The Finite Difference Time Domain Method for Electromagetics*, CRC Press, 1993.

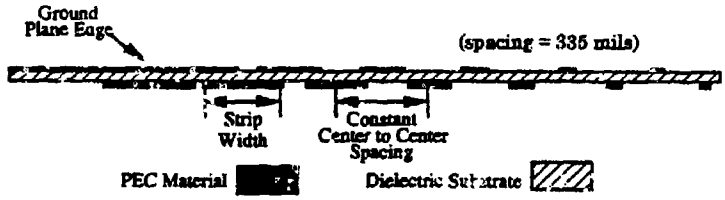

Figure 1. Taper design for parallel polarization, with constant center to center spacing.

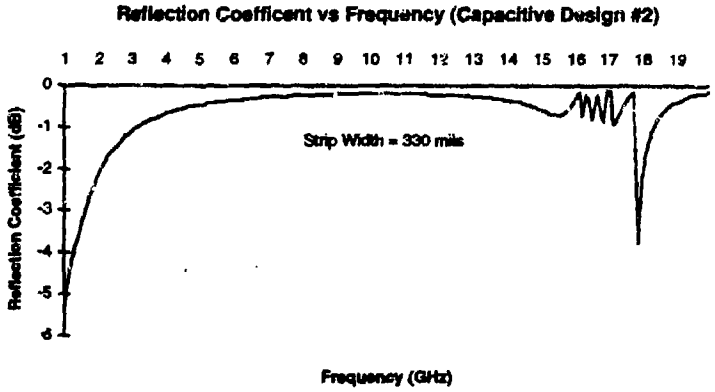

Figure 2. Reflection Coefficient vs. Frequency for Ground Plane Edge of Taper. This design was for two thin strip arrays of constant center-to-center spacing of 335 mils, with strip width of 330 mils.

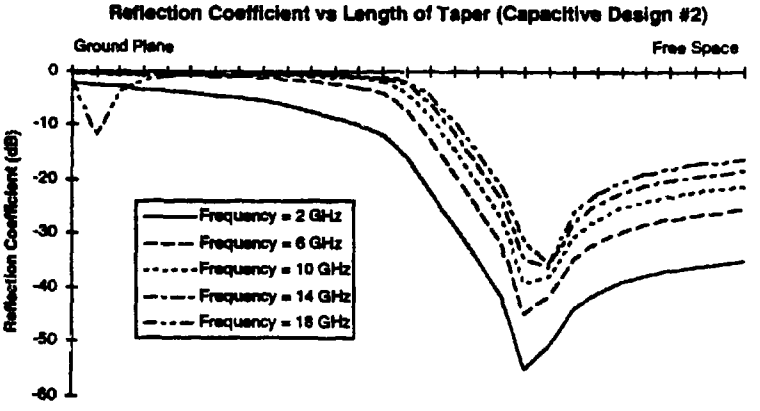

Figure 3. Reflection Coefficient vs. Length of Taper. Note that this taper is well behaved over most of the frequency range.

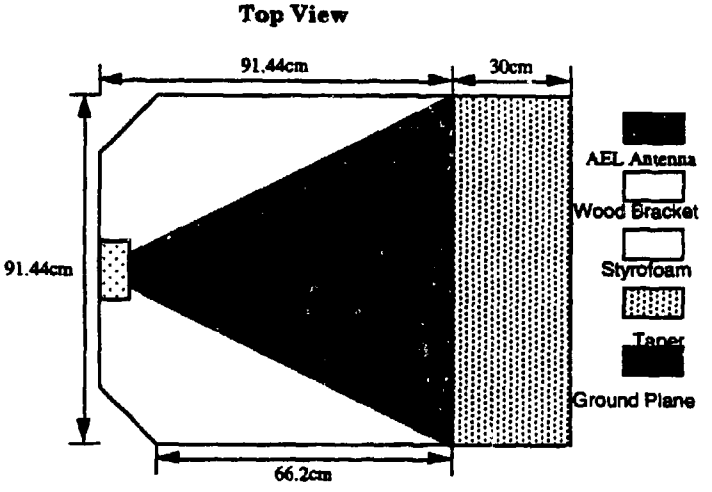

Figure 4. Antenna Platform used for measurements.

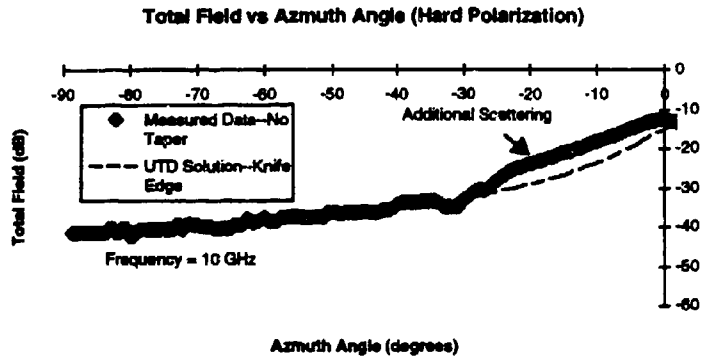

Figure 5. Comparison of UTD and Measured Results From the Knife Edge, showing additional scattering when the observation was less than 30° into the shadowed region.

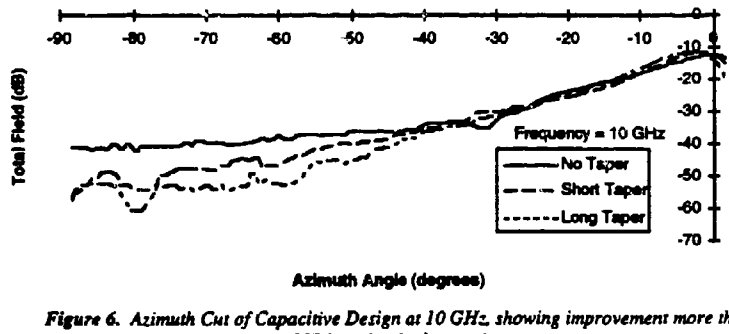

Figure 6. Azimuth Cut of Capacitive Design at 10 GHz, showing improvement more than 30° into the shadow region.

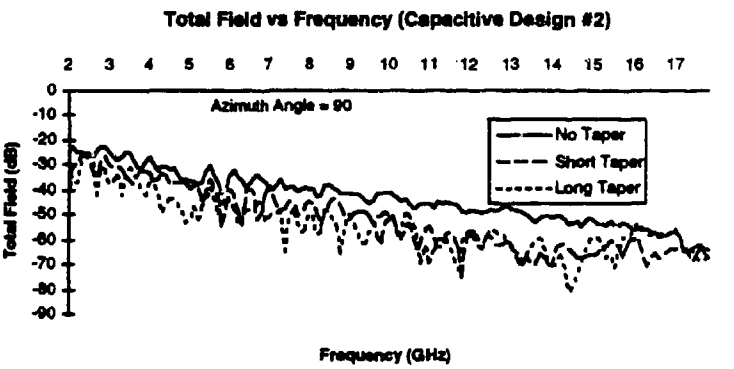

Figure 7. Frequency Sweep for Capacitive Design at 90° into the Shadow Region, showing a 10 dB reduction over for 6-16 GHz at 90° into the shadow region.

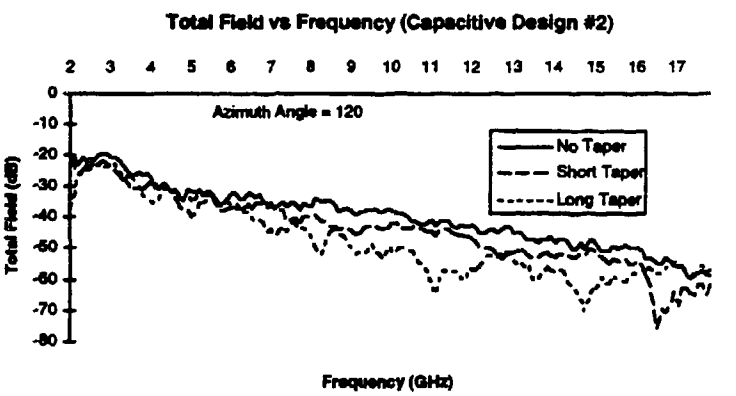

Figure 8. Frequency Sweep for Capacitive Design at 120° into the Shadow Region, showing a 5 dB improvement for 6-16 GHz at 120° into the shadow region.

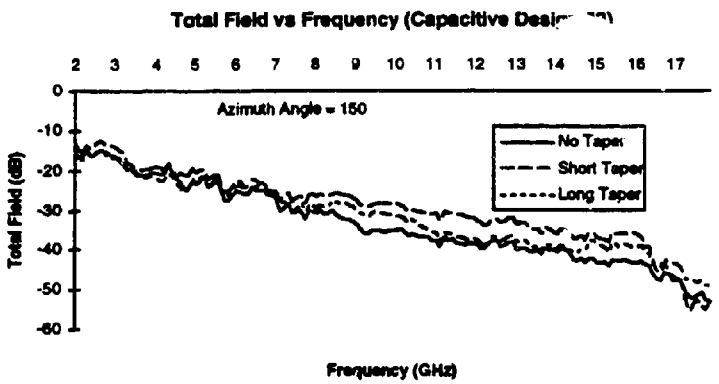

Figure 9. Frequency Sweep for Capacitive Design at 150° into the Shadow Region, showing no improvement for the entire frequency range at 150° into the shadow region.

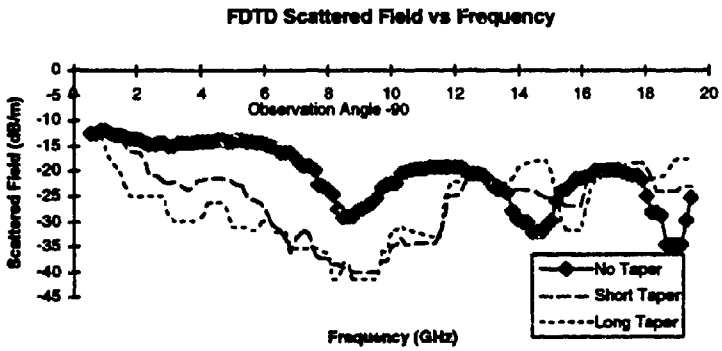

Figure 10. Comparison of FDTD Results for Taper, showing improvement for the capacitive taper design up to 13 GHz. The incident field was at 170° and the far field observation angle was -90°.

SESSION 10:

FINITE DIFFERENCE TIME DOMAIN I

Chair: Jiayuan Fang
Co-Chair: Bruce Archambeault

Application of an Upwind Leap-frog Method for Electromagnetics

Brian Nguyen and Philip Roe
Department of Aerospace Engineering
University of Michigan

1 Introduction

Advances in the computational sciences of the past decades have increased the feasibility of time domain solutions of Maxwell's equations. In the last few years, many studies and applications of finite difference time-domain (FDTD) method have been published. [3, 1, 5, 6, 8]. FDTD solutions can overcome the limits of older methods such as geometrical optics, physical optics and frequency domain methods. These limits are in particular, non-linear material response, ultra-high frequencies, continuous excitations and wide-band excitations. Recently proposed technologies such as electro-optical and all-optical devices demand solutions that cannot be given by the older methods [3]. Hence the time domain methods are required.

Three common families of FDTD methods are the leapfrog method [16], finite volume methods using Riemann solutions [10, 9], and finite element methods [4]. All three methods are currently receiving interest and gaining improvements. In this work, we apply a recently developed variation of the leapfrog family of methods to obtaining FDTD solutions of Maxwell's equations.

The upwind leapfrog (UL) method was developed originally to improve time domain solutions in computational aeroacoustics [14]. It addressed the issue of propagating a disturbance accurately and efficiently, that is, without numerical dissipation, very little numerical dispersion and on a coarse grid (with respect to the spatial wavelength of the disturbance).

The UL scheme works equally well for Maxwell's equations in 2D, where the equations are dual to the 2D acoustic equations. In 3D, its practical implementation in a computer program is slightly different.

2 Upwind Leapfrog Scheme

The various versions of the leapfrog scheme used by Yee [16] and Taflove and Goorjian [13, 12, 2, 3] all used a central difference (or symmetric) spatial stencil (although variations in grid staggering were employed). Works in fluid dynamics have shown the importance of treating hyperbolic partial

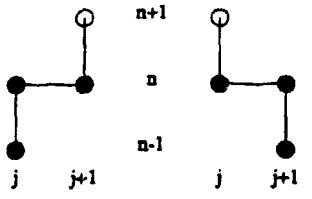

Figure 1: Upwind leapfrog stencils in 1 dimension

differential equations in an "upwind" manner (as opposed to symmetrically in space) when solving them with finite-difference methods [15, 7]. Accordingly, the stencil of Figure 1 is proposed for a 1D (in space) system. The first stencil is used for a right going wave, the second for a left going wave. The leapfrog scheme owes its dissipation-free characteristic to the fact that it is reversible in time. In Figure 1, the stencils are clearly reversible. Using this stencil, a 1D Maxwell's equation is written, in finite difference form as

$$u_j^{n+1} = u_{j-1}^{n-1} - (2\nu - 1)[u_j^n - u_{j-1}^n] \tag{1}$$

where u is any cartesian component of the charcteristic variable vector $\mathbf{G}^* = \mathbf{D} \mp \frac{\mathbf{a}\Delta\mathbf{B}}{c}$, and ν is the Courant number, constrained by stability to be less than 1. This scheme has no numerical dissipation. It's numerical dispersion error is a function of the frequency and the Courant number. A complete discussion of the UL scheme can be found in reference [14].

In two spatial dimensions, the situation is more complicated because the direction of the wave propagation, a deciding factor in upwinding, can vary continuously in $[0, 2\pi]$, whereas we must be limited to a finite number of discrete equations. One solution is to discretize the bicharacteristic equation along each grid direction using the stencil in Figure 2. In this manner, the characteristic variables are required on the cell interfaces (faces), thus all unknowns are kept on the faces. The resulting bicharacteristic equations for a transverse magnetic (TM) polarization are obtained by taking combinations of Maxwell's equations:

$$\frac{\partial}{\partial t}\left(D_z \mp \frac{H_y}{c}\right) \pm c\frac{\partial}{\partial x}\left(D_z \mp \frac{H_y}{c}\right) + \frac{\partial H_x}{\partial y} = 0 \tag{2}$$

$$\frac{\partial}{\partial t}\left(D_z \pm \frac{H_x}{c}\right) \pm c\frac{\partial}{\partial y}\left(D_z \pm \frac{H_x}{c}\right) - \frac{\partial H_y}{\partial x} = 0 \tag{3}$$

Upon applying the stencils of Figure 2 to these equations, we obtain the difference equations

$$P_i^{n+1} = P_i^n - (P_{i-1}^n - P_{i-1}^{n-1}) - 2\nu(P_i^n - P_{i-1}^n) - 2\Delta t\left[\frac{\partial H_x}{\partial y}\right]_{i-\frac{1}{2}}^n \tag{4}$$

$$Q_i^{n+1} = Q_i^n - (Q_{i+1}^n - Q_{i+1}^{n-1}) - 2\nu(Q_i^n - Q_{i+1}^n) - 2\Delta t\left[\frac{\partial H_x}{\partial y}\right]_{i+\frac{1}{2}}^n \tag{5}$$

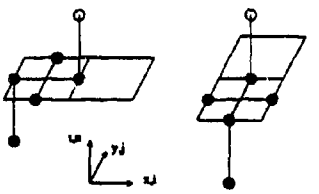

Figure 2: Upwind leapfrog stencils in 2 dimensions

$$R_j^{n+1} = R_j^n - (R_{j-1}^n - R_{j-1}^{n-1}) - 2\nu(R_j^n - R_{j-1}^n) + 2\Delta t \left[\frac{\partial H_z}{\partial x}\right]_{j-\frac{1}{2}}^n \tag{6}$$

$$S_j^{n+1} = S_j^n - (S_{j+1}^n - S_{j+1}^{n-1}) - 2\nu(S_j^n - S_{j+1}^n) + 2\Delta t \left[\frac{\partial H_z}{\partial x}\right]_{j+\frac{1}{2}}^n \tag{7}$$

where P, Q, R and S are the z components of the characteristic variable vector propagating in the $+x$, $-x$, $+y$ and $-y$ directions, respectively. Note the cross term in the direction orthogonal to the primary direction, which arises due to the extra term in the bicharacteristic equations. In three dimensions, we get a cross term in each of the two orthogonal directions. The cross terms are evaluated using a central difference in the appropriate half-integer indexed cell.

3 Analysis

An analysis of the UL scheme for acoustics is given in reference [14]. Here, we discuss its specific implementation for Maxwell's equations as on a staggered, face centered scheme, particularly with regard to the storage requirement. Indeed, some efficiency is lost when the variables are kept at the cell faces. A nodal (or cell centered), non staggered scheme will have 6 unknowns (3 in 2D) per node and 6 equations (3 in 2D). The UL scheme requires that at each face we store the tangential components of the magnetic and electric fields. This gives four unknowns per face in 3D, which is twice as many unknowns per cell as a nodal scheme. For a 2D problem the factor is $\frac{4}{3}$.

When we discretize the field with (say) $N = 8$ grid spacings per wavelength and we store $\frac{4}{3}$ times more unknowns than the unstaggered nodal scheme, a problem that required $n \times n$ units of storage now requires $\frac{4}{3}n \times n$ units, so that the storage requirement per wavelength is not 8, but $8\sqrt{\frac{4}{3}} = 9.24$. In 3D, the requirement would be $8\sqrt[3]{2} = 10.08$. This implies that the naive 1D measure of efficiency were slightly optimistic. However, resolution of the waves can still be done significantly more efficiently than it can be with the original leapfrog scheme.

4 Boundary Condition

4.1 Image Grid Elements

To implement certain boundary conditions in an upwind scheme, it is useful to set the field just outside the computational domain and let the upwind scheme separate what information is allowed to propagate inward and what information is ignored. This method simplifies the incidence and, in some cases, the exit boundary conditions. It also allows the boundary faces to be included in most loops without special treatments. We refer to the first face outside the computational domain as the image face. Likewise the first cell and the first point are the image cell and the image point.

4.2 Perfect Electric Conductor

At a perfect electric conductor (pec) surface, any wave hitting the surface is completely reflected. We think of this as having the wave penetrate the surface while another emerges such that the resulting electric field on the surface is zero. The two waves are shown in Figure 3 where the $\mathbf{G}^-$ wave is the former and the $\mathbf{G}^+$ wave is the latter. Denoting the conditions outside the pec with superscript "i" and the condition inside the pec with superscript "r", we have by definition

$$\mathbf{G}^- = \mathbf{D}^i + \frac{\mathbf{n} \times \mathbf{H}^i}{c} \tag{8}$$

$$\mathbf{G}^+ = \mathbf{D}^r - \frac{\mathbf{n} \times \mathbf{H}^r}{c} \tag{9}$$

The electric displacement on the surface, obtained from these characteristic variables are

$$\mathbf{D} = \mathbf{G}^+ + \mathbf{G}^- \tag{10}$$

Thus the zero electric tangential electric field amounts to requiring

$$\mathbf{G}_t^+ = -\mathbf{G}_t^- \tag{11}$$

where the subscript "t" denotes the components tangential to the boundary. This completely specifies the imaginary (or reflected) wave at the boundary of a pec.

This method applies to the total (incidence and scattered field). When the scattered field equations are solved, the solution is converted to the total field before applying this boundary condition.

4.3 Outer Boundary Condition

A very simple method for treating the outer boundary faces so that waves exiting the domain are not reflected is to set the image faces to a zero field. This method works very well when the

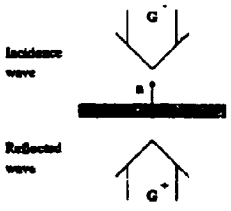

Figure 3: Incidence and reflected waves at a p.c.c. surface

wave is traveling normal to the boundary but generates some reflection when the angle is oblique. In the U shaped channel problem below, there are strong waves exiting the boundary at oblique angles. For this problem, the image face method was not used on the outer boundaries.

The outer boundary for the channel problem is treated as follows. For a wave traveling at an angle of θ with respect to the normal at the boundary, a simple plane wave assumption leads to the following fields (assuming the boundary surface normal, n, points along $+x$):

$$D_z = \mathrm{f}(x\cos\theta + y\sin\theta - ct) \tag{12}$$

$$B_x = -Z\sin\theta\,\mathrm{f}(x\cos\theta + y\sin\theta - ct) \tag{13}$$

$$B_y = Z\cos\theta\,\mathrm{f}(x\cos\theta + y\sin\theta - ct) \tag{14}$$

By differentiating with respect to x, y and t the results can be combined so that the unknown angle θ drops out, leaving

$$\frac{\partial D_z}{\partial t} + c\,\mathrm{sign}\left(\frac{\partial D_z}{\partial x}\right)\sqrt{\left(\frac{\partial D_z}{\partial x}\right)^2 + \left(\frac{\partial D_z}{\partial y}\right)^2} = 0 \tag{15}$$

$$\frac{\partial B_y}{\partial t} + c\,\mathrm{sign}\left(\frac{\partial B_y}{\partial x}\right)\sqrt{\left|\left(\frac{\partial B_y}{\partial x}\right)^2 - \frac{\partial B_y}{\partial x}\frac{\partial B_y}{\partial x}\right|} = 0 \tag{16}$$

As written, these equations are true of any wave leaving the domain, but false for any wave that is entering. It is the sign function that discriminates between the two cases. For the specified n and the face centered scheme used, no equation for B_x is necessary. The variables on the outer boundaries are then integrated according to these relations.

This boundary condition was used in all 2D results in this work, where it performed quite well. Unfortunately, its extension into three dimensions has not been done at this point.

It should be noted that a good non-reflecting outer boundary condition is highly desirable, especially for a non-dissipative scheme, such as this one. Usually, the dissipation in the other schemes help to damp out the small reflections. Such a mechanism is not available here, and reflections between outer boundaries can build up very fast.

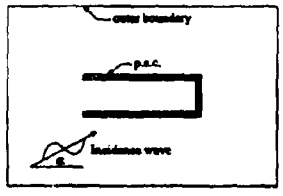

Figure 4: Geometry and grid of U shaped channel

4.4 Incidence Boundary Condition

All incidence boundary conditions in this work are treated by setting the image faces to the incident field. The upwind scheme then allows the incident waves in but simultaneously allows the interior waves to exit (to a certain degree, as noted in Section 4.3). For the solutions of 2D and 3D beams in Sections 5.2 and 5.3, this allows the surface of the boundary on the side of the incidence wave, but outside the beam, to act as far field boundaries. As noted in Section 4.3, waves approaching the boundary at an oblique angle do experience significant reflections with this treatment, but for the problems of Sections 5.2 and 5.3, the waves doing this have very low strengths.

5 Results

5.1 U Shaped Channel

The two dimensional result of a harmonic plane TM wave incident on a perfectly conducting U shaped channel is considered. The geometry of the problem is shown in Figure 4. The grid spacing was $h = 1$ for the geometry, and the wavelength $\lambda = 10$. The channel's outer dimensions are 42×12 and its wall thickness is 2. The grid size was 127×97 leaving about 42 cells between the body and the outer boundary. The wavelength of the incident field was 10. The incident plane wave was inclined at $\alpha = 30°$ with respect to the x axis. The scattered field equations were solved.

The problem was integrated forward with $\nu = .3125$ (although the stability limit in two dimensions is $\nu = .5$) in order to have one wavelength passing each point in exactly 32 time steps. This was done only to have the right sampling rate for conversion into a frequency domain solution via a fast Fourier transform (FFT).

The frequency domain solution was used to compute the radar cross section (RCS) of the channel, using the definition of the RCS, and the farfield solution can be obtained from the nearfield numerical solution using the Stratton-Chu integral [11] and equivalence principles.

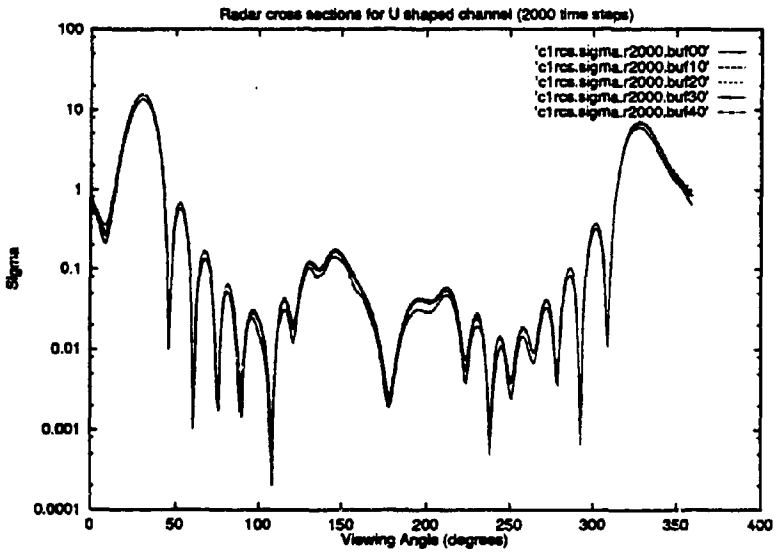

Figure 5: Radar cross sections from different contours

The contours chosen for the integral were taken at several places in the grid in order to test the accuracy with which the waves are propagated. Ideally, there would be no difference in the results of the RCS, but because the disturbances are specified on the body, we feel that placing the contour near the body does not sufficiently test the scheme. Any difference between the computed RCS of the close or far contours are assumed to be primarily due to errors incurred in the wave propagation.

The results for 5 different contours are shown in Figure 5. The first contour was taken on the outer boundary and each sucessive one was taken 10 cells inward. The contour closest to the body actually coincided with the back end of the channel. All but one of the curves agree (generally within about .1dB). The exception is that for the contour on the outer boundary. The difference there may be partly due to the boundary being treated differently from the rest of the computational domain.

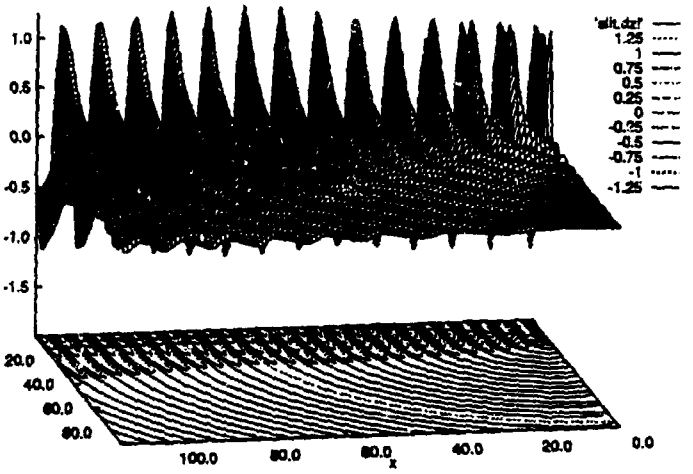

Figure 6: Near field electric field diffracted through a slit

5.2 Two Dimensional Coherent Beam

The present scheme was used to compute the near field of coherent light emerging from a slit aligned in the x direction. One half of the symmetric field was computed on a 111×91 grid. The disturbance had a wave length of $\lambda = 8$. The half width of the slit was 20. The integration was performed at $\nu = .4$, not at the stability limit of $\nu = .5$, where there is no dispersion error [14].

Figure 6 shows the distribution of D_z. The contours of Figure 6 shows that the far field boundary condition of Section 4.3 works quite well. (The far field boundary condition of setting the image faces to a zero field has been seen to reflect half the wave amplitude, for waves approaching the boundary at around 45°.) The non-dissipative characteristic of the scheme can be seen in that the beam is not being damped, even though the grid is very coarse compared to the roundness of the wave crests.

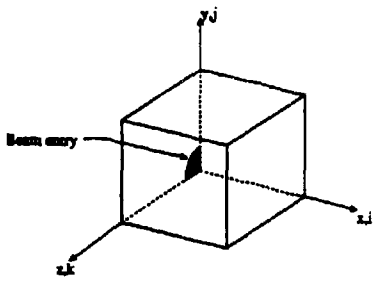

Figure 7: Round aperture problem

5.3 Three Dimensional Coherent Beam

The three dimensional scheme was used to compute the near field of a uniform coherent beam of circular cross section (Figure 7). Due to symmetry, it is only necessary to simulate a quarter of the beam. For this problem, the grid spacing was $h = 1$; the wave length was $\lambda = 8$; and the radius of the beam (before diffracting) was 2λ. The grid size was $32 \times 48 \times 48$. The solution was integrated at $\nu = .4$.

For all the boundaries, the conditions on the image faces were set. The incidence field boundary condition of Section 4.4 was used for the boundary at maximum x. For the boundaries at minimum y and minimum z, the images were set to the the conditions immediately inside the domain to simulate the symmetric half of the beam on the other side. All other boundaries are outer boundaries, and there, the image faces were set to the zero field. Although, as noted in Section 4.3, this type of outer boundary did not work well when there was a strong wave exiting the domain at an oblique angle, that is not the case here. The strong part of the field is in the core, which is exiting at the normal angle. Nevertheless, due to the unavailability of a reliable far field boundary condition at this point, only 100 iterations were taken to avoid reflected waves from possibly building up inside the domain. After 100 iterations, there are no visible reflections.

The magnitudes of D, B and $\mathbf{E} \times \mathbf{H}$ are shown in Figures 8, 9 and 10. It should be noted that, for the purpose of plotting the data, all face centered quantities have been averaged to the cell, where then all components of D and B could be made available.

Figures 10 and 11 shows that the strongest waves are in the core and exiting the boundary at reasonably normal angles. Outside the core, the strengths of the waves are negligible, in regards to producing recognizable reflections. Thus, from this at least, the far field boundary does not appear to be introducing significant errors.

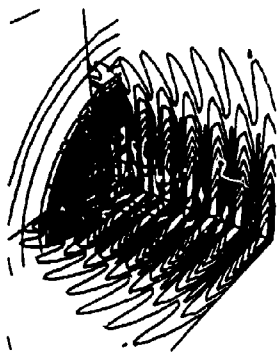

Figure 8: D vector magnitude

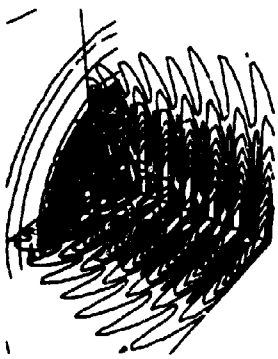

Figure 9: B vector magnitude

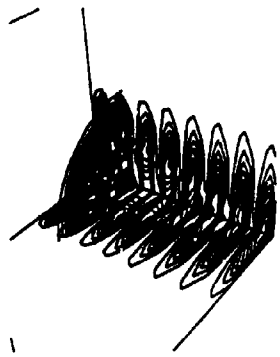

Figure 10: Poynting vector magnitude

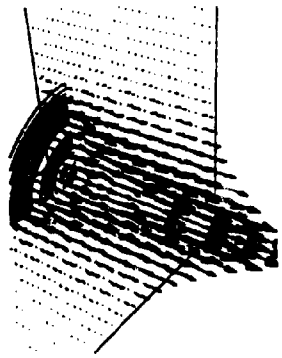

Figure 11: Poynting vector

6 Summary and Conclusions

The upwind leapfrog method, a non-dissipative, low dispersion error scheme was applied to Maxwell's equation in 2D and 3D. The scheme performed well, however, at this point, few quantitative comparisons was made.

It was found that due to the lack of dissipation, waves reflected back from far field boundaries can cause problems as they build up inside the domain. A far field boundary condition based on the assumption of a single exiting wave was tested and performed quite well in 2D, but a 3D extension is not yet available. However, simpler far field boundary conditions make workable substitutes if the conditions for strong reflections from far field boundaries are not present.

In the future, we plan to develop less reflective boundary conditions for use in 3D and to compare the results of this scheme to other analytical and numerical solutions.

Acknowledgement: This work has been supported through a fellowship granted by the Department of Energy.

References

[1] David G. Bishop and Dale A. Anderson. A Comparison of Finite-Volume Time-Domain Schemes for the Maxwell Equations. Technical Report 92-0456, AIAA, January 1992.

[2] Peter Goorjian and Allen Taflove. Computational Modeling of Nonlinear Electromagnetic Phenomena. Technical Report 92-0457, AIAA, January 1992.

[3] Peter M. Goorjian. Computational Modeling of Femtosecond Optical Solitons from Maxwell's Equations. *IEEE Journal of Quantum Electronics*, 28(10), October 1992.

[4] Nathan Ida and Joao P. A. Bastos. *Electromagnetics and Calculation of Fields*. Springer-Verlag, New York, NY, 1992.

[5] Ralph Noack and Dale A. Anderson. Time Domain Solutions of Maxwell's Equations Using A Finite-Volume Formulation. Technical Report 92-4151, AIAA, January 1992.

[6] Benoit PetitJean and Rainald Lohner. Finite Element Solvers for Radar Cross-Section (RCS) Calculations. Technical Report 92-0455, AIAA, January 1992.

[7] Philip L. Roe. Approximate Riemann Solvers, Parameter Vectors and Difference Schemes. *Journal of Computational Physics*, 43:357-3762, 1981.

[8] Vijaya Shankar. A Gigaflop Performance Algorithm for Solving Maxwell's Equations of Electromagnetics. Technical Report 91-1578, AIAA, 1991.

[9] Vijaya Shankar, William Hall, and Alireza Mohammadian. A CFD-Based Finite-Volume Procedure for Computational Electromagnetics – Interdisciplinary Applications of CFD Methods. Technical Report 89-1987, AIAA, 1989.

[10] Vijaya Shankar, Alireza Mohammadian, William Hall, and Roy Erickson. CFD Spinoff – Computational Electromagnetics for Radar Cross Section (RCS) Studies. Technical Report 90-3055, AIAA, 1990.

[11] Julius Adams Stratton. *Electromagnetic Theory*. McGraw-Hill, London, first edition, 1941.

[12] Allen Taflove and Morris Brodwin. Numerical Solution of Steady-State Electromagnetic Scattering Problems Using the Time-Dependent Maxwell's Equations. *IEEE Transactions on Microwave Theory and Techniques*, MTT-23(8):623–630, August 1975.

[13] Allen Taflove and Korada R. Umashankar. Review of FD-TD Numerical Modeling of Electromagnetic Wave Scattering and Radar Cross Section. *Proc. IEEE*, 77(5):682–699, May 1989.

[14] Jeffrey P. Thomas and Philip L. Roe. Development of Non-Dissipative Numerical Schemes for Computational Aeroacoustics. Technical Report 93-3282, AIAA, 1993.

[15] Bram van Leer, James L. Thomas, and Philip L. Roe. A Comparison of Numerical Flux Formulas for the Euler and Navier-Stokes Equations. Technical Report 87-1104, AIAA, 1987.

[16] Kane S. Yee. Numerical Solution of Initial Boundary Value Problems Involving Maxwell's Equations in Isotropic Media. *IEEE Transactions on Antennas and Propagation*, AP-14(3):302–307, May 1966.

Linear Superposition of Phased Array Antenna Near Field Patterns Using the FD-TD Method

C. E. Reuter, E. T. Thiele, A. Taflove
Department of Electrical Engineering and Computer Science
Northwestern University, McCormick School of Engineering
Evanston, Illinois 60208

M. J. Piket-May*
Department of Electrical and Computer Engineering
University of Colorado
Boulder, Colorado 80309

A. J. Fenn
Lincoln Laboratory
Massachusetts Institute of Technology
Lexington, Massachusetts 02173

1 Introduction

This paper generalizes the concept of linear superposition from circuit theory to 3-D FD-TD solutions to Maxwell's equations. The linear superposition principle is applied to FD-TD-simulated radiation patterns of two specific phased array antennas used in electromagnetic hyperthermia. The first is the BSD Sigma-60 annular phased array designed to heat cancerous tumors deep within the body. The second is an experimental prototype device in use at Lincoln Laboratory. It is a non-invasive monopole phased array designed to heat cancerous tumors near the surface of the skin. It is believed that the linear superposition technique has broad applications in FD-TD-based pattern synthesis, adaptive nulling, and design of phased array systems.

2 Linear Superposition

Because Maxwell's equations are linear, the resultant field distribution of any antenna array with all array elements radiating in a linear medium can be thought of as the linear superposition of the field distributions due to each element radiating individually. The demonstration of the superposition principle has not been rigorously reported in the literature for numerical simulation

of the full 3-D vector Maxwell's equations. Sullivan [1] qualitatively describes a superposition procedure in the context of FD-TD simulations. However, given the date of his paper (May 1991), it is clear that he did not employ resistive sources in his FD-TD model (which were developed approximately 2 years later [2]). Therefore, Sullivan's superposition treatment does not have the rigorous flavor of the work reported here.

The basic procedure consists of exciting one array element using a recently-developed resistive source feed representation [2]. The remaining elements are unexcited, but loaded with the nominal generator source impedance. Near-filed data are stored for this run. This procedure is repeated for each array element. Thus, an array with 8 elements would require 8 separate FD-TD runs. A subsequent post-processing step, not requiring a Cray FD-TD run, would merely scale each set of stored data by an arbitrary magnitude/phase distribution, and then transform to the far field (if desired) for the radiated pattern. In this manner, literally hundreds of amplitude/phase tapers across the phased array could be quickly examined. Or, a synthesis procedure involving adaptive nulling techniques [3] could be used to optimally provide the magnitude/phase taper. It is believed that this linear superposition approach employing resistive sources is novel relative to FD-TD modeling.

3 Source Representation

Two different source representations were investigated with regards to the linear superposition technique. These are described below.

The initial source considered is the "hard source." This source forces a specified field component that excites an antenna element to have a desired sinusoidal or impulsive time dependence at any time step, regardless of anything else happening in the FD-TD grid. The hard source is analogous to the ideal voltage source. That is, it has a zero source impedance and can source unlimited power regardless of the load that is placed on it.

The second source considered is the resistive source. This simulates a true physical source having a finite source impedance. It cannot supply unlimited power, and its output voltage is dependent on the load. The following modified FD-TD electric field update expressions were used for the electric field components representing a y-directed resistive source [2]. Here, V_s is the source voltage term or the forcing function:

$$E_y\Big|_{i,j,k}^{n+1} = C_a(m)E_y\Big|_{i,j,k}^{n} + C_b(m)\left(H_x\Big|_{i,j,k+1/2}^{n+1/2} - H_x\Big|_{i,j,k-1/2}^{n+1/2} + H_z\Big|_{i-1/2,j,k}^{n+1/2} - H_z\Big|_{i+1/2,j,k}^{n+1/2}\right) - C_c(m)V_s^{n+1/2} \qquad (1)$$

In this case the coefficients C_a, C_b, and C_c are as follows:

$$C_a|_{i,j,k} = \frac{1 - \dfrac{\sigma_{i,j,k}\Delta t}{2\varepsilon_{i,j,k}} - \dfrac{\Delta t}{2R_s\varepsilon_{i,j,k}\Delta x}}{1 + \dfrac{\sigma_{i,j,k}\Delta t}{2\varepsilon_{i,j,k}} + \dfrac{\Delta t}{2R_s\varepsilon_{i,j,k}\Delta x}} \tag{2a}$$

$$C_b|_{i,j,k} = \frac{\dfrac{\Delta t}{\varepsilon_{i,j,k}\Delta x}}{1 + \dfrac{\sigma_{i,j,k}\Delta t}{2\varepsilon_{i,j,k}} + \dfrac{\Delta t}{2R_s\varepsilon_{i,j,k}\Delta x}} \tag{2b}$$

$$C_c|_{i,j,k} = \frac{\dfrac{\Delta t}{\varepsilon_{i,j,k}(\Delta x)^2 R_s}}{1 + \dfrac{\sigma_{i,j,k}\Delta t}{2\varepsilon_{i,j,k}} + \dfrac{\Delta t}{2R_s\varepsilon_{i,j,k}\Delta x}} \tag{2c}$$

where R_s is the resistance in ohms of the resistive voltage source.

4 Demonstration of Superposition of the FD-TD Computed Fields of the Sigma-60 Using Hard Sources

The BSD Sigma-60 hyperthermia system [1] has four amplifiers each driving a pair of 44-cm long flared dipole antennas radiating in the frequency range of 60 to 120 MHz. The eight dipole antennas are equally spaced around a 60-cm diameter clear plastic annulus and are phased to provide constructive interference of the energy deep inside the body of a patient centered in the annulus. Energy is coupled from the antennas to the patient via a water bolus filling the space between the plastic annulus and the patient. For the case of our 3-D FD-TD simulations, a phantom model is used in place of the patient.

The following results show that unexcited hard sources in the FD-TD grid must be short circuited for the superposition principle to hold. Figure 1a shows the computed electric field pattern in a transverse plane through the Sigma-60 that results after two cycles of equal-magnitude and zero-phase hard-source excitation is simultaneously applied to all 4 dipole pairs of the Sigma-

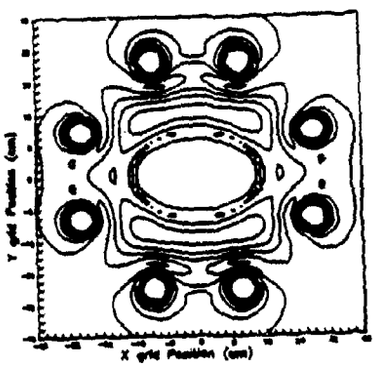

(a) All applicators excited.

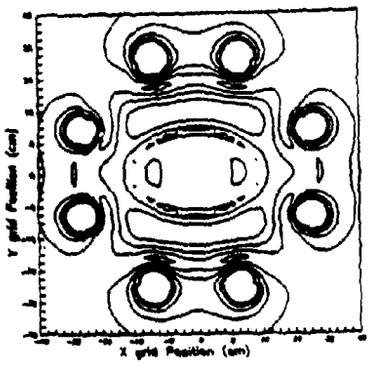

(b) Additive Superposition, but unexcited applicators open-circuited.

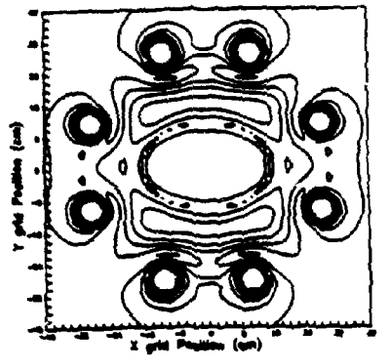

(c) Additive Superposition, same as (b), but unexcited applicators short-circuited.

Figure 1 FD-TD computed electric field distributions in the transverse plane of the Sigma-60. Comparison of the results for all applicators excited (a) with additive superposition of the fields due to individual applicators excited one at a time, and the remainder passive (b, c).

60. (This is not at the sinusoidal steady state; however, it is sufficient to demonstrate the superposition principle using the FD-TD method.) Figure 1b shows the results for the summation of the FD-TD computed electric field patterns of 4 runs, where each run represents the field distribution after 2 sinusoidal cycles of excitation of an individual dipole pair while the three unexcited dipole pairs are left open-circuited. Figure 1c shows the computed electric field pattern corresponding to the case of Figure 1b, with the exception that the dipole pairs have their center-gaps short circuited. It is clear that Figs. 1a and 1c are very similar. In fact, detailed analysis of the data indicates point-by-point agreement of the fields of Figs. 1a and 1c to 3 decimal places.

5 Demonstration of Superposition of the FD-TD Computed Fields of the Monopole Phased Array Using Resistive Sources

Here, the goal of our simulations is to provide theoretical support for the experiments performed at Lincoln Laboratory in phased-array technology for EM hyperthermia. These experiments are designed to focus a monopole phased array (MPA) to a point 2.5 cm deep in a muscle phantom.

The 915-MHz monopole phased array is shown in Figure 2. It consists of a semicircular metal disk hollowed out to form a cavity for 8 active monopole elements. The disk has an outer radius of 10.59 cm and an inner radius of 9.32 cm giving a wall thickness of 1.27 cm. The cavity can be viewed as a parallel-plate waveguide region (top and bottom plates of the disk) with a conducting back wall for the purpose of focusing the energy from the radiating elements towards the aperture of the applicator. The conducting back wall has a constant arc radius of 9.32 cm. The aperture is 2.54 cm wide by 18.64 cm long. The 8 active elements, each 1.27 cm long, penetrate through holes in one of the parallel plates, are positioned on an arc of radius of 8.66 cm centered at the center of the housing disk.

The cavity region of the housing of the monopole array applicator is filled with low-loss deionized or distilled water to provide impedance matching for the active array elements. The applicator is sealed with a solid dielectric cover. The muscle phantom is shown schematically in Figure 2b. It is a 15 x 36 x 13 cm box containing a saline solution having relative dielectric constant $\varepsilon_r = 50$ and electrical conductivity $\sigma = 1.3$ S/m.

The following results for the MPA show the validity of the linear superposition concept for FD-TD simulations with resistive sources. Figure 3 shows FD-TD computed electric fields along an H-plane cut parallel to the aperture of the MPA and 2.54 cm deep within the phantom. The squares depict fields for the phase-focused run wherein all elements are excited with a phase distribution selected to obtain maximum heating at the 2.54-cm depth. The circles depict the corresponding data points for the linearly superimposed results of 8 runs, where each run simulated the excitation of only one element at a time, leaving the 7 other elements unexcited but terminated in 50 Ω. There is excellent agreement of the two results even at the depths of the -30 dB nulls.

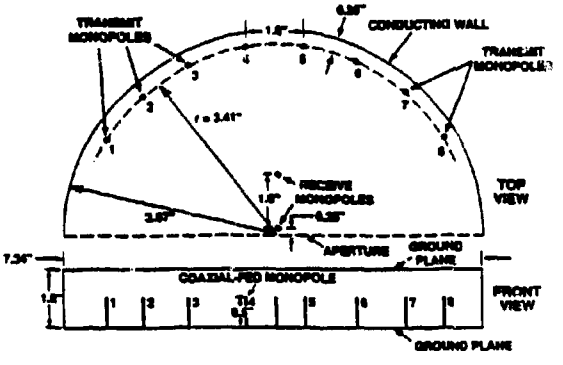

(a)

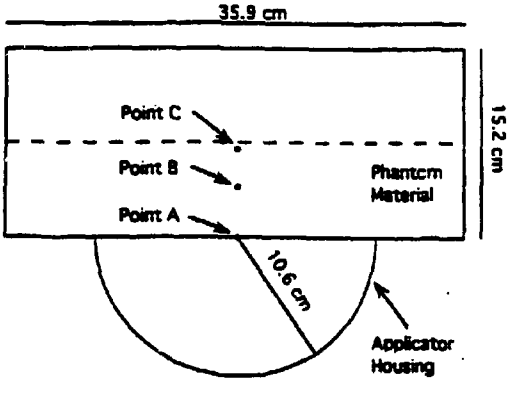

(b)

Figure 2 Schematic representation of the monopole phased array applicator showing the locations of the 8 active array elements (a). Schematic representation showing the dimensions of the muscle phantom material inside the plexiglas container with the monopole phased array applicator positioned below (b).

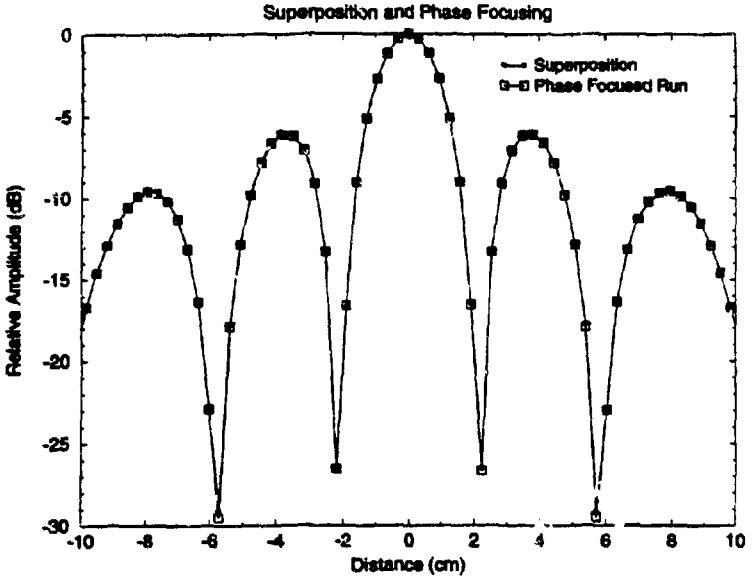

Figure 3 FD-TD computed electric field distributions in an H-plane cut of the monopole phased array, 2.54 cm deep into the phantom. Comparison of the results for all elements excited (squares) with additive superposition of the fields due to individual elements excited one at a time, and the remainder passive but terminated in 50 Ω (circles).

6 Conclusions

This work showed that the concept of linear superposition can be generalized from circuit theory to 3-D FD-TD simulations of phased array antennas. The presence of generator source resistance is accounted in a straightforward manner. It is believed that the linear superposition technique has broad applications in FD-TD-based pattern synthesis, adaptive nulling, and design of phased array systems. This procedure will be applied to a linear array antenna consisting of 8 crossed-pair Vivaldi flared horn antenna elements in the near future.

7 Acknowledgments

This work was supported in part by Cray Research Inc., ONR contract number N00014-93-0133, and the Department of the Air Force contract number F19628-90-C-0002.

8 References

[1] D. M. Sullivan, "Mathematical methods for treatment planning in deep regional hyperthermia," *IEEE Trans. Microwave Theory Tech.*, vol. 39, pp. 864-872, 1991.

[2] M. J. Piket-May, A. Taflove and J. Baron, "FD-TD modeling of digital signal propagation in 3-D circuits with passive and active loads," *IEEE Trans. Microwave Theory Tech.*, in press.

[3] A. J. Fenn, "Evaluation of adaptive phased-array antenna far-field nulling performance in the near-field region," *IEEE Trans. Antennas Propagat.*, vol. 38, pp. 173-185, 1990.

Radiation and Scattering from Curved Surface Scatterers with Stair-Cased FDTD

H. Scott Langdon* and Raymond J. Luebbers
The Pennsylvania State University
University Park, PA 16802

Results for FDTD calculations of radiation and scattering for some 2 and 3-dimensional canonical scatterers, with curved surfaces, will be presented. The objects are meshed using stair stepped, cubical FDTD cells. The FDTD results are compared with accepted values.

The authors hope to show that with care in meshing, the standard, simple, cubical FDTD mesh can yield good results for many shapes which include curved surfaces, at relatively low resolution, 20–30 cells/λ.

An examination of cylindrical and spherical objects meshed with different diameters shows marked changes in accuracy with a resolution change of only a few cells/λ. Comparative results with a 2-dimensional cylinder clearly show this change in accuracy.

It is possible to help account for the effects of partial filling of a cell volume by a dielectric scatterer by setting the constituitive parameters for that cell to a value between the values for the object and free space. A simple linear interpolation of the constituitive parameters is shown to improve the results. Some examples of curved and tilted surfaces are given which demonstrate this improvement. More accurate determination of the constituitive parameters, based on boundary conditions for the **E** and **H**-fields give better results.

Most of these techniques are simple and straightforward to use with a typical FDTD code. Computer time savings over more complicated methods, due to fewer computations per cell and to fewer cells needed for a given object may allow more intricate geometries to be modeled on a given computer.

Input Impedance, Radiation Pattern, and Radar Cross-Section of Spiral Antennas using FDTD

Christopher W. Penney* and Raymond J. Luebbers
Department of Electrical Engineering
The Pennsylvania State University
University Park, PA 16802

Abstract

A Finite-Difference, Time-Domain (FDTD) analysis of several spiral antennas was performed to calculate input impedance, antenna gain and scattering patterns. Broadband input impedance calculations were performed on an equiangular spiral slot antenna and compared to measured results [1]. Data from Finite Element calculations [2, 3, 4] of a square Archimedean spiral with a cavity backing was used for comparison to FDTD radiation gain pattern and RCS versus incidence angle computations.

Introduction

FDTD input impedance calculations were performed using a computer code developed at the Pennsylvania State University (PSU). This code uses a total field formulation and approximates the feed of the antenna by applying an electric field between two input terminals. The input electric field and resulting loop of magnetic fields are saved by the FDTD program and the input impedance is found by Fourier Transforming these values and dividing them. This gives the input impedance over a broad frequency range, necessary when dealing with spiral antennas.

The equiangular spiral slot antenna used for the input impedance calculations has an arm length of 42.3 cm and a rate of expansion of 30.3 cm/radian. The feedpoint separation is 0.5 cm and the ratio of the inner to outer radii of the arms is 0.75. The FDTD approximation of this antenna uses cubical cells measuring 0.1 centimeters on a side for a resolution at the maximum frequency of 40 cells/wavelength. The input impedance for the antenna has been measured to be approximately 80 + j0 Ω over a frequency range of 0.75 to 2.5 GHz [1]. A modulated Gaussian pulse was used as the input waveform for the FDTD simulation so that the spectrum of input frequencies would span the entire operating range of the antenna without introducing frequencies below the low frequency cutoff. This was necessary to avoid energy being trapped on the antenna and causing unwanted resonances.

The antenna used for the FDTD radiation and scattering computations was a 2.8125 cm square Archimedean spiral antenna mounted in a large conducting ground plane above a cavity. The cavity was both air-filled (0.9375 cm deep) and absorber-filled (2.7375 cm deep with a 0.9375 cm separation layer below the antenna and three 0.6 cm thick layers of absorber). Further calculations were performed on the absorber-filled cavity configuration with 1.0 Ω/square and 5.0 Ω/square resistive sheets covering the aperture of the antenna. The FDTD approximation of this antenna

used cubical cells measuring 0.09375 cm on a side for a minimum resolution of 70 cells/wavelength. A timestep of 1.8 ps (also the Courant limit) was used for all FDTD calculations on this antenna.

Results

The FDTD feedpoint current calculated on the equiangular spiral antenna used for the impedance results was completely converged after 1500 timesteps with the timestep size at the Courant limit of 1.93 ps (Figure 1). The resulting impedance plots varied slightly from the measured values (approximately 180 + j0), but did display the broadband behavior desired (Figure 2). The FDTD radiation pattern calculations used the same total field formulation of the input impedance, but the far-zone radiation patterns were calculated by saving the complete time record of the tangential electric fields in the aperture. These aperture electric fields are then Fourier transformed to give the complex tangential magnetic currents in the aperture. These currents can then be used to compute the radiation gain pattern at any frequency in any plane above the ground plane of the antenna [5]. Figure 3 displays FDTD results for the radiation patterns in the $\phi = 45$ plane (diagonal of the square) of the air-filled cavity backed antenna at 4.5 GHz. Very good agreement is shown between FDTD and the Finite Element-Boundary Integral [4] computations for this antenna.

Scattering was performed using an FDTD code modified for apertures above large ground planes [6]. The complete time records of the tangential aperture electric fields are saved and converted to the far-zone in the same manner used for radiation. Figure 4 shows a comparison of the FDTD and FE-BI [4] computations of RCS versus incidence angle for the air-filled cavity backed antenna in the $\phi = 45$ plane at 4.5 GHz with a θ-polarized Gaussian incident plane wave. Good agreement was found for all cases tested with better agreement in the calculations with resistive sheets covering the aperture.

Conclusions

This paper has shown that FDTD can be used for computing broadband antenna impedance, radiation patterns and radar cross-section. The results shown are for spiral antennas but can be extended to other types of antennas.

Acknowledgement

The authors would like to thank Dr. John Volakis of The University of Michigan for his assistance during this study. His results for the square spiral antenna, and his suggestions and comments, were extremely helpful in providing verification of the FDTD scattering and radiation results presented here.

References

[1] J. D. Dyson, "The equiangular spiral antenna," *IRE Trans. Antenna Propagat.*, vol. 7, pp. 181–187, April 1959.

[2] J. M. Jin and J. L. Volakis, "A hybrid Finite Element method for scattering and radiation by microstrip patch antennas and arrays residing in a cavity," *IEEE Trans. Antennas Propagat.*, vol. 39, pp.1598–1604, Nov. 1991.

[3] J. M. Jin, J. L. Volakis, C. L. Yu and A. C. Woo, "Modeling of resistive sheets in Finite Element solutions," *IEEE Trans. Antennas Propagat.*, vol. 40, pp. 727–731, June 1992.

[4] J. L. Volakis, J. Gong and A. Alexanian, "Electromagnetic scattering from microstrip patch antennas and spirals residing in a cavity," Accepted for publication in *Electromagnetics*.

[5] C. A. Balanis, *Advanced Engineering Electromagnetics*, Wiley, 1990.

[6] R. J. Luebbers and C. W. Penney, "Scattering from apertures in infinite ground planes using FDTD," *IEEE Trans. Antennas Propagat.*, accepted for publication.

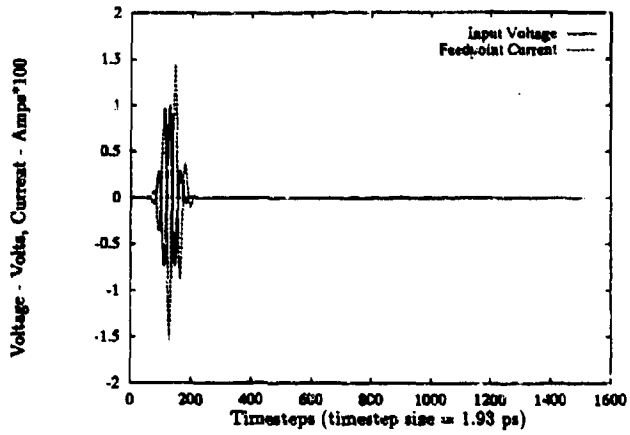

Figure 1: FDTD input voltage and current response for equiangular spiral slot antenna.

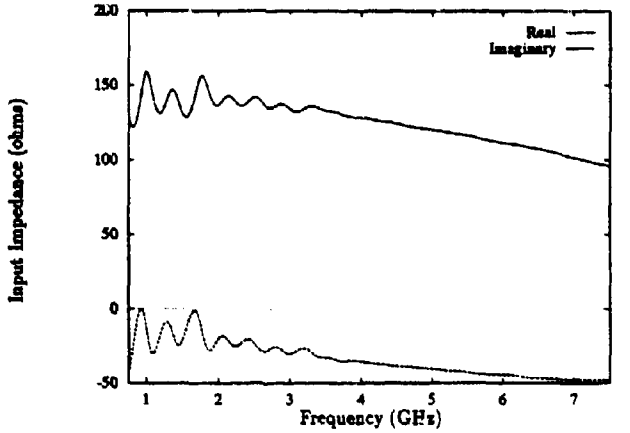

Figure 2: FDTD input impedance for equiangular spiral slot antenna. Measured value at approximately 80 + j0 Ω from 0.75 to 2.5 GHz.

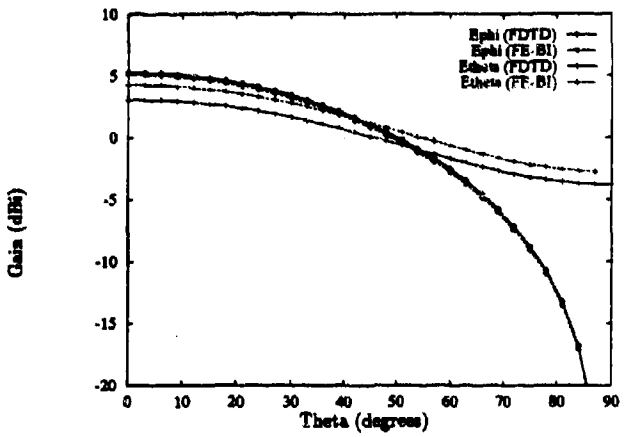

Figure 3: FDTD and FE-BI radiation gain patterns for square spiral antenna with air-filled cavity backing in $\phi = 45$ plane at 4.5 GHz.

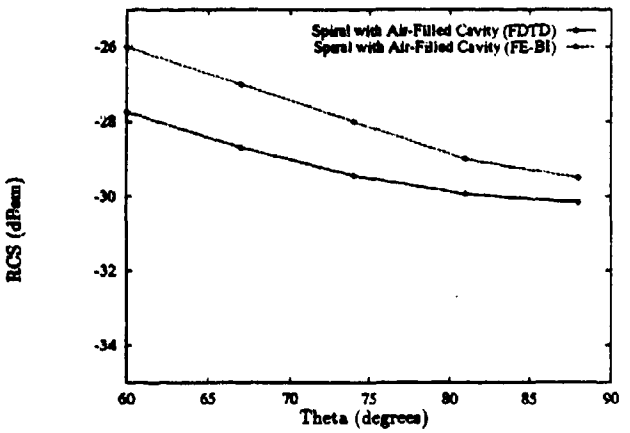

Figure 4: FDTD and FE-BI RCS versus Incidence Angle for square spiral antenna with air-filled cavity backing in $\phi = 45$ plane at 4.5 GHz. The incident plane wave was a θ-polarized, modulated Gaussian pulse.

FDTD SIMULATION OF AN OPEN-ENDED METALLIZED CERAMIC PROBE FOR BROADBAND HIGH-TEMPERATURE DIELECTRIC PROPERTIES MEASUREMENTS

Magdy F. Iskander, Shane Bringhurst, and Paul Gartside
Electrical Engineering Department
University of Utah
Salt Lake City, UT 84112

ABSTRACT

Open-ended coaxial probes have been conveniently used for broadband dielectric properties measurements for several years. A commercial probe and associated calibration and measurement software are now available from Hewlett-Packard Company. Several mathematical models for calculating the dielectric properties of materials from measured input impedance values are also available. In conjunction with our ongoing research activities in the area of microwave processing of materials and, in particular, in the microwave sintering of ceramics, we found it necessary to make dielectric properties measurements at temperatures as high as 1000°C. Available high-temperature procedures based on cavity perturbation methods are relatively narrow band and metallic coaxial probes are not suitable for these high-temperature measurements. This is not only because of the differential thermal expansion of the center and outer conductors in coaxial metallic probes, which make carrying out the probe calibration difficult, but also because metallic probes require long cooling sections to minimize heat transfer to measurement equipment (e.g., network analyzer).

We have developed a new metallized ceramic coaxial probe for broadband, high-temperature dielectric properties measurements. To help optimize the design of the probe and, in particular, to: develop a design that would increase the penetration of fields in samples under test, improve the probe sensitivity to variation in properties of a larger class of materials, and help determine the required minimum thicknesses of various samples for obtaining accurate results, we modeled and simulated the probe performance using the Finite-Difference Time-Domain (FDTD) method. A TEM mode was excited in the coaxial feed, and one end of the probe was terminated by an absorbing boundary. The sample under test was placed at the other end of the probe.

Numerical and graphical results illustrating the obtained FDTD results will be described and some of the identified guidelines regarding suitable probe design and sample dimensions will be discussed. Experimental results of broadband and high-temperature dielectric properties measurements will also be presented.

INTRODUCTION

Broadband dielectric property measurements are generally important in characterizing the atomic and molecular structure of materials. In the new and emerging technology of microwave processing of materials (including sintering of ceramics, curing of polymers, and remediation of hazardous waste), it is also important that these measurements be made as a function of temperature that sometime reaches as high a value as 1000°C. Data obtained from these measurements are used to support the numerical modeling and simulation activities as well as to characterize the absorption characteristics of ceramic polymers and glass materials during heating. Issues such as sample/insulation compatibility, and parameters involved in optimizing the heating process, may also benefit from the results of these

measurements. In particular, the dielectric behavior of samples may play a role in controlling the heating process and the possible prevention of problems such as the thermal runaway.

High-temperature dielectric properties, however, are only known for a limited number of materials and there are serious frequency gaps in the available dielectric property database. It is therefore crucial to develop adequate devices and testing procedures that would facilitate making these measurements accurately and on a routine basis [1-2]. Because of thermal expansion problems often encountered in making high-temperature dielectric properties measurements using metal probes, we have developed a novel metallized ceramic open-ended coaxial probe for making broadband dielectric property measurements for temperatures up to 1000°C. Dielectric properties measurements are made by placing the dielectric sample in contact with the open end of the coaxial dielectric probe. The analysis procedure assumes a sample under test of infinite thickness.

To help us design, optimize, and effectively use the developed dielectric probe, we simulated the probe performance using FDTD. Parameters such as minimum thickness of a sample, optimum probe dimensions in a given frequency range, and the role of a ground plane in improving the performance of the probe can be better understood using results from the FDTD simulations. In this paper, we will describe the probe design and operation, and graphically show some of the FDTD results that demonstrate the probe performance.

PROBE DESIGN

The more important design parameters of the proposed open-ended coaxial probe include: a good, broadband impedance matching at the junction connector, and an ability to carry out accurate and reproducible calibration procedures over a reasonably broad frequency band, and for temperatures as high as 1000°C. Therefore, instead of designing a special connector that fits the desired dimensions of our probe, we tested several commercially available connectors that may be easy to modify to fit the desired dimensions of the probe. To facilitate routine metallization procedures and to minimize possible excessive heating of the connector, a coaxial probe with the dimensions shown in Fig. 1 was designed.

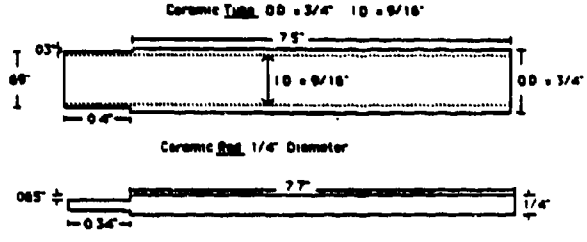

Fig. 1. Dimensions of the open-ended coaxial probe design for broadband dielectric measurements (500 MHz to 3 GHz) for temperatures up to 1000°C.

A GR-to-N type connector was selected to connect the designed probe to the standard accessories of a network analysis system. The broadband performance of the GR-to-N type connector was tested using time-domain gating and frequency to time-domain analysis capabilities of the HP8510B Network

Analyser. The inner and outer conductors of the GR half of the connector were removed, and a new adapter was machined to facilitate connecting the center and outer conductors of the probe to the N connector.

The metallized probe was fabricated of a standard alumina (Al-99) tube and center conductor rod. The alumina coaxial probe was machined to the design specifications. The diameters of the center and outer conductors were 6 mm and 11 mm, respectively. The probe was then metallized at Westgo Inc. The metallization was accomplished by painting the ceramics with a moly-manganese paint and then firing them at high temperatures in a controlled atmosphere (e.g., argon-hydrogen). The moly-manganese metallization is about 1 mil thick, and a protective layer of nickel plating with a thickness of about 0.1 mil was also added.

Using this metallization procedure, it was possible to repeatedly heat the probe up to 1000°C in a hydrogen environment without cracks or peel. Obtained input admittances of the probe, for a short, at 25°C and 1000°C are shown vs. frequency in Fig. 2. From these obtained results, it is clear that a successful metallization procedure has been achieved and the designed probe is adequate for complex permittivity measurements in the frequency range from 500 MHz to 3 GHz and at temperatures up to 1000°C.

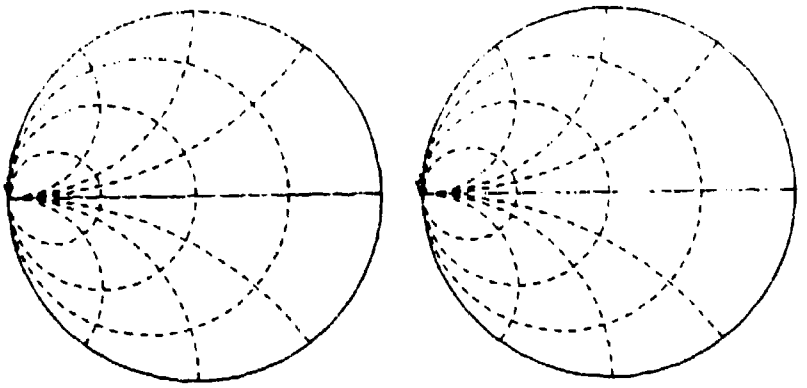

(a) (b)

Fig. 2. Input admittance of the designed metallized ceramic dielectric probe as a function of temperature. It can be seen that the short stays almost constant as the temperature increases from room temperature to 1000°C in the frequency range of 500 MHz to 3 GHz. (a) Room temperature (25°C); (b) 1000°C.

FDTD SIMULATION OF PROBE PERFORMANCE

As indicated earlier, FDTD simulation of the probe performance is necessary to optimize the design of the probe in a given frequency band. It will also help better identify a suitable sample thickness for a given dielectric material that maintains the validity of the assumption of an infinitely thick sample and further examine and quantify the effect of some commonly encountered experimental errors such as the probe contact with the sample.

The FDTD simulation was simply achieved by modifying an FDTD code available in our department. Modifications include the placement of a TEM field as an excitation which is located approximately three wavelengths from the open end of the probe, while the other end was terminated by a first-order Mur absorbing boundary condition. A forward direction (towards the open end) TEM wave was launched at the excitation plane, and field distributions in the coaxial probe and the sample were calculated using a standard Yee cell procedure. From the calculated fields, both the current on the center conductor ($\oint \bar{H} \cdot d\bar{l} = I$) and the potential difference between the coaxial conductors ($\int \bar{E} \cdot d\bar{l} = V$) are calculated and hence used to determine the input impedance of the probe. This input impedance calculation procedure is compared with rigorous analysis of the probe admittance when placed in direct contact with a dielectric sample [3].

FDTD RESULTS

Figure 3 shows some of the obtained FDTD results of the field distribution in the coaxial probe and sample under test. The figure shows the FDTD results for four different samples including alumina, deionized water, methanol, and teflon. From Fig. 3 it is estimated that the fields do not penetrate completely through the water and methanol samples, thus satisfying the infinite sample criteria. In the alumina sample, the fields penetrate very well in the first couple of mm and then manage to completely penetrate the whole sample. In the teflon sample, the fields easily penetrate through half of the sample (7 mm) and then continue to penetrate the rest of the sample. Therefore, it is estimated that the alumina sample should be about 17-18 mm to satisfy the infinite sample criteria and the teflon sample should be about 20 mm thick. These results were calculated at 2.45 GHz.

These, as well as many other FDTD and experimental results, will be presented. It is generally believed that we have achieved a successful metallized probe design, and the FDTD simulation has significantly enhanced our ability to understand and further optimize the probe performance in a given frequency band and for a typical class of dielectric materials.

REFERENCES

1. O. A. Andrade, M. F. Iskander, and S. Bringhurst, "High Temperature Broadband Dielectric Properties Measurement Techniques," in *Microwave Processing of Materials III*, R. L. Beatty, W. H. Sutton, and M. F. Iskander, eds. Materials Research Society Symposium Proceedings 269, 1992, pp. 527-539.

2. S. Bringhurst, O. A. Andrade, and M. F. Iskander, "High-Temperature Dielectric Properties Measurements of Ceramics," in *Microwave Processing of Materials III*, R. L. Beatty, W. H. Sutton, and M. F. Iskander, eds. Materials Research Society Symposium Proceedings 269, 1992, pp. 561-568.

3. H. Levine and C. H. Papas, "Theory of the Circular Diffraction Antenna," *Journal of Applied Physics*, Vol. 22, No. 1, 1951.

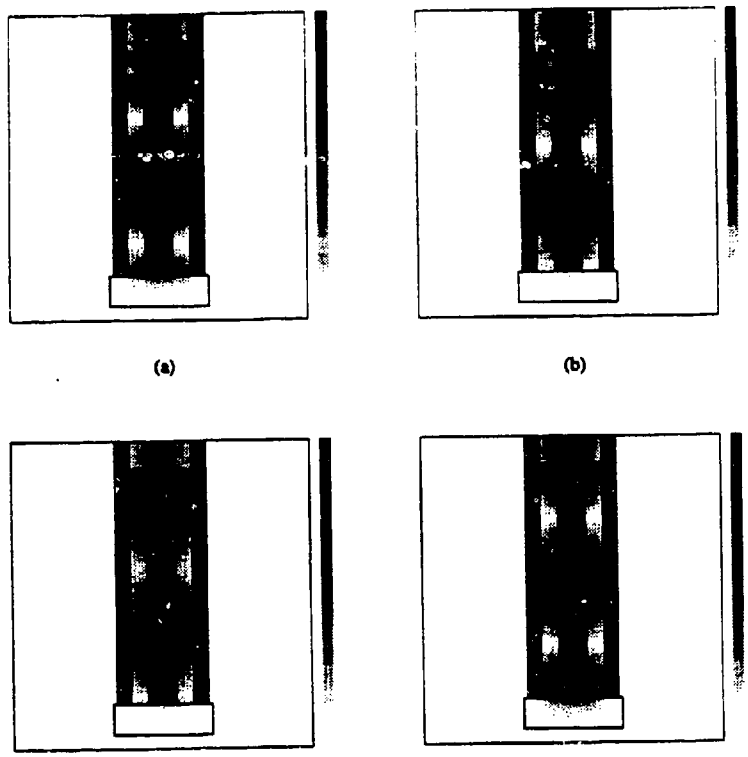

Fig. 3. Electric field distribution in the high-frequency coaxial probe and the sample. The results were obtained using FDTD calculations at f = 2.45 GHz. (a) Alumina sample; (b) deionized water; (c) methanol; (d) teflon.

FDTD SIMULATION OF RF DRYING AND INDUCTION HEATING PROCESSES

Magdy F. Iskander, Paul Gartside, Mikel White
Electrical Engineering Department
University of Utah
Salt Lake City, UT 84112

and

Christopher J. Markey
Corning, Inc.
Celpro Development - EJ 114
Corning, NY 14831

ABSTRACT

Radiofrequency (RF) drying and induction heating have been in industrial use for over 20 years. Relatively simple electrode and coil designs provided satisfactory results in many manufacturing facilities. As ceramic products continue to invade new markets and continue to be used in new hi-tech applications, more delicate drying and firing processes are often required. Business economics often demand drying at faster rates, which makes achieving the required uniformity of the drying process at economically viable rates very challenging. More sophisticated designs of the heating systems are required, and improved controls of drying systems are becoming essential.

In this paper, we use the Finite-Difference Time-Domain (FDTD) method to simulate RF drying and induction heating systems. The FDTD code was used to model realistic electrode designs and to investigate procedures for improving the uniformity, speed, and efficiency of heating relatively large-sized products. The effect of the product shape, type of material, and location and orientation between the electrodes of an RF dryer were simulated, and efforts are underway to provide guidelines towards increasing the efficiency and heating uniformity in existing dryers. A variety of options in feeding the RF heating electrodes was also simulated and their performance evaluated.

Similar simulations were made to help investigate ways and means for improving the performance of the induction heating process. In addition to the role of the geometrical and type of material factors in the heating process, the FDTD simulation was extended to include the optimization of the coil design and the operating frequency to increase the speed and improve the uniformity of the induction heating process. FDTD simulation is also intended to examine the effectiveness of the induction heating process in drying non-magnetic materials.

Results of these FDTD simulation efforts will be shown and described, and some guidelines that may help improve the performance and increase the efficiency of RF drying and induction heating systems will be discussed.

INTRODUCTION

Computer modeling and simulation of microwave processing systems provide significant advantages that are expected to play an important role in the development, scale-up, and effective utilization of radiofrequency heating technology. These advantages include the following:

1. Understanding of the physical aspects of RF [1] interaction with materials. Radiofrequency heating is a complex process, and computer modeling may help identify the role of materials properties, dimensions, input power, heating rates, etc. on the effective use of RF heating procedures.

2. Design, characterization, and optimization of the various RF drying and processing systems. Several RF processing systems -- including RF dryers and induction heating systems -- are presently available, and the selection and/or the design of the most suitable one for a specific application presents one of the challenges. Furthermore, characterization and evaluation of the performance of a specific design are crucial in performing controlled and reproducible heating.

3. Development of effective training and continued education in this highly interdisciplinary area. It is broadly accepted that visualization and animations based on computer simulation are important in providing effective training procedures.

It may be noted that for accurate and, in particular, experimentally relevant computer simulation, not only are adequate computer model and simulation analysis capabilities required, but also knowledge of the thermophysical properties of materials (including dielectric properties) and their variation with temperature and frequency is needed. With the availability of high-performance computers and three-dimensional modeling software, however, required materials properties should be measured, and more efforts need to be focused on the simulation, design, and optimization of RF processing systems.

This paper describes the use of FDTD simulation in modeling various aspects of RF heating of materials. Examples illustrating results from simulation of various heating systems, including RF dryers and induction heating systems, will be presented.

FINITE-DIFFERENCE TIME-DOMAIN METHOD AND EXAMPLES

Several analytical and numerical solutions are available and can be used to model RF processing systems [2-6]. Our efforts at the University of Utah, however, are focused on using the finite-difference time-domain (FDTD) method. An iterative solution of Maxwell's curl equations in both time and space, FDTD can be used to determine both the dynamic behavior of the heating process and also the steady-state values of the electromagnetic power deposition pattern in the sample and in the surrounding insulation. FDTD has also been shown to provide a suitable, accurate procedure for modeling inhomogeneous and electrically large objects of complex geometries [7]. These features are certainly important in simulating realistic heating experiments. The following will describe examples of applying FDTD to the modeling of some RF heating systems.

FDTD Simulation of RF Drying Process

For this simulation, we used several models of electrode dryers including the one shown in Fig. 1. A coaxial line is used to feed the RF energy, and the end tapers are used to limit the leakage of the RF radiation. The drying zone is basically beneath the central electrode fed by the coaxial line. Ceramic ware is placed on dielectric trays and carried through the dryer on a conveyer belt. The FDTD solution procedure involves placing an excitation plane along the coaxial feed, a first-order absorbing boundary

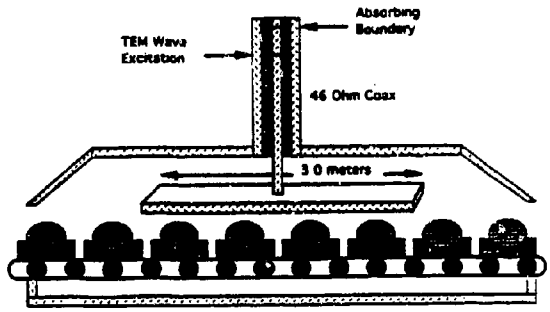

Fig. 1. Schematic diagram of an RF drying system.

at one end, and the drying electrode arrangement at the other end. The FDTD is then used to determine the steady-state RF field distributions in the dryer. The effects of parameters such as the sample shape, size, properties, location, orientation, and aspects of placement of multiple samples on the uniformity of drying and on the overall efficiency of the drying process are then examined. Figure 2 shows example results for samples of three different shapes. From this figure it may be seen that the most uniform heating may be achieved when elliptical ware is used and placed vertically parallel to the electric field. All presented results are at 25 MHz. Figure 3 shows the field distribution along the conveyer belt when the electrodes were separated by two different distances 12" and 15". In this figure, the dielectric properties of the ceramic ware were varied along the conveyer belt to simulate wet ware at one end and dry ware at the other end. Figure 4 shows the field distribution around the stub (coil) region. Figure 5 shows the FDTD field distribution in the coaxial feed and electrode area. These stubs are often used in practice to improve field uniformity along the dryer. These as well as other results illustrating the characteristics of various dryers and procedures to improve uniformity and efficiency of the drying process will be shown and described.

FDTD Simulation of Induction Heating

Although it may seem that the induction heating process has been well understood for many years, the application of this procedure in the delicate drying process of non-metallic and non-magnetic materials is challenging. Parameters such as the coil pitch and its effect on the magnitude of the axial E-field distribution that significantly contribute to uniformity of drying in the coil need to be examined. Also, the role of frequency on uniformity of resulting heating patterns as well as an optimum sample/coil diameter ratio that needs to be used to improve the uniformity of heating need to be studied.

We used FDTD simulation to study various important aspects of induction heating. The solution procedure in this case involves placing an excitation voltage at the two terminals of the coil and employing the Yee cell to calculate the various components of the electric and magnetic fields throughout the computation domain. Absorbing boundaries were placed outside the coil to limit the computation domain. Example results are shown in Figs. 6-8. While Fig. 6 shows marked

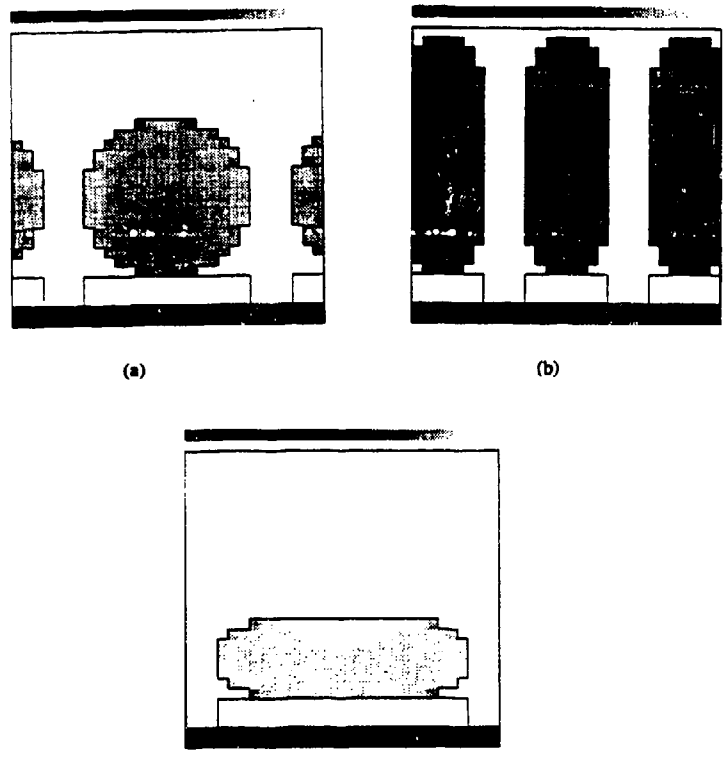

Fig. 2. FDTD results illustrating the electric field distribution in ceramic ware of different geometries. (a) Spherical ware; (b) elliptical ware placed vertically; (c) elliptical ware placed horizontally.

improvement in the uniformity of heating when a frequency around 25 MHz is used, Fig. 7 shows that increasing the coil pitch from 2" to 4" helps improve the uniformity of heating in the sample. Figure 8 shows results of employing multiple samples, where it is expected that separation distance between samples plays an important role in improving the drying pattern.

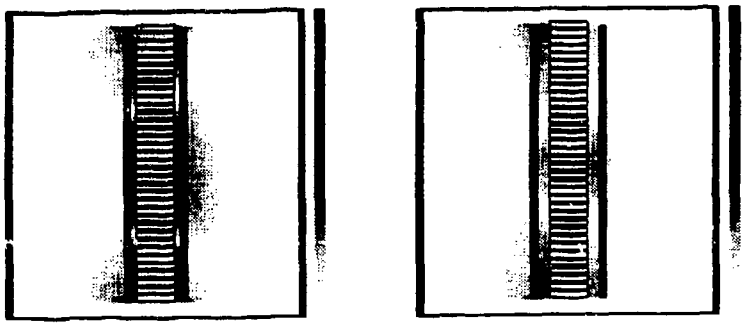

(a) (b)

Fig. 3. Field distribution along the axis of the dryer for two separation distances between the electrodes. Dielectric properties were varied from $\epsilon' = 25$, $\sigma = 0.04$ (wet ware) to $\epsilon' = 5$, $\sigma = 0.00$ (dry ware) along the dryer. (a) Electrode separation 12"; (b) electrode separation 15".

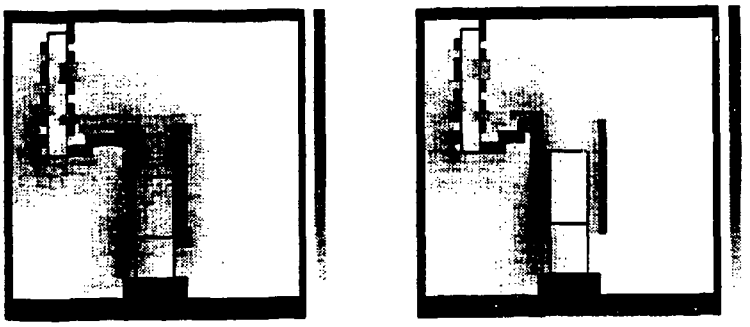

(a) (b)

Fig. 4. Field distribution around the electrodes and the stubs (coils) for two different separation distances. Stubs are often used to improve field distribution along electrodes. (a) Electrode separation 12"; (b) electrode separation 15".

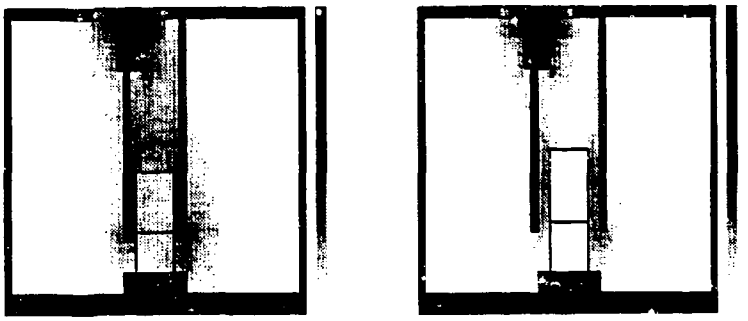

(a) (b)

Fig. 5. Field distribution around the feed coaxial line and the electrodes. (a) 12" separation; (b) 15" separation.

These, as well as many other results illustrating characteristics of induction heating systems, will be shown and described.

CONCLUSIONS

FDTD modeling and numerical simulation provide valuable tools for addressing various aspects of RF processing of materials. They help in understanding the physical aspects of RF interaction with materials, in examining issues involved in the dynamic heating process and in heating multiple samples, and in simulating, evaluating, and controlling the performance of different RF processing systems. Examples presented here have illustrated the application of FDTD in simulating heating systems for RF dryers and induction heating. FDTD results also are being used in conjunction with a 3-D finite-different heat transfer code to develop a dynamic model for calculating temperature distribution patterns in samples during heating.

ACKNOWLEDGMENTS

This work is a compilation of efforts by many individuals and is supported by two sponsors: Hal Kimrey of Oak Ridge National Laboratory and Chris Malarkey of Corning, Inc. The authors are indebted to them for their technical contributions and the financial support of their institutions. Graduate students working on this project include Tom Reed, Dan Roper, Shane Bringhurst, and Zhenlong Huang. Undergraduate Engineering Clinic students working on the project supported by Oak Ridge National Laboratory also contributed to this work. This work is supported by Corning, Inc. and the Oak Ridge National Laboratory (Metals and Ceramic Division) under the auspices of the Advanced Industrial Concepts Program.

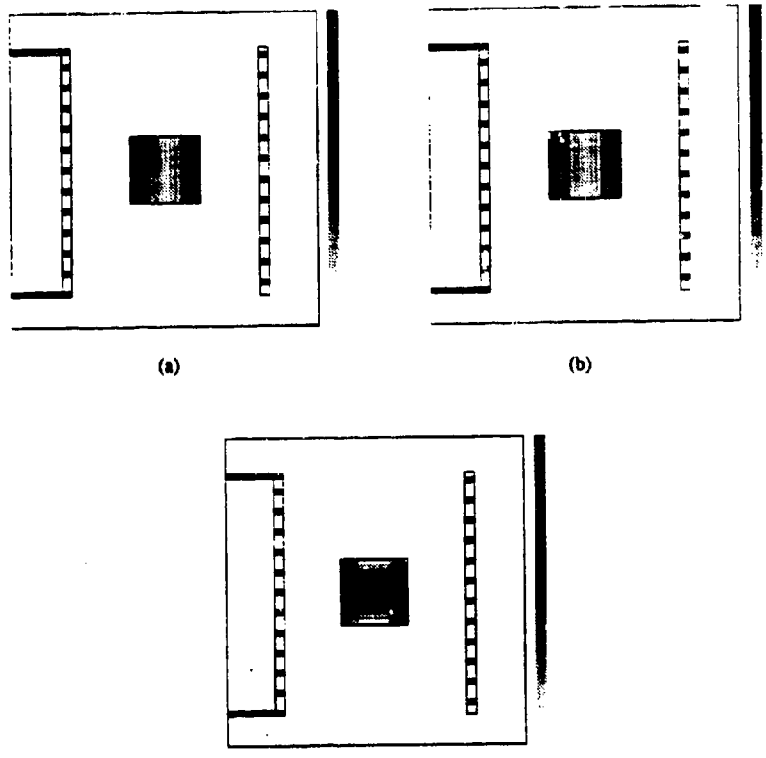

Fig. 6. FDTD results illustrating the role of frequency on improving the uniformity of heating using induction coils. (a) 300 kHz; (b) 2 MHz; (c) 25 MHz.

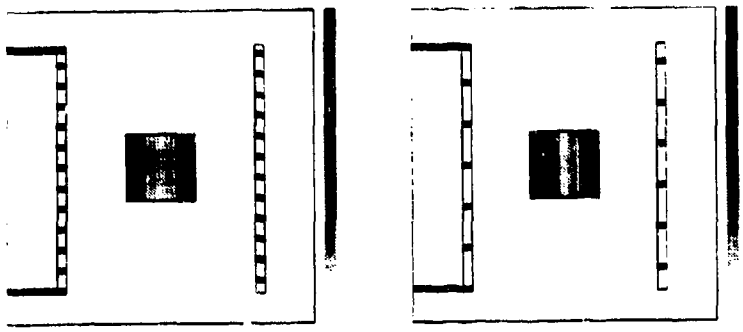

Fig. 7. FDTD results illustrating the fact that changing the coil pitch from 2" to 4" helped improve the uniformity of heating. Results are shown at 2 MHz. (a) Results for 2" pitch; (b) results for 4" pitch.

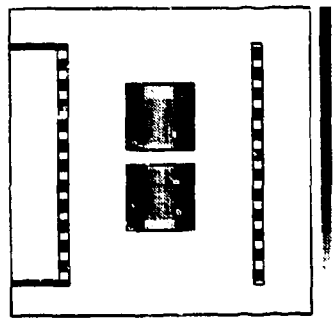

Fig. 8. FDTD results when multiple samples are placed inside the heating coil. The coil diameter is 10" and the operating frequency is 2 MHz. The sample/coil diameter ratio is 1/3.

REFERENCES

1. M. F. Iskander, O. Andrade, A. Virkar, and H. Kimrey, "Microwave Processing of Ceramics at the University of Utah -- Description of Activities and Summary of Progress," in *Microwaves: Theory and Application in Materials Processing*, D. E. Clark, F. D. Gac, and W. H. Sutton, eds. American Ceramic Society, Ceramic Transactions Vol. 21, 1991, pp. 35-48.

2. P. Chaussecourte, J. F. Lamaudiere, and B. Maestrali, "Electromagnetic Field Modeling of a Loaded Microwave Cavity," in *Microwave Processing of Materials III*, R. L. Beatty, W. H. Sutton, and M. F. Iskander, eds. Materials Research Society Symposium Proceedings 269, 1992, pp. 69-74.

3. C. Lorenson and C. Gallerneault, "Numerical Methods for the Modelling of Microwave Fields," in *Microwaves: Theory and Application in Materials Processing*, D. E. Clark, F. D. Gac, and W. H. Sutton, eds. American Ceramic Society, Ceramic Transactions Vol. 21, 1991, pp. 193-200.

4. B. Manring and J. Asmussen Jr., "Electromagnetic Modeling of Single-Mode Excited Material Loaded Applicators," in *Microwaves: Theory and Application in Materials Processing*, D. E. Clark, F. D. Gac, and W. H. Sutton, eds. American Ceramic Society, Ceramic Transactions Vol. 21, 1991, pp. 159-166.

5. M. Barmatz and H. W. Jackson, "Steady State Temperature Profile in a Sphere Heated by Microwaves," in *Microwave Processing of Materials III*, R. L. Beatty, W. H. Sutton, and M. F. Iskander, eds. Materials Research Society Symposium Proceedings 269, 1992, pp. 97-103.

6. M. F. Iskander, "Computer Modeling and Numerical Techniques for Quantifying Microwave Interactions with Materials," in *Microwave Processing of Materials II*, W. B. Snyder Jr., W. H. Sutton, M. F. Iskander, and D. L. Johnson, eds. Materials Research Society Symposium Proceedings 189, 1991, pp. 149-171.

7. P. C. Cherry and M. F. Iskander, "FDTD Analysis of Power Deposition Patterns of an Array of Interstitial Antennas for Use in Microwave Hyperthermia," *IEEE Transactions on Microwave Theory and Techniques*, Vol. 40, August 1992, pp. 1692-1700.

A Generalized Finite-Volume Algorithm for Solving the Maxwell Equations on Arbitrary Grids

Yen Liu
NASA Ames Research Center
Moffett Field, CA 94035

I. Abstract

A finite-volume formulation based on arbitrary basis functions for time-dependent problems on general two- and three-dimensional structured and unstructured grids is developed. The method is applied to the volume integrals of the time-domain Maxwell equations. Discrete unknowns are thus volume integrals or cell averages of the electric and magnetic field variables. Spatial terms are converted to surface integrals using the Gauss curl theorem. Arbitrary sets of basis functions are introduced in constructing local representations of the fields and evaluating the volume and surface integrals. Electric and magnetic fields are approximated by linear combinations of these basis functions. Unlike other unstructured formulations used in Computational Fluid Dynamics, the new formulation actually does not reconstruct the field variables at each time step. Instead, the spatial terms are calculated in terms of unknowns by precomputing weights as functions of cell geometry and basis functions to retain efficiency. The formulation is suitable for arbitrarily defined grids, either smooth or unsmooth. A centered scheme is applied in the interior, while an upwind matching scheme is employed at material interfaces and the Engquist-Majda non-reflecting boundary condition is implemented at the numerical outer boundaries. The staggered leapfrog scheme and the Runge-Kutta methods are utilized for the time integration. This new formulation is capable of achieving any order of accuracy on arbitrary grids. Several model electromagnetic scattering problems are computed and compared with analytical solutions. Examples are given for cases based on 0th to 3rd degree polynomial basis functions.

II. Finite-Volume Formulation

Governing Equations

The time-domain Maxwell equations in their vector form can be written as

$$\frac{\partial \mathbf{F}}{\partial t} + \nabla \times \mathbf{I} = -\mathbf{J}, \tag{1}$$

where

$$\mathbf{F} = \begin{bmatrix} \mathbf{D} \\ \mathbf{B} \end{bmatrix} \tag{2a}$$

contains the electric displacement and magnetic induction vectors (also referred as the electric and magnetic flux density vectors),

$$\mathbf{I} = \begin{bmatrix} -\mathbf{H} \\ \mathbf{E} \end{bmatrix} \tag{2b}$$

contains the magnetic and electric intensity vectors, and

$$\mathbf{J} = \begin{bmatrix} \mathbf{J} \\ \mathbf{0} \end{bmatrix} \tag{2c}$$

contains the electric current density vector. The vectors $\mathbf{D}$ and $\mathbf{H}$ are related to $\mathbf{E}$ and $\mathbf{B}$ by the constitutive relations

$$\begin{aligned} \mathbf{D} &= \epsilon \mathbf{E} \\ \mathbf{B} &= \mu \mathbf{H}, \end{aligned} \tag{3}$$

where ϵ is the permittivity and μ is the permeability of the material. The electric current density $\mathbf{J}$ is related to the electric intensity $\mathbf{E}$ by

$$\mathbf{J} = \sigma \mathbf{E}, \tag{4}$$

where σ is the electric conductivity of the material. Here we assume the problem is linear and all the properties are not functions of the fields.

General Properties of Grids

The Maxwell equations can be solved numerically based on the integral form of Eqs. (1). One first generates a grid which consists a set of discrete points and a set of lines or curves connecting the points. The connecting lines or curves must be chosen in a way that divides the region into a set of contiguous, non-overlapping, space filling cells. The discrete points are then called cell vertices (or nodes), and the connecting lines or curves are called cell edges. The surfaces common to two neighboring cells are called cell faces. Each cell is enclosed by a combination of faces. The bounding curve of each face is formed by a combination of edges, and each edge connects two vertices. Every cell, face, edge, and vertex is assigned an index to identify itself. To complete the geometric description of a grid, one must also specify the shapes of the edges and faces.

A grid can be structured or unstructured based on the ordering of cells, faces, edges, and vertices. For structured grids, the indices for these geometric elements are ordered; given one index, the others can be determined implicitly. For unstructured grids, such an order does not exist, and some information must be given explicitly. A simple way is to store the indices of the vertices and the two neighboring ("left" and "right") cells for each face. All other information, such as indices of faces and vertices for each cell, can then be determined from it. A special case of structured grids, which is called a regular grid, is that all cells have exactly the same shape and volume. There are a few regular three-dimensional shapes known to crystallographers which are space-filling. Those include the hexahedron, tetradecahedron (truncated octahedron), hexagonal prism, rhombic dodecahedron, and elongated rhombic dodecahedron [1]. The most structured grid is one that is topological equivalent to a generalized curvilinear coordinate system, which consists of ordered arrays of hexahedra. An example of a commonly used unstructured grid is one consisting of non-ordered tetrahedra.

Integrating Eqs. (1) over each and every cell defines a generalized finite volume method. Recalling that the Gauss curl theorem converts a volume integral over a cell V_j to a closed surface integral over its faces S_{ji}, one thus obtains

$$\frac{\partial}{\partial t}\int_{V_j} \mathbf{F}\,dV + \sum_i \int_{S_{ji}} d\mathbf{S} \times \mathbf{I} = -\int_{V_j} \mathbf{J}\,dV. \tag{5}$$

Here the subscript j denotes a generic index for a cell and the subscript i denotes a generic index for a face. If coordinates are defined by some analytical, differentiable transformation, then these shapes could be taken to be portions of the exact coordinate lines and coordinate surfaces. However, this procedure generally does not increase the accuracy of interior schemes but only complicates the process in evaluating the volume and surface integrals. Since Eqs. (5) are valid for any cell shapes, it is therefore preferable to construct *simple shapes* for the surfaces and cells that could facilitate integrations involving those elements. The only possible exception would be for the edges and faces involving grid points on a prescribed, curved, solid boundary or material interface. In order to obtain high accuracy in the solution on such a boundary, one may be willing to carry out the more cumbersome integrations involving the curved elements, particularly since special procedures have to be involved to satisfy the boundary and interface conditions. Line, triangle, and tetrahedron are the most fundamental shapes of edge, face, and cell, respectively. Integrations over these fundamental shapes are relatively simple and for some cases can be exact. We notice that general polyhedron, polygon, and edge is a union of tetrahedra, triangles, and lines, respectively. Any volume integral over a polyhedron is equal to the summation of the volume integrals over each individual tetrahedron, any surface integral over a polygon is equal to the summation of the surface integrals over each individual triangle, and any line integral over a edge is equal to the summation of the line integral over each line element. In this paper we shall formulate our method on arbitrary grids, but emphasis will be given to general polyhedral grids. The formulation is suitable for either smooth or unsmooth grids. Except for the bookkeeping of indices, whether the grid is structured or unstructured is irrelevant to our formulation.

Unknown Variables and Piecewise Local Representations

To solve Eq. (5) numerically, one first defines the discrete unknown variables which are to be advanced in time. One then obtains a set of equations to solve for the discrete unknowns by converting the spatial terms in terms of the unknowns. There are two methods of defining the unknown variables – either as values at

discrete nodal points or as discrete volume integrals (or volume averages). In the first method, one defines the unknown variables at vertices. For high order formulations, unknowns must also be defined at extra points on the surfaces and/or inside the cells. The volume and surface integrals are evaluated by quadratures using quantities at these nodal points. Unfortunately, this procedure couples the nodal unknowns. Therefore, even explicit time integrations are effectively implicit. For a time-dependent problem, this can be very inefficient. In this paper we choose the volume integrals, denoted by the symbol $\bar{}$,

$$\bar{\mathbf{F}}_j \equiv \int_{V_j} \mathbf{F}(\mathbf{r})\, dV = \begin{bmatrix} \int_{V_j} \mathbf{D}(\mathbf{r})\, dV \\ \int_{V_j} \mathbf{B}(\mathbf{r})\, dV \end{bmatrix} \equiv \begin{bmatrix} \bar{\mathbf{D}}_j \\ \bar{\mathbf{B}}_j \end{bmatrix} \tag{6}$$

as the unknown variables. In order to evaluate the volume and surface integrals in Eq. (5) consistently, we introduce an arbitrary set of basis functions $\phi_m(\mathbf{r})$ and assume that each field variable can be expressed by a piecewise local representation in terms of linear combinations of these basis functions

$$\begin{aligned} \mathbf{D}_j(\mathbf{r}) &= \sum_m \mathbf{d}_{jm}\phi_m(\mathbf{r}) \\ \mathbf{B}_j(\mathbf{r}) &= \sum_m \mathbf{b}_{jm}\phi_m(\mathbf{r}). \end{aligned} \tag{7}$$

The type and number of basis functions chosen depend on the desired accuracy. The most common form for Eqs. (7) is as a spatial polynomial in which the $\phi_m(\mathbf{r})$ are tensor products of the position vector. Depending on the nature of problems, other classes of functions, such as splines, wavelets, trigonometric, exponential, or other special functions, may also be used as a basis set. Our formulations will be given in terms of arbitrary basis functions, but numerical examples will be restricted to the polynomial representation. We shall leave the study of other types of representations to future research.

Reconstruction and Interpolation

Once the basis functions have been chosen, the coefficients $\mathbf{d}_{jm}$ and $\mathbf{b}_{jm}$ in Eqs. (7) can then be determined in terms of the discrete unknowns in the neighborhood of the cell j. This process is normally referred to as reconstruction [2,3]. The neighborhood of a cell is defined as an assemble of its neighboring cells. The first hierarchical neighborhood of the cell j is itself. The second hierarchical neighborhood consists the cell j and all its immediate neighbors. An immediate neighbor of a cell can be a common-face neighbor, which shares a common face with the cell, or a common-edge or common-node neighbor, which shares one or more edges or nodes with the cell, respectively. The third hierarchical neighborhood includes the second neighborhood and the immediate neighbors of all cells in the second neighborhood. Higher levels of neighborhood are built recursively. The list of the neighborhood can be sorted by the distance between the centroids of the parent and neighboring cells. The stencil for reconstruction is then selected from the neighborhood. The selection can be symmetrically around the parent cell j, or can be directionally biased in terms of the materials or solution fields. One should avoid choosing a stencil that is across a material interface, since some field components and derivatives may be discontinuous at the interface.

For simplicity, here we use one component in Eqs. (7) to illustrate the reconstruction. Let $f_j(\mathbf{r})$ be a component of $\mathbf{F}_j(\mathbf{r}) = \begin{bmatrix} \mathbf{D}_j(\mathbf{r}) \\ \mathbf{B}_j(\mathbf{r}) \end{bmatrix}$ and c_{jm} a component of $\begin{bmatrix} \mathbf{d}_{jm} \\ \mathbf{b}_{jm} \end{bmatrix}$. The local representation can be written in a vector form

$$f_j(\mathbf{r}) = \sum_m c_{jm}\phi_m(\mathbf{r}) \equiv \boldsymbol{\phi}^T(\mathbf{r})\mathbf{c}, \tag{8}$$

where and $\boldsymbol{\phi}^T(\mathbf{r})$ and $\mathbf{c}$ are the row vector of $\phi_m(\mathbf{r})$ and the column vector of c_{jm}, respectively. Let $\mathcal{N}_j$ denote the list of indices of the reconstruction stencil for the cell j. Integrating Eq. (8) over all the cells in $\mathcal{N}_j$, one forms a linear system of equations for the cell j. If the number of reconstruction cells present in $\mathcal{N}_j$, NC, is equal to the number of basis functions NB, the coefficients c_{jm} can be determined from a standard linear system solver. For general unstructured grids, it is more likely that those numbers are not the same. If NC > NB, one then solves an over-determined minimization problem with respect to some chosen norm. If the l_2 norm is used, this is equivalent to a least squares problem

$$\mathbf{A}\mathbf{c} \cong \mathbf{f}, \tag{9}$$

where A is a rectangular matrix of size MC x MB whih elements

$$A_{nm} = \int_{V_k} \phi_m(\mathbf{r})\, dV \tag{10}$$

and f is a column vector of size MC with elements

$$f_n = \bar{f}_k. \tag{11}$$

Here the subscript $k = N_j(n)$ is the nth member in the reconstruction stencil for the cell j and the symbol $\simeq$ denotes a least squares problem. Techniques for solving a least squares problem are well known and can be found in standard textbooks (e. g. Refs. 4–5). Here we use the method of singular value decomposition, and the solution for the coefficients can be written as

$$\mathbf{c} = A^{+}\mathbf{f}, \tag{12}$$

where the symbol $^{+}$ represents the pseudo inverse of a rectangular matrix. Thus, the field can be reconstructed by a piecewise analytic function

$$f_j(\mathbf{r}) = \boldsymbol{\phi}^{T}(\mathbf{r})A^{+}\mathbf{f}. \tag{13}$$

Notice that the pseudo inverse does not always give a correct answer if the rank of A is less than MB. It is unclear at the present time what kind of norm should be minimized for this type of under-determined system. Therefore, in our study we choose the reconstruction stencil such that the rank of A is always greater than or equal to the number of basis functions used. It is also possible to build some constrains in the minimization process. The most common one is the preservation of the volume integral, i. e., the volume integral of the resulting reconstruction Eq. (13) matches $\bar{f}_j$. Procedures for solving constrained least squares problems are also given in Refs. 4–5. Once the flux density vectors $\mathbf{D}_j(\mathbf{r})$ and $\mathbf{B}_j(\mathbf{r})$ have been reconstructed, the functions of the intensity and current density vectors can then be expressed as

$$\begin{aligned}
\mathbf{E}_j(\mathbf{r}) &= \frac{1}{\epsilon}\mathbf{D}_j(\mathbf{r}) \\
\mathbf{H}_j(\mathbf{r}) &= \frac{1}{\mu}\mathbf{B}_j(\mathbf{r}) \\
\mathbf{J}_j(\mathbf{r}) &= \frac{\sigma}{\epsilon}\mathbf{D}_j(\mathbf{r})
\end{aligned} \tag{14}$$

As we mentioned above, the reconstruction process involves solving an over-determined linear system of equations for each cell, which is a very time-consuming procedure. This process has been employed in several flow computations using polynomial basis functions for unstructured grids [e.g., 6–7]. However, because the reconstruction was carried out at every time step, those computations are very inefficient and become impractical for three-dimensional problems. Here we would like to emphasis that the reconstruction, except at the beginning and the end of computation, is actually unnecessary during the time integration if the reconstruction stencil is unchanged. What really are needed in the computations are not the reconstructed analytical representations, but their functional values such as point values of the representations or their derivatives at some points or integral values of the representations over some regions. These functional values can be expressed as the products of some weights and the unknowns. This process is known as interpolation. In our formulation, as we shall discuss in the next section, the spatial integrals can be expressed as

$$\int_{S_{jk}} \frac{1}{\epsilon} f_j(\mathbf{r})\, d\mathbf{S} = \mathbf{w}_{\epsilon}\mathbf{f}, \tag{15a}$$

$$\int_{S_{jk}} \frac{1}{\mu} f_j(\mathbf{r})\, d\mathbf{S} = \mathbf{w}_{\mu}\mathbf{f}, \tag{15b}$$

and

$$\int_{V_j} \frac{\sigma}{\epsilon} f_j(\mathbf{r})\, dV = \mathbf{w}_J f, \tag{15c}$$

where the weighus are defined as

$$\mathbf{w}_E \equiv \left[\int_{S_{j_n}} \frac{1}{\epsilon}\phi(\mathbf{r})\, d\mathbf{S}\right]^T A^+, \tag{16a}$$

$$\mathbf{w}_H \equiv \left[\int_{S_{j_n}} \frac{1}{\mu}\phi(\mathbf{r})\, d\mathbf{S}\right]^T A^+, \tag{16b}$$

and

$$\mathbf{w}_J \equiv \left[\int_{V_j} \frac{\sigma}{\epsilon}\phi(\mathbf{r})\, dV\right]^T A^+, \tag{16c}$$

respectively. From Eqs. (16) and (10), one immediately notices that the weights are functions of the cell geometry, reconstruction stencil, and surface and volume integrations of the basis functions only. Those weights can be calculated once for all and stored in the memory at the beginning of computation. As we mentioned earlier, the integration process can be simplified if polyhedral cells with polygonal faces are used. Each face can be divided into planar facets, in which each one has a constant unit normal vector. Thus, the vector surface integrations in Eqs. (16a) and (16b) are reduced to scalar surface integrations. Furthermore, if the material properties are constants within the cell, ϵ and μ can be taken outside the surface integrations, and the volume integration in Eq. (16c) is no longer needed since $\vec{J}_j = \frac{\sigma}{\epsilon}\vec{D}_j$. One therefore only needs to store

$$\mathbf{w} = \left[\int_S \phi(\mathbf{r})\, d\mathbf{S}\right]^T A^+ \tag{17}$$

for each planar facet. Notice that the weights are all constants for regular grids and thus they require no memory storage. The use of regular grids can also yield higher accuracy due to the symmetry. Therefore, we feel that the most efficient grid in practical three-dimensional computations involving complex geometry should be one that is regular except near the body, where an unstructured grid can be used to accommodate the boundary or interface conditions. The surface and volume integrations in Eqs. (16) and (17) can be carried out using quadratures. For some basis functions, such as polynomial or trigonometric functions, these integrations can even be performed analytically. Details are given in a separate paper [8].

Evaluation of Spatial Terms

The spatial terms in Eq. (5) involve closed surface integrations associated with the tangential intensity vector

$$\mathbf{I}_t(\mathbf{r}) \equiv \mathbf{n}(\mathbf{r}) \times \mathbf{I}(\mathbf{r}). \tag{18}$$

Here $\mathbf{n}$ is the outward unit normal vector of a cell face at $\mathbf{r}$. Based on the above least squares process, the local representations for the two neighboring cells separated by a face are not the same in general unless such constrain is built in the basis functions or the reconstruction process. However, the difference is bounded within the error of the approximation in Eqs. (7) or (8). Let the superscript * denote the field state on a face and the subscripts $_L$ and $_R$ the field states on the left and right of the face. Given the two left and right states of a cell face, there are two approaches to construct the local representations of intensity vectors on the surface. One corresponds to a centered scheme and the other to an upwind scheme. In the former approach we employ an arithmetic average

$$\mathbf{I}_t^*(\mathbf{r}) = \mathbf{n} \times \begin{bmatrix} -\frac{1}{2}(\mathbf{H}_R + \mathbf{H}_L) \\ \frac{1}{2}(\mathbf{E}_R + \mathbf{E}_L) \end{bmatrix}, \tag{19}$$

while in the latter we apply a Riemann solver

$$\mathbf{I}_t^*(\mathbf{r}) = \mathbf{n} \times \begin{bmatrix} -\frac{(\mu\epsilon)_R \mathbf{H}_R + (\mu\epsilon)_L \mathbf{H}_L - \mathbf{n}\times(\mathbf{E}_R - \mathbf{E}_L)}{(\mu\epsilon)_L + (\mu\epsilon)_R} \\ \frac{(\epsilon\epsilon)_R \mathbf{E}_R + (\epsilon\epsilon)_L \mathbf{E}_L + \mathbf{n}\times(\mathbf{H}_R - \mathbf{H}_L)}{(\epsilon\epsilon)_L + (\epsilon\epsilon)_R} \end{bmatrix}. \tag{20}$$

Riemann solvers have long been employed in Computational Fluid Dynamics calculations for capturing discontinuities. The Riemann solver here is based on the exact solution of the one-dimensional Maxwell equations at a material interface. A simple derivation was given in Ref. 9. This technique was first applied to electromagnetic computations by Shankar et al. [10]. Our schemes differ from conventional centered or upwind schemes in that all variables in Eqs. (19) and (20), instead of being point values at "face centers", are functions of $\mathbf{r}$. (Actually, there is no unique way to define a face center if the surface is not planar.) Integrating either equation over cell faces and utilizing Eqs. (15a) and (15b) with the pre-computed weights, one easily converts the intensity terms in Eq. (5) in terms of unknowns. The source term in Eq. (5) can be converted in a similar manner with Eq. (15c).

A Fourier analysis of the two schemes was given previously by the author [9]. While the centered scheme generally provides no dissipation for regular grids or very little dissipation for non-regular grids, the upwind scheme sometimes generates too much dissipation. The latter actually can be considered as the former plus an artificial damping (smoothing) terms. In a constant property material, the strength are equal to $\frac{1}{2}\varepsilon c$ and $\frac{1}{2}\mu c$ for the electric and magnetic fields, respectively. Although we prefer a non-dissipative scheme for problems involving wave propagations, a "right" amount of smoothing may be necessary if there is any oscillation generated from a boundary or interface. More detailed comparisons of the two schemes with various smoothing shall be reported in a separate paper [11]. In our numerical examples to be presented later, the centered scheme is applied in the interior and the upwind scheme at the material interface. At the numerical outer boundaries, we use the first-order Engquist-Majda non-reflecting boundary condition. For perfect conductors, we simply set the tangential component of the electric field equal to zero. Highly accurate boundary conditions are currently under investigation.

Time Discretization

Once the spatial discretization has been completed, a time integration scheme is then needed for Eq. (5) to advance the unknowns in time. For the purpose of efficiency, it is desirable to choose a time scheme that gives accurate solutions for a larger time step. Notice that the spatial and time discretizations both introduce numerical errors, which involve dispersion, dissipation, and anisotropy. The error for each discretization decreases as its spacing decreases. However, when combining the two with opposite sign of errors, the error from one can cancel the error from the other. This makes the full discretization more accurate at large time steps. The time discretization methods we use here include the standard staggered leapfrog method and the third- and fourth-order Runge-Kutta methods. The choice depends on the errors from the spatial discretization. For example, the staggered leapfrog or third-order Runge-Kutta is used if the spatial discretization has a phase lag, and the fourth-order Runge-Kutta method is used otherwise. The numerical errors can be analysed by the Fourier method. Again, details were given previously in Ref. 9.

III. Numerical Results

Based on the formulation given above, we have developed a general multi-dimensional, multi-media computer code. One can choose any type and any number of basis functions. Surface and volume integrations of these basis functions over simple shapes such as tetrahedron, triangle and line are used as building blocks. The code then automatically constructs surface and volume integrals over the cell geometry. All variables in the code are defined in their vector form. It is therefore capable of doing both two- and three-dimensional computations. Currently, the code runs 360 Mflops (single processor) on a Cray C90 computer.

Several model electromagnetic scattering problems are calculated and compared with analytical solutions. Shown here are two examples using 0th to 3rd degree polynomial (piecewise constant to piecewise cubic) basis functions for TM plane waves incident on a perfectly conducting cylinder and a dielectric cylinder. Three-dimensional results will be given elsewhere. Fig. 1 shows the grid used in our calculations, which contains 400 cells inside the cylinder and 2400 cells outside. For simplicity, the cylinder is approximated by an 80-edge polygon. The grid was constructed by perturbing a smooth grid through a random number generator. Certainly, this is one of the worst kind of grids, and we would not use this type of grid in any practical computations. Here our purpose is just to demonstrate the capability of the new formulation in handling unsmooth grids. The resolution of the grid per wave length is approximately $60/k'a$ cells inside the cylinder and $20/ka$ to $60/ka$ cells outside, where a is the radius of the cylinder, k the wave number of the incident plane wave, and k' the wave number of the transmitted wave.

In the perfectly conducting cylinder case, the incident wave has a value of ka 3 propagating from left to right. The analytical solution consists of an infinite series of Bessel functions of the first and second kinds [12]. Shown in Fig. 2a are the contour lines of the total electric field of the exact solution in the vicinity of the cylinder. Plotted in Fig. 2b through 2e are the same field from the numerical solutions using 0th to 3rd degree polynomial basis functions, respectively. With the 0th degree reconstruction the field is assumed to be piecewise constant and the solution therefore reflects the unsmoothness of the grid (Fig. 2b). However, the general features are well captured. By using 1st degree polynomial basis functions, the grid-scale noise is eliminated (Fig. 2c). With the next two higher order reconstructions, the solutions (Figs. 2d-2e) are hardly distinguishable from the exact solution. The magnitudes of these solutions at the centroids of cells along the negative x axis are compared in Fig. 2f. Those results with 2nd and 3rd degree polynomial basis functions closely reproduce the exact solution.

In the dielectric cylinder case, the incident wave has a value of ka 1. The permittivity ratio of the dielectric to the free space is set to 4, therefore, $k'a$ = 2. The analytical solution again consists of an infinite series of Bessel functions [12]. The same 0th to 3rd degree polynomial basis functions are used for computing the numerical solutions. Features of the comparisons among these results and the exact solution are similar to those in the previous case. Only the exact and the 0th and 1st degree solutions are given in Fig. 3.

References

[1] J.V. Smith, *Geometrical and Structural Crystallography*, (Wiley, New York, 1982), p. 77.
[2] B. van Leer, "Towards the Ultimate Conservative Difference Scheme... V. A Second Order Sequel to Godunov's Methods," *J. Comp. Phys.* 54, 101 (1979).
[3] A. Harten and S. Osher, "Uniformly High-Order Accurate Non-Oscillatory Schemes, I.," *SIAM J. Num.Analy.* 24, 279 (1987).
[4] C.L.Lawson and R.J. Hanson, *Solving Least Squares Problems*, (Prentice-Hall, Englewood Cliffs, 1974).
[5] G.H. Golub and C.F van Loan, *Matrix Computations*, 2nd Edition, (The Johns Hopkins University Press, Baltimore, 1989).
[6] T.J. Barth and P.O. Frederickson, "Higher Order Solution of the Euler Equations on Unstructured Grids Using Quadratic Reconstruction," AIAA paper 90-0013, (1990).
[7] S.R. Chakravarthy, K.Y. Ssema, and C.L. Chen, "A UNIVERSE-Series Code for Inviscid CFD with Space Shuttle Applications Using Unstructured Grids," AIAA paper 91-3340, (1991).
[8] Y. Liu, "Exact Integrations of Polynomial and Trigonometric Functions over Arbitrary Polyhedral Cells," in preparation, (1994).
[9] Y. Liu, "Fourier Analysis of Numerical Algorithms for the Maxwell Equations," AIAA paper 93-0368, (1993).
[10] V. Shankar, W.F. Hall, and A.H. Mohammadian, "A CFD-Based Finite-Volume Procedure for Computational Electromagnetics - Interdisciplinary Applications for CFD Methods," AIAA paper 89-1987, (1989).
[11] Y. Liu, "A Comparison of Centered and Upwind Schemes for Solving the Maxwell Equations," in preparation, (1994).
[12] R.F. Harrington, *Time-Harmonic Electromagnetic Fields*, (McGraw-Hill, New York, 1961), Chap 6.

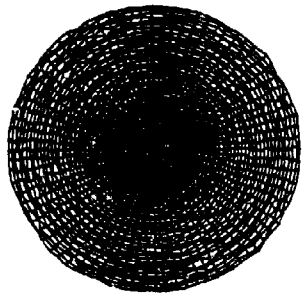

FIG. 1 An unsmooth grid for a cylinder

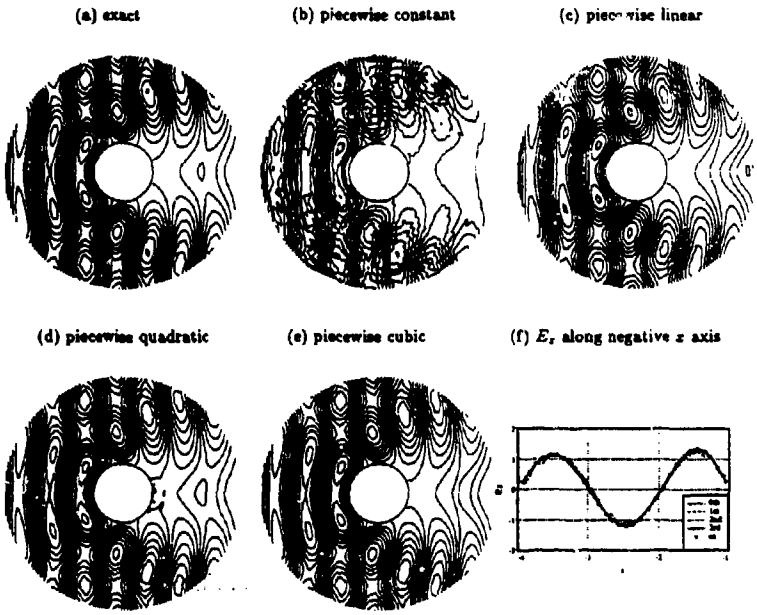

FIG. 2 Comparison of electric field for a plane wave incident on a perfectly conducting cylinder

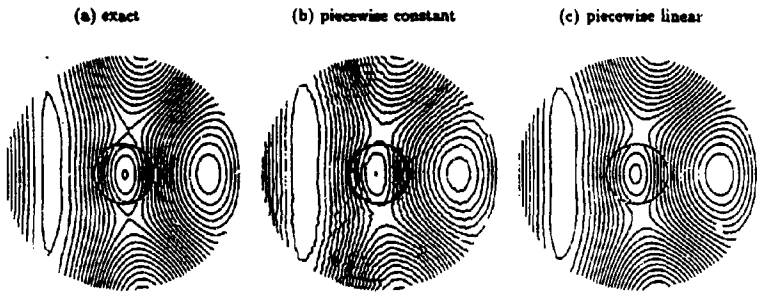

FIG. 3 Comparison of electric field for a plane wave incident on a dielectric cylinder

Massively parallel finite-difference time-domain methods for electromagnetic scattering problems.

R. S. David and L. T. Wille, Department of Physics, Florida Atlantic University, Boca Raton, FL 33431, USA.

Abstract: We discuss the development of finite-difference time-domain algorithms for massively parallel computers with a single-instruction multiple-data architecture. Various strategies are illustrated by parallelizing an existing sequential code, which is relatively simple yet of sufficient complexity to allow us to demonstrate the majority of parallelization issues and considerations. We give numerical values for the speedup obtained for a range of problem sizes and numbers of processors. Finally, we critically analyze these results and the promise they hold for the solution of more complex problems.

1. Introduction.

Time-domain electromagnetic problems include a wide variety of phenomena of great practical interest ranging from the electromagnetic pulse produced in nuclear explosions to radar target identification and whole-body human dosimetry, to mention just a few. Only in very rare cases, usually with high symmetry and simplified geometries, is an analytical solution feasible and for most situations occurring in typical applications a computational approach is necessary. The direct solution of such problems may be based on Maxwell's equations in a differential equation formulation, leading to finite element or finite difference calculations [1,2], or it may start from an integral equation approach, leading to the method of moments [2,3]. Generalizations of these schemes and hybrid techniques have also been proposed. For an accurate determination of transients as well as high spatial resolution these methods become quite demanding in terms of computer time and, to a lesser extent, storage. Thus, researchers in computational electromagnetics, just like their colleagues in many other fields, have been turning increasingly to high-performance computers, including vector and parallel machines (see the review articles [4,5,6] and references therein).

Parallelism is no panacea, however, and different techniques may be better suited for different types of architectures. The method of moments leads to a matrix equation which is well-suited for parallel computation [4-7] as many vendors have given careful attention to efficient implementation of vector and matrix operations on their products. Finite-difference time-domain (FDTD) methods also lead to a system of linear equations that needs to be solved for the fields as a function of space and time. Parallelization is possible at the level of the equations, but care must be taken because the matrices in question are sparse, or it may be performed at the physical level by assigning one (or more) spatial locations to each processor in a parallel machine. Parallel FDTD codes have been reported by a number of authors [4]. Similar strategies may be employed to parallelize finite element codes [4], for which the regularity of the grid becomes an important issue to decide which type of machine to use. A very general discussion on these and other techniques with a large bibliography (up to 1985) can be found in reference [8]. In the present paper the main emphasis is on the FDTD method in the original formulation of Yee [9] and the discussion will be for parallelization on computers with a single-instruction multiple-data architecture, specific programming examples being given for the MasPar family of machines.

The aim of this paper is threefold: to be a general introduction to parallel computing, to be a tutorial on how to parallelize an existing sequential Fortran-code, and to illustrate the kind of performance that may be realistically expected for FDTD applications. In the remainder of this paper we discuss the parallelization of FDTD algorithms on the MasPar class of computers, although most of the considerations hold equally well for other types of architectures. In section 2 we give a brief overview of various types of parallel computer architectures, discuss software issues, and describe the MasPar family of computers and their relation to other parallel machines with related architectures. Section 3 outlines the FDTD method and enumerates various approaches used to parallelize an existing FDTD

code. Section 4 presents and analyzes the timing results, while section 5 concludes the paper with a summary and a discussion of future work.

2. Issues in parallel computing.

Conventional single-CPU computers based on the so-called von Neumann architecture are rapidly approaching fundamental physical limitations posed by the finiteness of the speed of light and the lower limits put on miniaturization by quantum mechanical effects. Thus the only way to maintain the expected increase in computer speed with time is to get several computers to cooperate on a single task, i.e. to employ some form of parallelism [10]. Of course, even on sequential computers limited forms of parallelism have been used, for example by having bit-parallel arithmetic or by allowing for instruction pipelining, but the amount of speed-up to be obtained in this way is rather restricted. Computer architectures may be classified very conveniently in terms of a taxonomy first proposed by Flynn in 1972, based on the notions of an instruction stream and a data stream. In this scheme traditional single-processor machines are called SISD (single instruction single data), since there is a single instruction stream and each instruction operates on a single datum at a time. On the other hand, most parallel machines in current use either employ the SIMD (single instruction multiple data) or MIMD (multiple instruction multiple data) paradigm. In the first case a single instruction stream broadcast by a single control unit is executed by many processing elements (PE's) acting on different data elements. The PE's are arranged in some regular fashion such as a mesh, hypercube, tree, etc. and operate in a synchronous way. SIMD is very well suited for massively parallel programming, with many thousands of PE's working cooperatively, and for problems with a high degree of granularity and inherent parallelism. MIMD parallelism is a more general framework in which processors may be simultaneously executing different instructions on different data in essentially an autonomous manner, no centralized or global synchronization mechanism being present. Usually MIMD computers contain a relatively small number of processors (tens to hundreds) and they are considered to be better suited for coarse grained or irregular problems. Although by their very design they are more flexible, MIMD machines are quite difficult to program efficiently and great care needs to be taken that proper load balancing is achieved such that the number of idle processors is kept to a minimum. In both parallel paradigms it is also important that the amount of interprocessor data exchange is relatively small since communication is generally a slower process than computation and the communication channel usually has a small bandwidth and does not allow simultaneous communication between all processors. Moreover it is also important to keep communication distances short, an issue for which the interconnection topology plays an important role. Higher-dimensional networks are to be preferred for their short interprocessor distances, but need many more links than lower-dimensional ones making them harder to design and build. Most machines provide some fast communication mechanism between nearby processors and a slower global communication mechanism (a 'router') between any two processors. Another issue in which architectures differ is the memory organization: in shared memory systems, all processors share global memory in a tightly coupled or loosely coupled fashion and information exchange happens primarily through central memory, while in distributed memory systems, each processor has its own local memory and process cooperation occurs through message passing. Typically shared memory systems employ a single bus for interprocessor communication rather than a true interconnection network. Thus the number of possible designs is very large and numerous prototypes have been built at research institutions, while the number of commercially available machines also continues to increase [10,11].

From the software point of view the development of an efficient parallel algorithm is not an easy task which ideally should not start from porting a sequential code, but rather from a rethinking of the entire approach. Many problems and solution strategies possess a high degree of inherent parallelism which is often obscured when the solution is attempted by a sequential algorithm. A useful measure of the performance of a parallel program is the speed-up attained which is defined as the time necessary to execute the algorithm on a single processor divided by the time this takes on N processors. There are some problems with this definition since it is not clear how to obtain the time necessary for execution on a single processor and often some approximation is used or the scaling behavior over a range of

processor array sizes is measured. Also, although it might naively appear that the maximum possible speed-up with N processors would be N (a linear speed-up), there has been a vocal debate in the literature about the possibility of superlinear speed-up [12], which may occur in certain search problems with random elements. However, this issue need not concern us here since we are considered with deterministic calculations. In rare cases the problem breaks up into N independent, identical pieces, leading to so-called 'embarrassingly parallel' code. The speed-up in such cases is N since there is no overhead associated with communication or serial portions of the code. This may happen when an identical calculation needs to be done for a range of parameters or initial conditions, for example, to calculate averages. Such computational approaches have been called replication algorithms [13]. However, most problems do not fall in this class and more typically one needs to find an efficient mapping from the problem to the target parallel computer. Common approaches include geometric parallelism and data parallelism [13]. In the first case, the physical space in which the system to be investigated resides is broken up into cells, each cell associated with a processor, while in the latter case it is the parallelism in the mathematical formulation of the problem that is exploited. Other techniques include divide-and-conquer methods in which the task is subdivided in a tree-like fashion and results are passed from the leaves to the parents. Clearly most of these approaches, except data parallelism, are well suited for MIMD computers, since the tasks allocated to each processor are not necessarily identical.

The emergence of parallel computing has also necessitated the development of new computer languages or extensions to old ones, to allow parallel constructs. Originally there was a considerable lack of standardization with each machine having its own programming language, but recently more and more effort is being made to establish some uniformity and compatibility. In particular, the Fortran community has adopted a powerful new standard, Fortran 90, which contains several features of primary interest for parallel programming [14,15]. Of particular relevance are the powerful array operations supported by this language. For example, the sum, C, of two arrays, A and B, of the same size may be accomplished simply by the statement C = A + B, rather than by the standard nested loops running over all elements. Likewise, the statement C = A*B assigns to the element C_{ij} the value A_{ij}*B_{ij}. Note that this is not the matrix product. The WHERE statement may be used to assign values to only those array elements where a certain logical expression evaluates to true. For example, the following statement fills each element of the array A with the inverse of the corresponding element in array B as long as the latter is non-zero: WHERE (B/=0) A = 1.0/B. A similar instruction is FORALL, which was part of the original Fortran 8X draft, but was not retained for the Fortan 90 standard, although it is being used by a number of manufacturers as an extension. It allows the conditional assignment of array elements based on a condition that itself may contain explicit subscript expressions. Many more innovative features are present in the language, but the ones just discussed are of special relevance to the discussion in this paper. A new standard is currently under development by the High Performance Fortran Forum.

In the present work the main interest is in the MasPar MP-1 and MP-2 (DECmpp 12000) class of massively parallel computers [10,11,16,17]. In brief, the machines in this class are based on the SIMD paradigm and consist of a PE-array arranged in a two-dimensional mesh with toroidal wrap-around boundary conditions. They are made out of 1, 2, 4, 8, or 16 processor boards, each of which holds 1,024 PE's and their associated memory (16 kbyte or 64 kbyte in Dynamic RAM as well as forty 32-bit registers). The control of the PE-array is performed by the Array Control Unit (ACU). This is a register-based load/store 12-MIPS scalar RISC processor which fetches and decodes the machine instructions, handles address and scalar computations, monitors the status of the PE array, and broadcasts control signals to it. In addition it contains 128 kbyte of data memory and 1Mbyte of code store. The combination of the PE-array, the communication mechanism, and the ACU is called the Data-parallel Unit (DPU). Interprocessor communication between nearest-neighbor PE's is possible through the so-called X-net which links each PE to its eight nearest neighbors and provides a fast communication path with a bandwidth between 1 and 20 Gbytes/s depending on the model. Data interchange between arbitrary PE's is provided by a global router based on a multi-stage hierarchical crossbar switch. At most 1,024 simultaneous links are possible and the system is able to operate at an aggregate bandwidth of 1.5 Gbytes/s. The global router is also responsible for data transfer to the high-speed I/O subsystem.

Clearly, whenever possible, router communications should be avoided since they are slower than X-net operations and necessitate a large fraction of the PE-array to remain idle. The computer is frontended by a Unix workstation with standard I/O which provides the user interface and network communication. Only when there is need for massively parallel execution is the DPU invoked, all other sequential computation is performed on the frontend. The latter also acts as the host for the MasPar Programming Environment (MPPE), a powerful debugging and code development aid, as well as the language compilers. Currently two languages are supported: MPL, a version of Kernighan and Ritchie C with parallel extensions, and MPF, a version of Fortran 90 with extensions (including FORALL). In MPL the computer architecture is accessible to the user who has control over the locations where data will reside with the possibility to address individual PE's. In MPF on the other hand the array size and PE contents are hidden from the user. This has the advantage of increasing code portability between models and even to and from other architectures, but it means that the burden of the parallelization effort consists of putting the code in such a format that the compiler stores data, especially arrays, in the desired format. Compiler directives are available to assist in this task. The recently announced MP-2 machines are binary compatible with the MP-1, but are about 5 times faster.

In terms of architecture the MasPar computers are very similar to the Distributed Array Processor (DAP) for which a good deal of expertize has been accumulated [18] as well as a number of computers that were mainly used in academic or research laboratory environments (Illiac IV, MPP, etc.). Perhaps the best-known class of SIMD computers is the Connection Machine CM-2 family. These machines are based on a hypercube architecture: single-bit processors are connected in a twelve-dimensional hypercube each node of which may have up to 16 processors. They are not to be confused with the more recent CM-5 family which uses a mixed SIMD/MIMD paradigm (sometimes called SAMD: Synchronous/Asynchronous Multiple Data [12]). It might seem that algorithms developed for a mesh computer would not be easily adapted for other geometries, but fortunately it turns out that many of the connectivity graphs may be embedded into others [19], so that an algorithm for one may be ported relatively easily to another one. In particular, the two-dimensional mesh can be embedded quite straightforwardly into the hypercube and this mapping is supported by the Fortran environment on the CM-2. Thus the algorithms and approaches to be discussed here, although implemented on the MasPar computers, have much wider applicability.

3. Massively parallel FDTD methods.

To illustrate the parallelization of an existing sequential code, we decided to take a program listed in ref. [2] (pages 199-203) which involves the penetration of a plane wave into a lossless dielectric sphere. Although this is by no means a very complicated or time-consuming calculation, it is of sufficient generality and complexity to take considerable effort to parallelize it efficiently and it also allows us to illustrate some of the typical strategies that may be used to accomplish this. As mentioned before, it is not always best to try to port an existing sequential code to a parallel machine, a process aptly described as 'rejuvenating a sequential code' by Lu *et al.* [7]. In the first place, there is no guarantee that the most efficient parallel algorithm is also the best sequential algorithm. Also, it is not always easy to discern the existing parallelism in a particular algorithm; sometimes the mathematical notation itself obscures the presence of parallel operations. Even if an algorithm is parallel in nature and a sequential code exists, the idiosyncrasies of the computer language used may render parallelization of this code less than trivial: constructs such as IF-statements and GOTO's in Fortran need to be replaced by 'FORALL' or 'WHERE' instructions in Fortran 90 and this may be a daunting and time-consuming task. Dataflow to and from subroutines is another issue that needs to be handled carefully: COMMON blocks in particular are often a source of errors, leading many programmers to pass all arguments explicitly in the subroutine call. In fact, COMMON blocks are considered obsolete in Fortran 90, along with various GOTO statements, the CONTINUE statement, and others. Also in order to accomplish an efficient mapping of the data arrays to the processor array one needs to understand the way this is done by the compiler. Clearly it is important to maximize the number of active processors and so it may be necessary to re-arrange the order of the subscripts in an array in order to accomplish this.

It will be assumed that the reader is familiar with the general ideas behind the FDTD method; further details may be found in the original paper by Yee [9] or the review by Taflove and Umashankar [20], as well as the text by Sadiku [2]. As is known the method works directly from Maxwell's time-dependent curl equations and uses second-order central-difference approximations for the spatial and temporal derivatives of the electric and magnetic fields. Thus it is a relatively simple, yet fast and accurate, method to approximately determine the waves propagating in physical space by a time-stepping procedure on a discrete grid. In Yee's original notation the grid points are denoted by integers i, j, and k as follows:

$$(i,j,k) = (i\Delta x, j\Delta y, k\Delta z), \tag{1}$$

where Δx, Δy, and Δz are the lattice increments in the x, y, and z direction. The grid spacing is typically taken to be eight or sixteen cells per wavelength. Likewise, any function of space and time will be denoted as:

$$F^n(i,j,k) = F(i\Delta x, j\Delta y, k\Delta z, n\Delta t), \tag{2}$$

where n is an integer and Δt is the time increment chosen to ensure stability of the time-stepping algorithm. Since the physical domain involved is usually unbounded, some form of boundary conditions needs to be imposed. Here we only consider the most widely used form, the absorbing boundary conditions developed by Taflove and collaborators [20].

The six FDTD equations at interior grid points are all quite similar to each other and can be found in the references mentioned earlier [2,9,20]. For the sake of discussion we just list one of these equations, which gives the x-component of the magnetic field, H_x, at time n in terms of H_x at the previous timestep and the y and z components of the electric field, E_y and E_z, at previous time steps and nearby grid points (equations (3.86) in [2]):

$$H_x^n(i,j,k) = H_x^{n-1}(i,j,k) + E_y^{n-1}(i,j,k+1) - E_y^{n-1}(i,j,k) - E_z^{n-1}(i,j+1,k) + E_z^{n-1}(i,j,k). \tag{3}$$

Clearly these equations are well suited for parallel computation since only data from previous time steps and from nearest-neighbor grid points are needed. The absorbing boundary conditions (equations (3.82) in [2]) are similar except that all fields are calculated in terms of quantities two time steps prior (for propagation in free space) and spatial interaction is with grid points that differ by 1 from the current one in one or two directions, for example:

$$H_y^n(0,j,k) = (H_y^{n-2}(1,j,k-1) + H_y^{n-2}(1,j,k) + H_y^{n-2}(1,j,k+1))/3. \tag{4}$$

As can be seen this expression is still well suited for parallelization as it involves short-range communications. In the particular code that was parallelized the initial field consists of a single-frequency incident plane wave. The program starts by putting all field components at the grid points equal to zero, while the plane wave source is activated at the first time step and left on for the duration of the calculation. This problem is of course exactly solvable and numerical results obtained were compared to Mie's exact solution.

The parallelization of the FDTD code proceeded in a number of stages. First the original Fortran 77 code was compiled with MPF and executed to establish a baseline for future comparison. Since only Fortran 90 constructs actually run on the DPU no parallelization was obtained at this level. Next all DO loops were converted to Fortran 90 by eliminating CONTINUE statements. At the same time simple loop assignment operations were converted. For example, initialization of the fields is performed by a single statement of the form: EY = 0, which initializes to zero all elements of the four-dimensional array EY (0:IMAX+1, 0:JMAX+1, 0:KMAX+1, 0:NMAX). The compiler directive CMPF ONDPU EY instructs the compiler to put this array on the PE-array. The default assignment on the MasPar is that the first index goes along the x-direction of the grid, the second one along the y-direction, and further indices are put in PE-memory. At all stages it was checked that the numerical results still agreed with those produced by the sequential code. Next a number of more complex loops were parallelized by using the subscript triplet notation which allows one to refer to a range of subscript values within an area, delimited by a lower bound, an upper bound, and an increment. For example, the double loop over I and K to handle the boundary condition on EX near J = 1 is written in MPF as follows: EX (0:IMAX, 0,

0:KMAX, NCUR) = EX (0:IMAX, 1, 0:KMAX, NPR2). Here the integers separated by colons are part of the triplet (the third element in the triplet, the increment, is 1 in this case and may therefore be omitted). In order to measure immediately the effects of parallelization the main loop over I, J, and K in the sequential code was broken up in several smaller loops and each loop individually tackled. In this way the loop for the interior grid points could be completely parallelized and the same was possible for many of the absorbing boundary conditions. However, for a number of boundary conditions it was possible to eliminate one of the loops, but not the other because of the way loop variables were organized. For those cases, partial parallelization is obtained, i.e. a number of PE's all in the same row or column will be active simultaneously but most will be idle. There appears to be no easy way to avoid this from occurring and these loops (which will be included in the sequential timings to be presented) at present put a limit on the amount of parallelization that can be obtained. Finally, the computation of the maximum of the absolute values of the field components which is a combination of a loop and if-tests in the sequential code can be performed quite elegantly by a WHERE construction in the parallel code.

4. Results.

We now turn to a discussion of some of the performance results of the parallel code. All calculations were performed on a 4,096-node MP-1 at Florida Atlantic University and a 8,192-node MP-1 at MasPar headquarters in Sunnyvale (CA). The former machine has 16 kbyte of memory for each PE, while the latter has 64 kbyte of PE-memory.

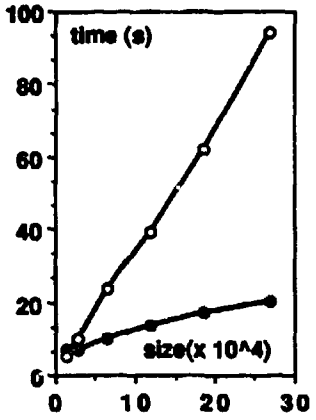

Fig. 1: Execution time (in seconds) as a function of problem size (number of grid points). Solid circles: parallel portion of code; open circles: sequential potion of code.

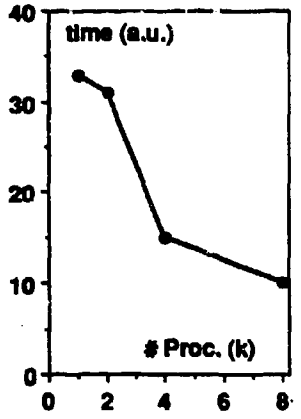

Fig. 2: Execution time of fully parallelized loop for interior grid points on various machine sizes. Time is measured in arbitrary units, the number of processors is in multiples of 1,024.

Fig. 1 shows the execution time for 10 time steps on the 8,192-node MP-1 of the parallel and sequential portions of the code as a function of problem size (measured as the total number of grid points). Based on a comparison with sequential runs we estimate that the code currently is about 95% parallel. As can be seen the execution time for moderately sized problems is essentially dominated by the

5% of the code that is sequential. This is an illustration of Amdahl's law [12], which states that the possible speed-up by using parallelism is limited since eventually a small, but non-negligible, sequential portion of the code will dominate the execution time and thus limit the gains attained by the parallel parts. The time spent in the sequential portions increases nearly linearly with problem size as is to be expected and this is what ultimately limits attainable speed-up. Fig. 1 shows that the parallel portion of the code has a much milder increase with problem size. In fact it exhibits plateaus (only one of which is shown) since the execution time of a parallel statement will remain constant with increasing problem size as long as not all PE's are busy. Only when the array size exceeds a multiple of the PE-array size does wrap-around occur and the execution time of the parallel statements increases discontinuously.

For many years, Amdahl's law was considered a major obstacle towards exploiting parallelism until it was realized that the hidden assumption in its derivation is that the percentage of sequential code remains constant as the number of processors increases. It was argued by Gustafson and collaborators that it is more sensible to scale up the problem size with the number of processors, thereby keeping the workload per processor constant, and this leads to the Gustafson-Barsis law which is much more optimistic in its prediction of possible speed-up (now called 'scaled speed-up') [12]. While we have not yet performed measurements of scaled speed-up, Fig. 2 shows the effect of increasing the number of processors for fixed problem size. To clearly display this we have only timed the parallelized loop over interior grid points (Eq. (3) above). The calculation was performed for the 19x39x19 grid also used in the original code listed in Sadiku [2]. This problem size does not fit very well onto the PE-array sizes (32x32 and multiples of it) and thus the speed-up is not linear as might be expected since the number of idle PE's and consequent router calls vary on different machine sizes. In particular the time difference in going from 1,024 to 2,048 processors is very small. Beyond that however, the speed-up is close to 2 when going from 2,048 to 4,096, and approximately 3.3 when going from 2,048 to 8,192 processors. Preliminary calculations show that if grid-sizes are multiples of the PE-array size a more linear trend is obtained, but we feel that it is of more interest to show what is possible with realistic grid-sizes.

5. Conclusions.

Summarizing, we have shown that for a relatively simple case of the FDTD electromagnetic scattering algorithm, major speed improvements are possible on a parallel computer. This is mainly because of the matrix formulation of the underlying equations and the fact that only values on nearby grid points are needed to update the fields at a certain grid point. The main loop of the calculation at interior points is completely straightforward to parallelize, but greater care is needed to handle the absorbing boundary conditions. Because there is fine grain parallelism and calculations are repeated in a regular fashion this approach is well suited for SIMD architectures. The amount of work involved in parallelizing the code was not negligible, but it was very satisfying to see what could be attained with some persistence.

Lest the reader think that SIMD parallelism is the cure to all ills it is also important to point out some of its shortcomings for FDTD calculations. Clearly, the approach is not well suited for irregular regions or objects, nor for adaptive meshes. One may have to use MIMD computers in those cases although load-balancing and synchronization will then be difficult to control. In rectangular coordinates the mapping to a mesh (or hypercube) is natural and straightforward, but in other coordinate systems this may not be the case. Also, as Fig. 1 shows, Amdahl's law still applies in that the sequential part of the code eventually becomes a dominating factor. On the MasPar we were restricted in grid sizes that could be handled by the limited amount of PE-memory and similar constraints apply on other machines. The transfer of the massive amount of data stored on a parallel machine to I/O devices is often a bottleneck and has a detrimental effect on code performance if swapping occurs. Clearly, many challenges remain, both algorithmic and architectural in nature. It is to be expected, however, that massively parallel computations will only gain in importance for computational electromagnetics over the next few years.

Acknowledgements: Robert S. David is the recipient of a Motorola Partnerships in Research Grant.

References.

[1] M. A. Morgan (ed.), 'Finite Element and Finite Difference Methods in Electromagnetic Scattering', Elsevier, New York (1990).
[2] M. N. O. Sadiku, 'Numerical Techniques in Electromagnetics', CRC Press, Boca Raton (1992).
[3] R. F. Harrington, 'Field Computation by Moment Methods', Macmillan, New York (1968).
[4] K. D. Tzanlias and J. M. Bornholdt, IEEE Trans. Magnetics, 25, 2901 (1989).
[5] D. B. Davidson, IEEE Antennas Propagation Magazine, 32, 6 (1990).
[6] D. B. Davidson, IEEE Antennas Propagation Magazine, 34, 9 (1992).
[7] Y. Lu, A. G. Mohamad, G. Fox, and R. F. Harrington, in 'Parallel Processing for Scientific Computing', eds. R. F. Sincovec, D. E. Keyes, M. R. Leuze, L. R. Petzold, and D. A. Reed, SIAM, Philadelphia, 1993, pp. 216-220.
[8] J. M. Ortega and R. G. Voigt, 'Solution of Partial Differential Equations on Vector and Parallel Computers', SIAM, Philadelphia (1985).
[9] K. S. Yee, IEEE Trans. Ant. Prop., AP-14, 302 (1966).
[10] K. Hwang, 'Advanced Computer Architecture - Parallelism, Scalability, Programmability', McGraw-Hill, New York (1993).
[11] A. Trew and G. Wilson (eds.), 'Past, Present, Parallel - A Survey of Available Parallel Computing Systems', Springer-Verlag, Berlin (1991).
[12] J. R. Smith, 'The Design and Analysis of Parallel Algorithms', Oxford University Press, Oxford (1993).
[13] D. W. Heermann and A. N. Burkitt, 'Parallel Algorithms in Computational Science', Springer-Verlag, Berlin (1991).
[14] W. S. Brainerd, C. H. Goldberg, and J. C. Adams, 'Programmer's Guide to Fortran 90', McGraw-Hill, New York (1990).
[15] M. Metcalf and J. Reid, 'Fortran 90 Explained', Oxford University Press, Oxford (1990).
[16] T. Blank, in Proceedings of the CompCon Spring 1990, 35th IEEE Computer Society International Meeting, 20 (1990).
[17] J. R. Nicholls, in Proceedings of the CompCon Spring 1990, 35th IEEE Computer Society International Meeting, 25 (1990).
[18] D. Parkinson and J. Litt (eds.), 'Massively Parallel Computing with the DAP', Pitman, London (1990).
[19] F. T. Leighton, 'Introduction to parallel algorithms and architectures: arrays • trees • hypercubes', Morgan Kaufmann, San Mateo (1992).
[20] A. Taflove and K. R. Umashankar, in 'Finite Element and Finite Difference Methods in Electromagnetic Scattering', ed. M. A. Morgan, Elsevier, New York (1990).

SESSION 11:

ARRAYS

Chair: Vaughn Cable

Computation of Phased Array Active Impedances and Comparison with Measurements *

Paul Elliot[1], Peter Koert[1], James Cha[1], Richard Groff[2], and Thomas Collins[3]

[1] ARCO Power Technologies
1250 24th St. NW Ste 850
Washington, D.C. 20037

[2] Applied Research Laboratory
The Pennsylvania State University
North Atherton St.
State College, PA 16803

[3] Center for Electronic Design,
Communications & Computing
The Pennsylvania State University
University Park, PA 16802

Abstract

Measured and calculated input impedances of a phased array antenna are compared. The calculations were done using the Numerical Electromagnetic Code - NEC-4. The maximum array size was a 7x7 over a ground plane. Active impedances, mutual coupling as a function of distance, the effect of different NEC segmentation models, and sources of error are also described. The measurement frequency was from 56 MHz to 200 MHz, with array spacing of 4 feet between elements, which is a 1/20 size scale model of a larger size element to be built. Each element consists of two stacked broadband crossed grid dipoles. The larger, upper crossed grid dipole is used over the lower portion of the frequency band and the smaller crossed grid dipole is used for the higher frequencies. Impedances were measured and calculated separately for each dipole (two dipoles per element for each frequency band). Overall there is good agreement between the measured and calculated results, including for the 7x7 active impedances, with better agreement over the low frequency band than the high band.

Introduction

Input impedance measurements of a 1/20 scale model phased array antenna are compared with calculations using the Numerical Electromagnetic Code - NEC-4[1]. The NEC computer models were run on SUN SPARCstation 10, DEC Alpha, and other computers to predict the performance of the array. Results for 1x1, 2x2 and 7x7 array sizes in a square lattice are shown. The measurement frequency was from 56 MHz to 200 MHz, with array spacing of 4 feet between elements, although the data is plotted at 1/20 these frequencies (from 2.8 MHz to 10 MHz) since this antenna is intended as a 1/20 size scale model. Following the Introduction, Section 2 describes how the S-parameters and active impedances were computed. Section 3 compares the accuracy of different NEC models for small arrays. Section 4 then compares the full 7x7 array measurements with NEC calculations and describes coupling as a function of distance in the 7x7 array. Sources of NEC modeling errors are discussed in Section 5, followed by conclusions in Section 6.

Figures 1 and 2 show two NEC models of one radiating element**. These NEC element models were used with various numbers of segments and numbers of elements, and calculated over an infinite ground plane. The element consists of two stacked

---

* Work performed under contract # N00014-92-C-0210 with the Office of Naval Research.

** Element designed under ARCO Power Technologies IR&D funding, patent application has been filed.

Acknowledgement: The authors wish to acknowledge Dr. Leon Susman of ARCO Power Technologies, Dr. Walter Kahn of ANRO Inc, Sarasota, FL, and Mr. Ed Kennedy and Dr. Adrian Eley of the Naval Research Laboratory, Washington DC for their suggestions, and Mr. Ross Bell and Mr. Anthony Medina of Antenna Products Corp., Mineral Wells, TX for design assistance and fabrication of the antenna.

C:\HAARP7\WORDS\SCALEAPC\ACES\PAP.WPD

broadband crossed grid dipoles. The larger, upper crossed grid dipole is used over the lower portion of the frequency band (2.8 to 7 MHz in the plots), and the smaller crossed grid dipole is used for the higher frequencies (7 to 10 MHz in the plots).

2. Computation of S-Parameters and Active Impedances

The method used to compute S-parameters and active impedances are described in this section. S-parameters were measured at the dipole feed points by calibrating out the baluns and feed lines. NEC however does not compute S-parameters directly, but the S-parameters for the array can be derived from the NEC output currents and the loads and voltages placed in the NEC input file as described below[2]. Measured or calculated S-parameters are then summed to obtain active impedances.

2.1 Computation of S-Parameters from NEC Output Currents

S-Parameters are widely used at RF due to the ease and accuracy with which they can be measured. To calculate them from NEC results, the NEC model was run with one dipole in the array excited using a voltage source V_g. The other dipoles are not excited, but they are terminated in a generator impedance as seen from the dipole R_g (50 ohms was used). Figure 3a and 3b show the NEC model feed circuits. With the driven dipole designated using the subscript 1, and the other dipoles by subscript n, the voltages directly across the dipoles are:

$$V_1 = V_g - I_1 R_g$$
$$V_n = -I_n R_g \qquad n \neq 1$$

The currents I_n on the undriven dipoles are generated by coupling from dipole #1. V_1 (the voltage across the excited dipole) is not equal to the NEC excitation voltage V_g due to the voltage drop across R_g. All voltages and currents including for dipole #1 are then normalized using the square root of R_g:

$$V_n' = V_n / \sqrt{Rg}$$

$$I_n' = I_n \sqrt{Rg}$$

The forward and reverse traveling waves are then defined as

$$a_n = (V_n' + I_n') / 2.$$
$$b_n = (V_n' - I_n') / 2.$$

and the S-Parameters coupling between ports n and 1 is:

$$S_{n,1} = b_n / a_1$$

2.2 Active Input Impedances

The term "active impedance" is used throughout to refer to the active reflection coefficient or antenna load impedance if all the dipoles were radiating. The active reflection coefficient is equal to the sum of the individual S-Parameters with each S-parameter weighted by the amplitude and phase of the forward traveling wave a_n. This summation was done using the S-parameters from NEC and using the measured S-parameters to yield the NEC and measured active impedances respectively. All "measured" active impedances shown in this paper are therefore actually obtained by summing the individually measured S-parameters. This procedure is highly accurate and widely used in antenna measurements for obtaining active array impedances[3].

The a_n (complex forward voltage amplitudes and phases) are selected to provide the desired illumination function, polarization and scan angle. The active impedance and active reflection coefficient are therefore somewhat different for different tapers, scan angles and polarizations. All the plots shown are for uniform amplitude illumination and either Left or Right Hand Circular Polarization (LHCP or RHCP). Tapered illumination functions would produce slightly different active impedances than the uniform cases shown. Linear polarizations also differ a little but not much from the circularly polarized impedances shown.

C:\HAARP\WORDS\SCALEAPC\ACESPAP.WPD

For the a_n to be determined, the positive reference direction for the dipole excitations must be known. In NEC these are the positive reference directions for currents on the source segments, which are determined by the NEC input file and shown in the NEC output. In the measurements it may be taken as the dipole half which is connected to the center pin of the feed coax on the feed side of the balun (the other half dipole is connected to the coax outer conductor).

3. Comparison of NEC Segmentation Models

Figures 1 and 2 showed two NEC models used and Figure 3 shows a closeup top view of the feed region and tower of Figure 1. The feed region consists of feed wires in their correct positions and metalic support structure in the vicinity of the dipole feed point. These NEC element models were used with various numbers of segments and numbers of elements, and run over an infinite ground plane. Impedances were measured and calculated seperately for each dipole (two per element). Unless otherwise specified in the figures, marker symbols not linked by a curve are from NEC, whereas all continuous curves with or without markers are measured. Corner and center dipole results are included. The side dipoles are not plotted since they have impedances that are intermediate between the corner and center. The NEC data is shown in 0.6 MHz increments while the measured data is shown in .025 MHz increments. The measurements were actually taken at 20 times the frequency plotted and at 0.5 MHz increments since the fabricated model is inteded as a 1/20 scale model.

1x1 and 2x2 active impedance results are presented first to illustrate the effect of different NEC models and segmentation. Figure 5 shows the high band 1x1 self impedance. The model with tower and feed details (300 segments/element) is seen to provide a much better agreement with measurements, especially at the higher frequencies, than the 130 segments/element model which has no tower or feed details.

Figures 6 and 7 compare high band 2x2 calculations for different NEC models, and Figure 8 shows the same impedances in a different format for greater magnitude resolution but with no phase information. The same measured data is shown in all three figures. As for all the active impedances in this paper, the North-South dipole with Right Hand Circular Polarization (RHCP) has the same impedance in theory on broadside as the East-West Dipole with Left Hand Circular Polarization (LHCP), so the NEC points apply to both, and the two measured curves are nearly identical.

All the NEC cases in Figure 6 used the same segmentation for the radiating portions of the element, the only difference is in the tower and feed models. Similarly, all the NEC cases in Figure 7 used the same segmentation for the radiating portions of the element. The 130 and 174 segment/element models do not include any tower or feed region details, with the 174 segment model being more finely segmented for the radiating portions of the element. Similarly, the 300 and and 342 segment NEC models used identical tower and feed region models, just the segmentation of the radiating portions is different. A second 342 segment model labeled "as built" used the measured dimensions of the scale model element, whereas all the other NEC cases in this paper used the slightly different "as designed" dimensions. The 254 segment model is identical to the 300 segment model except it has no tower, but it does include the same feed region.

Not surprisingly the 342 segment models show the best agreement with measurements for the high frequency element, especially the 342 "as built" model. The 254 segment model compared with the 300 segment model shows that the tower increases the capacitance slightly for the high band active impedance, yielding better agreement with measurements. A comparison of the 130 and 254 segment models shows that the effect of the feed region is also to increase capacitance, and to reduce input resistance as well, both of which improve accuracy for the high band element. The comparison between the 174 and 342 segment models supports the above conclusions.

Figures 9 through 12 show comparisons for the low band 1x1 and 2x2. The tower and feed region, which improved accuracy when included in the high band NEC models, actually reduce accuracy in the low band NEC models. Athough both models in Figure 9 are quite accurate, the 114 segment model which has no tower or feed region is more accurate than the 300 segment model which has tower and feed detail. Similarly in Figures 10 and 11 (which show different polarizations), the 342 segment "as built" model is more accurate than the 300 segment model at resonance, but neither is as accurate as the 114 segment model. This difficulty with the low band NEC tower and feed region model has not been explained as yet.

However for orthogonal dipoles showing very low coupling, the NEC model with feed details is more accurate due to a

peculiarity in the feed region. This result is shown in Figure 12 which is the same S_{11} data as in Figure 9 using the 300 segment NEC model, but plotted in dB magnitude format, and Figure 12 also shows the S_{12} coupling term to the orthogonal dipole. It is seen that the S_{12} coupling between the orthogonal crossed dipoles is measured and calculated by the 300-segment model to be about -40 dB. The 114 segment model calculated about -130 dB (out of range), so the model with tower and feed was much closer in this instance. This high -40 dB coupling between orthogonal dipoles is probably due to a slight asymmetry in the scale model feed design which was faithfully incorporated into the NEC 300 segment and other models which include tower and feed region details: as shown in Figure 4 each dipole half is driven against a corner of the square tower instead of against the middle of the tower face. This asymmetry results in higher coupling between nominally orthogonal dipoles. This feed asymmetry will not be present in the full size element design.

In general the comparison between NEC and measured impedances is quite close, the main discrepancy being that the measured curves tend to show a slightly higher resistance. For any results below about -40 dB the agreement with measurements is not very close due to the relatively large effect of noise and other small errors at low signal levels.

For the NEC results shown in the rest of this paper, unless stated otherwise the smaller arrays (3x3 or smaller) used the 300 segments per element model with tower and feed region. The 7x7 used the simpler NEC models without tower or feed region which are the 114 segment for the low band and 130 segment for the high band. This compromise in the larger NEC models were done due to the long computer runs required for larger arrays, especially an odd number of array rows and columns such as a 7x7.

4. 7x7 Array Results

Measured vs NEC active impedances and mutual coupling are compared below for the 7x7 array. These are significant because the active impedance is the antenna load impedance when the array is under operation.

4.1 Low Band 7x7

Figures 13, 14 and 15 show active low band broadside impedances for the full 7x7 array. Both dipoles in the corner and center element are shown, each for both Left and Right Hand Circular Polarization (LHCP and RHCP) broadside illumination. The corner dipole active impedance shows dependence on polarization but the center does not on broadside due to cancellation of diagonal orthogonal dipole coupling.

Surprisingly, the agreement with NEC does not seem to be adversely affected for the corner element despite the nearby truncation of the ground screen, since NEC modeled an infinite ground. Symmetry was used to obtain the 7x7 low band active impedances, so not all S-parameters were measured directly, some were determined by inference to be identical in theory to symmetrically placed elements. The center element active impedance includes contributions from the whole array, but the corner 7x7 measured active impedance only includes coupling terms up to 3 elements away. More distant elements were neglected for the corner element. Figure 16 compares impedances for the array if it were scaning a conical pattern at a constant 30 degrees off of zenith (broadside) over all 360 azimuth angles. The agreement with measurement is seen to be of about the same precision as for broadside.

4.2 High Band 7x7

For the high band 7x7 results, which begin with Figure 17, symmetry was not required to obtain all the S-parameters for the corner element active impedances since all S-parameters were measured, but symmetry was used for the corner element. Also, as for the low band 7x7, the center element active impedance includes contributions from the whole array but the corner measured active impedance only includes coupling terms up to 3 elements away. Figure 21 compares impedances for the array if it were scaning a conical pattern at a constant theta off of zenith (broadside) over all 360 azimuth angles, with theta equal to 30 degrees at 7 MHz and 10 degrees at 10 MHz. Agreement is about the same as for broadside.

The high band agreement for the most part is not as good as for the low band, but the same trends are evident: better agreement for small arrays than larger arrays, better agreement for S_{12} coupling terms than for the S_{11} self impedance for the most part, and

better agreement for S_{12} between dipoles in the same row or column than between dipoles on the diagonal, very poor or no agreement for coupling below about -40 dB due to noise.

4.3 Coupling as a Function of Distance

Figures 22 through 25 show the 7x7 mutual coupling (S12) terms from the corner dipoles to other dipoles along the side and on the diagonal for both the low and high bands. The reduction in coupling with distance is sufficient to ensure the convergence of the active impedance summation with increasing array size. It also provides the justification for not including elements more than 3 rows away in the active impedance summations for the corner dipoles. The calculated results in these four figures are actually from a 6x6 NEC array model which introduces a small amount of error when compared to the 7x7 measured array. The best agreement between NEC and the measurements is seen for the dipoles along the side. The coupling to the closest element on the diagonal is also accurately predicted. The two cases plotted (side parallel and diagonal orthogonal) are the best and worst cases in terms of agreement between NEC and measurements. Similar plots for the colinear dipoles along the side and the parallel dipoles on the diagonal are intermediate in accuracy.

5. Discussion of Modeling Errors

Errors between the measured and calculated results are generally small considering the number and complexity of elements. The worst errors typically occur for the active impedance of the largest array in the high frequency band. Possible sources of NEC modeling errors are listed below and discussed in more detail in the paragraphs that follow. One or more of these error sources working simultaneously, plus measurement errors, are the likely cause of the small discrepancies between NEC and the measurements. With several error sources occuring simultaneously it becomes more difficult to pinpoint the effect of each one and improve the NEC model.

NEC Model Sources of Error

Limitations of NEC algorithm: segmentation etc
Antenna feed region model
Ground screen mesh and truncation
Mechanical tolerances and alignment
Use of Symmetry for Active Impedance Sum
Truncation of Summation for 7x7 Active Impedances

The foremost limitation of the NEC code is that the antenna must be segmented into a finite number of match points. The match points are located at the center of each wire segment. Currents on the structure are solved only at the match points. This discretization of the currents on the structure results in some sacrifice of accuracy, with greater accuracy when using more segments. The total number of segments is limited by the computer resources available (RAM, disk size, and CPU speed). Another limitation of NEC is that only axial currents are computed on each wire; circumferential currents are neglected. For a fuller discussion the NEC algorithm the reader is referred to the NEC manual[1].

The modeling of the feed region of the antenna is critical for several reasons: The input impedance and mutual coupling terms are computed from the NEC output currents flowing on the feed point wire segments, so any errors there result directly in errors in the impedances and S-parameters. The currents are also largest near the feed region so it is critical that these be accurately modeled. Unfortunately, the structure in the feed region is also the most intricate and difficult to reproduce in NEC due to the large number of small, irregularly shaped, very thin or very wide conductors, such as printed circuit metalization for the scale model. The feed region of the scale model feed includes a fiberglass printed circuit board which cannot be included in NEC. The exact terminating impedance of the feed (looking back from the dipole feed points through the balun) is assumed to be

exactly 50 ohms for the NEC computation, but that is only approximated in the actual scale model by the coax feed and balun and by resistors with tolerances making a friction fit into a plated through hole in the pc board. The tower is difficult to model accurately in NEC because it it much wider than the conductors connected to it, but the resulting approximations in the tower model also affect the placement of other NEC conductors in the vicinity of the feed.

The infinite, perfectly conducting ground screen used in the NEC model is an approximation necessary because of the excessive number of wire segments that would be required to model the actual mesh used. The scale model ground screen was not completely planar since it sagged in places and also had slightly elevated platforms at the base of each tower, which may have contributed somewhat to errors in the comparison to NEC. The conductivity of the screen does not appear to have been a significant source of error since changing the conductivity of the ground plane in NEC did not make much difference in the input impedances. The 7x7 is the only array size that approached the truncated edge of the screen. Most of the evidence indicates that the infinite screen used in NEC was not a significant source of error when compared to the measured results which used a truncated screen. For the low band 7x7 the corner elements which are closest to the truncated edge actually showed better agreement with NEC active impedances than the center elements, although this was not the case for the high band. However, the self impedance and active impedances did show increasing errors with the number of elements, which may have been due to the edge truncation since a larger array would provide a coupling path for energy to reach the edge of the screen, whereas a smaller array at the center of the screen might be less affected by the edge.

The calibration of the network analyzer removes the effect of the balun and feed up to the feed point of the dipoles. However the measurement system is not completely error-free. Typical measurement uncertainties ranged from from +/- 1 dB and 4 degrees phase for the low band S_{11} to +/- .33 dB and 2.5 degrees phase for the high band S_{11}. Much of this is due to mechanical tolerances and alignment of the dipoles: for example the dipole tips were often about 2 inches off from their desired position due to rotation of the dipole arms.

The active impedances are obtained by summing the S-parameters as explained earlier. Symmetry in the array geometry permitted substitution of S-parameters in the summation, greatly reducing the number of measurements required. However this may have introduced some errors into the measured active impedances since an error in one measured S-parameter would be repeatedly included in the summation instead of being averaged out by different errors in other S-parameters. The use of symmetry as a source of error is supported by the 7x7 data shown, since the low band corner active impedance was more accurate than the low band center (which made more use of symmetry), and the high band corner was less accurate than the high band center (which made less use of symmetry). The truncation of the active impedance summation beyond 3 elements may have also contributed to the errors for the 7x7 array.

6. Conclusions

Overall there is good agreement between the measured and calculated results, including for the 7x7 active impedances. The agreement is better over the low band than the high band. Measurement and mechanical tolerances limit the measurement accuracy to about -40 dB. Mutual coupling is usually more accurately predicted by NEC than the S_{11} self impedance or the active impedance. Small arrays also show better agreement than large arrays even when differences in NEC segmentation is accounted for. For the largest arrays the NEC element model was simplified, which resulted in some additional calculated errors for the high band 7x7. The rms error for all the NEC scale model vs measurements appears to be in the vicinity of 15%.

7. References

1. "Numerical Electromagnetic Code - NEC-4 Method of Moments", Gerald Burke, Lawrence Livermore National Laboratory Report #UCRL-MA-109338, January 1992. Refer requests to Commander, US Army Information Systems Engineering Command, Attn: ASQB-OSE-TP, Fort Huachuca, AZ 85613-5300.

2 Collin, R E., "Foundations for Microwave Engineering", McGraw-Hill, New York, 1966. p.171

3 Hansen, R.C., "Microwave Scanning Antennas", vol. II, Peninsula Publishing, Los Altos, CA. 1985. p.213.

C:\HAARP7\WORDS\SCALEAPC\ACESPAP.WPD

Fig. 1. NEC Model of One Element with Tower and Feed Region.

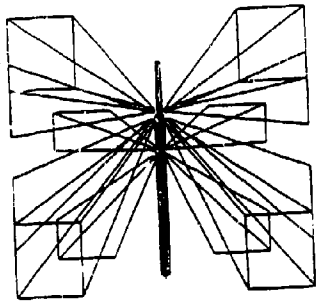

Fig. 2. NEC Model of One Element without Tower or Feed Region

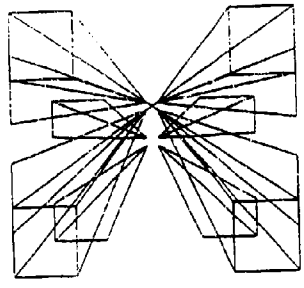

Fig. 3. Closeup Top View Showing NEC Model Tower Crossection and Feed Region.

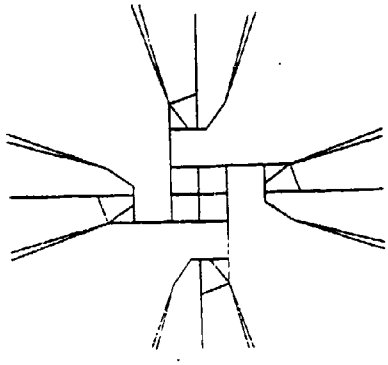

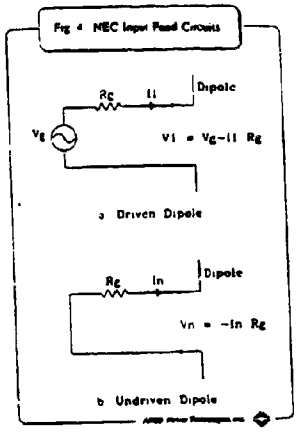

Fig 5. 1x1 High Band Crossed Dipole: S11, 7 - 10 MHz

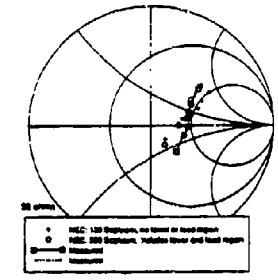

Fig 6. 2x2 High Band Active Impedance Comparing NEC Element Models

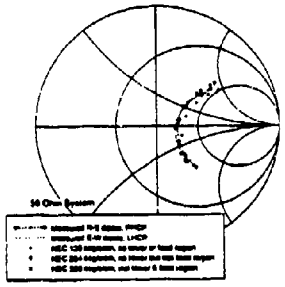

Fig 7 2x2 High Band Active Impedance Comparing NEC Element Models

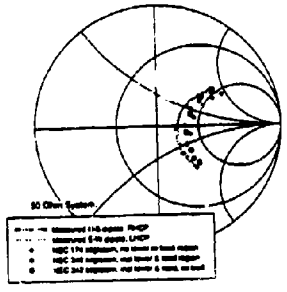

Fig 8 2x2 High Band Active Reflection Coefficient Magnitude

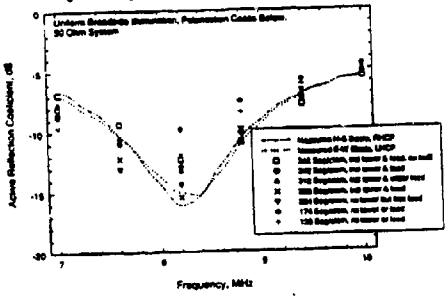

Fig. 9 1x1 Low Band Crossed Dipole S11, 2.8 - 7 MHz

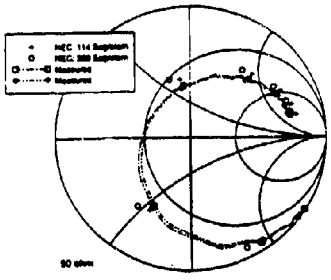

Fig. 10. 2x2 Low Band Active Impedances 2.8 - 7 MHz

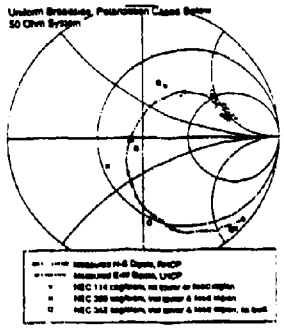

Fig. 11. 2x2 Low Band Active Impedances 2.8 - 7 MHz

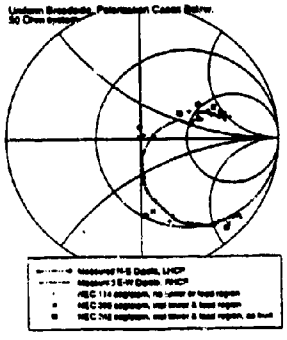

Fig. 12. 1x1 Low Band Crossed Dipole

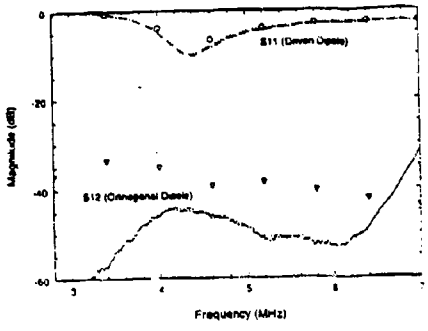

Fig. 13. 7x7 Low Band Active Impedance for Corner Dipoles 2.8 - 7 MHz

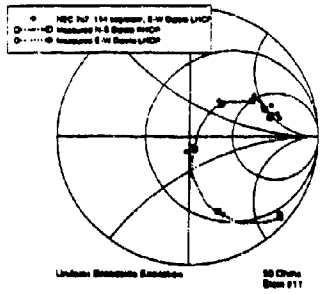

Fig. 14. 7x7 Low Band Active Impedance for Corner Dipoles 2.8 - 7 MHz

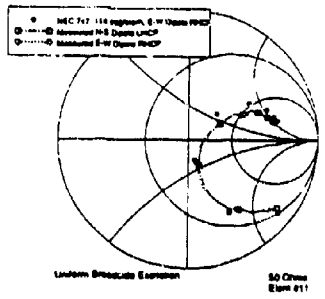

Fig. 15. 7x7 Low Band Active Impedance for Corner Dipoles 2.8 - 10 MHz

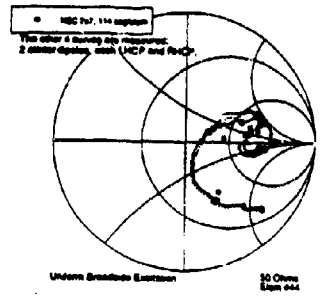

Fig. 16. 7x7 Low Band Full Scan Active Impedance for Center Dipoles

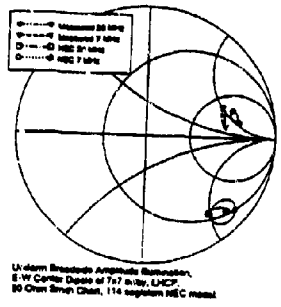

Fig. 17. 7x7 High Band Active Impedance for Corner Dipoles 7 - 10 MHz

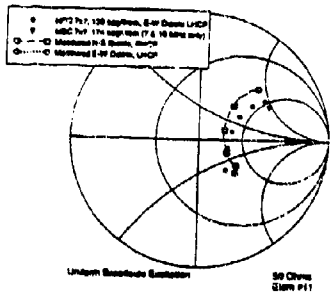

Fig. 18 7x7 High Band Active Impedance for Corner Dipoles 7 - 10 MHz

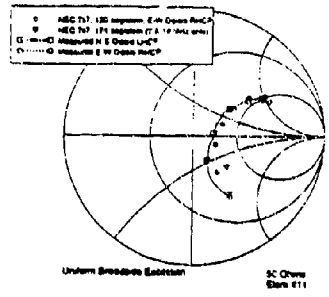

Fig. 19. 7x7 High Band Active Impedance for Center Dipoles 7 - 10 MHz

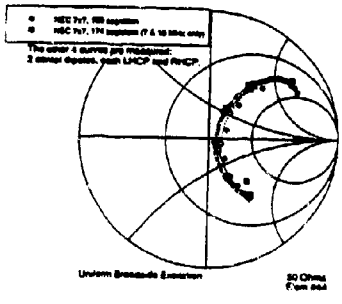

Fig. 20. 7x7 High Band Full Scan Active Impedance for Center Dipoles

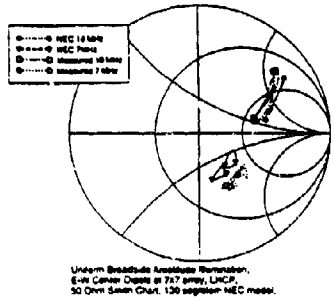

Fig. 21 Coupling from Corner Element (#11) to Parallel Dipoles along Side

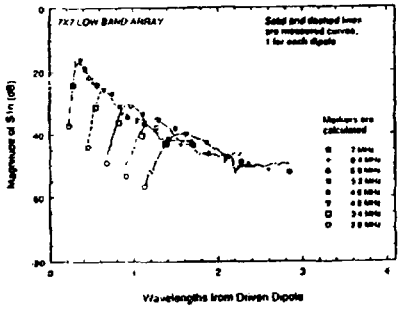

Fig. 22 Coupling from Corner Element (#11) to Orthogonal Dipoles along Diagonal

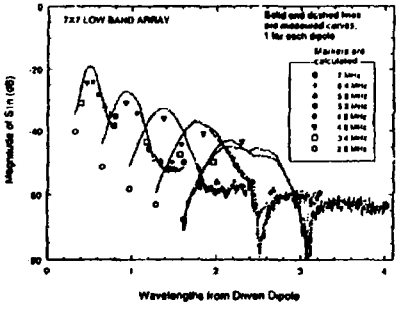

Fig. 23 Coupling from Corner Element (#11) to Parallel Dipoles along Side

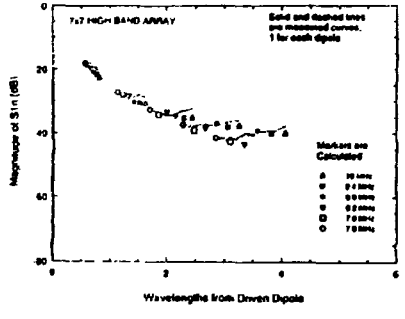

Fig. 24. Coupling from Corner Element (#11) to Orthogonal Dipoles along Diagonal

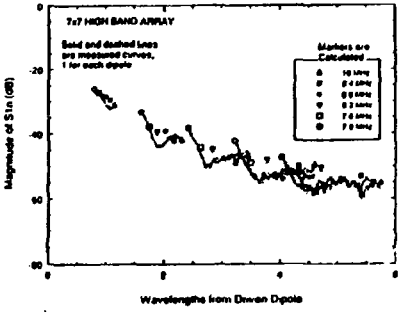

The Effects of Exceeding Mechanical Design Constraints on the Performance of HF Log-Periodic Dipole Arrays.

Duncan C. Baker[1], J. Tobias de Beer[1] and Nielen Stander[2]

[1]Department of Electrical and Electronic Engineering,
[2]Department of Mechanical Engineering,
University of Pretoria, 0002 Pretoria, South Africa.
e-mail: duncan.baker@ee.up.ac.za

ABSTRACT: Conventional practice requires that fairly stringent mechanical tolerances be adhered to in the design and manufacture of HF log periodic dipole array (LPDA) antennas. The effects of sagging, changes in element length and spacing of elements along the feedline, are examined for two HF LPDA's deployed in horizontal and sloping planes. Preliminary results indicate that in practice the mechanical design tolerances can be relaxed considerably, without significantly affecting the characteristics of the LPDA's. While further study is required it would appear that the tolerances could be relaxed by a factor of at least 5, or even more, without excessively degrading antenna performance in practice.

1 INTRODUCTION

This brief study of the effects of exceeding the design constraints recommended by Smith [1] for HF log-periodic dipole arrays (LPDA's), was prompted by problems caused by wind-induced vibrations in LPDA's designed and installed to conform to these recommendations [2]. When solutions for the problem of extreme vibration were sought, it was by no means certain what the effect of relaxing the recommended tolerances for element length, height above ground (sag) or spacing along the feedline would be on gain, take-off angles or input impedances of the LPDA's. Simple mechanical vibration dampers were found to be an effective interim solution to the problem [2].

In order to provide guidelines for future mechanical designs of LPDA's, the effects of exceeding the recommended tolerances of ±2.5% of element halflength for height above ground (sag), ±0.5% for the element length itself and ±0.1% for the spacing between elements, were investigated using NEC2 [3]. This exercise also offered an opportunity for further comparison of gain predictions obtained using the antenna design routines from HFMUFES4 [4] with those from NEC2. The subroutines from HFMUFES4 have the advantage of being easy to implement on a personal computer, and several orders of magnitude faster to run than NEC2. The basic design of the antenna is the same as that used in [5]. The design parameters of the 4-30 MHz LPDA are:- (a) rear element total length = 42.13m, (b) element length reduction factor = 0.87, (c) angle between element tips and feedline = 15 degrees, and (d) number of elements = 20. Unless otherwise stated all computations were made at 1MHz increments in the HF band.

In order to investigate the effects of sag of the LPDA structures, use was made of the program TOWEROPT developed by one of the authors (NS) for the design of mechanical structures. The program uses finite element structural modelling for non-linear analysis of an arbitrarily shaped guyed truss or cable structure. Allowance is made in the program for arbitrary grouping of structure members in design groups. Assumed masses per metre were 117 gm and 275 gm for the conductors and catenary/stay wires respectively. Appropriate loading allowance for mechanical connection components was made. The maximum breaking strain of the catenaries and staywires was about 20 KiloNewton.

Two cases were selected for this study. The first case is for an LPDA intended for use over a long distances, and the second for shorter distances of about 1200km.

2 EFFECTS OF SAGGING ON THE PERFORMANCE OF TWO DIFFERENTLY DEPLOYED LPDA'S

2.1 CASE 1 - LONG RANGE LPDA IN A HORIZONTAL PLANE

Figure 1 illustrates the statistical distribution of arrival angles of HF signals used in ionospheric communications over distances from several hundreds of km to 4000 km (after 6). Figures 2a and 2b show the gain contours, in dBi, predicted using NEC2 and HFMUFES4 respectively, as a function of take-off angle and frequency for an LPDA which has the same basic design as that used in [5]. The predictions are for a LPDA deployed in a horizontal plane 20 metres above smooth level ground with conductivity of 0.005 Siemens and relative dielectric constant of 15, corresponding to average ground, and with all elements lying in the horizontal plane. The predicted contour patterns for the two methods are in excellent agreement and are also well-matched to the required take-off angles.

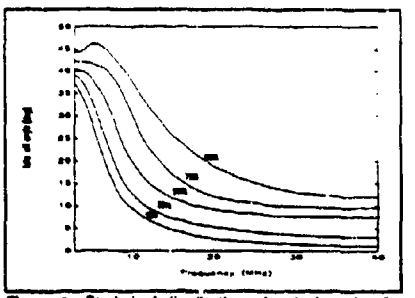

Figure 1. Statistical distribution of arrival angles for ionospherically propagated HF signals (after 6).

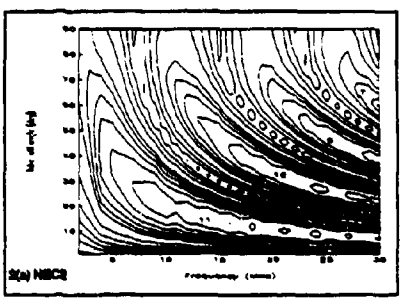

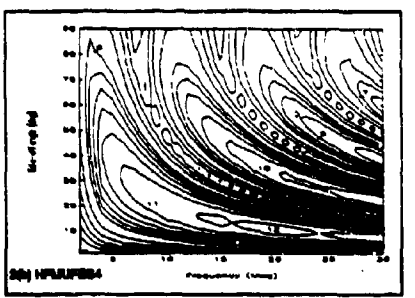

Figure 2. Gain contours predicted using (a) NEC2, and (b) HFMUFES4 for horizontally deployed LPDA 20m above the ground.

Figures 3(a), (b) and (c) illustrate the effect of raising and lowering the plane of the LPDA by 2m, or 10% of height, on the maximum gain, the take-off angle for maximum gain and the input impedance respectively. The induced changes in antenna performance are not expected to be significant in practice.

A real structure will of course sag under its own weight, as illustrated in Figure 4. The program TOWEROPT was used to analyse the effects of three cases of structural sag on the antenna characteristics. These cases are:- (a) an extreme case of maximum sag where the LPDA is considered to have been deployed on the ground with no prestress in any of the support wires or catenaries and raised into the design position 20m above the ground, (b) moderate prestressing such as could readily be achieved in practice, and (c) high prestressing with the catenaries prestressed to to a condition in which the strain in the final position was about 79% of the breaking strain of the catenary material.

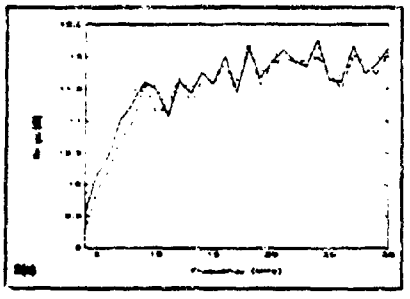

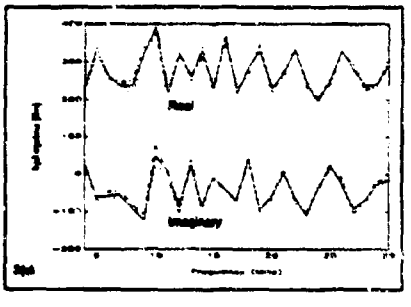

Figures 5(a), (b) and (c) illustrate the effects of sagging on the antenna performance predicted using NEC2. The maximum sag in height with no prestressing was found to be 4.33m at the sixteenth element, with the first element being the shortest. The length of the sixteenth element is

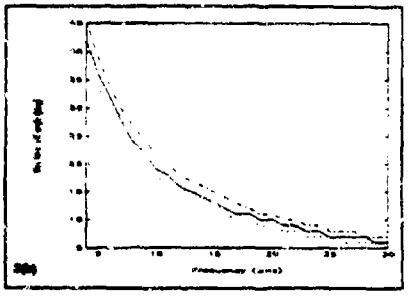

Figure 3. Effects of changing the height of horizontally deployed LPDA by +/- 2m on (a) maximum gain, (b) take-off angle at maximum gain, and (c) input impedance.

——— 20m above ground (reference height)
– – – 10m above ground
• • • 22m above ground

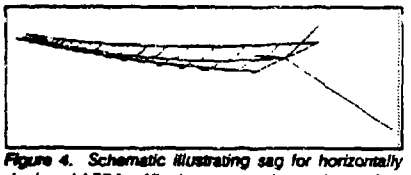

Figure 4. Schematic illustrating sag for horizontally deployed LPDA. All wires, catenaries and staywires are shown.

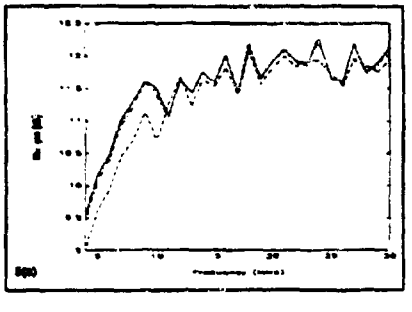

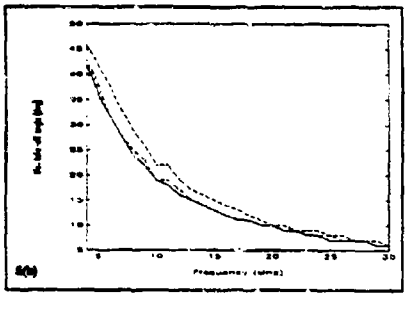

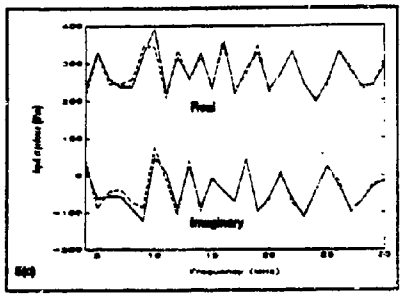

Figure 5. Predicted antenna performance for horizontally deployed LPDA for various conditions of strain in supporting catenaries and staywires.

——— *ideal case no sagging*
• • • • • *minimal sagging, final strain = 79% of breaking strain*
– • – • *moderate sagging, final strain = 40% of breaking strain*
– – – *maximum sagging, final strain = 8% of breaking strain*

24.14m, thus the sag is about 18% of the total element length. In terms of percentage the maximum sag was about 28% of the total element length at the fourth element. For this structure a decrease of 0.8 dB was predicted in the maximum gain at 10 MHz, with an average decrease of about 0.5 dB between 5 and 10 MHz. The predicted take-off angle at maximum gain increased by a maximum value of about 6 degrees at about 5 to 6 MHz. No significant changes were predicted in the antenna impedance. In practice it is expected that it will be relatively easy to reduce the sag to the order of 1-2m or 5-10% of height in this example, without placing excessive mechanical strain on the catenaries and/or staywires.

2.2 CASE 2 - SLOPING LPDA FOR USE OVER A DISTANCE OF 1200 KILOMETRES.

Figure 6 shows the expected range of take-off angles for distances of 400 to 4000 km for single hop ionospheric propagation via the E- and F-regions, for all frequencies, times of day and seasons, and for low to high solar activity. The figure is based on results from HFMUFES4 for temperate latitudes. At 1200 km the take-off angles lie between about 18 and 32 degrees, measured from the horizon. The highest probable frequency predicted over this distance using HFMUFES4, is 23 MHz. Optimum matching of the antenna take-off angles to the required angles for communications is expected with the front element at a height of 1.5m and an array slope of 33.8 degrees, as measured from the horizontal.

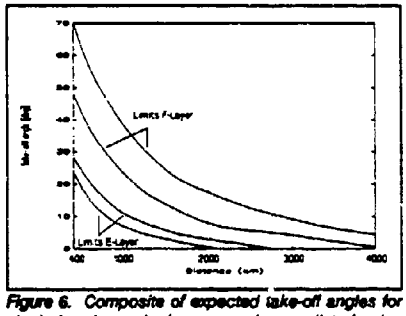

Figure 6. Composite of expected take-off angles for single hop ionospheric propagation predicted using HFMUFES4 - all frequencies, times of day, seasons and solar activity.

Figures 7(a) and (b) show the gain contours, in dBi, as a function of take-off angle and frequency as obtained using NEC2 and HFMUFES4 respectively. The results are in reasonable agreement only at the low frequency end and at lower take-off angles. The predicted gain contours differ increasingly at higher take-off angles as the frequency increases. The differences are believed to be due to the simplified approach used in HFMUFES4 to estimate the effect of ground reflection on antennas which are ground arrayed. The vertical radiation pattern is computed by summing the contributions for the direct and ground reflected rays using the appropriate reflection coefficient for horizontal polarisation. As far as can be determined from [7], which predates and gives a detailed description of the approach used in [4], this method does not appear to take into account fully the orientation of the plane of the LPDA relative to the ground. This aspect requires further investigation. It is fortuitous that the measured results and those predicted using HFMUFES4 and NEC2 for a frequency of 5.27 MHz as reported in [5] were in reasonable agreement. From

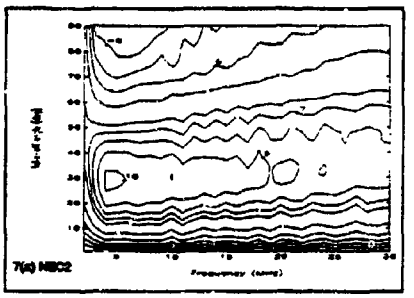

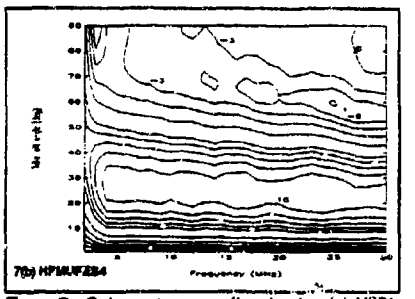

Figure 7. Gain contours predicted using (a) NEC2, and (b) HFMUFES4 for sloping LPDA

a practical point of view, it is also fortunate that there is reasonable agreement at the lower take-off angles used for HF communications between results predicted using NEC2 and HFMUFES4.

Figure 8 illustrates the sloping LPDA configuration with a condition of severe sagging. All antenna elements, catenaries, support wires and stays are shown. As with Case 1 the antenna was simulated in a horizontal plane on the ground with all elements, catenaries and back stays in a condition of zero extension or stress and then raised into the final position. Figures 9(a), (b) and (c) compare the changes in the LPDA characteristics for the ideal case, maximum sag corresponding to no prestressing of the catenaries and/or stays, a condition of moderate prestressing such as could be easily achieved in practice, and extreme prestressing such that the strain of the catenaries in the final position is about 88% of the breaking strain of the catenary and strywire material. For the case of extreme sagging, the greatest effect is generally observed

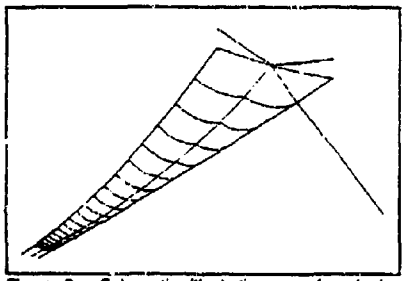

Figure 8. Schematic illustrating sag for sloping deployed LPDA. All wires, catenaries and strywires are shown.

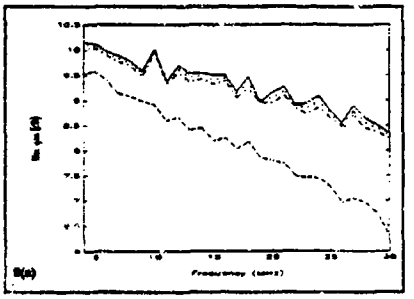

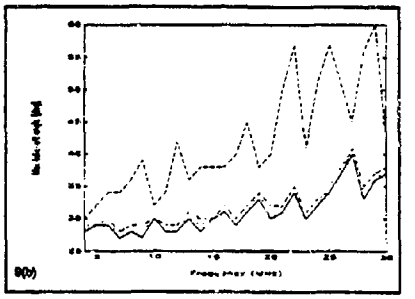

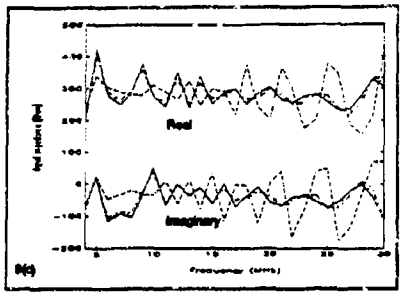

Figure 9. Predicted antenna performance for sloping LPDA for various conditions of strain in supporting catenaries and staywires.

———	*ideal case no sagging*
• • • •	*minimal sagging, final strain = 88% of breaking strain*
– • –•	*moderate sagging, final strain = 45% of breaking strain*
– – –	*maximum sagging, final strain = 8% of breaking strain*

at the high frequency end. For the case considered this occurred at the third element where a sag of 33% of total element length is predicted. The LPDA performance predictions for moderate prestressing, such as could be achieved in practice, show very little difference compared to the ideal case.

3 THE EFFECTS OF CHANGING ELEMENT LENGTH

In order to examine the effects of changes in element length, the length of the thirteenth element, with length 15.894m, was changed by plus and minus 6.5%, or half of the 13% by which successive elements are progressively shortened. Element number one is the shortest element at a length of 2.988m. The reason for this somewhat drastic change in element length is because little significant changes were predicted for length changes of the order of 2.5%, or about five times the recommended tolerance of 0.5%. Significant effects were noted for the larger length variations for the

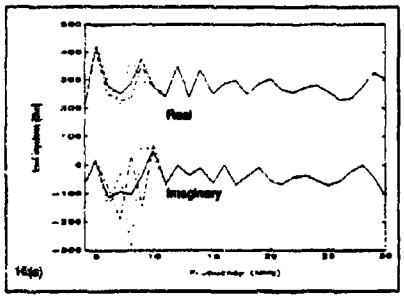

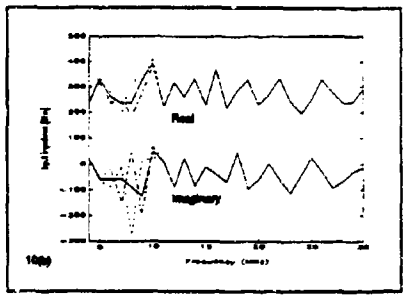

Figure 10. Comparison of predicted input impedances for +/- 6.5% changes in length of element 13, (a) sloping LPDA, (b) horizontally deployed LPDA

———	*ideal case*
– – – –	*+ 6.5%*
• • • • •	*- 6.5%*

predicted input impedance, but not the gain performance, between 5 and 10 MHz for both the sloping and horizontally deployed LPDA. These results are shown in Figures 10(a) and (b) respectively for the sloping LPDA and the LPDA in the horizontal plane. Balmain and Nkeng [8] have shown experimentally that asymmetrical sharply resonant modes can occur due to transmission line resonances. In order to investigate this aspect, the predictions of input impedance

were repeated for the LPDA deployed in a horizontal plane 20m above ground, in 0.2 MHz increments between 5 and 12 MHz only, for an increase in length of the thirteenth element of 6.5%. The results are shown in Figure 11 and suggest that this phenomenon could occur on the antenna structure.

4 THE EFFECTS OF CHANGING ELEMENT SPACING

The last aspect investigated in this short study was the effect of displacing the thirteenth element by 10% of the design spacing of 3.855m between it and the next shortest element of length 13.828m. The permitted tolerance in this case is plus or minus 0.19%. The positions of all other elements were left unchanged. Once again the most significant changes predicted from a practical point of view were in the input impedances of the two antennas. By way of illustration Figures 12(a) and (b) show the predicted input impedances for the sloping and horizontally deployed LPDA's. No attempt was made to check for transmission-line resonances of the type described in [8].

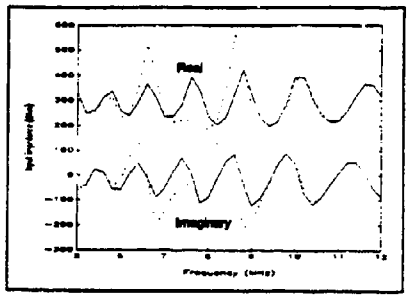

Figure 11. Comparison of predicted input impedances for ideal case and 6.5% increase in length of element 13 for horizontally deployed antenna at 0.2 MHz increments.

——— *ideal case*
• • • • + 6.5%

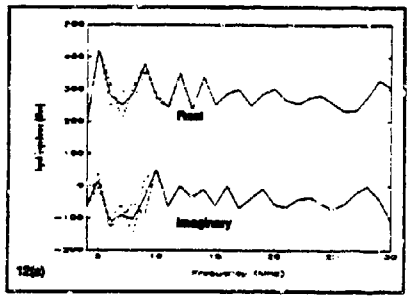

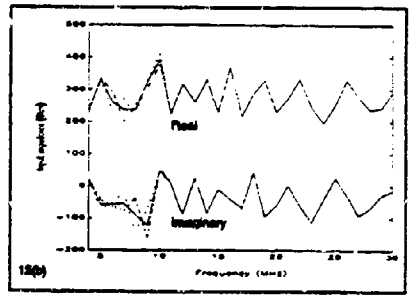

Figure 12. Predicted input impedances for +/- 10% changes in spacing between elements 12 and 13, (a) sloping LPDA, (b) horizontally deployed LPDA

——— *ideal case*
– • – • *+ 10%*
• • • • • *- 10%*

5 DISCUSSION AND CONCLUSIONS

Gain contours predicted using NEC2 and HFMUFES4 were compared for two cases. The first case is a horizontally deployed HF LPDA 20m above the ground, such as could be used for long distance ionospheric communication. The second case was for a sloping LFDA similar to that which would be used over a range of about 1200 km, where the vertical radiation pattern must stay reasonably constant over the usable HF band. Excellent agreement is achieved between the two methods for the horizontally deployed antennas. For the sloping LPDA agreement at the higher frequencies and elevation angles is poor. This is probably due to the fact that the effect of the slope is not properly accounted for in the HFMUFES4 formulation. It is fortuitious that the agreement at the lower frequencies and

elevation angles between NEC2 and HFMUFES4 predictions, is acceptable for practical HF communications applications.

Results predicted using NEC2 for cases in which the arrays are allowed to sag, or the element length or spacings are allowed to vary by more than the recommended tolerances, suggest that these tolerances could be relaxed substantially. Until further studies are made it is suggested that a factor of five greater than the values given in [1] would not lead to excessive and unacceptable degradation of antenna performance. From a practical point of view it is easier to maintain relatively high tolerances in the case of element length and spacing. In the case of sagging of the antenna structure, an effort to adhere to the strict specification of [1] will lead to high stresses in catenaries and staywires for HF antennas. Failure could result from metal fatigue induced by wind driven mechanical resonances on the structure.

It is suggested that the strong coupling between the various elements account for the slow degradation in performance of the antennas. However, the possibility of asymmetric resonance effects of the type described in [8], resulting from the relaxation of the design tolerances, need to be investigated further.

6 REFERENCES

[1] **Smith, C.E.**, 'Log Periodic Antenna Design Handbook', First Edition, Smith Electronics Inc., Cleveland, Ohio, 44141, 1966.

[2] **Baker, D.C.**, 'Mechanical damping of vibration of staywires on antenna masts', ACES Newsletter, Vol. 7, No. 1, pp.41-42, 1992.

[3] **Burke, G.J. and A.J. Poggio**, 'Numerical Electromagnetics Code (NEC) - Method of Moments', NOSC Technical Document TD 116, Naval Ocean Systems Center, San Diego, California, 1981.

[4] **Peters, L.R., J.L. Lloyd, G.W. Haydon and D.L. Lucas**, 'Estimating the performance of telecommunication systems using the ionospheric transmission channel', NTIA Report 83-127, US Department of Commerce, Boulder, Colorado, 1983.

[5] **Baker, D.C.**, 'A Limited comparison of predicted and measured results for an HF ground-arrayed log periodic dipole array', ACES Journal, Vol. 5, No. 1, pp.25-38, Summer, 1990.

[6] **Stark, A.**, 'Rotatable log-periodic dipole antennas for 5 to 30 MHz', News from Rohde and Schwarz, No. 63, p. 16-22, No year given.

[7] **Haydon, G.W., M. Leftin and R. Rosich**, 'Predicting the performance of high frequency skywave telecommunications systems', OT Report 76-102, US Department of Commerce, Boulder, Colorado, 1976.

[8] **Belmain, K.G. and J.N. Nkeng**, 'Asymmetry phenomenon of log-periodic dipole antennas', IEEE Trans. Antennas and Propagat., Vol. AP-24, pp. 402-410, 1976.

Modeling of a Cylindrical Waveguide Slot Array, a Loop-Fed Slot Antenna and an Annular Slot Antenna with the BSC and ESP Codes

Wendy L. Lippincott
Naval Research Laboratory
Washington, D.C. 20375

Dr. Joseph A. Bohar
Antenna Corporation of America
Harleysville, PA, 19438

Abstract

Experimental data and modeling results from the Ohio State BSC[1] (Basic Scattering Code) and the Ohio State ESP[2] (Electromagnetic Surface Patch) code were compared for three antennas: a cylindrical waveguide slot array, a loop-fed cylindrical slot antenna, and an annular slot antenna. The BSC code gave good results for the antennas alone on a small ground plane. It tended to mispredict by a few dB the ripple in the azimuth pattern caused by a large scatterer placed a few wavelengths away. The ESP code modeling for the loop-fed slot antenna gave good results for both the antenna alone and in the presence of a large scatterer.

1. Introduction

The cylindrical waveguide slot array, loop-fed cylindrical slot antenna, and annular slot antenna are omni-directional antennas that can be placed on complex platforms where considerable effort must be made to ensure the surrounding structures do not unduly affect the radiation patterns. Decisions regarding antenna placement can be made through anechoic chamber studies or computer EM (electromagnetic) simulations. This study was designed to validate the use of the BSC and ESP codes in modeling these antennas and their surroundings. The BSC code is based on the Uniform Geometrical Theory of Diffraction (UTD) and is a HF (high frequency) ray tracing/diffraction code. The ESP code uses the method of moments. In general, the BSC code is better suited for structures many wavelengths in dimension. The ESP code provides more exact modeling, but becomes computationally impractical for large structures.

2. Cylindrical Waveguide Slot Array

The cylindrical waveguide slot array can have either horizontal or vertical polarization depending on the slot orientation. Both polarizations were modeled. This antenna was only modeled with the BSC code. Modeling with the ESP code would require a complex mesh, and it is doubtful whether it would model the internal waveguide cavity appropriately. This antenna has a relatively high frequency compared to the surrounding structures, so the added complexity and computational burden of using the ESP code was not warranted.

2.1 Horizontally Polarized Cylindrical Slot Array

Fig. 1 shows a horizontally polarized slot array. The array is fed at the bottom by a short stub inside the tube. Machined onto the hollow tube are 8 columns of slots and 14 rows. The slots are tilted both as an aid in packing and also to control the amount of radiation of each slot. The amount of tilt increases vertically to offset the decreasing EM energy in the tube. The tilt is designed so that the amplitude out of the column of slots follows a truncated cosine distribution. The average slot tilt angle is 12.8°, so some cross polarization does exist.

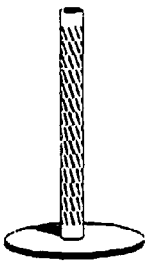

Fig. 1. Horizontally polarized cylindrical slot array

The slot length is $\lambda/2$ and the distance between the rows is 0.54 λ. The tube outer radius is 0.52 λ. The array is relatively ground plane independent because little of the radiation pattern intercepts the ground plane. The phases in the individual slots for the array are calculated knowing the cutoff frequency of the TM_{01} mode in a circular waveguide. These values and the truncated cosine amplitude distribution are then used as input data for the BSC code.

As stated in the BSC code manual, one limitation of the code is that it does not accurately model radiating elements mounted on curved surfaces. However, for this antenna, reasonable results were obtained by positioning the radiating elements a short distance away from the curved surface. The slots were positioned on the measured outer radius, and the cylinder radius was adjusted inward 5% so that the radiators were not directly on the surface of the cylinder. Once this was done, good matches were obtained between the experimental and modeling data. Figs. 2 and 3 show the azimuth and elevation patterns using this method versus the experimental data on a 43 λ diameter ground plane. These runs were done at the center frequency, f_c, of the antenna. The azimuth pattern was taken 60° from boresight. As can be seen, excellent agreement is obtained for both patterns. The BSC code only computes relative gain. This is then scaled to match the known gain of the antenna.

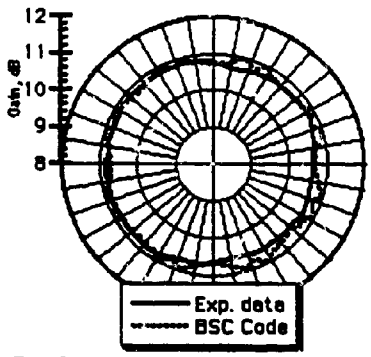

Fig. 2 Horizontally polarized Slot Array, Azimuth Pattern

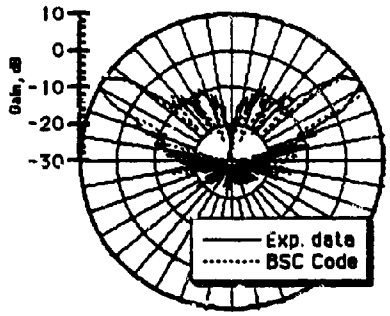

Fig. 3 Horizontally polarized Slot Array, Elevation Pattern

Each of these runs took 20 minutes on a 486 PC at 50 MHz or 2 hours on a Mac IIfx computer. The results of the BSC code also compared well to results of a program that uses a harmonic series expansion for an infinite cylinder.

This antenna was also modeled as an eight-sided cylinder, with the slots mounted directly on the plates. The size of the plates was first adjusted so that the perimeter matched the circumference of the actual cylinder. Slight variations of the plate sizes were then made to better match the experimental data. For modeling on a 43 λ diameter ground plane, the elevation patterns matched the experimental data well. The computed azimuth pattern at 60° from boresight had 2 dB of ripple. When the array was modeled with 16 sides instead of 8, the ripple in the azimuth pattern increased. This increase in error is believed to be due to the edges of the plates being too near to the center of the slots. For accurate modeling, plate dimensions in the BSC code should be no less than one wavelength.

2.2 Vertically Polarized Cylindrical Slot Array

The vertically polarized slot array is similar to the horizontally polarized slot array except that its slots are oriented horizontally. Fig. 4 shows this antenna. This slot array has 6 columns of 18 slots each. The slot length is 0.35λ and the spacing between the rows is 0.39λ. The tube inside and outside radii are 0.418λ and 0.462λ respectively.

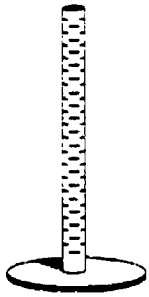

Fig. 4 Vertically polarized cylindrical slot array

The phases in the individual slots for the array are calculated knowing the effective cutoff frequency of the TM_{01} mode in a circular waveguide. For this antenna, an additional phase shift is introduced by the slots, effectively changing the cutoff frequency of the waveguide. Once this effective cutoff frequency is determined empirically, the phases are then calculated and used as input to the BSC code. The amplitude of the slots along the axis of the tube is known to follow a truncated cosine distribution.

This antenna was modeled with the BSC code using both a cylindrical center and flat plates. For the cylindrical center modeling, good results were obtained by modeling the antenna as slots placed a short distance from a

cylinder. The slots were positioned on the measured radius, and the cylinder radius was adjusted inward 2.5% so that the radiating elements were not mounted directly on the cylinder surface. Once this was done, good matches were obtained between the experimental and modeling data. Figs. 5 and 6 show the elevation and azimuth patterns compared to experimental data. The azimuth pattern was taken 60° from boresight. There is a strong central lobe on the modeling data not seen experimentally. The actual antenna has a choke ring on top of it to suppress radiation along the tube. In the modeling, a small plate on top of the antenna was used to model the choke, but this did not have much effect in suppressing the central lobe. With vertical polarization, the ground plane has more of an effect on the far-field pattern than for horizontal polarization.

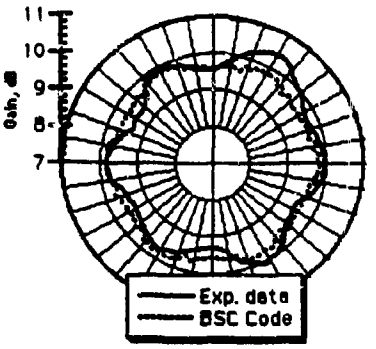

Fig. 5 Vertically polarized Slot Array, Azimuth Pattern

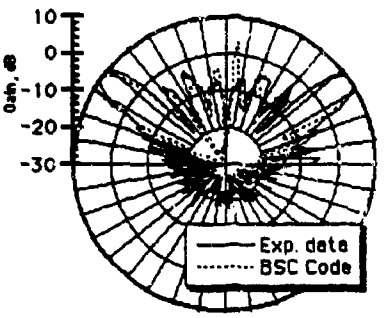

Fig. 6 Vertically polarized Slot Array, Elevation Pattern

This antenna was also modeled with slots mounted on six flat plates. The computed elevation patterns for the vertically polarized antenna matched the experimental data well. For the azimuth pattern at an angle of 60° from boresight, the computed ripple was 2.5 dB compared to 1.1 dB determined experimentally. This error is due to the interaction of the slot radiation with the edges of the plates. With vertical polarization, the diffraction off the side plate edges is much more pronounced than for the horizontal polarization case and causes a poor match to the experimental data. The antenna was also modeled with 12 sides instead of 6. This did not change the results substantially.

3. Dual-polarized cylindrical slot Antenna

The loop-fed cylindrical slot and annular slot antennas form a combination structure with the annular slot antenna placed below the loop-fed slot. Fig. 7 shows this antenna. The loop-fed slot gives horizontal polarization and the annular slot gives vertical polarization. The loopfed slot antenna is fed by four wires printed on a circuit board (only two loops are seen in the figure because the other two loops are on the other side of the circuit board). The annular slot is fed by a small stub underneath the main cylinder.

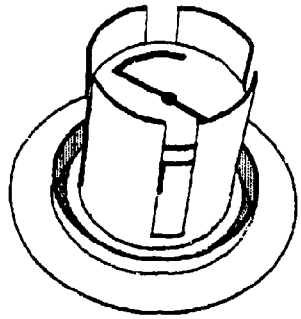

Figure 7. Loop-fed cylindrical slot/annular slot antenna

3.1 Loop-fed Slot Antenna

The radius of the cylinder is 0.256 λ. The loopfed slot antenna was modeled in the BSC code as an 8-plate approximation to a cylinder (8-sided cylinder). The slots were placed directly on the plates. When modeled as a four-sided cylinder, the peaks in the omni pattern occurred between the slots instead of directly out from the slots as seen in the experimental data. The 8-sided cylinder modeling compared to experimental data is shown in figs. 8 and 9 for the elevation pattern and azimuth pattern 60° from boresight. The peaks in the azimuth pattern occur directly out from the slot positions. The antenna was mounted on a 9 λ diameter ground plane. Good agreement was obtained.

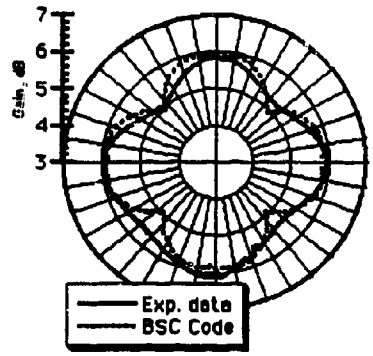

Fig. 8 Horizontally polarized Loop-fed Slot, Azimuth Pattern

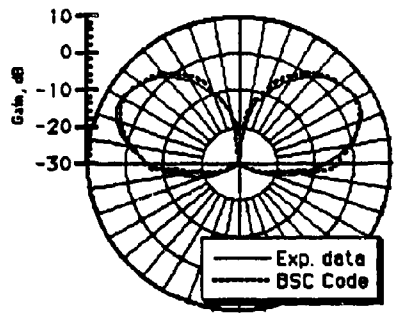

Fig. 9 Horizontally polarized Loop-fed Slot, Elevation Pattern

Modeling this antenna with a cylindrical center was also tried. This method did not work well for this antenna. Large notches occurred in the azimuth pattern.

Results were also obtained with a large scatterer on the ground plane. As shown in Fig. 10, a large 2.3 λ x 1.9 λ width plate was placed near the edge of the ground plane, directly out from a slot.

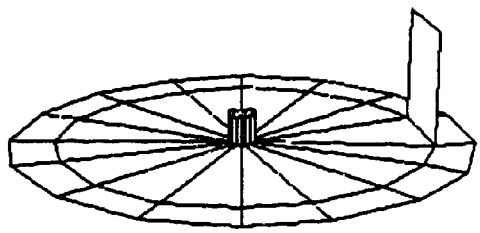

Fig. 10 Loop-fed/Annular Slot Antenna on 9 wavelength diameter ground with large plate scatterer

Figs. 11 and 12 shows comparisons of experimental and modeling data for 2 frequencies for the azimuth pattern at 60° from boresite. The BSC code in general predicts less ripple than the experimental data.

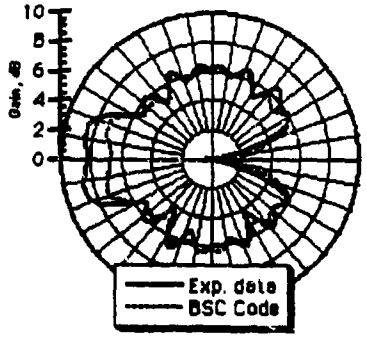

Fig. 11 Horizontally polarized Loop-fed Slot, at f_c with large plate scatterer

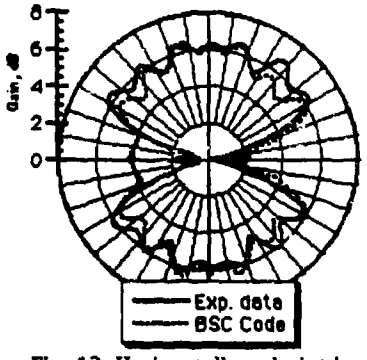

Fig. 12 Horizontally polarized Loop-fed Slot, at 0.9 f_c with large plate scatterer

A smaller 1.16 λ by 0.93 λ plate was also used in place of the larger 2.3 λ x 1.9 λ plate. For this case, the BSC code matched the data better, with a maximum error in the azimuth patterns of 1 dB.

The loopfed slot antenna was also modeled with the ESP MOM code. Fig. 13 shows the antenna as it was modeled with flat plates and wires.

The ESP code has a built-in mesh generator. For the mesh generator to work efficiently, it is necessary to break up the structure into plates that are close to rectangular. Otherwise, too many modes are used to mesh the surface. Wedge-shaped plates are particularly bad. A maximum of 6800 modes could be modeled on the a CRAY YMP with 0.5 GBytes of RAM.

Fig. 13 ESP Code Plate and Wire Model of Loop-Fed/Annular Slot Antenna

Figs. 14 and 15 show the results of the experimental and ESP code modeling data for the loop fed slot antenna mounted on an 9 wavelength diameter ground plane alone. The peaks in the azimuth pattern occur directly out from the slot positions. The ESP code predicts more power towards boresight, as seen in the elevation plot. When a top plate was placed on the antenna to try and suppress some of the radiation towards boresight, poor results were obtained.

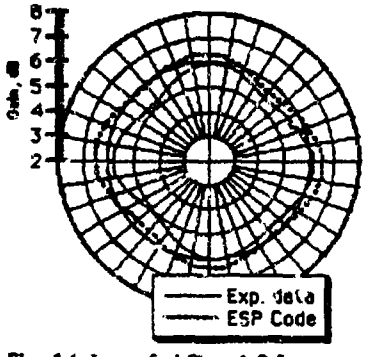

Fig. 14 Loop-fed Slot, 1.0 f_C on 9 wavelength dia. ground alone, 60° azimuth pattern

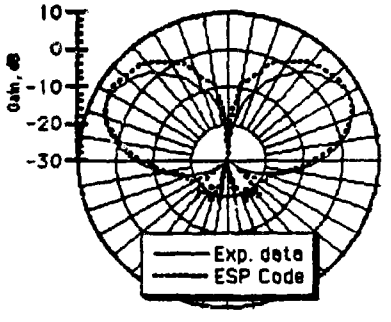

Fig. 15 Loop-fed Slot, 1.0 f_C on 9 wavelength dia. ground alone, elevation pattern

Figs. 16 and 17 compare experimental and modeling data when a large 2.3 λ x 1.9 λ width plate was added near the edge of the ground plane. The elevation pattern for this case is the cut through the plate scatterer. Figs. 18 and 19 show the results for a lower frequency, 0.9 f_C. Figs. 20 and 21 show the results for a higher frequency, 1.13 f_C. Good agreement was obtained for all these cases. For all these figures, the actual calculated gain is plotted, unlike the RSC code results, which were normalized.

For runs on the 9 wavelength diameter ground plane, the code was set to mesh the plates for 0.2 modes/λ. With fewer modes/λ, the code would bomb with a floating point exception during the run. For the 1.13 f_C runs, 7900 modes were needed. This run needed ~63 MWords and 10 hours on a Cray C90. For the 0.9 f_C runs, 5054 modes were needed. This run needed ~45 MWords and 28 hours on a Cray YMP.

Another option when using the ESP code is to approximate the finite ground plane with an infinite ground. For this case, the method of images is

used and the ground plane does not need to be meshed. This saves both in the number of modes to be solved for and also in the complexity of specifying the ground plates.

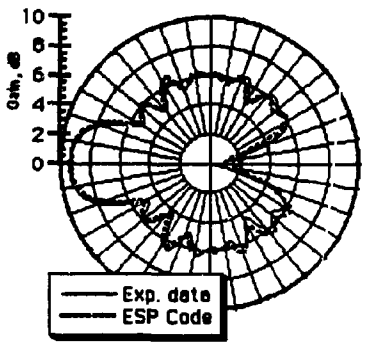

Fig. 16 Horizontally polarized Loop-fed Slot, 1.0 f_c with large plate scatterer, 60° azimuth pattern

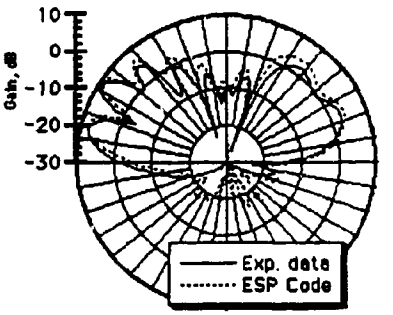

Fig. 17 Horizontally polarized Loop-fed Slot, 1.0 f_c with large plate scatterer ,elevation pattern

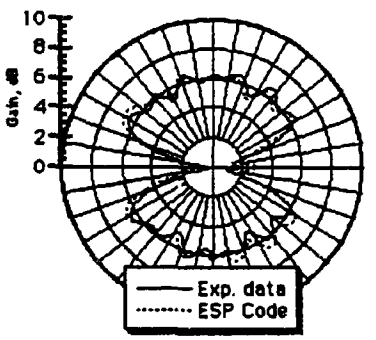

Fig. 18 Horizontally polarized Loop-fed Slot, 0.9 f_c with large plate scatterer, 60° azimuth pattern

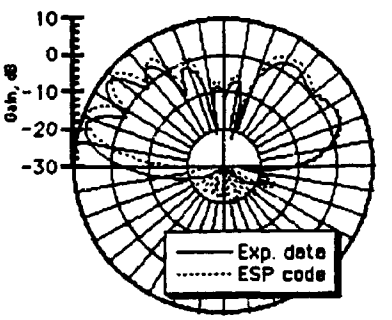

Fig. 19 Horizontally polarized Loop-fed Slot, 0.9 f_c with large plate scatterer ,elevation pattern

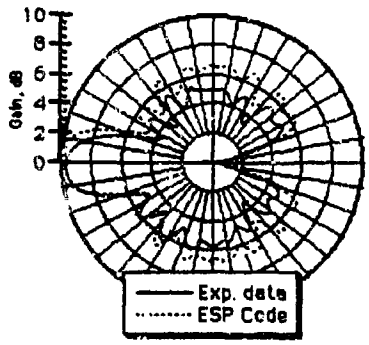

Fig. 20 Horizontally polarized Loop-fed Slot, 1.13 f_c with large plate scatterer, 60° azimuth pattern

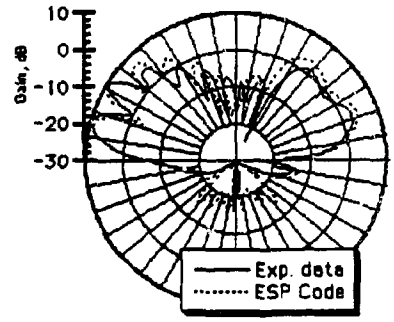

Fig. 21 Horizontally polarized Loop-fed Slot, 1.13 f_c with large plate scatterer ,elevation pattern

3.2 Annular Slot

The annular slot antenna is part of the dual polarization antenna shown in Fig. 7. The annular slot is fed by a small stub underneath the main cylinder. The slot aperture circles around the main cylinder of the loop-fed slot antenna. For the BSC code annular slot modeling, a cylinder is placed on top of a ground plate. To simulate the annular ring, a set of 64 slots are placed flat on the ground plane surrounding the cylinder, with their short dimension aligned radially. Fewer than 64 slots caused the azimuth pattern to have too much ripple. This antenna could be modeled accurately with as few as 8 slots (or as an annular ring source) when the cylindrical center was omitted. However, the cylindrical center could interact with other scatterers in a complex setting, and so it was thought best to include it. The annular ring source provided in the BSC code gave zero output when a cylinder was placed in the center of it, presumably because the model approximates the annular ring as a point source at its center.

Figs. 22 and 23 compare the azimuth and elevation patterns for the modeling and experimental data. The azimuth pattern was computed 60° from boresite. A 9 λ diameter ground plane was used. Good agreement was obtained. The BSC modeling results exhibited a slightly non-symmetric azimuth pattern, the cause of which is unknown at this time. The number of significant digits of the input data was increased and this had no effect on the output.

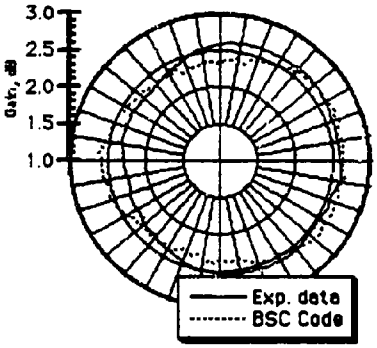

Fig. 22 Vertically polarized Annular Slot, Azimuth Pattern

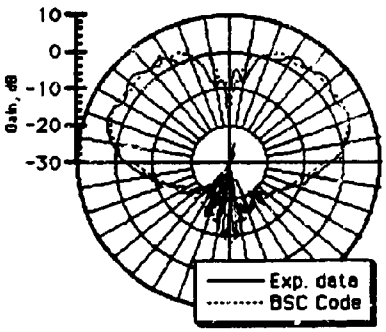

Fig. 23 Vertically polarized Annular Slot, Elevation Pattern

Results were also obtained with another scatterer on the 9 λ ground plane. As shown in Fig. 10, a large 2.3 λ x 1.9 λ width plate was placed near the edge of the ground plane. Figs. 24 and 25 show comparisons of experimental and modeling data for 2 frequencies for the azimuth pattern at 60° from boresite. The BSC code in this case predicts a deeper null in the direction of the plate than the experimental data.

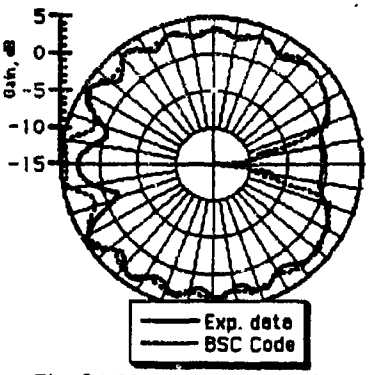

Fig. 24 Vertically polarized Annular Slot, 1.0 f_c with large plate scatterer

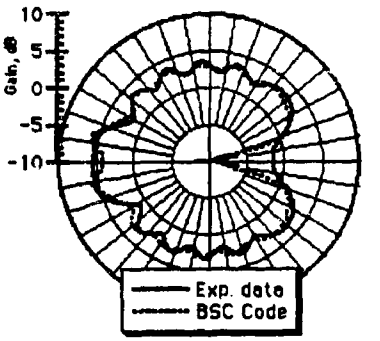

Fig. 25 Vertically polarized Annular Slot, 0.9 f_c with large plate scatterer

The annular slot antenna was also modeled with the ESP code, using a small monopole as the source. Fig. 13 shows the antenna as it was modeled with flat plates and wires. The source is underneath the center plate. The results so far have shown the code predicting on the average 6 dB of ripple both in the elevation and azimuth patterns which is much greater than the 1 dB ripple seen experimentally. Other techniques are currently being examined to improve this.

4.0 Conclusion

For the three antennas discussed, the BSC code gave good results for the antennas alone on a small ground plane. It tended to inaccurately predict by a few dB the ripple in the azimuth pattern caused by a large scatterer placed a few wavelengths away. The BSC code was found to be easy to use, did not require much computation time, and was well suited for modeling structures of several wavelengths in dimension. The ESP code modeling for the loop-fed slot

antenna gave good results for both the antenna alone and in the presence of a large scatterer. This code requires more time to implement, since the structure must be broken down into plates and wires. It is computationally intensive, but with our current maximum resource of a CRAY C90 with 96 MWords of memory, could model a structure ~ 15 λ x 15 λ in size.

5.0 References

[1] R. J. Marhefka, J. W. Silvestro, *Near Zone - Basic Scattering Code, User's Manual with Space Station Applications*, Version 3.2, Ohio State University, Report No. 716199-13, Performed under Grant No. NSG 1498, March 1989.

[2] E. H. Newman, A User's Manual for the Electromagnetic Surface Patch Code: ESP Version IV, Technical Report 716199-11 (Grant No. NSG 1498), August 1988.

ACKNOWLEDGMENT

The authors are grateful to Bruce Folk and Jim Barnes of the Naval Research Laboratory for many helpful discussions regarding the antennas and for taking the experimental anechoic chamber data presented here.

This work was sponsored by Art Boland of SRDO. It was supported in part by a grant of HPC time from the DoD HPC Shared Resource Center (CEWES Cray C90, NRL Cray YMP).

Multiple FSS and Array Analysis Program (MFAA)[1]

Henry A. Karwacki and Roland Gilbert
Lockheed Sanders, Inc.

Gerald Pirrung and Jack Abbasi
Naval Air Warfare Center Aircraft Division (NAWC-ADWAR)

INTRODUCTION

The MFAA program is a user-oriented computer code for the electromagnetic (EM) analysis of planar layered composite structures which are comprised of all or a combination of dielectric layers, thin frequency selective surfaces (FSS's), a perfectly conducting ground plane layer, and an antenna array layer. The code calculates the EM field scattered from or transmitted through the structures for an incident, arbitrarily polarized (TE & TM) plane wave. The code can also predict the radiation pattern of an antenna element. As part of the computation, the code computes the wave numbers for a forward and reverse plane wave and the coefficients of the basis functions representing the currents on the scatterers. The FSS and array are represented as finite length and width, infinitesimally thin, perfectly conducting rectangular strips or crossed strips. Each FSS and antenna array layer is considered to be an infinitely large planar array of these strips or scatterers. The material layers which make up the composite structure are lossless and isotropic dielectric substrates. To approximate a finite structure, one can select a subset of the infinite array. The assumption is made that all elements have the same mutual coupling. Hence the edge effects of side elements in a physical array are not represented.

The code uses a Floquet harmonic modal expansion of the scattered fields from each layer of the infinite periodic structure to solve for the total scattered field. The fields are matched at each interface except where the H-fields are discontinuous by the currents on the strips. The maximum number of Floquet modes can be utilized by the code is truncated to 361, any one of which can be the incident mode. In general, the solution converges with fewer modes.

The currents which are excited on the FSS and array scatterers are determined through a Galerkin method of moments approach utilizing up to 9 sets of full range sinusoidal basis and testing functions. The number of basis function sets used in the computation is selected by the user at the start of the program. Obviously, computation time increases dramatically with added sets of basis functions. In most cases, one or two sets is all that is needed for convergence to a solution.

The MFAA code was written in FORTRAN as a PC based analysis/synthesis tool, but can also be used on mainframe computers if recompiled with minor changes to the I/O portions.

ELECTRICAL MODEL

The analysis assumes the array is large, therefore, infinite array theory is used to expand the EM fields as summation of Floquet space harmonic modes. This approach was chosen primarily because it inherently includes mutual coupling between the dipole elements. Although a method of moments approach could be used (for reasonable accuracy, the segmentation of the conductors must be on the order of one tenth of a wavelength); it requires the inversion of extremely large matrices to provide a solution for even a small array of elements.

This work was supported by the Naval Air Warfare Center (NAWC) under contract No. N62269-90-C-0580

The Floquet mode approach considers the array and/or FSS as a periodic lattice with a unit cell geometry, characterized by length, width, and offset angle, and chosen to make the structure repetitive from cell to cell (Figure 1). To be exact, the summation must be infinite, and for negligible error, must converge to a solution when truncating to an essential number of modes. The fields in each unit cell are periodically related to every other cell. This requires the solution of the fields in a single cell only to obtain the total field, resulting in a relatively rapid computation as compared to a method of moments computation.

The structure is illuminated by a plane wave incident from a known direction. The transverse (x,y component) field variation of the (p,q)th space harmonic is given by

$$Q_{p,q}(x,y) = e^{-j(u_{pq}x+v_{pq}y)} \qquad p,q = 0,\pm1,\pm2 \cdots \tag{1}$$

where

$$u_{pq} = \frac{2p\pi}{a} + k_0\sqrt{\epsilon_r\mu_r}\sin(\theta)\cos(\phi) \tag{2}$$

$$v_{pq} = \frac{-2p\pi}{a}\cot(\Omega) + \frac{2q\pi}{b} + k_0\sqrt{\epsilon_r\mu_r}\sin(\theta)\sin(\phi) \tag{3}$$

The z-component variation is $e^{\pm\gamma_{mn}z}$, where the propagation constant is

$$\gamma_{pq} = \sqrt{k^2 - w_{pq}^2} \tag{4}$$

where

$$k = k_0\sqrt{\epsilon_r\mu_r}\ , \quad w_{pq}^2 = u_{pq}^2 + v_{pq}^2 \tag{5}$$

The scattered field can also be decomposed into transverse electric (TE) and transverse magnetic (TM) components. Expressing the scalar magnetic and electric potentials in terms of Floquet space harmonics (the overbar denotes the TM component) :

$$\begin{matrix}(TE)\\(TM)\end{matrix}\begin{bmatrix}\Psi(z)\\ \overline{\Psi}(z)\end{bmatrix} = \sum_{p=-\infty}^{\infty}\sum_{q=-\infty}^{\infty}\begin{bmatrix}C_{pq}\\ \overline{C}_{pq}\end{bmatrix}e^{\pm\gamma_{mn}z}\,Q_{pq}(x,y) \tag{7}$$

The fields for the r-th layer can then be expressed as:

$$\begin{bmatrix}E_x^{(r)}\\ E_y^{(r)}\\ E_z^{(r)}\\ H_z^{(r)}\end{bmatrix} = \begin{bmatrix}E_{pq} & E_{pq} & \frac{\gamma_{pq}^{(r)}\beta_{pq}}{k_0\epsilon_r} & \frac{-\gamma_{pq}^{(r)}\beta_{pq}}{k_0\epsilon_r}\\ 0 & 0 & \frac{-w_{pq}}{k_0\epsilon_r} & \frac{-w_{pq}}{k_0\epsilon_r}\\ \frac{\gamma_{pq}^{(r)}\beta_{pq}}{k_0\epsilon_r} & \frac{-\gamma_{pq}^{(r)}\beta_{pq}}{k_0\epsilon_r} & \frac{-E_{pq}}{\eta_0} & \frac{-E_{pq}}{\eta_0}\\ \frac{-w_{pq}}{k_0\eta_0} & \frac{-w_{pq}}{k_0\eta_0} & 0 & 0\end{bmatrix}\begin{bmatrix}C_{pq}^{(r)}\,e^{-\gamma_{mn}z}\\ D_{pq}^{(r)}\,e^{\gamma_{mn}z}\\ \overline{C}_{pq}^{(r)}\,e^{-\gamma_{mn}z}\\ \overline{D}_{pq}^{(r)}\,e^{\gamma_{mn}z}\end{bmatrix} \tag{8}$$

$$\alpha_{pq} = \frac{\gamma_{xx}^2 - \omega^2\mu\varepsilon}{\gamma_{pq}} \quad , \quad \beta_{pq} = \frac{\gamma_{xx}^2 - \omega^2\mu\varepsilon}{\gamma_{pq}} \tag{9}$$

The problem then becomes one of determining the unknown field coefficients C_{pq} and D_{pq}. The dominant space harmonic with p = 0, q = 0 is the one of primary interest since it is associated with the main beam propagating mode while the other harmonics are related to grating lobes. The next step in the analysis is to relate the fields in each layer by matching the tangential fields (E and H) at the interfaces. The simple dielectric-to-dielectric boundaries lead to transmission/reflection matrices of the form (for TE to z) :

$$\begin{bmatrix} C_{pq}^{(r)} \\ D_{pq}^{(r)} \end{bmatrix} = \frac{1}{2} \begin{bmatrix} (1 + \frac{\gamma_{pq}^{(s)}}{\gamma_{pq}^{(r)}}) e^{-j(\gamma_{pq}^{(s)} - \gamma_{pq}^{(r)}) t_r} & (1 - \frac{\gamma_{pq}^{(s)}}{\gamma_{pq}^{(r)}}) e^{j(\gamma_{pq}^{(s)} + \gamma_{pq}^{(r)}) t_r} \\ (1 - \frac{\gamma_{pq}^{(s)}}{\gamma_{pq}^{(r)}}) e^{-j(\gamma_{pq}^{(s)} + \gamma_{pq}^{(r)}) t_r} & (1 + \frac{\gamma_{pq}^{(s)}}{\gamma_{pq}^{(r)}}) e^{j(\gamma_{pq}^{(s)} - \gamma_{pq}^{(r)}) t_r} \end{bmatrix} \begin{bmatrix} C_{pq}^{(s)} \\ D_{pq}^{(s)} \end{bmatrix} \tag{10}$$

and similarly for TM to z.

These matrix equations relate the fields in the r-th layer to the fields in the s-th layer. The first boundary condition to be satisfied at a strip layer is continuity of tangential E-field :

$$E_t^{(s)}(x, y, 0^+) = E_t^{(r)}(x, y, 0^-) \tag{11}$$

over the area of the cell.

A boundary condition that must be satisfied is that the tangential component of the electric-field must be zero on the conductors. For the PEC ground, this leads to a pair of specialized transmission/reflection matrices. The FSS or array is assumed to be conductive strips that are centered in their respective unit cells. Applying the zero tangential field condition yields on unloaded strips:

$$E_t^{(s)}(x, y, 0_+) = 0 \tag{12}$$

(over the area of the strip)
To allow for loads on the strips, the tangential field on the array strip satisfies :

$$E_t^{(s)}(x, y, 0_+) = I_0 \cdot Z_0 \cdot f(x, y) \cdot [Z_0 \cdot \delta(x) + Z_{d1} \cdot \delta(x - d1) + Z_{d2} \cdot \delta(x + d2)] \tag{13}$$

where $\delta(x)$ is the Dirac delta function.

The loads in the present model are assumed to be pure resistive point loads. The last boundary condition to be satisfied is the continuity of tangential H-field on the strip.

$$H_t^{(r)}(x, y, 0_+) - H_t^{(s)}(x, y, 0_-) = \frac{-2jab}{Z_0} \cdot I_0 \cdot f(x, y) \tag{14}$$

I_0 is the current maximum and Z_0 is the free space impedance. Each equation is tested with an inner product defined as follows :
when applied to equation (11)

$$\int_{-a/2}^{a/2} \int_{b/2}^{b/2} dx dy \Phi_{mn}^*(x, y) \begin{bmatrix} E_{mn}^{(r)} \\ E_{mn}^{(s)} \end{bmatrix} \tag{15}$$

when applied to equations (12,13)

$$\int_{-l/2}^{l/2}\int_{h/2}^{h/2} dxdy\,(\hat{z} \times \bar{F}(x,y)) \cdot \tag{16}$$

when applied to equation (14)

$$\int_{-a/2}^{a/2}\int_{b/2}^{b/2} dxdy\,\bar{t}_{mn}^{*}(x,y) \begin{bmatrix} \hat{x}_{mn} \\ \hat{z}_{mn} \end{bmatrix} \tag{17}$$

The current basis function f (x,y) is selected such that

$$\hat{z} \cdot \bar{F}(x,y) = 0, \quad \iint_{strip} (\bar{J} \cdot \bar{F}^{*})\, dxdy = 1 \tag{18}$$

The equation for a single basis function set, simplified by introducing a rotation and translation of the coordinate axes to align with the strip centers, is defined by :

$$\begin{aligned} \bar{F}(x,y) = \sqrt{\frac{1}{N}} \cdot [(-\hat{x}\sin(\psi) - \hat{y}\cos(\psi)) \cdot \sum_{m} I_{xm} \cdot \sin(\frac{r \cdot \pi}{l_1} \cdot [x' + \frac{l_1}{2}]) \\ - I_{xm} \cdot \text{sgn}([x']) \cdot \cos(\frac{\pi}{l_1} \cdot x')] \\ + (-\hat{x}\cdot\cos(\psi) - \hat{y}\cdot\sin(\psi)) \cdot \sum_{n} I_{yn} \cdot \sin(\frac{r \cdot \pi}{l_2} \cdot [y' + \frac{l_2}{2}]) \\ - I_{xn} \cdot \text{sgn}([y']) \cdot \cos(\frac{\pi}{l_2} \cdot y')] \end{aligned} \tag{19}$$

where I_m, I_n, I_m, I_n, are the unknown current magnitudes in the x and y directions of the r^{th} symmetric and asymmetric modal basis functions. A normalization constant must be derived from the integral over the strip area of the dot product of the basis function (19) with itself.

The appropriate inner products ((15), (16), (17)) are then applied to the basis function set (19). Once the inner products are formed, and the equations are manipulated with substitution of the appropriate transmission/reflection matrices(10), a set of equations result :

$$C_{pq}^{i}(A_{11} + A_{21}) + D_{pq}^{i}(A_{12} + A_{22}) = C_{pq}^{0i}(B_{11} + B_{21}) + D_{pq}^{0i}(B_{12} + B_{22}) \tag{20}$$

$$\frac{\gamma_{pq}^{0i} s_x}{\gamma_{pq}^{0i} s_y}(\bar{C}_{pq}^{i}(\bar{A}_{11} - \bar{A}_{21}) + \bar{D}_{pq}^{i}(\bar{A}_{12} - \bar{A}_{22})) = \bar{C}_{pq}^{ri}(\bar{B}_{11} - \bar{B}_{21}) + \bar{D}_{pq}^{ri}(\bar{B}_{12} - \bar{B}_{22}) \tag{21}$$

$$\sum_p \sum_q \Big\{ w_{pq} \Big[-\sigma_{pq}^{(m)} \big(C_{pq}^{(m)} (\bar{A}_{11} + \bar{A}_{21}) + D_{pq}^{(m)} (\bar{A}_{12} + \bar{A}_{22}) \big) \Big] + \Big[-\frac{\sigma_{pq}^{(m)} \gamma_{pq}^{(m)}}{k_0 \epsilon_0} \big(C_{pq}^{(m)} (\bar{A}_{11} + \bar{A}_{21}) - D_{pq}^{(m)} (\bar{A}_{12} + \bar{A}_{22}) \big) \Big] \Big\} = \begin{matrix} 0 & \text{on metal} \\ I_q \bar{Z} & \text{on resistor} \end{matrix} \quad (22)$$

$$w_{mn} \Big\{ \big[C_{mn}^{(m)} (\bar{B}_{11} + \bar{B}_{21}) + D_{mn}^{(m)} (\bar{B}_{12} + \bar{B}_{22}) \big] - \big[C_{mn} (\bar{A}_{11} + \bar{A}_{21}) + D_{mn} (\bar{A}_{12} + \bar{A}_{22}) \big] \Big\} = -2 \sigma_{mn}^{(m)} I_n \quad (23)$$

$$w_{mn} \Big[\frac{\gamma_{mn}^{(m)}}{k_0} \big[C_{mn}^{i} (A_{11} - A_{21}) - D_{mn}^{i} (A_{12} - A_{22}) \big] - \frac{\gamma_{mn}^{(m)}}{k_0} \big[C_{mn}^{(m)} (B_{11} - B_{21}) + D_{mn}^{(m)} (B_{12} - B_{22}) \big] \Big] = -2 \sigma_{mn}^{(m)} I_n \quad (24)$$

where the sigma functions have the form

$$\sigma_{pqi}^{(m)} = \sqrt{\frac{1}{N}} \cdot \frac{\delta_{pq}^{1} h_{i-1}}{w_{pq} \pi} \cdot \frac{\sin\left(\frac{\delta_{pq}^{2} h_{i-1}}{2}\right)}{\left(\frac{\delta_{pq}^{2} h_{i-1}}{2}\right)} \cdot \sum_{n=1}^{N} \frac{\left(\cos\left(\frac{\delta_{pq}^{1} I_n}{2}\right)(1 - \cos(n\pi)) + j \sin\left(\frac{\delta_{pq}^{1} I_n}{2}\right)(1 + \cos(n\pi))\right)}{n\left(1 - \left(\frac{\delta_{pq}^{1} I_n}{\pi}\right)^2\right)} \cdot \exp^{-j(x_{pq} h_{i-1} + y_{pq} h_{j-1})} \quad (25)$$

$$\sigma_{pqi} = \sqrt{\frac{1}{N}} \cdot \frac{\delta_{pq}^{1} h_{i-1}}{w_{pq} \pi} \cdot \frac{\sin\left(\frac{\delta_{pq}^{2} h_{i-1}}{2}\right)}{\left(\frac{\delta_{pq}^{2} h_{i-1}}{2}\right)} \cdot 2j \cdot \frac{\left(\left(-\delta_{pq}^{1} \frac{I_n}{\pi}\right) + \sin\left(\frac{\delta_{pq}^{1} I_n}{2}\right)\right)}{\left(1 - \left(\frac{\delta_{pq}^{1} I_n}{\pi}\right)^2\right)} \cdot \exp^{-j(x_{pq} h_{i-1} + y_{pq} h_{j-1})} \quad (26)$$

Where A_{ij} and B_{ij} are the transmission/reflection matrix coefficients and the superscript i denotes the incident wave. A method of moments approach is then used to solve for the unknown current magnitudes by testing according to Galerkins method.

This results in two sets of matrix equations :

$$[I_{mn}]\,[I_n] = [\Delta H_p] \quad , \quad [I_{pn}]\,[E_p] \quad (27)$$

which can be represented as :

$$\begin{bmatrix} \langle w_1 g_1 \rangle & \langle w_1 g_2 \rangle & - & \langle w_1 g_n \rangle \\ \langle w_2 g_1 \rangle & \langle w_2 g_2 \rangle & - & \vdots \\ \vdots & \vdots & \vdots & \vdots \\ \langle w_m g_1 \rangle & - & - & \langle w_m g_n \rangle \end{bmatrix} \begin{bmatrix} I_1 \\ I_2 \\ \vdots \\ \vdots \\ I_n \end{bmatrix} = \begin{bmatrix} \langle w_1 \Delta H_i \rangle \\ \langle w_2 \Delta H_i \rangle \\ \vdots \\ \langle w_m \Delta H_i \rangle \end{bmatrix} \quad (28)$$

for the H-field set, with a similar form for the E-field equations. The solutions for the unknowns I_n are then found by matrix inversion.

The matrix elements consist of double sums of products of the sigma functions resulting from the integration of the continuity equations (inner product) over the cell. A typical element has the form :

$$\langle W_i , f_j \rangle = (\sum_p \sum_q \overline{A_{pq}}\, \sigma^{(v)}_{pqi} \cdot \sigma^{(u)*}_{pqi} + A_{pq}\, \sigma^{(v)}_{pqj} \cdot \sigma^{(u)*}_{pqj}) \cdot F_i \cdot F^*_i \cdot \overline{Z} \qquad (29)$$

This element would be associated with the I_i unknown current coefficient. The matrix size is a function of the number of basis function sets r, having r elements of the symmetric type and one of the asymmetric type for both the TE and TM portions of the equations resulting in a 2(r+1) by 2(r+1) matrix. Where $\overline{A}_{pq}$ and A_{pq} are formed from products and sums of the transmission and reflection matrices, and F_j , F_i^* , and $\overline{Z}$ are the basis functions and the impedance function.

Upon solving for the unknown currents the results are used to solve for the transmitted and reflected fields. By cascading the combined structure of FSS's and array, a solution is developed with only propagating space harmonics allowed to transmit or reflect. This approach simplifies the analysis for unequal cell sizes of the array and FSS structures and is still valid since most of the non-propagating modes are highly attenuated over the separation distances of the structures.

The monostatic scattering of a finite array can be modeled by applying an array factor to the scattered field calculated for the single cell over a range of incidence angles. This makes the assumption that the infinite array can be truncated and that the scattered field for each element of the finite size array is the same as in the infinite array. In reality the edge elements of the finite array experience a different mutual coupling, and hence scatter differently than the center elements; however as array size increases this approximation improves.

The gain of the finite array can be approximated in a similar manner by using the calculated excitation current at boresight of the infinite array element as the current on each element of the finite array. The gain, radiation resistance and other parameters of the finite array can then be computed by applying the appropriate array factor.

CONCLUSION

The code has been used to model several published FSS and array geometries as well as a multiband crossed and single dipole arrays with multiple FSS and PEC ground planes which were built and tested under company IR&D. The calculated results of these models proved to be comparable to the published data and within approximately five percent of the measured data. Sample plots of these data are shown in figures 2 through 7. The code is presently being used to design a more complex multiband array/FSS structure. The code has been compiled on a VAX mainframe and an HP 700 series workstation as well as on PC's and is proving to be a useful analysis and design tool. Enhancements to the code to improve efficiency and utility of the code are being made.

REFERENCES

[1] Pelton, E. L. and Munk, B.A. , "Scattering from Periodic Arrays of Crossed Dipoles", IEEE Transactions on Antennas and Propagation, Vol. AP-27, No. 3, May 1979. pp. 323-330

[2] Tsao, Chich-Hsing and Mittra, R., "Spectral Domain Analysis of Frequency Selective Surfaces Comprised of Periodic Arrays of Cross Dipoles and Jerusalem Crosses", IEEE Transactions on Antennas and Propagation, Vol. AP-32, No. 5, May 1984. pp. 478-486

[3] Zarillo, G., and Lee, S.W., "Closed-Form High-Frequency and Low-Frequency Solutions For Electromagnetic Waves Through a Frequency Selective Surface", Electromagnetics Laboratory, Department of Electrical Engineering, Engineering Experiment Station, University of Illinois at Urbana-Champaign, October 1982.

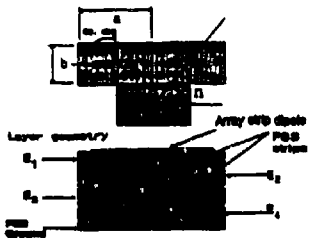

Figure 1 Typical Unit Cell Geometry

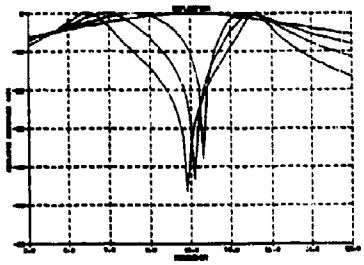

Figure 2 Example from reference 1 Figure 7a.

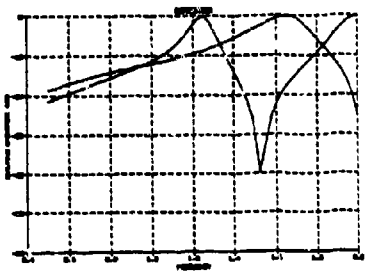

Figure 3 Overlay of reflected field for strip dipoles resonant @ 1.2 and 1.7 Ghz

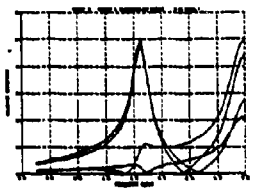

Figure 4 Current amplitude vs frequency for 1.2 Ghz strip dipole

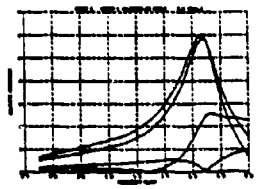

Figure 5 Current amplitude vs frequency for 1.7 Ghz strip dipole

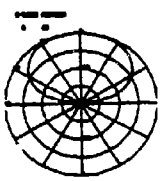

Figure 7 E-plane pattern at 1.7 Ghz

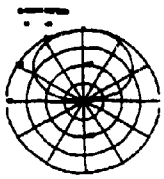

Figure 6 E-plane pattern at 1.2 Ghz

FREQUENCY PERTURBATION FOR CIRCULAR ARRAY OF COUPLED CYLINDRICAL DIPOLE ANTENNAS

DR FATMA M. EL-HEFNAWI
ELECTRONICS RESEARCH INSTITUTE
DOKKI / CAIRO / EGYPT

1. INTRODUCTION :

This paper presents a procedure for calculating efficiently the frequency perturbation of a circular coupled cylindrical dipole. This is commonly done through subsequent application of the algorithm at different values of frequency. A novel technique is developed to avoid such repeated computation, hence saving computer time, storage and effort. This is done by solving the coupled integral equation at a single frequency and then extending the solution to cover a band of frequencies, by implementing Taylor series expansion for the current distributions on the different antenna elements as a function of frequency. The derivatives needed for Taylor expansions are calculated using the same impedance matrix calculated for the solution at a single frequency.

Convergence of Taylor series expansion is guaranteed by two transformations. The first one requires a knowledge of pole location, to extract the singularity out, then applying Taylor series on the analytic part only is straight forward. The second one utilizes the fact that the poles of a function are the zeros of its inverse, hence, Taylor series is applied on the inverse of the current distribution. Both transformations do not require repeated computation of the impedance matrix or its inverse.

Coupled improved Pocklington integral equation is suggested for the solution using the method of moments [1]. Kernel singularity is overcome using extended boundary condition [2] resulting in a regular kernel. Current expansion basis is chosen to be of the entire-domain type to save computer storage and time [3],[4]. The increase in the expected time to carry out such integration numerically is fairly reduced by a semi-analytic technique similar to that used by Duncan and Minchey [5] with some modifications. This is done by expanding the kernel in Fourier series . Infinite Fourier Series (IFS) is chosen for the self kernel, while Finite Fourier Series (FFS) is use for the mutual kernel. The behavior of the kernel is behind the choice of IFS or FFS.

The method of feeding suggested is such that it is in the operator range [6] which represents the electric field distribution in the aperture of a coaxial fed monopole over a ground plane [7].

2. COUPLED INTEGRAL EQUATION IN CIRCULAR ARRAY:

Consider n symmetrically identical antennas of a circular array of dipoles equally spaced as shown in fig.(1). Each antenna has a half length h and radius a, relative to the wave length. The antennas are assumed to be thin such that $a<<\lambda$, $h/a >>\lambda$. Assume ρ is the radius of the circular array. the set of coupled Pocklington has the following form:

$$\sum_{m=1}^{N} \int_{-h}^{+h} I_m(z',k) K_{in}(z,z',k)\, dz' = \frac{-j4\pi k E_{inc(i)}(z,k)}{z_0} \qquad i = 1,2,\ldots,N(1)$$

where, I_m is the current distribution on the m^{th} antenna, $K_{in}(z,z')$ is the Kernel between the i^{th} and the m^{th} antenna respectively and is given by:

$$K_{in}(z,z',k) = (k^2 + \frac{\partial^2}{\partial^2}) \frac{e^{-jkR_{in}}}{R_{in}} \qquad (2)$$

and R_{in} is the distance between the i^{th} and the n^{th} antenna. Also, $E_{inc(i)}$ is the z-component of the incident field on the axis of antenna i resulting from the method by chang (3) which is equal to

$$E_{inc(i)}(z,k) = \frac{V_i}{2\ln(b/a)}\left(\frac{e^{-jkR_a}}{R_a} - \frac{e^{-jkR_b}}{R_b}\right) \quad (3)$$

where $R_a = \sqrt{\rho_i^2 + z^2}$ (4)

and $R_b = \sqrt{\rho_i^2 + z^2}$ (5)

The kernel in equation (1) suffers from singularity when both the observation and the source points coincide. This is overcome using extended line type boundary condition making use of the fact that the electric field vanishes on the axis of the dipole and within the dipole surface. Thus the observation point can be taken on the dipole axis. While the source point is taken on the antenna surface. Hence, the distance R can be written as:

$$R_{in} = \sqrt{(z-z')^2 + b_{in}^2} \qquad i \neq n \quad (6)$$

$$R_{nn} = \sqrt{(z-z')^2 + b_{in}^2} \qquad i = n \quad (7)$$

where $b_{in}^2 = 2a^2 \sin^2(\phi_i - \phi_n)/2$ (8)

The set of coupled integral equation (1) is solved using the method of moments in the following sections.

3. CURRENT DISTRIBUTION ON CIRCULAR ARRAY :

The set of coupled integral equations (1) is solved using the method of moments [1]. The kernel is expanded using Fourier series making use of the fact that z,z' enter only as the square term of their difference. Since h>z>-h and h>z'>-h. Then let $\xi = z - z'$ yields $2h > \xi > -2h$. Thus the kernel can be expanded in Fourier series of period 4h giving :

$$k_{in}(\xi_r, k) = \sum_{q=0}^{N} D_q^{in} \cos\left(\frac{q\pi\xi_r}{2h}\right) \quad (9)$$

where $\xi_r = \frac{2h}{Q} r$, (10)

and 2Q+1 are the total number of points. While D_q's in equation (9) are calculated using the least squares for mutual kernal. For the self kernel, infinite Fourier series expansion is used with the same period giving:

$$K_{ii}(\xi,k) = \sum_{q=0}^{\infty} D_q^{ii} \cos\left(\frac{q\pi\xi}{2h}\right) \quad (11)$$

where $D_q^{ii} = \frac{1}{2h}\int_{-2h}^{+2h} k_{ii}(\xi,k)\cos\left(\frac{q\pi\xi}{2h}\right) d\xi$ (12)

using a procedure similar to that applied before by Ducan-Hincy [5] gives:

$$D_q^{ii} = \frac{1}{h} + \frac{\pi}{2}\left[(k^2-a^2)A_{1q}(k^2-a^2)B_{1q} + C_q\right] \quad (13)$$

where $\alpha = q\pi/2h$, and A_{1q}, B_{1q} for $\alpha < k$ are given by

$$A_{1q} = -j\frac{\pi}{2} H_0^{(2)}(\sqrt{k^2-\alpha^2}\, a) \quad (14)$$

$$B_{1q} = \frac{-1}{\sqrt{2\pi}}\left[C_i((k+\alpha)2h) - C_i((k-\alpha)2h) + j\pi - jSi((k+\alpha)2h) - jSi((k-\alpha)2h)\right] \quad (15)$$

$$C_q = -\frac{2}{\pi}\cos(\alpha z')\exp(-jkR_{2h})\left(\frac{1}{R_{2h}} + jk\right)\frac{2h}{R_{2h}^2} \quad (16)$$

And for $\alpha > k$, one has

$$D_q^{ii} = \frac{1}{h} + \frac{\pi}{2}\left[(\alpha^2-k^2)A_{2q} + (\alpha^2-k^2)B_{2q} + C_q\right] \quad (17)$$

where $A_{2c} = \frac{2}{\pi} K_0(\gamma^2 - k^2 a)$ (18)

$B_{2c} = \frac{-1}{\pi/2}$ [illegible] (19)

where Si(x), Ci(x) are defined as

$$Si(x) = \int_0^x \frac{\sin(x)}{x}\, dx \quad (20)$$

$$Ci(x) = \int_\infty^x \frac{\cos(x)}{x}\, dx \quad (21)$$

and $H_0^{(2)}$ k_0 are Hankel function of second kind and modified Bessel function [8]. The current is also expanded in Fourier series of the same period as the kernel in odd cosine Fourier serves giving:

$$I_n(z',k) = \sum_{r=1}^{R} A_{nr} \cos\left(\frac{r\pi z'}{2h}\right) \quad (22)$$

now, inserting equations (9),(11), and (22) in equation (1) gives :

$$\sum_{n=1}^{N} \sum_{r=1,3}^{R} A_{nr} \cos\left(\frac{r\pi z'}{2h}\right) \sum_{q=0}^{Q} \frac{D_q^{ni}}{\varepsilon_q} \cos\left(\frac{q\pi z'}{2h}\right) \cos\left(\frac{q\pi z}{2h}\right) = \frac{-j4\pi E_{inc(i)}}{\omega Z_0} \quad i = 1,2,\ldots,N \quad (23)$$

where the sine term in equation (23) vanishes for symmetrical feeding. Now, to solve equation (23) by the method of moments, both sides are multiplied by cos(pπz/2h) where p is taken as odd number p=1,3,....,R. giving :

$$\sum_{n=1}^{N} \sum_{r=1,3}^{R} A_{nr}\left(\varepsilon_{pr} D_r^{in} - \sum_{q=0,2}^{Q} \frac{1}{\varepsilon_q} D_q^{in} I_{rq} I_{pq}\right) = \frac{-j4\pi}{\omega Z_0}\left(D_{ip}^a - D_{ip}^b\right)$$

where $p = 1,3,\ldots,R$ $i=1,2,\ldots,N$ (24)

$$(Z)(A) = (W) \quad \ldots \quad (25)$$

$$D_{ip}^c = \int_{-h}^{+h} \exp(-jkR_c)/R_c \cos(p\pi z/2h)\, dz \quad (26)$$

where c=a for inner radius, c=b for outer radius of feeding method suggested. Also

$$I_{rq} = \int_{-h}^{+h} \cos(r\pi z'/2h) \cos(q\pi z'/2h)\, dz' \quad (27)$$

which simplifies to

$$I_{rq} = \frac{4r}{\pi} \frac{\sin(r\pi/2)\cos(q\pi/2)}{r^2 - q^2} \quad \text{for } r \text{ odd}, \ q \text{ even}$$

$$= 1 \quad r \text{ odd}, \ q \text{ odd}$$

$$= 0 \quad \text{otherwise} \quad (28)$$

The integration in equation (25) to calculate D_{ip}^a ,D_{ip}^b are calculated in a manner similar to that used before by Duncan and Hinchy [5] giving :

$$D^{a}_{ip} - D^{o}_{ip} = -j\frac{\pi}{2}\left(H_o^{2}(\nu k^2-\nu^2 a)-H_o^{(2)}(\nu k^2-\nu^2 a)-H_o^{(2)}(k^2-\nu^2 b)\right)$$

where $\nu = p\pi / 2h$ and for $\nu < k$ (29)

$$D^{a}_{ip} - D^{b}_{ip} = -\frac{2}{\pi}\left(K_o(\nu^2-k^2 a) - K_o(\nu^2-k^2 b)\right) \quad \text{for } \nu > k \quad (30)$$

and for $\nu = k$

$$D^{a}_{ip} - D^{b}_{ip} = \ln(b/a) \quad (31)$$

Thus equation (24) can be solved making use of symmetries in circular array, where the resultant matrix is circulant. Applying the procedure used by Sinnot [7], one can easily get the current distribution of the circular array.

4. CALCULATING OF CURRENT DERIVATIVES :

Differentiating equation (1) with respect to k,ν times gives :

$$\sum_{n=1}^{N}\int_{-h}^{+h} I_n^{(\nu)}(z',k)\,k_{in}(z,z',k) = f_i^{(\nu)}(z,k) - \sum_{n=1}^{N}\int_{-h}^{+h}\sum_{\nu'=1}^{\nu}\frac{\nu!}{(\nu-\nu')!\nu'!} I_n^{(\nu-\nu')}(z',k)k_{in}^{\nu'}(z,z',k)dz' \quad (32)$$

where $f_i^{(\nu)}(z,k)$ is the ν^{th} derivative with respect to k of the right hand side of equation (1), $I_n^{(\nu)}$ is the derivative of the current on the n^{th} element and $k_{in}^{(\nu)}$ ν^{th} derivative of kernel between the i^{th} and the n^{th} element respectively.

Equation (32) can be applied for increasing values of r from r=1 to higher values to get current derivatives. It is to be noted that the kernel in equation (32) is the same as the kernel of equation (1). Hence eaploying the same procedure applied in section 3 by expanding the kernels and the current derivatives in Fourier series yields the same matrix [z] obtained in equation (25), but with different right hand side. Hence, it is only needed to calculate for each derivative value ν a new right hand side of equation (32). Applying the procedure described in section 3 on equation (32) yields :

$$\sum_{n=1}^{N}\sum_{r=1,3}^{R} A_{nr}^{\nu}\left(\varepsilon_{pr} D_r^{in} + \sum_{q=0,2}\frac{1}{\varepsilon_q} D_q^{in}\,\varepsilon_{rq}\right) I_{pq} = \int_{-h}^{+h} fi^{\nu}(z,k)\cos(p\pi z/2h)dz - \sum_{n=1}^{N}\sum_{\nu'=1}^{\nu}\frac{\nu!}{(\nu-\nu')!\nu'!}\sum_{r=1,3}^{R} A_{nr}^{(\nu-\nu')}\left(\varepsilon_{pr} D_r^{in(\nu')} - \sum_{q=0,2}\frac{1}{\varepsilon_q} D_q^{in(\nu')} I_{rq}\right) I_{pq} \quad p = 1,3,\ldots,M,\ i = 1,2,\ldots,N \quad (33)$$

where A_{nr} is the r^{th} harmonic of the ν^{th} derivative on the n^{th} element and $D_q^{in(\nu)}$ is the q harmonic of the ν^{th} derivative of the kernel between elements (i&n) and is calculated using least squares. Also $fi^{\nu}(z,k)$ is expanded infinite Fourier series

$$f_n(z,k) = \sum_{q=0,1,2} \frac{1}{q!} F_q^{(v)} \cos\left(\frac{q\pi z}{2h}\right) \qquad (34)$$

where F_q's are calculated using least squares. Thus equation (33) reduces to

$$[\ Z\ ][\ A^{v'}\ ] = [\ W^{v'}\ ] \qquad (35)$$

where $W^{v'} = \sum_{q=0,1} F_q^{(v)} \left[\sum_{n=1}^{N} \sum_{v'=1}^{v} \frac{v!}{(v-v')!v'!} \sum_{r=1,3} \lambda_{nr}^{v-v'} \right.$

$$\left. \epsilon_{pr} D_r^{in^{v'}} - \sum_{q=0,2} \frac{1}{q!} D_q^{in^{(v')}} I_{rq} I_{pq} \right)$$

$$p = 1,3,\ldots,R \quad i = 1,2,\ldots,N \qquad (36)$$

5. FREQUENCY PERTURBATIONS :

Taylor series representation of the current on each antenna element is built up as function of K gives:

$$I_n(z'k) = I_n(z',k)\Big|_{k=k_o} + (k-k_o) \cdot I_n^{(1)}(z',k)\Big|_{k=k_o} + \frac{(k-k_o)^2}{2} I_n^{(2)}(z',k)\Big|_{k=k_o}$$

$$+ \ldots \quad n = 1,2,\ldots,N \qquad (37)$$

The value of $I_n(z',k)$ at k=ko is calculated at section 3, While $I_n^{(1)}$, $I_n^{(2)}(z',k)$, ... are calculated in section 4. thus the current on each element of the circular array is directly obtained. Due to the existence of pole location in the coaplex frequency plane, divergence occurs in equation (37) which is overcose by building up another Taylor series of the inverse of the current, provided it is analytic at that point. Expansion of $1/In(z',k)$ is built up where :

$$Z_n(z'k) = Z_n(z',k)\Big|_{k=k_o} + (k-k_o) Z_n^{(1)}(z',k)\Big|_{k=k_o} + \frac{(k-k_o)^2}{2} Z_n^{(2)}(z'k)\Big|_{k=k_o}$$

$$+ \ldots \quad n = 1,2,\ldots,N \qquad (38)$$

making use of $Z_n(z'k) = 1/I_n(z'k)$ (39)

or $Z_n(z'k) \cdot I_n(z'k) = 1$ (40)

differentiation equation (40) v times with respect to k gives

$$\sum_{v'=0}^{v} \frac{v!}{(v-v')!v'!} Z_n^{(v-v')} I_n^{(v-v')} I_n^{(v')}(z',k) = 0 \qquad (41)$$

which can be written as :

$$Z_n^{(v)}\Big|_{k=k_o} = -\frac{1}{I_n(z',k)}\Big|_{k=k_o} \sum_{v'=1}^{v} \frac{v!}{(v-v')!v'!} Z_n^{(v-v')} \cdot I_n^{(v)}(z',k) \qquad n \ldots \qquad (42)$$

Hence equation (42) can be applied for n=1,2,3,....,N to get the inverse of the

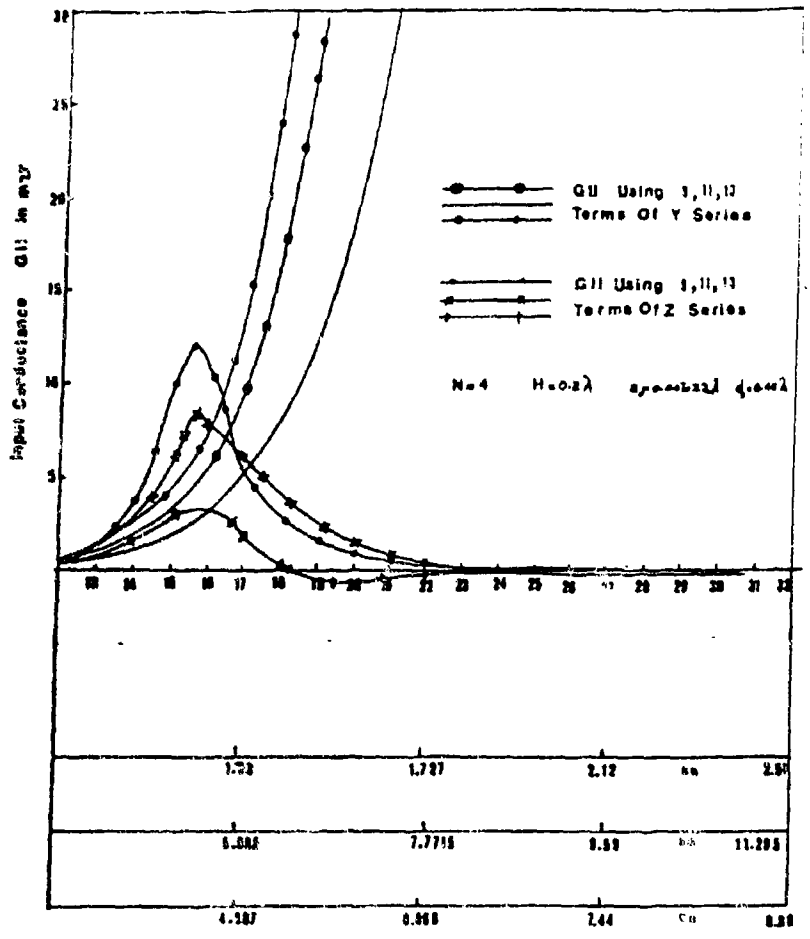

Terminal Conductance G11 Against Normalized Dipole Spacing kd

For A Four Element Circular Array Antenna

Fig. (1)

Table 1 INPUT ADMITTANCE IN mU

N=4 $h/a = 74.2$ $\rho_c = 0.125\ \lambda$ $h = 0.01\ \lambda$

Method	Y_{11}	$Y_{12} = Y_{14}$	Y_{13}
Author	$1.531\times10^{-4} - j0.4544$	$1.17319\times10^{-4} - j0.8643\times10^{-4}$	$8.6545\times10^{-5} - j6.5379\times10^{-5}$
Cummins[19]	$1.490\times10^{-4} - j0.5032$	$1.145\times10^{-4} - j1.386\times10^{-4}$	$8.445\times10^{-5} - j8.944\times10^{-5}$

Table 2 INPUT ADMITTANCE IN mU

N=4 $h/a = 74.2$ $\rho_c = 0.125\ \lambda$ $h=0.125\ \lambda$

Method	Y_{11}	$Y_{12} = Y_{14}$	Y_{13}
Author [19]	0.0846 + 2.5165	0.0619 - j0.0517	-0.0423 - j0.052097
Cummins	0.07973 + j2.689	0.05837 - j0.05038	0.03978 -j0.04942

Table 3 INPUT ADMITTANCES IN m U

N=4 $h/a = 74.2$ $\rho_c = 0.25\ \lambda$ $h= 0.03\ \lambda$

Method	Y_{11}	$Y_{12} = Y_{14}$	Y_{13}
Author	$1.53\times10^{-4} + j0.454$	$3.725\times10^{-5} - j8.662\times10^{-5}$	$-2.334\times10^{-5} - j6.550\times10^{-5}$
Cummins[19]	$1.492\times10^{-4} - j0.532$	$3.634\times10^{-5} - j8.451\times10^{-5}$	$-2.281\times10^{-5} - j6.392\times10^{-5}$

Table 4 INPUT ADMITTANCES IN m U

N=4 $h/a = 74.2$ $\rho_c = 0.25\ \lambda$ $h= 0.125\ \lambda$

Method	Y_{11}	$Y_{12} = Y_{14}$	Y_{13}
Author	0.09139 +j2.521	0.01792 -j0.05023	-0.01998 -j0.035527
Cummins [19]	0.08663 + j2.693	-0.01699 -j0.04750	-0.01878 - j0.03376

current derivatives for v=1,2,3.....N. Thus , equation (38) can be calculated for all antenna elements. Hence its inverse gives the current distribution on each element of the circular array.

6. NUMERICAL RESULTS AND CONCLUSION:

The methods presented infrequency perturbation give the solution at a band of frequencies without repeated calculation of the impedance matrix Z or its elements. The second method which uses Taylor series of the inverse of the current gives better results when compared with experimental and other published numerical results as shown in tables 1-4 and figure (1) .

REFERENCES:

[1] R.F.Harington ,Field computation by moment methods ,N.Y., Macaillan,1968.

[2] K.A.Al-Badwaihy and J.L.Yen ," Extended boundary condition integral equation for perfectly conducting and dielectric bodies : formulation and uniqueness ", IEEE AP-23 , No 4 , pp 546-551, July 1975.

[3] R.E.Collin ,"Equivalent line current for cylindrical dipole antennas and it's asymptotic behavior ," IEEE AP-32 ,No 2 ,pp 200-204 , Feb.1984 .

[4] E.K.Miller ,"A selective survey of computational electromagnetics ," IEEE AP-36 , No 9 ,pp 1281-1305 , Sept 1988 .

[5] R.H.Duncan and F.A.Hinchey ,"Cylindrical antenna theory ", J.Res. NBS, Sec.D (Radio Propagation) , Vol. 64 ,pp 569-584 , Sept./Oct. 1960.

[6] T.K.Sarkar ,"A study of the various methods for computing electromagnetic field utilizing thin wire integral equation ," Radio Science , Vol. 18 , pp 28-38 , 1983 .

[7] D.C.Chang ,"On the electrically thick monopole : Part I theoretical solution ," IEEE AP-16 , No 1 , pp 58-64 , Jan. 1968.

[8] D.H.Sinnot ,"Analysis and design of circular array by matrix method", Ph.D. dissertation , electrical engineering department , Syracuse University , N.Y. , Jan. 1972.

On Effect of Phase Quantization Upon Peak Sidelobe Level in Phased Array Antennas

GAO Tie GUO Yanchang LI Jianxin
Nanjing Research Institute of Electronics Technology
P.O.Box: 1315—403, Nanjing, 210013, P.R.China

ABSTRACT

In this paper, the peak sidelobe level degradation due to the phase quantization in scanning phased array antenna is described. The several computation formulas which estimate the peak sidelobe level degradation and the some simulated computation results are given. It is shown that the theoretical analysis are in good agreement with the simulated computation results.

I. INTRODUCTION

Beam steering for phased arrays normally employs electronically switchable digital shifters in a few microseconds. Most of the phase shifters in use are digital, the digital phase shifter consist of P fixed phase shifters whose volues are individually equal to $2\pi/2$, $2\pi/2^2$, $\cdots,2\pi/2^P$, P is called the bit number of the phase shifter. In order to steer the beam to a given direction, we must set up the phases computed according to the steering direction in the phase shifters. But all the values cannot be exactly phased in the digital phase shifter. Therefore, the phase should be set up in the element must be quantized, it introduces parasitic sidelobes due to the phase quantization, and the peak sidelobe of the array will be degradated.

In the early phased array research, many techniques are proposed to analysis the effect of the phase quantization on the peak sidelobe level. It is well known that, when the rounding off is used, the parasitic sidelobe is $-6P$ (dB), when the random phase shift technique is used, the parasitic sidelobe is $-12P$ (dB). In fact, these results are effective for a large array, when the array is not large, the above conclusions are not accurate.

In this paper, using the principle of the probability and the statistics, the peak sidelobe degradation due to the phase quantization in scanning phased array antenna is described. The several computation formulas (for rounding off, rounding up, rounding to the nearest bits and random phase quantization) which estimate the peak sidelobe level degradation are given. It is shown that the sidelobe level degradation is the function of ideal designed sidelobe, array aperture efficiency, the elements number of an array antenna and the bit number of the phase shifter. Some simulated computation results are given and they confirm the theoretical analysis.

II. THEORETICAL ANALYSIS

For simplicity, suppose that there is a linear array antenna with N isotropic elements spaced at distance d, the field pattern can be written as

$$E = \sum_{n=1}^{N} I_n e^{j n(u-u_0)} \tag{1}$$

Where $u = kd_x(\sin\theta)$, $u_0 = kd_x(\sin\theta_0)$, I_n is the amplitude at the n-th element, $k = 2\pi / \lambda$, λ and θ_0 are the wave length and scanning angle respectively. In general, the phase quantization function of array antenna can be expressed as

$$\theta_n = \mathrm{Int}\left(\frac{n\theta_0}{\Delta} + f_i(n) \right) \cdot \Delta \tag{2}$$

where, θ_n is the quantized phase at the n-th element, $\Delta = 2\pi / 2^P$, P and Int(*) stand for the bit number of phase shifter and integralization respectively, θ_0 is the accurate phase shift.

For rounding off, rounding up and rounding the to the nearest bits, the phase quantization function is

$$f_1(n) = C, \qquad 0 \leq C \leq 1 \tag{3}$$

$$\left.\begin{array}{ll} C = 0, & \textit{for rounding off} \\ C = 1, & \textit{for rounding up} \\ C = 0.5, & \textit{for rounding to the nearest bits} \end{array}\right\} \tag{4}$$

For random phae quantization, the phase quantization function is

$$f_2(n) = \zeta_n \tag{5}$$

In equ.(5), the ζ_n is the random number uniformly distributed in region (0,1). Due to the phase quantization, the array pattern can be written as

$$E' = \sum_{n=1}^{N} I_n e^{j\theta'_n} e^{j n(u-u_0)} \tag{6}$$

where u_0 is the accurate phase shift, θ'_n is phase error due to phase quantization.

Using the principle of probability and statistic theory, it is known that, for rounding off, rounding up and rounding to the nearest bits, the phase error θ'_n in equ.(5) is random number uniformly in region $[-\pi / 2^P, \pi / 2^P]$. So

$$< E'(u) > = \sum_{n=1}^{N} I_n < e^{j\theta'_n} > e^{j n(u-u_0)} \tag{7}$$

$< * >$ stands for mean value, it is obvious

$$< e^{j\theta'_n} > = \frac{2^P}{\pi} \cdot \sin\left(\frac{\pi}{2^P} \right) \tag{8}$$

According to the definition of variance

$$D(E'(u)) = < E'(u)E'^{*}(u) > - < E'(u) > < E'^{*}(u) > = \sum_{n=1}^{N} D(I_n) \tag{9a}$$

$$D(J_n) = < J_n J_n^* > - < J_n > < J_n^* > \tag{9b}$$

In the above formula, $J_n = I_n e^{j\theta'_n}$. Using the equ.(9), we can obtain

$$\left.\begin{aligned} &< J_n \cdot J_n^* > = < I_n e^{j\theta'_n} \cdot I_n e^{-j\theta'_n} > = I_n^2 \\ &< J_n > < J_n^* > = < I_n e^{j\theta'_n} > < I_n e^{-j\theta'_n} > = I_n^2 \cdot \left[\frac{2^P}{\pi} sin\left(\frac{\pi}{2^P}\right)\right]^2 \end{aligned}\right\} \tag{10}$$

So

$$\sigma_{E'}^2 = D(E'(u)) = \left[1 - \left(\frac{2^P}{\pi} sin\frac{\pi}{2^P}\right)^2\right] \sum_{n=1}^{N} I_n^2 \tag{11}$$

The sidelobe level degradation due to phase quantization is

$$SLL_{max} = \frac{|< E'(u) >| + 3\sigma_{E'}}{\sum_{n=1}^{N} < J_n >} = \frac{\left|\frac{2^P}{\pi} sin\left(\frac{\pi}{2^P}\right) \sum_{n=1}^{N} I_n e^{j n(u-u_0)}\right| + 3\sigma_{E'}}{\frac{2^P}{\pi} sin\left(\frac{2\pi}{2^P}\right) \cdot \sum_{n=1}^{N} I_n}$$

$$= SLL_0 + \frac{3\sigma_{E'}}{\frac{2^P}{\pi} sin\left(\frac{\pi}{2^P}\right) \sum_{n=1}^{N} I_n} = SLL_0 + A \tag{12}$$

In equ.(12)

$$A = 3\sqrt{\frac{\left[1 - \left(\frac{2^P}{\pi} sin\frac{\pi}{2^P}\right)^2\right] \cdot \sum_{n=1}^{N} I_n^2}{\left(\frac{2^P}{\pi} sin\left(\frac{2\pi}{2^P}\right)\right)^2 \cdot \left(\sum_{n=1}^{N} I_n\right)^2}} = 3\sqrt{\left[\frac{\pi^2}{2^{2P} sin^2\left(\frac{\pi}{2^P}\right)} - 1\right] \cdot \frac{1}{N \cdot \eta}} \tag{13}$$

where $\eta = \left(\sum_{n=1}^{N} I_n\right)^2 / N \sum_{n=1}^{N} I_n^2$ is array aperture efficiency. So, we have

$$SLL_{max} = SLL_0 + 3\sqrt{\frac{1}{N \cdot \eta}} \cdot \sqrt{\frac{\pi^2}{2^{2P} sin^2\left(\frac{\pi}{2^P}\right)} - 1} \tag{14}$$

When the bit number of phase shifter is large, equ.(14) can be simplified as follows

$$SLL_{max}(dB) = 20 \cdot log(10^{\frac{SLL_0}{20}} + \sqrt{\frac{3}{N \cdot \eta}} \cdot \frac{\pi}{2^P}) \tag{15}$$

where

SLL_0 is the ideal designed sidelobe level

N is the total number of the array element

η is the array aperture efficiency

P is the bit number of the phase shifter

It can be seen that, from equs.(14) and (15), the sidelobe level degradation due to the phase quantization is the function of array aperture efficiency η, the number of array element, the ideal designed sidelobe level and the bit number of phase shifter. According to equ.(15), we can estimate the effect of phase quantization on the sidelobe level degradation for rounding off, rounding up and rounding to the nearest bits. Similarly, based on the above method, for the case of planar array, suppose that $M \times N$ elements are arranged along the X and Y axes with equal spacing d_x and d_y, the formula of sidelobe level degradation due to the phase quantization can be written as

$$SLL_{max} = SLL_0 + 3\sqrt{\frac{1}{M \cdot N \cdot \eta}} \cdot \sqrt{\frac{\pi^2}{2^{2P} \sin^2\left(\frac{\pi}{2^P}\right)} - 1} \tag{16}$$

where $\eta = \left(\sum_{m=1}^{M}\sum_{n=1}^{N} I_{mn}\right)^2 / MN \sum_{m=1}^{M}\sum_{n=1}^{N} I_{mn}^2$ is the aperture efficiency of a planar array antenna. When the bit number of phase shifter is large, equ.(16) can be simplified as follows

$$SLL_{max}(dB) = 20 \cdot log(10^{\frac{SLL_0}{20}} + \sqrt{\frac{3}{M \cdot N \cdot \eta}} \cdot \frac{\pi}{2^P}) \tag{17}$$

When the random phase is used, for a linear array, the formula estimated for the sidelobe level degradation is

$$SLL_{max} = SLL_0 + 3\sqrt{\frac{1}{N \cdot \eta}} \cdot \sqrt{\frac{\pi^2}{2^{2P-2} \sin^2\left(\frac{2\pi}{2^P}\right)} - 1} \tag{18}$$

when the bit number of phase shifter is large, equ.(18) can be simplified as

$$SLL_{max}(dB) = 20 \cdot log(10^{\frac{SLL_0}{20}} + \sqrt{\frac{3}{N \cdot \eta}} \cdot \frac{2\pi}{2^P} \tag{19}$$

For the planar array antenna, the formula estimated for sidelobe level degradation can be expressed as

$$SLL_{max} = SLL_0 + 3\sqrt{\frac{1}{M \cdot N \cdot \eta}} \cdot \sqrt{\frac{\pi^2}{2^{2P-2} \sin^2\left(\frac{2\pi}{2^P}\right)} - 1} \tag{20}$$

When the bit number of phase shifter is large, we have

$$SLL_{max} = 20 \cdot log(10^{\frac{SLL_0}{20}} + \sqrt{\frac{3}{M \cdot N \cdot \eta}} \cdot \frac{2\pi}{2^P}) \tag{21}$$

Ⅲ. SIMULATED COMPUTATION

In the followi some typical examples are given. The total number N of linear array elements is 32, the ideal pattern is −30(dB) taylor, the array aperture efficiency is $\eta = 0.8488$ and the bit number of phase shifter $P = 5$. When the array is scanning from $0^\circ \sim 60^\circ$, the peak sidelobe level is calculated using the FFT, the results are shown in Fig.1 (a) (b) ~ Fig4 (a) (b), where, from Fig.1 ~ Fig.4, the rounding to the nearest bits, rounding off, rounding up and random phase quantization are used respectively. In these Figures, (a) is the peak sidelobe level distribution in region $0^\circ \sim 60^\circ$, (b) is the probability of PSLLs less than the specified sidelobe. From Fig.1 to Fig.3, we can see that the peak sidelobe level is −24.3(dB) in region $0^\circ \sim 60^\circ$, the sidelobe level degradation estimated by equ.(15) is −23.84(dB), the simulated values differ from the prediction by no more than a few percent in analysis of PSLLs degradation. The Fig.5 ~ Fig.6 are typical quantization pattern in which the array is scanning to 35° when the rounding to nearest bits and the random phase quantization are used respectively. It can be seen that, from Fig.5 ~ Fig.6, the effect of phase quantization on peak sidelobe level cannot be neglected.

Ⅳ. CONCLUSION

In this paper, the effect of phase quantization on the sidelobe level for phased array antennas are described, some formulas of estimating sidelobe level degradation due to phase quantization and some typical simulated computation results are given. It can be seen that the sidelobe level degradation due to the phase quantization is the function of array aperture efficiency η, the bit number of phase shifter P, the ideal designed sidelobe SLL_0 and the total number N of array elements, the simulated computation results are in good agreement with the theoretical analysis. It is effective and practical for designing phased array antennas.

REFERENCES

1 Guo, Y.C., et al. Principles of phased array and frequency scanning antennas. Chinese Defence Press, 1978, 48~141

2 Guo, Y.C., et al. Sidelobe reduction for phased array antenna using digital shifters. IEE Proc., PtH, 1983, 130(5): 343~351

3 Guo, Y.C., et al. Sidelobe reduction for phased array antenna using digital shifters. IEE Proc., PtH, 1983, 130(5): 351~357

4 Smith, M.S. and Guo, Y.C. A comparison of methods for randomizing phased quantization errors in phased arrays. IEEE Trans. Antennas Propagat., Vol. AP-31, 821~828, Nov. 1983

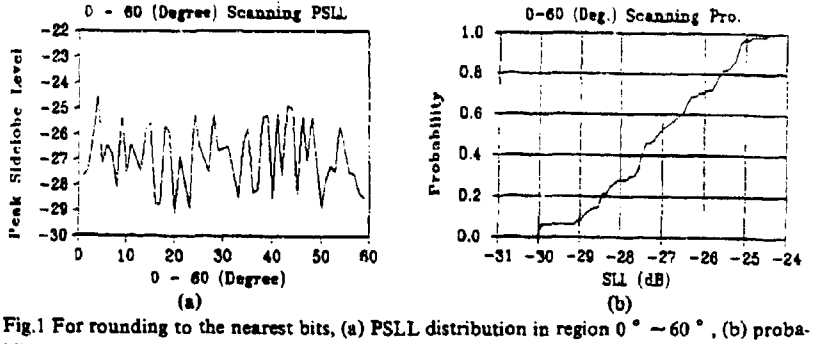

Fig.1 For rounding to the nearest bits, (a) PSLL distribution in region $0^\circ \sim 60^\circ$, (b) probability curve of PSLL

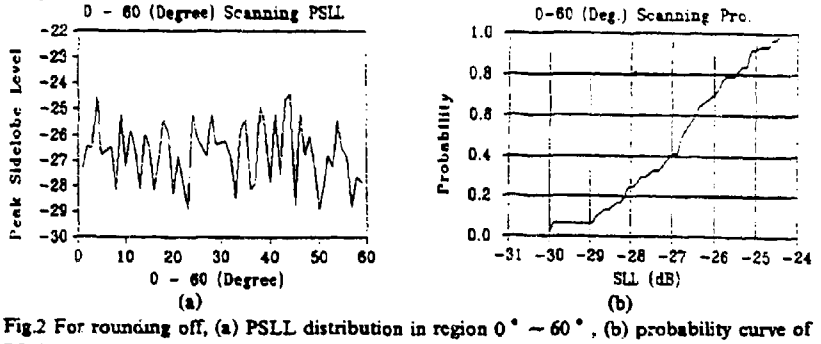

Fig.2 For rounding off, (a) PSLL distribution in region $0^\circ \sim 60^\circ$, (b) probability curve of PSLL

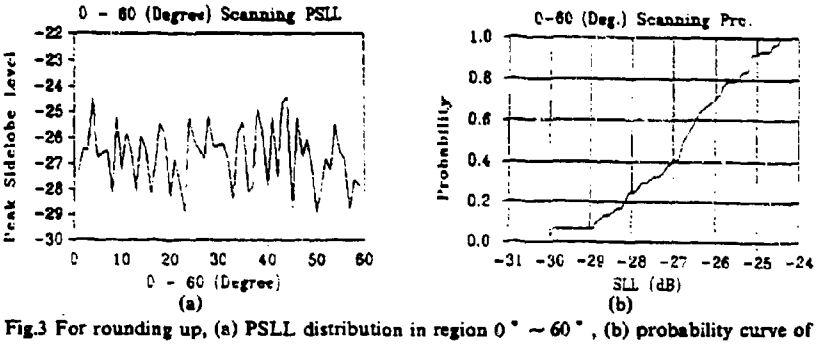

Fig.3 For rounding up, (a) PSLL distribution in region $0^\circ \sim 60^\circ$, (b) probability curve of PSLL

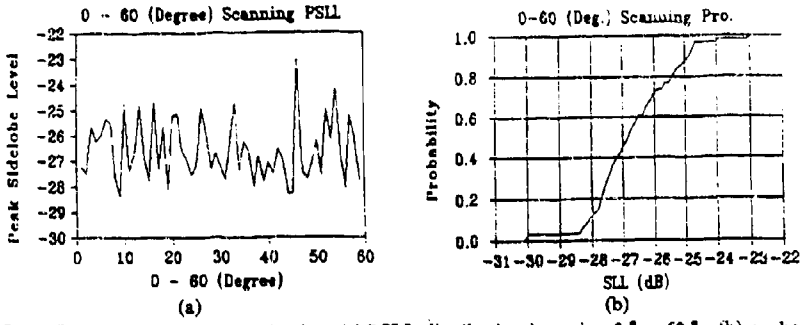

Fig.4 For random phase quantization, (a) PSLL distribution in region $0^\circ \sim 60^\circ$, (b) probability curve of PSLL.

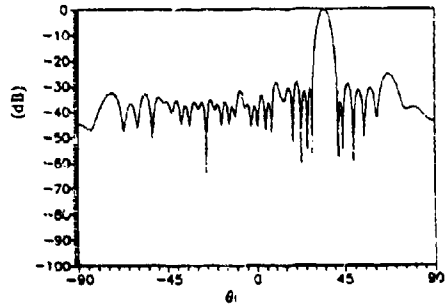

Fig.5 The pattern of scanning to 35° when the rounding to the nearest bits is used.

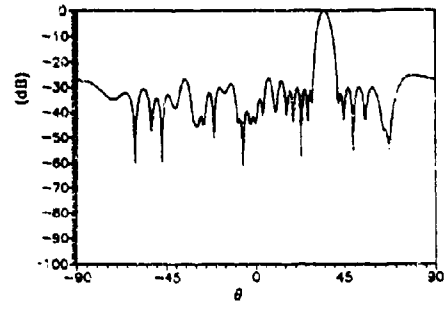

Fig.6 The pattern of scanning to 35° when the random phase quantization is used.

A Closed Loop Algorithm for Real Phase–Only Weighted Nulling Synthesis in Phased Array Antennas

Gao Tie Guo Yanchang Fang Nenghang

Nanjing Research Intitute of Electronics Technology
P.O.Box: 1315–403, Nanjing, 210013, P.R.China

ABSTRACT

In this paper, a novel algorithm of real phase–only nulling synthesis for phased array antennas is proposed, which is based on the "Element Null Vector" and modified Gram–Schmidt orthogonalization, it is effective to set wide null and low notch. In addition, the increase of notch level due to the phase quantization is investigated too.

I. INTRODUCTION

The antijammer technique is one of the important research subject in modern radar. To suppress the jammer signal, many techniques were utilized[1–11]. Now we are engaged in study of developing a novel algorithm which only controls the phases at elements in the array.

In phased array antenna, the phase is set for beam steering. If we use phase weighting method to set up nulls in field patterns, the required phases can be added to the scanning phases at no extra cost, and the signal from jammers can be suppressed.

In this paper, a closed loop algorithm for real phase–only weighted nulling synthesis is proposed. Its main ideas are (1) In the inner product normalized space, a set of linear independent vectors (element null vectors) is constituted. (2) The constituted complex inner product space is linearly transformed and divided into the real and imaginary parts. (3) The constituted vector are expanded into Taylor series and the nonlinear equations are converted into the linear ones. (4) The orthogonalization is iterated using the modified Gram–Schmidt method and the optimization is used to deepen the nulls. (5) The increase of the null depth due to the phase quantization is analysed and the appropriate random technique (ART) is used to alleviate the phase quantization effect.

II. PHASE–ONLY NULLING——THE ELEMENT NULL VECTOR METHOD

Suppose that there is a linear array antenna with N isotropic elements spaced at distance d, let that the array pattern nulls are located at K directions $(\theta_1, \theta_2, \cdots, \theta_K)$ in space, so, the signal received by the n–th element in K direction is

$$x_n = a_n \sum_{k=1}^{K} a_k \exp(j\, b_n u_k + \varphi_k) \tag{1}$$

where

$$u_k = 2\pi d \sin\theta_k / \lambda$$
$$b_n = n - \frac{(N+1)}{2}$$

λ is the wave number, a_k and φ_k are the received signal amplitude and phase respectively, a_n is the n-th element excitation. From equ.(1), we can know that the signal received by each element from K space direction is linear combination of $\{\exp j\ (nu_k)\}$ $(k=1,2,\cdots,K)$. In order to set up nulls in K space direction, it is necessary to make signal received at each element equal to zero in the K direction (as a transmitting array, it is the same). Thus, using the DBF ideas in paper [9], we constitute a set of N dimensional column vectors and assume that the number of N dimensional column vectors constituted is M. We have

$$Span\{X\} = (X_1, X_2, \cdots, X_M) \tag{2}$$

where

$$\left.\begin{aligned} X_m &= (x_{1m}, x_{2m}, \cdots, x_{Nm}) \\ x_{nm} &= a_n \sum_{k=1}^{K} \exp(j\, b_n u_k + \varphi_{km}) \end{aligned}\right\} \tag{3}$$

In equ.(3), φ_{km} $(k=1,2,\cdots,K,\ m=1,2,\cdots,M)$ are random number uniformly in $(0, 2\pi)$ generated by computer and we call it as "Phase Adjustment Factor of Linearly Independent Vector".

To set up the K nulls, suppose that a small phase Ψ_n is created at the n-th element, these Ψ_n's $(n=1,2,\cdots,N)$ form a N dimensional vector

$$\Psi = (\exp j\ \Psi_1, \exp j\ \Psi_2, \cdots, \exp j\ \Psi_N)^T \tag{4}$$

and

$$(\Psi, X_m) = 0 \qquad m = 1,2,\cdots,M \tag{5}$$

i.e,

$$\sum_{n=1}^{N} x_{nm} \exp j\ \Psi_n = 0 \qquad m = 1,2,\cdots,M \tag{6}$$

In equ.(5), (a, b) stand for inner product. To expand the equ.(6), we have

$$\sum_{n=1}^{N} a_n \sum_{k=1}^{K} \exp j\ [b_n u_k + \varphi_{km} + \Psi_n] = 0 \qquad m = 1,2,\cdots,M \tag{7}$$

Now we take out the real component and imaginary ones from equ.(7), we have

$$\left.\begin{aligned}\sum_{n=1}^{N} a_n \sum_{k=1}^{K} cos[b_n u_k + \varphi_{km} + \Psi_n] = 0 \\ \sum_{n=1}^{N} a_n \sum_{k=1}^{K} sin[b_n u_k + \varphi_{km} + \Psi_n] = 0\end{aligned}\right\} \quad m = 1,2,\cdots M \tag{8}$$

We assume that φ_{km} and Ψ_n are anti-symmetric to the centre of the array antenna. Therefore, equ.(8) can be simplified as follows

$$\sum_{n=1}^{N} a_n \sum_{k=1}^{K} cos[b_n u_k + \varphi_{km} + \Psi_n] = 0 \tag{9}$$

Equ.(9) is nonlinear problem, since Ψ_n'S are the small phases, equ.(9) are expanded into Taylor series and the nonlinear equations are converted into the linear ones, and two term are kept. We obtain

$$\sum_{n=1}^{N} a_n \sum_{k=1}^{K} cos[b_n u_k + \varphi_{km}] - \sum_{n=1}^{N} a_n \sum_{k=1}^{K} \Psi_n sin[b_n u_k + \varphi_{km}] = 0 \tag{10}$$

which constitutes a linear problem, it can be solved by using the modified Gram-Schmidt orthogonalization[2]. Because of equ.(5) or (10), Ψ is orthogonal to all X_m's, from equ.(3), it can be seen that X_m is a linear combination of the K element nulls vectors, i.e

$$\left.\begin{aligned}V_1 &= (expj\ b_1 u_1, expj\ b_2 u_1, \cdots, expj\ b_N u_1)^T \\ V_2 &= (expj\ b_1 u_2, expj\ b_2 u_2, \cdots, expj\ b_N u_2)^T \\ &\cdots \\ V_K &= (expj\ b_1 u_K, expj\ b_2 u_K, \cdots, expj\ b_N u_K)^T\end{aligned}\right\} \tag{11}$$

Then we have

$$(\Psi, V_k) = 0 \qquad k = 1,2,\cdots,K \tag{12}$$

It means that if we use the weighting phases Ψ_n the received signal at array antenna are zero in K direction and the object of setting up nulls is achieved. In addition, in equ.(3), by means of the basic criteria of optimal weights[5-8], we select the number M of initial constructional vectors.

III. THE EFFECT OF PHASE QUANTIZATION ON NULL DEPTH

Because the phase-only nulling synthesis is employed, most of the phase shifters are digital. The digital phase shifter consist of P fixed phase shifters whose values are individually equal to $2\pi/2, 2\pi/2^2, \cdots, 2\pi/2^P$, P is called the bit number of the phase shifter. Thus, all the values cannot be exactly phased in the digital phase shifter. Therefore, the phase should be set up in the element must be quantized. In this section, the effect of phase quantization on the null depth is analysied.

In general, the phase quantization function of array antenna can be expressed as

$$\Psi'_n = Int\left(\frac{\Psi_n}{\Delta} + a + b \cdot R\right) \cdot \Delta \tag{13}$$

where, $\Delta = 2\pi/2^P$, Int($\cdot$) stand for integralization, Ψ_n is the accurate phase shift, Ψ_n' is the quantized phase, R is the random number uniformly in region (0, 1), a and b are unknown constant. When $a=0$ and $b=0$, the phase quantization is rounding off. When $a=0.5$ and $b=0$, the phase quantization is rounding to the nearest bits. When $a=1$ and $b=0$, the phase quantization is rounding up. When $a=0$ and $b=1$, the phase quantization is random phase quantization. A vast amount of computation results show that, when $a=0.25$ and $b=0.5$, the effect of phase quantization on null depth is smallest, this method is called as Appropriate Random Technique (ART).

Due to the phase quantization, the array pattern can be written as

$$E(u) = \sum_{n=1}^{N} a_n e^{j\Delta\Psi_n} e^{j(b_n u + \Psi_n)} \tag{14}$$

where, $\Delta\Psi_n$ is phase error due to phase quantization, when $a=0.25$ and $b=0.5$, using the principle of peobability and statistics, the phase error is random number uniformly in region $[-3\pi/2^{P+2}, 3\pi/2^{P+2}]$. So

$$\langle E(u) \rangle = \sum_{n=1}^{N} a_n \langle e^{j\Delta\Psi_n} \rangle e^{j(b_n u + \Psi_n)} \tag{15}$$

it is obvious

$$\langle e^{j\Delta\Psi_n} \rangle = \frac{2^{P+2}}{3\pi} \cdot \sin\left(\frac{3\pi}{2^{P+2}}\right) \tag{16}$$

according to the definition of variance

$$\left.\begin{aligned} D(E(u)) &= \langle E(u)E^*(u)\rangle - \langle E(u)\rangle\langle E^*(u)\rangle = \sum_{n=1}^{N} D(J_n) \\ D(J_n) &= \langle J_n J_n^*\rangle - \langle J_n\rangle\langle J_n^*\rangle \end{aligned}\right\} \tag{17}$$

we have

$$\sigma_E^2 = D(E(u)) = \left[1-\left(\frac{2^{P+2}}{3\pi}\sin\frac{3\pi}{2^{P+2}}\right)^2\right]\sum_{n=1}^{N} a_n^2 \tag{18}$$

therefore, the increase of null depth due to phase quantization is

$$\overline{SLL} = \frac{|\langle E(u_k)\rangle| + \sigma_E}{\sum_{n=1}^{N}\langle J_n\rangle} = \sqrt{\frac{1}{N\eta}}\cdot\sqrt{\frac{9\pi^2}{2^{2P+4}\sin^2\left(\frac{3\pi}{2^{P+2}}\right)}-1} \tag{19}$$

where $\eta = \left(\sum_{n=1}^{N} a_n\right)^2 / N\left(\sum_{n=1}^{N} a_n^2\right)$ is array aperture efficiency

When the bit number of phase shifter is larger, equ.(19) can be simplified as follows

$$\overline{SLL}(dB) = 2.673 - 10\log(N\eta) - 6P \tag{20}$$

IV. SIMULATED COMPUTATION

In the following, some typical examples are given. In Fig.1, the total number N of linear array elements is 20, (a) shows the quiescent pattern, its distribution is −30 (dB) Taylor ones, $\eta = 0.8488$, (b) is the pattern with 3 nulls which are located at $\theta = 33.37^\circ$, 34.03° and -44.43°, (c) is the pattern with 4 close nulls which are located from -33.36° to -37.58°. It is obvious that null depth to suppress interferences is about −80 (dB). The effect of phase quantization on null depth are shown in Fig.2, (a) (b) (c) which are the patterns of Fig.1 (c) with 6, 8 and 10 bit phase quantization respectively. Because $N = 20$ and $\eta = 0.8488$, equ.(20) can be expressed as

$$\overline{SLL}(dB) = -9.625 - 6P \tag{21}$$

When the $P = 6$, 8 and 10, the $\overline{SLL}$ are −45.625 dB, −57.625 dB and −69.625 dB. From Fig.2, it can be seen that the theoretical prediction are in good agreement with simulated computation results.

V. CONCLUSION

It can be seen from the above discussion that it is possible to creat nulls in the given directions to suppress jammers through controlling the phase at each array elements.

The algorithm presented in this paper has an advantage that the real arithmetic operations are only used in computation. So this algorithm converges fast. In addition, the resulted phases can be added to the phases of the beam steering, and the production cost can be reduced. The simulated values differ from the prediction by no more than a few percents in analysis of the effect of phase quantization on null depth.

REFERENCES

1 Hung. E.K.L., et al. A fast beamforming for large array. IEEE Trans., 1984, AES-19(4): 598~607

2 Li Jianxin and Guo Yanchang. Real amplitude-only nulling algorithm (RAMONA) for pattern synthesis. Proc. of Asia-Pacific Microwave Conf., Japan, 1990: 81~84

3 Gao Tie, et al. A amplitude-only synthesis of nulling pattern for arbitrary convex surface array. Inter. Conf. of Microwave and Communication, Nanjing, 1992: 344~439.

4 Gao Tie, et al. A novel algorithm for digital beamforming in conformal array. 5-th Asia-Pacific Microwave Conf. Proc., Australia, 1992

5 Gao Tie, et al. A fast beamforming algorithm for adaptive sum and difference pattern in conformal antennas. 1992 IEEE AP-S Inter. Symp. Digest, Chicago, USA, 1992: 450~453

6 Gao Tie, et al. Pattern nulling synthesis based on adaptive array theory. The 1993 IEEE Region 10 Inter. Conf. on "Computer, Communication and Automation", Beijing, 1993: 1142~1145

7 Gao Tie, et al. Wide null and low sidelobe pattern synthesis for phased array antennas 1993 Asia-Pacific Microwave Conf., Taiwan, 1993: Session Arrays.

[8] Gao Tie and Guo Yanchang, "Real amplitude-only weight algorithm for adaptive digital beamforming in conformal array", 《Modern Radar》, Vol.13, No.6, pp.43~52.

9 Guo Yanchang and Li Jianxin. Real phase-only nulling algorithm (REPONA) for adaptive beamforming. 1990 ICSP, Beijing, 1990: 661~662

10 Guo Yanchang, et al. Real phase-only nulling algorithm (REPONA) for pattern synthesis, 1990 IEEE AP-S Inter. Symp. Digest, USA, 1990: Session ARRAYS

11 Guo Yanchang, et al. Real phase-only nulling algorithm (REPONA) for adaptive sum and difference patterns. 1991 IEEE AP-S Inter. Symp. Digest, Canada, 1991: 94~97

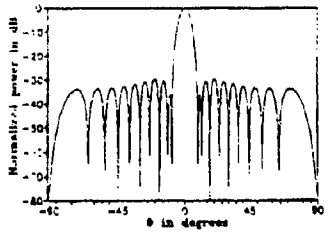

(a)

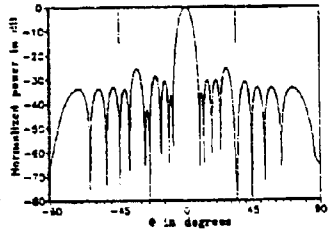

(b)

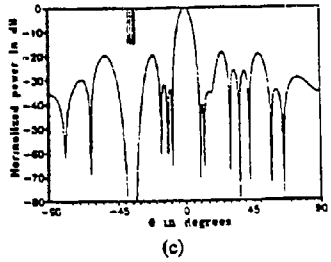

(c)

Fig.1 Pattern for 20 array element with phase-only weight. (a) quiescent pattern, (b) (c) pattern with nulls.

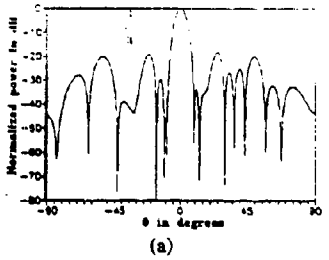

(a)

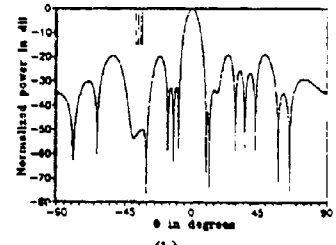

(b)

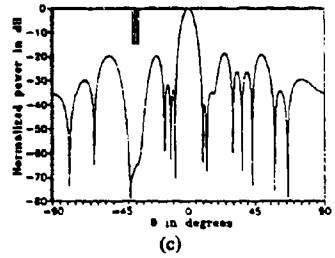

(c)

Fig.2 The effect of phase quantization on field pattern of Fig.1 (c), here, the bit number of phase shifter are 6, 8 and 10 respectively.

FULL WAVE ANALYSIS OF INFINITE PHASED ARRAY

OF ARBITRARY SHAPE PRINTED LINE MICROSTRIP ANTENNAS

Prof. Elhilaly M. Eid , Ahmed M. Attiya , Essam Eldiwany
Fatma Elhefnawi

ELECTRONICS RESEARCH INSTITUTE
ELTAHREER ST. \ DOKKI \ CAIRO \ EGYPT

ABSTRACT

This paper presents full wave analysis of infinite array of arbitrary shape microstrip line antenna based on moment method. The active element parameters are found using the current distribution on the radiating element. Comparison is made between the parameters for different infinite arrays when the array element is a linear microstrip dipole and when it is of arbitrary shape line such as circular loop, zigzag, spiral, and meander for the same substrate parameters.

I INTRODUCTION

Microstrip antenna structures are suitable as radiating elements for phased array due to their light weight, compact structure and low cost, compared with other types of radiating elements. Another important feature of microstrip antenna structures is the ability of integrating different devices such as phase shifters and amplifiers on the antenna substrate.

Some forms of microstrip antenna structures; such as rectangular patch, circular patch and linear dipole; were studied as a single element and as an array structure. H.Nankano et al [1,2] and H.A.Ragheb et al [3] studied arbitrary shaped printed line microstrip single element antennas. They show the properties of single radiating element for several configurations such as circular loop, meander , zigzag, and spiral. D.M.Pozar et al studied the array structure of linear microstrip dipole [4,5] and the array structure of rectangular patch [6]. The studies in [4] and [5] are concerned with finite and infinite array structures of a linear dipole respectively. Comparing the results of [4] and [5] it can be concluded that for almost all practical finite microstrip array structures the properties of the infinite array structure can represent to a good degree of approximation those of each of most of the finite array elements except those elements near the edge of the finite array. On the other hand, solving for an infinite array requires solving for only one element in a periodic structure which takes implicitly the coupling among the elements, while solving for the finite array requires solving for all the elements in addition to solving for the coupling among them. This means the increase of the order of the moment method matrix by a factor equals the number of the array elements. The situation becomes worse when solving radiating elements structures that need large number of basis functions to describe their current distributions such as the case of arbitrary shape radiating elements.

This paper presents the moment method solution of an infinite array composed of arbitrary shape printed radiating elements. The solution is based on the technique of Poisson's sum formula [5]. It is assumed that the radiating element is excited by a delta function generator placed at arbitrary point along its length. The current distribution on the radiating element is found by solving the moment method matrix. Then one can determine the active input impedance and the active radiation pattern , which represent the radiating element parameters in the presence of the array structure. The variation of the

input impedance with scanning angle is studied also. Results are presented for some special cases where the array element is a circular loop, a zigzag, a spiral, or a meander.

II THEORY & ANALYSIS

Fig.(1) shows the geometry of the infinite planar array of identical arbitrary shape microstrip antenna elements. The radiating elements are assumed to lie in a rectangular grid with spacing a&b in x&y directions, respectively.

For scanning angle (θ,ϕ); as shown in fig.(1); the current on the mn^{th} radiating element is phased as :

$$e^{jko(mau+nbv)} \qquad (1)$$

where ko is the free space wave number ($ko=2.*\pi/\lambda o$ λo is the free space wave length) and u&v are defined as:

$$u=\sin(\theta)\cos(\phi) \qquad (2\text{-a})$$

$$v=\sin(\theta)\sin(\phi) \qquad (2\text{-b})$$

The electric field at any observation point (x,y) on the surface of the substrate is given by :

$$E_{(x,y)}=\sum_{m=-\infty}^{m=+\infty}\sum_{n=-\infty}^{n=+\infty} \int_1 \overline{G}^{mn} \cdot J_{(xo,yo)}\, e^{jko(mau+nbv)} \qquad (3)$$

where $\overline{G}^{mn}$ is the dyadic Green's function for the mn^{th} element. Applying the boundary condition that the total tangential electric field is zero along any radiating element except at the feeding point, the above electric field integral equation is solved for the unknown current distribution $J_{(xo,yo)}$ where (xo,yo) represents the location of the excitation point .

For such planar structure the solution requires only four elements of the dyadic Green's function G_{pq}^{mn}, which represent the electric field in each of the (p = x or y) direction due to elements in each of the (q=x or y) direction. The elements of the dyadic Green's functions are given in reference [6] .

The Green's function for the field at (x,y) on the substrate due to an infinite array of infinitesimal dipole on the substrate phased at (θ,ϕ) is given by :

$$G_{pq}=\frac{-jZo}{koab}\sum_{m=-\infty}^{m=+\infty}\sum_{n=-\infty}^{n=+\infty} e^{jko(mau+nbv)} \int_{-\infty}^{+\infty}\int Q_{pq}(kx,ky)\, e^{jkx(x-xo-ma)}\, e^{jky(y-yo-nb)}\, dkx\, dky \qquad (4)$$

where Qpq(kx,ky) is the dyadic Green's function for single element in spectral domain representation [6]. Using Poisson's sum formula [5] equation (4) can be rewritten as follows :

$$pq=\frac{-jZo}{koab}\sum_{m=-\infty}^{m=+\infty}\sum_{n=-\infty}^{n=+\infty} Q_{pq}(kx,ky)\, e^{jkx(x-xo)}\, e^{jky(y-yo)} \qquad (5)$$

where kx and ky in equation (5) are given by :

$$kx=\frac{2\pi\, m}{a}+kou \quad , \quad ky=\frac{2\pi\, n}{b}+kov \qquad (6)$$

The moment method can now be applied to a single radiating element structure in a single unit cell, and then by periodicity the effects of all the radiating elements in the infinite array are taken into account [5].The length of the radiating element is divided into small equal linear segments as shown in fig.(2).The position of each segment is defined by its x&y coordinates and its angle α with respect to the x axis. The tangential

electric current on the antenna is expanded into a set of overlapping piecewise sinusoidal expansion functions in the form :

$$J(l,W)=\sum_{I} Ii\ Ji(l)\ f(W) \qquad (7\text{-}a)$$

Ii is the unknown amplitude of the basis function and Ji(l) is given by

$$Ji(l) = \frac{\sin ke(s-|l-li|)}{\sin kes} \quad \text{for } |l-li| \le s \qquad (7\text{-}b)$$

where s is the length of each segment and ke is the wave number of the expansion function which is taken here to be $ko\sqrt{(\varepsilon r+1)/2}$. The feeding point should lie at the center of one of the expansion functions. The dependence of the current on the radiating element across its width satisfies the edge behavior which is given by :

$$f(W)= \frac{1}{\sqrt{\left(\frac{Wo}{2}\right)^2 - (2W)^2}} \quad \text{for } -Wo/2 \le W \le Wo/2 \qquad (8)$$

where Wo is the width of the radiating element and W is the location across the width of the radiating element w.r.t. its center. The testing functions are taken to be the same as the expansion functions in both directions; the length and the width of the antenna element. The advantage of this choice is to make use of every symmetry to reduce the computational time as much as possible. The feeding is taken to be a Dirac delta function.

By integration w.r.t. l over the "e" source segment and integration w.r.t. l' over the "f" observation segment, it can be shown that the general term Zef of the moment method impedance matrix is given by the following equations :

$$Z_{ef}= \frac{jZo}{kosb} \sum_{i=0}^{i=i} \sum_{j=0}^{j=l} U_{e+i,f+j} \qquad (9)$$

$$U_{e+i,f+j}= \sum_{m=-\infty}^{m=+\infty} \sum_{n=-\infty}^{n=+\infty} C_{e+i,f+j}\ A_{fj}\ A^{*}_{ei}\ I_f\ I^{*}_e\ \frac{1}{\sin^2 koa}$$
$$e^{jkx(xe+i\ -\ xf+j)}\ e^{jky(ye+i-yf+j)} \qquad (10)$$

$$C_{r,s}= \cos\alpha r\ \cos\alpha s\ Qxx(kx,ky) + \sin(\alpha r+\alpha s)\ Qxy(kx,ky)$$
$$+\sin\alpha r\ \sin\alpha s\ Qyy(kx,ky) \qquad (11)$$

$$A_{r0}= \frac{e^{-j(kx\ \cos\alpha r+ky\ \sin\alpha r)a}}{ke^2 -(kx\ \cos\alpha r+ky\ \sin\alpha r)^2} (-j(kx\ \cos\alpha r+ky\ \sin\alpha r)-ke\ \cos ke a +$$
$$e^{j(kx\ \cos\alpha r+ky\ \sin\alpha r)a}\ ke\ ) \qquad (12)$$

$$A_{r1}= \frac{1}{ke^2 -(kx\ \cos\alpha r+ky\ \sin\alpha r)^2} (j(kx\ \cos\alpha r+ky\ \sin\alpha r)\sin ke a-ke\ \cos ke a+$$
$$e^{-j(kx\ \cos\alpha r+ky\ \sin\alpha r)a}\ ke\ ) \qquad (13)$$

$$I_r=J_o([kx\ \sin\alpha r-ky\ \cos\alpha r]Wo/2) \qquad (14)$$

where kx & ky are given by equation (6). The elements for the excitation vector [V] are zero ;since the electric field on the surface of strip antenna is zero; except at the feeding point where it equals unity.

Now solving the matrix equation :

$$[Z][I]=[V] \qquad (15)$$

the current distribution and consequently the input impedance can be calculated .

Studying equations (6,9-14) it can be concluded that the moment method matrix is not symmetric except at the broadside direction (scanning angle $\theta=0.$ and $\phi=0.$). However, $C_{r,s}$ equals $C_{s,r}$ for all scanning angles so that

equation (10) can be used effectively for calculating Zef and Zfe by changing the conjugate operation during summation process. Toeplitz property which holds for moment method matrix of linear dipole[5] is not valid for the case of arbitrary shape printed antenna. For the broadside direction, similar pairs of elements which have the same spacing between each other and the same orientation with respect to each other; as shown in fig(3); have equal impedance element. For any direction other than the broadside, *all the moment method matrix should be calculated.*

Variation of the impedance and consequently the reflection coefficient of the radiating element with scanning angle is studied. The worst case for the phased array occurs when the reflection coefficient approaches unity. This represents what is called scan blindness. In an infinite phased array scan blindness is due to excitation of surface wave along the array structure. Microstrip structure supports at least one surface wave because the dominant mode TMo has zero cutoff frequency. Scan blindness is therefore an expected behavior for an infinite phased array of microstrip radiating elements. At scan blindness the radiating elements are highly reactive with zero resistive impedance part since all the incident power is captured as surface wave and no radiation exists. It can be explained mathematically due to the roots of the Te and Tm functions which appear in the denominator of the Green's function [equations (5-7)]. If one of the terms of the series in equation (20) has kx,ky satisfying the root of Te or Tm ,it causes an infinite increase in the imaginary part of the impedance elements which causes the highly reactive behavior of the radiating element. An exception exists when there is a zero in the numerator of this term that can cancel this root. Physically, the cancellation means that the polarization of the array is such that it is orthogonal to the excited surface wave [5].

The active radiation pattern of a single radiating element in an infinite array structure is actually the radiation pattern of a single element with the current distribution derived from an infinite array analysis.The total antenna radiation pattern for practical cases is given by multiplication of active radiation pattern of the radiating elements by the array factor for the actual array size. The method used for calculating the active radiation pattern for unit cell is the same as that described in [1-3].

III RESULTS AND DISCUSSION

The above theory is implemented in a computer code for calculating the active input impedance and the active current distribution of several shapes of radiating elements. The active current distribution is used by another computer code for calculating and plotting the active radiation pattern. Results for different configurations are presented throughout this section. For the sake of simplicity of comparison the substrate parameters , the lattice dimensions and the width of the radiating elements are kept constant for all cases studied. Hence for all the cases, the dielectric constant εr=2.55, the dielectric thickness d=.14λo, the lattice dimensions a=b=.5λo and the width of the radiating elements Wo=.002λo. For these substrate parameters there is only one surface wave pole corresponding to the TMo mode. For the above lattice dimensions and substrate dimensions ,this surface wave pole is excited for θ scan angle equals 56.203 at the two principal planes (ϕ = 0"xz plane" and ϕ=90 "yz plane").

The cases studied here are :

1- linear dipole of length .35λo , (fig. 4-a).
2- Circular loop of radius .135λo , (fig. 5-a).
3- Zigzag of total length 1.29λo and 3 zigzag sections. The angle between any two adjacent elements of the studied zigzag is 45° , (fig6-a).
4- Rampart(two sections meander)of total length 1.0λo and 5 equal sections,

(fig. 7-a).

5- Spiral of total length 1 91λo The straight part at its center is 04064λo The spiral function is ρ=A φs ,where A is the spiral constant and φs is the spiral winding angle. A = 0077616 λo/rad , (fig 8-a)

Variation of the active impedance of the array element with scan angles is presented as the reflection coefficient w.r.t the broadside impedance So that

$$R(\theta,\phi)=\frac{Z(\theta,\phi)-Z(0,0)}{Z(\theta,\phi)+Z^{*}(0,0)} \qquad (16)$$

where $R(\theta,\phi)$ & $Z(\theta,\phi)$ are the reflection coefficient and the input impedance respectively for scanning angle (θ,ϕ) .

The five figures 4b-8b present the reflection coefficient versus scan angle for the two principal planes for the above five cases. By comparison it can be seen that the reflection coefficients for the circular loop, the rampart and the spiral do not reach unity in the two principal planes at the angle corresponding to excitation of surface wave and at which scan blindness is supposed to take place. But for the linear dipole and the zigzag the reflection coefficient reaches unity at scan blindness for the plane $\phi=90$.

The explanation for this behavior of the reflection coefficient is that the current distribution along the radiating element tends to rotate along the element in the direction orthogonal to the surface wave polarization if the positions of the segments of the radiating elements allow this rotation. This property is obvious by studying the current distribution and the active radiation pattern presented here for the case of the spiral at the broad side direction and at the angle corresponding to the excitation of surface wave (figs 8-c:f). Due to this property ,the real part of the current at the feeding point does not reach zero and consequently the real part of the impedance does not reach zero either For the zigzag and the linear dipole, the property of rotation of the current dose not exist because all the segments of the radiating elements are not orthogonal to the surface wave polarization at the yz-plane

By studying Figures (7-b & 8-b) other peaks in the reflection coefficients are shown not to concide with the angle corresponding to the excitation of the surface wave and these peaks are lower than the peaks corresponding to the surface wave in the other scanning plane. These peaks are due to a leaky wave excited along the array structure [7]. The difference between the peak reflection due to leaky wave and the peak reflection due to surface wave is that for the former the real part of the active impedance increases rapidly w.r.t the broadside one while for the later the imaginary part increases rapidly w.r.t the broadside one. Figs (8 g-h) show the current distribution and the active radiation pattern for the spiral at the angle corresponding to the leaky wave.

IV CONCLUSION

Full wave analysis of infinite phased array of arbitrary shape printed antenna is presented based on solving the integral equation for the current distribution using moment method. Results are obtained for special cases where the radiating element is a circular a loop,rampart (two sections meander), a zigzag or a spiral Comparison is made between the results obtained for these configurations and the linear dipole with the same substrate parameters and the same lattice dimensions. It is found that the infinite array of arbitrary shape configuration tends to rotate the real part of the current distribution along its length to be orthogonal to the surface wave polarization if the rotation is possible for the element configuration. This results in reducing the reflection coefficient less than unity at the scanning angles corresponding to the excitation of the surface wave.

REFERENCES:
[1] HISAKATSU NAKANO et Al, "The Moment Method Solution for Printed Wire Antennas of Arbitrary Configuration,"IEEE Trans.Antennas Propagat.,vol. AP-36, pp.1667-1673, Dec. 1988.
[2] HISAKATSU NAKANO et Al. "Numerical Analyses of Printed Line Antennas,"IEE Proc.,Vol.136 , Pt. H, pp.98-104, Apr. 1989.
[3] HASSAN A.RAGHEB and LOTFOLLAH SHAFAI "Analysis of Arbitrary shape Printed Line Microstrip Antennas ,"IEEE Trans. Antennas Propagat., Vol. AP-36, pp. 269-274, Feb. 1990.
[4] D.M.POZAR ,"Analysis of Finite Phased Arrays of Printed Dipoles ," IEEE Trans. Antennas Propagat. Vol. AP-33 , pp 1045-1053, Oct. 1985.
[5] D.M.POZAR and D.H.SCHAUBERT ,"Scan Blindness in Infinite Phased Arrays of Printed Dipoles ,"IEEE Trans. Antennas Propagat., Vol. AP-32 , pp 602-610. June 1984.
[6] D.M.POZAR and D.H.SHAUBERT ,"Analysis of an Infinite Array of Rectangular Microstrip Patches with Idealized Probe Feeds ," IEEE Trans. Antennas Propagat. Vol. AP-32 , pp 1101-1107 ,Oct 1984.
[7] C.Liu ,A.Hessel and J.Shmoys ,"Performance of prop-fed microstrip-patch element phased arrays ," IEEE Trans. Antennas Propagat., Vol. AP-36 ,pp 1501-1507 , Nov. 1988.

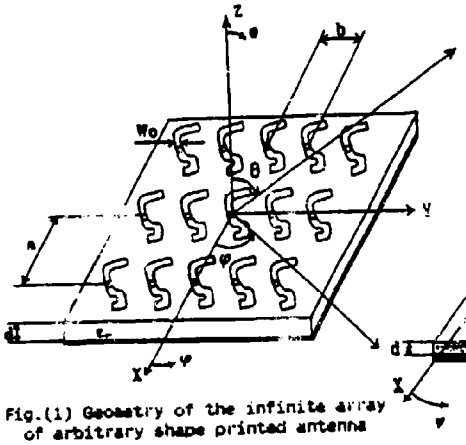

Fig.(1) Geometry of the infinite array of arbitrary shape printed antenna

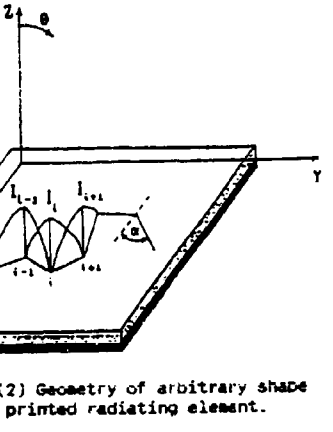

Fig.(2) Geometry of arbitrary shape printed radiating element.

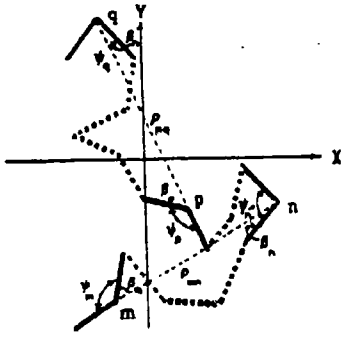

Fig.(3) Orientation of similar pairs of segments

For Broadside scanning angle if $\rho_{mn}=\rho_{pq}$, $\psi_m=\psi_p$, $\psi_n=\psi_q$, $\psi_m=\psi_p$ and $\beta_n=\beta_q$ then $Z_{mn}=Z_{pq}$.

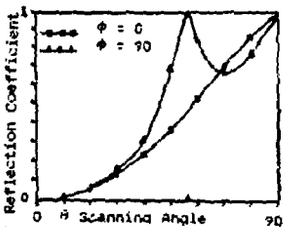

Fig(4-b) Reflection Coefficient V.S. Scan Angles

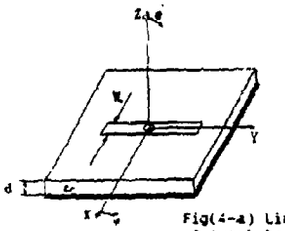

Fig(4-a) Linear dipole of total length .35λ₀

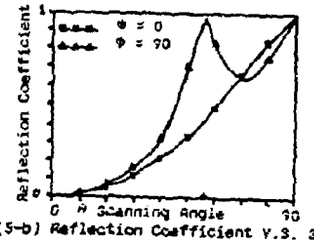

Fig(5-b) Reflection Coefficient V.S. Scan Angles

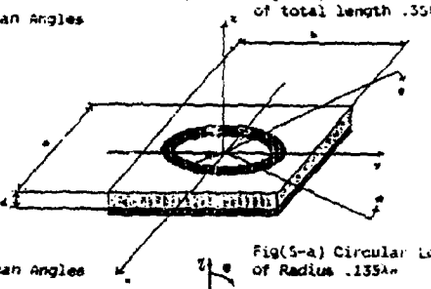

Fig(5-a) Circular Loop of Radius .135λ₀

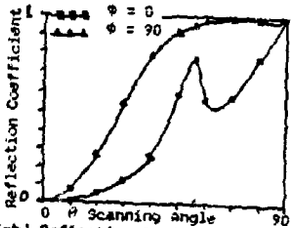

Fig(6-b) Reflection Coefficient V.S. Scan Angles

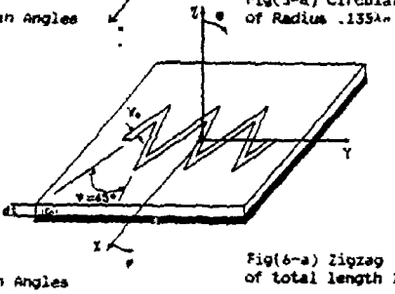

Fig(6-a) Zigzag of total length 1.29λ₀

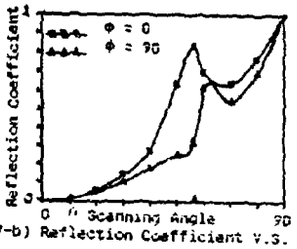

Fig(7-b) Reflection Coefficient V.S. Scan Angles

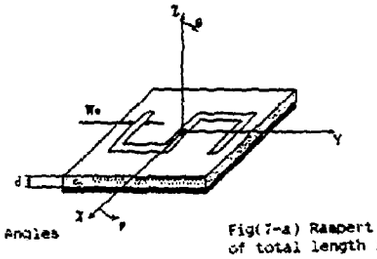

Fig(7-a) Rampert of total length 1.0λ₀

For all the above configurations a=b=.5λ₀ ,d=.14λ₀, W₀=.002λ₀ & εr=2.55

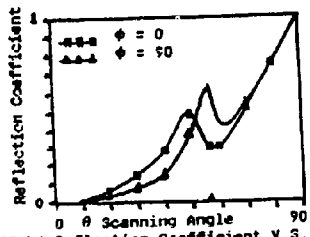

Fig(8-b) Reflection Coefficient V.S. Scan Angles

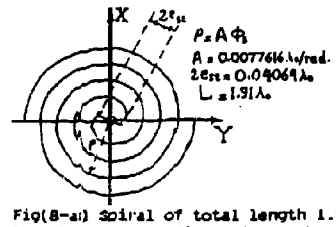

Fig(8-a) Spiral of total length 1.91λ₀ For the above configurations a=b=.5λ₀, d=.14λ₀, W₀=.002λ₀ & εr=2.55

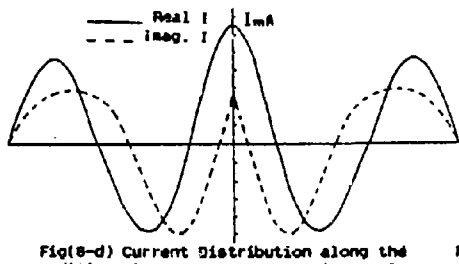

Fig(8-d) Current Distribution along the raditing element for the scanning angle (θ=0 , φ=0)

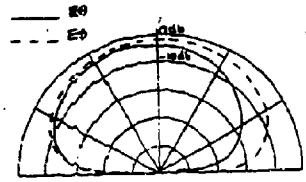

Fig(8-c) Active Radiation Pattern in the yz plane for a single radiating element. The scanning angle is (θ=0 , φ=0)

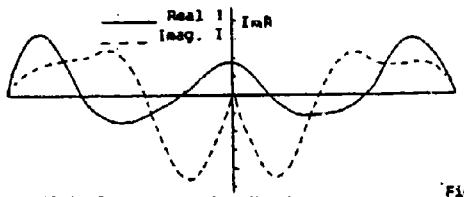

Fig(8-f) Current Distribution along the raditing element for the scanning angle (θ=56.2 , φ=90)

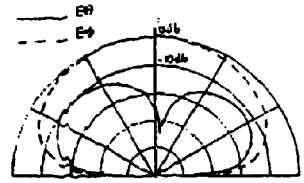

Fig(8-e) Active Radiation Pattern in the yz plane for a single radiating element. The scanning angle is (θ=56.2 , φ=90) which is corresponding to S.W. excitation.

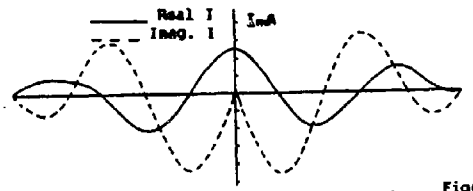

Fig(8-h) Current Distribution along the raditing element for the scanning angle (θ=50 , φ=0)

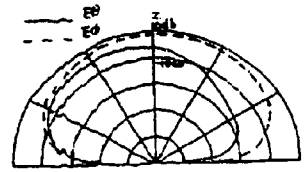

Fig(8-g) Active Radiation Pattern in the yz plane for a single radiating element. The scanning angle is (θ=50 , φ=0) which is corresponding to L.W. excitation.

EFFICIENT MUTUAL COUPLING COMPUTATION FOR SYMMETRICAL ARRAYS

S CHRISTOPHER DHANYASHREE VVS PRAKASH

ELECTRONICS AND RADAR DEVELOPMENT ESTABLISHMENT
BANGALORE-93, INDIA

ABSTRACT:

A method has been presented in this paper to reduce the computational time involved in the evaluation of external mutual coupling. Symmetry property of the arrays has been used to bring down the time. As there is no approximation used, the present method does not effect the accuracy. Certain cases of linear and planar arrays have been considered here and the theoritical and practical results are presented. The analysis presented in this paper has significant application in the design of large planar arrays.

INTRODUCTION:

The slotted arrays find extensive applications in rader and satellite communications due to their high efficiency and elegent feeding network. The present day designs include slot-to-slot external mutual coupling. In a synthesis procedure such as Elliot's, evaluation of external mutual coupling between slots account for most of the computationl effort [1]. Therefore fast and accurate computation of mutual computation has been a topic of discussion in the prior literature. Dipole analogy has been employed by Hansen and Brunner[2]. The mutual coupling between i^{th} and j^{th} slot is a four fold integral. Mazzarella and Panariello have evaluated this integral by a Taylor series expression around half wavelength long slots[3].

Most of the practical antennas that we encounter are symmetric with respect to their axes. Linear arrays are symmetric about their center and the planar arrays have quadrant symmetry. This method exploits the symmetry property of the practical antennas and thus reduces the computer time. This algorithm provides 50% to 75% computation reduction time, with no loss of accuracy. Since this exploits the symmetric property of the array, earlier time reduction techniques can also be used[4]. This paper explains the algorithm and compares the time considerations.

THEORY:

In the design of slot arrays, the length and the offset of each of the slots have to be computed by an iterative procedure. It involves the computation of external mutual coupling matrix a number of times. Thus, any percentage reduction of time in this computation reflects in the over-all computational time in a big way. In the algorithm presented below, the only assumption made that the array is having quadrant symmetry or one plane symmetry.

It is obvious that in the computation of external mutual coupling matrix, we have,

$$Y_{ij} = Y_{ji} \qquad \ldots\ldots(1)$$

where Y_{ij} is the coupling from i^{th} element to j^{th} element.

This equation gives 50% reduction. Apart from the above mentioned property, the symmetry of the array can be exploited to give more than 50% reduction.

CASE-1:LINEAR ARRAY:

Let the number of elements be 2N in the case of even n.o elementsand (2N+1) in case of odd number of elements. The complete external mutual coupling matrix is:

$$Y^{ext} = \begin{bmatrix} Y_{11} Y_{12} Y_{13} \cdots\cdots Y_{1M} \\ Y_{21} Y_{22} Y_{23} \cdots\cdots Y_{2M} \\ \cdots\cdots\cdots\cdots \\ Y_{M1} Y_{M2} Y_{M3} \cdots\cdots Y_{MM} \end{bmatrix} \qquad \ldots\ldots(2)$$

where M is 2N in even case and (2N+1) in odd case.

EVEN CASE:

We can use $Y_{ij} = Y_{ji}$ for $i > j$, i.e. upper triangular matrix.

For $i > N$, we can use $Y_{ij} = Y_{pq}$ where

$$p = 2N + 1 - i \quad \text{and} \quad q = 2N + 1 - j \qquad \ldots\ldots(3)$$

Out of 2N rows,We have to compute only a portion of the first N rows of external coupling matrix and the rest of the N rows are filled up using (3).

ODD CASE:

We can use $Y_{ij} = Y_{ji}$ for $i > j$.

For $i = (N+1)$ and $j > (N+2)$ and for $i > (N+1)$ and $1 \leq j \leq (2N+1)$

We use, $Y_{ij} = Y_{pq}$ where $p = 2N + 2 - i$ and $q = 2N + 2 - j$.

....(4)

CASE-2: PLANAR ARRAY:

EVEN CASE:

Let the number of elements be N^2. The complete coupling matrix will be of (N^2, N^2) size. We have,

$$Y_{ij} = Y_{pq}$$

For $1 \leq j \leq N^2$,

if $(N.K + N/2) < i \leq N(K+1)$; for $K = 0,1,2,\ldots,(N-1)$

then $p = (N.K+1) + (N.K + N) - j$

$q = (N+1) + 2(L - 1)N - j$

for $(L.N+1-N) \leq j \leq L.N$ for $L = 1,2,3,\ldots,N$

else

if $(N^2/2 + K.N) < i \leq (N^2/2+N(K+1))$ for $K = 0,1,2,\ldots,(N/2-1)$

then $p = i - 2.K.N - N$

$q = j - 2.N.L + N(N+1)$. .....(5)

Those elements not covered by (5) are to be computed. The numbering of the elements is done from left to right and top to bottom as shown in Fig.1c. For a typical case of 16 element planar array, the elements for which mutual coupling integral has to be evaluated is shown in Fig.1c. Even for these elements, only a portion of the row elements have to be computed.The equations for Odd number of elements and one plane symmetry are not presented here as they are simple extension of the above mentioned cases. Even though the equations appear to be complex, they are quite easy to program.

RESULTS:

For a Linear slot array of N elements, the Time Reduction Code (TRC) is implemented by using an array Ichek(N,N) of integer type. If Ichek(i,j) = 1 then that particular element of coupling matrix has to be computed and if Ichek(i,j) = 0, it need not be computed The percentage saving in computatic ' time for even number of elements, computed using Eq.(3) is ' wn in Fig.2. A comparision is made between theoritical data ' the practical data which considers the time taken to run the time reduction code. In Fig.3, for the case of odd number f elements,the time reduction (%) is presented as a function of number of elements of the linear array. To compute the mutual coupling between elements, the equations derived in [4] have been used. In the case of Planar array, the time reduction is presented in Fig.4. The Quadrant symmetry as well as Half-plane symmetry have been shown. For a trivial case of 4 element planar array, quadrant symmetry and Half-plane symmetry are one and same. The practical results taken into consideration the finite run time of TRC are presented. Even though, the run time of TRC is significant, the over-all time reduction is considerable as can be visualized. All the programs are written in Fortran and run on 386 machine.

CONCLUSION:

A method has been presented to design slot arrays with rapid computation of mutual coupling in the linear and planar cases. As there are no assumptions made on the element properties itself, there is no loss of accuracy. It is found that the computational time is dependent on how efficiently the equations are programed. The difference between the theoritical computational time and the time taken practically is attributed to the run time of the equations given in this paper.

REFERENCES:

[1] R.S.Elliot,"An Improved Design Procedure for small Arrays of Shunt Slots," IEEE Trans.Antenna Propagat., vol.31,Jan.1983, pp.48-53.

[2] R.C.Hansen and G.Brunner,'Dipole Mutual Impedance for Design of Slot Arrays', Microwave Journal,vol.22, Dec.1979, pp.54-58.

[3] Mazzarella and G.Panariello,"Fast computation of Mutual coupling in Slot Arrays,"Microwave Journal,vol.31,June 1988, pp.192-196.

[4] S.R.Rengarajan and E.Gabrelian,:Efficient and Accurate Evaluation of External Mutual Coupling Between Compound Broad Wall Slots," IEEE Tran. Antenna Propagat.,vol. 40,June 1992, pp.733-737.

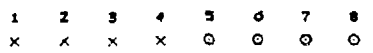

Fig.(1a) Symmetric Linear Array with Even Number of Elements.

$$\begin{bmatrix} 0 & 1,2 & 1,3 & 1,4 \\ 0 & 0 & 2,3 & 2,4 \\ 0 & 0 & 0 & 3,4 \\ 0 & 0 & 0 & 0 \end{bmatrix} \qquad \begin{bmatrix} 0 & 1,2 & 1,3 & 1,4 \\ 0 & 0 & 2,3 & 0 \\ 0 & 0 & 0 & 0 \\ 0 & 0 & 0 & 0 \end{bmatrix}$$

Using $Y_{ij} = Y_{ji}$ only. Using present method.

Fig.(1b) Comparision between Coupling Matrices using present method and Upper Triangular matrix for 4 element Linear Array.

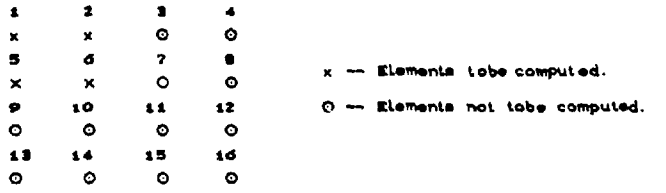

Fig.(1c) Quadrant Symmetric Planar Array with 16 Elements.

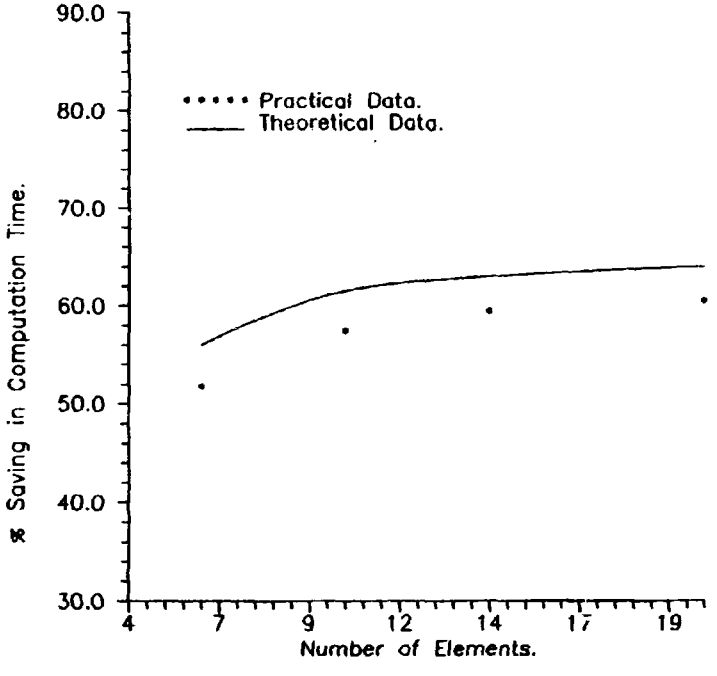

Fig.2 Computational Saving For Linear Array with Even Number of Elements.

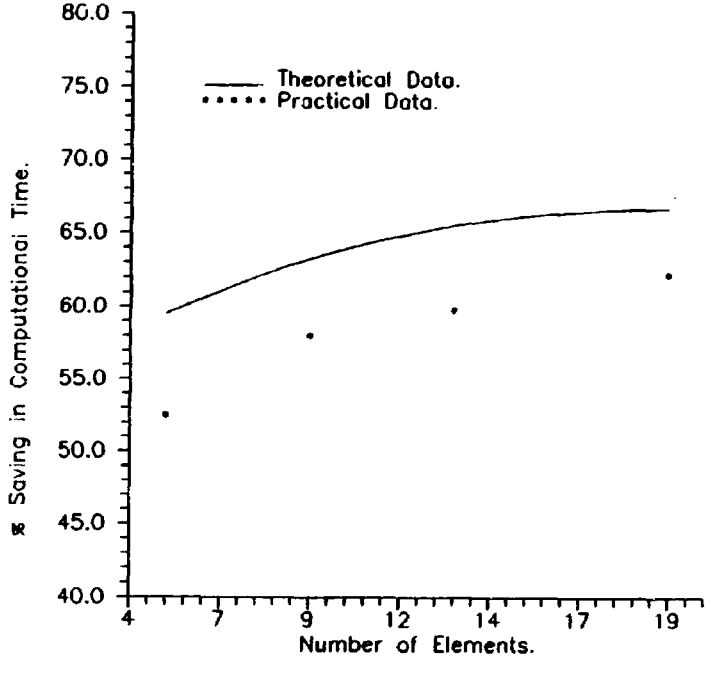

Fig.3 Computational Saving for Linear Array of Odd Number of Elements.

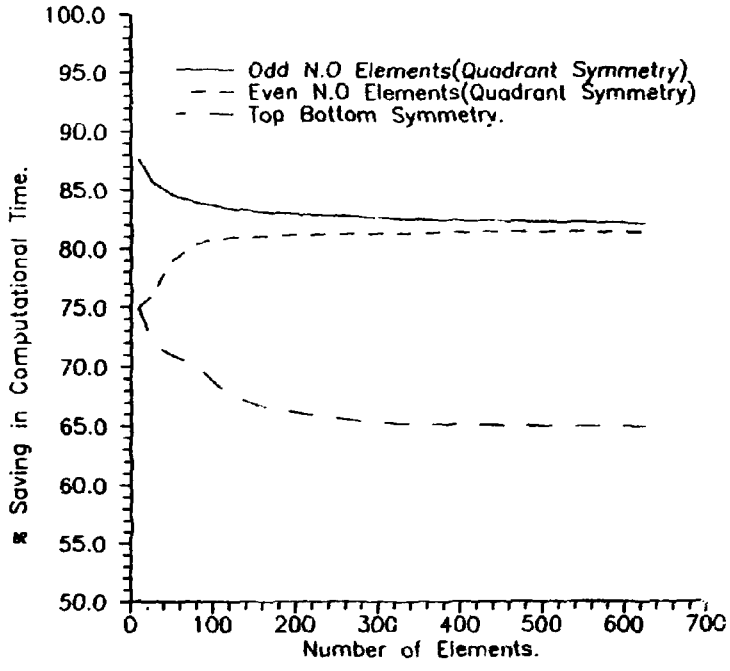

Fig.4 Planar Array of N * N Elements With Quadrant and Half Plane symmetry.

AUTHOR INDEX

VI = Volume I
VII = Volume II